UNIVERSITIES OF GLASGOW AND STRATHCLYDE
DEPARTMENT OF NAVAL ARCHITECTURE AND MARINE ENGINEERING

HULL GIRDER ULTIMATE STRENGTH AND FRACTURE TOUGHNESS OF DAMAGED MARINE STRUCTURES

By
Özgür Özgüç

A THESIS SUBMITTED IN PARTIAL FULFILMENT OF THE REQUIREMENTS FOR THE DEGREE OF DOCTOR OF PHILOSOPHY

GLASGOW, UNITED KINGDOM
MARCH 2006

CONTENTS

Contents.....i

Abstract.....vi

List of Tables.....viii

List of Figures.....xii

Symbols.....xx

Acknowledgements.....xxv

1. Introduction.....1

1.1. Background.....1

1.2. Motivation.....8

1.3. Objectives and Scope of Work.....9

1.4. Organization of the Thesis.....11

2. Buckling and Ultimate Strength Behaviour of Stiffened Plates.....14

2.1. Introduction.....14

2.2. Imperfections of Stiffened Plates.....26

2.2.1. Initial deflections.....26

2.2.2. Welding-induced residual stress.....32

2.3. Finite Element Model for Inelastic Buckling Analyses.....35

2.4. Applied Boundary Conditions.....40

2.4.1. Boundary conditions for simply supported under longitudinal compression (For 1+1/2 bay model).....41

2.4.2. Boundary conditions for clamped under longitudinal compression (For 1+1/2 bay model).....41

2.4.3. Boundary conditions for simply supported under transverse compression and lateral pressure loads (For 1/2 + 1 + 1 +1/2 bay model).....42

2.5. Collapse Strength of Stiffened Plates.....42

2.5.1. Elastic-plastic collapse of the structural elements.....45

2.5.2. Beam – column buckling failure mode.....46

2.5.3. Plate induced buckling failure mode.....47

2.5.4. Flexural – torsional (tripping) buckling failure mode.....48
2.5.5. Web local buckling failure mode.....50
2.6. Simple Design Equations to Predict the Ultimate Strength of Imperfect Stiffened Plates.....51
2.7. Comparison between ANSYS FEM and Proposed Simple Equations.....54
2.8. Effects of Load Combinations on the Ultimate Strength Capacity.....67
2.8.1. Influence of transverse compression and lateral pressure on the ultimate strength.....68
2.8.2. Biaxial compression.....72
2.8.3. Effect of shear loading.....74
2.9. Ultimate Capacity of Transversally Stiffened Plates.....76
2.10. Discussion & Conclusion 79
3. Verification of The Proposed Simple Design Equations with Experiment Results.....81
3.1. Introduction.....81
3.2. The Smith Mechanical Collapse Tests.....82
3.3. The Tanaka & Endo Mechanical Collapse Tests.....87
3.4. Discussion & Conclusion 91
4. Hull Girder Ultimate Strength Under Vertical Bending Moment.....92
4.1. Introduction.....92
4.2. Direct Method to Evaluate Ultimate Hull Girder Strength.....93
4.2.1. Caldwell's method.....93
4.2.2. Improved methods.....94
4.2.3. Empirical formulations and interaction formulations.....95
4.3. Progressive Collapse Analysis.....95
4.3.1. Idealized structural unit method (ISUM).....96
4.3.2. Smith's method.....97
4.3.3. Non-linear finite element method.....103
4.4. A Developed Computer Code for Assessment of the Ultimate Strength *(NEPTUNE)*.....105
4.5. Benchmark Calculations on the Hull Girder Ultimate Strength.....106
4.6. Applied Methods of Analyses.....109

4.7. Calculated Results.....117
4.8. Effects of In-service Damage on Hull Girder Ultimate Strength.....124
4.9. Discussion & Conclusion 129
5. Investigation of Coupled Bending Moment on Hull Girder Ultimate Strength.....131
5.1. Introduction.....131
5.2. Collapse Analysis under Combined Bending.....132
5.2.1. Features of the method.....133
5.2.2. The followed steps.....134
5.3. Structural Modelling of Vessels.....137
5.3.1. Bulk carriers.....138
5.3.2. Tankers.....148
5.3.3. General cargo & Container ships.....161
5.4. Discussion & Conclusion 167
6. Residual Strength Analysis Using Non-linear Finite Element Method for Collision Damage Condition.....169
6.1. Introduction.....169
6.2. Description of the Analyses.....171
6.2.1. Vessel particulars.....171
6.2.2. Analysis codes.....173
6.2.3. Finite element model.....174
6.2.4. Boundary conditions.....177
6.2.5. Summary of the results.....178
6.3. Discussion & Conclusion 186
7. A Case Study: A comparative study on the structural integrity of single and double side skin bulk carriers under collision damage.....188
7.1. Introduction.....188
7.2. Collision Problem.....190
7.2.1. State of art.....191
7.3. Validation of ANSYS LS-DYNA using ISSC Benchmark Collision Test.....193
7.3.1. Finite element procedure.....193

7.3.2. Results.....193
7.4. SSS & DSS Bulk Carrier Designs.....194
7.4.1. Assumed collision scenarios.....197
7.4.2. Failure criterion.....202
7.4.3. Modified Minorsky correlation.....203
7.4.4. Calculation of internal energy for every collision cases.....204
7.5. Residual Strength Analysis.....212
7.5.1. State of art.....212
7.6. The Analysis of Residual Strength of SSS & DSS Bulk Carriers under Collision Damage.....215
7.7. Discussion & Conclusion 229
8. Fracture Assessment on Hull Girder Ultimate Strength Subject to Collision Damage.....232
8.1. Introduction.....232
8.2. Fundamentals of Fracture Mechanics.....236
8.3. Basic Concepts for Fracture Mechanics Analysis.....241
8.3.1. Energy-based concept.....242
8.3.2. Stress intensity factor concept.....243
8.3.3. Fracture toughness testing.....249
8.4. Elastic-Plastic Fracture Mechanics.....251
8.4.1. Crack tip opening displacement.....251
8.4.2. Other EPFM measure: J-integral.....255
8.5. The Crack Growth Resistance Curve.....257
8.5.1. Modelling of fatigue crack growth.....257
8.5.2. The Paris Law.....257
8.6. Failure Assessment.....259
8.7. Finite Element Analyses.....263
8.8. Loading Assessment.....267
8.9. Assumed Fracture Scenarios.....270
8.10. Parametric Studies.....275
8.11. Failure Assessment Diagrams.....285
8.12. Discussion & Conclusion 289

9. Conclusions and Recommendations.....291

9.1. Conclusions.....291

9.2. Recommendations for Future Work.....294

A. The Nonlinear Finite Element Method.....296

A.1. Introduction.....296

A.2. Solution procedures for nonlinear problems.....297

A.2.1. The direct method.....298

A.2.2. The incremental method.....299

A.2.3. The Newton-Raphson method.....300

A.2.4. The modified Newton-Raphson method.....302

A.2.5. The Arc Length method.....302

A.3. Formulation of nonlinear rectangular plate-shell element.....304

A.3.1. Nodal forces and nodal displacements.....304

A.3.2. Strain-displacement relationship.....305

A.3.3. Stress-strain relationship.....307

A.3.4. Elastic tangent stiffness matrix.....308

A.3.5. Displacement (Shape) function.....312

A.3.6. Yield condition.....312

A.3.7. Elastic-plastic tangent stiffness matrix.....316

A.3.8. Treatment of the Bauschinger effect.....323

A.3.9. Local to global transformation matrix.....324

References.....325

List of Author's Articles Published or Submitted during this Ph.D. Study.....338

ABSTRACT

This thesis addresses the structural performance of the hull structure of a vessel in extreme response state of a combined loading consisting of vertical and horizontal moments for intact and damaged conditions, where fracture mechanics of ships with large damage openings are investigated in great detail.

The motivation for conducting this research task is the importance of the ultimate and post-ultimate strength in relation to the reliability of intact as well as damaged vessels. Moreover, in an emergency situation, knowledge of the structural capacity of the vessel in whatever damaged or intact condition it may be in, is crucial to allow for a rational decision to be made regarding possible salvage, or at worst disembarkation of the crew, in the interest of safety for human life, environmental protection, and capital investment.

To facilitate these requirements, the overall objective of the present research therefore becomes to build a rapid computer based analysis tool for calculation of the ultimate and post-ultimate capacity of the hull girder in intact and damaged states of combined bending moment loading. Then, to verify the accuracy of the procedure developed against available experimental results and by comparison with other theoretical results. To meet this objective essentially requires five sub-tasks to be completed. Hence, the scope of the work to be carried out becomes

- A study of literature for the available methods usable to evaluate the ultimate and post-ultimate capacity of the stiffened plates.
- Developing the new simple design equations for predicting the ultimate strength of stiffened plates with imperfections in the form of imperfections, where a non-linear finite element method is employed on a wide range of typical ship panel geometries. The new simplified analytical method must be generalized to deal with such combined load cases. The performance of the proposed equations must be also verified by experimental results.

- Establishing a rapid computer code based on simplified formulas developed for calculation of the ultimate capacity of the hull girder. This program must be capable of considering initial imperfections and must be compared with other theoretical approaches developed.
- The influence of the coupled bending moment on the intact & damaged ship structures must be extensively investigated. The rational interaction equations must be developed, which based on the extensive ship types.
- Accidents such as collision, grounding and explosions occur and can have major consequences to the ship structure. The effect of such large damages on the hull girder must be assessed under time pressure. The recent accident with the PRESTIGE shows the importance of being able to reliably assess the longitudinal strength of damaged vessels. The procedures for this must be developed. A major drawback is lack of knowledge of the failure mechanism that may play a role in such circumstances. Therefore, the fracture mechanism of damaged ships is essential. Key effects must be identified and if possible, included in the procedure.

When these five points have been addressed, and the objectives solved, all that is needed for the development of a computer code for the ultimate strength. The remaining final task will thus to be benchmark the code against available experimental results and other theoretical methods.

List of Tables

Table 2.1: Initial deflection amplitudes for various initial deflection shapes based on Figure 2.5 (Paik & Pedersen, 1996)

Table 2.2: Geometric properties of stiffened panels analysed in this study

Table 2.3: Torsional buckling of axially loaded stiffeners – Number of m half waves

Table 2.4: The comparisons between ANSYS FEM, Faulkner's, Soares & Gordo`s and new proposed formulas with only initial deflection without considering residual stress under only longitudinal compression

Table 2.5: The comparisons between ANSYS FEM, Faulkner's, Soares & Gordo`s and new proposed formulas with initial deflection with considering residual stress ($\mu = 0.1$) under only longitudinal compression

Table 2.6: Summary of the prediction methods

Table 2.7: The differences between simply supported and clamped boundary conditions in ANSYS FEM

Table 2.8: The comparison between ANSYS FEM and Present study in clamped case

Table 2.9: The main particulars of DW 5120 analysed in ANSYS FEM

Table 2.10: The comparison of ANSYS FEM with the present study for transverse compression capacity of stiffened plate

Table 2.11: The main particulars of the Tanker bottom panel

Table 2.12: The main particulars of the Bulk Carrier side panel

Table 2.13 Comparison of ultimate capacity for transversally stiffened plates

Table 3.1: Mean values of geometric properties and material yield stresses for the Smith test grillages

Table 3.2: Other geometric characteristics of the Smith test grillages

Table 3.3: Initial imperfections of plating, longitudinal and transverses for the Smith test grillages

Table 3.4: Comparison of Present study, FEA, Soares & Gordo, Paik and Faulkner with the Smith experiments for the ultimate strength of grillages

Table 3.5: Comparison of Present study, FEA, Soares & Gordo, Paik and Faulkner with the Smith experiments for the ultimate strength of grillages

Table 3.6: Summary of the design methods with the Smith experiments for the ultimate strength of grillages
Table 3.7: Experimental results and finite element solutions of the ultimate compressive strengths for the stiffened panels obtained by Tanaka & Endo (1988)
Table 3.8: Comparison of Present study, FEA, Gordo & Soares, Paik and Faulkner with the Tanaka - Endo experiments for the ultimate compressive strengths for stiffened panels
Table 3.9: Comparison of Present study, FEA, Gordo & Soares, Paik and Faulkner with the Tanaka - Endo experiments for the ultimate compressive strengths for stiffened panels
Table 3.10: Summary of the design methods with the Tanaka - Endo experiments for the ultimate compressive strengths for stiffened panels
Table 4.1: Comparison of different methods considering the assumptions in each one
Table 4.2: Principal dimensions of five vessels for calculations
Table 4.3: Dimensions of longitudinals of Bulk Carrier (dimensions in mm)
Table 4.4: Dimensions of longitudinals of Container Ship (dimensions in mm)
Table 4.5: Dimensions of longitudinals of double hull VLCC (dimensions in mm)
Table 4.6: Dimensions of longitudinals of *Energy Concentration* (dimensions in mm)
Table 4.7: Location of longitudinals of 1/3-scale Frigate model (dimensions in mm)
Table 4.8: Ultimate hull girder strength of bulk carrier
Table 4.9: Ultimate hull girder strength of container ship
Table 4.10: Ultimate hull girder strength of single hull VLCC, *Energy Concentration*
Table 4.11: Ultimate hull girder strength of double hull VLCC
Table 4.12: Ultimate hull girder strength of 1/3-scale welded steel frigate model
Table 4.13: Safety factor assessment against hull girder ultimate strength for case (2)
Table 4.14: Corrosion additions t_c , in mm. (Bureau Veritas Rules)
Table 5.1: Hull sectional properties of the Tankers
Table 5.2: Hull sectional properties of the Bulk Carriers, Container ships and General Cargo
Table 6.1: Material properties of plastic – kinematics used in LS-DYNA
Table 7.1: Principal dimensions of SSS & DSS bulk carrier vessels
Table 7.2: The scantlings of longitudinal of SSS bulk carrier vessel

Table 7.3: The scantlings of longitudinal of DSS bulk carrier vessel
Table 7.4: Material properties of plastic – kinematics used in this study
Table 7.5: Bow shape 1at direct web longitudinal position
Table 7.6: Bow shape 1 at between webs long. Position
Table 7.7: Bow shape 2 at direct web longitudinal position
Table 7.8: Bow shape 2 at between webs longitudinal position
Table 7.9: Proposed failure strain versus mesh size, GL 2003
Table 7.10: Internal energy for SSS at hitting direct web at t = 0. 1 second
Table 7.11: Internal energy for DSS at hitting direct web at t = 0.1 seconds
Table 7.12: Internal energy for SSS at hitting between web at t = 0.3 seconds
Table 7.13: Internal energy for DSS at hitting between at t = 0.3 seconds
Table 7.14: The summary of the rupture energies of DSS & SSS bulk carrier designs
Table 7.15: Bow shape 1at direct web longitudinal position
Table 7.16: Bow shape 1 at between web longitudinal position
Table 7.17: Bow shape 1at direct web longitudinal position
Table 7.18: Bow shape 1 at between web longitudinal position
Table 7.19: Bow shape 1at direct web longitudinal position
Table 7.20: Bow shape 1 at between web longitudinal position
Table 7.21: Bow shape 1at direct web longitudinal position
Table 7.22: Bow shape 1 at between web longitudinal position
Table 7.23: Residual strength of SSS & DSS bulk carriers both in intact and damage states without corrosion effect
Table 7.24: Residual strength of SSS & DSS bulk carriers both in intact and damage states with corrosion effect
Table 7.25: Safety assessment of SSS & DSS bulk carriers without JBP Rules corrosion effect
Table 7.26: Safety assessment of SSS & DSS bulk carriers with JBP Rules corrosion effect
Table 8.1: Values of C present in different sources
Table 8.2: Wave induced bending moments obtained by USAS-L program
Table 8.3: All cases investigated in this study

Table 8.4: Stress summaries subject to wave induced bending moment in hogging and sagging cases

Table 8.5: Numeric and Analytic through crack fracture parameters for MC1 (H_s=8.5m)

Table 8.6: Numeric and Analytic through crack fracture parameters for MC2 (H_s=8.5m)

Table 8.7: Numeric and Analytic through crack fracture parameters for MC3 (H_s=8.5m)

Table 8.8: Numeric and Analytic through crack fracture parameters for MC4 (H_s=8.5m)

Table 8.9: Numeric and Analytic through crack fracture parameters including 25 MPa compressive residual stress level (Hs=8.5 m)

Table 8.10 Numeric and Analytic through crack fracture parameters for 1800 x 1000 damage shape (H_s=8.5 m)

Table 8.11: Numeric and Analytic through crack fracture parameters for unstiffened plate (H_s=8.5 m)

Table 8.12: Short-term north-sea stress spectrum

Table 8.13: Numeric and Analytic through crack fracture parameters for sea state, H_s=7.0 m

Table 8.14: Numeric and Analytic through crack fracture parameters for sea state, H_s=5.5 m

Table 8.15: Numeric and Analytic through crack fracture parameters for sea state, H_s=4.0 m

Table 8.16: Numeric and Analytic through crack fracture parameters for sea state, H_s=2.5 m

Table 8.17: Allowable crack length (mm) versus time period (days)

Table 8.18: Crack sizes versus time period under various sea states

List of Figures

Figure 1.1: Complete hull failure in a stranded bulk carrier, *NEW CARISSA*

Figure 1.2: Loss of bulk carrier, *DERBYSHIRE*

Figure 1.3: Deck plate buckled on *BUFFALO 286*

Figure 1.4: *BUFFALO 292* after buckling on March 18, 1996

Figure 1.5: Collision at sea, *US Navy Destroyer and Saudi Arabian Container Vessel*

Figure 1.6: *US Navy LST 1179* Class Stranding in Chile

Figure 1.7: *MT PRESTIGE* accident (left) and clean-up operations after *MT ERIKA* accident (right)

Figure 2.1: A stiffened steel plate in ship hull

Figure 2.2: A cross-stiffened panel under combine in plane and lateral pressure loads Paik & Thayamballi (2003)

Figure 2.3(a): Mode I-1: Overall collapse of an unaxially stiffened panel (Paik & Thayamballi, 2003)

Figure 2.3(b): Mode I-2: Overall collapse of a cross-stiffened panel (Paik & Thayamballi, 2003)

Figure 2.3(c): Mode II: Plate induced failure –yielding at the corners of plating between stiffeners (Paik & Thayamballi, 2003)

Figure 2.3(d): Mode III: Plate induced failure –yielding of plate – stiffener combination at mid – span (Paik & Thayamballi, 2003)

Figure 2.3(e): Mode IV: Stiffener induced failure –local buckling of the stiffener web (Paik & Thayamballi, 2003)

Figure 2.3(f): Mode V: Stiffener induced failure –lateral-torsional buckling of stiffener (Paik & Thayamballi, 2003)

Figure 2.4: A comparison of the ultimate strength formulations for the plate-stiffener combinations under axial compression (Paik & Thayamballi, 2003)

Figure 2.5: Some selected initial deflection patterns in steel plating between stiffeners in the plate length direction, based on the measurements of Ueda & Yao (1985)

Figure 2.6: A simplified initial deflection pattern in steel plating between stiffeners in the plate breadth direction

Figure 2.7: Idealization of welding induced residual stress distribution inside plating in the x and y directions (Paik & Thayamballi, 2003)
Figure 2.8: Faulkner's model used in this work for residual stress distribution
Figure 2.9: ANSYS solid model for three-bay grillages in this study
Figure 2.10(a): Linear eigenvalue buckling mode shape 1 in SP7 (overall mode)
Figure 2.10(b): Linear eigenvalue buckling mode shape 2 in SP7
Figure 2.10(c): Linear eigenvalue buckling mode shape 3 in SP7
Figure 2.10(d): Linear eigenvalue buckling mode shape 4 in SP7
Figure 2.10(e): Linear eigenvalue buckling mode shape 5 in SP7
Figure 2.11: Load versus deformation behaviour (Murray, 1973)
Figure 2.12: Von Misses stress distribution in SP37, where neglected residual stress
Figure 2.13: Von Misses stress distribution in SP45, where neglected residual stress
Figure 2.14: Von Misses stress distribution in SP46, where neglected residual stress
Figure 2.15: Von Misses stress distribution in SP55, where neglected residual stress
Figure 2.16: Comparison of ANSYS FEM with approximate formulation for SP37
Figure 2.17: Comparison of ANSYS FEM with approximate formulation for SP45
Figure 2.18: Comparison of ANSYS FEM with approximate formulation for SP46
Figure 2.19: Comparison of ANSYS FEM with approximate formulation for SP55
Figure 2.20: The comparison between FEM and simplified methods respect to beam-column slenderness ratio without residual stress effect for $\beta = 1.183$
Figure 2.21: The comparison between FEM and simplified methods respect to beam-column slenderness ratio with residual stress effect for $\beta = 1.183$
Figure 2.22: The comparison between FEM and simplified methods respect to beam-column slenderness ratio without residual stress effect for $\beta = 1.553$
Figure 2.23: The comparison between FEM and simplified methods respect to beam-column slenderness ratio with residual stress effect for $\beta = 1.553$
Figure 2.24: Fig.2.22. The comparison between FEM and simplified methods respect to beam-column slenderness ratio without residual stress effect for $\beta = 1.774$
Figure 2.25: The comparison between FEM and simplified methods respect to beam-column slenderness ratio with residual stress effect for $\beta = 1.774$

Figure 2.26: The comparison between FEM and simplified methods respect to beam-column slenderness ratio without residual stress effect for $\beta = 2.329$

Figure 2.27: The comparison between FEM and simplified methods respect to beam-column slenderness ratio with residual stress effect for $\beta = 2.329$

Figure 2.28: The comparison between FEM and simplified methods respect to beam-column slenderness ratio without residual stress effect for $\beta = 2.484$

Figure 2.29: The comparison between FEM and simplified methods respect to beam-column slenderness ratio with residual stress effect for $\beta = 2.484$

Figure 2.30: The comparison between FEM and simplified methods respect to beam-column slenderness ratio without residual stress effect for $\beta = 3.726$

Figure 2.31: The comparison between FEM and simplified methods respect to beam-column slenderness ratio with residual stress effect for $\beta = 3.726$

Figure 2.32: Linear eigenvalue buckling for DW 5120, mode shape 1

Figure 2.33: Effect of lateral pressure on axial capacity for DW 5120 tanker bottom panel

Figure 2.34: Tanker bottom panel, biaxial compression without lateral pressure

Figure 2.35: Tanker bottom panel, biaxial compression with lateral pressure, $p = 0.151$ MPa

Figure 2.36: Bulk Carrier side panel, transverse compression and shear loading without lateral pressure

Figure 2.37: Bulk Carrier side panel, transverse compression, shear with lateral pressure, p=0.157 MPa

Figure 2.38: Typical cross-section of bulk carrier

Figure 2.39: Typical cross-section of container

Figure 3.1: A schematic of the Smith test grillage (1976, 1992)

Figure 3.2: The Tanaka & Endo test structure for longitudinally stiffened panels under uniaxial compression, incorporating two dummy panels away from the transverse frames (Tanaka & Endo, 1988)

Figure 4.1: Flow chart of procedure for the evaluation of curve Moment versus Curvature

Figure 4.2: A computer code developed NEPTUNE for calculating hull girder ultimate strength
Figure 4.3: Cross-section of Bulk Carrier
Figure 4.4: Cross-section of Container Ship
Figure 4.5: Cross-section of double hull VLCC
Figure 4.6: Cross-section of single hull VLCC, *Energy Concentration*
Figure 4.7: Cross-section of 1/3-scale steel welded frigate model
Figure 4.8: Moment curvature relationship for Bulk Carrier
Figure 4.9: Moment-curvature relationships for Container Ship
Figure 4.10: Moment – curvature relationships for Single Hull VLCC, *Energy Concentration*
Figure 4.11: Moment – curvature relationships for Double Hull VLCC
Figure 4.12: Moment-curvature relationships for 1/3-scale Frigate model
Figure 4.13: Effect of corrosion level on ultimate bending moment for Bulk Carrier and Container, respectively
Figure 4.14: Effect of corrosion level on ultimate bending moment for Double Hull VLCC and Single Hull VLCC, respectively
Figure 4.15: Effect of corrosion level on effective area and section modulus for Bulk Carrier and Container, respectively
Figure 4.16: Effect of corrosion level on effective area and section modulus for Double Hull VLCC and Single Hull VLCC, respectively
Figure 5.1: Initial and at collapse position of the neutral axis under combined bending moment
Figure 5.2: Midship cross-section of five bulk carriers
Figure 5.3: Components of bending moment at $\theta = 20$ degree in hogging case for BULK1
Figure 5.4: The magnitude of the moment components with respect to angle of curvature vector
Figure 5.5: Relationship between angle of resultant bending moment and angle of curvature vector
Figure 5.6: Interaction curves for bulk carriers under coupled bending moment
Figure 5.7: Midship cross-section of nine tankers

Figure 5.8: The magnitude of the moment components with respect to angle of the curvature vector
Figure 5.9: Relationship between angle of the resultant bending moment and angle of curvature vector
Figure 5.10: Interaction curves for tankers under coupled bending moment
Figure 5.11: Midship cross -section of two container ships and one general cargo
Figure 5.12: The magnitudes of the moment components with respect to angle of the curvature vector
Figure 5.13: Relationship between angle of curvature and resultant bending moment
Figure 5.14: Interaction curves for general cargo & container ships under coupled bending moment
Figure 6.1: Midship cross section of 5600 DWT chemical tanker
Figure 6.2: Longitudinal section of 5600 DWT chemical tanker
Figure 6.3: The one cargo hold ANSYS model geometry used in the analyses
Figure 6.4: Dynamics impact analysis conducted in LS-DYDA explicit FEM code
Figure 6.5: The Multi Point Constraints (MPCs) introduced to damaged tanker vessel
Figure 6.6: The two-dimensional model for hull girder strength of damaged tanker vessel
Figure 6.7: The three-dimensional model for hull girder strength of damaged tanker (remove element)
Figure 6.8: The three-dimensional model for hull girder strength of damaged tanker (no remove element)
Figure 6.9: Damaged hull girder ultimate strength of the tanker in hogging case
Figure 6.10: Damaged hull girder ultimate strength of the tanker in sagging case
Figure 6.11: Hogging condition: moment 471 MNm, curvature 0.25 x 10^{-3} 1/m (Von Mises stress)
Figure 6.12: Hogging condition: moment 471 MNm, curvature 0.25 x 10^{-3} 1/m (longitudinal stress)
Figure 6.13: Hogging condition: moment 567 MNm, curvature 0.40 x 10^{-3} 1/m (longitudinal normal stress)
Figure 6.14: Hogging condition: moment 567 MNm, curvature 0.40 x 10^{-3} 1/m (Von Mises stress)

Figure 6.15: Sagging condition: moment 458 MNm, curvature 0.30 x 10^{-3} 1/m (Von Mises stress)
Figure 6.16: Sagging condition: moment 458 MNm, curvature 0.30 x 10^{-3} 1/m (longitudinal normal stress)
Figure 7.1: Collision force versus penetration (*left*) and absorbed energy versus penetration (*right*)
Figure 7.2: Finite element model with very fine mesh (left) and penetration of 500 mm (right)
Figure 7.3: Midship cross section of SSS Bulk carrier
Figure 7.4: Midship cross section of DSS Bulk carrier
Figure 7.5: ANSYS one cargo tank geometry model for SSS & DSS bulk carrier vessels
Figure 7.6: Bow shape 1 and bow shape 2
Figure 7.7: Draft differences between striking and struck ships, (GL 2003)
Figure 7.8: Deformations in case 1 for DSS at t = 0.1 and t = 0.3 seconds, respectively
Figure 7.9: Deformations in case 1 for SSS at t = 0.1 and t = 0.3 seconds, respectively
Figure 7.10: Internal energy versus penetration curves for all investigated collision case
Figure 7.11: Moment – curvature relationship of DSS vessels in Case 1
Figure 7.12: Moment – curvature relationship of SSS vessels in Case 1
Figure 8.1: M V Kurdistan tanker failure (www.twi.co.uk)
Figure 8.2: M V Kurdistan failure induced by fracture initiation (www.twi.co.uk)
Figure 8.3: A schematic representation of the cracking damage effect on the ultimate strength behaviour of steel structures
Figure 8.4: A schematic of appropriate approaches for fracture analysis as a function of material fracture toughness (LEFM = linear elastic fracture mechanics, EPFM = elastic-plastic fracture mechanics, LLA = limit-load analysis)
Figure 8.5: A cracked infinite plate under tensile loading
Figure 8.6: Local coordinate system and the resulting stress components for a cracked body (B = plate thickness)

Figure 8.7: Three basic loading modes for a cracked body: (a) Mode I, opening mode; (b) Mode II, sliding mode; (c) Mode III, tearing mode
Figure 8.8: Typical crack locations in a plate under tensile stress: (a) center crack; (b) crack on one side; (c) crack on both sides
Figure 8.9: A schematic representation of the critical K_I value versus the plate thickness, B
Figure 8.10: Crack opening displacement and CTOD
Figure 8.11: A schematic representation of the Dugdale approach (the shaded areas represent the plastic zones)
Figure 8.12: Contour path used for J evaluation
Figure 8.13: A schematic of the generic FAC, the FAP and safety margin (Reemsnyder, 2002)
Figure 8.14: Simplified Level 2B, BS 7910
Figure 8.15: The global finite element modelling created by ANSYS
Figure 8.16: Possible crack propagations induced by ship collision incident
Figure 8.17: Through-crack finite element model for damaged side shell of tanker
Figure 8.18: PLANE82 geometry
Figure 8.19: Boundary condition adopted into FEA (One transverse frame spacing)
Figure 8.20: Assumed crack location (C200)
Figure 8.21: Assumed crack location (C200s)
Figure 8.22: Assumed crack location (CC80)
Figure 8.23: Assumed crack location (CC80s)
Figure 8.24. Crack extension versus cycles between perfect and imperfect including residual stress cases
Figure 8.25: Crack extension versus cycles between 1800 x 1000 and 1500 x 600 damage geometries
Figure 8.26: The structural arrangement of stiffened panel investigated
Figure 8.27: Crack extension versus cycles between stiffened and unstiffened panels
Figure 8.28: Crack extension versus cycles for five loading cases
Figure 8.29: Simplified Level 2B FAD for Main case-1 (MC1)
Figure 8.30: Simplified Level 2B FAD for Main case-2 (MC2)
Figure 8.31: Simplified Level 2B FAD for Main case-3 (MC3)

Figure 8.32: Simplified Level 2B FAD for Main case-4 (MC4)
Figure 8.33: Simplified Level 2B FAD for residual stress level (25 MPa) on MC1
Figure 8.34: Simplified Level 2B FAD for 1800 x 1000 damage extent effect on MC1
Figure 8.35: Simplified Level 2B FAD for ignoring stiffeners (unstiffened plate) on MC1
Figure 8.36: Simplified Level 2B FAD for sea state, H_s = 7.0 m on MC1
Figure 8.37: Simplified Level 2B FAD for sea state, H_s = 5.5 m on MC1
Figure 8.38: Simplified Level 2B FAD for sea state, H_s = 4.0 m on MC1
Figure 8.39: Simplified Level 2B FAD for sea state, H_s = 2.5 m on MC1
Figure A.1: A nonlinear spring, $k_0 = cons\tan t, k_N = f(u)$
Figure A.2: The incremental method (Cook *et al.* 1989)
Figure A.3: The (a) original and (b) modified Newton-Raphson methods (Cook *et al.* 1989)
Figure A.4: (a) The arc length method; (b) Application example of the arc length method to the so-called 'snap-through' problem
Figure A.5: The local coordinate system for the rectangular plate element with its nodal forces and displacements
Figure A.6: A diagram of the yield surface
Figure A.7: The elastic-perfectly plastic model for the stress-strain relationship
Figure A.8: (a) The drift in the value of the yield function; (b) A two-step procedure for convergence to the yield condition
Figure A.9: The isotropic hardening versus the kinematic hardening

Symbols

The symbols used in this thesis are explained when they are first introduced. The following is a list of the main symbols used.

σ_C	critical stress
σ_E	Euler column buckling stress
β	plate slenderness ratio
b	plate breadth
t	plate thickness
E	young's modulus
σ_o	material yield stress of plate
t_w	thickness of stiffener web
w_{opl}	initial plate deflection
σ_{rtx}	residual stress in the x direction
σ_{rty}	residual stress in the y direction
$\eta \times t_{plate}$	a tension block having base width proportional to the plate thickness
ν	poisson ratio
λ	beam-column slenderness
α	aspect ratio
σ_{ow}	material yield stress of web
σ_{of}	material yield stress of flange
b_E	effective width of plating
ε	the relative strain
ε_E	element strain
ε_o	strain including yield stress in the element
Φ	edge function
σ_{CR1}	beam-column induced buckling stress
σ_{C1}	critical stress in MPa
A_S	net sectional area of a stiffener
b	spacing of stiffeners

σ_{E1}	Euler column buckling stress
I_E	net moment of inertia of ordinary stiffeners with attached shell plating
A_E	net sectional area of stiffeners with attached shell plating
a	length of stiffened plate
σ_{CR2}	plate induced buckling failure mode stress
σ_{CR3}	Flexural – torsional (tripping) buckling failure mode stress
σ_{C3}	critical stress
σ_{E3}	euler torsional buckling stress
I_W	net sectional moment of inertia of the stiffener
I_P	net polar moment of inertia of the stiffener
I_t	St. Venant's net moment of inertia of stiffener without attached plating
m	number of half waves
K_C	torsional buckling of axially loaded stiffeners
C_0	a spring stiffener of the attached plating
σ_{CP}	buckling stress of attached plating
σ_{CR4}	Web local buckling failure mode stress
h_{we}	effective height of the web
$\left(\frac{\sigma_r}{\sigma_o}\right)$	normalized compressive welding-induced stress
$\left(\frac{w_o}{t}\right)$	non-dimensional initial deflection
τ	shear stress
b_E	effective width of imperfect stiffened plate
R_d	reduction factor due to initial deflection
R_r	reduction factor due to welding-induced residual stress
R_y	reduction factor due to bi-axial compression
R_τ	reduction factor due to shear stress present

R_q	reduction factor due to lateral pressure load
$\xi = \left(\frac{\rho E}{\sigma_o^{\,2}}\right)$	normalized value of pressure
$\sigma_{transv}(\varepsilon)$	an average stress at compressed edge of transversely stiffened plates
${}^{(i)}\kappa$	curvature of a given section
z	vertical coordinate of element
${}^{(i)}z_C$	actual vertical co-ordinate of the centre of gravity of the section
${}^{(i)}\sigma$	direct strain
Z_{red}	reduced section modulus of the deck
z_d	vertical distance to the mean deck height measured from the baseline
g	the vertical distance to the neutral axis of the reduced section measured from the baseline
σ_{Yd}	specified yield stress of the steel in the deck
I_y	moment of inertia with respect to horizontal neutral axis, in m^4
z_G	location of neutral axis above keel under vertical bending, in m
M_P	Fully plastic bending moment of cross-section, in MN.m
M_{YS}	Initial yield strength of deck, in MN.m
M_{YH}	Initial yield strength of bottom, in MN.m
M_{BS}	Local buckling strength of deck, in MN
M_{BH}	Local buckling strength of bottom, in MN.m
M_{US}	Ultimate bending moment of cross-section under sagging, in MN.m
M_{UH}	Ultimate bending moment of cross-section under hogging, in MN.m
φ	angle that the bending moment vector makes with the baseline
θ	angle of the curvature vector
C_x	curvature in the x-direction
C_y	curvature in the y-direction
C	overall curvature, $C = \sqrt{C_x^2 + C_y^2}$

M_P	plastic bending moment
M_U	Ultimate bending moment
$T_{1\max}$	design draft of the striking ship
$T_{1\min}$	ballast draft of the striking ship
$T_{2\max}$	the design of the struck ship
$T_{2\min}$	the ballast draft of the struck ship
ε_P^{eff}	effective plastic strain
E_P	plastic hardening modulus
β	hardening parameter between 0 (kinematics) and 1 (isotropic)
C , P	cowder – symonds strain rate parameters
ε_g	the uniform strain
ε_e	the necking
l_e	an individual element length in mesh
W_C	the total energy absorbed by damage and striking and struck vessels
R_T	the damaged volume of structural steel
P_N , P_n	depth of damage for N-th member of striking vessels or for the n-th member of struck vessel, respectively
L_N , L_n	length of damage for the N-th member of the striking vessel or for the n-th member of struck vessel, respectively
t_N , t_n	thickness of the N-th member of the striking vessel or of the n-th member of the struck vessel, respectively
H	height of rupture aperture in the side shell
G	strain energy release rate
G_C	material's resistance to crack growth
a	half crack length
σ_f	failure stress
K_I	the Mode I stress intensity factor
u, v, w	translational displacements in the x, y and z directions
F	geometry factor for stress intensity factor

K_C	fracture toughness
r_p^*	size of the crack plastic zone
J	J – integral value
Γ	the contour path in J – integral calculation
W	strain energy density
T_i	components of the traction vector which is normal to the contour
u_i	components of the displacement vectors
ds	length increment along the contour Γ
σ_{ij} , ε_{ij}	the stress and the strain tensors
$\frac{da}{dN}$	fatigue crack growth formulae
ΔK	Stress intensity factor range
C	An experimentally determined coefficient
N	Number of cycles
K_r	fracture ratio
δ_c	CTOD fracture toughness
L_r	collapse ratio

Acknowledgements

This thesis is submitted as partial fulfilment of the requirements for the degree of Doctor of Philosophy at the Universities of Glasgow and Strathclyde. My sincere appreciation goes to my supervisors, Professor Purnendu K. Das and Professor Nigel Barltrop. Their guidance, patience and encouragement were invaluable to the progress and completion of this study.

I am grateful to Professor Tetsuya Yao for his kind help and his valuable discussions. I deeply thank to Dr. Ge (George) Wang for his kind support. Thanks to Professor A. Yucel Odabasi, Professor Ahmet Ergin, and Professor Manolis Samuelides for their helpful discussions. I also thank to all fellow students in Marine Structures & Reliability Research Group for their help and the great time we shared together.

I am indebted to my parents for love, support and encouragement. I would like to dedicate this study to my family.

Özgür Özgüç

March 2006

Chapter 1

Introduction

1.1 Background

The structural design of any vessel is strongly regulated both by class rules and regulations from both national and international authorities. All this goes to insure safe operation within an acceptable safety level of the vessel. While it is mainly the task of the authorities to set the standards for what constitutes an acceptable safety level, it falls upon the classification societies to formulate the appropriate design rules insuring this level of safety.

The focusing on the design rules, these are chiefly based on rational design principles developed over the years and are continually revised and updated according to the latest achievements in knowledge. Hence, for the structural aspects of a vessel, the fulfilment of the class rules insures safe operation given a specific design load level also set by the class rules.

Thus, it can be reasonably expected that a vessel will not undergo buckling / plastic collapse while the working load is below the design load. However, there is a risk that the vessel will experience extreme loading conditions far beyond the design load in an unintended, accidental, or emergency situation.

On July 21st 1980, the VLCC *Energy Concentration* broke into two parts during discharge of oil at Rotterdam, The Netherlands. This is an excellent illustration of how irresponsible cargo handling caused transgressing of the design load and is well documented by Rutherford & Caldwell (1990). Collision and grounding also constitutes a dangerous situation for any vessel, as it did on the morning of March 24th 1989, where the VLCC *Exxon Valdez* went aground onto a reef and spilled some 10.1 million barrels of oil into Price William Sound, Alaska, USA. Although she suffered extensive damage to her hull, overall structural integrity remained uncompromised by the accident. Less fortunate was the oil tanker *Braer*, which on January 5th 1993 ran aground off Sumburgh Head in Shetland, UK. Seven days later, on January 12th she broke up into three sections after having been continually thrown against the rocks of the island and the entire cargo of some 620 thousand barrels of oil was spilled into the sea around the southern end of the main Shetland Island.

The Ship Structure Committee has selected the following case studies which it represent a wide range of structural failures, casualties and solutions. The goal is to increase appreciation of structural issues that are unique to the shipbuilding industry and provide a forum for the dissemination of information to universities and practicing naval architects (www.shipstructure.org).

- Case Study I: *NEW CARISSA*

On February 3, 1999, the NEW CARISSA was inbound from Japan to pick up a load of wood chips at Coos Bay, Oregon. Due to high winds and heavy seas from a winter storm, the Coos Bay pilot decided that the vessel should stand off until February 4 before attempting to enter Coos Bay. On the morning of February 4, the *NEW CARISSA* dragged anchor and grounded approximately 300 yards off a stretch of remote, undeveloped sandy beach 3 miles north of Coos Bay, Oregon, which is shown in Figure 1.1. Within a few hours, the vessel was fully broached (broadside) to the incoming seas. There were approximately 400,000 gallons of fuel on board the vessel at the time of grounding; of which 350,000 gallons was Bunker C and 50,000 gallons was diesel.

Figure 1.1: Complete hull failure in a stranded bulk carrier, *NEW CARISSA*

Catastrophic failure of the hull girder in two-mode global cyclic bending resulting from wave forces and sea floor scouring, and impact loading from bottom pounding while stranded on an exposed coast, probably exacerbated or hastened by exposure to extreme heat and rapid quenching during attempts to burn fuel bunkers.

- Case Study II: *DERBYSHIRE*

MV DERBYSHIRE was a British Oil/Bulk/Ore, (OBO), carrier transporting ore from Canada to Japan when she was lost during the typhoon ORCHID on the 9th or 10th of September 1980. She went down with all 44 on board without any distress signal. DERBYSHIRE is the largest British bulk carrier ever lost and has been the object of several investigations and discussions regarding bulk carrier safety, which is shown in Figure 1.2.

Two possible explanations for the loss of the MV DERBYSHIRE during a severe storm, both of which postulate foundering due to structural failure of critical components. One scenario assumes the break-up of the ship due to fatigue failure of longitudinal structural members in the aft portion of the ship, while the other

assumes foundering resulting from collapse of hold covers under sea loading. The two loss scenarios were compared in the light of the results of recent technical investigations and wreckage surveys.

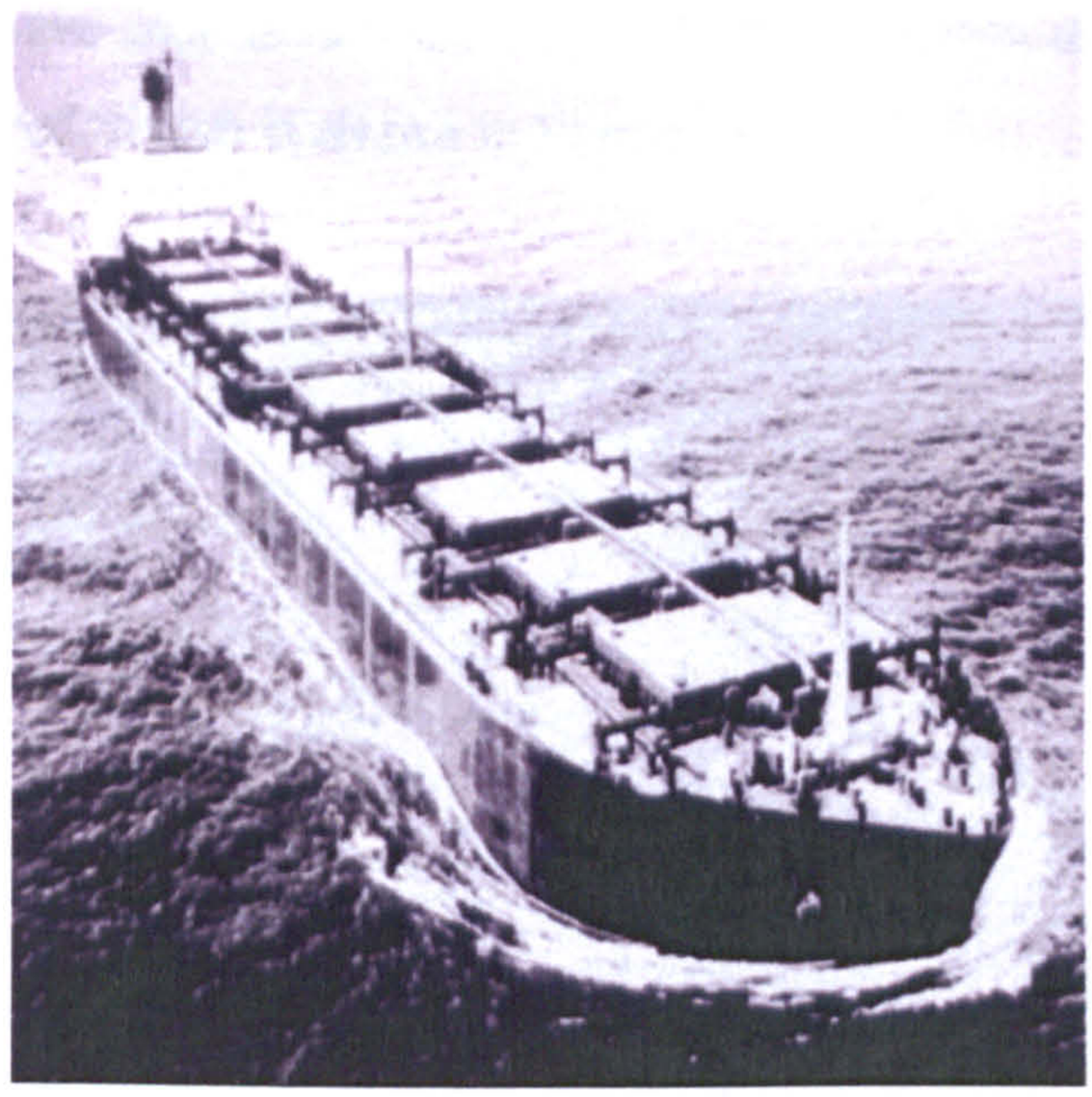

Figure 1.2: Loss of bulk carrier, *DERBYSHIRE*

- Case Study III: *BUFFALO 286 and 292*

BUFFALO 286

On March 18, 1996, the barge was being towed outbound in the Houston Ship Channel to be offloaded in Port Arthur, Texas. Winds were blowing at 35 knots and waves were 2 to 3 feet high. As the vessel was transiting, the bow and stern began rising significantly and rose to form an angle of about 30 degrees with the horizontal position. The deck had buckled about one foot aft of the transverse bulkhead separating the #2 and #3 cargo tanks. The hull was breached and nearly 5000 barrels of oil were spilled into the channel, which is shown in Figure 1.3.

BUFFALO 292

In May of 1996, the barge was being towed outbound in the Houston Ship Channel when the same type of failure occurred as exhibited by the BUFFALO 292. The weather and wave conditions were very mild, compared to that of the 292, when this casualty occurred, which is shown in Figure 1.4.

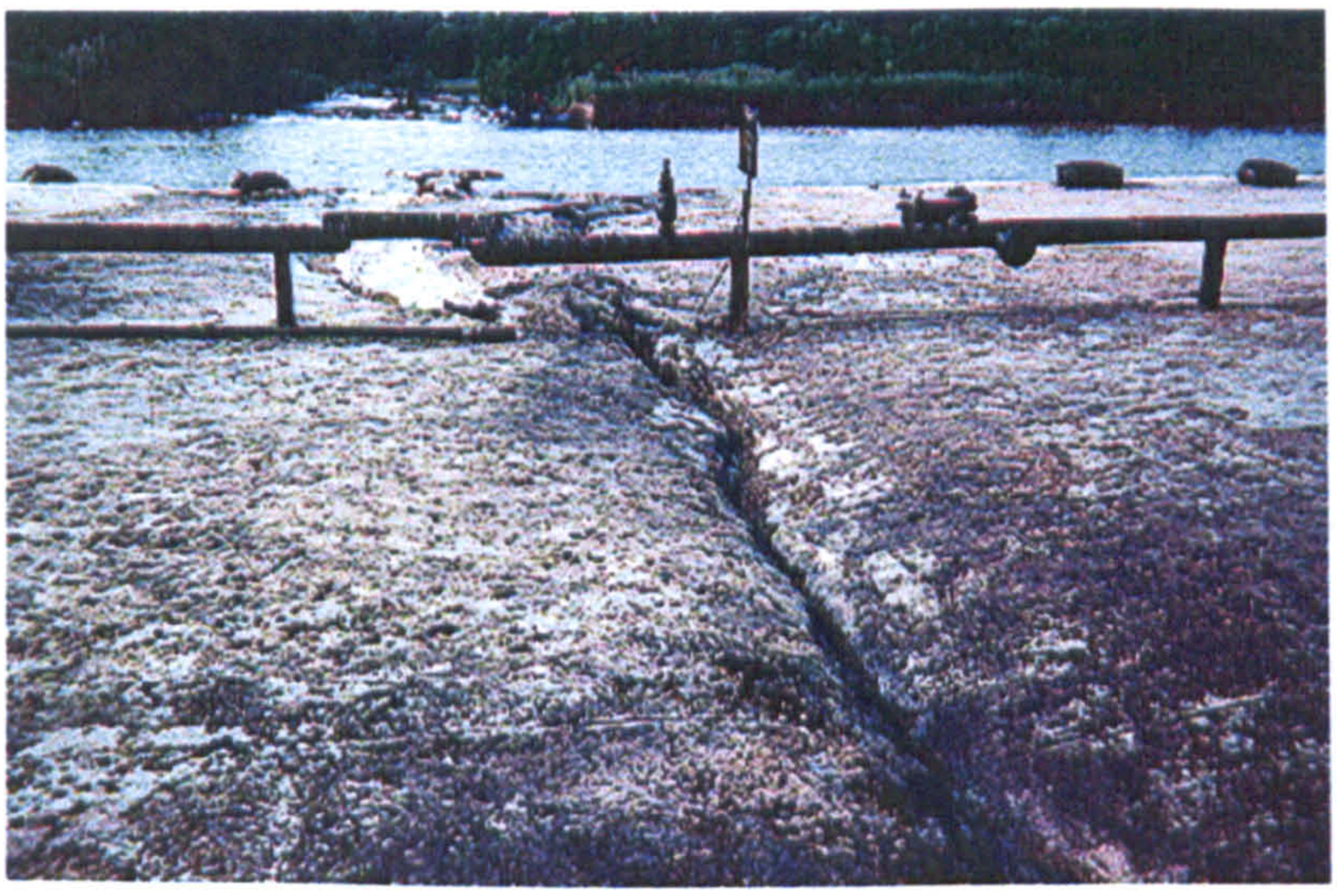

Figure 1.3: Deck plate buckled on *BUFFALO 286*

Figure 1.4: *BUFFALO 292* after buckling on March 18, 1996

- Case Study IV: *USS RADFORD*

On 5 February 1999,while conducting exercises off Hampton Roads, VA, the USS Arthur W. Radford was involved in a collision at sea with a Saudi Arabian container vessel. The Saudi vessel 's stem and bulbous bow penetrated the starboard side of the Radford, centered near frame 69. As a result of the collision, the Radford experienced significant structural damage and flooding from frames 58 through 94,with additional flooding within sonar equipment spaces between frames 29 and 58. Post damage inspections indicated that flooding was complete (free-flooded to the waterline). Structural damage from the stem of the Saudi vessel consisted of complete penetration of the side shell and main deck from the 1st platform deck on the side shell to the ship 's centreline on the strength deck, with damage extending mainly from frames 52 through 84. Additional structural damage below the waterline from the bulbous bow of the Saudi vessel consisted of complete penetration of the side and bottom shell from the 2nd platform deck to the centre vertical keel at the baseline, with damage extending mainly from frames 64 through 82.Outside these primary penetration areas, there was significant buckling of decks and tripping of stiffeners caused by the transverse force of the collision. Thus, many of the structural members outside the primary penetration area provided reduced effective strength to the hull girder, which is shown in Figure 1.5.

Figure 1.5: Collision at sea, *US Navy Destroyer and Saudi Arabian Container Vessel*

➢ Case Study V: *VALDIVIA*

LST 93 VALDIVIA ran aground after an engine failure during beaching exercises. The incident occurred near the town of Pisagua, on the shore of Northern Chile, on 17 May 1997. Breaking waves caused the crippled ship to broach, with the heading almost parallel to the beach. Preliminary estimates placed the vessel at least 1500 tons aground, which is shown in Figure 1.6.

Figure 1.6: *US Navy LST 1179* Class Stranding in Chile

The consistent pounding of breaking waves caused severe hull damage to 30 tanks. The hull girder experienced longitudinal buckling along the keel and the seaward sideshell. This athwartships buckling was caused by the unusual load condition of having the hull supported by the beach on the port side, while the sea continuously impacted the starboard side. Detailed structural modelling was done to assess the effects of this hull damage on residual strength.

European research project DEXTREMEL (1997-2000) addressed three main topics such as collision & grounding, wave induced damage and structural integrity to identify the safety of RO-RO ferries as a key priority by the European Commission and the Maritime Industry R & D Masterplan. This research work provided numerical methods to predict the residual structural strength of damaged

Ro-Ro passenger ferries in extreme conditions. The results of risks associated with total loss of the structural integrity due to extreme and / or accidental loads, such as collision and grounding loads and loads on deck structure caused by green water shipping.

The consequences of tanker accidents are often catastrophic, as can be vividly attested by the recent disasters of the *MT ERIKA* and *MT PRESTIGE,* raising the issue of oil spills to the highest priority for the EU Community. Recently, POP & C (2003-2006) project aims to address this issue head on by focusing on prevention and operation for both existing and new vessels, which is shown in Figure 1.7.

Figure 1.7: *MT PRESTIGE* accident (left) and clean-up operations after *MT ERIKA* accident (right)

It is an important task to perform a thorough safety analysis of a ship hull. A number of catastrophic basic events, of which only a few are mentioned above, need to be identified and analysed. It is one of the objectives of the present thesis to contribute to the safety analysis of ship hulls by addressing the event of hull girder collapse caused by collision accidental loading.

1.2 Motivation

In an emergency situation at sea, the course of best action to save crew, cargo, and ship, while protecting the marine environment, may not immediately be obvious. Time wasted or an ill-informed decision made, could cause irretrievable damage.

Hence, precise technical information about the ship and its damage condition will be of paramount importance in restraining the crisis.

Collision, grounding, fire and explosion, all presents extreme crisis situations for vessels damaged stability and damaged strength is essential before decision are taken about transferring cargo or initiating other remedial actions to salvage the vessel. Thus, using a computer model of the vessel, which will allow rapid calculation of damaged stability, damage strength will render the possibility of determining how the vessel will respond under various rescue option. Further, pre-analyses of likely emergency scenarios are advisable to keep on the vessel for ready reference during a crisis when human stress factors and time limitations might impair crew actions. This preparation is part of standard crisis management planning required by MARPOL 73/78 and OPA 90 (Oil Pollution Act of 1990, USA, 1990).

Hence, it is of interest to develop an efficient computer code suitable for repeated structural analyses of intact as well as especially damaged ship structures with different stages of initial imperfections and corrosion, where possible crack propagation is taken into account.

It is important that the underlying ultimate strength analyses can be performed fast and effective. Just as it is the requirement in the case of emergency scenarios. This observation is substantiated by current efforts by e.g. Paik *et al.* (1998), Paik & Pedersen (1996) and Paik & Mansour (1995) where a simple formulation for the evaluation for the evaluation of the ultimate strength is applied to predict the residual strength of e.g. collided ship hulls.

1.3 Objectives and Scope of Work

The whole objective is to establish the variety of local and global failure modes that in combination determine the overall ultimate longitudinal bending strength of ship hulls, both in new, aged and damaged conditions, where fracture mechanics of ships with large damage openings are investigated in great detail. Then, to verify the

accuracy of the procedure against available experimental results and by comparison with non-linear finite element method. To meet this objective essentially requires five sub-tasks to be completed. Hence, the scope of the work to be performed becomes

- A study of literature for the available methods usable to evaluate the ultimate and post-ultimate capacity of the stiffened plates.
- Developing the new simple design equations for predicting the ultimate strength of stiffened plates with imperfections in the form of imperfections, where a non-linear finite element method is employed on a wide range of typical ship panel geometries. The new simplified analytical method must be generalized to deal with such combined load cases. The performance of the proposed equations must be also verified by experimental results.
- Establishing a rapid computer code based on simplified formulas developed for calculation of the ultimate capacity of the hull girder. This program must be capable of considering initial imperfections and must be compared with other theoretical approaches developed.
- The influence of the coupled bending moment on the intact & damaged ship structures must be extensively investigated. The rational interaction equations must be developed, which based on the extensive ship types.
- Accidents such as collision, grounding and explosions occur and can have major consequences to the shipstructure. The effect of such large damages on the hull girder must be assessed under time pressure. The recent accident with the PRESTIGE shows the importance of being able to reliably assess the longitudinal strength of damaged vessels. The procedures for this must be developed. A major drawback is lack of knowledge of the failure mechanism that may play a role in such circumstances. Therefore, the fracture mechanism of damaged ships is essential. Key effects must be identified and if possible, included in the procedure.

When these five points have been addressed, and the objectives solved, all that is needed for the development of a computer code for the ultimate strength. The

remaining final task will thus to be benchmark the code against available experimental results and other theoretical methods.

1.4 Organization of the Thesis

The thesis is compiled as follows: Chapter 2 develops the new simple design equations for predicting the ultimate strength of stiffened plates with imperfections in the form of welding-induced residual stress and geometric deflections. A non-linear finite element method is used to investigate on 60 ANSYS elastic-plastic buckling analyses of a wide range of typical ship panel geometries. Reduction factors of the ultimate strength are produced from the results of 60 ANSYS inelastic finite element analyses. The proposed design equations have been developed based on these reduction factors. For the real ship structural stiffened plates, the most general loading case is a combination of longitudinal stress, transverse stress, shear stress and lateral pressure. The new simplified analytical method is generalized to deal with such combined load cases. Comparisons indicate that the adopted method has sufficient accuracy for practical applications in ship design.

Chapter 3 continues to investigate the performance of the proposed method as applied to 60 ANSYS elastic-plastic non-linear buckling analyses of wide range typical ship panel geometries using test data and related numerical results pertaining to an extensive series of mechanical tests performed and reported Smith (1976,1992) and Tanaka & Endo (1988).

In Chapter 4 hull girder ultimate strength on five ISSC benchmark vessels is analysed by using proposed formulas, where a computer code NEPTUNE is developed. The moment – curvature curve and the ultimate bending moment at ultimate state are calculated with initial imperfections in the form of geometric deflection and welding – induced residual stresses for both hogging and sagging cases subject to vertical bending. The effect of corrosion damage is also assessed by sensitivity study on the influence of plate and stiffener thickness on the hull girder

ultimate capacity. The accuracy of adopted procedure is examined by seven different methods on the examples used in the benchmark calculations.

Chapter 5 presents the most extensive investigation of the hull girder ultimate strength under coupled bending moment. The main objective is to develop hull girder ultimate strength interaction relationships useful for the ship designs subject to a combination of vertical and horizontal bending moments, where the ordinary Smith's method is employed using a developed computer code NEPTUNE with average stress – average strain relationship of element. The procedure adopted is applied to analyse on the seventeen ships such as nine tankers, five bulk carriers, one general cargo and two container vessels. The findings obtained are used to develop a rapid procedure for the assessment of the ultimate capacity of the hull girder. The interaction expressions proposed by other researchers are also addressed to discuss simple equations presented by this thesis.

Chapter 6 presents a new procedure capable of considering damage effect properly on the ultimate strength capacity using a combination of LS-DYNA explicit FE and ANSYS implicit FE codes. When Smith & Dow's method is applied to damaged ships, the damaged part of the ship is normally assumed being fully cut off. This simplified way to consider the effects of damage may be quite conservative. To investigate the accuracy of Smith & Dow's method in this case, explicit-to-implicit sequential finite element solution is used to predict the ultimate strength of the hull girder with the extent of damage determined.

Chapter 7 investigates the collision resistance and residual strength subject to collision damage of single side skin (SSS) and double side skin (DSS) bulk carriers. The impact dynamics analyses are conducted by means of a non-linear explicit finite element code, ANSYS LS-DYNA for the evaluation resistance forces, energy absorption and penetration depth for various collision scenarios. The struck vessels of Capsize SSS and DSS designs are assumed to be entirely standstill and the striking vessels of an Aframax type oil tanker with different bulbous bow shapes are modelled as rigid bodies. The numerical procedure adopted, findings are compared.

Chapter 8 mainly focuses on developing a procedure how to take into account fracture assessment on damaged marine structures using elastic-plastic fracture mechanics (EPFM), where extensive non-linear finite element analyses are performed. The models developed in this research are aimed at predicting the growth of cracks after they become through-thickness cracks, and investigating effect of residual stresses, damage extent, structural arrangement, sea states, and redundancy on the crack growth.

Finally, conclusions from the present study and recommendations for future work are offered in Chapter 9.

To further facilitate the reading of this thesis, a selected topic is presented in appendix part. Appendix A that explains the theory of the basics of the non-linear finite element method.

Chapter 2

Buckling and Ultimate Strength Behaviour of Stiffened Plates

2.1 Introduction

Stiffened plates is the main structural building block in ship hulls and their structural response subject to combined loads is a topic of significant practical interest in ship design. Figure 2.1 shows an example of such construction where the stiffened plate spans between girders.

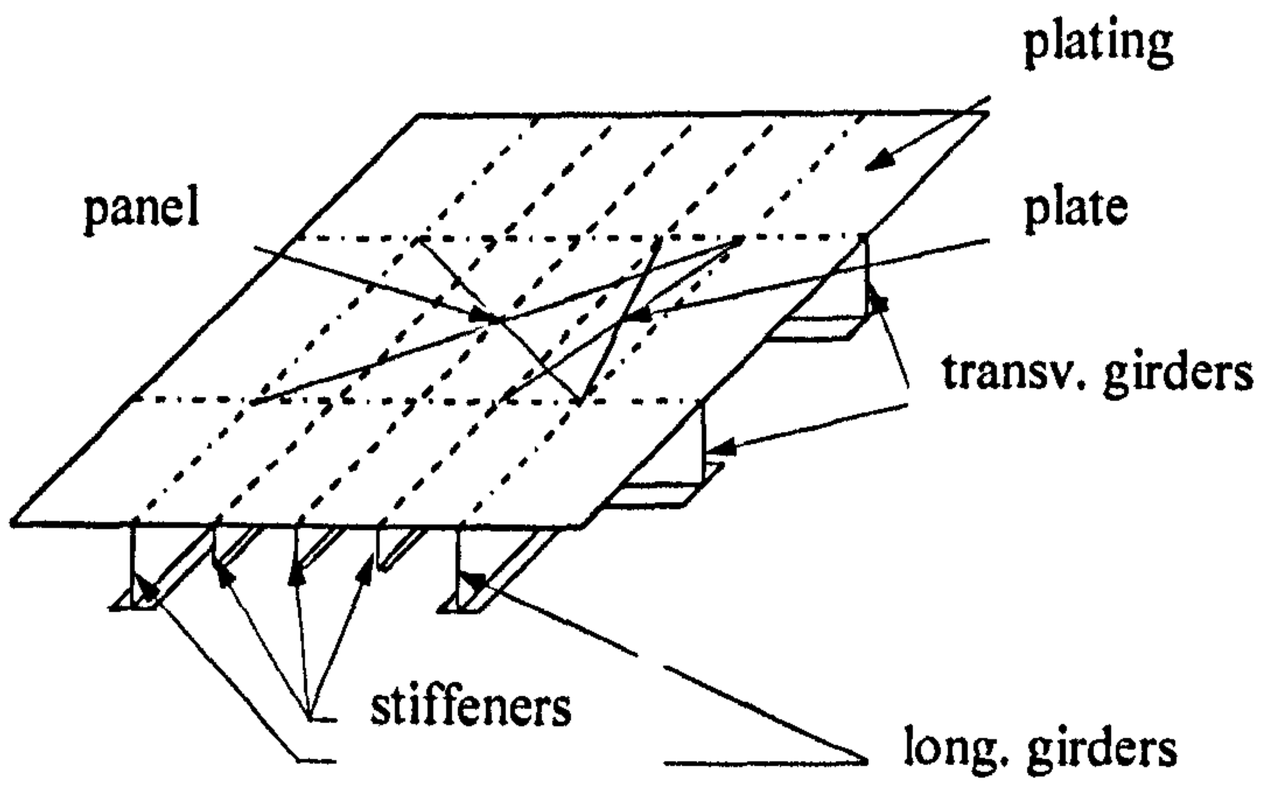

Figure 2.1: A stiffened steel plate in ship hull

Since the overall failure of a ship hull is normally governed by buckling and plastic collapse of the deck, bottom and sometimes the side shell stiffened plates, it is of importance to accurately calculate the ultimate strength of stiffened panels in deck, bottom and side shell in order to achieve a more advanced structural design of ships.

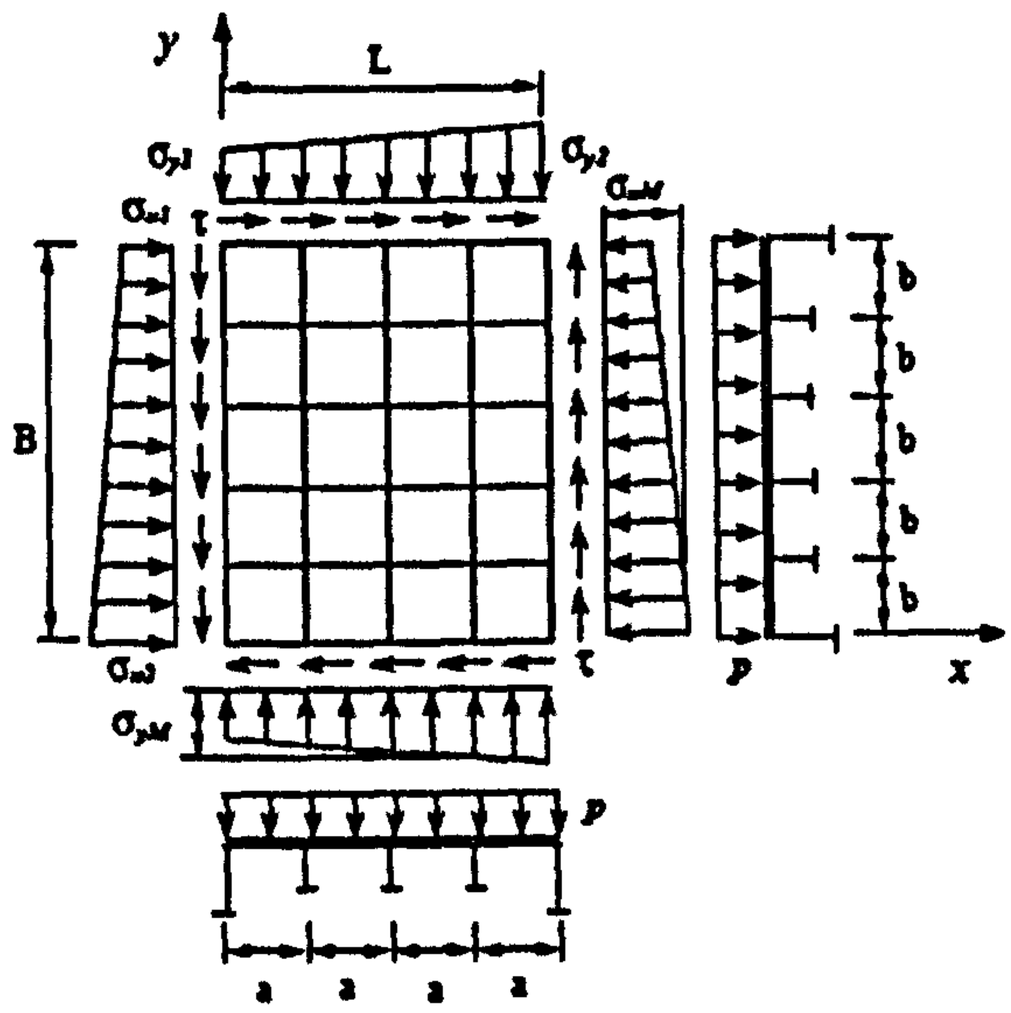

Figure 2.2: A cross-stiffened panel under combine in plane and lateral pressure loads Paik & Thayamballi (2003)

A stiffened panel in ships is generally subjected to combined in plane and lateral pressure loads, as shown in Figure 2.2. Loads are mainly induced by overall hull girder bending and/or torsion, ballast / seawater and cargo. Combined loads on a panel can be biaxial compression / tension, biaxial in-plane bending, edge shear and lateral pressure. These load components are not always applied simultaneously, but more than one normally exist and interact. Therefore, the strength formulations need to account for combined load effects.

The ultimate strength of ship plates is very important from the design and safety viewpoint because the collapse loads of plates can often act as an indicator of the ultimate strength of the whole stiffened panel in ship structures (Soares, 1992). The problem has been addressed for centuries for the general plated structures and for several decades even with regard to ship structures (Ueda & Tall, 1967; Mansour,

1971). The methods which have been proposed can be divided into: (1) finite element method, (2) experiments, (3) empirical formulae which are based on either on numerical or experimental results and (4) analytical or semi-analytical approaches. While most of the researchers studied on longitudinal compression only, some of them did consider the combined load cases (Steen & Valsgard, 1984; Fujikubo *et al.* 1999), but they used empirical approaches based on FE or experiment results.

Precise modelling of stiffened panels can be achieved by means of analysis tools and computing power. Initial imperfections such as welding induced residual stress and initial deflections of the cross section can be explicitly incorporated into numerical models. In a series of studies, Grondin *et al.* (1998, 1999) have considered the behaviour of structural elements under axial compression, both experimentally and numerically. The goal of that study was to investigate the tripping failure mode and validate with experiments, a sophisticated non-linear finite element model that would allow a more extensive study of the behaviour to be conducted numerically.

Many simplified design methods to predict the ultimate strength of stiffened have been improved, considering one or more of the failure modes. Some of those methods have been addressed by the ISSC technical committee III.1 on the ultimate hull girder strength (ISSC 2000).

Sheikh *et al.* (2003) have studied the stability of steel stiffened plates of T – shape section under uniaxial compression and combined uniaxial compression and bending using FEM analysis. A compression of numerical analysis results with API and DNV design guidelines indicates that the guidelines lack the potential interaction – buckling phenomenon between various failure modes i.e. plate, stiffener or overall buckling, which can cause a sudden loss of capacity.

Dunbar *et al.* (2004) have addressed the influence of local corrosion on stability of a plate and then on a combination of plates forming a stiffened panel. Local corrosion was applied to a stiffened panel with typical residual stress and initial

deflection values. A finite element model was verified through comparison to an experimental model, followed by the creation of several models with local corrosion.

Hughes *et al.* (2004) derived modifed expressions for elastic local plate buckling and overall panel buckling expressions form 55 Abaqus eigenvalue buckling analyses. Inelastic RISK analysis for the ulimate collapse stress and post collapse behaviour using Abaqus FEM was conducted on their models. Ultimate stress was also calculated using Orthotropic methods. It was found that for panels having crossover proportions, Orthotropic based methods are unsatisfactory.

Steen *et al.* (2004) have performed a direct calculation model (PULS) for determination of ultimate capacity of stiffened panels was developed using energy principles and non-linear plate theory according to Marguerre and Von Karman. Extensive verifications were conducted by means of more advanced numerical programs were found. This code is also recognized by ABS and Lloyds and is available advanced analysis method in the Joint Tanker Project (JTP) launched by ABS/DNV/Lloyds since January 2004.

Paik & Thayamballi (2003) categorized the primary modes of overall failure for a stiffened panel subject to predominantly compressive loads into the following six types, namely:

- Mode I: Overall (grillage) buckling collapse, see Figure 2.3(a-b)
- Mode II: Plate induced failure yielding at corners of plating between stiffeners, see Figure 2.3(c)
- Mode III: Plate induced failure yielding of the plate-stiffener combination at mid-span, see Figure 2.3(d)
- Mode IV: Stiffener induced failure local buckling of stiffener web, see Figure 2.3(e)
- Mode V: Stiffener induced failure –tripping of stiffener, see Figure 2.3(f), and
- Mode VI: Gross yielding.

Mode I typically represents the collapse pattern when the stiffeners are relatively weak. In this case, the stiffeners can buckle together with plating, the overall (grillage) buckling behaviour initially remaining elastic. The stiffened panel can normally sustain further loading even after overall (grillage) buckling in the elastic regime occurs and the ultimate strength is eventually reached by formation of a large yield region inside the panel and/or along the panel edges. In mode I, the stiffened panel may be considered to behave as an 'orthotropic plate'.

Mode II represents the collapse pattern wherein the panel collapses by yielding along the plate-stiffener intersection at panel edges, with no stiffener failure. This type of collapse can be important in some cases when the panel is predominantly subjected to biaxial compressive loads. Mode III indicates a failure pattern in which the ultimate strength is reached by plate induced failure of the plate-stiffener combination due to yielding at mid-span.

Mode IV and V failures typically arise from the stiffener induced failure when the ratio of stiffener web height to stiffener web thickness is large and/or when the type of the stiffener flange is inadequate to remain straight so that the stiffener web buckles or twist sideways. Mode V can occur when the ultimate strength is reached subsequent to lateral-torsional buckling (also called tripping) of stiffeners, while Mode IV represents a failure pattern in which the panel collapses by local compressive buckling of the stiffener web.

Mode VI typically takes place when the panel slenderness is very small (i.e., the panel is very stocky) and/or when the panel is predominantly subjected to the axial tensile loading so that neither local nor overall (grillage) buckling occurs until the panel cross section yields entirely.

The collapse of stiffened panels is usually postulated to take place at the lowest value among the various ultimate loads calculated for each of the above collapse patterns.

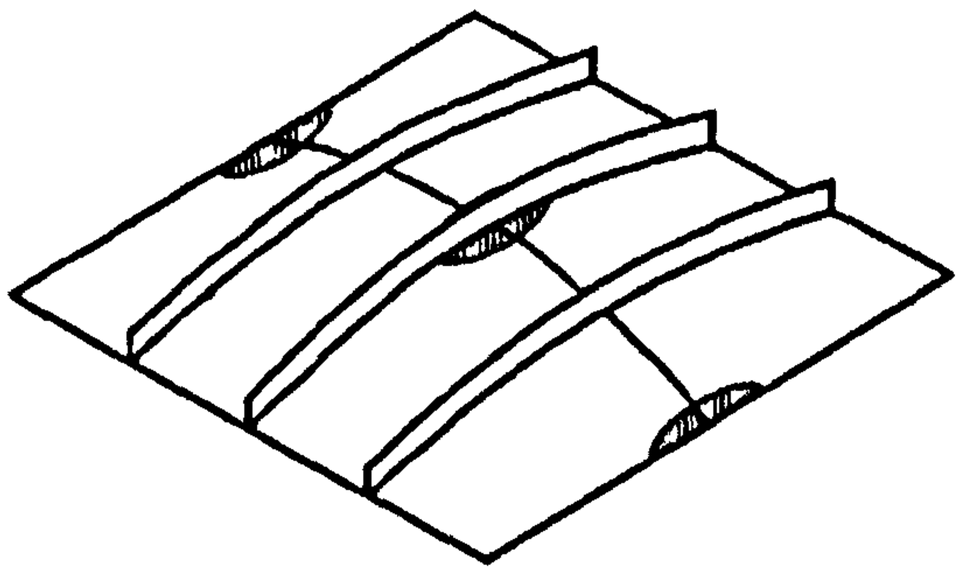

Figure 2.3(a): Mode I-1: Overall collapse of an unaxially stiffened panel (Paik & Thayamballi, 2003)

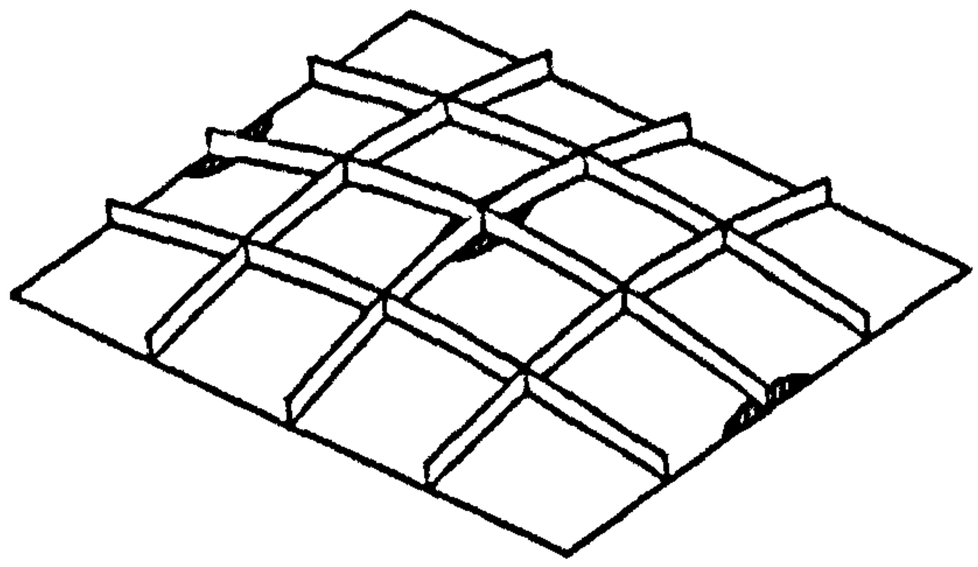

Figure 2.3(b): Mode I-2: Overall collapse of a cross stiffened panel (Paik & Thayamballi, 2003)

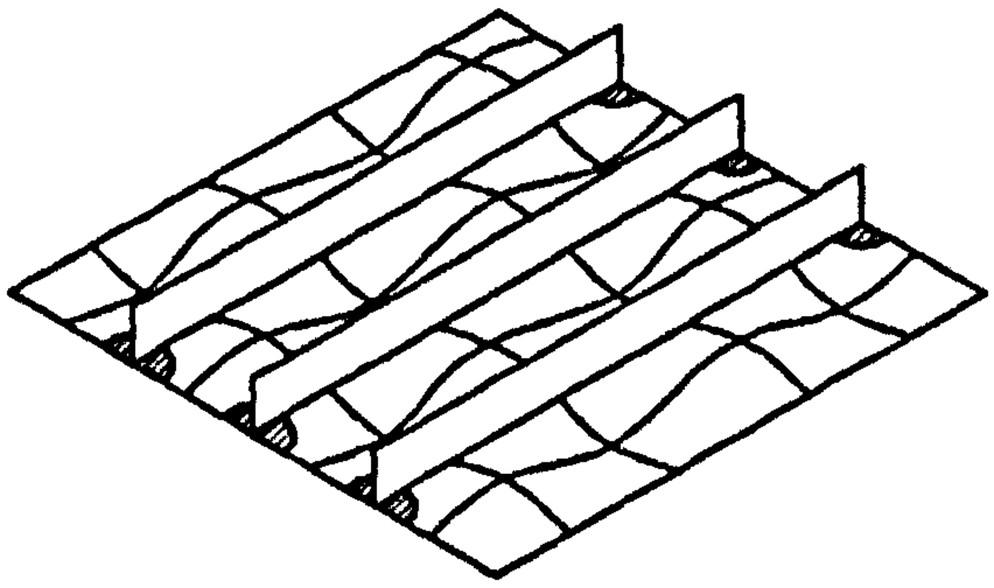

Figure 2.3(c): Mode II: Plate induced failure –yielding at the corners of plating between stiffeners (Paik & Thayamballi, 2003)

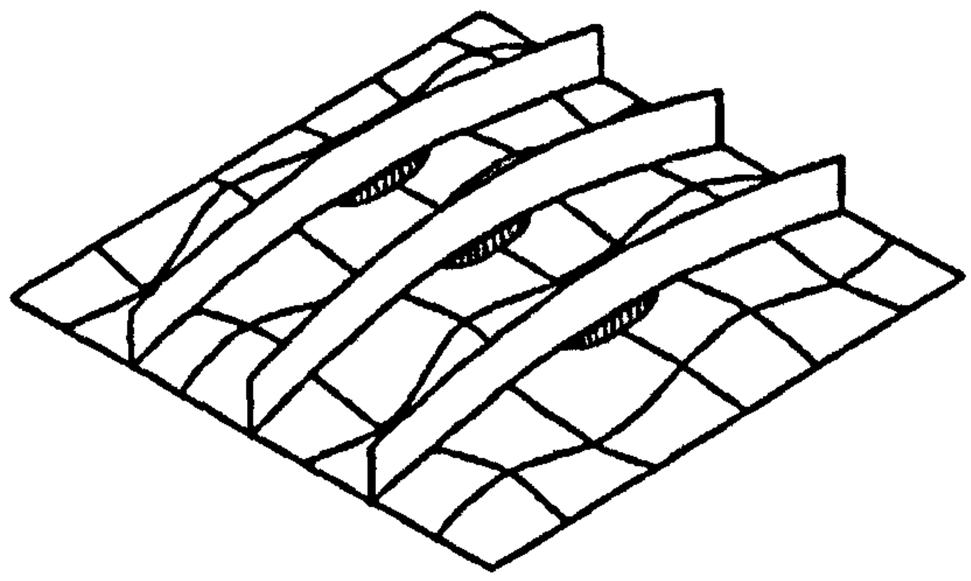

Figure 2.3(d): Mode III: Plate induced failure –yielding of plate – stiffener combination at mid – span (Paik & Thayamballi, 2003)

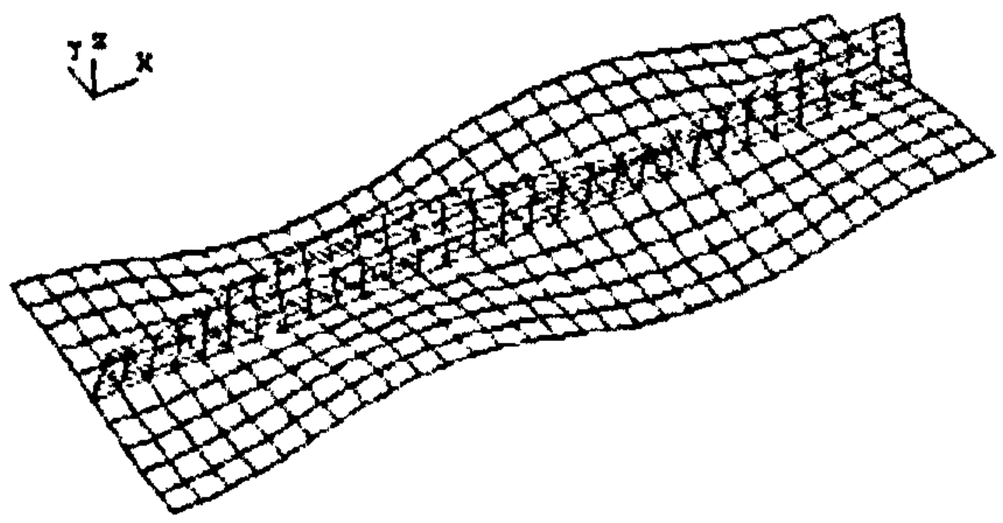

Figure 2.3(e): Mode IV: Stiffener induced failure –local buckling of the stiffener web (Paik & Thayamballi, 2003)

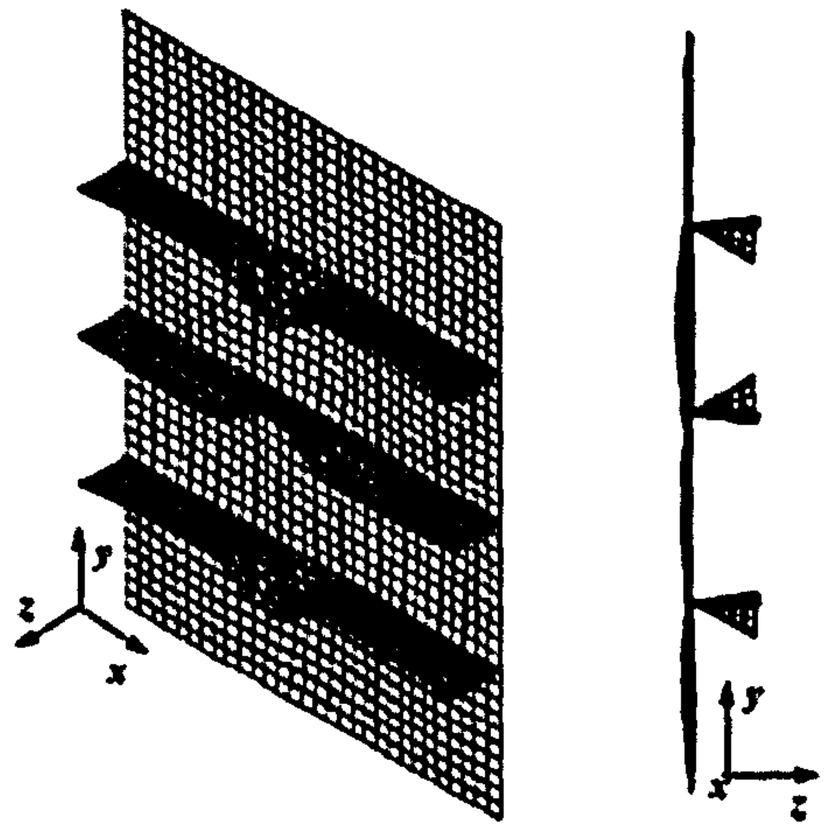

Figure 2.3(f): Mode V: Stiffener induced failure –lateral-torsional buckling of stiffener (Paik & Thayamballi, 2003)

While several methods deal with a condition of combined loading with two or more load components, most of them are limited to the application of a single load

component such as uniaxial compression. However, since the stiffened panels in marine structures are normally subjected to combined loads including in-plane and lateral pressure loads, it is of crucial importance to establish stiffened panel ultimate strength design formulations taking into account combined loading effects. It is perhaps in his area that this study has some major contributions when compared with other existing methods.

One major theoretical method used for predicting the ultimate strength of stiffened panels is the so-called plate stiffener combination approach (also called beam-column approach), which will be used in this study as well. This approach uses a representative plate-stiffener combination to represent the behaviour of a stiffened panel since the spacing of stiffeners is normally the same in each direction. Various column strength formulations have been used as the basis of such approaches. Three common types are:

- Johnson – Ostenfeld formulation
- Perry – Robertson formulation
- An empirical formulation obtained by curve fitting experimental or numerical data.

A stocky panel that has a high value of computed elastic buckling strength will not buckle in elastic domain, but will actually reach the ultimate strength with a certain degree of plasticity. In the most design rules of classification societies, the Johnson – Ostenfeld formulation is used to account for this behaviour, which is given by:

$$\sigma_C = \begin{cases} \sigma_E \quad for \quad \sigma_E \le 0.5\sigma_o \\ 1 - \dfrac{\sigma_o}{4\sigma_E} \quad for \quad \sigma_E > 0.5\sigma_o \end{cases} \tag{2.1}$$

Where σ_C is critical stress in MPa, σ_o is yield stress of element, and σ_E is Euler column buckling stress, which can be taken as $\sigma_E = \frac{\sigma_o}{\lambda^2}$ for a plate-stiffener combination pin-joined at both ends under axial compression. In ship rules from different sources (e.g., ABS 2000), the above equation may appear with somewhat different constants depending on the structural proportional limit value assumed; the above form assumes a structural proportional limit of 50% of the applicable yield value.

The Perry – Robertson formulation assumes that the stiffener with associated plating will collapse as a 'beam - column' when the maximum compressive stress in the extreme fiber reaches the yield strength of the material. The two possible collapse modes for the Perry – Robertson formulation are usually considered depending on the failure of the most highly stressed fiber, i.e., 'plate induced failure', and 'stiffener induced failure'. The plate induced failure mode is related to yielding of associated plating due to compression. The stiffener induced failure mode may result from either yielding of the extreme stiffener fiber (without rotation of stiffener) or tripping of stiffener (with rotation of stiffener). For a pin-ended plate stiffener combination under axial compression in the x direction, the Perry – Robertson formulae accounting for the effect of initial deflection (without either local buckling or tripping of stiffener) may be given with compression taken as positive, as follows (Paik & Thayamballi, 2003).

$$\frac{\sigma_u}{\sigma_{ox}} = \frac{1}{2}\left(1+\frac{1+\eta}{\lambda^2}\right) - \left[\frac{1}{4}\left(1+\frac{1+\eta}{\lambda^2}\right)^2 - \frac{1}{\lambda^2}\right]^{0.5} \tag{2.2}$$

where $\eta = \frac{w_{osx} z_c}{k^2}$ is initial deflection related parameter, z_c is distance from the neutral axis to the extreme fiber, which may be taken as $z_c = z_{px} + 0.5t$ for the plate induced failure or $z_c = z_{fx} + 0.5t_{fx}$ for the stiffener induced failure.

In empirical approaches, the ultimate strength formulations are developed by curve fitting based on mechanical collapse test results or numerical solutions. These types of empirical formulae can often be cast as simple closed-form expressions, which have certain advantages including getting quick first-cut estimates, while their use may be restricted to a specified range of dimensions or be subject to other limitations.

While a vast number of empirical formulations for ultimate strength of simple beams in steel framed structures have been developed (e.g., CRC, 1971; Chen & Atsuta; 1976; among others), relevant empirical formulae for plate-stiffener combination models are also available. As an example of the latter type, Paik & Thayamballi (1997, 2003) developed empirical formulae for predicting the ultimate strength of a plate-stiffener combination under axial compression in terms of both column and plate slenderness ratios, based on existing mechanical collapse test data for the ultimate strength of stiffened panels under axial compression and with initial imperfections at an 'average level'.

Since the ultimate strength of columns must be less than the elastic column buckling strength, the Paik – Thayamballi empirical formulae for a plate – stiffener combination in the x direction is given by Paik & Thayamballi (2003).

$$\frac{\sigma_u}{\sigma_{ox}} = \frac{1}{\sqrt{0.995 + 0.936\lambda^2 + 0.170\beta^2 + 0.188\lambda^2\beta^2 - 0.067\lambda^4}} \le \frac{1}{\lambda^2} \qquad (2.3)$$

where λ is determined for the plate-stiffener combination with full cross – section (i.e., without considering the effective width of attached plating). In contrast Equations (2.1) or (2.2) refer to the effective cross-section.

Figure 2.4 compares the Johnson – Ostenfeld formulae, the Perry – Robertson formulae and the Paik – Thayamballi empirical formulae for the column ultimate strength for a plate – stiffener combination varying the column slenderness ratios, with selected initial eccentricity and plate slenderness ratios. In usage of the Perry –

Robertson formulae, the lower strength as obtained from either plate induced failure or stiffener-induced failure was adopted. λ of Equation (2.3) was determined for the same plate-stiffener combination, i.e., with effective cross-section, because of convenience in this comparison.

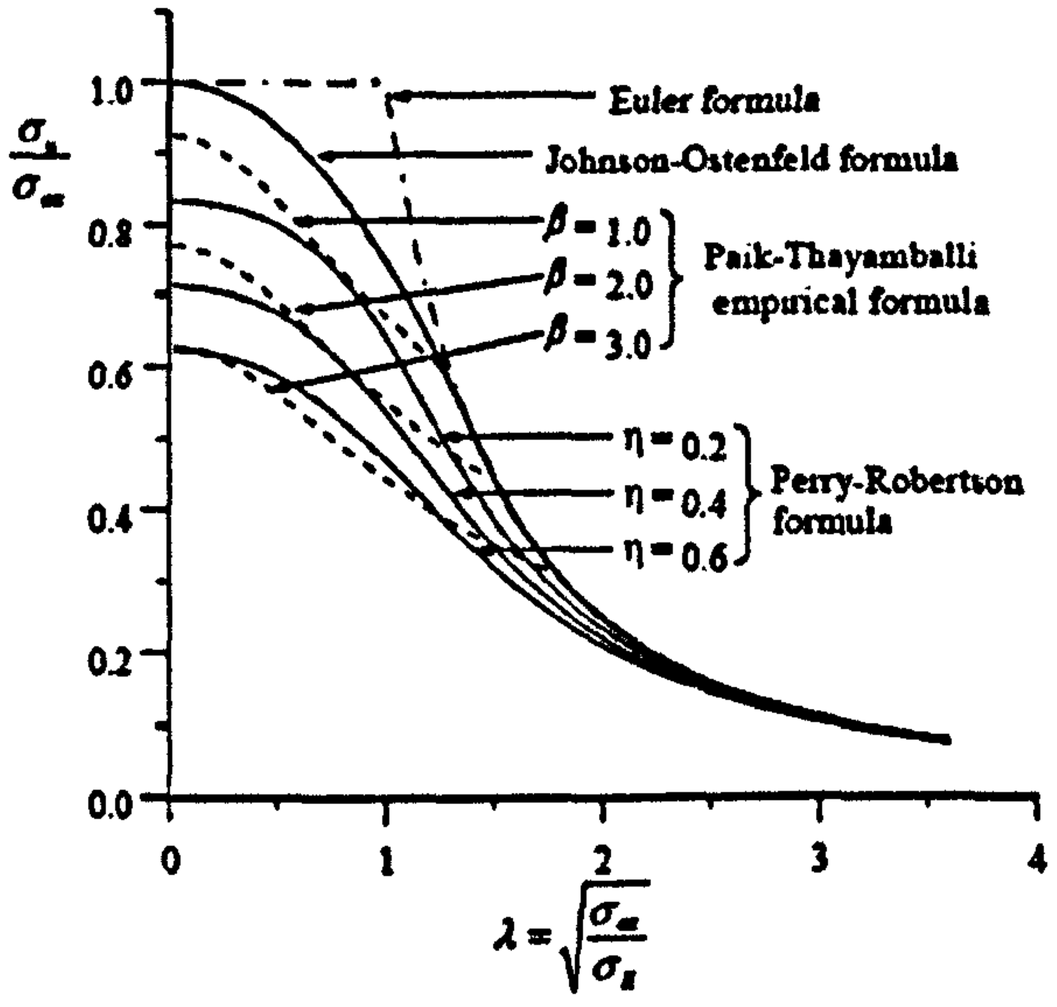

Figure 2.4: A comparison of the ultimate strength formulations for the plate-stiffener combinations under axial compression (Paik & Thayamballi, 2003)

While the Perry – Robertson and empirical formulations are not directly employed in this study, the Johnson – Ostenfeld formulae is utilised for the computation of the panel ultimate strength based on the behaviour of Modes III, IV and V.

Any method for the prediction of the stiffened panel ultimate strength has its own level of accuracy. Except for inherent variability in the structural properties and phenomena involved, the following four aspects are the primary reasons for such differences.

- Collapse modes that need to be considered, and their interactions,
- Differences in treatment of the effective width of plating,
- Consideration of post-weld initial imperfections, and

- Consideration of the rotational restraints between plating and stiffeners and /or between stiffener web and flange.

First, not all theoretically possible collapse modes are usually considered in the development of any particular design oriented strength prediction method.

Second, it is important to accurately predict the effective width of plating in calculating the effective cross-sectional area of a plate-stiffener combination. As the compressive loads increase, the effective width of the buckled plating would vary because it is a function of the applied compressive stress. However, most of simplified methods assume that effective width of plating does not depend on the applied compressive loads, the ultimate effective width of plating being used instead as a convenient 'constant'.

Third, initial deflections and welding induced residual stress are not always treated as parameters of influence in the development of the method. Most methods take into account the influence of initial imperfections for the plating between stiffeners, but only some of them include the initial imperfection effect for the stiffener.

Finally, the stiffener has some rotational restraints at its line of attachment to the plating and/or along the stiffener web-flange intersection. Such restraint affects the failure of stiffener, but most methods neglect this effect.

This chapter develops the new simple design equations for predicting the ultimate strength of stiffened plates with imperfections in the form of welding-induced residual stress and geometric deflections. A non-linear finite element method is used to investigate on 60 ANSYS elastic-plastic buckling analyses of a wide range of typical ship panel geometries. Reduction factors of the ultimate strength are produced from the results of 60 ANSYS inelastic finite element analyses. The proposed design equations have been developed based on these reduction factors. For the real ship structural stiffened plates, the most general loading case is a

combination of longitudinal stress, transverse stress, shear stress and lateral pressure. The new simplified analytical method is generalized to deal with such combined load cases. Comparisons indicate that the adopted method has sufficient accuracy for practical applications in ship design.

2.2 Imperfections of Stiffened Plates

Steel structures are typically fabricated by flame cutting and welding, and thus initial imperfections in the form of initial distortions and residual stresses may develop and will reduce the collapse capacity. Therefore, these initial imperfections should be included in structural design as parameters of influence.

When local heating is input to structural steels, the heated part will expand, but because of adjacent cold parts it will be subjected to compressive stress and distortion. When the heated part is cooled down, it will be locally shrunk rather than revert to its initial shape and thus now be subjected to tensile stress. (Paik *et al.* 2001).

Approximate methods based on the insights from measurements are usually adopted for design purposes because of the complexity of the phenomena involved, while some efforts have been performed to estimate the initial imperfections theoretically or numerically (Ueda, 1999; Masubuchi, 1980).

2.2.1 Initial deflections

A number of contributors (Carlsen & Czujko, 1978; Antoniou *et al.* 1984; Ueda & Yao, 1985; Kmiecik *et al.* 1995) previously measured welding-induced initial deflections in merchant ship plating. It is noticed that the initial deflection shapes strongly depend on the aspect ratio of plating as well as material properties and welding condition. According to available measurements, although the geometric configuration of such initial deflection is very complex, a multiwave shape is predominant in the plate length direction. Figure 2.5 shows some selected initial

deflection patterns in the plate length direction, which is based on the measurements of Ueda & Yao (1985).

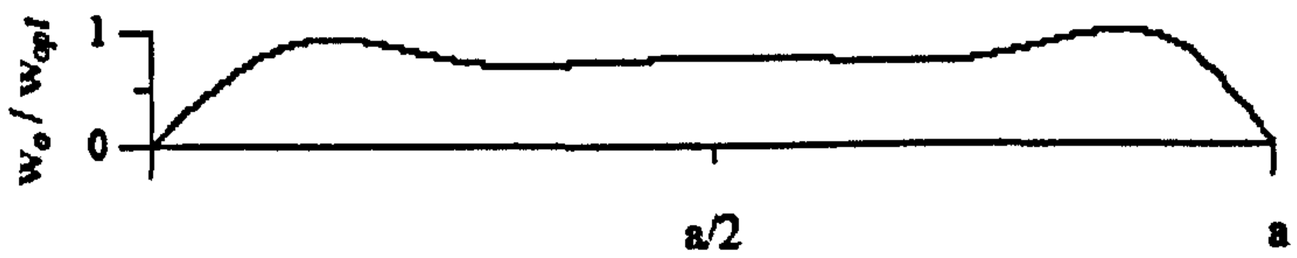

(a) Initial deflection shape 1

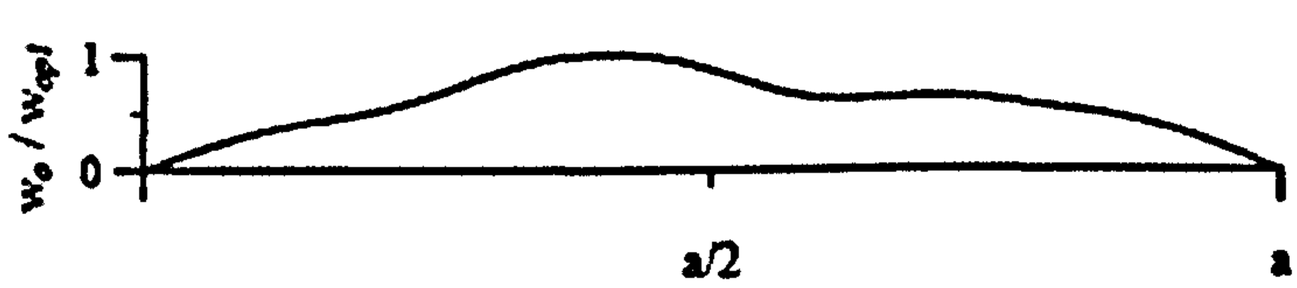

(b) Initial deflection shape 2

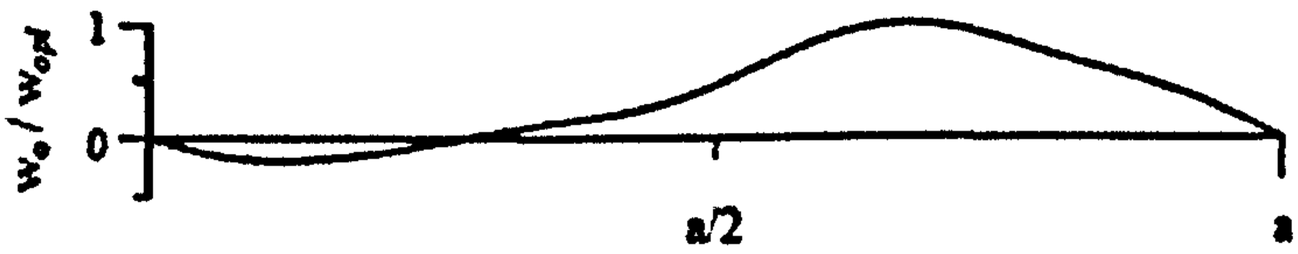

(c) Initial deflection shape 3

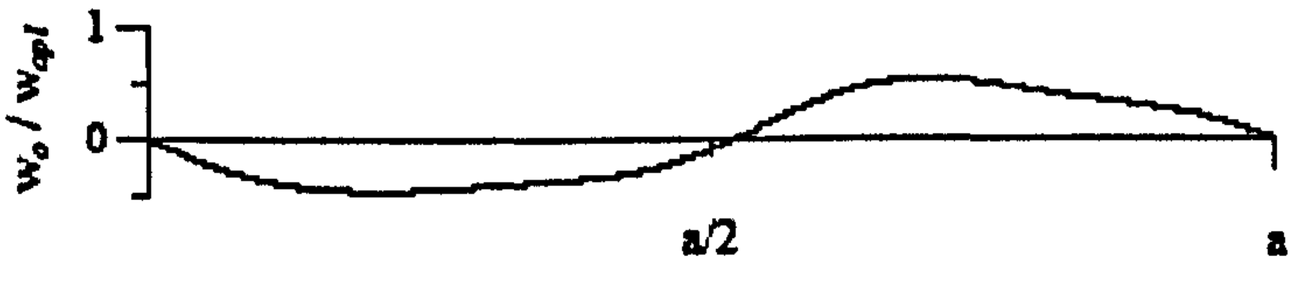

(d) Initial deflection shape 4

Figure 2.5: Some selected initial deflection patterns in steel plating between stiffeners in the plate length direction, based on the measurements of Ueda & Yao (1985)

The insights developed by such measurements support the use of the following mathematical expression for the weld-induced initial deflection of steel plating between stiffeners, namely (Paik *et al.* 2004).

$$\frac{w_o}{w_{opl}} = \sum_{i=1}^{M}\sum_{j=1}^{N} B_{oij} \sin\frac{i\pi x}{a}\sin\frac{j\pi y}{b} \tag{2.4}$$

where B_{oij} indicates the weld-induced initial deflection amplitude normalized by the maximum initial deflection, w_{opl} , which can be determined based on the initial

deflection measurements. The subscripts, i and j, denote the corresponding half wave numbers in the x (longitudinal) and y (transverse) directions.

If measured data for the initial deflection for plating are available, the initial deflection amplitudes of Equation (2.4) can be determined by expanding equation (2.4) approximately using a selected number of terms, M and N, depending on the complexity of the initial deflection shape. Although a two or more –wave shape of initial deflection is sometimes found in the plate breadth direction of some plates, it is often simplified to one half wave in the short direction in case of relatively long plating, as shown in Figure 2.6. For a long plate element with a multiwave shape in the x direction and one half wave in the y direction, therefore, Equation (2.4) would be simplified as follows,

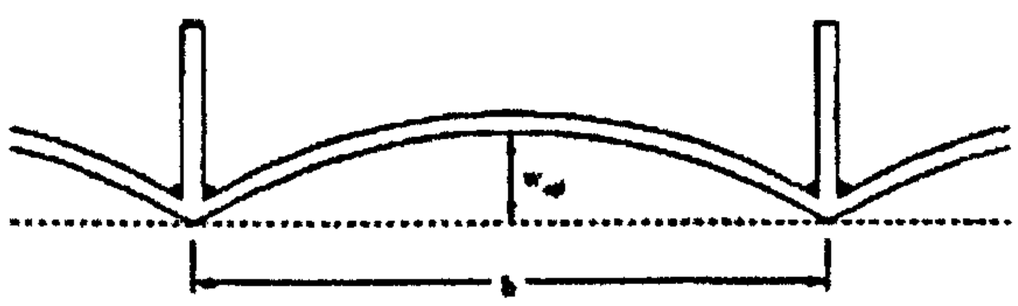

Figure 2.6: A simplified initial deflection pattern in steel plating between stiffeners in the plate breadth direction

$$\frac{w_0}{w_{0pl}} = \sum_{i=1}^{M} B_{oi} \sin\frac{i\pi x}{a} \sin\frac{\pi y}{b} \tag{2.5}$$

In practice, M in Equation (2.5) may be taken as an integer that corresponds to about three or more times the a/b ratio greater than 1 (Paik & Pedersen). On this basis, B_{oi} of equation (2.5) can be determined for the assumed M if the initial deflection measurements are available. The values of coefficients, B_{oi}, for the plate initial deflection shapes shown in Figure 2.5 are given in Table 2.1, by taking $M = 11$, for instance, because the aspect ratio of plating considered in Figure 2.5. was about 3.0.

It has been recognized that for the plates under predominantly longitudinal axis compressive loads, the deflection term associated with the lowest bifurcation mode plays a dominant role in elastic large deflection response (Paik & Pedersen, 1996). For the purposes of theoretical ultimate strength prediction where the plate deflection itself is not of primary interest, therefore, the initial deflection function, that is, Equation (2.5), is often simplified by including only the buckling mode initial deflection components as follows,

$$\frac{w_o}{w_{opl}} = B_{om} \sin\frac{m\pi x}{a} \sin\frac{\pi y}{b} \tag{2.6}$$

where B_{om} is buckling mode initial deflection component, that is, $B_{om} = B_{oi}$ for $i = m$ in Equation (2.5), and $m =$ buckling mode half wave number in the x (longitudinal) direction. For pessimistic evaluation of the plate ultimate strength, however, $B_{om} = 1.0$ is sometimes adopted no matter what the actual initial deflection shape may be.

Table 2.1: Initial deflection amplitudes for various initial deflection shapes based on Figure 2.5 (Paik & Pedersen, 1996)

Coefficients	Initial deflection shape 1	Initial deflection shape 2	Initial deflection shape 3	Initial deflection shape 4
B_{o1}	1.0	0.8807	0.5500	0.0
B_{o2}	-0.0235	0.0643	-0.4966	-0.4966
B_{o3}	0.3837	0.0344	0.0021	0.0021
B_{o4}	-0.0259	-0.1056	0.0213	0.0213
B_{o5}	0.2127	0.0183	-0.0600	-0.0600
B_{o6}	-0.0371	0.0480	-0.0403	-0.0403
B_{o7}	0.0478	0.0150	0.0228	0.0228
B_{o8}	-0.0201	-0.0101	-0.0089	-0.0089
B_{o9}	0.0010	0.0082	-0.0010	-0.0010
B_{o10}	-0.0090	0.0001	-0.0057	-0.0057
B_{o11}	0.0005	-0.0103	-0.0007	-0.0007

The initial deflection amplitudes may be approximately defined by assuming an appropriate initial deflection configuration when relevant initial deflection measurements are not available. For this purpose, some empirical formulations of the maximum plate initial deflection are relevant for steel plates between stiffeners, namely:

- Faulkner (1975):

$$\frac{w_{opl}}{t} = \begin{cases} k\beta^2 (t_w / t) & for\ t_w < t \\ k\beta^2 & for\ t_w \geq t \end{cases} \tag{2.7}$$

where $\beta = (b/t)\sqrt{(\sigma_o / E)}$, b is plate breadth between stiffeners, t is plate thickness, E is Young's modulus, σ_o is material yield stress, t_w is thickness of stiffener web, k is coefficient which may be in the range 0.05-0.15 for marine structures and less than 0.1 for land-based structures. Faulkner (1975) adopted for his sample calculations $k = 0.12$ for $\beta \leq 3$ and $k = 0.15$ for $\beta > 3$, while Antoniou (1980) suggested $k = 0.091$ for $t_w < t$ and $k = 0.0628$ for $t_w \geq t$.

- Carlsen & Czujko (1978):

$$\frac{w_{opl}}{t} = 0.016\frac{b}{t} - 0.36 \quad \text{for } \frac{b}{t} > 40 \tag{2.8}$$

- Antoniou (1980) (modified Carlsen & Czujko's formula):

$$\frac{w_{opl}}{t} = \begin{cases} 0.018b/t - 0.55 & for\ t \leq 14\,mm \\ 0.014b/t - 0.32 & for\ t > 14\ mm \end{cases} \tag{2.9}$$

- Smith *et al.* (1988):

$$\frac{w_{opl}}{t} = \begin{cases} 0.025\beta^2 & for\ slight\ level \\ 0.1\beta^2 & for\ average\ level \\ 0.3\beta^2 & for\ serious\ level \end{cases} \tag{2.10}$$

- Masaoka (1996):

$$\frac{w_{opl}}{t} = k\left(\frac{b}{t}\right)^2 \tag{2.11}$$

where k is coefficient, which may be taken as 8×10^{-5} for merchant ship structures.

Classification societies or other regulatory bodies specify construction tolerances of strength members as related to the maximum initial deflection with the intention that the initial distortions in the fabricated structure must be less than the corresponding specified values. Some examples of the limit for the maximum plate initial deflection are as follow:

- Det Norske Veritas (DNV):

$$\frac{w_{opl}}{b} \leq 0.01 \tag{2.12}$$

where b is as defined in Equation (2.7).

- Shipbuilding quality standards of Germany and Japan:

$$w_{opl} \leq 7 \text{ mm for bottom plate}$$
$$w_{opl} \leq 6 \text{ mm for deck plate} \tag{2.13}$$

- Steel box girder bridge quality standards of the UK:

$$w_{opl} \leq \min\left(\frac{t}{6}+2, \frac{t}{3}\right),\ t \text{ in mm} \tag{2.14}$$

2.2.2 Welding-induced residual stress

Two types of residual stresses exist in a ship structures such as mechanical stresses, which are introduced through construction sequencing and welding-induced residual stresses. There is an intimate relationship between mechanical residual stress and welding-induced residual stress, the first often affected by welding distortion. Welding residual stress arises from heat introduced by the welding process. The heat input used for the welding process as well as the sequence at which the stiffeners are welded to the plates can have a great influence on the distribution of residual stresses in the plate. High tensile residual stresses exist in the vicinity of the stiffener-to-plate weld, while compressive residual stresses exist between the stiffeners.

For practical design purposes, the welding-induced residual stress distributions of a plate element between support members for which welding has been carried out along its four edges may be idealized to be composed of tensile and compressive stress blocks as shown in Figure 2.7 (Paik & Thayamballi, 2003).

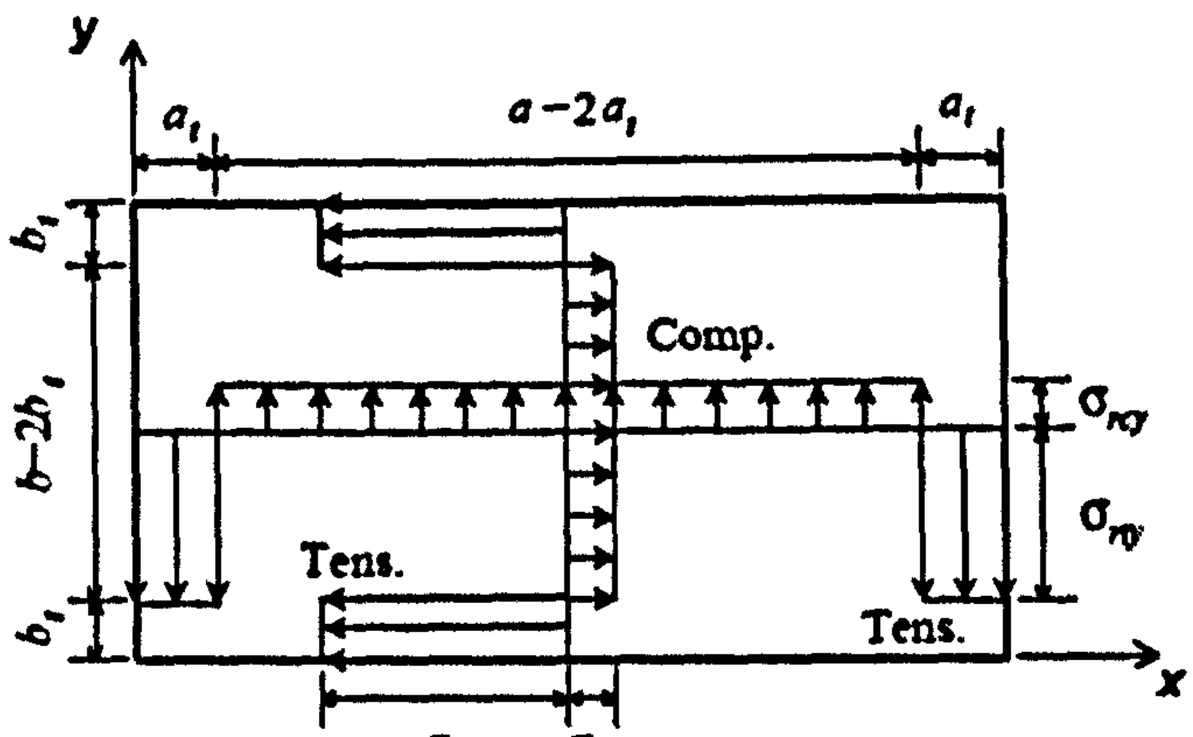

Figure 2.7: Idealization of welding induced residual stress distribution inside plating in the x and y directions (Paik & Thayamballi, 2003)

Along the welding, tensile residual stresses are usually developed with magnitude σ_{rtx} in the x direction and σ_{rty} in the y direction since welding is normally performed in both x and y directions. In order to obtain equilibrium, corresponding compressive (negative) residual stress with magnitude σ_{rcx} in the x direction and σ_{rcy} in the y direction are developed in the middle part of plating. The breadths of related tensile residual stress blocks in the x and y directions can be shown to be as follows:

$$\frac{2b_t}{b} = \frac{\sigma_{rcx}}{\sigma_{rcx} - \sigma_{rtx}}, \quad \frac{2a_t}{a} = \frac{\sigma_{rcy}}{\sigma_{rcy} - \sigma_{rty}} \tag{2.15}$$

where the tensile residual stress normally reaches the yield stress of material for mild steel plating (e.g., $\sigma_{rtx} = \sigma_{rty} \approx \sigma_o$), while it is usually somewhat less (approximately 80% of the material yield stress) for high tensile steel plating (e.g., $\sigma_{rtx} = \sigma_{rty} \approx 0.8\sigma_o$).

$$\sigma_{rx} = \begin{cases} \sigma_{rtx} & for\ 0 \le y < b_t \\ \sigma_{rcx} & for\ b_t \le y < b - b_t \\ \sigma_{rtx} & for\ b - b_t \le y \le b \end{cases} \tag{2.16}$$

$$\sigma_{ry} = \begin{cases} \sigma_{rty} & for\ 0 \le x < a_t \\ \sigma_{rcy} & for\ a_t \le x < a - a_t \\ \sigma_{rty} & for\ a - a_t \le x \le a \end{cases} \tag{2.17}$$

Smith (1987) also suggested the following representative values of welding-induced compressive residual stress in the longitudinal (x) direction:

$$\frac{\sigma_{rcx}}{\sigma_o} = \begin{cases} -0.05 & for\ slight\ level \\ -0.15 & for\ average\ level \\ -0.30 & for\ serious\ level \end{cases} \tag{2.18}$$

The magnitude of welding-induced residual stresses in the longer direction will normally be higher because the weld length is longer. Therefore, the plate breadth direction residual stresses may be approximated as below:

$$\sigma_{rcy} = \frac{b}{a}\sigma_{rcx} \tag{2.19}$$

In this work, Faulkner's model for residual stress distribution has been used to represent the distribution of the stresses, and has been incorporated into the finite element model as a simple representation of the actual residual stress present in the stiffened panels. Figure 2.8 shows Faulkner's model with the tensile regions around the stiffeners represented as a tension block having base width proportional to the plate thickness ($\eta \mathrm{x} t_{plate}$) where the value of η typically ranges 3.5 and 4 in a ship structures.

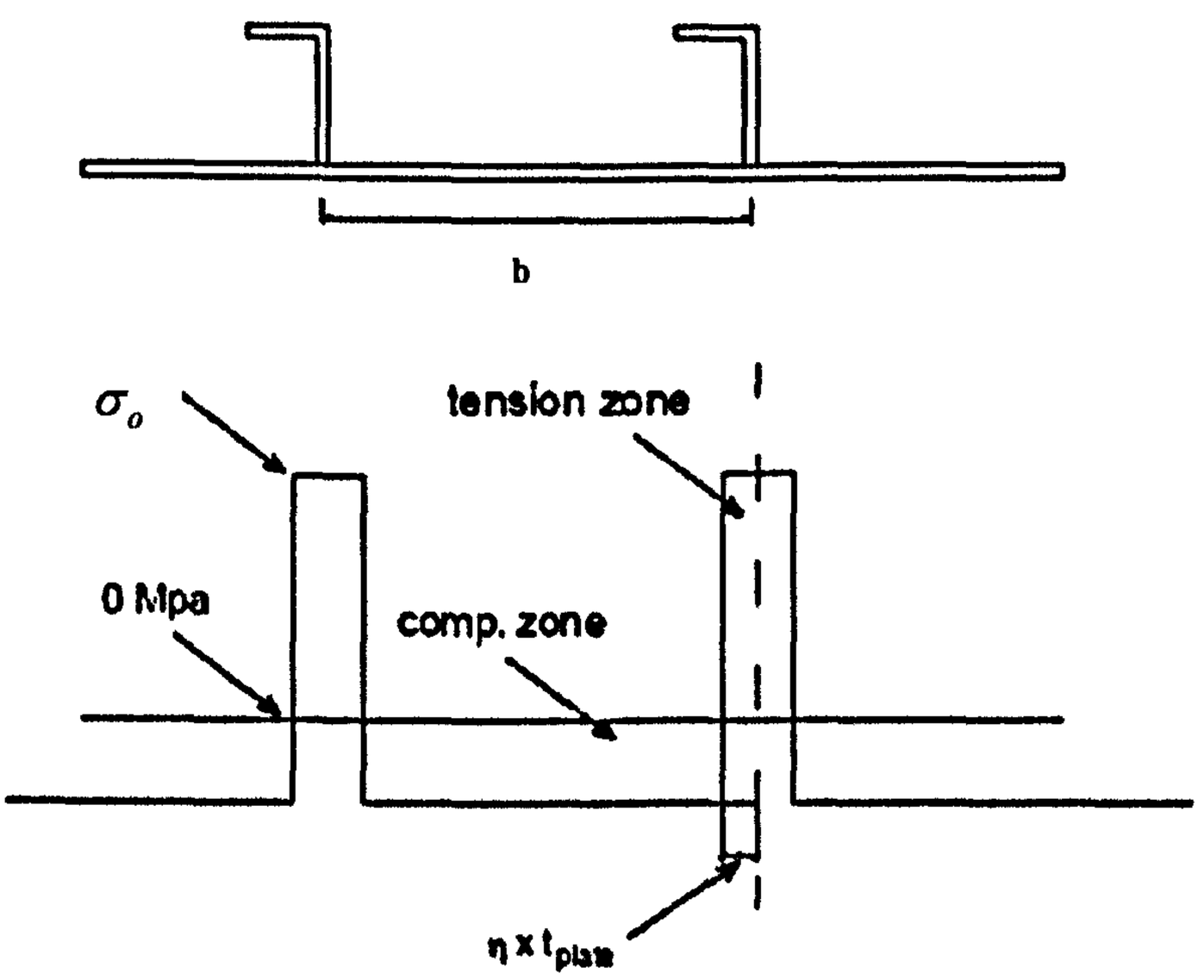

Figure 2.8: Faulkner's model used in this work for residual stress distribution

2.3 Finite Element Model for Inelastic Buckling Analyses

The geometrical properties of the 60 three-bay panels having three and five equally spaced T-stiffeners investigated in this study are shown in Table 2.2. They are all 3600 mm wide. It is intended that they represent the full range of proportions of typical ship plates. The material yielding stress, σ_o, is 352.8 MPa, Young's modulus, E, 205800 MPa and the poisson ratio, υ, is assumed to be 0.30. Four-nodded shell elements are used to model stiffened plate, and a fine mesh is conducted to adequately capture the stress and deformations. An elastic perfectly plastic material model without strain hardening may be considered enough for pessimistic strength assessment of stiffened plates. Arc-length method is applied to the solving of non-linear finite element stiffness equations.

The panels modelled should be capable to take into account all the mechanisms that cause to collapse of the structure in inelastic buckling analysis. Subjected to longitudinal compression, a transverse frame may deflect in an upward or downward half-sine wave, which are the plate-induced and stiffener-induced modes, respectively, while the next bay would deflect in the opposite direction.

Hughes *et al.* (2004) demonstrated using 107 FE ABAQUS models that a multi-bay structure with unbiased (equal upward and downward) initial eccentricities is weaker in the stiffener-induced buckling mode and that failure of this bay may cause to collapse of the structure. The other hands, if the initial eccentricity is the same in the upward and downward directions, collapse of a multi-bay panel is always caused by a stiffener-induced failure. Therefore, a one bay model as used by Grondin (2002) and some other researchers which could undergo either plate-induced or stiffener-induced collapse depending on the initial eccentricity could be misleading and conclusions for a multi-bay structure would be inappropriate. Moreover, the boundary conditions at a transverse frame are intermediate between simply supported and clamped and cannot be accurately modelled as a simply supported loaded edge. Therefore, for elastic-plastic buckling analysis a three-bay model is the most suitable, which can be represented as a symmetric 1 ½ bay model (Chen, 2002) as shown in

Figure 2.9. Due to considering of the inelastic properties, which contribute on collapse mechanisms, Chen (2002) found that edge stiffening of the panels was not essential.

In this study for ANSYS FE calculations, a linear eigenvalue buckling analysis is performed first to determine the critical load, as well as using the modes as an initial geometrical imperfection to be applied to model. A non-linear static buckling analysis is then carried out on the model.

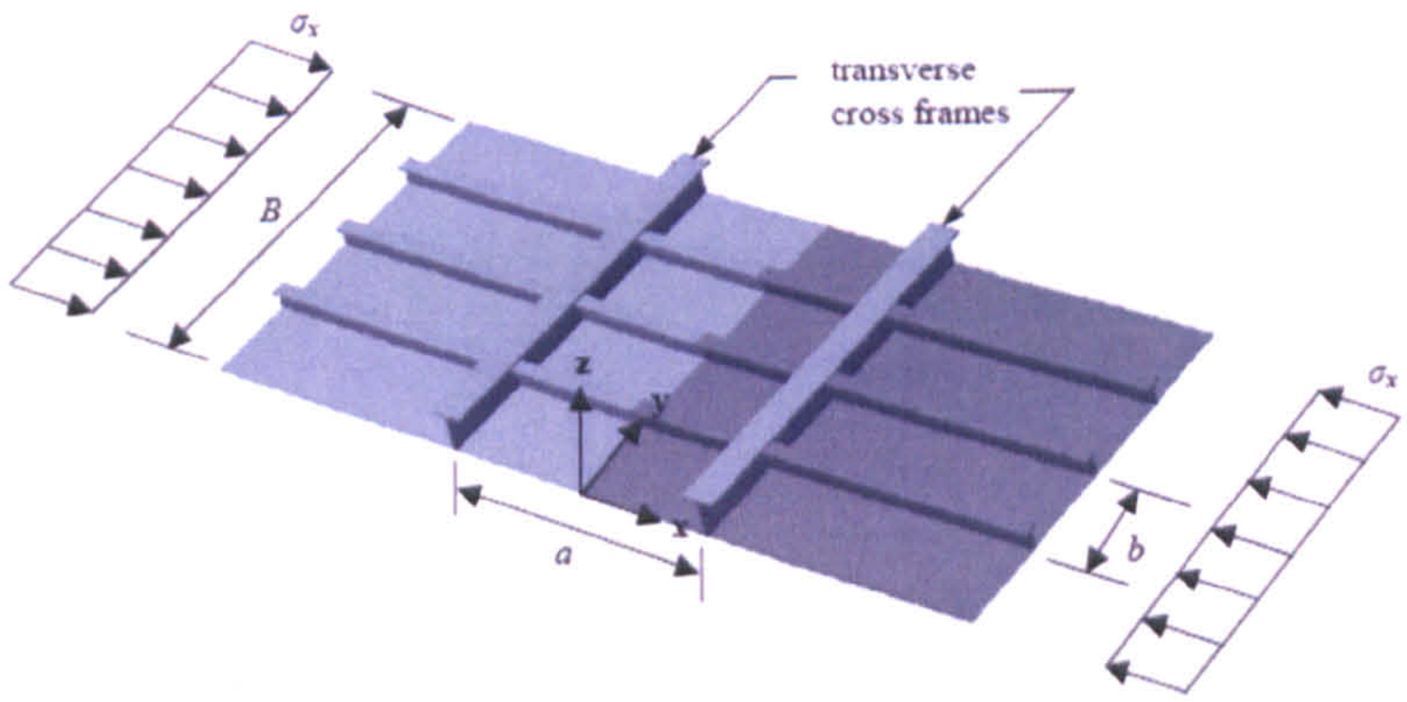

Figure 2.9: ANSYS solid model for three-bay grillages in this study

In ANSYS finite element analyses, initial deflection is assumed that plating has the overall buckling mode initial deflection, which corresponds to $0.05\beta^2 t$. The column-type or sideways initial deflection of the stiffeners is taken into account to be $0.0025a$, where a is the length of one-bay. Initial deflection of plating and stiffeners is automatically accounted once the scaling factor is applied which corresponds to above assumed equations. The imperfection patterns are determined from an overall buckling mode shape of a linear eigenvalue buckling analysis. The considered mode shape has an upward half wave deflection in the full bay and a downward deflection in the half bay, which is shown with the first buckling mode shapes in Figure 2.10(a-b-c-d-e) as well. Faulkner's model for residual stress distribution has been used to represent the distribution of the stresses, and has been incorporated into ANSYS finite element model as a simple representation of the actual residual stress present in the stiffened panels.

Table 2.2: Geometric properties of stiffened panels analysed in this study

Specimen no.	β (Plate Slenderness)	λ (Beam-column slenderness)	α (Aspect ratio)	ω_{op}, plate ($0.05\beta^2 t$)	ω_{os}, stiffener ($0.0025a$)	σ_{op} (MPa)	σ_{ow} (MPa)	σ_{of} (MPa)
SP1	1.774	0.489	2.00	3.30	4.50	352.8	352.8	352.8
SP2	1.183	0.427	3.00	1.47	4.50	352.8	352.8	352.8
SP3	1.774	0.718	2.94	3.30	6.60	352.8	352.8	352.8
SP4	1.183	0.627	4.40	1.47	6.60	352.8	352.8	352.8
SP5	1.774	0.979	4.00	3.30	9.00	352.8	352.8	352.8
SP6	1.183	0.855	6.00	1.47	9.00	352.8	352.8	352.8
SP7	1.774	0.859	2.00	3.30	4.50	352.8	352.8	352.8
SP8	1.183	0.744	3.00	1.47	4.50	352.8	352.8	352.8
SP9	1.774	1.141	2.94	3.30	6.60	352.8	352.8	352.8
SP10	1.183	0.989	4.40	1.47	6.60	352.8	352.8	352.8
SP11	1.774	1.718	4.00	3.30	9.00	352.8	352.8	352.8
SP12	1.183	1.488	6.00	1.47	9.00	352.8	352.8	352.8
SP13	2.329	0.582	2.00	4.34	4.50	352.8	352.8	352.8
SP14	1.553	0.508	3.00	1.93	4.50	352.8	352.8	352.8
SP15	2.329	0.650	2.94	4.34	6.60	352.8	352.8	352.8
SP16	1.553	0.571	4.40	1.93	6.60	352.8	352.8	352.8
SP17	2.329	1.374	4.00	4.34	9.00	352.8	352.8	352.8
SP18	1.553	1.197	6.00	1.93	9.00	352.8	352.8	352.8
SP19	3.726	0.818	2.00	6.94	4.50	352.8	352.8	352.8
SP20	2.484	0.709	3.00	3.08	4.50	352.8	352.8	352.8
SP21	3.726	0.911	2.94	6.94	6.60	352.8	352.8	352.8
SP22	2.484	0.793	4.40	3.08	6.60	352.8	352.8	352.8
SP23	3.726	0.996	4.00	6.94	9.00	352.8	352.8	352.8
SP24	2.484	0.872	6.00	3.08	9.00	352.8	352.8	352.8
SP25	2.329	1.060	2.00	4.34	4.50	352.8	352.8	352.8
SP26	1.553	0.920	3.00	1.93	4.50	352.8	352.8	352.8
SP27	2.329	1.555	2.94	4.34	6.60	352.8	352.8	352.8
SP28	1.553	1.349	4.40	1.93	6.60	352.8	352.8	352.8
SP29	1.774	0.739	4.00	3.30	9.00	352.8	352.8	352.8
SP30	1.183	0.650	6.00	1.47	9.00	352.8	352.8	352.8

Specimen no.	β (Plate Slenderness)	λ (Beam-column slenderness)	α (Aspect ratio)	ω_{op}, plate ($0.05\beta^2 t$)	ω_{os}, stiffener ($0.0025a$)	σ_{op} (MPa)	σ_{ow} (MPa)	σ_{of} (MPa)
SP31	3.726	1.659	2.00	6.94	4.50	352.8	352.8	352.8
SP32	2.484	1.430	3.00	3.08	4.50	352.8	352.8	352.8
SP33	3.726	1.735	2.94	6.94	6.60	352.8	352.8	352.8
SP34	2.484	1.497	4.40	3.08	6.60	352.8	352.8	352.8
SP35	2.329	0.790	4.00	4.34	9.00	352.8	352.8	352.8
SP36	1.553	0.696	6.00	1.93	9.00	352.8	352.8	352.8
SP37	1.774	0.825	2.00	3.30	4.50	352.8	352.8	352.8
SP38	1.183	0.473	3.00	1.47	4.50	352.8	352.8	352.8
SP39	1.774	1.581	2.94	3.30	6.60	352.8	352.8	352.8
SP40	1.183	0.563	4.40	1.47	6.60	352.8	352.8	352.8
SP41	3.726	2.365	4.00	6.94	9.00	352.8	352.8	352.8
SP42	2.484	2.041	6.00	3.08	9.00	352.8	352.8	352.8
SP43	2.329	1.163	2.00	4.34	4.50	352.8	352.8	352.8
SP44	1.553	0.690	3.00	1.93	4.50	352.8	352.8	352.8
SP45	1.774	0.864	2.94	3.30	6.60	352.8	352.8	352.8
SP46	1.553	0.724	4.40	1.93	6.60	352.8	352.8	352.8
SP47	1.774	0.888	4.00	3.30	9.00	352.8	352.8	352.8
SP48	1.183	0.585	6.00	1.47	9.00	352.8	352.8	352.8
SP49	1.183	0.540	3.00	1.47	4.50	352.8	352.8	352.8
SP50	1.774	1.089	2.94	3.30	6.60	352.8	352.8	352.8
SP51	2.484	1.111	6.00	3.08	9.00	352.8	352.8	352.8
SP52	2.484	1.198	3.00	3.08	4.50	352.8	352.8	352.8
SP53	3.726	1.880	2.94	6.94	6.60	352.8	352.8	352.8
SP54	1.553	0.740	6.00	1.93	9.00	352.8	352.8	352.8
SP55	2.484	1.220	4.40	3.08	6.60	352.8	352.8	352.8
SP56	3.726	1.900	4.00	6.94	9.00	352.8	352.8	352.8
SP57	1.774	0.718	2.94	3.30	6.60	352.8	352.8	352.8
SP58	1.183	0.576	6.00	1.47	9.00	352.8	352.8	352.8
SP59	2.329	1.122	4.00	4.34	9.00	352.8	352.8	352.8
SP60	1.183	0.562	6.00	1.47	9.00	352.8	352.8	352.8

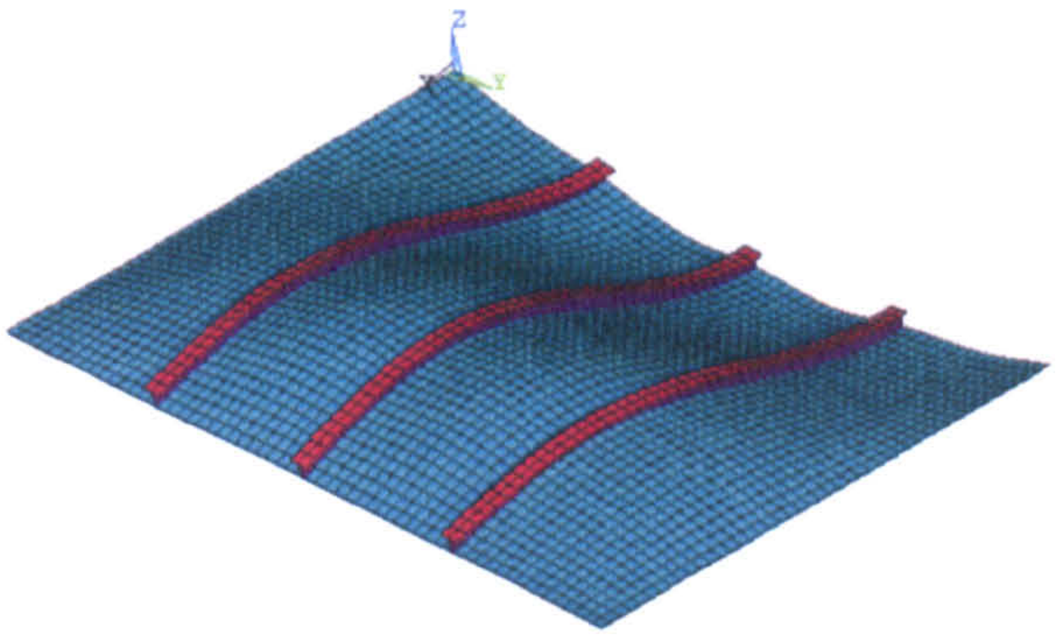

Figure 2.10(a): Linear eigenvalue buckling mode shape 1 in SP7 (overall mode)

Figure 2.10(b): Linear eigenvalue buckling mode shape 2 in SP7

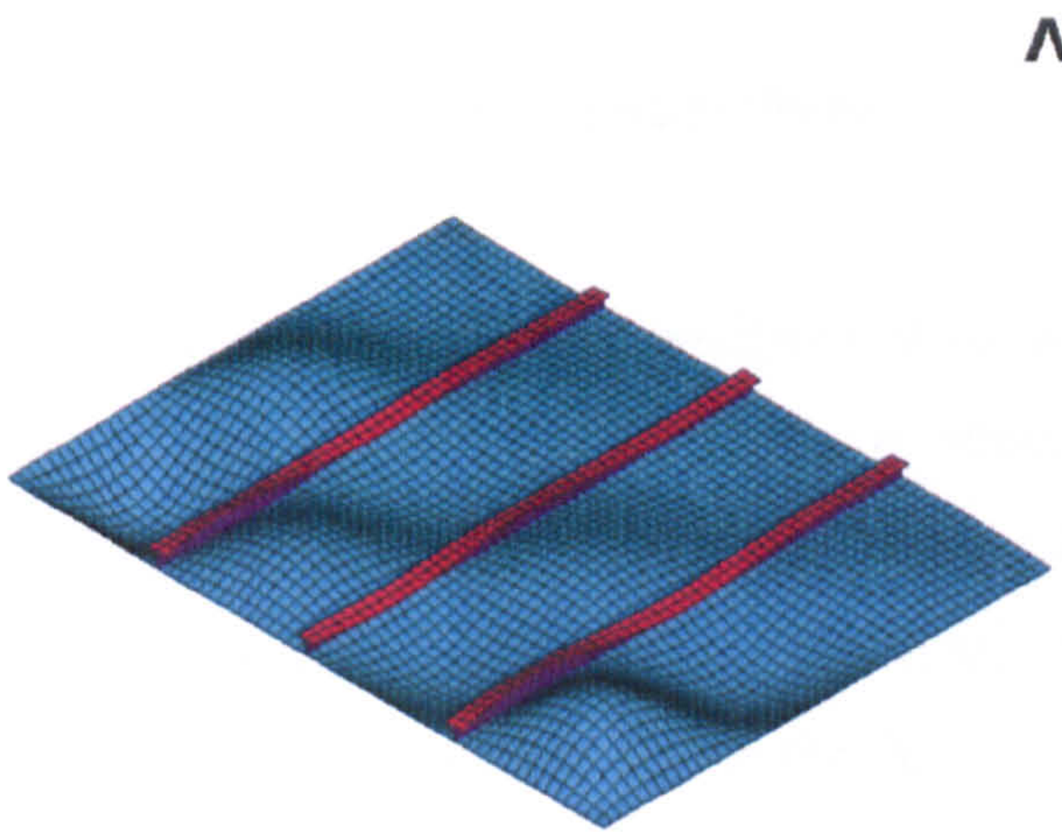

Figure 2.10(c): Linear eigenvalue buckling mode shape 3 in SP7

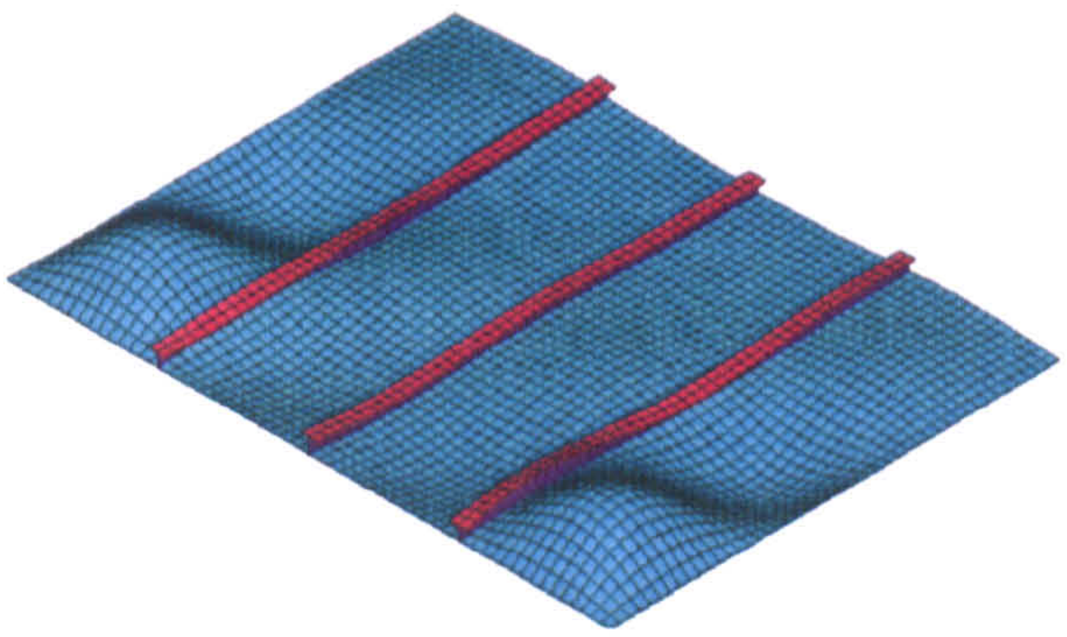

Figure 2.10(d): Linear eigenvalue buckling mode shape 4 in SP7

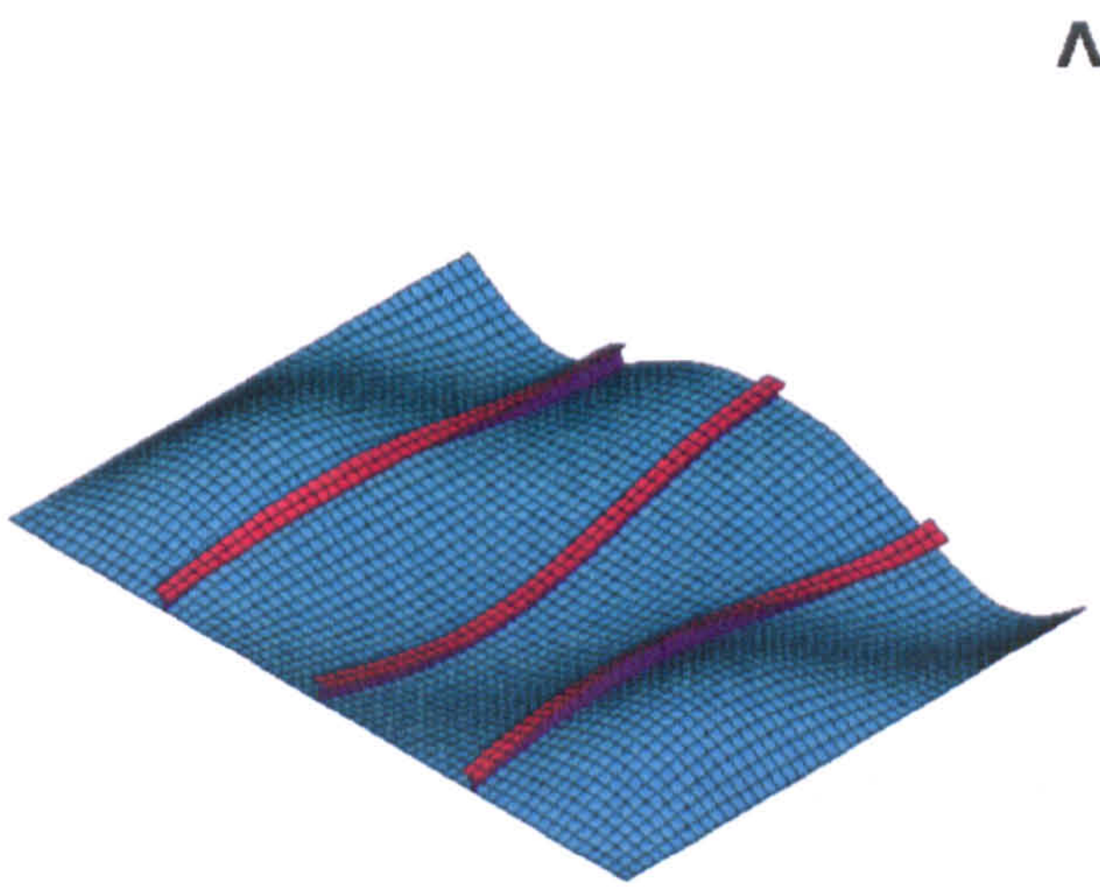

Figure 2.10(e): Linear eigenvalue buckling mode shape 5 in SP7

2.4 Applied Boundary Conditions

In this study, two kinds of boundary conditions are accounted into 1 ½ ANSYS FE model such as simply supported and clamped when subjected to longitudinal, transverse compression and lateral pressure loads. Hughes *et al.* (2004) also suggested similar boundary conditions for 1 ½ ABAQUS FE model in their studies. Their proposals have been considered in this thesis.

2.4.1 Boundary conditions for simply supported under longitudinal compression (For 1+1/2 bay model)

Let a "0" on $T[x,y,z]$ indicate translation constraints and on $R[x,y,z]$ indicate rotational constraints about the $x-$, $y-$ and $z-$ coordinates in Figure 2.10(a). Let a "1" indicate no constraint.

- The mid-width node in each of the two transverse edges has $T[1,0,1]$ to prevent rigid body motion in the y-direction.
- The longitudinal edges are simply supported with $T[1,1,0]$ and $R[1,0,0]$, with all the nodes along each edge having equal $y-$ displacement.
- The transverse edge on the left hand side, which is midlength of the mid-bay of the full three-bay model, has symmetric boundary conditions. This is simulated with $T[0,1,1]$ and $R[1,0,1]$.
- The transverse edge on the right hand side, which is the loaded edge, is simply supported with $T[1,1,0]$ and $R[0,1,0]$. Only the plate nodes have equal $x-$ displacements.
- The transverse cross-frame is not modelled, but is simulated with $T[1,1,0]$.

2.4.2 Boundary conditions for clamped under longitudinal compression (For 1+1/2 bay model)

- Simulating the maximum rotational restraint, set the loaded edge as clamped with $T[1,1,0]$ and $R[0,0,0]$. All the plate nodes and stiffener nodes have equal $x-$ displacements.
- Ignoring the rotational restraint, set the loaded edge as simply supported with $T[1,1,0]$ and $R[0,1,0]$. Only the plate nodes have equal $x-$ displacements.

2.4.3 Boundary conditions for simply supported under transverse compression and lateral pressure loads (For 1/2 + 1 + 1 +1/2 bay model)

- The short edges have symmetric boundary conditions being simulated with $R[1,0,0]$ and all nodes have the same $x-$displacements.
- The panel is clamped along the long edges, being simulated with $R[0,0,0]$ and all nodes have the same $y-$displacement.
- The middle frame is not modelled but symmetric boundary conditions are simulated with $T[0,1,0]$ and $R[1,0,1]$.
- The other two transverse frames are also not modelled but are simulated with $T[1,1,0]$.
- As the stiffeners pass through the three frames, they are constrained to remain vertical for equal $y-$ displacements at all stiffener nodes at the frame locations.

2.5 Collapse Strength of Stiffened Plates

In the plate panels, the longitudinal stiffeners have the main function of providing the necessary support to the plates ensuring that they retain the required strength. To fulfil this function, stiffeners must have adequate rigidity, and the spacing between them must be selected according to the main characteristics of the plate, namely, its thickness and yield stress. The slenderness of the plate has to be designed in such a way that the ultimate average stress is kept closer to the yield stress as much as possible.

The primary modes for the ultimate limit state of a stiffened panel subject to predominantly axial compressive loads are usually classified as plate induced failure, column or beam-column type collapse of the plate-stiffener combination, tripping of stiffeners and overall collapse after overall buckling. This last one is normally

avoided by ensuring that transverse frames are of adequate size therefore it is not considered in this study. The first one takes place when the stiffener is sufficiently stocky and plate has a critical elastic stress lower than yield stress. The second failure mode is mainly due to excessive slenderness of the column (stiffener and effective associated plate acting together) and failure may be towards the plate or towards the stiffener, depending on the column's initial shape and the type of loading considered, i.e., eccentrically applied or not, following the shift of neutral axis or not. In a continuous panel it is usual that the failure is towards the plate in one span and towards the stiffener in the adjacent span. The third mode of failure is the consequence of a lack of torsional rigidity of the stiffener. Interaction with the plate-buckling mode may also take place inducing premature tripping.

The plate buckling failure mode tends to experience a more significant drop in load-carrying capacity in the post-buckling range than the overall buckling failure modes. As opposed to the other modes of failure, stiffener tripping generally results in sudden loss of load-carrying capacity as shown in Figure 2.11. This behaviour was also observed experimentally (Grondin *et al.* 1998; Murray, 1973). Because of the sudden drop in load-carrying capacity accompanying stiffener tripping, this mode of failure is considered a more critical failure mode than the other stiffened plate failure modes identified above.

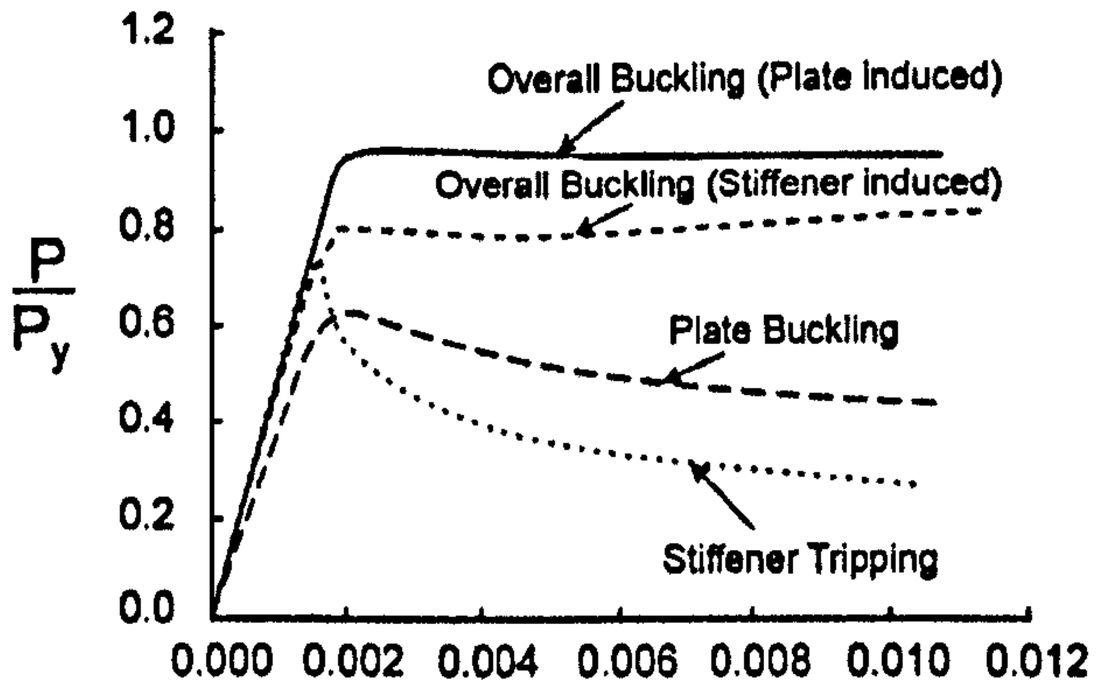

Figure 2.11: Load versus deformation behaviour (Murray, 1973)

The effective width approach is a commonly used method in predicting the ultimate strength of ship plating. It is assumed that the loading acting on the plate is taken by the areas of the plate situated close to the longitudinal supports. The total width of the areas is the effective width of the plating. The effective width is described by Faulkner's equation (1975), presently used in the form proposed as follows:

$$b_E = \begin{cases} b & for \quad \beta < 1 \\ \left(\frac{2}{\beta} - \frac{1}{\beta^2}\right) b & for \quad \beta \geq 1 \end{cases} \tag{2.20}$$

where $\beta = \frac{b}{t}\sqrt{\frac{\sigma_o}{E}}$ is called the plate slenderness ratio. Values of the coefficients in Equation (2.20) vary dependant on the support conditions and other effects influencing the ultimate strength. Frankland proposed his approach, widely used in practise.

$$b_E = \begin{cases} b & for \quad \beta < 1 \\ \left(\frac{2.25}{\beta} - \frac{1.25}{\beta^2}\right) b & for \quad \beta \geq 1 \end{cases} \tag{2.21}$$

Based on the effective width concept and having an appropriate equation, formula for the ultimate capacity of plates is derived as follows,

$$\sigma_{cp} = \left(\frac{2.25}{\beta} - \frac{1.25}{\beta^2}\right)\sigma_0 \tag{2.22}$$

The presented equations provide the ultimate capacity of the plates. However, for evaluation of the ship hull ultimate capacity, it is necessary to have an approach for definition of the stress-strain curve of the compressed panels as the hull structural elements are subject to various loading (in terms of strain) in the moment of collapse; some are in pre-buckling range and the others in the post-buckling. A method was

proposed by Gordo & Soares (1993) for evaluation of the curve. A basic concept of the method is to replace the slenderness of the plate given by Equation (2.21) with the actual slenderness depending on the strain of the element.

$$\beta_E = \frac{b}{t}\sqrt{\frac{\varepsilon\sigma_o}{E}} \tag{2.23}$$

Thus the effective width of the plate depends on the relative actual strain

$$b_E = \frac{2.25}{\beta_E} - \frac{1.25}{\beta_E{}^2} \tag{2.24}$$

ε is the relative strain, $\varepsilon = \frac{\varepsilon_E}{\varepsilon_o}$, ε_E, is element strain and ε_o is strain including yield stress in the element, $\varepsilon_o = \frac{\sigma_o}{E}$ and the actual average stress acting on the compressed edge is:

$$\sigma/\sigma_0 = \frac{2.25}{\beta_E} - \frac{1.25}{\beta_E{}^2} \tag{2.25}$$

The values of the critical buckling stresses for plate, beam-column, torsional-flexural (tripping) and web local failure modes are evaluated according to the formulas given in Bureau Veritas for perfect case only, in which chapters 'Ultimate Strength of Ship Structures' and 'Buckling Criteria'. Effective width, b_E, based on the Frankland's approach is developed in this study to get a better result.

2.5.1 Elastic-plastic collapse of the structural elements

The equation describing the load-end shortening curve $\sigma - \varepsilon$ or the elastic-plastic collapse of structural elements composing the hull girder transverse section can be

obtained from the following formula, valid for both positive (shortening) and negative (lengthening) strains.

$$\sigma = \Phi \sigma_o \tag{2.26}$$

where, Φ is edge function, σ_o is yield stress of element.

$$\Phi = \begin{cases} -1 & for \quad \varepsilon < -1 \\ \varepsilon & for \quad -1 < \varepsilon < 1 \\ 1 & for \quad \varepsilon > 1 \end{cases} \tag{2.27}$$

2.5.2 Beam – column buckling failure mode

The equation describing the load-end shortening curve $\sigma_{CR1} - \varepsilon$ for the beam-column buckling of the stiffeners composing the hull girder transverse section can be obtained from the following formula:

$$\sigma_{CR1} = \Phi \sigma_{C1} \left(\frac{A_S + b_E t}{A_S + bt} \right) \tag{2.28}$$

where, Φ is edge function defined in 2.26, σ_{C1} is critical stress in MPa, A_S is net sectional area of a stiffener and b is spacing of stiffeners.

$$\sigma_{C1} = \begin{cases} \dfrac{\sigma_{E1}}{\varepsilon} & for \quad \sigma_{E1} \le \dfrac{\sigma_o}{2} \varepsilon \\ \sigma_o \left(1 - \dfrac{\Phi \sigma_o \varepsilon}{4 \sigma_{E1}} \right) & for \quad \sigma_{E1} > \dfrac{\sigma_o}{2} \varepsilon \end{cases} \tag{2.29}$$

where σ_{C1} is based on the Johnson-Ostenfeld formulation accounting for inelastic effects on the column's buckling. In equation (2.28) the second term computes the

loss of efficiency of plate due to compression loading. Effective width, b_E, based on the Frankland`s approach developed to the plate strength and given by,

$$b_E = \begin{cases} b \quad for \quad \beta_E \le 1.25 \\ \left(\frac{2.25}{\beta_E} - \frac{1.25}{\beta_E^{\,2}}\right) b \quad for \quad 1.25 < \beta_E \le 3.25 \\ \left(\frac{1.91}{\beta_E}\right) b \quad for \quad \beta_E > 3.25 \end{cases} \tag{2.30}$$

where, σ_{E1} is Euler column buckling stress, which is calculated as below,

$$\sigma_{E1} = \pi^2 E \frac{I_E}{A_E a^2} \tag{2.31}$$

where, I_E is net moment of inertia of ordinary stiffeners with attached shell plating of width b_{E1}, A_E is net sectional area of stiffeners with attached shell plating of effective width b_E, and a is length of stiffened plate.

$$b_{E1} = \begin{cases} \frac{b}{\beta_E} \quad for \quad \beta_E > 1 \\ b \quad for \quad \beta_E \le 1 \end{cases} \tag{2.32}$$

where, $\beta_E = \frac{b}{t}\sqrt{\frac{\varepsilon\sigma_o}{E}}$ is defined.

2.5.3 Plate induced buckling failure mode

The equation describing the load-end shortening curve $\sigma_{CR2} - \varepsilon$ for the plate buckling composing the hull girder transverse section can be obtained the following formula:

$$\sigma_{CR2} = \Phi\left(\frac{A_S + b_E t}{A_S + bt}\right) \tag{2.33}$$

2.5.4 Flexural – torsional (tripping) buckling failure mode

The equation describing the load-end shortening curve $\sigma_{CR3} - \varepsilon$ for the flexural – torsional (tripping) buckling of stiffeners composing the hull girder transverse can be obtained according to following formula:

$$\sigma_{CR3} = \Phi\left(\frac{A_S\sigma_{C3} + bt\sigma_{CP}}{A_S + bt}\right) \tag{2.34}$$

where, σ_{C3} is defined as critical stress.

$$\sigma_{C3} = \begin{cases} \dfrac{\sigma_{E3}}{\varepsilon} & for \quad \sigma_{E3} \le \dfrac{\sigma_o}{2}\varepsilon \\ \sigma_o\left(1 - \dfrac{\Phi\sigma_o\varepsilon}{4\sigma_{E3}}\right) & for \quad \sigma_{E3} > \dfrac{\sigma_o}{2}\varepsilon \end{cases} \tag{2.35}$$

where, σ_{E3} is Euler torsional buckling stress, defined as follows.

$$\sigma_{E3} = \frac{\pi^2 EI_W}{I_P a^2}\left(\frac{K_C}{m^2} + m^2\right) + 0.385E\left(\frac{I_t}{I_P}\right) \tag{2.36}$$

where, I_W is net sectional moment of inertia of the stiffener about its connection to the attached plating and is defined as follows.

$$I_W = \begin{cases} \dfrac{h_w{}^3 t_w{}^3}{36} & for \quad flat \quad bars \\ \dfrac{t_f b_f{}^3 h_w{}^2}{12} & for \quad T-\text{sec}tions \\ \dfrac{b_f{}^3 h_w{}^2}{12(b_f+h_w)^2}\left[t_f b_f{}^2 + 2b_f h_w + 4h_w{}^2 + 3t_w b_f h_w\right] & for \quad angles\ and\ bulb\ \text{sec}tions \end{cases} \tag{2.37}$$

where, I_p is net polar moment of inertia of the stiffener about its connection to the attached plating, defined as follows.

$$I_P = \begin{cases} \dfrac{h_w{}^3 t_w}{3} & for \quad flat\ bars \\ \left(\dfrac{h_w{}^3 t_w}{3} + h_w{}^2 b_f t_f\right) & for \quad stiffeners \quad with \quad face\ plate \end{cases} \tag{2.38}$$

where, I_t is St. Venant's net moment of inertia of stiffener without attached plating, defined as follows:

$$I_t = \begin{cases} \dfrac{h_w t_w{}^3}{3} & for \quad flat \quad bars \\ \dfrac{1}{3}\left[h_w t_w{}^3 + b_f t_f{}^3\left(1-0.63\dfrac{t_f}{b_f}\right)\right] & for \quad stiffeners \quad with \quad face\ plate \end{cases} \tag{2.39}$$

where, m is number of half waves, may be taken equal to the integer number and K_C is torsional buckling of axially loaded stiffeners, calculated by following, also see Table 2.3.

$$m^2(m-1)^2 \le K_C < m^2(m+1)^2 \qquad \text{and} \qquad K_C = \left(\frac{C_0 a^4}{\pi^4 E I_W}\right) \tag{2.40}$$

where, C_0 is a spring stiffener of the attached plating and can be expressed as follows,

$$C_0 = \frac{Et^3}{2.73b} \tag{2.41}$$

Table 2.3: Torsional buckling of axially loaded stiffeners – Number of m half waves

K_C	$0 \le K_C < 4$	$4 \le K_C < 36$	$36 \le K_C < 144$
m	1	2	3

where, σ_{CP} is buckling stress of attached plating, which can be determined by following formula.

$$\sigma_{CP} = \begin{cases} \sigma_o \quad for \quad \beta_E \le 1.25 \\ \left(\frac{2.25}{\beta_E} - \frac{1.25}{\beta_E^{\,2}}\right)\sigma_o \quad for \quad 1.25 < \beta_E \le 3.25 \\ \left(\frac{1.91}{\beta_E}\right)\sigma_o \quad for \quad \beta_E > 3.25 \end{cases} \tag{2.42}$$

2.5.5 Web local buckling failure mode

The equating describing the load-end shortening curve $\sigma_{CR4} - \varepsilon$ for the web local buckling of flanged stiffeners composing the hull girder transverse section can be obtained from the following formula.

$$\sigma_{CR4} = \Phi\sigma_o\left(\frac{b_E t + h_{we}t_w + b_f t_f}{bt + h_w t_w + b_f t_f}\right) \tag{2.43}$$

where, h_{we} is effective height of the web, which can be determined by following formula:

$$h_{we} = \begin{cases} h_w \quad for \quad \beta_W \le 1.25 \\ \left(\frac{2.25}{\beta_E} - \frac{1.25}{\beta_E^{\,2}}\right) h_w \quad for \quad 1.25 < \beta_W \le 3.25 \\ \left(\frac{1.91}{\beta_E}\right) h_w \quad for \quad \beta_W > 3.25 \end{cases} \tag{2.44}$$

$\beta_W = \frac{h_w}{t_w}\sqrt{\frac{\varepsilon\sigma_o}{E}}$ is defined while ε is relative strain as described in 2.5.1.

2.6 Simple Design Equations to Predict the Ultimate Strength of Imperfect Stiffened Plates

The collapse behaviour of stiffened plates with initial imperfection is parametrically investigated by inelastic finite element analysis. The ultimate strength of a stiffened plate with initial imperfection can be expressed in general by following equation:

$$\phi_u = \phi_u(\beta, \lambda, \frac{\sigma_r}{\sigma_o}, \frac{w_o}{t}, \tau, \sigma_y, \rho) \tag{2.45}$$

where β is the slenderness ratio, λ is beam-column slenderness ratio, $\left(\frac{\sigma_r}{\sigma_o}\right)$ is normalized compressive welding-induced stress, $\left(\frac{w_o}{t}\right)$ is non-dimensional initial deflection, τ is shear stress, σ_y is transverse stress and ρ is lateral pressure load. Effective width, b_E is multiplied by reduction factors so as to introduce initial imperfections for stiffened plates, namely,

$$b_E' = b_E R_d R_r R_y R_\tau R_q \tag{2.46}$$

where b_E is the effective width of imperfect stiffened plate, b_E is the effective width of perfect stiffened plate, R_d is a reduction factor due to initial deflection, R_r is a reduction factor due to welding-induced residual stress, R_y is a reduction factor due to bi-axial compression, R_r is a reduction factor due to shear stress present, and R_q is a reduction factor due to lateral pressure load. All reduction factors proposed are expressed by the following equations:

$$R_d = 1.0 - 0.2323 f(\lambda) g(\beta) \tag{2.47}$$

$$f(\lambda) = \begin{cases} 0.015 \quad for \quad 0 < \lambda \le 0.35 \\ \left(-1.03 + 2.341\lambda - 1.344\lambda^2 + 0.212\lambda^3\right) \quad for \quad \lambda > 0.35 \end{cases} \tag{2.48}$$

$$g(\beta) = \begin{cases} \left(10.818 + 0.204\beta - 5.177\beta^2\right) \quad for \quad 1 < \beta \le 1.5 \\ \left(4.594 - 0.805\beta + 0.255\beta^2\right) \quad for \quad 1.5 < \beta \le 2.0 \\ \left(6.404 - 1.847\beta + 0.371\beta^2\right) \quad for \quad 2 < \beta \le 2.5 \\ \left(5.435 - 1.213\beta + 0.202\beta^2\right) \quad for \quad 2.5 < \beta \le 4.0 \end{cases} \tag{2.49}$$

$$R_r = 1.0 - \left[\frac{\mu}{8.1(\beta - 1.901)^2 + 1}\right] \tag{2.50}$$

where $\mu = \left(\frac{\sigma_r}{\sigma_o}\right)$ is defined as normalized welding residual stress.

$$R_y = 1.0 - \left(\frac{\sigma_y}{\sigma_{yu}}\right)^2 \tag{2.51}$$

which is proposed by Faulkner (1975), where $\sigma_y \le 0.25\sigma_0$

$$\sigma_{yu} = \sigma_o \left(\frac{0.9}{\beta^2} + \frac{1.9}{\alpha\beta} \left(1 - \frac{0.9}{\beta^2} \right) \right) \tag{2.52}$$

$$R_q = \left(1.0 + 0.0262\xi - 0.3232\xi^2 \right) \tag{2.53}$$

where $\xi = \left(\frac{\rho E}{\sigma_o^{\,2}} \right)$ is defined as normalized value of pressure. (2.54)

$$R_\tau = \left[1 - \left(\frac{\tau}{\tau_o} \right)^2 \right]^{0.5} \tag{2.54}$$

where $\tau_o = \frac{\sigma_o}{\sqrt{3}}$ is given by Faulkner (1975).

Initial deflection value is taken into account for plating and stiffeners implicitly in this study. For clamped stiffened plates, b_E, effective width may be re-arranged by the following simple equations as well.

$$b_E = \begin{cases} 1.035b \quad for \quad \beta_E \le 1.25 \\ \left(\frac{2.65}{\beta_E} - \frac{1.95}{\beta_E^{\,2}} \right) b \quad for \quad 1.25 < \beta_E \le 3.25 \\ \left(\frac{1.95}{\beta_E} \right) b \quad for \quad \beta_E > 3.25 \end{cases} \tag{2.55}$$

2.7 Comparison between ANSYS FEM and Proposed Simple Equations

The "Ultimate Capacity" can be defined as the maximum load the panel can carry without suffering major permanent set and is effectively the maximum load carrying capacity of a panel. In FEM calculations, the ultimate capacity value is taken as the load that results in the first occurrence of membrane yield stress anywhere in the stiffened panel. The ultimate capacity values calculated from ANSYS FEM, Faulkner (1975), Soares & Gordo (1993) and the proposed equations are now compared for 60 different stiffened plates and are shown in Table 2.4, Table 2.5 and Table 2.6.

Table 2.4: The comparisons between ANSYS FEM, Faulkner's, Soares & Gordo`s and new proposed formulas with only initial deflection without considering residual stress under only longitudinal compression

Specimen No.	$(\sigma_{xu}/\sigma_{oeq})$ ANSYS FEM	$(\sigma_{xu}/\sigma_{oeq})$ Faulkner	$(\sigma_{xu}/\sigma_{oeq})$ Soares & Gordo	$(\sigma_{xu}/\sigma_{oeq})$ Present Study	Collapse Modes	
					ANSYS FEM	Present Study
SP1	0.949	0.803	0.839	0.968	M4a4	I
SP2	0.965	0.940	0.940	0.949	M4a4	I
SP3	0.791	0.763	0.797	0.790	M3a1	I
SP4	0.888	0.894	0.893	0.935	M4a4	I
SP5	0.660	0.699	0.730	0.649	M3b1	I
SP6	0.748	0.819	0.818	0.767	M3b3	I
SP7	0.658	0.728	0.762	0.703	M1a1	I
SP8	0.790	0.858	0.858	0.842	M3a1	I
SP9	0.513	0.650	0.680	0.583	M3b1	I
SP10	0.636	0.765	0.765	0.684	M3b1	I
SP11	0.517	0.419	0.438	0.412	M3b3	I
SP12	0.547	0.494	0.495	0.441	M3b3	I
SP13	0.777	0.686	0.745	0.776	M1a1	I
SP14	0.940	0.854	0.876	0.987	M4a4	I
SP15	0.755	0.681	0.738	0.738	M1a1	I
SP16	0.903	0.843	0.865	0.935	M4a4	I
SP17	0.503	0.518	0.564	0.481	M3b1	I
SP18	0.588	0.647	0.664	0.580	M3b3	I
SP19	0.516	0.492	0.611	0.499	M1a1	I
SP20	0.697	0.652	0.713	0.687	M1a1	I
SP21	0.478	0.487	0.601	0.475	M1a1	I
SP22	0.654	0.642	0.700	0.645	M1a1	I
SP23	0.457	0.480	0.589	0.459	M1a1	I
SP24	0.650	0.631	0.684	0.620	M1a1	III
SP25	0.505	0.597	0.651	0.546	M1b1	I

SP26	0.633	0.749	0.770	0.703	M3a1	I
SP27	0.471	0.559	0.609	0.504	M3b1	I
SP28	0.582	0.701	0.718	0.632	M3a1	I
SP29	0.790	0.761	0.794	0.783	M3a3	I
SP30	0.879	0.887	0.887	0.911	M1c4	I
SP31	0.281	0.362	0.454	0.359	M2b2	I
SP32	0.372	0.484	0.532	0.455	M1b1	I
SP33	0.301	0.345	0.434	0.352	M1b1	I
SP34	0.400	0.462	0.499	0.433	M3b1	I
SP35	0.700	0.660	0.714	0.667	M3a1	I
SP36	0.839	0.815	0.835	0.843	M4a4	I
SP37	0.683	0.737	0.771	0.721	M3b1	I
SP38	0.961	0.932	0.932	1.040	M4a4	I
SP39	0.437	0.481	0.504	0.452	M3b3	I
SP40	0.930	0.911	0.910	0.987	M4a4	I
SP41	0.333	0.209	0.262	0.292	M2b2	I
SP42	0.447	0.433	0.473	0.416	M3b1	I
SP43	0.401	0.575	0.631	0.513	M1b1	I
SP44	0.816	0.815	0.836	0.847	M3a1	I
SP45	0.680	0.729	0.762	0.702	M3b1	I
SP46	0.809	0.808	0.828	0.823	M3a3	I
SP47	0.704	0.724	0.756	0.692	M3b1	I
SP48	0.905	0.905	0.905	0.968	M3a3	III
SP49	0.940	0.916	0.916	1.015	M4a4	I
SP50	0.537	0.666	0.697	0.602	M1b1	I
SP51	0.589	0.569	0.612	0.532	M3a3	I
SP52	0.430	0.549	0.606	0.497	M1a1	I
SP53	0.281	0.326	0.411	0.346	M1b1	I
SP54	0.811	0.805	0.824	0.812	M3a3	I
SP55	0.446	0.545	0.599	0.494	M3b1	I
SP56	0.320	0.320	0.401	0.342	M2b2	I
SP57	0.788	0.763	0.797	0.790	M3a1	I
SP58	0.908	0.907	0.907	0.972	M4a4	III
SP59	0.570	0.586	0.635	0.537	M3b1	I
SP60	0.921	0.911	0.910	0.974	M3a3	III

Table 2.5: The comparisons between ANSYS FEM, Faulkner's, Soares & Gordo`s and new proposed formulas with initial deflection with considering residual stress ($\mu = 0.1$) under only longitudinal compression

Specimen No.	$(\sigma_{xu}/\sigma_{oeq})$ ANSYS FEM	$(\sigma_{xu}/\sigma_{oeq})$ Faulkner	$(\sigma_{xu}/\sigma_{oeq})$ Soares & Gordo	$(\sigma_{xu}/\sigma_{oeq})$ Present study
SP1	0.884	0.717	0.777	0.897
SP2	0.947	0.907	0.936	0.938
SP3	0.735	0.682	0.738	0.733
SP4	0.868	0.862	0.889	0.924
SP5	0.614	0.623	0.676	0.602
SP6	0.730	0.788	0.703	0.753
SP7	0.614	0.646	0.713	0.651
SP8	0.771	0.825	0.850	0.828
SP9	0.484	0.577	0.627	0.538

SP10	0.632	0.736	0.761	0.675
SP11	0.464	0.372	0.404	0.382
SP12	0.532	0.474	0.490	0.432
SP13	0.758	0.578	0.651	0.756
SP14	0.906	0.791	0.838	0.961
SP15	0.719	0.577	0.647	0.719
SP16	0.877	0.783	0.829	0.907
SP17	0.476	0.436	0.491	0.461
SP18	0.559	0.598	0.635	0.560
SP19	0.501	0.423	0.538	0.488
SP20	0.674	0.554	0.625	0.670
SP21	0.470	0.421	0.531	0.471
SP22	0.635	0.548	0.616	0.635
SP23	0.453	0.417	0.522	0.458
SP24	0.616	0.542	0.605	0.605
SP25	0.483	0.499	0.565	0.531
SP26	0.604	0.691	0.731	0.677
SP27	0.442	0.468	0.530	0.491
SP28	0.554	0.646	0.687	0.610
SP29	0.731	0.682	0.736	0.724
SP30	0.851	0.855	0.883	0.902
SP31	0.271	0.308	0.397	0.349
SP32	0.345	0.406	0.462	0.440
SP33	0.285	0.297	0.380	0.341
SP34	0.387	0.390	0.442	0.417
SP35	0.665	0.560	0.627	0.643
SP36	0.810	0.758	0.801	0.816
SP37	0.632	0.654	0.711	0.668
SP38	0.941	0.905	0.929	1.011
SP39	0.400	0.426	0.464	0.420
SP40	0.904	0.877	0.905	0.971
SP41	0.315	0.178	0.229	0.252
SP42	0.422	0.366	0.414	0.403
SP43	0.387	0.475	0.541	0.494
SP44	0.790	0.796	0.800	0.819
SP45	0.631	0.649	0.704	0.651
SP46	0.781	0.751	0.795	0.796
SP47	0.651	0.647	0.700	0.644
SP48	0.881	0.873	0.901	0.948
SP49	0.927	0.882	0.911	0.985
SP50	0.499	0.591	0.643	0.556
SP51	0.545	0.501	0.550	0.526
SP52	0.411	0.458	0.524	0.477
SP53	0.277	0.276	0.359	0.339
SP54	0.780	0.750	0.790	0.790
SP55	0.430	0.457	0.520	0.484
SP56	0.300	0.272	0.351	0.332
SP57	0.733	0.681	0.738	0.733
SP58	0.896	0.877	0.903	0.957
SP59	0.532	0.497	0.555	0.521
SP60	0.906	0.884	0.907	0.955

Table 2.6: Summary of the prediction methods

Prediction method	Mean Value	Std. Deviation	Variance
Faulkner (Only Initial deflection)	1.043	0.136	0.019
Faulkner (Residual stress with initial deflection)	0.976	0.121	0.015
Soares & Gordo (Only Initial deflection)	1.119	0.176	0.031
Soares & Gordo (Residual stress with initial deflection)	1.077	0.144	0.021
Present study (Only Initial deflection)	**1.037**	**0.092**	**0.008**
Present study (Residual stress with initial deflection)	**1.043**	**0.091**	**0.008**

In the sixth column of Table 2.4 labelled collapse mode of ANSYS FEM is denoted using the following nomenclature:

K: Stiffeners elastic in middle bay

L: Web partially plastic in middle bay

M: Approximate plastic hinge in middle bay

1: Plate elastic in middle bay

2: Plate corners yielded in middle bay

3: Plate mid-longitudinal edges yielded in middle bay

4: Plate gross yield in middle bay

a: Stiffeners elastic in end bay

b: Web partially plastic in end bay

c: Approximate plastic hinge in end bay

1: Plate elastic in end bay

2: Plate corners yielded in end bay

3: Plate mid-longitudinal edges yielded in end bay

4: Plate gross yield in end bay

In the seventh column of Table 4 labelled collapse mode of present study describes as (I) is beam-column buckling failure, (II) is plate induced buckling failure, (III) is tripping buckling failure and (IV) is web local buckling failure.

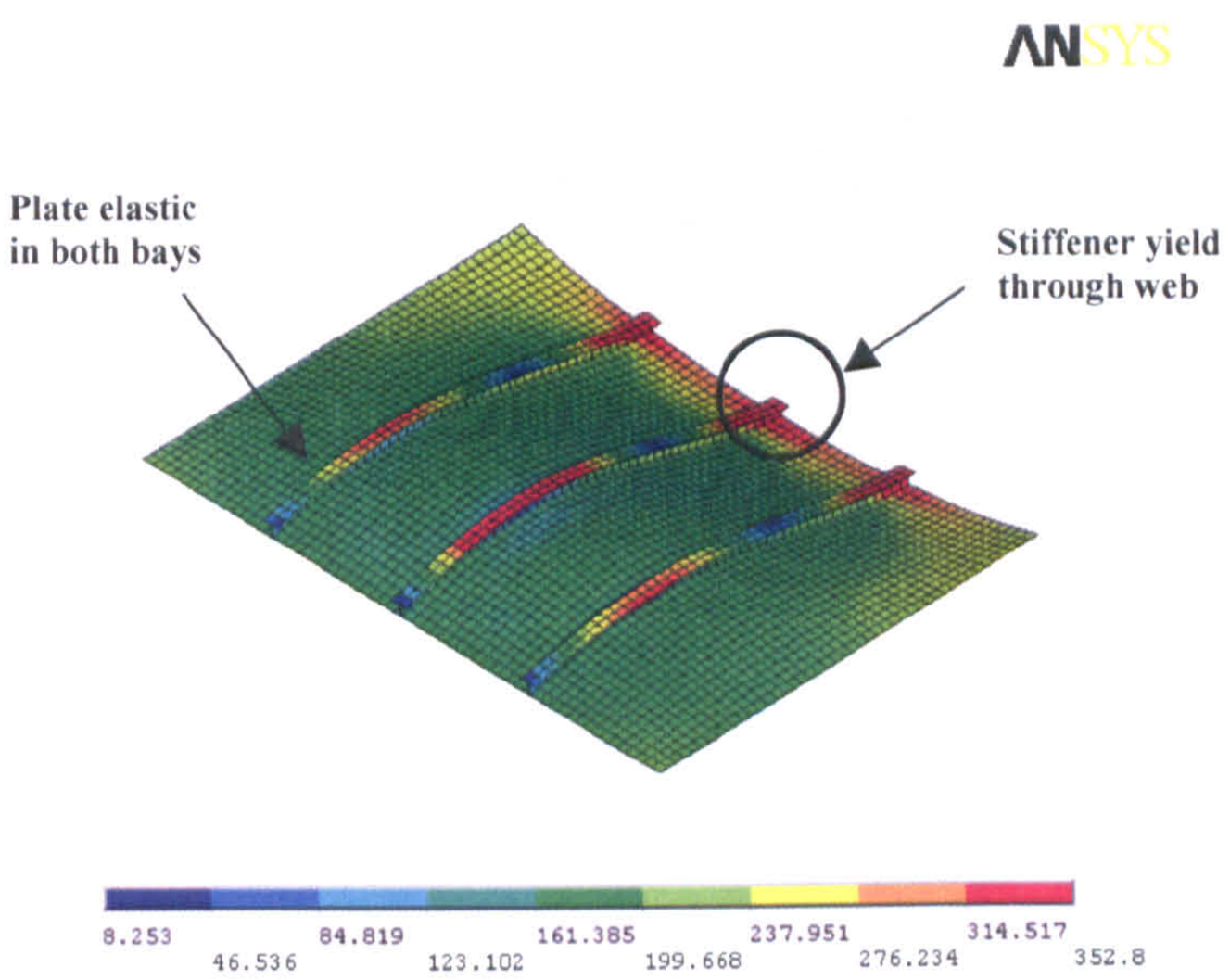

Figure 2.12: Von Misses stress distribution in SP37, where neglected residual stress

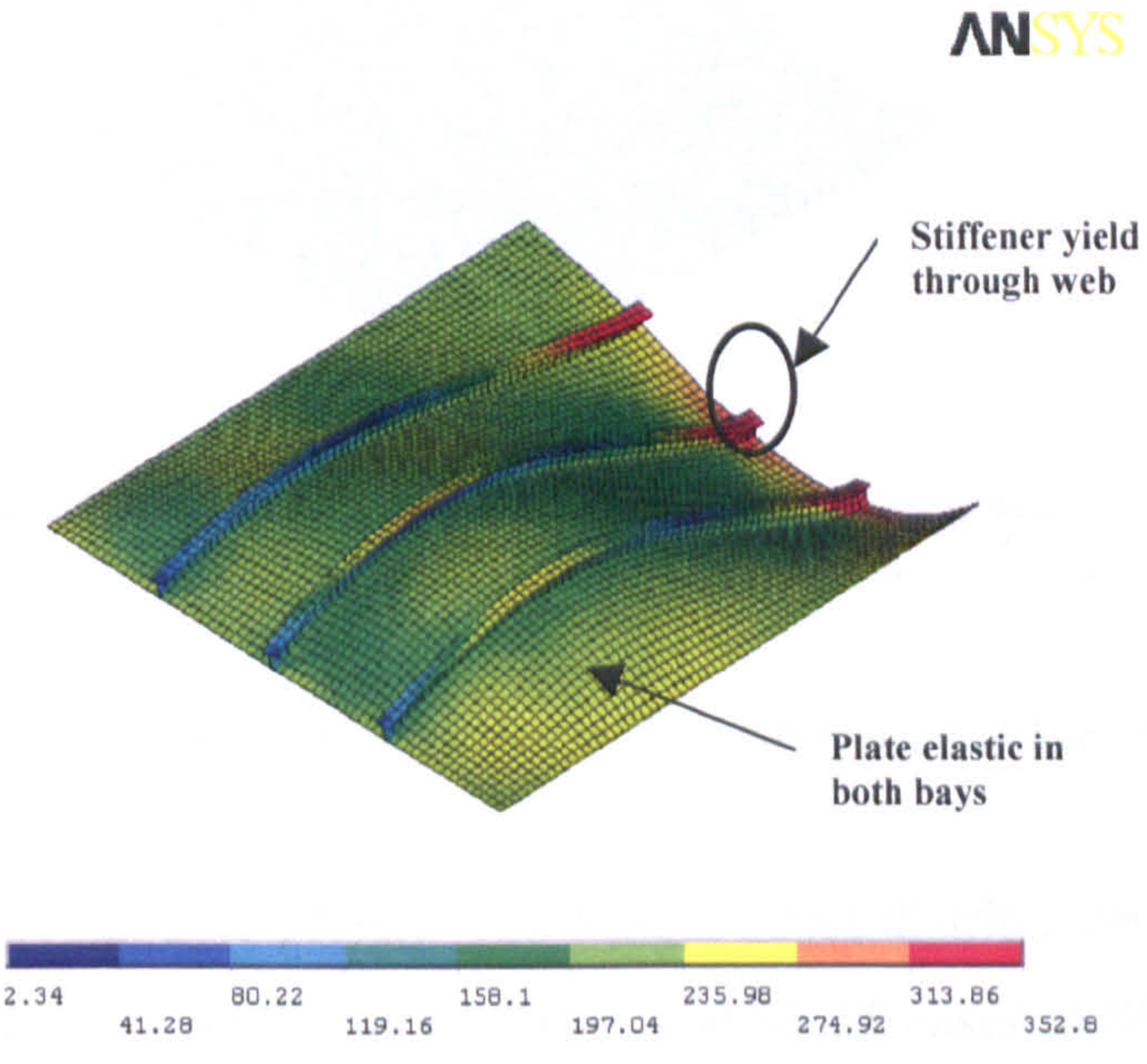

Figure 2.13: Von Misses stress distribution in SP45, where neglected residual stress

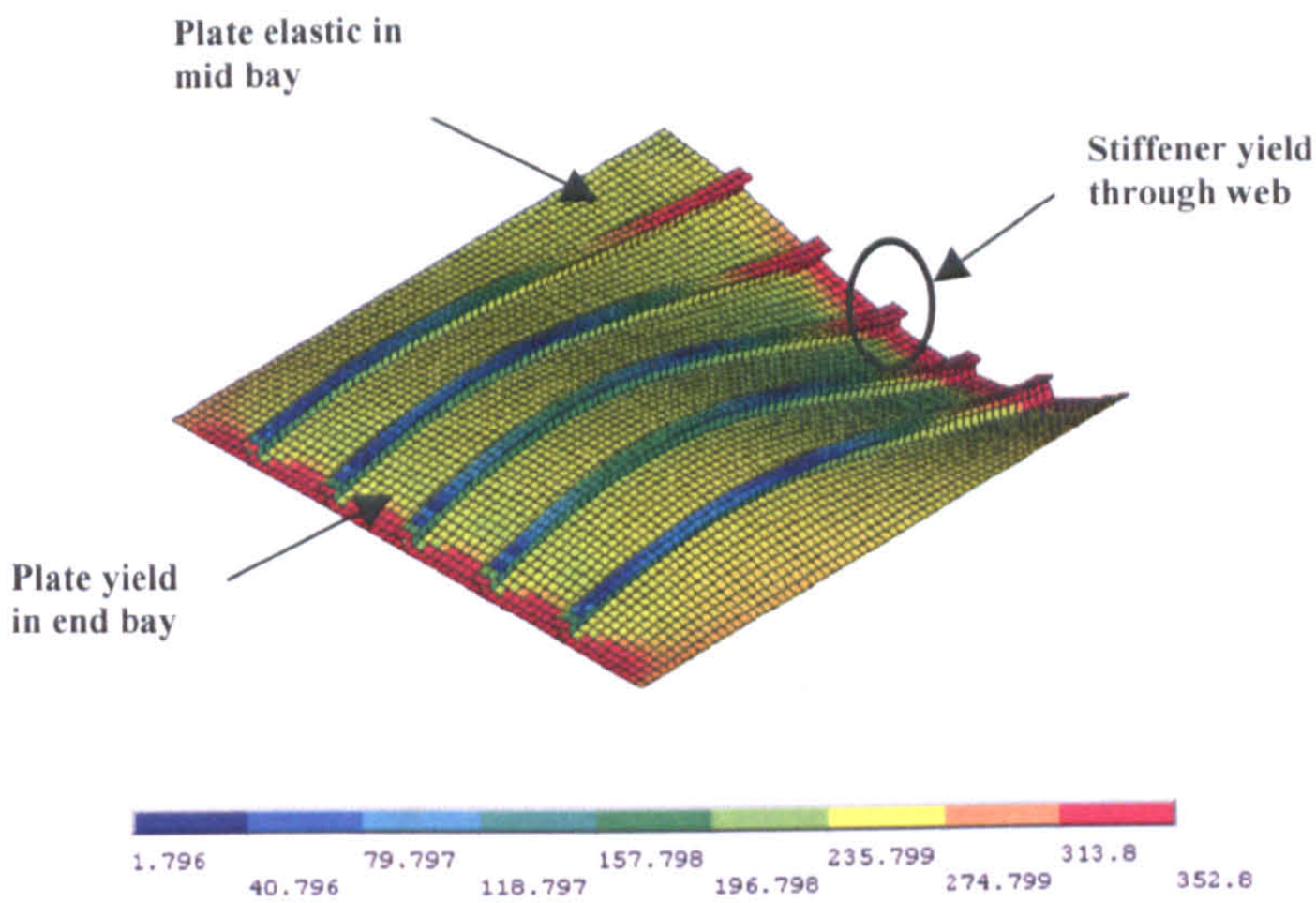

Figure 2.14: Von Misses stress distribution in SP46, where neglected residual stress

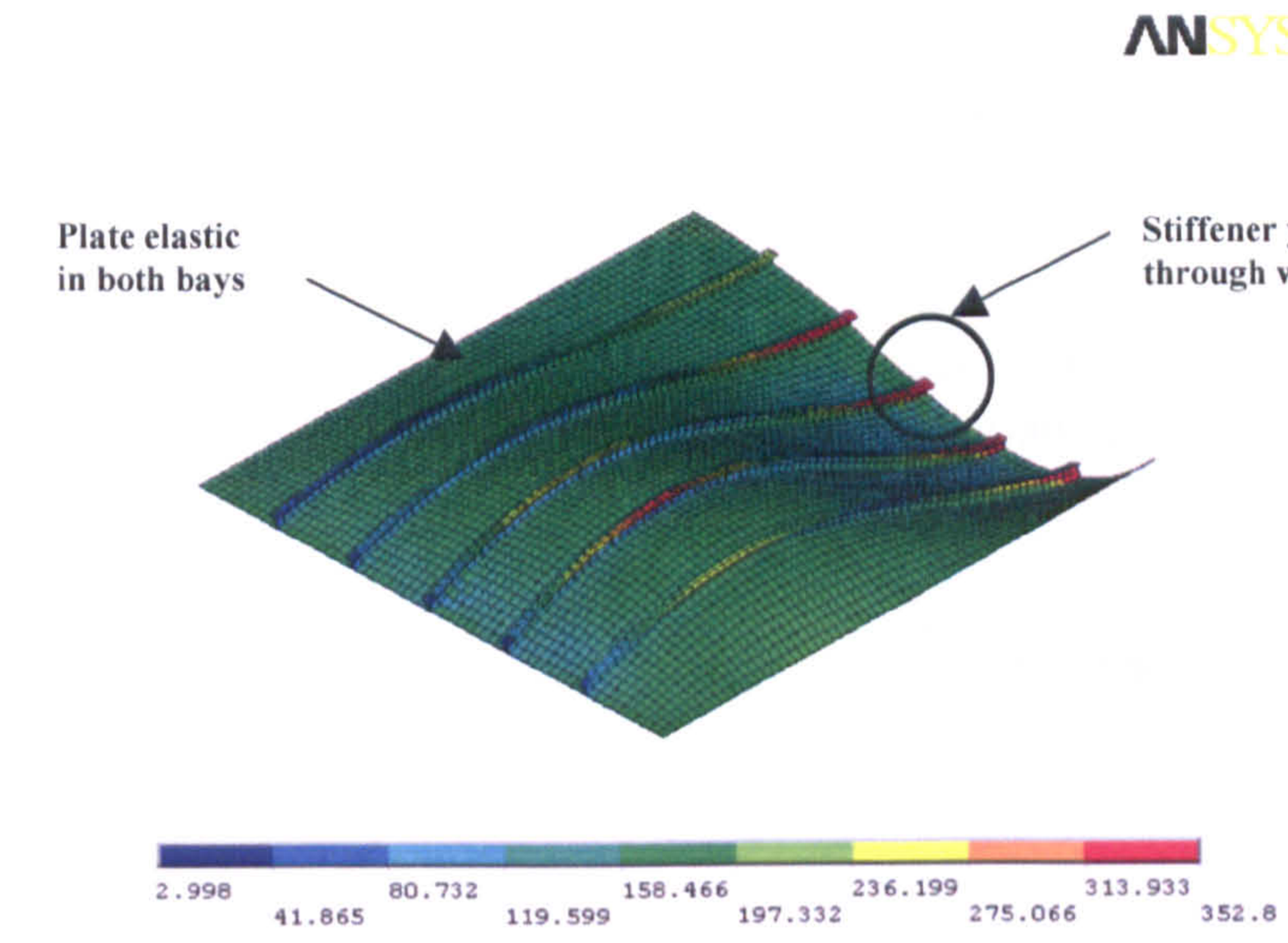

Figure 2.15: Von Misses stress distribution in SP55, where neglected residual stress

Figures 2.12 through 2.15 present Von Misses stress distribution, where residual stresses are ignored for in SP37, SP 45, SP46, and SP 55 cases. ANSYS FE models with considering only overall buckling initial deflection where ignoring welding-induced residual stress, respectively, while Figure 2.16 through 2.19 illustrate stress-strain curves in SP37, SP45, SP46 and SP55 for ANSYS FE models and proposed simple expressions under longitudinal compressive loading. Figure 2.20 through 2.31

illustrates the ultimate capacity respect to vary with beam-column slenderness ratio without and with considering welding-induced residual stress.

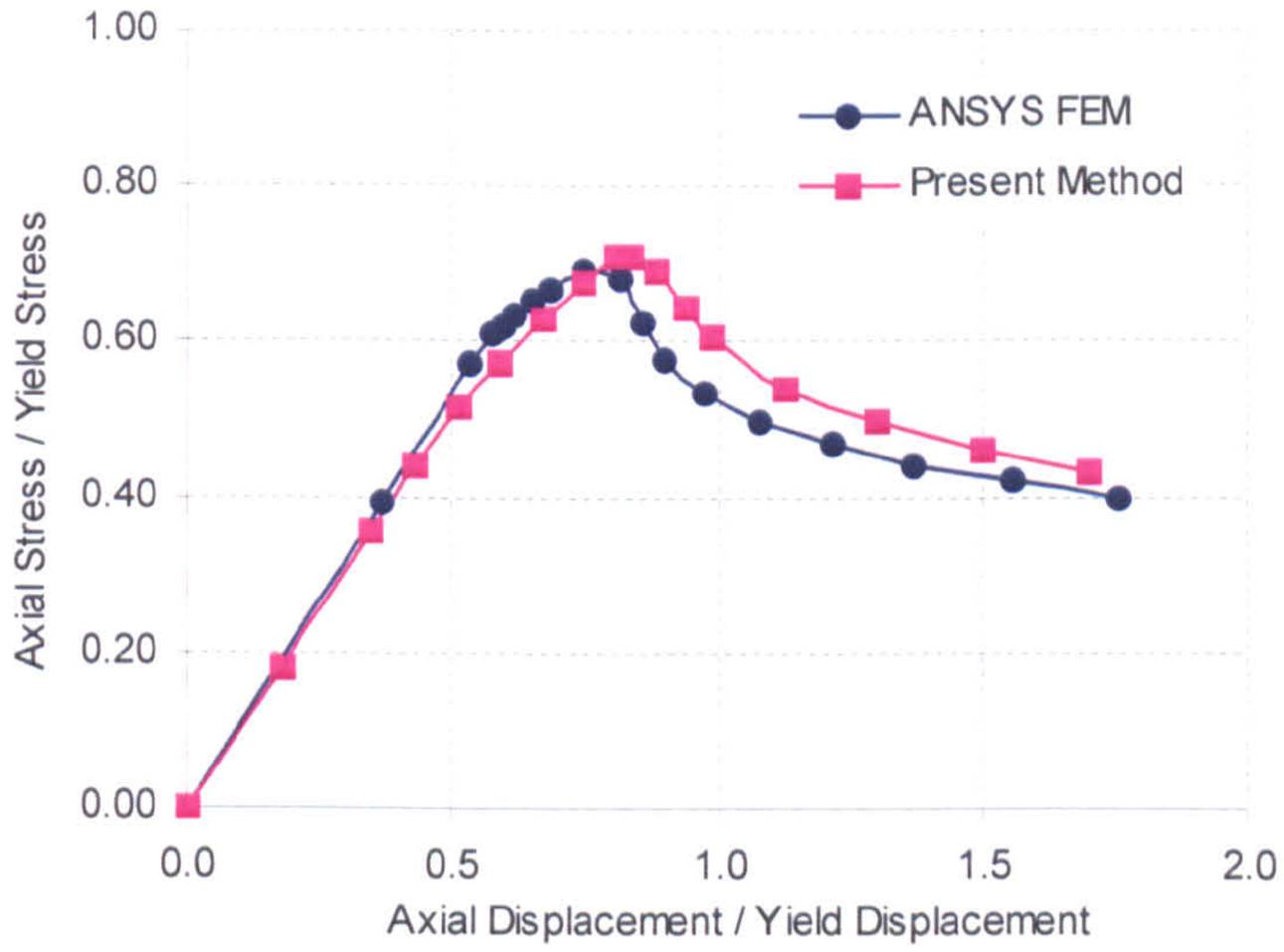

Figure 2.16: Comparison of ANSYS FEM with approximate formulation for SP37

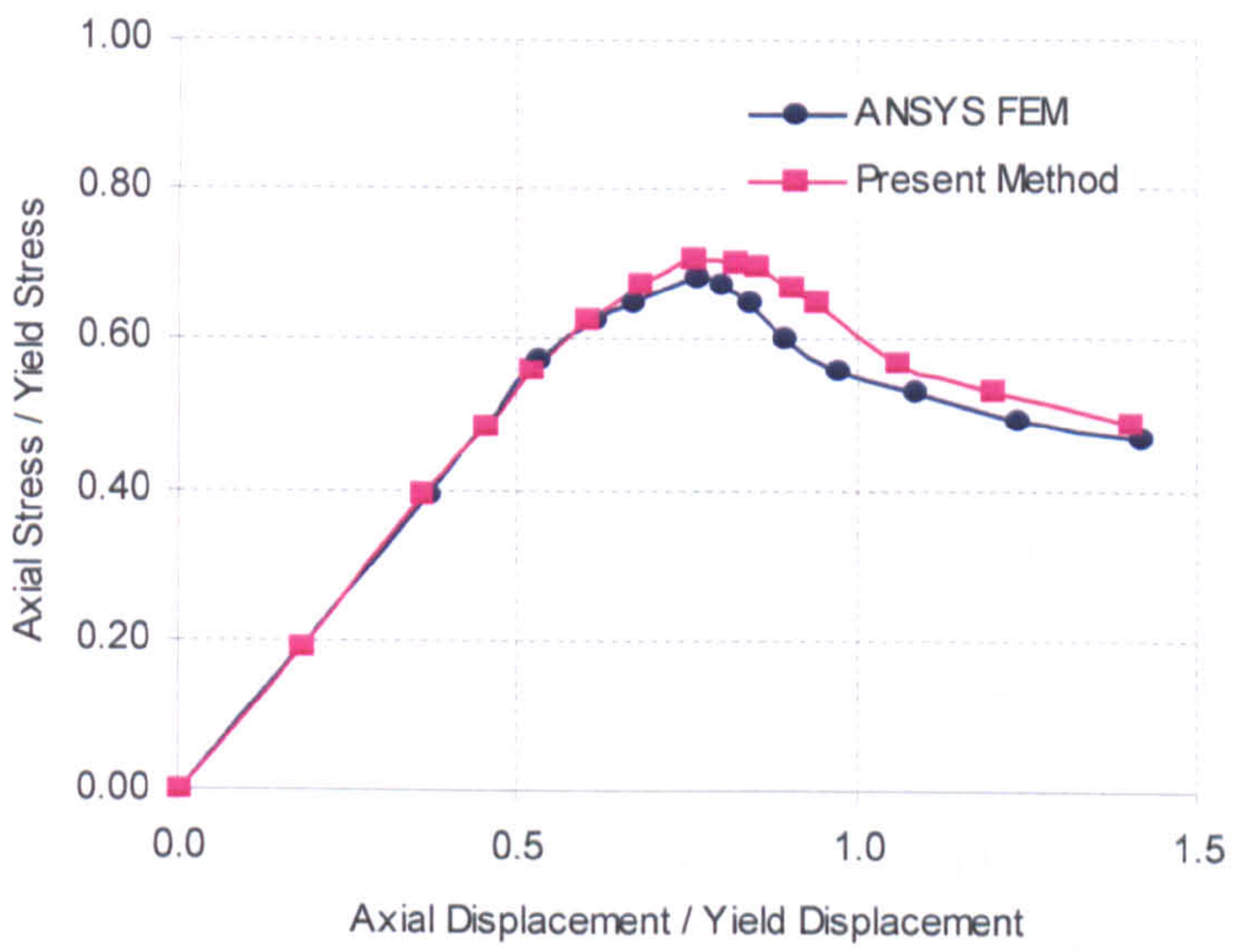

Figure 2.17: Comparison of ANSYS FEM with approximate formulation for SP45

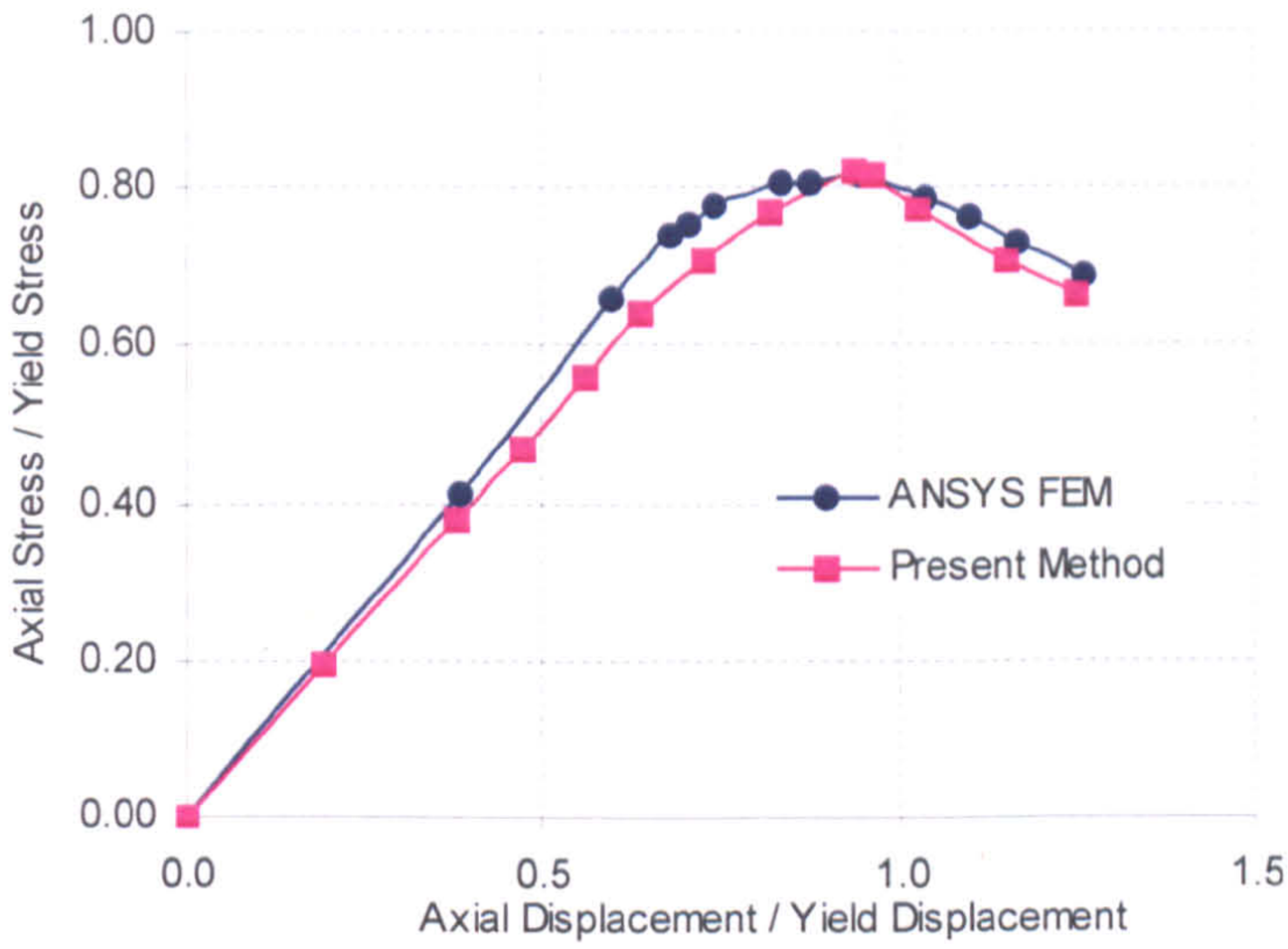

Figure 2.18: Comparison of ANSYS FEM with approximate formulation for SP46

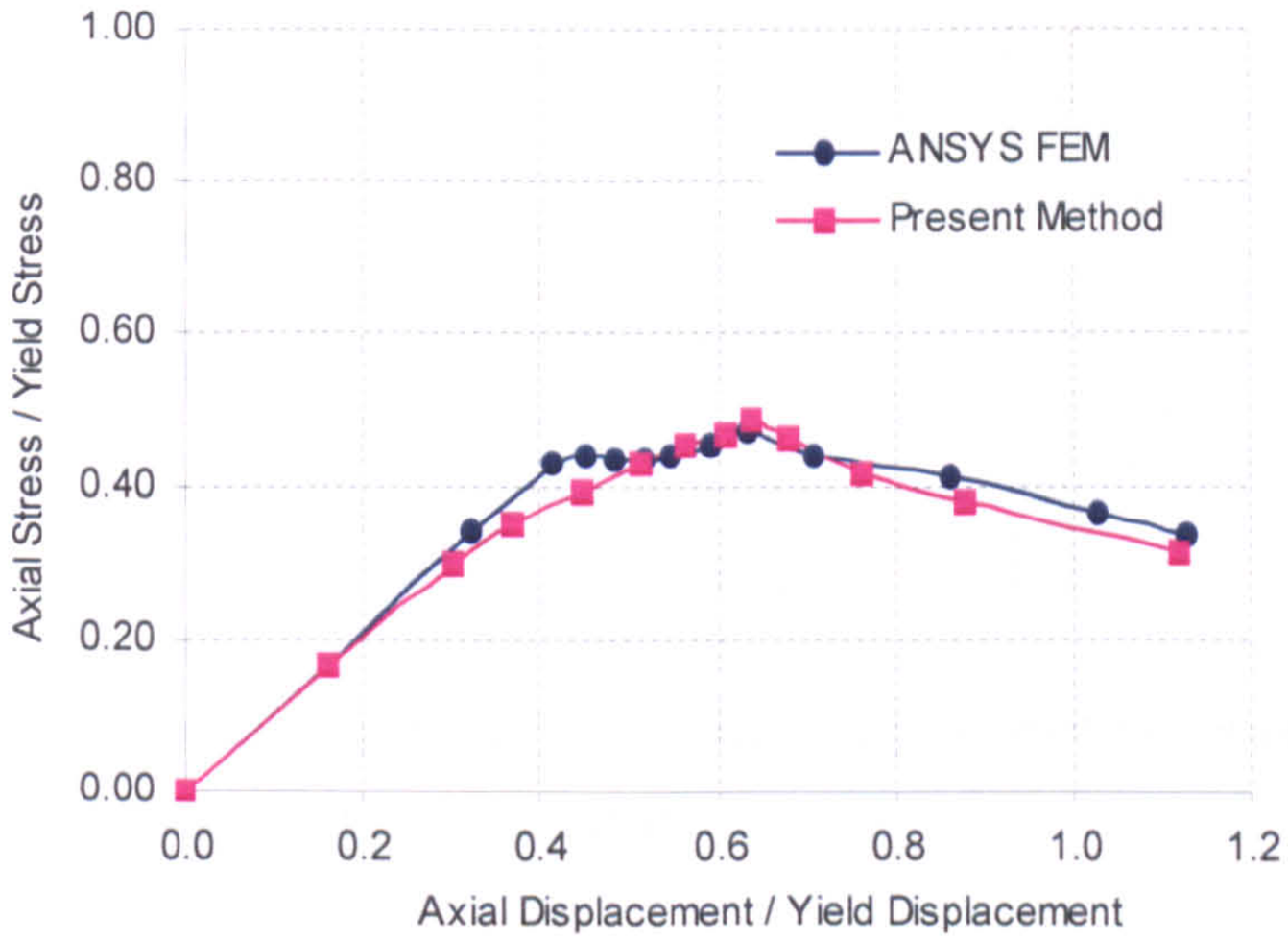

Figure 2.19: Comparison of ANSYS FEM with approximate formulation for SP55

The boundary conditions represent the actual response of the plate or stiffened plate. Simply supported and clamped boundary conditions are considered in this project. The influence of clamped boundary condition has also been investigated on 36 ANSYS FE model and has been compared with new simplified method, which is shown in Table 2.7 and Table 2.8.

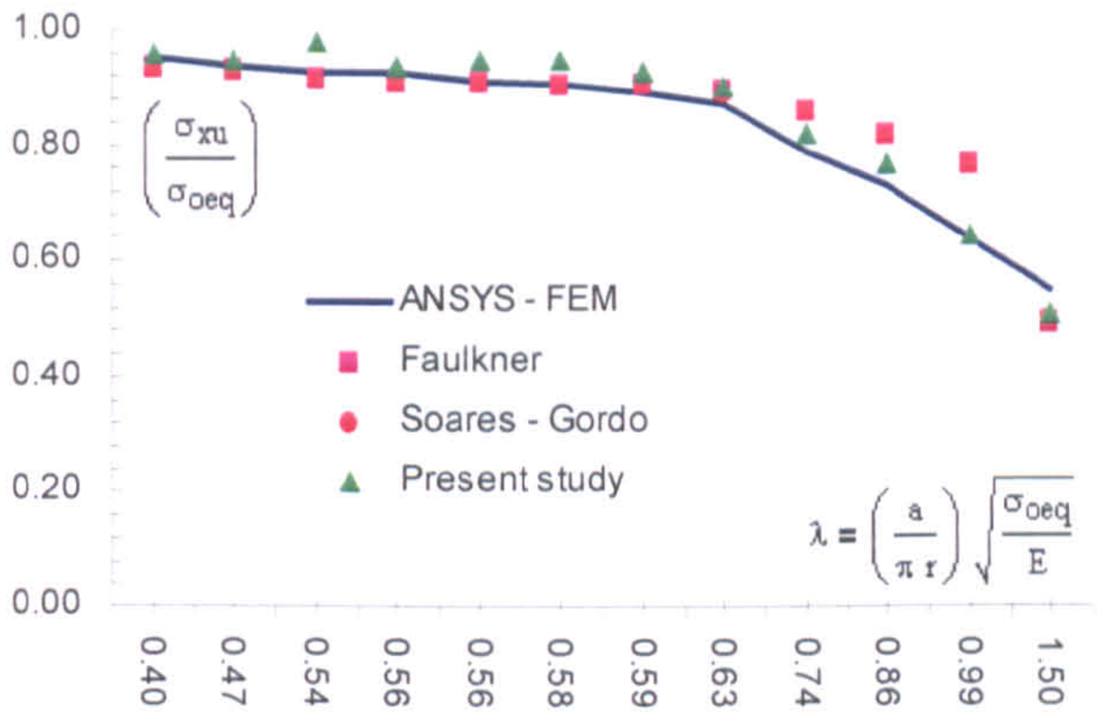

Figure 2.20: The comparison between FEM and simplified methods respect to beam-column slenderness ratio without residual stress effect for $\beta = 1.183$

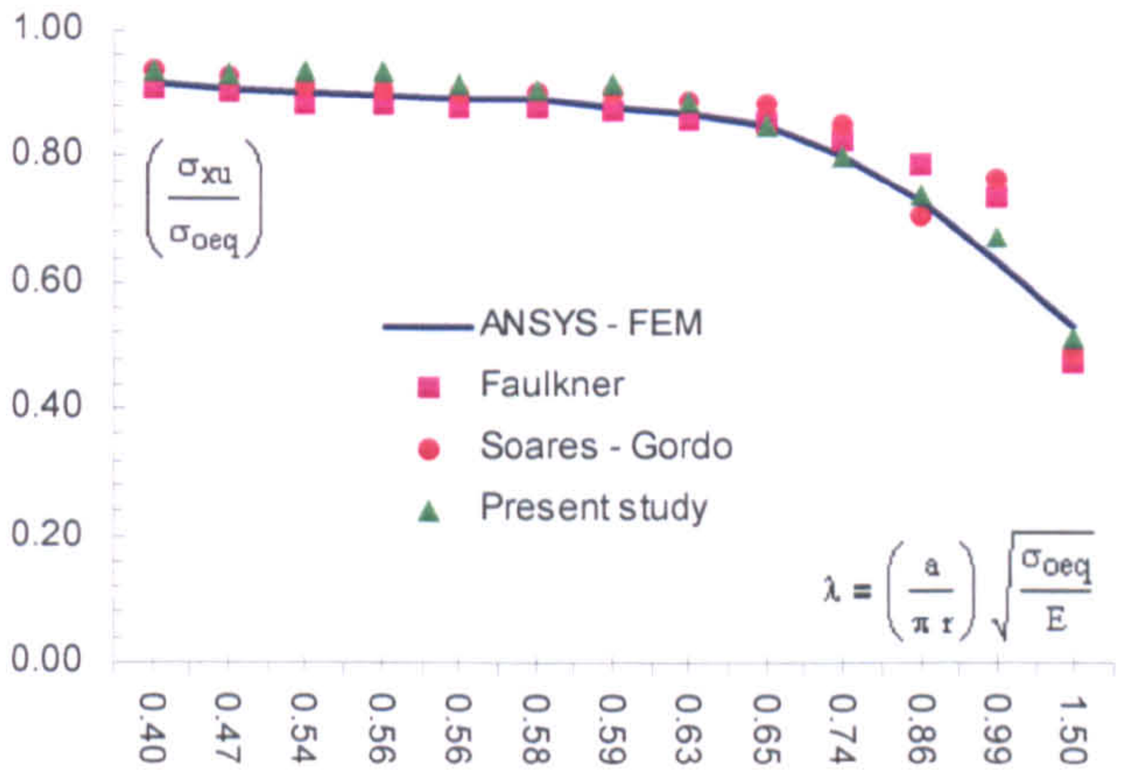

Figure 2.21: The comparison between FEM and simplified methods respect to beam-column slenderness ratio with residual stress effect for $\beta = 1.183$

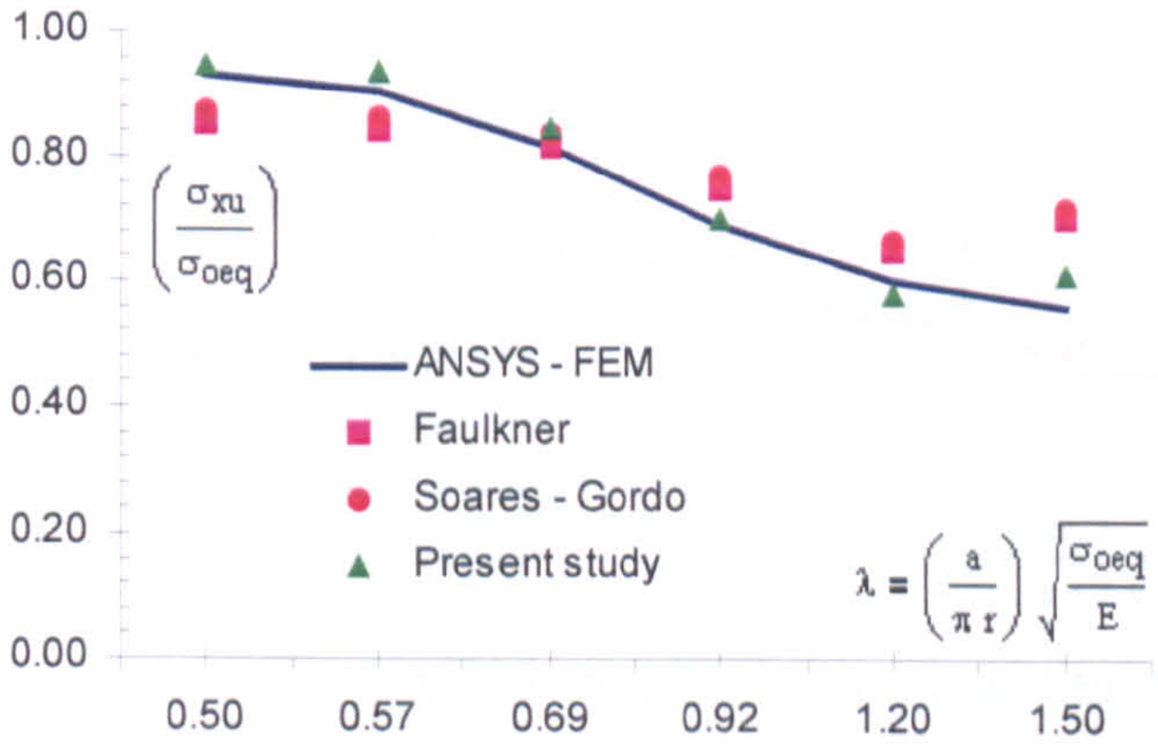

Figure 2.22: The comparison between FEM and simplified methods respect to beam-column slenderness ratio without residual stress effect for $\beta = 1.553$

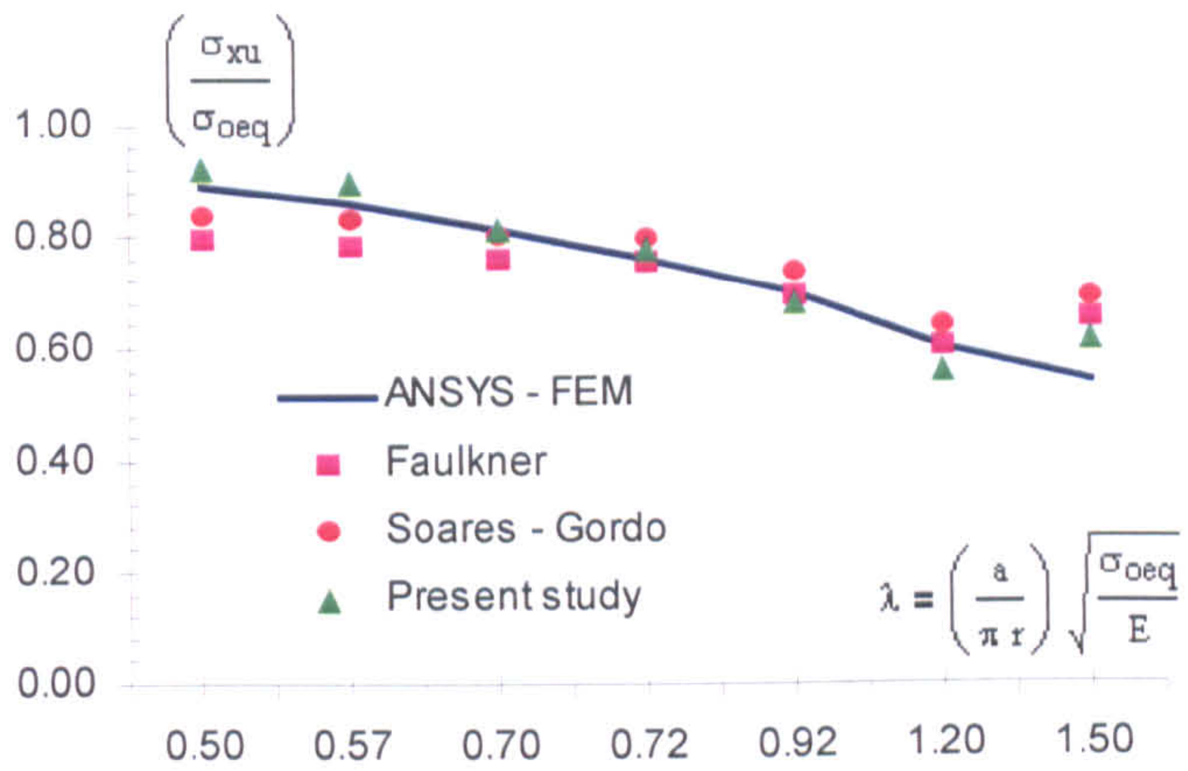

Figure 2.23: The comparison between FEM and simplified methods respect to beam-column slenderness ratio with residual stress effect for $\beta = 1.553$

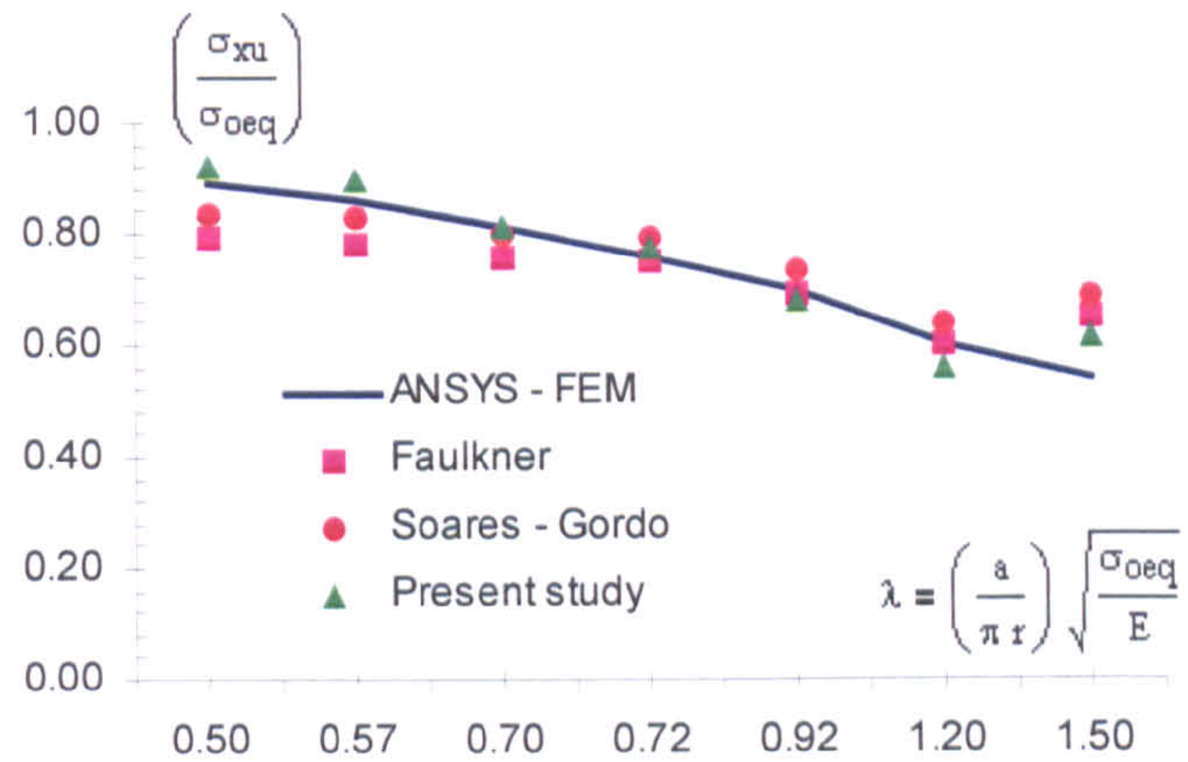

Figure 2.24: Fig.2.22. The comparison between FEM and simplified methods respect to beam-column slenderness ratio without residual stress effect for $\beta = 1.774$

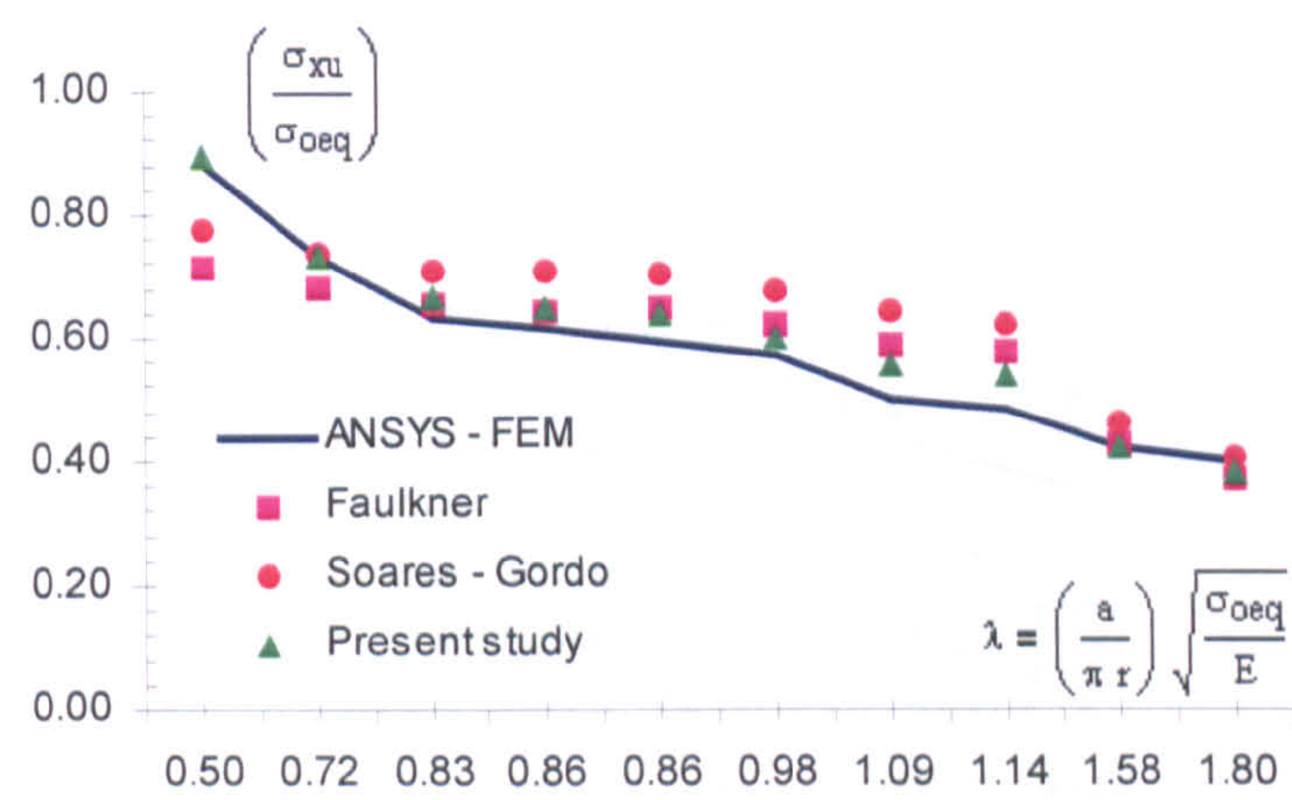

Figure 2.25: The comparison between FEM and simplified methods respect to beam-column slenderness ratio with residual stress effect for $\beta = 1.774$

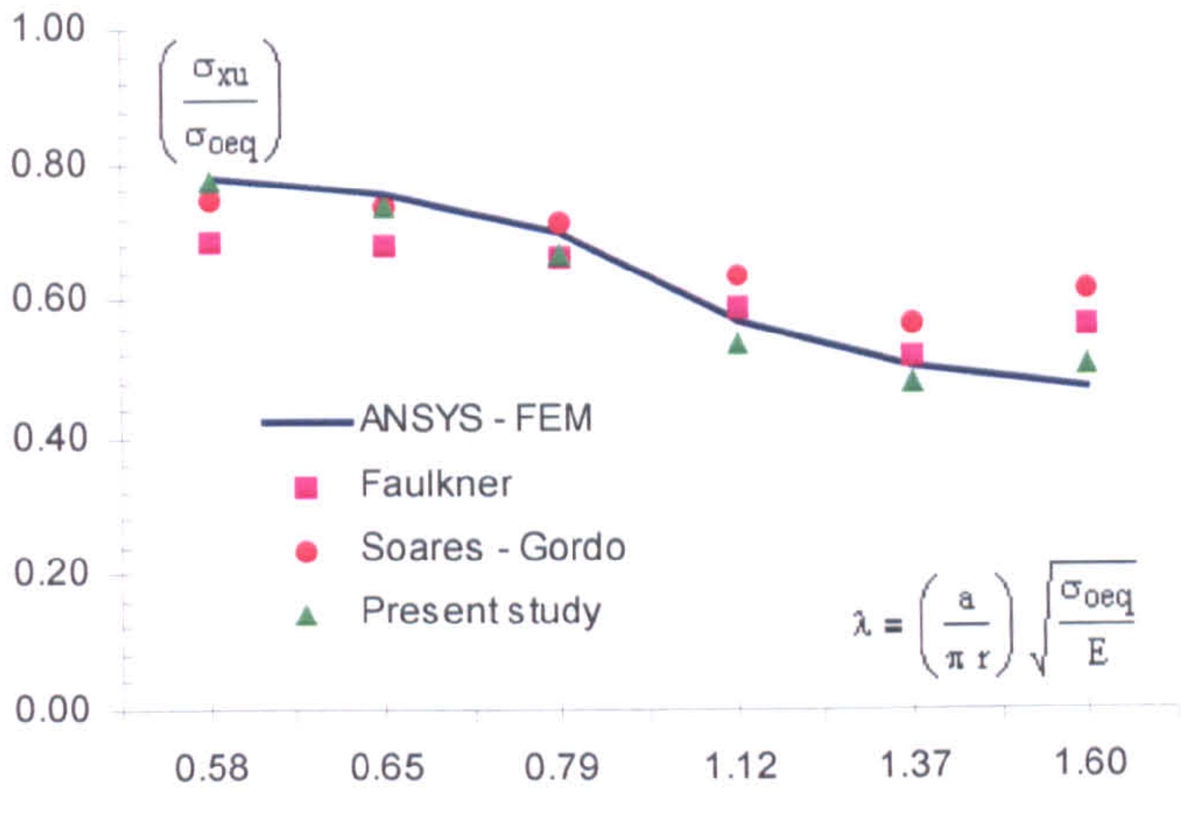

Figure 2.26: The comparison between FEM and simplified methods respect to beam-column slenderness ratio without residual stress effect for $\beta = 2.329$

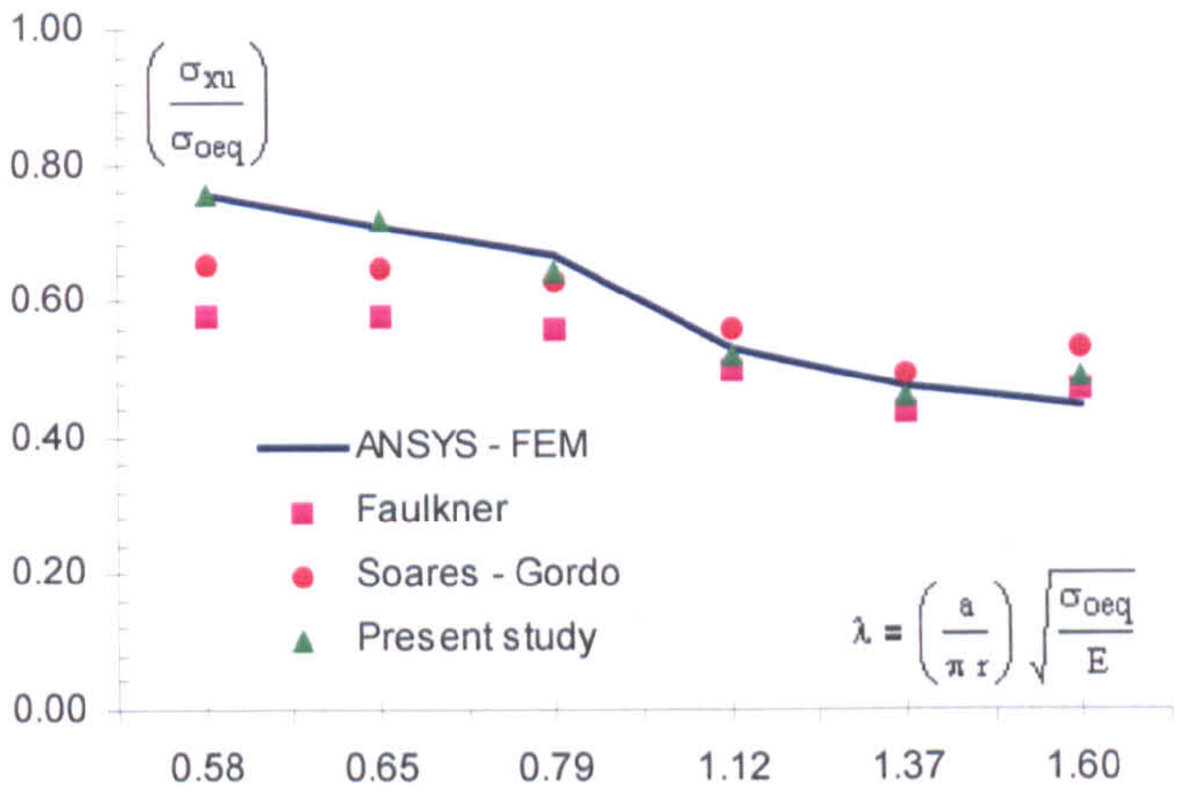

Figure 2.27: The comparison between FEM and simplified methods respect to beam-column slenderness ratio with residual stress effect for $\beta = 2.329$

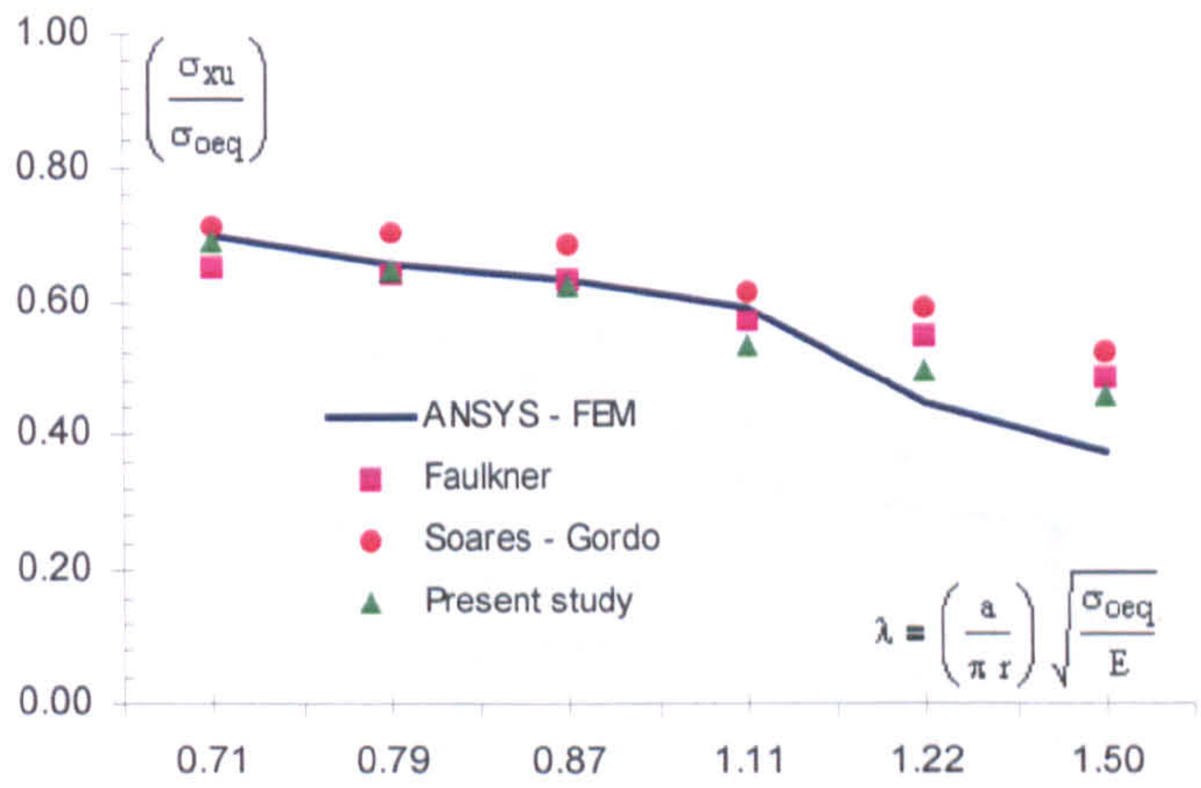

Figure 2.28: The comparison between FEM and simplified methods respect to beam-column slenderness ratio without residual stress effect for $\beta = 2.484$

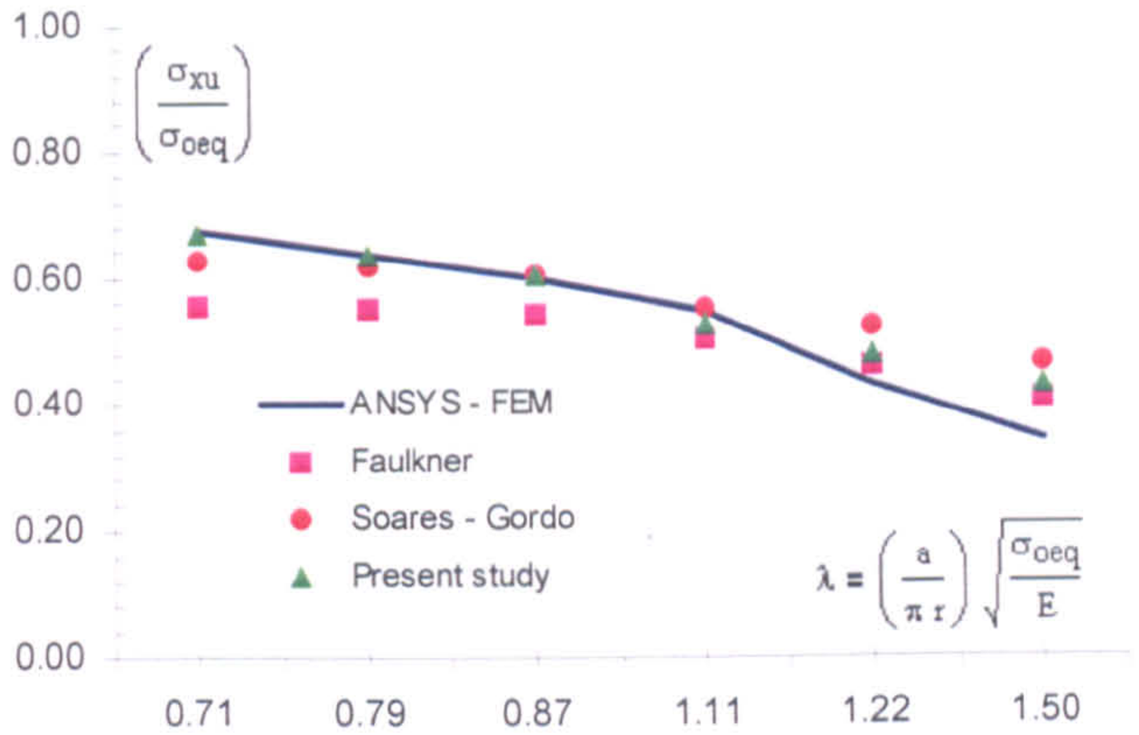

Figure 2.29: The comparison between FEM and simplified methods respect to beam-column slenderness ratio with residual stress effect for $\beta = 2.484$

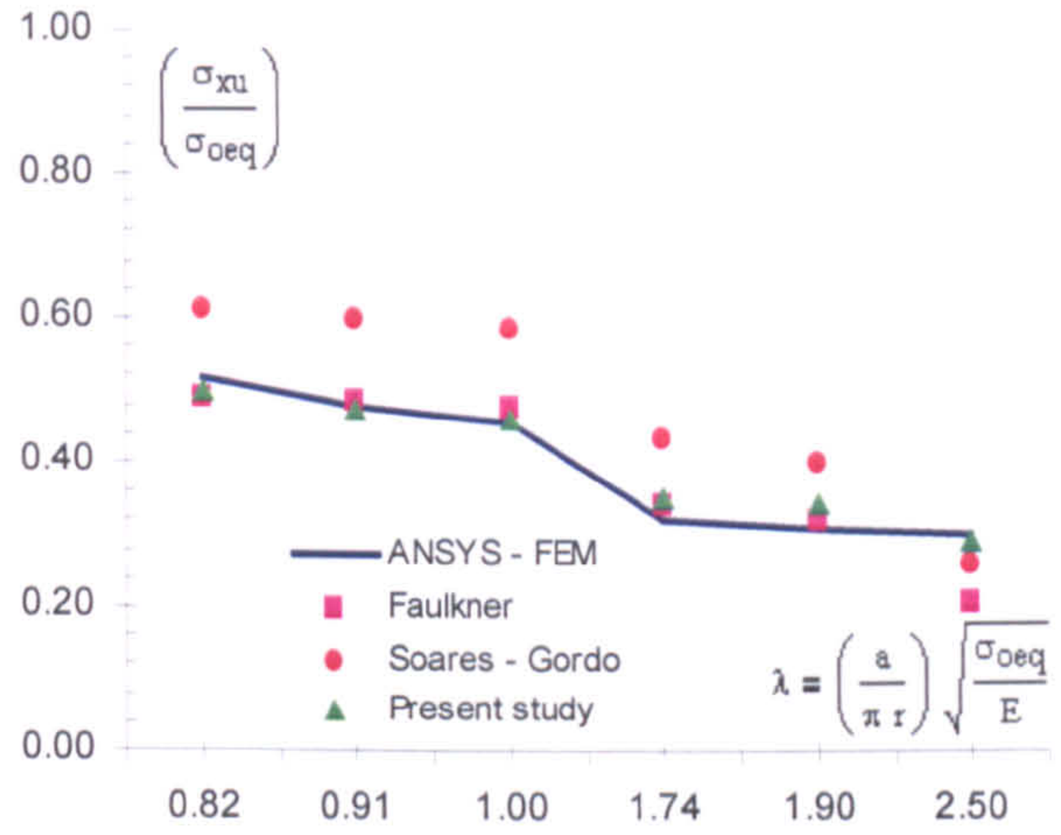

Figure 2.30: The comparison between FEM and simplified methods respect to beam-column slenderness ratio without residual stress effect for $\beta = 3.726$

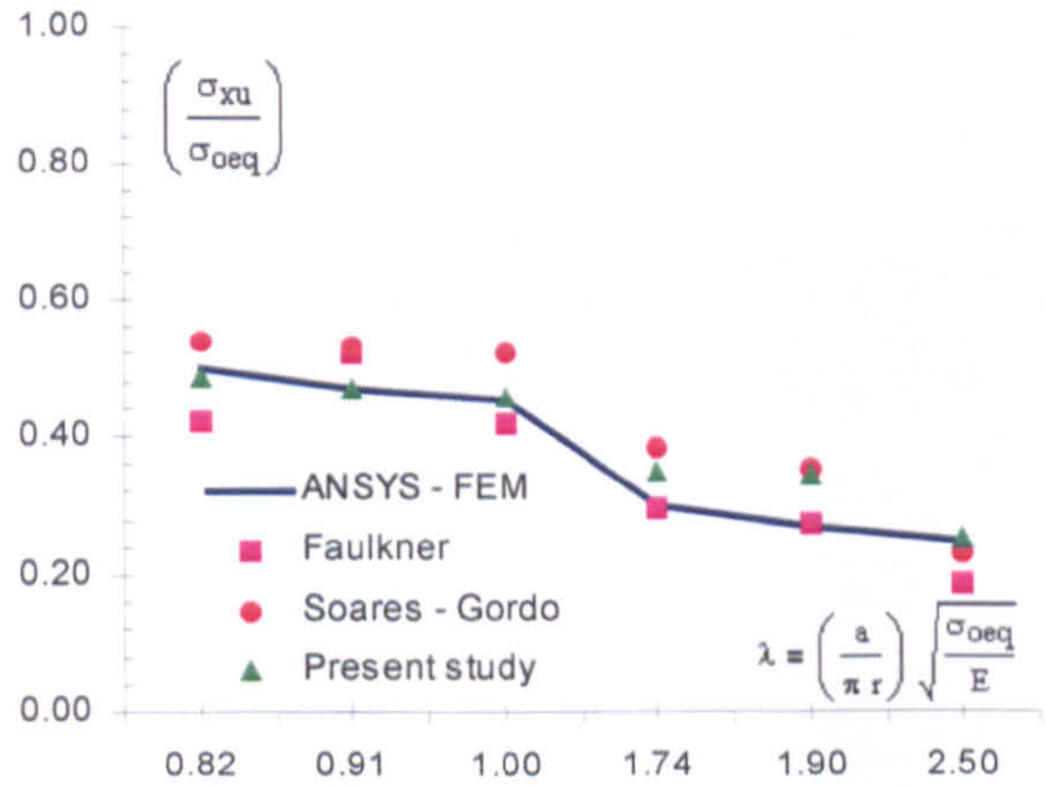

Figure 2.31: The comparison between FEM and simplified methods respect to beam-column slenderness ratio with residual stress effect for $\beta = 3.726$

Table 2.7: The differences between simply supported and clamped boundary conditions in ANSYS FEM

Specimen No.	Simply supported (ANSYS - FEM)	Clamped (ANSYS - FEM)	% Increase
SP1	0.949	0.978	+3.06
SP2	0.965	0.973	+0.83
SP3	0.791	0.808	+2.15
SP4	0.888	0.898	+1.13
SP5	0.660	0.674	+2.12
SP6	0.748	0.766	+2.41
SP7	0.658	0.685	+4.10
SP8	0.790	0.813	+2.91
SP9	0.513	0.561	+9.36
SP10	0.636	0.669	+5.19
SP11	0.517	0.526	+1.74
SP12	0.547	0.566	+3.47
SP13	0.777	0.791	+1.80
SP14	0.940	0.949	+0.96
SP15	0.755	0.767	+1.59
SP16	0.903	0.915	+1.33
SP17	0.503	0.522	+3.78
SP18	0.588	0.609	+3.57
SP19	0.516	0.522	+1.16
SP20	0.697	0.715	+2.58
SP21	0.478	0.485	+1.46
SP22	0.654	0.674	+3.06
SP23	0.457	0.468	+2.41
SP24	0.650	0.661	+1.70
SP25	0.505	0.524	+3.76
SP26	0.633	0.651	+2.84
SP27	0.471	0.497	+5.52
SP28	0.582	0.601	+3.26
SP29	0.790	0.803	+1.65
SP30	0.879	0.898	+2.16
SP31	0.281	0.299	+6.41
SP32	0.372	0.392	+5.38
SP33	0.300	0.305	+1.67
SP34	0.401	0.420	+4.74
SP35	0.700	0.715	+2.14
SP36	0.839	0.856	+2.03

Table 2.8: The comparison between ANSYS FEM and Present study in clamped case

Specimen No.	Clamped (ANSYS - FEM)	Clamped (Present study)	Clamped (Present study) / FEM
SP1	0.978	0.970	0.992
SP2	0.973	1.030	1.058
SP3	0.808	0.792	0.980
SP4	0.898	0.940	1.046
SP5	0.674	0.651	0.966
SP6	0.766	0.787	1.027
SP7	0.685	0.705	1.029
SP8	0.813	0.865	1.064
SP9	0.561	0.585	1.042
SP10	0.669	0.694	1.037
SP11	0.526	0.427	0.812
SP12	0.566	0.456	0.806

SP13	0.791	0.810	1.024
SP14	0.949	0.961	1.012
SP15	0.767	0.770	1.004
SP16	0.915	0.914	0.999
SP17	0.522	0.496	0.950
SP18	0.609	0.568	0.933
SP19	0.522	0.505	0.967
SP20	0.715	0.714	0.999
SP21	0.485	0.483	0.996
SP22	0.674	0.676	1.003
SP23	0.468	0.467	0.998
SP24	0.661	0.643	0.973
SP25	0.524	0.572	1.092
SP26	0.651	0.682	1.047
SP27	0.497	0.528	1.062
SP28	0.601	0.616	1.025
SP29	0.803	0.781	0.973
SP30	0.898	0.936	1.042
SP31	0.299	0.364	1.220
SP32	0.392	0.390	0.995
SP33	0.305	0.355	1.167
SP34	0.420	0.457	1.088
SP35	0.715	0.694	0.971
SP36	0.856	0.824	0.963
		Mean Value:	*1.010*
		Std. Deviation:	*0.074*
		Variance:	*0.007*

2.8 Effects of Load Combinations on the Ultimate Strength Capacity

The stress picture in real ship structures tends to become very complicated. The load bearing capacity of the stiffened panel depends on the actual stress distribution, and may be result of several load actions. The main load component for the deck structure, the bottom structure and longitudinal bulkheads close to the deck and bottom is axial compression. Therefore, in standard design analyses of the ultimate hull girder moments, the only load components considered are longitudinal stresses. However, the external bottom plating and the lower parts of the side shells can in addition be subjected to relatively high external lateral pressure and the inner bottom and inner longitudinal bulkheads to lateral pressure loads from the cargo. These lateral pressures also either directly or through bending in web frames introduce transverse in-plane loads on the plate fields.

The task of determining the detailed stress distribution in a part of the ship structures, will in reality involve large-scale numerical analysis using the Finite Element method. For some structures, it may be necessary to perform fully non-linear FE analyses to determine the actual stress distribution due to the local non-linear response rising from the initial deformations, residual stresses and fabrication tolerances. This picture becomes more complicated when the aim is to assess the ultimate carrying capacity of the structures.

It is therefore important that the simplified capacity models should be developed which cover the combine load components. This study establishes the ultimate strength interaction relationship of a stiffened plate subject to combine loads with imperfections in the form of geometric deflections and welding induced residual stresses. The accuracy of the interaction expressions is confirmed by use of inelastic finite element calculations. Comparison is carried out with existing ship rules used by Classification Societies as well.

2.8.1 Influence of transverse compression and lateral pressure on the ultimate strength

Ultimate strength analyses have been carried out by using ANSYS FEM on a typical panel called DW 5120, subjected to transverse axial compression without and with pressure, which has also been analysed by DNV and Hughes *et al.* (2002) using ABAQUS. Following Table 2.9 summarizes main particulars of FE model and is shown in Figure 2.32.

Two load cases have been investigated, namely, Case 1 is panel under only transverse load without lateral pressure and Case 2 is panel under combined transverse compression and lateral pressure ($\rho = 0.2531$ MPa).

Table 2.9: The main particulars of DW 5120 analysed in ANSYS FEM

Number of bays modelled	1/2 + 1 + 1 +1/2
Length of each bay (mm)	5120
Panel breadth (mm)	9100
Plate thickness (mm)	20
Web height (mm)	598.5
Web thickness (mm)	12
Stiffeners	9 longitudinal T-stiffeners
Flange breadth (mm)	200
Flange thickness (mm)	20
Yield stress (MPa)	315
Young's modulus (MPa)	208000
Poisson ratio	0.30

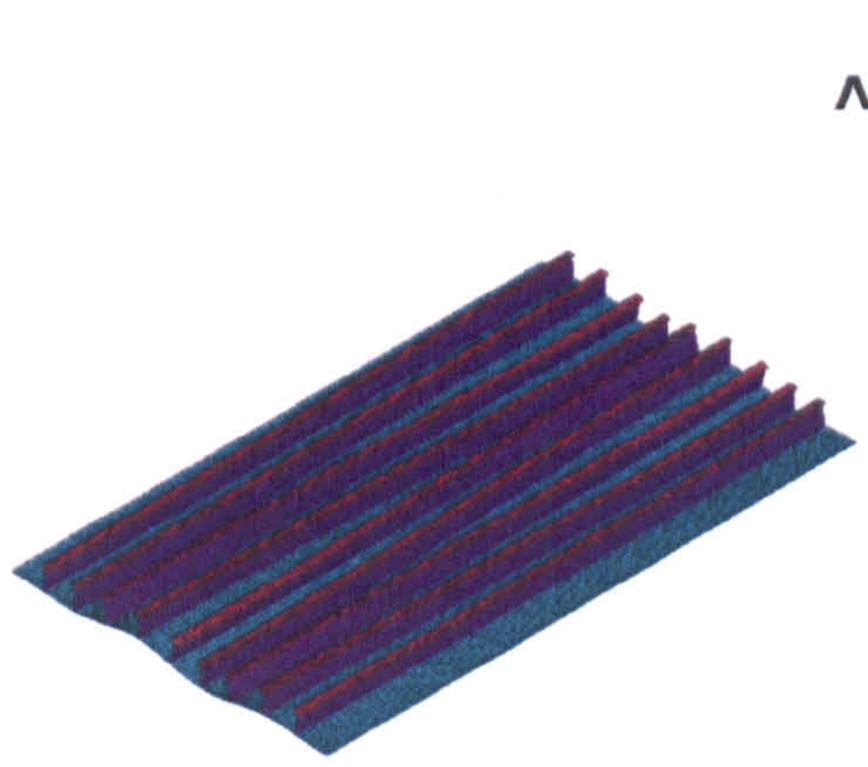

Figure 2.32: Linear eigenvalue buckling for DW 5120, mode shape 1

In case 1, ultimate strength 121.3 MPa and collapse is due to buckling of subpanels, in alternating directions, with full yield along their short edges. In case 2, ultimate strength has been calculated to be 105.5 MPa and collapse is due to a localized upward buckling of alternate subpanels in a checkerboard pattern, which the subpanels have an upward initial local imperfection. Table 2.10 presents transverse compression capacity of stiffened plates under combine loading.

Table 2.10: The comparison of ANSYS FEM with the present study for transverse compression capacity of stiffened plate

	P (MPa)	$\frac{\sigma_{ANSYS-FEM}}{\sigma_o}$	$\frac{\sigma_{Present\ study}}{\sigma_o}$	$\frac{\sigma_{Present\ study}}{\sigma_{ANSYS-FEM}}$
DW 5120	0	0.396	0.419	1.058
	0.05	0.383	0.415	1.083
	0.10	0.377	0.409	1.084
	0.15	0.358	0.401	1.120
	0.20	0.355	0.383	1.078
	0.25	0.347	0.371	1.069
	0.30	0.343	0.362	1.055
SP3	0	0.522	0.545	1.044
	0.123	0.515	0.538	1.044
	0.245	0.499	0.515	1.032
	0.368	0.478	0.476	0.995
SP27	0	0.389	0.396	1.017
	0.079	0.387	0.391	1.010
	0.157	0.378	0.377	0.997
SP33	0	0.241	0.229	0.950
	0.031	0.240	0.225	0.937
	0.061	0.239	0.218	0.912
SP2	0	0.779	0.821	1.053
	0.304	0.755	0.815	1.079
	0.456	0.726	0.798	1.099
SP26	0	0.542	0.626	1.155
	0.176	0.515	0.615	1.194
	0.264	0.457	0.595	1.302
SP32	0	0.366	0.363	0.992
	0.069	0.359	0.358	0.997
	0.103	0.352	0.352	1.000

According to above numerical results, an interaction formula is proposed for transverse compression and lateral pressure as follows:

$$\left(\frac{\sigma_y}{\sigma_{yu}}\right)^2 + \left(\frac{p}{p_u}\right)^{1.5} = 1 \tag{2.56}$$

where p_u is defined as critical (ultimate) lateral pressure of plating between stiffeners clamped at all edges from rigid plastic theory proposed by Wood (1961) as below:

$$p_u = C_p \frac{\sigma_{op}{}^2}{E\beta^2}, \text{ where } C_p = \frac{12}{\left[\sqrt{3+(b/a)^2} - b/a\right]^2} \tag{2.57}$$

It is noticed that moderate lateral pressure has very small effect on the transverse ultimate capacity. The degree of reduction depends on pressure value. When water head is increased, bending stresses become larger. Because of this, yielding will take place earlier, which results in reduced ultimate strength capacity. It is seen that proposed an empirical formulae to calculate the transverse buckling strength of a continuous stiffened plate field including the effect of lateral pressure which shows good correlation with numerical FEM analyses.

Capacity curves for the longitudinal buckling capacity for DW 5120, which is a tanker bottom panel are also presented as a function of lateral pressure in Figure 2.33.

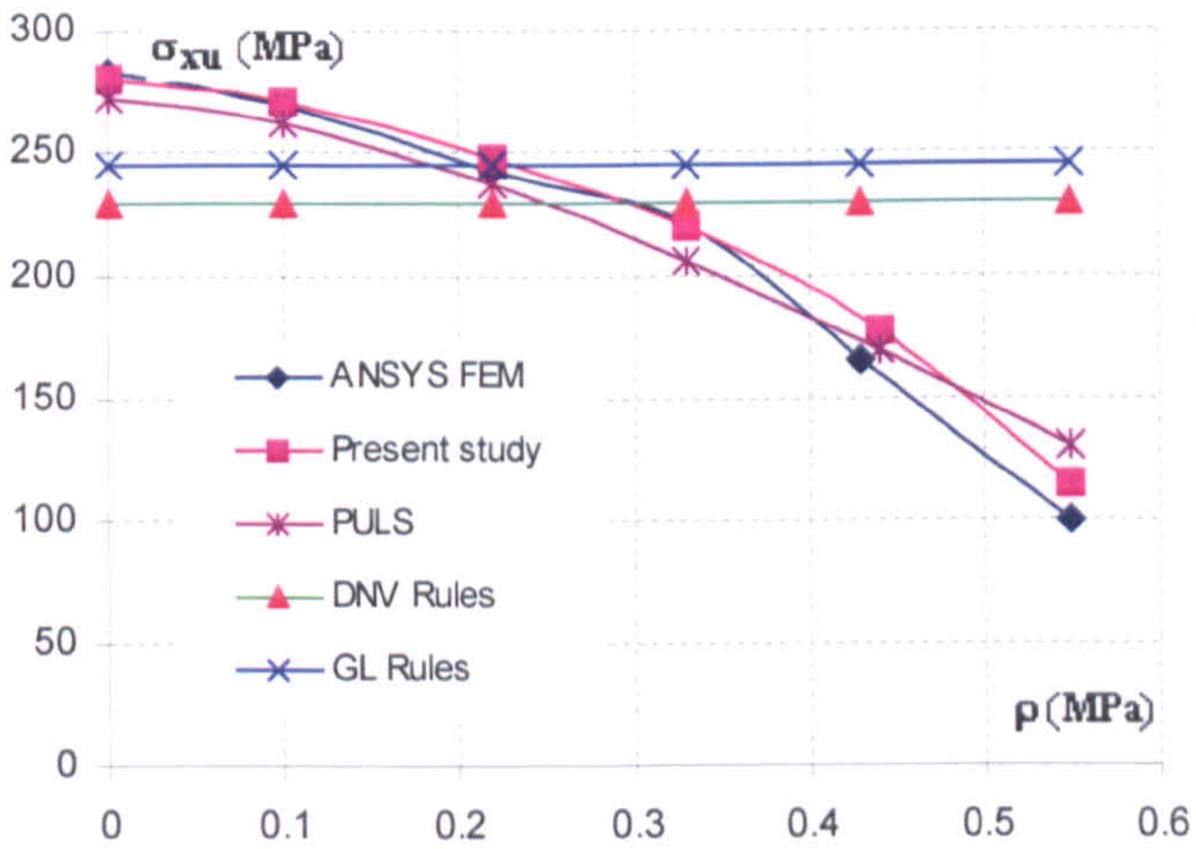

Figure 2.33: Effect of lateral pressure on axial capacity for DW 5120 tanker bottom panel

It is seen that present method in the axial capacity predicts very well results as compared to ANSYS FEM, while the rule formulations overpredict the capacity of the stiffened panel since they are not affected by influence of lateral pressure. Following an expression is proposed for longitudinal compression and lateral pressure for practical applications in ship design.

$$\left(\frac{\sigma_x}{\sigma_{xu}}\right)^2 + \left(\frac{p}{p_u}\right)^{1.5} = 1 \qquad (2.58)$$

2.8.2 Biaxial compression

Capacity curves for bi-axial compression of bottom panel of a 173 m Tanker are presented in Figure 2.34, while Table 2.11 summarizes main particulars of investigated model. Results for the same panel under combined in-plane compression and lateral pressure are presented in Figure 2.35.

Table 2.11: The main particulars of the Tanker bottom panel

Length of stiffened panel	2400 mm
Stiffener spacing	800 mm
Plate thickness	13.5 mm
Web height	240 mm
Web thickness	11 mm
Stiffeners	6 longitudinal Bulb profiles
Yield stress	355 MPa
Young's modulus	208000 MPa
Poisson ratio	0.3

The new proposed interaction formula is suggested and validated FEM results reported by DNV Research Team (2004), where ABAQUS and PULS were employed.

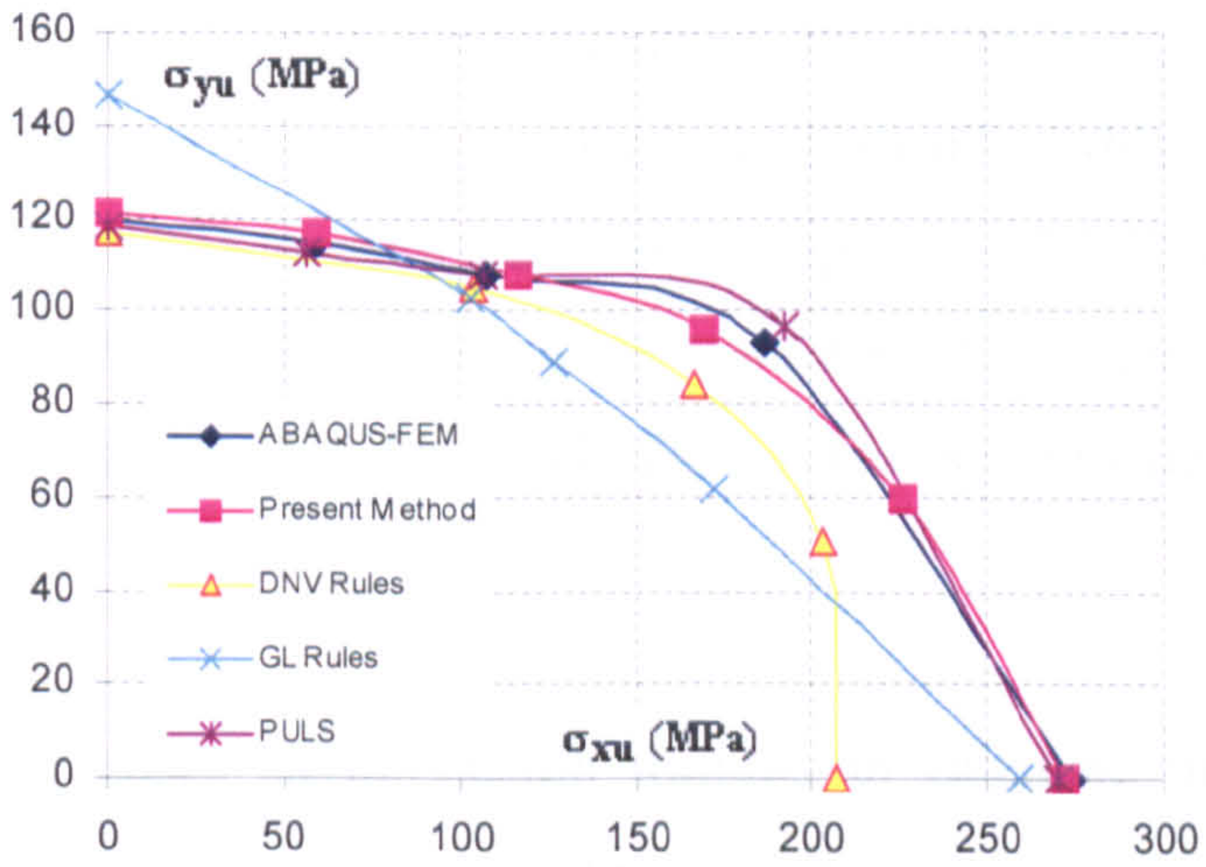

Figure 2.34: Tanker bottom panel, biaxial compression without lateral pressure

The comparisons of ultimate strength capacities using ABAQUS FEM, PULS and present method are very consistent. Such deviations are to be expected since the

applied methods are very different. Typically the largest deviations are for regions in load space where the failure mode is not unique and obtained results depend strongly on how the geometrical imperfections are modelled especially with respect to shape and definition of boundary condition.

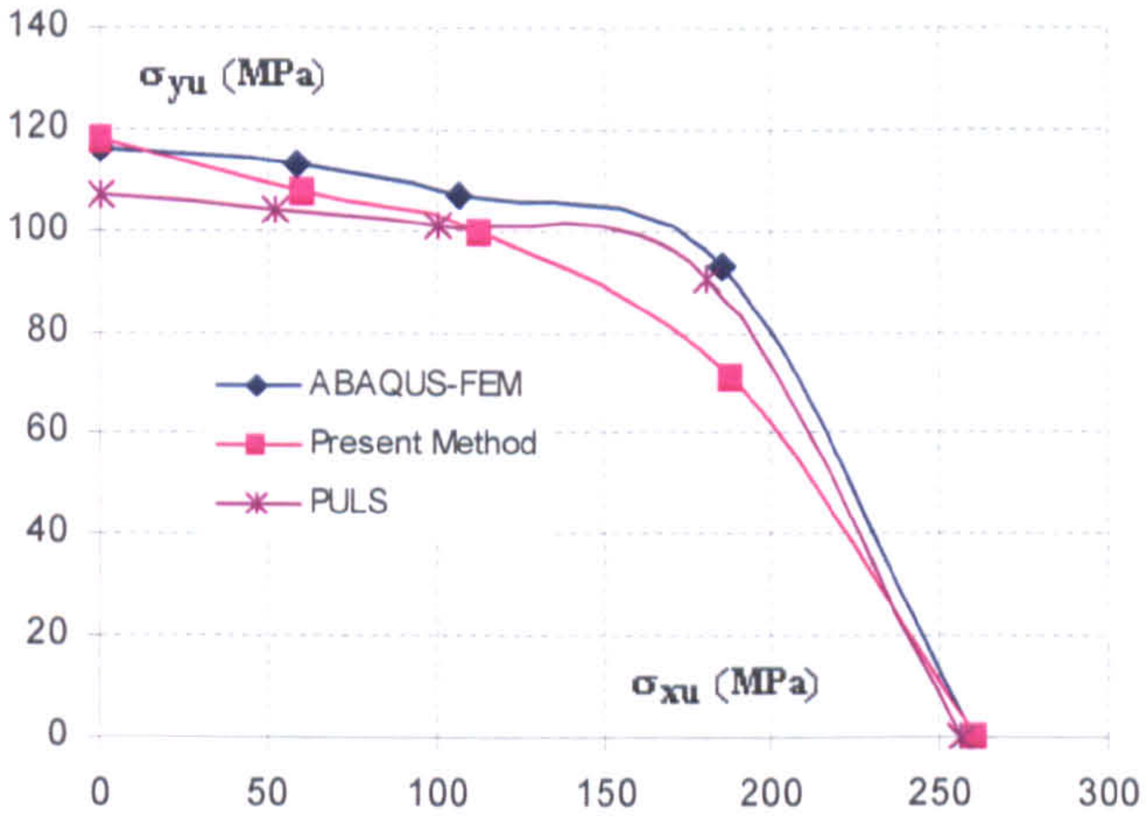

Figure 2.35: Tanker bottom panel, biaxial compression with lateral pressure, $p = 0.151$ MPa

It is seen that reduction in the in-plane capacity is not very much reduced when the design lateral pressure is employed. The reduction is somewhat lesser for present method than ABAQUS and PULS. It is noticed that present approach predicts more capacity than both of the rule formulations in the bi-axial region. For pure axial compression, DNV Rules seem to be overly conservative when compared with all prediction methods, while for pure transverse compression GL Rules seem to be non-conservative. The present method curve is more convex, which is also the case for ABAQUS, PULS and DNV Rules, while the GL Rules interaction curve is close to linear.

This study proposes an interaction formula to calculate biaxial compression capacity considering lateral pressure loading as follows:

$$\left(\frac{\sigma_x}{\sigma_{xu}}\right)^2 + \left(\frac{\sigma_y}{\sigma_{yu}}\right)^2 + \left(\frac{p}{p_u}\right)^{1.5} = 1 \qquad (2.59)$$

2.8.3 Effect of shear loading

Available results on the effect of shear loads on the ultimate capacity of stiffened panels are scarce. Some results are reported by Steen & Engelsen (1997) for un-stiffened plates using non-linear Finite Element Method. Plates with aspect ratio 3 and 5 and slenderness ratio varying from 0.2 to 2.0 have been studied. The general observation made in Steen's paper is that the ultimate shear capacity is close to the shear yield strength for all plates.

Capacity curves for combined shear load and transverse compression of a bulk carrier side panel are presented in Figure 2.36, while Table 2.12 summarizes main particulars of investigated model. The loading is typically compression perpendicular to the stiffener transverse direction acting simultaneously with in-plane shear and lateral pressure from the sea. Results for the same panel under combined transverse compression, shear and lateral pressure are presented in Figure 2.37.

Table 2.12: The main particulars of the Bulk Carrier side panel

Length of stiffened panel	8800 mm
Stiffener spacing	890 mm
Plate thickness	14.5 mm
Web height	700 mm
Web thickness	13 mm
Stiffeners	5 longitudinal Tee profiles
Flange breadth	150 mm
Flange thickness	18 mm
Yield stress	355 MPa
Young's modulus	208000 MPa
Poisson ratio	0.3

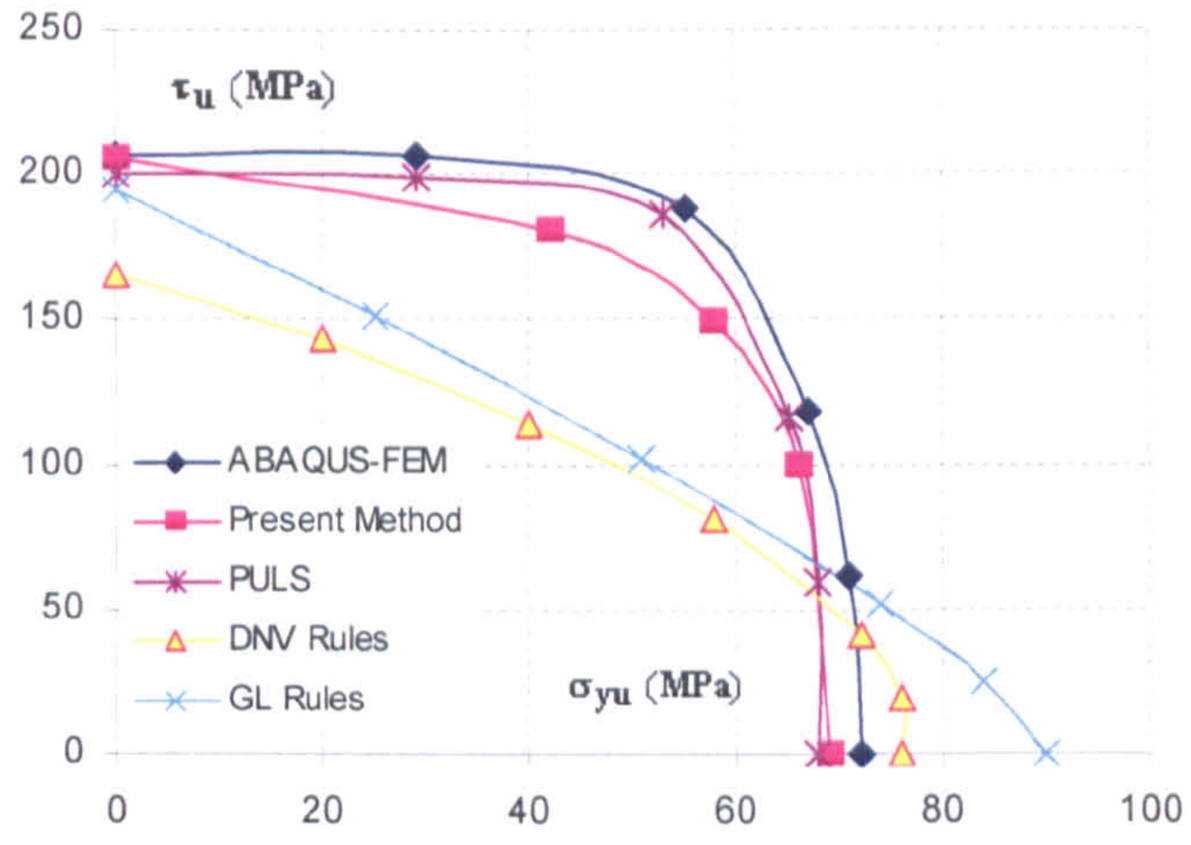

Figure 2.36: Bulk Carrier side panel, transverse compression and shear loading without lateral pressure

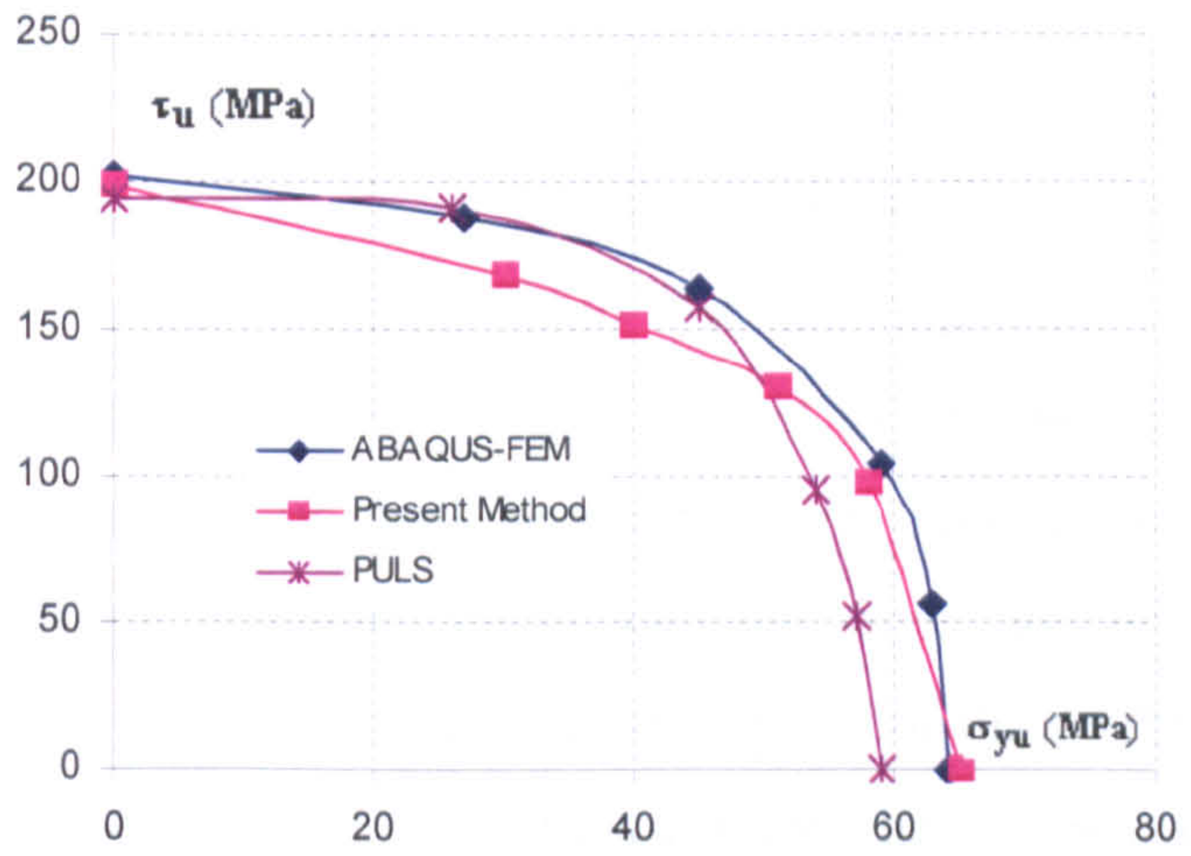

Figure 2.37: Bulk Carrier side panel, transverse compression, shear with lateral pressure, p=0.157 MPa

An expression is finally produced to describe ultimate strength interaction relationship for a stiffened panel under combined biaxial loads, shear and lateral pressure, which applicable format is as follows:

$$\left(\frac{\sigma_x}{\sigma_{xu}}\right)^2+\left(\frac{\sigma_y}{\sigma_{yu}}\right)^2+\left(\frac{\tau}{\tau_u}\right)^{3.5}+\left(\frac{p}{p_u}\right)^{1.5}=1 \qquad (2.60)$$

It can be seen that present method shows very reasonable results as compared to ABAQUS and PULS analyses covering load combinations covering load combinations dominated by shear loading as well as load combinations dominated by transverse compression. The presence of lateral pressure is not very significant for the in-plane capacity of this pane, though more so for transverse dominated loading than for pure shear. It is seen that both the rule formulations overpredict the capacity for pure transverse compression, while they significantly underestimate the capacity in the combined load region of the capacity curve.

2.9 Ultimate Capacity of Transversally Stiffened Plates

Two types of stiffening systems can be applied when designing and building ship hull such as transverse and longitudinal. The choice of the system is associated with predominant loading carried by structural members. Transversally stiffened ships were built until sixties/seventies. With the growing size of merchant vessels application of longitudinal system became a must, at least in regions carrying largest stresses due to overall ship hull bending. Some regions are still transversally stiffened. Most typical examples are bulk-carrier sides, and precisely a part of the side between hopper and wing tank, and some parts of the double sides of container ships Figure 2.38 and Figure 2.39. In bulk-carriers the side is transversally stiffened due to exploitation and strength reasons - large shear forces appear for this type of ship, which is more effectively carried by transversally rather than longitudinally stiffened plating. In container ships it is due to manufacturing. Transversally stiffened plates are generally much less resistant to buckling, induced by overall bending stresses, however their influence must be also taken into consideration. Moreover, a part of the plate can be subject to compression while other to tension what makes the problem more complex.

Papers by Schultz (1964) and Faulkner (1973) can be given as examples of early attempts of investigation on behaviour of transversally stiffened plates. First practical formula was cast by Valsgaard (1979) who presented a design equation for the

ultimate strength of simply supported plates in compression with unrestrained shorter edges.

$$\sigma_{transv} = \sigma_o \left[\frac{a}{b} \left(\frac{2}{\beta_E} - \frac{1}{\beta_E{}^2} \right) + 0.08 \left(1 - \frac{a}{b} \right) \left(1 + \frac{1}{\beta_E{}^2} \right)^2 \right] \tag{2.61}$$

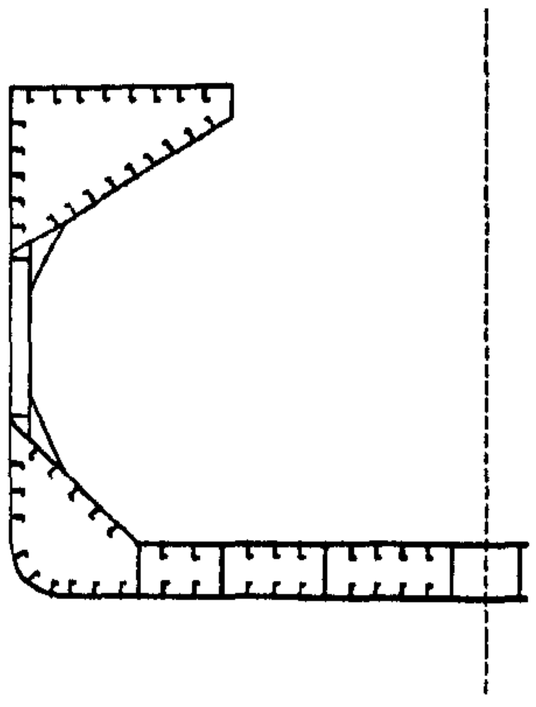

Figure 2.38: Typical cross-section of bulk carrier

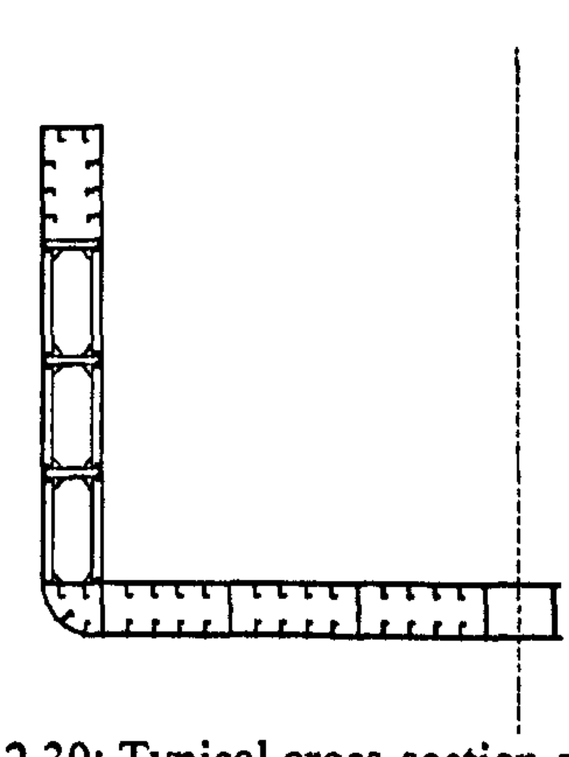

Figure 2.39: Typical cross-section of container

The formula was based on the results of numerical investigation performed using non-linear shell computer code. The formula covered the range of plate aspects and slenderness ratios typical for ship and offshore structures. Where a is length of shorter, unloaded edge of the plate and b is length of longer, loaded edge. Buckling and post-buckling behaviour of plates under non-uniform compressive edge stress were also addressed to by Bedair (1996), following earlier contribution by Walker (1967). Galerkin method was applied for solution; however, all investigations were restricted to elastic range. Narayan & Chan (1985) examined behaviour of plates containing holes under linearly varying edge displacements in pre- and post-buckling range. They assumed that the ultimate capacity of plate is equivalent to load level when edge strips reached yield. No other papers concerning the problems are available; especially plates subject to both tension and compression are not treated. This type of loading occurs for plates being bulk-carriers side. For the purpose of calculations performed in the present paper it was assumed for transversally stiffened plate that the actual stress for a given co-ordinate (distance from the neutral axis) could be evaluated using generalised form of modified Valsgaard equation for evaluation of average critical compressive stress as follows:

$$\sigma_{transv}(\varepsilon) = \sigma_o \Phi(\varepsilon) \Phi_{we}(\varepsilon) \tag{2.62}$$

For plate-induced failure of transversely stiffened plates, the equation for evaluation of the average stress at a given strain takes the form:

$$\sigma_{transv}(\varepsilon) = \sigma_o \Phi(\varepsilon) \Phi_{we}(\varepsilon) \tag{2.63}$$

where $\sigma_{transv}(\varepsilon)$ is an average stress at compressed edge, is a normalised collapse load for transvversally stiffened plate (modified Valsgaard equation).

$$\Phi_{we}(\varepsilon) = \left[\frac{a}{b}\left(\frac{1.8}{\beta_E} - \frac{0.8}{\beta_E^{\,2}} \right) + 0.1\left(1 - \frac{a}{b}\right)\left(1 + \frac{1}{\beta_E^{\,2}}\right)^2 \right] \tag{2.64}$$

Calculations were performed for models of plates covering the whole range of dimensions of all transversally stiffened plates occurring in the analysed ships. Exemplary results for 3 plates of the double side of the container ship (L=225 m) are shown in Table 2.13. The values given there are representative for the whole set of results.

Table 2.13 Comparison of ultimate capacity for transversally stiffened plates

Items	a (mm)	b (mm)	t_p (mm)	Ultimate capacity according to (MPa)		
				Valsgaard equation (2.61)	Modified Valsgaard equation (2.64)	FEM
1	800	1880	8.0	64.5	63.5	62.8
2	800	1880	13.5	93.7	92.9	102.7
3	800	1880	24.0	136.1	142.8	167.5

A good agreement of results obtained using finite element method and approximate formulations can be noticed. The value of the ultimate capacity according to modified Valsgaard equation is slightly overestimated for slender plates and, on the other hand, underestimated for more stocky plates comparing to the finite element results.

2.10 Discussion & Conclusion

The objective of the present chapter has been to develop a simplified analytical method for calculating the ultimate strength of a stiffened plate subject to combine loads, where any type of stiffener profile may be used. A non-linear finite element method has been employed to investigate on 60 ANSYS elastic-plastic buckling analyses of a wide range of typical ship panel geometries. The reduction factors of the collapse strength have been produced from the results of 60 ANSYS inelastic FE calculations. Through this investigation, the following conclusions can be discussed:

- ✓ The simplified analytical method is able to predict the ultimate strength of stiffened plates under combined loading accurately.
- ✓ Initial deflection and residual stress have significant reduction influence on the perfect stiffened plate capacity. The collapse strength of stiffened plate the slenderness ratios of which are around $\beta = 2$ is sensitive to the initial imperfections.
- ✓ Moderate lateral pressure has very small influence on the longitudinal and transverse ultimate strength capacity. The prediction of this effect has also been compared with numerical results and it has very consistent correlation.
- ✓ Simplified closed-form interaction formulations for the ultimate capacity assessment of stiffened panels has been developed based on a large number of non-linear finite element analyses using the commercial program ANSYS. It is believed that full non-linear finite element codes are able to predict buckling deflection an accuracy which is sufficient for advanced design purposes, on condition that the analyses are done properly such as boundary conditions, mesh size, model extent, element types and imperfections.
- ✓ Validation of the proposed interaction model is conducted by use of non-linear finite element calculations and by existing ship rules used by DNV and GL Rules. It is found that present model is generally consistent with results obtained from by ABAQUS and PULS.
- ✓ The rules used by Classification Societies are found to be conservative for some case and non-conservative for other cases as compared with ABAQUS

and PULS. Therefore it is difficult to assess the actual safety margin using these formulations.

- ✓ The main advantage of the approximate method relative to FEM results from the time consumption both in the creation of model and in the CPU time, so it can be used for practical applications in ship design.
- ✓ Using the present method, it has also been shown that the average stress – average strain relation required in applying the Smith's method to estimate ultimate strength of ship hulls and the interaction relation between longitudinal stress, transverse stress, shear stress and lateral pressure can be obtained. Furthermore, for the convenience of design application, simplified formula is able to provide for quick prediction of the ultimate strength of stiffened plates under combined loading.

Chapter 3

Verification of The Proposed Simple Design Equations with Experimental Results

3.1 Introduction

The performance of the proposed method as applied to 60 ANSYS elastic-plastic non-linear buckling analyses of a wide range typical ship panel geometries is now considered using test data and related numerical results pertaining to an extensive series of mechanical tests performed and reported Smith (1976,1992) and Tanaka & Endo (1988). The test grillages were stiffened with flat bar, angle or T-type directions. Such cross-stiffened panels are particularly relevant to the design of naval vessels, small craft and high-speed vessels. The Smith and Tanaka & Endo test data are recorded for the sake of completeness.

ALPS / ULSAP program (Paik *et al.* 2003), which is used for non-linear analysis of large plated structures ultimate analysis of stiffened panels, as well as simplified analytical methods developed by Faulkner and Gordo & Soares.

3.2 The Smith's Mechanical Collapse Tests

Smith (1976) carried out a series of collapse tests using a total of 11 full scale welded steel grillages representing typical warship deck structures under axial compression, or bottom structures under combined axial compression and lateral pressure. The test structures include four pairs of nominally identical grillages (numbers 1a, 1b, 2a, 2b, 3a, 3b, 5, 7) representing frigate strength decks and one grillage (number 6) corresponding to a light superstructure deck. The typical grillage model that Smith tested is as that shown in Figure 3.1.

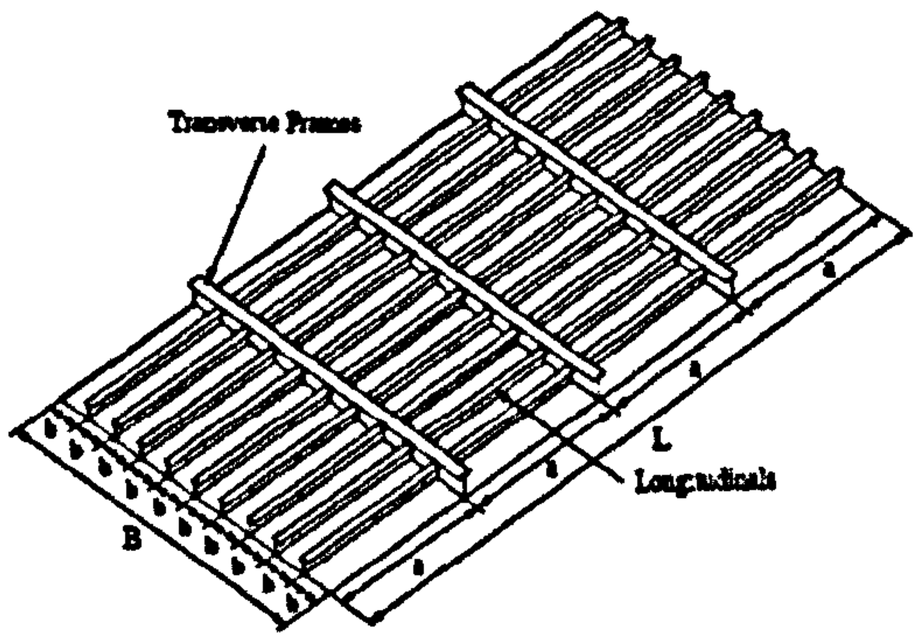

Figure 3.1: A schematic of the Smith test grillage (1976, 1992)

Smith *et al.* (1992) later computed the ultimate strengths of the Smith test grillages using the non-linear finite element method as well, where they used the two-bay beam-column model as representative of the grillages. The overall dimensions of each grillage were $L = 6096$ mm long by $B = 3048$ mm wide; excluding the panel ends which are bolted to the test frames along the edges. Except for numbers 4a and 4b, which have both large girders and small stiffeners in the longitudinal direction, all test grillages have identical T-type longitudinal stiffeners and identical T-type transverse frames.

Table 3.1 indicates the geometric properties of longitudinals and transverses and the material yield stresses for the plating and stiffeners, where numbers 4a and 4b are represented by the longitudinally stiffened panel between two adjacent longitudinal girders and two adjacent transverse frames. Table 3.2 presents the important ultimate

strength related geometric characteristics for each grillage. The initial deflections of plating, longitudinals or transverses were measured in these tests. There was reportedly a high degree of variability associated with the plate initial deflection measurements, with the COVs of w_{opl} and w_{osx} in the range of 0.22 - 0.63 and 0.29 – 1.04, respectively. Specifically, it is reportedly observed that plating and stiffener imperfections for model number 3b were abnormally large, with an 'unfavourable' relative stiffener distortion as well. Also, number 6, representing a light superstructure deck, had a 'serious level' of initial imperfections which would be untypical in a real structure. The welding induced residual stresses of plating were also measured for selected grillages. The corresponding COV of the compressive residual stress, σ_{rcx}, in the longitudinal direction was in the range of 0.12-0.52.

Table 3.3 summarizes the initial imperfections of plating and stiffeners for each grillage, on the basis of the measurements and insights provided in Smith (1976) and Smith *et al.* (1992). Based on the measured initial deflection patterns of plating, Table 3.3 represents the buckling mode initial deflection component of each grillage also. It is noted that in the FEA of Smith *et al.* (1992), two types of computations was tried with different levels of initial deflections, namely FEA-1 with average initial imperfections and FEA-2 with actual initial imperfections.

Table 3.4 and Table 3.5 compares the present design procedure predictions with Smith mechanical test result as well as FE analysis results and simplified analytical approaches.

Table 3.6 presents a summary of the design methods with the Smith experiments for the ultimate strength of grillages. Proposed simplified formula has 0.061 values for standard deviation and 0.004 values for variance. The other hand, it gives excellent correlation among all considered methods including finite element analysis. It is also noted that the stiffener-induced failure based on Mode III predictions using the ALPS/ULSAP (Perry-Robertson formula) are too pessimistic compared to the test results.

Table 3.1: Mean values of geometric properties and material yield stresses for the Smith test grillages

Grillage no.	L (mm)	B (mm)	t (mm)	n_{sx}	h_{wx} (mm)	t_{wx} (mm)	b_{fx} (mm)	t_{fx} (mm)	n_{sy}	h_{wy} (mm)	t_{wy} (mm)	b_{fy} (mm)	t_{fy} (mm)	σ_{Yp} (MPa)	σ_{Ys} (MPa)	σ_{Yeq} (MPa)
1a	6096	3048	8.00	4	153.67	153.67	78.99	14.22	4	257.56	9.37	125.48	18.29	249.1	253.7	250.4
1b	6096	3048	7.87	4	152.40	152.40	76.20	14.22	4	254.00	9.14	127.00	18.29	252.2	252.4	252.3
2a	6096	3048	7.72	9	115.57	115.57	45.97	9.53	3	204.98	8.31	102.62	16.26	261.3	268.9	263.1
2b	6096	3048	7.37	9	114.30	114.30	44.70	9.53	3	203.71	8.33	102.62	16.26	259.7	274.9	263.3
3a	6096	3048	6.38	9	77.72	77.72	25.91	6.35	3	156.21	6.81	78.99	14.22	250.6	227.9	246.8
3b	6096	3048	6.40	9	77.22	77.22	27.94	6.35	3	153.92	6.88	79.25	14.22	252.2	223.3	247.3
4a	1219.2	1016	6.43	3	76.71	76.71	27.69	6.35	-	-	-	-	-	259.7	223.9	252.5
4b	1219.2	1016	6.40	3	76.96	76.96	26.16	6.35	-	-	-	-	-	264.3	227.9	257.3
5	6096	3048	6.43	4	116.08	116.08	46.23	9.53	3	154.18	6.76	77.22	14.22	247.6	230.9	244.9
6	6096	3048	6.32	4	76.20	76.20	27.43	6.35	4	114.55	5.36	46.23	9.53	256.7	241.5	255.2
7	6096	3048	6.30	4	115.06	115.06	45.21	9.53	3	153.92	6.65	78.74	14.22	290.1	305.3	303.3

Notes: Grillage Numbers 4a and 4b represent longitudinally stiffened panels between two adjacent longitudinal girders and two adjacent transverse frames, v=0.3, E=205.8 GPa.

Table 3.2: Other geometric characteristics of the Smith test grillages

Grillage no.	b/t	β	a/r	λ	A_{sx}/bt
1a	76.2	2.67	21	0.24	0.42
1b	77.4	2.72	21	0.23	0.43
2a	39.5	1.42	36.5	0.42	0.40
2b	41.4	1.48	36	0.42	0.42
3a	47.8	1.68	66	0.70	0.24
3b	47.6	1.68	66	0.70	0.24
4a	39.5	1.41	50	0.54	0.28
4b	39.7	1.43	50	0.53	0.28
5	94.9	3.31	42	0.45	0.24
6	96.4	3.42	68	0.75	0.12
7	96.8	3.65	42	0.52	0.24

Table 3.3: Initial imperfections of plating, longitudinal and transverses for the Smith test grillages

Grillage no.	ω_{0pl}/b	ω_{0sx}/a	$\omega_{0sy}/\omega_{0sx}$	σ_{rcx}/σ_{Yp}	$\sigma_{rcy}/\sigma_{rcx}$	σ_{rsx}/σ_{Ys}	$\sigma_{rsy}/\sigma_{rsx}$	A_{0m}/ω_{0pl}
1a	0.0060	0.0007	0.7	-	-	-	-	0.1
1b	0.0077	0.0011	-	-	-	-	-	0.1
2a	0.0044	0.0025	-	0.48	0.10	-	-	0.1
2b	0.0060	0.0010	-	0.33	0.10	-	-	1.0
3a	0.0093	0.0028	0.2	0.38	0.10	-	-	0.7
3b	0.0150	0.0019	0.8	0.43	0.10	-	-	1.0
4a	0.0081	0.0023	0.5	0.38	0.10	-	-	0.8
4b	0.0063	0.0008	0.5	0.41	0.10	-	-	0.7
5	0.0100	0.0008	0.4	0.16	0.10	-	-	0.1
6	0.0125	0.0020	0.4	0.31	0.10	-	-	1.0
7	0.0094	0.0007	-	0.08	0.10	-	-	0.1

Sources: Smith (1976) and Smith *et al.* (1992)

Table 3.4: Comparison of Present study, FEA, Soares & Gordo, Paik and Faulkner with the Smith experiments for the ultimate strength of grillages

Grillage no.	ρ (MPa)	$(\sigma_{xu}/\sigma_{oeq})$ Experiment	$(\sigma_{xu}/\sigma_{oeq})$ FEA - 1	$(\sigma_{xu}/\sigma_{oeq})$ FEA - 2	$(\sigma_{xu}/\sigma_{oeq})$ Paik	$(\sigma_{xu}/\sigma_{oeq})$ Faulkner	$(\sigma_{xu}/\sigma_{oeq})$ Gordo & Soares	$(\sigma_{xu}/\sigma_{oeq})$ Present study
1a	0	0.76	0.65	0.69	0.76	0.65	0.72	0.76
1b	0.103	0.73	0.57	0.57	0.62	0.65	0.71	0.74
2a	0.048	0.91	0.81	0.81	0.79	0.85	0.87	0.84
2b	0	0.83	0.82	0.82	0.79	0.84	0.86	0.81
3a	0.021	0.69	0.69	0.63	0.69	0.69	0.73	0.71
3b	0	0.61	0.71	0.60	0.58	0.69	0.73	0.64
4a	0	0.82	0.80	0.75	0.80	0.85	0.87	0.87
4b	0.055	0.83	0.73	0.76	0.81	0.84	0.86	0.85
5	0	0.72	0.51	0.55	0.52	0.53	0.62	0.70
6	0	0.49	-	-	0.37	0.45	0.56	0.53
7	0	0.65	0.49	0.53	0.52	0.50	0.61	0.56

Table 3.5: Comparison of Present study, FEA, Soares & Gordo, Paik and Faulkner with the Smith experiments for the ultimate strength of grillages

Grillage no	$\frac{(\sigma_{xu})_{FEA-1}}{(\sigma_{xu})_{Exp}}$	$\frac{(\sigma_{xu})_{FEA-2}}{(\sigma_{xu})_{Exp}}$	$\frac{(\sigma_{xu})_{Paik}}{(\sigma_{xu})_{Exp}}$	$\frac{(\sigma_{xu})_{Faulkner}}{(\sigma_{xu})_{Exp}}$	$\frac{(\sigma_{xu})_{Soares-Gordo}}{(\sigma_{xu})_{Exp}}$	$\frac{(\sigma_{xu})_{Ozguc-Das}}{(\sigma_{xu})_{Exp}}$	Collapse modes	
							Exp.	Present study
1a	0.86	0.91	1.00	0.86	0.95	1.00	V	I
1b	0.78	0.78	0.85	0.88	0.98	1.01	V	V
2a	0.89	0.89	0.87	0.94	0.95	0.92	III+V	V
2b	0.99	0.99	0.95	1.01	1.03	0.98	III+V	V
3a	1.00	0.91	1.00	0.99	1.05	1.03	III+V	V
3b	1.16	0.98	0.95	1.13	1.19	1.05	III+V	V
4a	0.98	0.91	0.98	1.03	1.06	1.06	III+V	V
4b	0.88	0.92	0.98	1.01	1.04	1.02	III+V	V
5	0.71	0.76	0.82	0.73	0.87	0.97	III+V	V
6	-	-	0.75	0.92	1.14	1.08	I+V	I
7	0.75	0.82	0.80	0.77	0.94	0.86	III+V	V

Table 3.6: Summary of the design methods with the Smith experiments for the ultimate strength of grillages

Prediction method	Mean Value	Std. Deviation	Variance
FEA – 1	0.899	0.137	0.019
FEA – 2	0.887	0.076	0.006
Paik (ALPS/ULSAP)	0.895	0.101	0.010
Faulkner	0.935	0.118	0.014
Gordo & Soares	1.018	0.095	0.009
Present study	**1.001**	**0.062**	**0.004**

3.3 The Tanaka & Endo's Mechanical Collapse Tests

Tanaka & Endo (1988) carried out a series of experiment and numerical FE investigations related to the ultimate compressive strength of longitudinally stiffened panels having three flat bar stiffeners, which were intended to fail by local web buckling or tripping of longitudinal stiffeners. Figure 3.2 shows a typical test structure from the Tanaka & Endo study. In order to account for the effect of adjacent panels on the collapse behaviour of the central panel, a three bay model with two adjacent (dummy) stiffened panels on either side of the transverse support frames is employed. The plate thickness of two adjacent panels prior to the collapse of the centre panel was prevented. Table 3.7 review the geometric / material properties and initial imperfections for the Tanaka & Endo test structures.

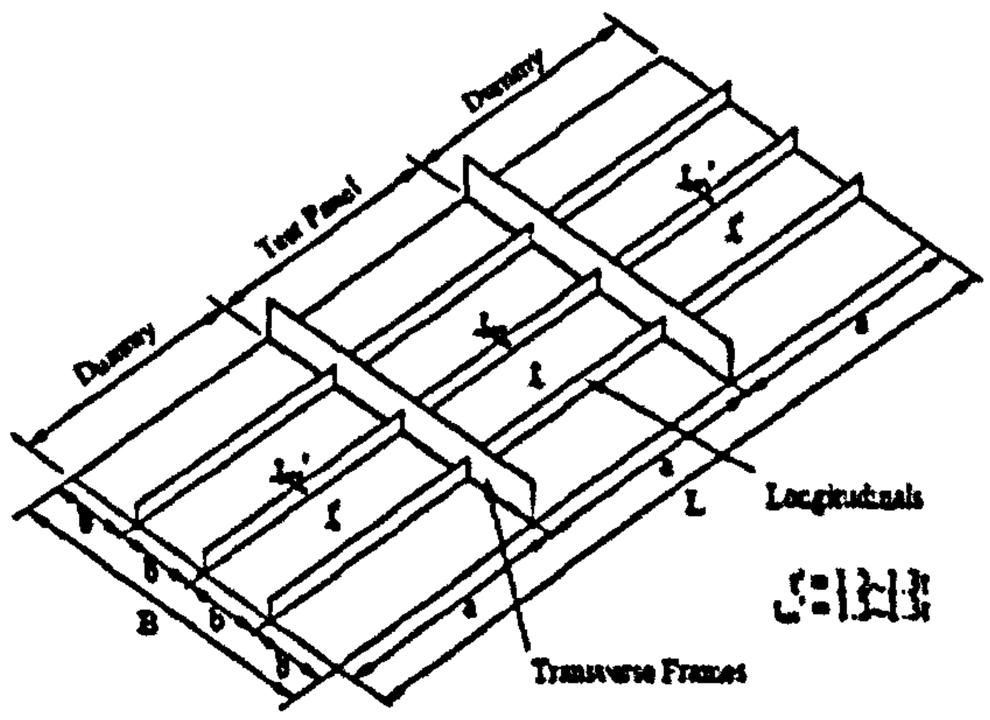

Figure 3.2: The Tanaka & Endo test structure for longitudinally stiffened panels under uniaxial compression, incorporating two dummy panels away from the transverse frames (Tanaka & Endo, 1988)

Table 3.8 indicates the comparison results for the present ultimate strength formulations with the experiments, non-linear FE solutions, and other methods. Apart from one case, the present study predicts that all test structures will fail by Mode III (Local buckling of stiffener web, tripping), which corresponds well to the intent of the experiments. Table 3.9 presents the correlations between present method when compared to the corresponding experimental, numerical as well as simplified analytical approaches proposed by Faulkner and Gordo & Soares.

For Nos. D1 and D3, the specimen's ultimate strength values are nominally greater than the material yield stress from a coupon test. For No.D4, the panel ultimate strength as obtained by the experiments is 99% of the yield stress. Aside from yield stress variability, such observations may also be due to the strain – hardening effect. Table 3.10 shows that mean, standard deviation and variance of the Tanaka & Endo FEA against their experiments is 0.977, 0.136 and 0.018, respectively. Also, the present method correlated with mean is 0.983, standard deviation is 0.062 and variance is 0.004.

Table 3.7: Experimental results and finite element solutions of the ultimate compressive strengths for the stiffened panels obtained by Tanaka & Endo (1988)

Specimen No.	a (mm)	B (mm)	n_{st}	b (mm)	t_p (mm)	h_w (mm)	t_w (mm)	b_f (mm)	t_f (mm)	w_{op}/t_p	w_{os}/a	λ	β	σ_{rs}/σ_{Yp}	σ_{rs}/σ_{Ys}	σ_{Yp} (MPa)	σ_{Ys} (MPa)	σ_{Yeq} (MPa)
D0(F0B)	1080	1440	3	360	6.15	110	9.77	-	-	0.0912	1.0	0.367	1.975	0.088	0.050	234.2	287.1	251.5
D0A(FB)	1080	1440	3	360	5.65	110	10.15	-	-	0.2458	1.0	0.343	2.220	0.300	0.050	249.9	196.0	230.8
D1(FB)	1080	1200	3	300	5.95	110	10.19	-	-	0.1335	1.0	0.351	1.771	0.102	0.050	253.8	250.9	252.7
D2(FB)	1080	1560	3	390	5.95	110	10.19	-	-	0.2689	1.0	0.369	2.302	0.073	0.050	253.8	250.9	252.9
D3(FB)	1080	1440	3	360	5.95	103.5	11.84	-	-	0.2913	1.0	0.397	2.125	0.091	0.050	253.8	326.3	280.2
D4(FB)	1080	1440	3	360	5.95	118.5	7.98	-	-	0.1111	1.0	0.357	2.125	0.134	0.050	253.8	284.2	263.1
D4A(FB)	1080	1440	3	360	5.65	118.5	8.08	-	-	0.3727	1.0	0.351	2.220	0.300	0.050	249.9	274.4	257.7
D10(FB)	1080	1200	3	300	4.38	65	4.38	-	-	0.6532	1.0	1.028	3.174	0.084	0.300	442.0	442.0	442.0
D11(FB)	1080	1200	3	300	4.38	90	4.38	-	-	0.6380	1.0	0.678	3.174	0.057	0.300	442.0	442.0	442.0
D12(FB)	1080	1440	3	360	4.38	65	4.38	-	-	0.6634	1.0	1.097	3.809	0.085	0.300	442.0	442.0	442.0

Table 3.8: Comparison of Present study, FEA, Gordo & Soares, Paik and Faulkner with the Tanaka - Endo experiments for the ultimate compressive strengths for stiffened panels

Specimen no.	$(\sigma_{xu}/\sigma_{oeq})$ Experiment	$(\sigma_{xu}/\sigma_{oeq})$ FEM	$(\sigma_{xu}/\sigma_{oeq})$ Paik	$(\sigma_{xu}/\sigma_{oeq})$ Faulkner	$(\sigma_{xu}/\sigma_{oeq})$ Soares & Gordo	$(\sigma_{xu}/\sigma_{oeq})$ Present study
D0(F0B)	0.931	0.910	0.883	0.735	0.797	0.943
D0A(FB)	0.843	0.867	0.841	0.734	0.791	0.816
D1(FB)	1.095	0.952	0.818	0.810	0.856	1.017
D2(FB)	0.900	0.842	0.888	0.693	0.797	0.935
D3(FB)	1.032	0.888	0.891	0.713	0.758	0.925
D4(FB)	0.990	0.784	0.851	0.706	0.774	0.933
D4A(FB)	0.875	0.758	0.838	0.703	0.751	0.865
D10(FB)	0.547	0.631	0.580	0.452	0.525	0.535
D11(FB)	0.527	0.618	0.462	0.518	0.592	0.554
D12(FB)	0.510	0.571	0.583	0.402	0.501	0.465

Table 3.9: Comparison of Present study, FEA, Gordo & Soares, Paik and Faulkner with the Tanaka - Endo experiments for the ultimate compressive strengths for stiffened panels

Specimen no.	$\frac{(\sigma_{xu})_{FEM}}{(\sigma_{xu})_{Exp}}$	$\frac{(\sigma_{xu})_{Paik}}{(\sigma_{xu})_{Exp}}$	$\frac{(\sigma_{xu})_{Faulkner}}{(\sigma_{xu})_{Exp}}$	$\frac{(\sigma_{xu})_{Soares-Gordo}}{(\sigma_{xu})_{Exp}}$	$\frac{(\sigma_{xu})_{Ozguc-Das}}{(\sigma_{xu})_{Exp}}$	Collapse modes	
						Exp.	Present study
D0(F0B)	0.977	0.948	0.789	0.856	1.013	III	III
D0A(FB)	1.028	0.998	0.871	0.938	0.968	III	III
D1(FB)	0.869	0.747	0.740	0.782	0.929	III	III
D2(FB)	0.936	0.987	0.770	0.886	1.039	III	I
D3(FB)	0.860	0.863	0.691	0.734	0.896	III	III
D4(FB)	0.792	0.860	0.713	0.782	0.942	III	III
D4A(FB)	0.866	0.958	0.803	0.858	0.989	III	III
D10(FB)	1.154	1.060	0.826	0.960	0.978	III	III
D11(FB)	1.173	0.877	0.983	1.123	1.051	III	III
D12(FB)	1.120	1.143	0.788	0.982	0.912	III	III

Note: Collapse mode:
I = Plate induced failure, II = Stiffener induced failure, III = Local buckling of stiffener web (or tripping)

Table 3.10: Summary of the design methods with the Tanaka - Endo experiments for the ultimate compressive strengths for stiffened panels

Prediction method	Mean Value	Std. Deviation	Variance
FEM	0.977	0.136	0.018
Paik (ALPS/ULSAP)	0.944	0.113	0.013
Faulkner	0.797	0.084	0.007
Soares & Gordo	0.890	0.115	0.013
Present study	**0.983**	**0.062**	**0.004**

3.4 Discussion & Conclusion

The accuracy of the proposed method is examined by mechanical test results. The comparisons show that adopted procedure has excellent correlation when compared to the experimental results. The other approaches developed by Paik *et al.* (2003), Faulkner (1975) and Gordo & Soares (1993) are employed to compare with performance of present work, where Faulkner and Gordo & Soares' methods are unable to consider lateral pressure effect. Therefore, it is believed that this work establishes to include combine-loading effects properly for the evaluation of structural response of stiffened plates.

According to two different mechanical experimental results, new expressions have 0.061 value for standard deviation and 0.004 value for variance. Also, comparisons indicate that adopted method presents better results as compared with non-linear finite element analyses.

For practical purposes in ship design, it could be employed to achieve reliable results as well as for the evaluation of the ultimate hull girder strength calculations using Smith's method.

Chapter 4

Hull Girder Ultimate Strength Under Vertical Bending Moment

4.1 Introduction

A ship hull is a structure composed of plating stiffened by girders and stiffeners. The hull is subject to loading generated by hull weight, cargo, equipment etc. and buoyancy force. The loading cause vertical and horizontal bending moments, vertical and horizontal shear forces, and torsional moment. Essential in estimation of the hull strength is the vertical bending moment as generating the largest stresses in the ship structures, especially in the middle part of the ship hull.

The conventional assessment of the ship hull girder longitudinal strength is based on comparison of maximum elastic stress in the hull section with allowable stress, defined as a fraction of yield stress. Thus the elastic section modulus calculated for horizontal axis may be treated as a measure of longitudinal bending strength. This attitude, though widely applied, does not provide with information concerning resistance of the ship hull in extreme conditions. This can be achieved by evaluation of ultimate capacity - maximum bending moment a hull can carry - which

becomes an important parameter in ship structural rational design. With this value it is possible to estimate a safety margin above maximum still water and wave bending moment. It should be clearly explained that the term ultimate capacity is addressed to ductile collapse of hull.

With the increase in the applied longitudinal bending moment, the structural members composing a hull cross-section begin to collapse one by one due to buckling or yielding, and finally, the maximum capacity of the cross-section has been attained. This implies that the behaviour of the structural members affects that of the cross-section.

There exist two methods to evaluate the ultimate hull girder strength of a ship's hull under longitudinal bending. One is to calculate the ultimate hull girder strength directly, and the other is to perform progressive collapse analysis on a hull girder. In this chapter, existing methods are firstly introduced with a brief historical review. Secondly, hull girder ultimate strength on five ISSC benchmark vessels is analysed by using proposed formulas, where a computer code NEPTUNE is developed. The moment – curvature curve and the ultimate bending moment at ultimate state are calculated with initial imperfections in the form of geometric deflection and welding – induced residual stresses for both hogging and sagging cases subject to vertical bending. The effect of corrosion damage is also assessed by sensitivity study on the influence of plate and stiffener thickness on the hull girder ultimate capacity. The accuracy of adopted procedure is examined by seven different methods on the examples used in the benchmark calculations.

4.2 Direct Method to Evaluate Ultimate Hull Girder Strength

4.2.1 Caldwell's method

Caldwell (1965) was the first who tried to theoretically evaluate the ultimate hull girder strength of a ship subjected to longitudinal bending. He introduced a so-called

Plastic Design considering the influence of buckling and yielding of structural members composing a ship's hull. He idealised a stiffened cross-section of a ship's hull to an unstiffened cross-section with equivalent thickness. If buckling takes place at the compression side of bending, compressive stresses cannot reach the yield stress, and fully plastic bending moment cannot be attained. Caldwell introduced a stress reduction factor at the compression side of bending, and the bending moment produced by the reduced stress was considered as the ultimate hull girder strength. He performed a series of calculations changing the reduction factors, and discussed the influence of buckling on the ultimate hull girder strength.

In Caldwell's method, reduction in the capacity of structural members beyond their ultimate strength was not taken into account. This causes an overestimation of the ultimate strength in general. In addition to this, in Caldwell's time, the exact values of reduction factors for structural members were not available, and the real ultimate strength itself could not be evaluated. However, Caldwell's original method seems to be rational, and has since been improved with respect to:

- The derivation of exact reduction factors due to buckling,
- The introduction of phase lag in collapse of individual structural members,
- The introduction of load-shedding effect of structural members beyond their ultimate strength.

4.2.2 Improved methods

Twenty-four years later, Maestro & Marino (1989) extended the Caldwell's formulation to the case of bi-axial bending, and modified the method to estimate the influence of damage due to grounding and collision on the ultimate hull girder strength. Nishihara (1983) applied Caldwell's method to calculate the ultimate strength of a ship's hull improving the accuracy of the strength reduction factors. Many researchers proposed similar formulae. For examples, Endo *et al.* (1988) and Mansour *et al.* (1990) proposed simple calculation methods to evaluate the ultimate

hull girder strength using hull girder strength. Applying this method, Paik *et al.* (1998) performed reliability analysis considering corrosion damage.

Although these methods described above do not explicitly take into account of strength reduction in the members beyond their ultimate strength, the evaluated ultimate hull girder strength showed good correlation with the measured / calculated results in many cases. For instance, Paik & Mansour (1995) compared the predicted results with those by experiments and ISUM analysis, and the differences were reported to be between –1.9% and +9.1%.

4.2.3 Empirical formulations and interaction formulations

Another class of methods, different from the rational Caldwell's method (and improved methods), are some empirical formulations usually assessed for a type of specific vessels (Viner, 1986; Frieze *et al.* 1991). In order to raise the problem of combined loads (vertical, horizontal bending moments, and shear forces), several authors have proposed interaction equations to predict the ultimate strength associated with each load (supposed to act separately).

4.3 Progressive Collapse Analysis

In Caldwell's method (and later improvements), the ultimate hull girder strength is calculated without considering the strength reduction in individual members after they have attained their ultimate strength locally. This does not represent the real collapse behaviour of the structural members. Neglecting of the reduction in capacity of individual members beyond their ultimate strength greatly affects the ultimate strength of the whole cross-section. For this reason, it is very important to take into consideration the strength reduction (load shedding) of each structural member when the collapse behaviour of a ship's hull is simulated. This simulation method is called Progressive Collapse Analysis. In the following, major methods of progressive collapse analysis and some calculated results are introduced.

4.3.1 Idealized structural unit method (ISUM)

The Idealized Structural Unit Method (ISUM) was proposed by Ueda & Rashed (1984), who had initially derived and introduced an ISUM element for the plate girders. The key concept of ISUM, i.e. to divide the structure into as large elements as possible keeping the main features of the nonlinear structural members behaviors in their formulation, was afterwards employed in the development of various types of plate elements (Paik, 1995). The common aim was to develop elements significantly larger than in FEM, therefore to obtain a drastic reduction in the calculation time.

An efficient ISUM rectangular plate element, recently developed and proven accurate in predicting buckling/plastic behavior of stiffened plate panels, is employed here to model the inner and outer plating. In its original formulation, (Masaoka *et al.*, 1988) the intra-element lateral deflection is treated as additional degree of freedom and approximated by its elastic buckling mode throughout the collapse behavior.

The new ISUM rectangular stiffened plate model proposed by Fujikubo & Kaeding (2002) is used. The ISUM rectangular plate element was improved by new lateral shape functions based on the collapse modes, new element subdivision technique keeping the continuity of deflection, introduction of plate/stiffener interactions etc. The stiffeners are modeled with beam-column elements. This new model can cope with the buckling/collapse behavior of the stiffener and plate panel and is accurate in the post-ultimate strength behavior, thus useful for system analysis.

The collapse behavior of double-bottom structures under lateral loads depends mainly on the behavior of inner and outer plating under large in plane stress occurred from the overall bending. The aforementioned ISUM plate elements accurately capture local failures such as buckling and yielding, including their post-buckling and post-ultimate behavior that is crucial to simulate correct load redistribution.

Another principal failure is that of web plates in shear. The floors and girders are made of stiffened webs with or without perforations of various types. The behavior of double-bottom girders in shear/bending is known from prior detailed nonlinear Finite Element Analyses (FEA) (Yanagihara et. al, 2002). In the present approach, the webs are modeled by Timoshenko beam elements provided with elastic-plastic layers in depth direction. The holes in the web plates can also be considered in this approach. The web buckling in bending is taken into account with the aid of the effective width concept.

The ISUM stiffened plate models for inner and outer plating and Timoshenko beam elements for floors and girders are connected assuming that the cross sections remain plane. The accuracy of this approach is validated for several flange/web combinations using single- and multi-span girder models under shear and bending.

The combined model of Timoshenko beam and ISUM stiffened plate models is applied to predict the collapse behavior of double-bottom structure of a bulk carrier. The longitudinal stiffeners on the inner and outer plating are considered. The uniform pressure load is increased up to the collapse. The ultimate strength and the reserved strength after the initial local failure are discussed.

Pei & Fujikubo (2005) have developed the new stiffened plate model that consist of large plate elements for local plate panels and beam-column elements for stiffeners is applied to the progressive collapse analysis of a ship's hull girder under longitudinal bending. The employed ISUM model was characterized by the shape functions for the deflection of local plate panels based on the collapse modes and ability to regard the localization of plastic deformation. Adopted model was validated by 1/3 –scale welded steel frigate model and Abaqus FE analysis as well.

4.3.2 Smith's method

After Caldwell, more exact information is obtained regarding the strength reduction factor representing the influence of buckling. However, the problem caused by the

above-mentioned time lag had not been solved until Smith (1977) proposed a simplified method, which is now commonly called the Smith's method. This method enables to perform progressive collapse analysis on the cross-section of a hull girder subjected to longitudinal bending. In Smith's method, a cross-section is divided into small elements composed of stiffener(s) and attached plating. At the beginning, the average stress–average strain relationships of individual elements are derived under the axial load considering the influences of yielding and buckling. Then, a progressive collapse analysis is performed assuming that a plane cross-section remains plane and each element behaves according to its average stress–average strain relationships. After Smith, many research papers have been published, in which new methods are proposed to constitute the average stress–average strain relationship of element composed of stiffener(s) and attached plating.

It is assumed in the Smith method that the behaviour of the ship hull girder follows the behaviour of a beam according to the Euler beam theory extended to elastic plastic range. The method is briefly characterized below:

The framing system is assumed to be longitudinal. The collapse of a girder section is assumed to occur between two adjacent frames, being induced either by the inter-frame flexural beam-column collapse of panels under compression or by the inter-frame yielding of panels under tension. This hypothesis is based on two other assumptions, namely: the overall grillage instability stress is higher than the inter-frame beam-column collapse stress, which requires sufficient rigidity of the transverse frames to provide supports to the longitudinal stiffeners; and the tripping stress of stiffeners is also higher than the inter-frame collapse stress. Both criteria can be achieved during design, satisfying appropriate design constraints on the relative sizes of the transverse frames and the longitudinal structure. The computations for the moment-curvature relationship of the hull girder are described according to the following sequence (Rahman & Chowdhury, 1996).

- Divide the hull girder into stiffened elements. One stiffener with its attached plating is considered as a panel element. Any left-out portion of plating at the

junctions of deck and side structures, bottom and side structures, and other junctions of two perpendicular plating panels can be considered as corner elements.

- Define stress-strain relationships for all of these elements as shown in Chapter 2.
- Initialise the total curvature with the initial limit curvature, and the instantaneous neutral axis with the effective elastic neutral axis. The initial limit curvature is considered to be the curvature that produced the first elemental limit state in the section.
- Calculate the corresponding strain for every element of the section using the distance to the instantaneous neutral axis. Corresponding element stress is obtained using the stress-strain relationships of the element.
- Determine the current position of the instantaneous neutral axis in an iterative manner, establishing force equilibrium over the whole cross section, by updating the position of elements relative to the current step neutral axis, and recalculating the values of strain and stress for every element as mentioned above. The calculation of the position of the instantaneous neutral axis starts from the previous neutral axis position and continues until the equilibrium of force in section is established with some specified accuracy.

According to the theory of beams in bending total direct strain in step (i) is equal to

$$^{(i)}\varepsilon = {}^{(i)}\kappa\left(z - {}^{(i)}z_C\right) \tag{4.1}$$

where $^{(i)}\kappa$ is curvature of a given section, z is the vertical coordinate of element, $^{(i)}z_C$ is the actual vertical co-ordinate of the centre of gravity of the section.

Thus the direct strain increment is found as,

$$\Delta^{(i+1)}\varepsilon = {}^{(i+1)}\varepsilon - {}^{(i)}\varepsilon = {}^{(i+1)}\kappa\left(z - {}^{(i+1)}z_C\right) - {}^{(i)}\kappa\left(z - {}^{(i)}z_C\right) \tag{4.2}$$

Iterative change of position of the neutral axis can be expressed as,

$$^{(i+1)}\Delta z_C = {}^{(i+1)}z_C - {}^{(i)}z_C \tag{4.3}$$

The strain increment can be split into two parts; dependant on the curvature increment and neutral axis position change

$$\begin{aligned}&\Delta^{(i+1)}\varepsilon = {}^{(i+1)}\kappa\left(z - {}^{(i)}z_C - {}^{(i+1)}\Delta z_C\right) - {}^{(i)}\kappa\left(z - {}^{(i)}z_C\right) = \\ &\left({}^{(i+1)}\kappa - {}^{(i)}\kappa\right)\left(z - {}^{(i)}z_C\right) - {}^{(i+1)}\kappa\,{}^{(i+1)}\Delta z_C = {}^{(i+1)}\Delta\kappa\left(z - {}^{(i)}z_C\right) - {}^{(i+1)}\kappa\,{}^{(i+1)}\Delta z_C\end{aligned} \tag{4.4}$$

The iterative correction of the neutral axis position is calculated using the condition of the zero net force normal to the cross section

$$\int_A {}^{(i)}\sigma dA = 0 \tag{4.5}$$

where ${}^{(i)}\sigma$ is the direct strain and A is the cross-section-area. Expanding the direct stress in the Taylor series

$${}^{(i)}\sigma\left({}^{(i)}z_C + {}^{(i)}\Delta z_C\right) = {}^{(i)}\sigma_k\left({}^{(i)}z_C\right) + \frac{\partial\,{}^{(i)}\sigma}{\partial\,{}^{(i)}z_C}\Delta^{(i)}z_C = 0 \tag{4.6}$$

the value of $\Delta^{(i)}z_C$ is evaluated

$$\Delta\,{}^{(i)}z_{C,k} = -\left[\int_A \frac{\partial\,{}^{(i)}\sigma_k}{\partial\,{}^{(i)}z_{C,k}} dA\right]^{-1} \int_A {}^{(i)}\sigma_k\left({}^{(i)}z_{C,k}\right) dA \tag{4.7}$$

- Calculate the overall bending moment corresponding to a certain curvature by integrating the contribution of all component stiffened panel elements of the cross section of the box girder.

- Compare the value of moment in the current increment (k) with the value of moment in the previous increment (k-1) and identify peak values.
- If the slope in the moment-curvature relationship is zero or negative, terminate the process defining the ultimate moment, by the highest peak value. Otherwise increment the curvature to obtain the total progressive curvature and repeat from point 4.

The curve Moment versus Curvature is obtained by means of an incremental – iterative approach, summarized in the flow chart in Figure 4.1.

The accuracy of the calculated results by the Smith's method depends largely on the accuracy of the average stress – average strain relationships of elements. Main difficulties concern the modeling of initial imperfections (deflection and welding residual stress) and the boundary conditions (multi-span model, interaction between adjacent elements, etc.). This is the reason why most of the recent works are focusing on the development of more reliable stress-strain curves (Gordo & Soares, 1993; Paik, 1999).

Smith himself performed a series of elastic-plastic large deflection analysis by FEM to derive average stress-average strain relationships of elements. On the other hand, some analytical methods have been proposed to get average stress-average strain relationships of stiffened plate elements. Ostapenko (1981) applied analytical solutions with some assumptions, and derived the average stress-average strain relationships of compression flange under combined in plane bending and shear as well as under combined thrust and hydraulic pressure. Rutherford & Caldwell (1990) proposed an analytical method combining the ultimate strength formulae and solution of the rigid-plastic mechanism analysis. In both methods, the strength reduction after the ultimate strength is considered. To evaluate the ultimate hull girder strength by the Smith's method, Gordo & Soares (1993, 1996), and Gordo *et al.* (1996) applied a simplified approach to represent collapse behaviour of a beam-column subjected to axial compression.

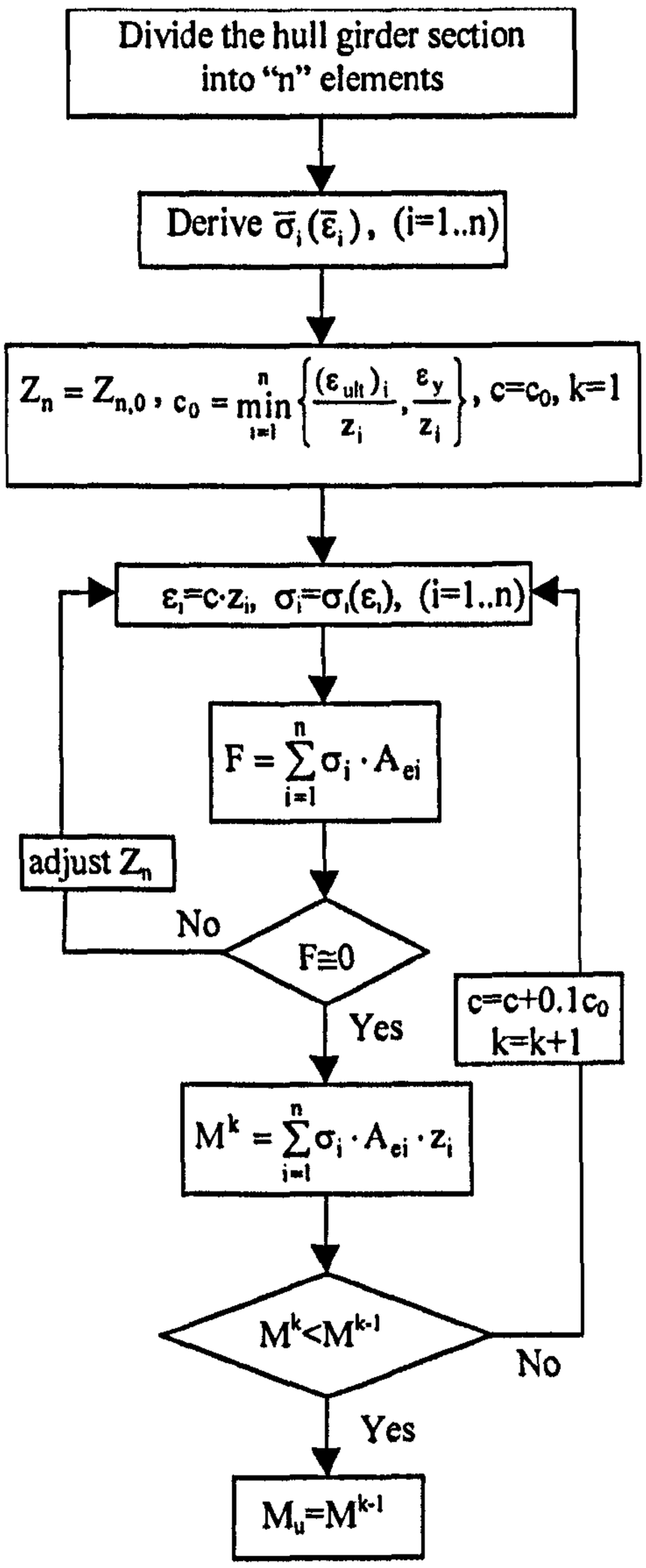

Figure 4.1: Flow chart of procedure for the evaluation of curve Moment versus Curvature

Yao & Nikolov (1993) proposed an analytical method to derive average stress-average strain relationship for the element composed of a stiffener and attached plating. In this method, the average stress-average strain relationship of the panel surrounded by stiffeners is first derived combining the elastic large deflection analysis and the rigid-plastic mechanism analysis in analytical forms. Then, considering the equilibrium condition of forces and bending moments acting on the element, the average stress-average strain relationship of a stiffener element is derived. This method is implemented in the computer code HULLST for progressive collapse analysis.

Rahman & Chowdury (1996) combined the Smith's method with simplified average stress-average strain curves based on the calculation of the ultimate strength of a stiffened panel developed by Hughes (1988). A few practical applications are summarised: Smith (1983) discussed the advantage of the longitudinal stiffening systems from the viewpoint of ultimate longitudinal strength and he derived a strength interaction curve for combined vertical and horizontal bending moments; Dow *et al.* (1981, 1991) studied a British destroyer and a frigate model applying the Smith's method; Faulkner *et al.* (1984) carried out analysis by the same method on a British torpedo-boat-destroyer and Okamoto *et al.* (1985) performed a progressive collapse analysis to assess the strength of a new unidirectional girder structural system.

Hu & Chen (2001) performed the limit state analysis, and the evaluated torsional strength was compared with the design loads given by the Classification Society Rules. Ultimate hull girder strength in torsion was discussed also by Paik (2001). Committee III.1 of ISSC'94 also performed a series of progressive collapse analyses on ten vessels (Jensen *et al.* 1994) and noticed that the initial yielding strength cannot be a conservative measure of the ultimate hull girder strength especially when a cross-section is subjected to the sagging bending moment. Many ultimate longitudinal strength design formulations have been investigated in detail under vertical bending moment by Yao *et al.* (2000).

4.3.3 Non-linear finite element method

Usually, simplified methods are applied for the progressive collapse analysis of a ship's hull under longitudinal bending, and the applications of ordinary FEM are very few. This is because the influences of both material and geometrical nonlinearities have to be considered in the analysis applying an incremental procedure. A ship's hull girder may be too large for such kind of analysis to get rational results easily. Nevertheless, some results have been reported.

Chen *et al.* (1983) performed static and dynamic FEM analyses modelling a part of the ship hull with plate and beam-column elements. They also used orthotropic plate elements to represent stiffened plates. This reduced the numbers of nodal points and elements. The yielding condition was represented by sectional forces such as axial force, shear force and bending moment. This also reduced the computation time by avoiding numerical integration towards the thickness direction. The computer code, USAS was developed for this analysis. Kutt *et al.* (1985) performed the same analysis also using USAS on two general cargo vessels. They discussed the sensitivities of the ultimate hull girder strength with respect to yield stress, plate thickness and initial imperfection based on the calculated results. Valsgaard *et al.* (1991) applied a non-linear code FENCOL to analyse the compressive collapse behaviour of the girder models tested by Mansour *et al.* (1990) and *Energy Concentration.*

The results of the FEM analysis to evaluate ultimate hull girder strength are not so many at the moment because the number of elements and nodal points become very huge if rational results are required. However, the Investigation Committee of the Cause of Casualty on *Nakhodka* performed elastic-plastic large deflection analysis in an incremental manner with nearly 200000 elements (JMT 1997) using the computer code LSDYNA-3D. Similar analysis was performed on existing handy size tanker, panamax size tanker and VLCC to investigate into the influence of corrosion damage on ultimate hull girder strength (JSRA 2000).

Moan *et al.* (2005) have conducted a critical review of ultimate strength models; especially including the approach used in the Joint Tanker Project (JTP) was accomplished, by considering separately the bending and shear capacities, where the focus was on sagging state. See Table 4. In the JTP Rules (2005), the ultimate hull girder bending capacity, in sagging, is to be assessed by the single step procedure. The single step procedure or linear first approach, so-called HULS-1, is a simplified method based on a reduced hull girder bending stiffness accounting for buckling of the deck.

$$M_{u,JTP} = Z_{red}\sigma_{Yd} \tag{4.8}$$

where Z_{red} is the reduced section modulus of the deck (to the mean deck height) defined as $\frac{I_{red}}{z_d - g}$, z_d is the vertical distance to the mean deck height measured from the baseline, g is the vertical distance to the neutral axis of the reduced section measured from the baseline and σ_{Yd} is the specified yield stress of the steel in the deck.

Table 4.1: Comparison of different methods considering the assumptions in each one

System Model Assumption	Hull Girder Collapse Analysis Method					
	A	B	C	D	E	F
Simplified average stress-average strain relationship	-	-	-	+	-	+
Utilization of Navier's hypotheses	-	-	-	-	-	+
Negligence of the interaction between adjacent element	-	-	-	-	-	+
Negligence of load shedding / Time lag	-	+	+	+	+	+
Negligence of progressive collapse	-	+	+	+	+	+
Computationally inefficient algorithm	+	+	+	-	+	+
Modelling difficulty	+	+	+	+	+	-
Negligence of the presence of transverse/lateral/shear	-	+	+	+	+	-
Points	2	5	5	5	5	6

NOTE: A= Linear approaches; B = Semi – progressive collapse approach; C = Smith approach – Simplified load – end shortening; D = Smith approaches – FE load – end shortening; E = ISUM; F = Finite Element approach (- = Yes, + = No)

4.4 A Developed Computer Code for Assessment of the Ultimate Strength (NEPTUNE)

Theoretical background of the code with respect to evaluation of the stress-strain curves is expressed in Chapter 2. The method adopted in the code NEPTUNE uses the Smith's method. A few simplifying assumptions are made in the program. Transverse cross-sections of the ship hull remain plane and perpendicular to the neutral surface. Collapse takes place for panels located between transverse primary members. The midship cross-section is divided into panel elements and hard-corner

elements to construct an analytical model in the simplified method. Material is assumed to be an elastic-plastic. No interaction is taken into account among stiffened panels. The influence of shear forces is neglected.

After a series of calculation at different curvatures, a moment – curvature curve can be obtained. The position of the instantaneous neutral axis should be determined by iteration or trial-and-error according to the case that the sum of stresses on all elements of the cross-section equals zero.

The latest version of computer code NEPTUNE calculates values of the moment versus curvature function of a ship hull subject to longitudinal bending in the elastic-plastic range for vertical and horizontal bending. The developed program is presented in Figure 4.2.

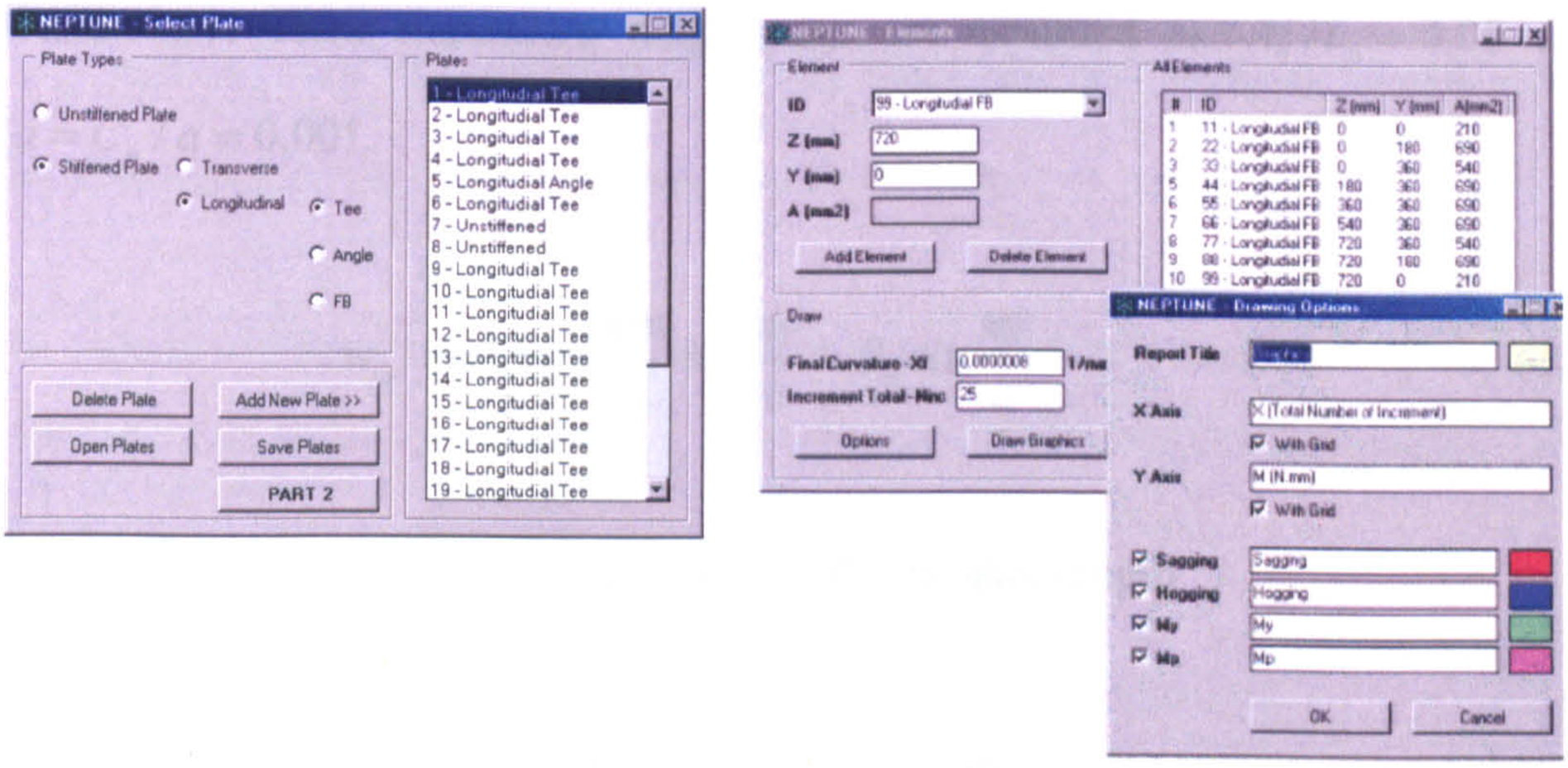

Figure 4.2: A computer code developed NEPTUNE for calculating hull girder ultimate strength

4.5 Benchmark Calculations on the Hull Girder Ultimate Strength

Hull girder ultimate strength on five ISSC benchmark vessels is analysed where a computer code NEPTUNE is developed. Hull girders of five vessels indicated in Table 4.2 while the cross-sections of the five hull girders are shown in Figures 4.3

through 4.7. Dimensions of stiffeners in the Tables 4.3 through 4.7 are defined. Among five vessels, the ultimate hull girder strength of the Frigate Model under sagging condition is measured by Dow (1991). The single Hull VLCC is *Energy Concentration* who sank at Rotterdam harbour in 1980, and the working bending moment at collapse under the hogging condition was estimated by Rutherford & Caldwell (1990).

Two cases are investigated for five hull girders, which are:

- Case (1): with small initial deflection and no welding residual stress
- Case (2): with actual initial deflection and welding residual stress

The assumed initial deflection in panels and stiffeners for Case (1) are the same, which is global buckling failure mode shape and are represented by Equations 4.9, 4.10 and 4.11. Their maximum magnitudes are assumed as $A_o / t_p = 0.01$ and $B_o / a = C_o / a = 0.001$.

$$w_{op} = A_o \sin\frac{m\pi x}{a}\sin\frac{\pi y}{b} + B_o \sin\frac{\pi x}{a} \tag{4.9}$$

w_{op} is defined as initial deflection for plate and a is span length

$$w_{os} = B_o \sin\frac{\pi x}{a}, \qquad v_{os} = C_o \sin\frac{\pi x}{a} \tag{4.10}$$

The magnitudes of initial deflection are taken as:

$$A_o = 0.01 x t_p; \quad B_o = 0.001 x a; \quad C_o = 0.001 x a \tag{4.11}$$

For Case (2), the same initial deflection is assumed for stiffeners.

The assumed welding residual stress in Case (2) is represented by Equations (4.12) through (4.15).

$$\sigma_{cp} = \frac{2b_t}{b-2b_t}\sigma_{op}, \qquad \sigma_{cs} = \frac{2b_s}{b-2b_s}\sigma_{os} \tag{4.12}$$

$$\sigma_{cp} = \sigma_{cs} = \frac{2b_t t_p \sigma_{op} + b_s t_w \sigma_{os}}{(b-2b_t)t_p + A_s - b_s t_w} \tag{4.13}$$

$$b_t = t_w/2 + 0.26\Delta Q/(t_w + 2t_p) \qquad b_s = (t_w/t_p)x(b_t - t_w/2) \quad \Delta Q = 78.8l^2 \tag{4.14}$$

$$l = \begin{cases} 0.7xt_w \ (mm) & (when 0.7xt_w < 7.00mm) \\ 7.0 \ \ (mm) & (when 0.7xt_w \geq 7.00mm) \end{cases} \tag{4.14}$$

σ_{op} and σ_{os} are the yield stress of the plate and the stiffener, respectively. Young's modulus of the material is taken as 205.8 GPa.

In case (2) of Single Hull VLCC *(Energy Concentration)*, thickness of the panel and the stiffener web is reduced by 1 mm and that of the stiffener flange by 2 mm according to the measured results (Rutherford & Caldwell, 1990).

Table 4.2: Principal dimensions of five vessels for calculations

Type	Length (m)	Breath (m)	Depth (m)
Bulk Carrier	285	50	26.7
Container ship	230	32.2	21.5
Double hull VLCC	315	58	30.3
Single hull VLCC *(Energy Concentration)*	313	48.2	25.2
Frigate Model	18	4.2	2.8

4.6 Applied Methods of Analyses

- **Astrup:**

A computer code NAUTICUS is used to evaluate the ultimate longitudinal strength of a hull girder. The program calculates the ultimate hull girder bending moment capacity based on DNV Rules for Ships Part 3 Chapter 1 Section 16 D300. A cross-section of the hull girder is divided into panels with stiffener. It is assumed that the capacity of each panel in compression is equal to the critical buckling capacity calculated according to DNV Class Note 30.1 (1995). On the other hand, that in tension is assumed to be the yield strength. Assuming that all the structural components in the cross-section are at their state either in compression or tension, the neutral axis for pure bending is calculated. The bending moment with respect to this neutral axis is considered as the ultimate hull girder strength.

- **Chen:**

This method is a variation of the Idealized Structural Unit Method (ISUM) generally attributed to Ueda *et al.* (1984) and was further developed by Paik (1990). The specific method employed here is a subset of Paik's work that is identified as Analysis of Large Plated Structures (ALPS; Paik, 1992).

In the present analysis, five types of ISUM elements are in use; namely, beam-column element, unstiffened plate element, hard element, and virtual element. The detail of these elements can be found in ALPS (Paik, 1992). Failure modes simulating instability and plasticity imbedded in the formulation include local buckling, panel buckling, overall buckling, yielding (including necking), ultimate tensile rupture, and ductile fracture. An element may fail in one of these modes initially and progressive to another mode subsequently in the manifestation of the progressive collapse process.

Table 4.3: Dimensions of longitudinals of Bulk Carrier (dimensions in mm)

Stif. No.	Dimensions	Type	Yield Stress	Stif. No.	Dimensions	Type	Yield Stress
1	390x27	Flat-bar	392.0	8	283x9+100x17	Tee-bar	352.8
2	333x9+100x16	Tee-bar	352.8	9	333x9+100x18	Tee-bar	352.8
3	283x9+100x14	Tee-bar	352.8	10	333x9+100x19	Tee-bar	352.8
4	283x9+100x18	Tee-bar	352.8	11	383x9+100x17	Tee-bar	352.8
5	333x9+100x17	Tee-bar	352.8	12	383x10+100x18	Tee-bar	352.8
6	283x9+100x16	Tee-bar	352.8	12	383x10+100x21	Tee-bar	352.8
7	180x32.5x9.5	Bulb-bar	235.2	14	300x27	Flat-bar	392.0

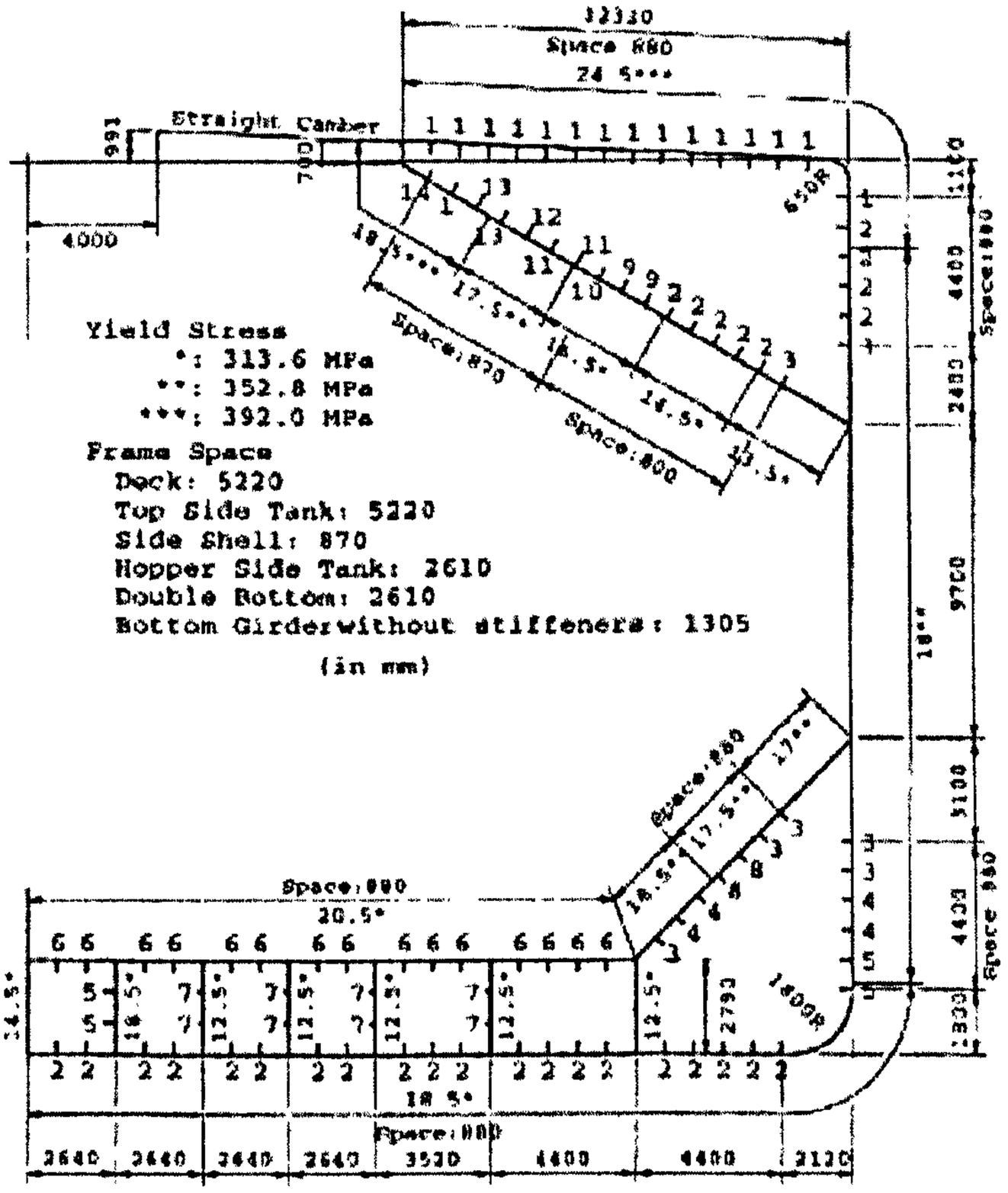

Figure 4.3: Cross-section of Bulk Carrier

Table 4.4: Dimensions of longitudinals of Container Ship (dimensions in mm)

Stif. No.	Dimensions	Type	Yield Stress	Stif. No.	Dimensions	Type	Yield Stress
1	300x38	Flat bar	352.8	9	230x10	Flat bar	313.6
2	300x28	Flat bar	313.6	10	300x90x13/17	Angle bar	313.6
3	250x90x10/15	Angle bar	313.6	11	150x90x12/12	Angle bar	313.6
4	250x90x12/16	Angle bar	313.6	12	250x90x12/15	Angle bar	313.6
5	300x90x11/16	Angle bar	313.6	13	150x12	Flat bar	313.6
6	350x100x12/17	Angle bar	313.6	14	150x90x9/9	Angle bar	313.6
7	350x100x12/17	Angle bar	313.6	15	150x10	Flat bar	313.6
8	400x100x11.5/16	Angle bar	313.6	16	300x90x11/16	Angle bar	313.6

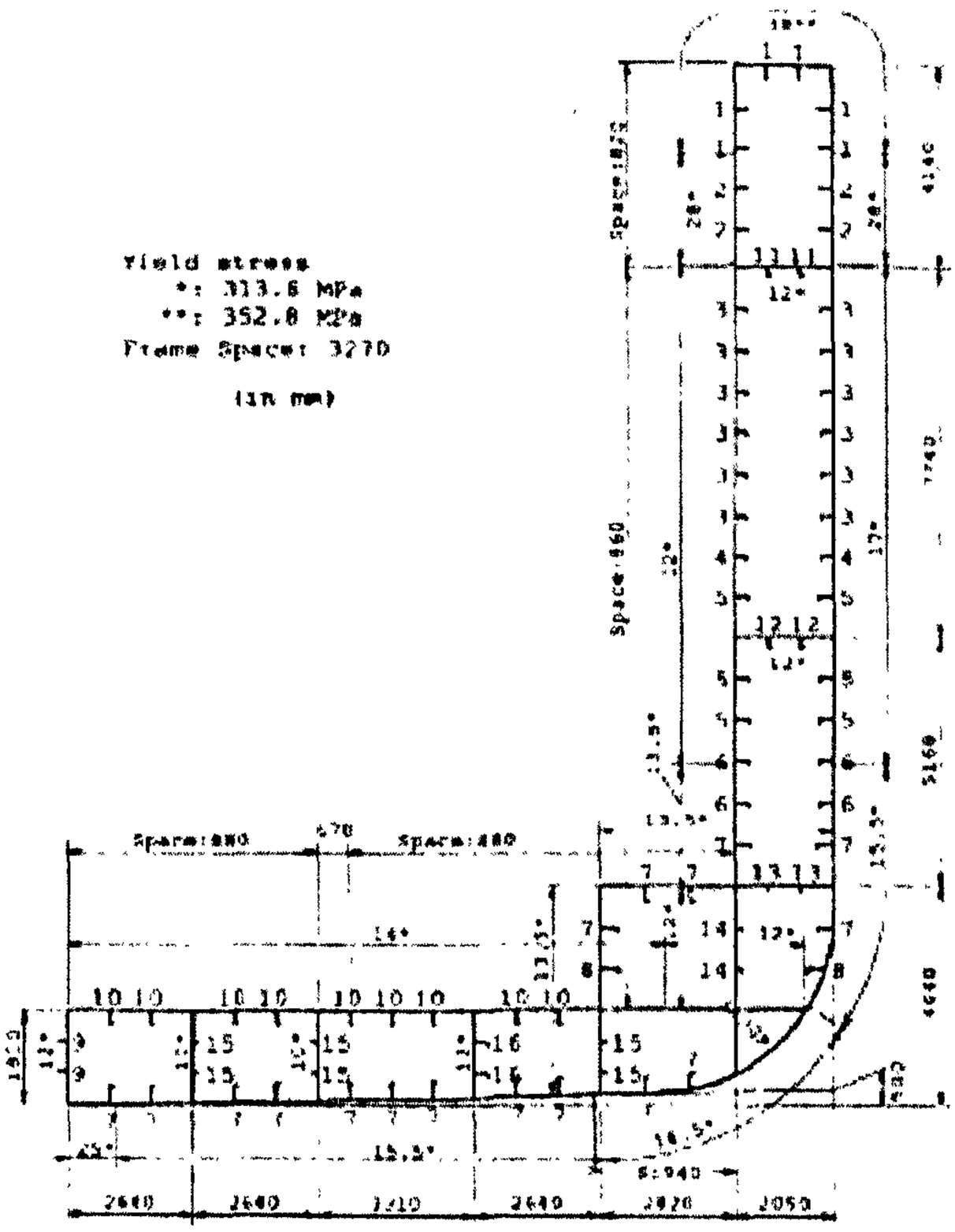

Figure 4.4: Cross-section of Container Ship

Table 4.5: Dimensions of longitudinals of double hull VLCC (dimensions in mm)

Stif. No.	Dimensions	Type	Yield Stress	Stif. No.	Dimensions	Type	Yield Stress
1	300x90x13/17	Angle bar	313.6	25	250x90x12/16	Angle bar	313.6
2	350x100x12/17	Angle bar	313.6	26	450x11+150x22	Tee bar	352.8
3	400x100x11.5/17	Angle bar	313.6	27	450x11+150x19	Tee bar	352.8
4	400x11+150x12	Tee bar	313.6	28	450x11+150x16	Tee bar	352.8
5	400x11+150x14	Tee bar	313.6	29	450x11+150x14	Tee bar	352.8
6	450x11+150x12	Tee bar	313.6	30	450x11+150x12	Tee bar	352.8
7	450x11+150x14	Tee bar	313.6	31	450x11+150x14	Tee bar	352.8
8	450x11+150x16	Tee bar	313.6	32	400x100x11/16	Angle bar	352.8
9	450x11+150x19	Tee bar	313.6	33	350x100x12/17	Angle bar	352.8
10	450x11+150x22	Tee bar	313.6	34	300x90x13/17	Angle bar	352.8
11	450x11+150x25	Tee bar	313.6	35	850x17+150x19	Tee bar	352.8
12	500x11+150x28	Tee bar	313.6	36	250x90x12/16	Angle bar	352.8
13	500x11+150x30	Tee bar	313.6	37	300x90x12/16	Angle bar	352.8
14	500x11+150x32	Tee bar	313.6	38	400x11+150x14	Tee bar	352.8
15	500x11+150x34	Tee bar	313.6	39	450x11+150x12	Tee bar	352.8
16	550x12+150x30	Tee bar	313.6	40	450x11+150x14	Tee bar	352.8
17	550x12+150x25	Tee bar	313.6	41	450x11+150x16	Tee bar	352.8
18	350x100x12/17	Angle bar	313.6	42	450x11+150x19	Tee bar	352.8
19	550x12+150x32	Tee bar	352.8	43	450x11+150x22	Tee bar	352.8
20	500x11+150x30	Tee bar	352.8	44	450x11+150x25	Tee bar	352.8
21	500x11+150x25	Tee bar	352.8	45	450x11+150x28	Tee bar	352.8
22	500x11+150x25	Tee bar	352.8	46	500x11+150x25	Tee bar	352.8
23	450x11+150x28	Tee bar	352.8	47	500x11+150x28	Tee bar	352.8
24	250x12.5	Flat bar	313.6	48	230x12.5	Flat bar	313.6

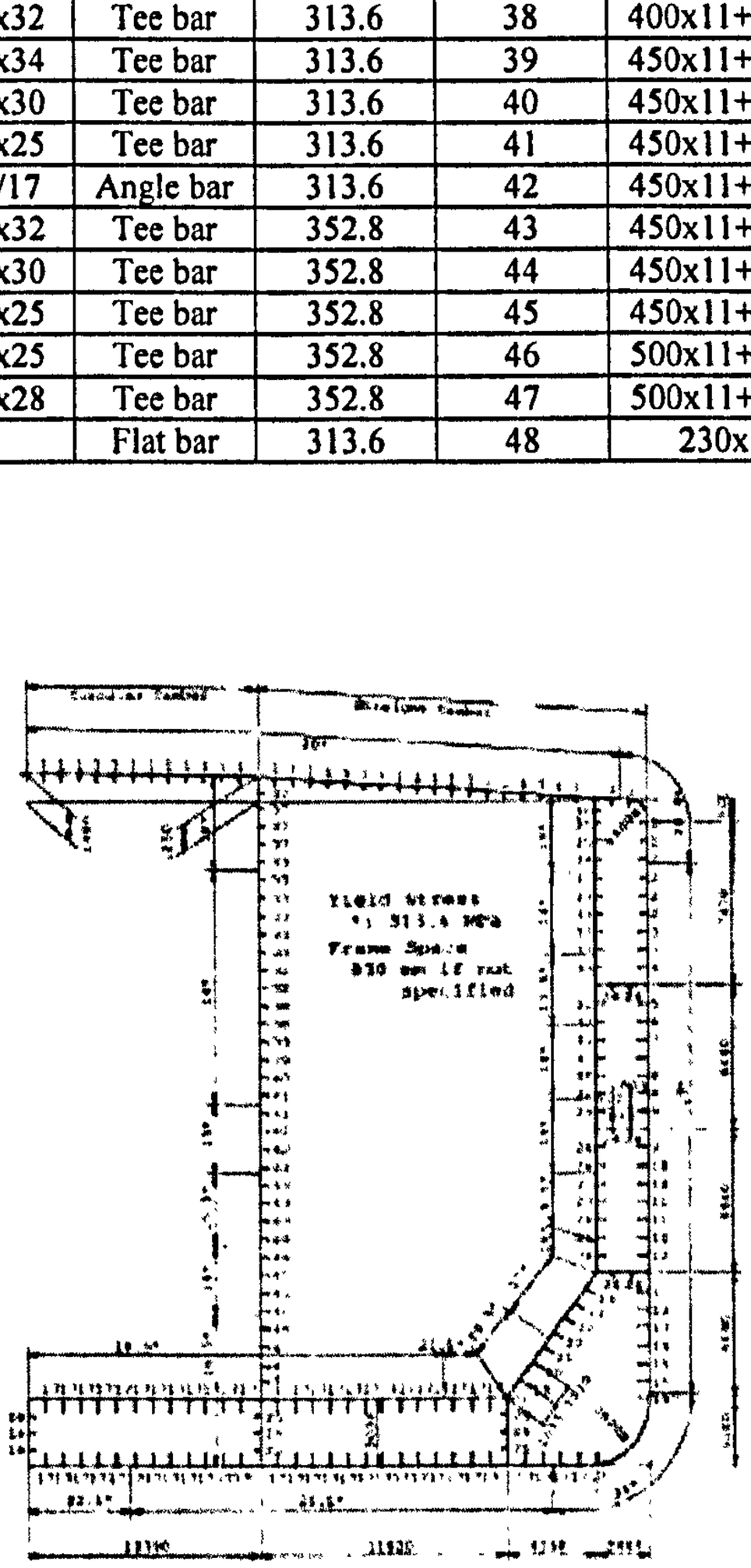

Figure 4.5: Cross-section of double hull VLCC

Table 4.6: Dimensions of longitudinals of *Energy Concentration* (dimensions in mm)

Stif. No.	Dimensions	Type	Yield Stress	Stif. No.	Dimensions	Type	Yield Stress
1	797x15+200x33	Tee bar	313.6	17	747x12+180x25	Tee bar	235.2
2	300x100x11/16	Angle bar	313.6	18	797x14+180x25	Tee bar	235.2
3	370x16	Flat bar	313.6	19	847x14+180x25	Tee bar	313.6
4	425x25	Flat bar	313.6	20	847x14+180x32	Tee bar	235.2
5	480x32	Flat bar	313.6	21	847x15+180x32	Tee bar	313.6
6	300x100x11/16	Angle bar	313.6	22	847x15+180x32	Tee bar	313.6
7	370x16	Flat bar	313.6	23	897x15+200x25	Tee bar	253.2
8	447x11+125x22	Tee bar	313.6	24	945x16+200x25	Tee bar	253.2
9	549x11+125x22	Tee bar	235.2	25	897x15+200x25	Tee bar	313.6
10	597x11+125x22	Tee bar	235.2	26	797x15+180x25	Tee bar	313.6
11	597x11+125x22	Tee bar	235.2	27	347x11x125/22	Tee bar	313.6
12	647x11+125x22	Tee bar	235.2	28	397x25	Flat bar	313.6
13	350x25.4	Flat bar	235.2	29	300x25	Flat bar	253.2
14	646x12+150x25	Tee bar	235.2	30	230x12.7	Flat bar	253.2
15	697x12+150x25	Tee bar	235.2	31	230x12.7	Flat bar	253.2
16	747x12+150x25	Tee bar	313.6	32	397x11+100x25	Tee bar	313.6

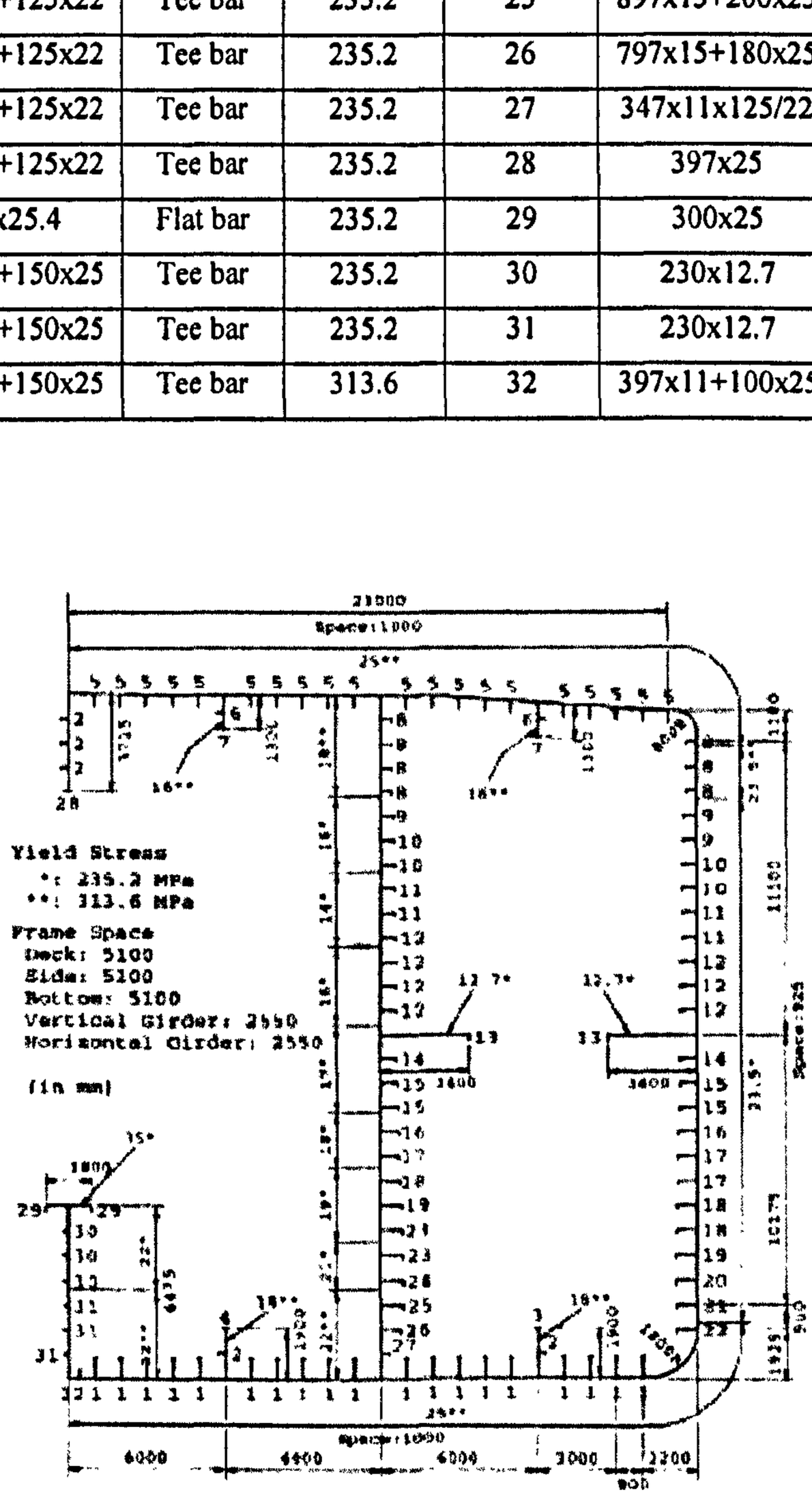

Figure 4.6: Cross-section of single hull VLCC, *Energy Concentration*

Table 4.7: Location of longitudinals of 1/3-scale Frigate model (dimensions in mm)

Stif.ID	Y (mm)	Z (mm)	Stif.ID	Y (mm)	Z (mm)	Stif.ID	Y (mm)	Z (mm)
Keel	0.0	0.0	No.4 DK	1685.9	493.5	29L	2050.0	2264.5
1L	98.4	12.9	16L	1741.7	584.5	30L	2050.0	2264.5
2L	249.3	41.9	17L	1807.3	622.6	31L	2050.0	2658.1
3L	373.9	67.7	18L	1863.0	709.7	No. 1 DK	2050.0	2800.0
4L	472.3	87.1	19L	1909.0	793.5	32L	1948.3	2800.0
5L	574.0	106.5	20L	1945.0	883.9	33L	1823.7	2800.0
6L	675.7	125.8	21L	1974.6	977.4	34L	1621.6	2800.0
7L	774.1	145.2	22L	1994.2	1077.4	35L	1418.3	2800.0
8L	882.3	167.7	23L	2010.6	1174.2	36L	1216.2	2800.0
9L	984.0	190.3	24L	2023.8	1274.2	37L	1012.9	2800.0
10L	1089.0	216.1	25L	2033.6	1367.7	38L	810.8	2800.0
11L	1197.2	241.9	26L	2040.2	1471.0	39L	607.5	2800.0
12L	1292.3	277.4	27L	2050.0	1671.0	40L	405.4	2800.0
13L	1394.0	316.1	28L	2050.0	1867.7	41L	202.0	2800.0
14L	1492.4	364.5	No. 2 DK	2050.0	2064.5	42L	0.0	2800.0
15L	1587.5	419.4						

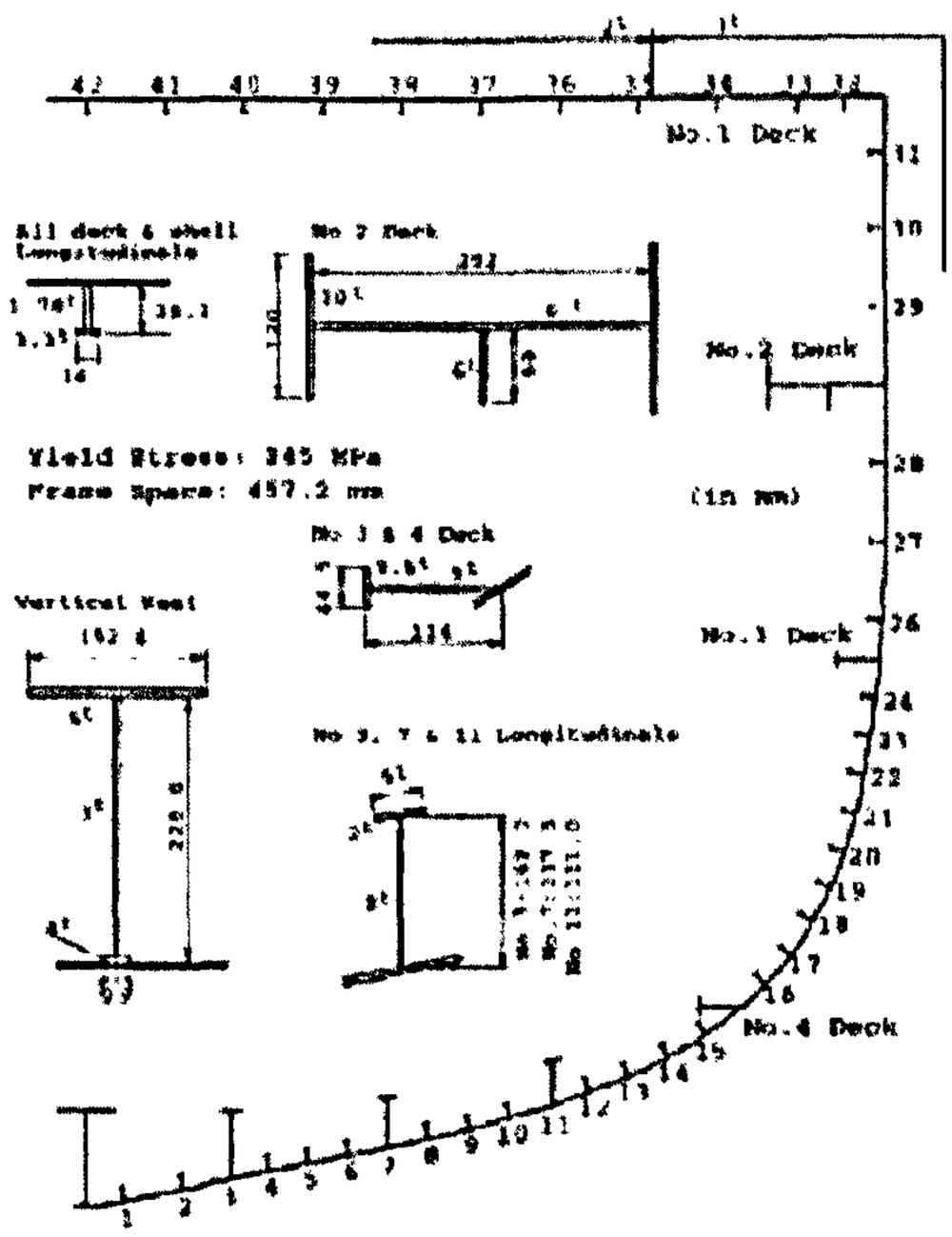

Figure 4.7: Cross-section of 1/3-scale steel welded frigate model

- **Cho:**

The ordinary Smith's method is applied to simulate the progressive collapse behaviour of the hull girder cross-section using average stress-average strain relationships derived for the stiffener elements with attached plating (Cho *et al.* 1998).

- **Dow:**

The method used to carry out the analysis is the Smith's method, which enables to calculate the progressive collapse behaviour of a ship hull girder subjected to combined vertical and horizontal bending incorporating the effects of shear and lateral loads (Dow, 1980).

- **Masaoka:**

The ISUM is applied for the analysis. The cross-section is divided into ISUM rectangular plate elements and elastoplastic beam elements. To derive the stiffness matrix of all the panel members, edges of the plate elements are assumed to be simply supported. Stiffeners are also modelled by plate elements with a free edge and simply supported edges.

Detail of the ISUM rectangular plate element used for the present analysis is described in the paper by Ueda & Masaoka (1995). In this analysis, overall buckling as a stiffened plate and tripping of stiffeners are not accounted. Geometrical nonlinearity is considered in ISUM element only locally by using eigen-function for deflection. Arc length method is applied for the nonlinear incremental calculation taking into account a shift of the neutral axis during progressive collapse.

- **Rigo (1):**

The ordinary Smith's method is applied with a simplified structural modelling proposed by Rahman & Chowdhury (1996), and a progressive collapse analysis is performed. The modelled structure is composed of only three components, which are the deck, the bottom and the side shell plating. The average stress-average strain relationships are derived for these three components applying the Hughes' method (1988). Special approximation and simplification have to be performed when the analysed midship section is complex or composed of large curved part.

- **Rigo (2):**

For each component composing a cross-section, the ultimate strength is estimated applying Paik's method (Paik & Thayamballi, 1997). Then, based on the credibly assumed stress distribution across the cross-section, the hogging and the sagging ultimate bending moments are directly calculated by a simple formulation (Paik & Mansour, 1995). A progressive collapse analysis is not performed.

In this method, the stress-strain relationships are not defined, but the reduction in capacity beyond the ultimate strength in individual compressed components is implicitly and approximately accounted for by introducing an "assumed stress distribution" which may represent the real situation of the structural failure at the ultimate limit state. If the reduction of capacity is not considered, the assumed stress distribution could not be obtained.

- **Soares:**

The ordinary Smith's method is applied using the average stress-average strain relationships based on a beam-column approach (Gordo & Soares, 1996). The influence of the panel buckling is accounted introducing effective width after local buckling.

- **Yao:**

The ordinary Smith's method is applied using a computer code HULLST with the average stress-average strain relationships of elements composed of a stiffener and attached plating, which are derived analytically (Yao & Nikolov, 1991; 1992). The bi-axial bending can be applied, and the influence of shear force can be accounted when it is necessary.

- **Ozguc:**

The ordinary Smith's method is employed using a computer code NEPTUNE with the average stress-average strain relationships of elements composed of a stiffener and attached plating, which were derived semi analytically based on ANSYS non-linear elastic-plastic buckling analyses of a wide range of typical ship panel geometries. The moment-curvature curve and the ultimate bending moment at ultimate state are calculated with initial imperfections in the form of initial deflection and welding induced residual stresses for both hogging and sagging cases subject to vertical and horizontal bending moments (Ozguc *et al.* 2005c).

4.7 Calculated Results

The calculated results of ultimate hull girder strength are presented in Table 4.6 through 4.10. The items in the tables are as follows:

I_y : Moment of inertia with respect to horizontal neutral axis, in m^4

z_G : Location of neutral axis above keel under vertical bending, in m

M_P : Fully plastic bending moment of cross-section, in MN.m

M_{YS} : Initial yield strength of deck, in MN.m

M_{YH} : Initial yield strength of bottom, in MN.m

M_{BS} : Local buckling strength of deck, in MN.

M_{BH} : Local buckling strength of bottom, in MN.m

M_{US} : Ultimate bending moment of cross-section under sagging, in MN.m

M_{UH} : Ultimate bending moment of cross-section under hogging, in MN.m

(1): With small initial deflection without welding residual stress, Case (1)

(2): With specified initial deflection and welding residual stress, Case (2)

The moment-curvature relationships obtained by different methods for Case (2) are plotted in Figures 4.8 through 4.12.

Table 4.8: Ultimate hull girder strength of bulk carrier

Items	Chen	Cho	Masaoka	Rigo (1)	Rigo (2)	Soares	Yao	Present method
I_y	694.87	693.44	689.80	-	702.48	679.31	682.50	682.11
Z_g	11.20	11.06	11.03	10.94	10.66	11.15	10.87	11.02
M_P	20.87	19.90	19.86	20.26	20.03	19.64	20.12	20.22
M_{YS}	15.82	15.64	15.53	-	15.45	15.41	15.21	15.19
M_{YH}	21.58	21.83	21.79	-	23.04	21.20	21.91	19.41
M_{BS}	13.19	13.05	12.95	-	12.89	12.85	12.79	12.06
M_{BH}	16.43	16.63	16.59	-	17.55	16.14	16.68	16.20
M_{US-1}	15.35	14.40	16.82	15.03	-	13.72	15.67	14.28
M_{UH-1}	18.71	19.55	18.90	19.13	-	17.43	17.78	17.52
M_{US-2}	15.20	13.69	16.02	14.34	14.84	-	14.45	14.19
M_{UH-2}	19.06	18.99	18.56	18.71	17.08	-	17.36	17.34

MOMENT (x 1000 MN-m)

Table 4.9: Ultimate hull girder strength of container ship

Items	Chen	Cho	Masaoka	Rigo (1)	Rigo (2)	Soares	Yao	Present method
I_y	250.94	226.70	235.60	-	254.30	238.73	238.21	246.53
Z_g	8.86	8.84	8.54	8.13	8.10	8.51	8.63	8.69
M_P	9.36	8.39	8.64	9.06	9.01	8.76	8.95	8.39
M_{YS}	7.00	6.32	6.41	-	6.70	6.48	6.53	6.38
M_{YH}	8.88	8.04	8.65	-	9.85	8.80	8.66	8.85
M_{BS}	6.72	6.06	6.16	-	6.43	6.22	6.28	6.05
M_{BH}	6.54	5.92	6.37	-	7.25	6.48	6.37	6.32
M_{US-1}	5.54	5.29	7.79	6.93	-	6.68	6.84	6.52
M_{UH-1}	6.82	7.05	8.06	8.00	-	7.75	6.90	7.12
M_{US-2}	5.47	5.13	7.75	6.51	6.91	-	6.72	6.70
M_{UH-2}	6.56	6.69	8.07	7.60	7.20	-	6.72	6.79

MOMENT (x 1000 MN-m)

Table 4.10: Ultimate hull girder strength of single hull VLCC, *Energy Concentration*

Items	Chen	Cho	Dow	Masaoka	Rigo (1)	Rigo (2)	Soares	Yao	Present method
I_{y-1}	851.5	860.0	-	869.8	-	857.76	848.71	840.28	851.46
Z_{g-1}	12.06	12.12	-	11.99	12.81	12.75	12.17	12.24	12.31
M_{P-1}	22.63	22.85	21.03	23.08	21.29	21.53	22.62	22.73	22.54
M_{YS-1}	20.32	20.62	-	20.65	-	21.61	20.43	20.33	20.70
M_{YH-1}	22.14	22.25	-	22.75	-	21.10	21.87	21.53	21.69
M_{BS-1}	16.90	17.14	-	17.17	-	17.96	16.98	16.90	16.91
M_{BH-1}	18.41	18.50	-	18.91	-	17.54	18.18	17.90	18.27
M_{US-1}	20.49	17.98	-	18.02	19.52	18.15	15.83	18.98	16.96
M_{UH-1}	20.67	20.53	-	20.44	20.02	18.58	18.79	20.82	18.78
								MOMENT (x 1000 MN-m)	
I_{y-2}	-	819.70	743.8	828.3	-	812.86	-	800.89	808.46
Z_{g-2}	-	12.15	11.85	12.01	12.31	12.81	-	12.27	12.34
M_{P-2}	-	21.76	19.85	21.96	20.35	20.39	-	21.75	21.57
M_{YS-2}	-	19.70	17.47	19.69	-	20.57	-	19.43	18.94
M_{YH-2}	-	21.16	19.68	21.63	-	19.90	-	20.47	19.88
M_{BS-2}	-	16.09	14.28	16.09	-	16.81	-	15.87	14.91
M_{BH-2}	-	17.29	16.08	17.67	-	16.26	-	16.73	16.44
M_{US-2}	18.54	16.75	16.32	19.00	17.90	17.10	-	16.84	16.45
M_{UH-2}^{*}	20.23	20.09	18.80	20.01	18.46	17.54	-	19.03	17.89

- Estimated applied load at collapse in hogging: 17.94×10^3 MN.m (Rutherford & Caldwell, 1990)

Table 4.11: Ultimate hull girder strength of double hull VLCC

Items	Chen	Cho	Masaoka	Rigo (1)	Rigo (2)	Soares	Yao	Present method
I_y	1347.3	1340.1	1360.0	-	1382.3	1355.8	1344.7	1354.9
Z_g	12.88	12.92	12.79	12.83	13.18	13.03	12.84	12.93
M_P	32.40	31.74	32.07	30.99	32.86	31.77	32.96	32.77
M_{YS}	24.12	24.04	24.22	-	25.17	24.48	24.02	24.33
M_{YH}	32.80	32.53	33.35	-	32.89	32.63	32.84	32.84
M_{BS}	19.74	19.68	19.82	-	20.61	20.24	19.66	20.05
M_{BH}	27.14	26.91	27.59	-	27.21	26.99	27.17	27.12
M_{US-1}	23.83	22.11	26.82	20.62	-	19.85	21.23	21.86
M_{UH-1}	28.28	29.59	30.88	28.90	-	27.61	29.22	29.17
M_{US-2}	24.33	20.80	26.59	19.57	24.07	-	20.42	21.15
M_{UH-2}	27.40	28.66	30.59	28.32	25.61	-	28.88	27.45

MOMENT (x 1000 MN-m)

Table 4.12: Ultimate hull girder strength of 1/3-scale welded steel frigate model

Items	Chen	Cho	Masaoka	Rigo (1)	Rigo (2)	Dow	Yao	Present method
P	0.0649	0.0595	0.0638	-	0.0676	0.0627	0.0608	0.0627
Z_g	1.376	1.44	1.398	1.433	1.42	1.407	1.424	1.422
M_P	13.77	12.81	13.72	14.32	14.39	17.01	13.24	12.93
M_{YS}	11.17	10.72	11.08	-	12.00	11.03	10.83	11.05
M_{YH}	11.55	10.12	11.25	-	11.66	10.92	10.46	10.41
M_{BS}	3.32	3.19	3.30	-	3.57	3.28	3.22	3.26
M_{BH}	10.48	9.18	10.20	-	10.58	9.90	9.48	9.77
M_{US-1}	-	10.10	11.72	9.84	-	-	9.88	9.89
M_{UH-1}	-	11.61	13.21	13.45	-	-	11.24	12.35
M_{US-2}	9.54	9.48	11.50	9.47	9.88	9.67	8.58	9.60
M_{UH-2}	12.49	11.32	12.49	13.26	12.12	11.39	10.90	12.01

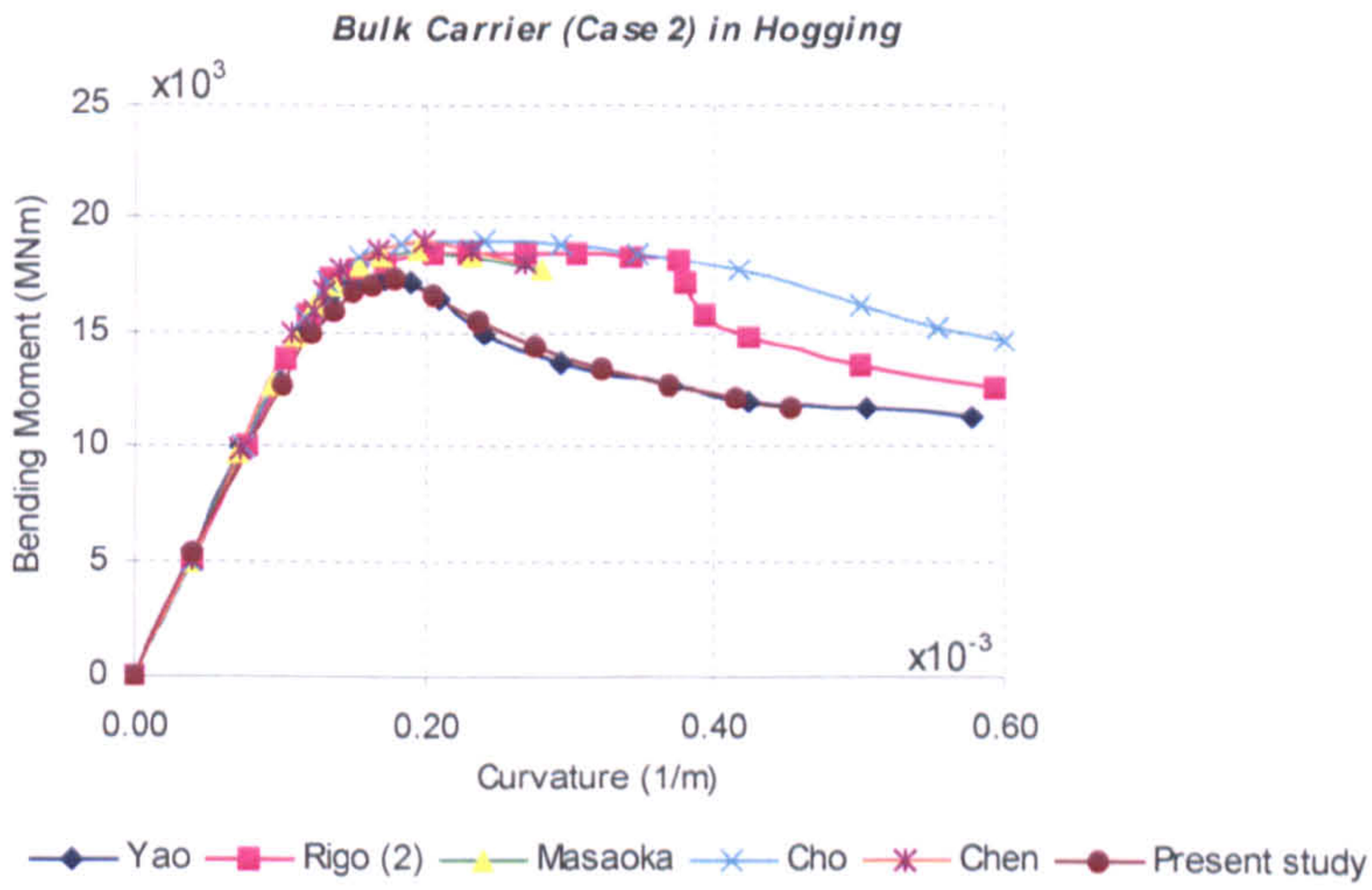

Figure 4.8: Moment curvature relationship for Bulk Carrier

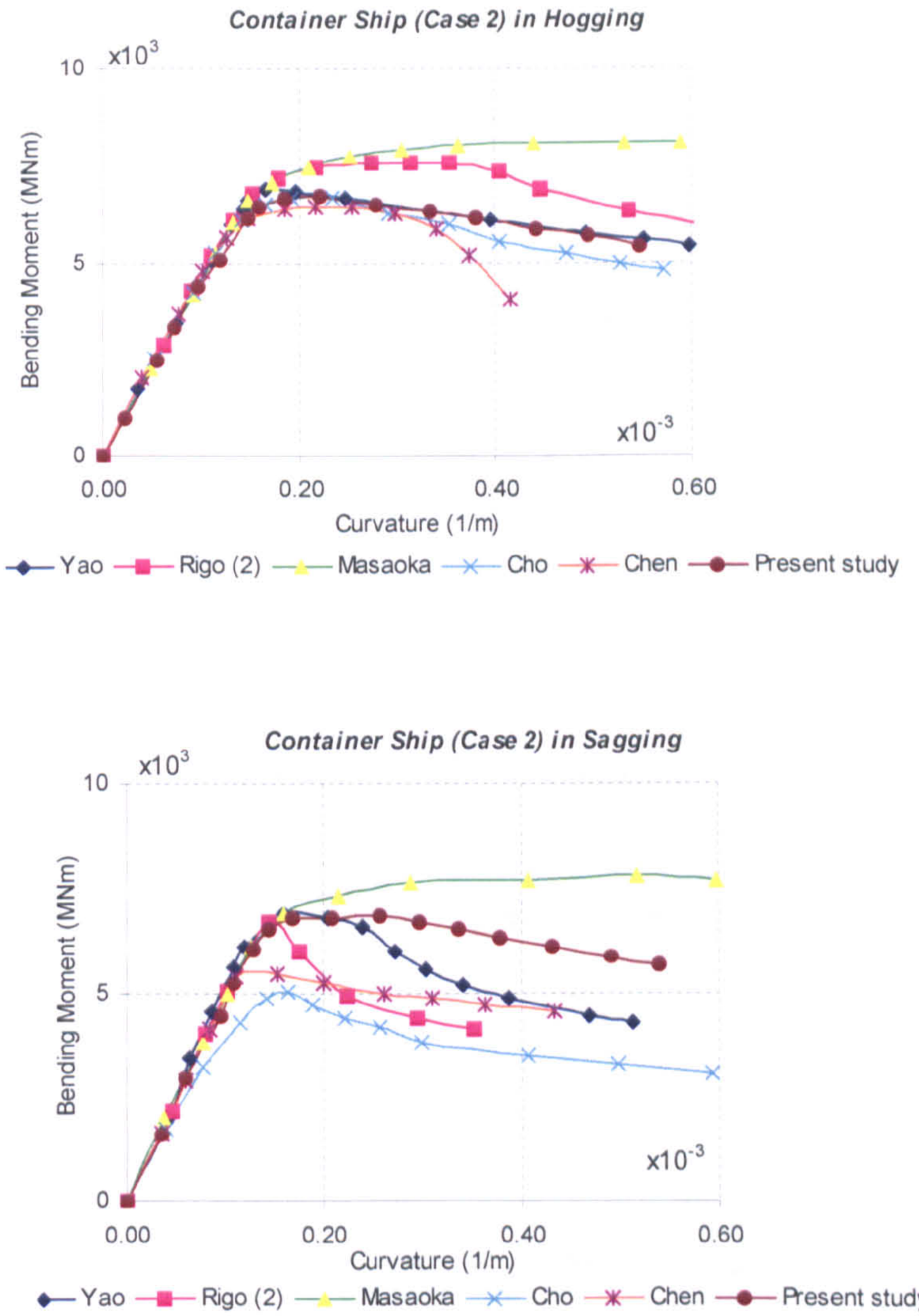

Figure 4.9: Moment-curvature relationships for Container Ship

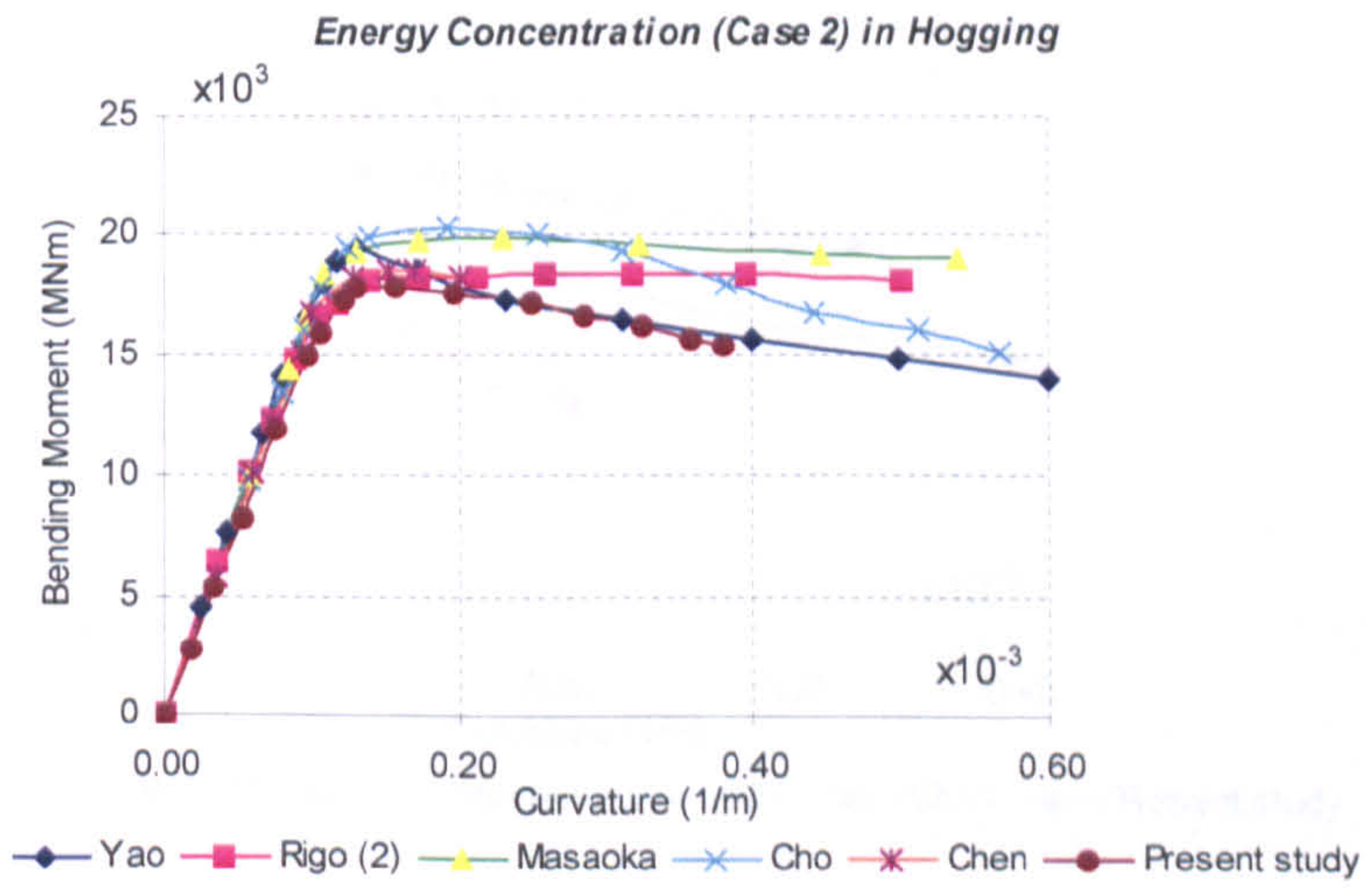

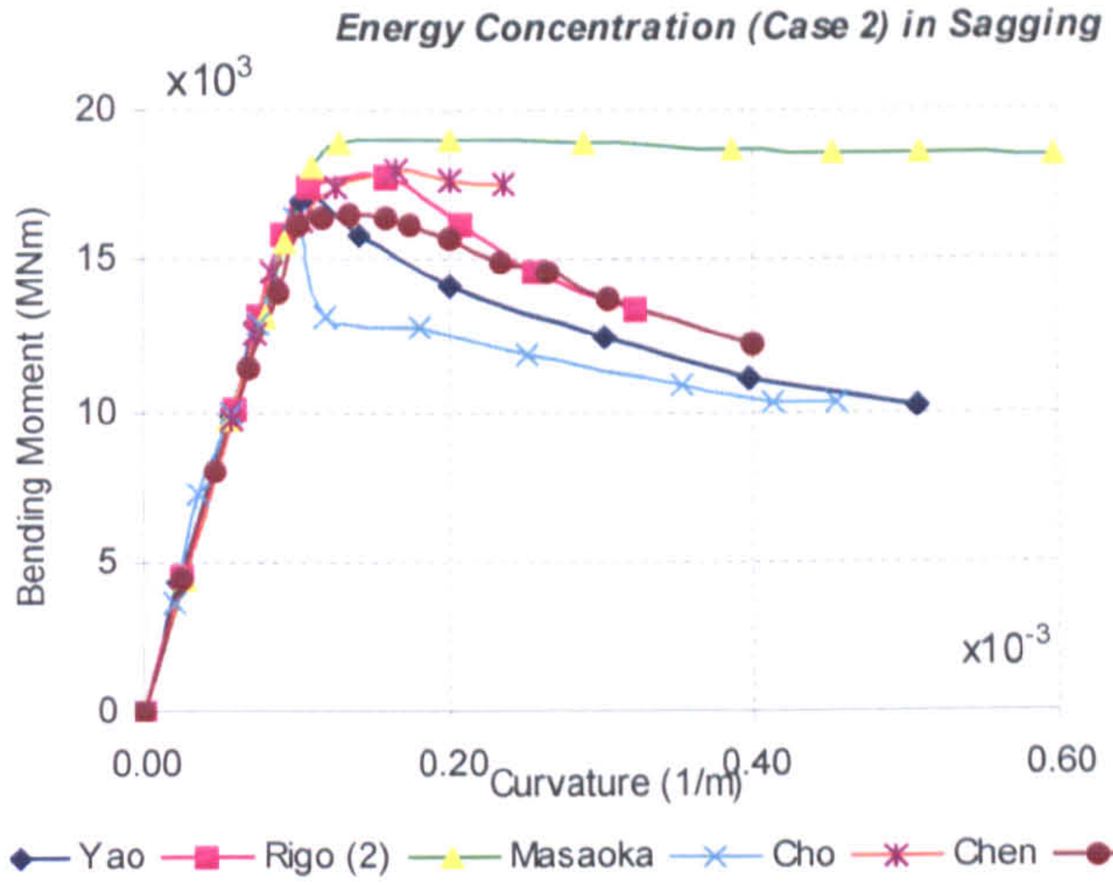

Figure 4.10: Moment – curvature relationships for Single Hull VLCC, *Energy Concentration*

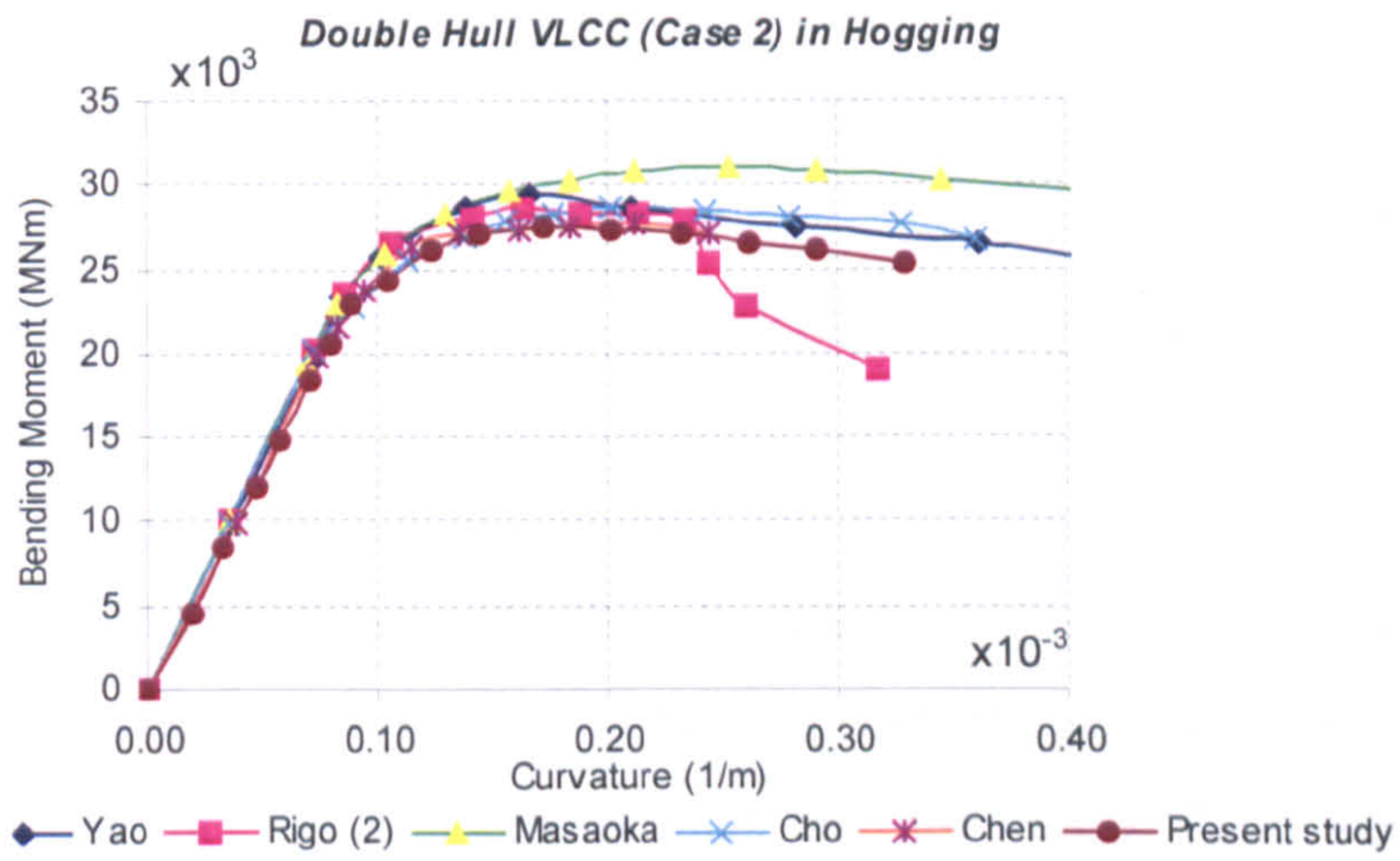

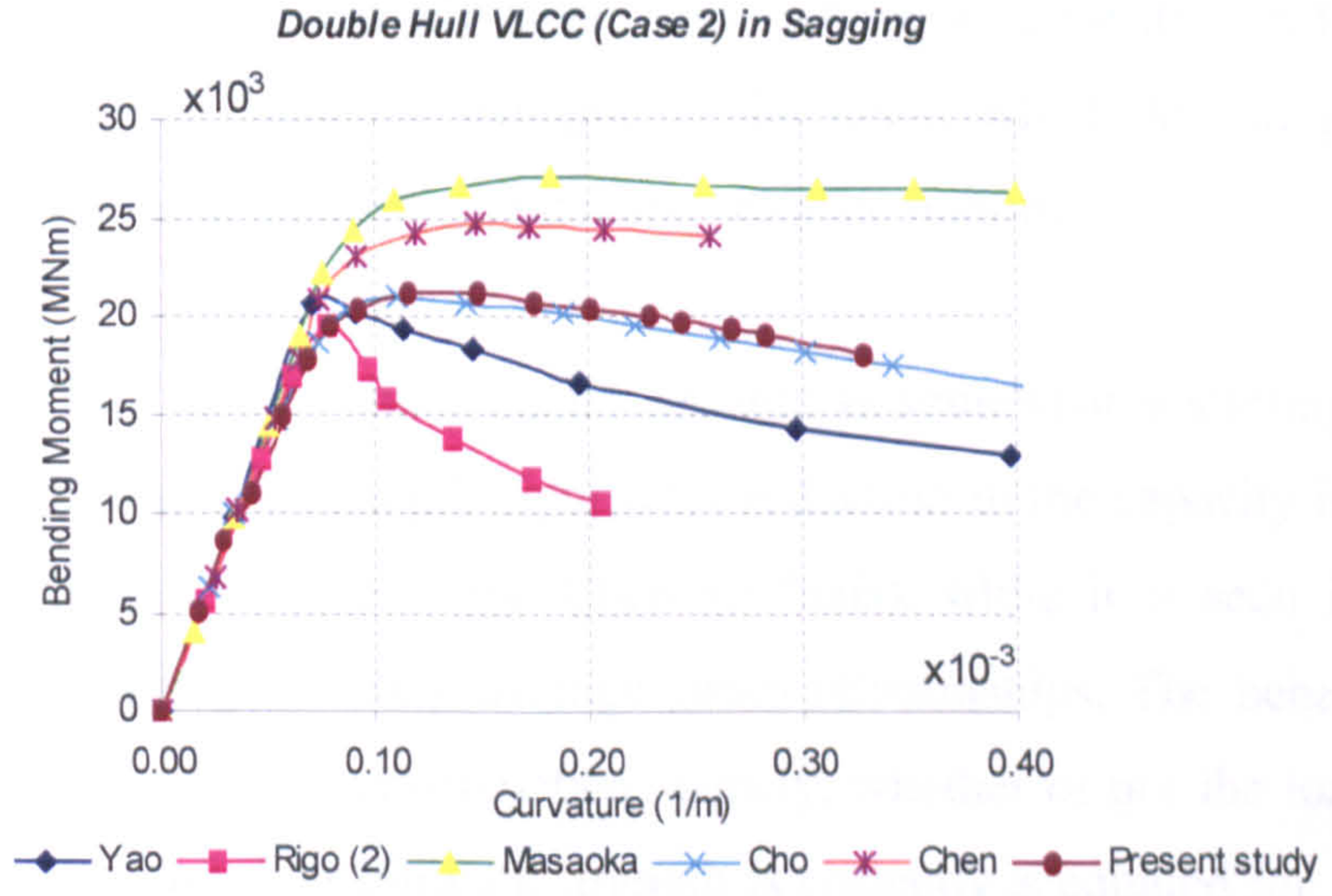

Figure 4.11: Moment – curvature relationships for Double Hull VLCC

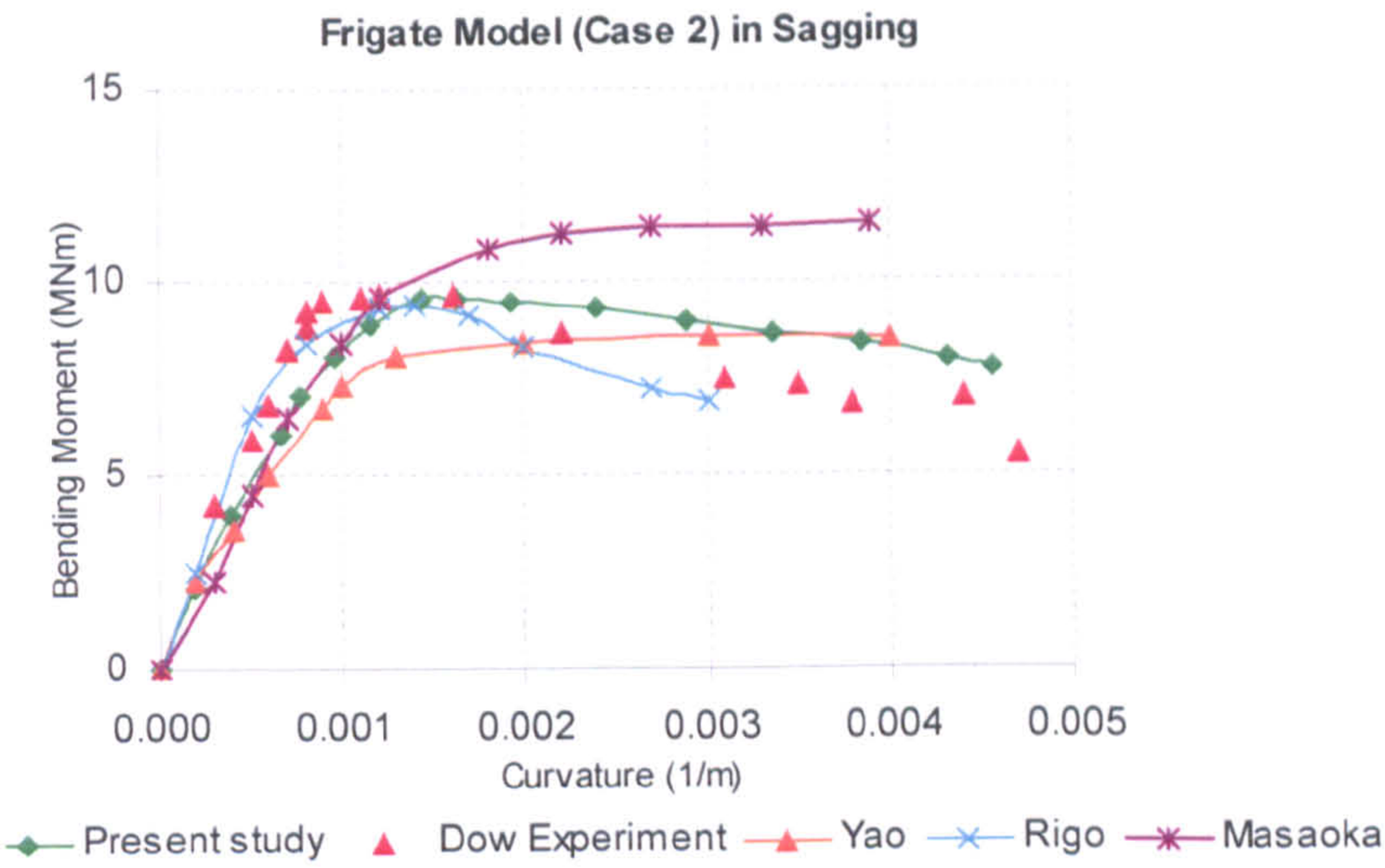

Figure 4.12: Moment-curvature relationships for 1/3-scale Frigate model

The simplified procedure used in this work to predict the behaviour of the hull girder under vertical bending seems to be quite accurate when the results are compared with those obtained by seven different approaches and also in the case of a real ship failure.

It is seen that the scatter in the ultimate hull girder strength is not so large especially when the hull is subject to hogging bending moment. This may be partly because the bottom plate is relatively thick, and the hull buckling strength is nearly equal to the yield strength. On the other hand, the scatter of the ultimate hull girder strength in sagging is relatively large. This may be because different methods give somewhat different buckling strength of the deck, which has in general lighter scantling and is more sensitive to buckling than the bottom.

The capacity beyond the ultimate strength is somewhat scattering compared to the ultimate hull girder strength significant reduction in the capacity is not observed with ISUM results (Masaoka and Chen methods), while it is seen in the Smith's method using average stress – average strain relationships. The behaviour strongly depends on the element characteristics, namely, whether or not the load shedding in the elements beyond their ultimate strength is correctly accounted for. Therefore, the presented ISUM elements seem to have been failed to simulate load-shedding

behaviour of element. However, recently more sophisticated elements are proposed and still under development. To simulate the load shedding (capacity reduction) beyond the ultimate hull girder strength, it is necessary to account the influences of the localisation of yielding and deformation after the ultimate strength has been reached.

The next point, which should be noticed, is the relationships between initial yielding strength and calculated hull girder ultimate strength. Even though, there are some exceptional cases, it can be said that, under sagging case, the initial yielding strength shows relatively good correlation with the hull girder ultimate and in general gives a little lower estimation value. On the other hand, under the hogging case, the initial yielding strength is sometimes higher than the fully plastic bending moment. This is the case when neutral axis of the cross section is located at lower part of the cross-section and stress based on elastic moment of inertia near the deck is higher than yield stress. For this fictitious stress distribution is, M_{YH} is higher than M_P. In this case, the initial buckling strength, M_{BH}, gives a better estimate of the hull girder ultimate strength than M_{YH} in general on the conservative side.

Hull girder ultimate strength is very important when safety of a ship structure is considered. Calculated results are summarised in Table 4.12 together with design bending moments in accordance with Bureau Veritas Rules. It is seen that the safety factor under the hogging case is higher than that under the sagging case. This is because, under the hogging case, hull girder strength is higher owing to the double bottom structure even if design moment equals when they are compared with those under the sagging case.

4.8 Effects of In-service Damage on Hull Girder Ultimate Strength

Ships are subjected to the action of a corrosive environment during their lives. The external structures at the water line and upper deck, as well as internal tank structures, are the areas most exposed to corrosion. Therefore, a steady reduction of

thickness takes place. The effect of corrosion damage can be assessed by sensitivity study on the influence of plate and stiffener thickness on ultimate hull girder capacity. Jensen *et al.* (1994) performed a sensitivity study on the ultimate hull girder capacity of four typical merchant ships. Yao *et al.* (1994) reported on a case study of a double hull tanker where the effect of corrosion damage on the hull girder capacity has been assessed. The effect of corrosion damage is also assessed by a sensitivity study on the influence of plate and stiffener thickness on the hull girder ultimate capacity. The present approach considers the Bureau Veritas corrosion allowance, between 0.5 and 2 mm depending on the position of plate element, the nature of tank and surrounding tanks. Table 4.13 shows corrosion additions in mm for each exposed side. Each level of corrosion is reduced the thickness of plating and stiffener by values indicated in Table 4.13.

The study clearly shows that a thickness reduction in the bottom plating largely affects the hogging strength, while a thickness reduction in the deck plating largely reduces the sagging strength. Figure 4.13 through 4.16 shows the linear correlation of corrosion level and ultimate moment variation.

It is seen that 20 % reduction on the effective area in double hull VLCC promotes a reduction of 24.3 % and 20.1 % in the sagging and the hogging cases, respectively. The inclusion of tripping formulation in the behaviour of stiffened panels is noticed to be very important in the particular case investigated here. Since the deck stiffeners do not have much torsional rigidity and calculated tripping stress is lower than beam-column stress of the stiffener with associated plate. This fact leads to a high reduction of the ultimate bending moment in sagging compared with the moment in hogging, where the deck is in tension.

It is noted that 20 % reduction on the effective area in single hull VLCC promotes a reduction 17.7 % and 15.8 % in the sagging and the hogging cases, respectively.

It is seen that 20 % reduction on the effective area in container ship promotes a reduction of 18 % and 25.2 % in the sagging and hogging case, respectively.

It is noted that 20 % reduction on the effective area in bulk carrier promotes a reduction of 21.9 % and 25.3 % in the sagging and hogging cases, respectively.

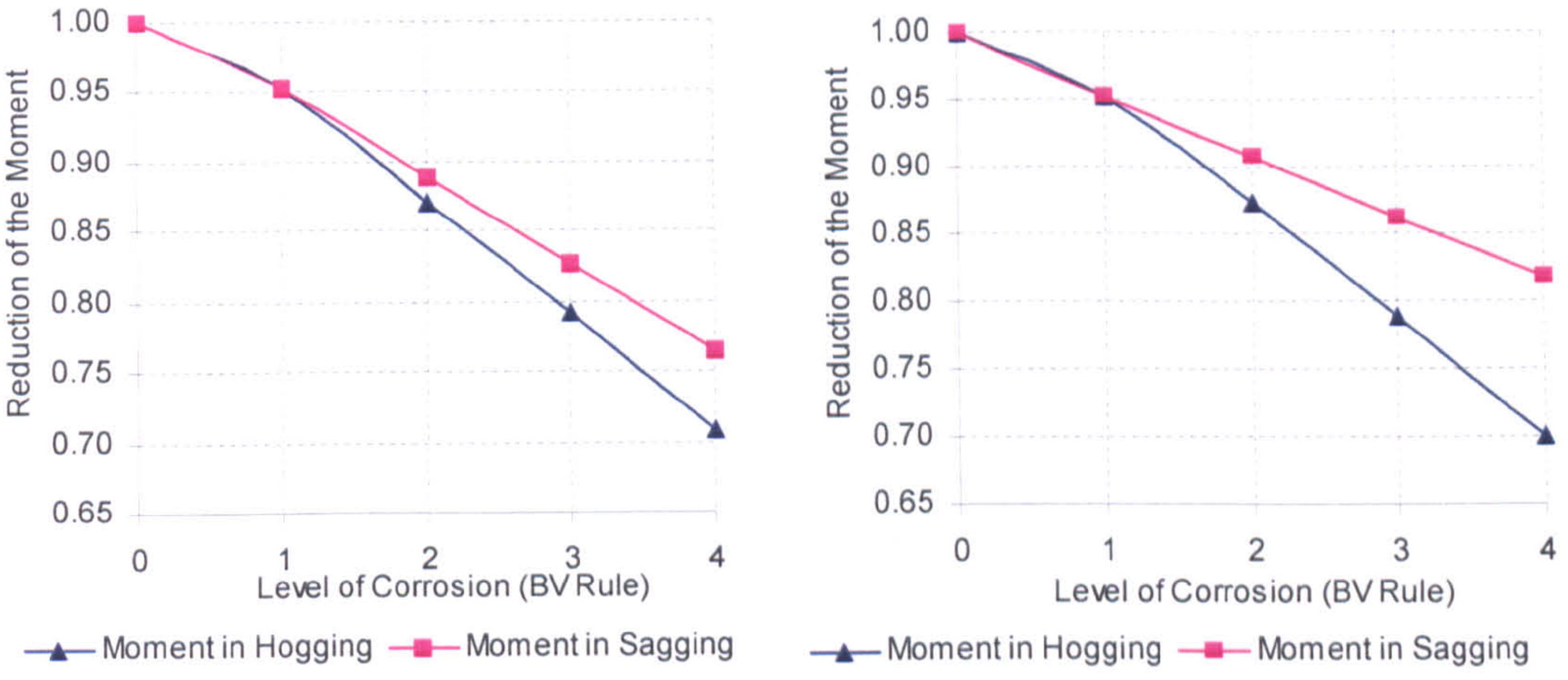

Figure 4.13: Effect of corrosion level on ultimate bending moment for Bulk Carrier and Container, respectively

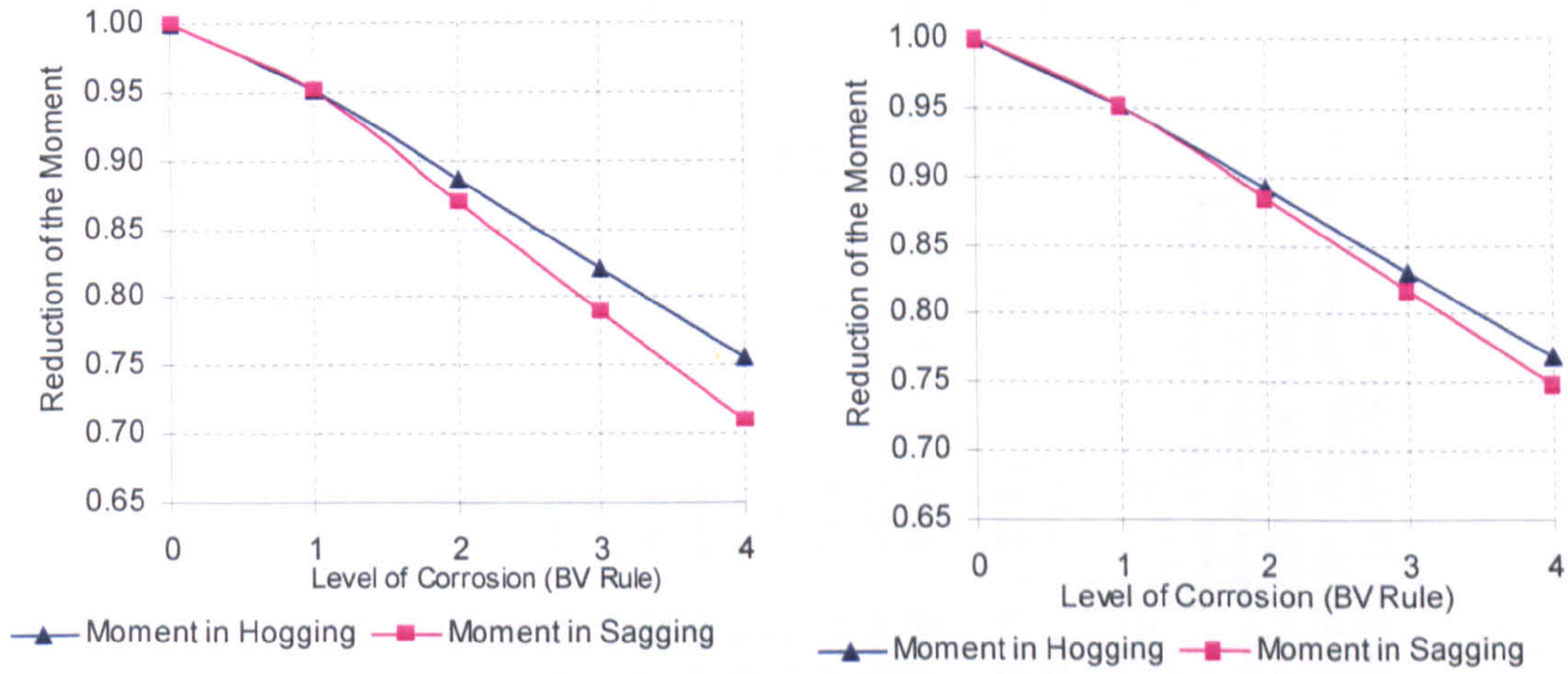

Figure 4.14: Effect of corrosion level on ultimate bending moment for Double Hull VLCC and Single Hull VLCC, respectively

Table 4.13: Safety factor assessment against hull girder ultimate strength for case (2)

		Double Hull VLCC			Single Hull VLCC *(Energy Concentration)*			Container Ship			Bulk Carrier			Remarks
		Hog.	Sag.	Hog. / Sag.	Hog.	Sag.	Hog. / Sag.	Hog.	Sag.	Hog. / Sag.	Hog.	Sag.	Hog. / Sag.	
M_{Design} (BV)	M_{swbm}	6.78	6.23	1.09	5.54	5.21	1.06	1.94	1.55	1.25	4.75	4.43	1.07	
	M_{wvbm}	9.99	10.54	0.95	8.48	8.82	0.96	2.23	2.62	0.85	7.17	7.49	0.96	
	M_{Total}	16.77	16.77	1.00	14.02	14.02	1.00	4.17	4.17	1.00	11.92	11.92	1.00	
$M_{Ultimate}$	A	27.40	24.33	1.13	20.23	18.54	1.09	6.56	5.47	1.20	19.06	15.20	1.25	Chen
	B	28.66	20.80	1.38	20.09	16.75	1.20	6.69	5.13	1.30	18.99	13.69	1.39	Cho
	C	30.59	26.59	1.15	20.01	19.00	1.05	8.07	7.95	1.02	18.56	16.02	1.16	Masaoka
	D	28.32	19.57	1.45	18.46	17.90	1.03	7.60	6.51	1.17	18.71	14.34	1.30	Rigo (1)
	E	25.61	24.07	1.06	17.54	17.10	1.03	7.20	6.91	1.04	17.06	14.34	1.15	Rigo (2)
	F	28.88	20.42	1.41	19.03	16.84	1.13	6.72	6.72	1.00	17.36	14.45	1.20	Yao
	G	**27.45**	**21.15**	**1.30**	**17.89**	**16.45**	**1.09**	**6.79**	**6.70**	**1.01**	**17.34**	**14.19**	**1.22**	**Present method**
	Mean	28.13	22.42	1.27	19.04	17.51	1.09	7.09	6.48	1.11	18.15	14.60	1.24	
	(%) COV	5.4	11.2	12.1	5.1	4.9	5.6	7.7	14.5	9.9	4.3	5.0	6.7	
Safety Factor		1.68	1.34		1.36	1.25		1.70	1.55		1.52	1.23		

NOTE:
1- $M_{Total} = M_{swbm} + M_{wvbm}$ (According to BV Rules)
2- $M_{Ultimate}$: refer to Table 4.8 to Table 4.11
3- COV = Coefficient of Variation
4- Safety Factor = $M_{Ultimate}$ (Mean) / M_{Total}
5- MOMENT (x 1000 MN-m)

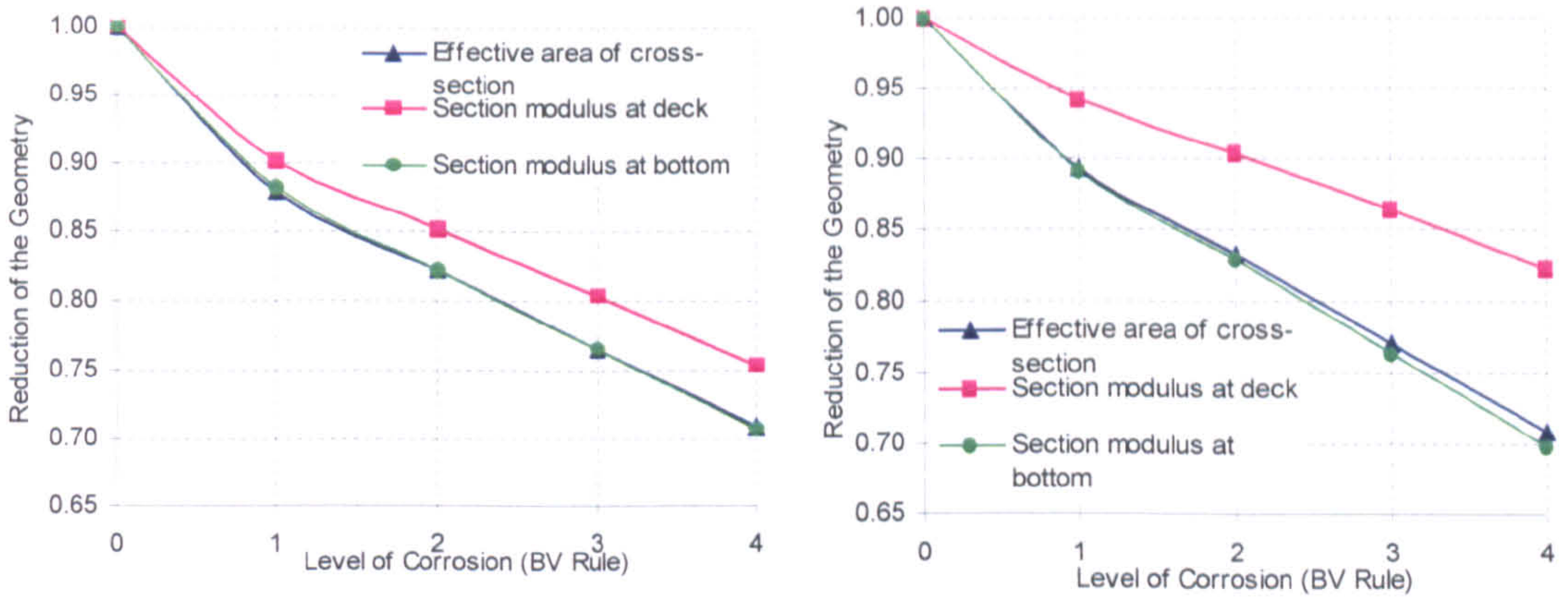

Figure 4.15: Effect of corrosion level on effective area and section modulus for Bulk Carrier and Container, respectively

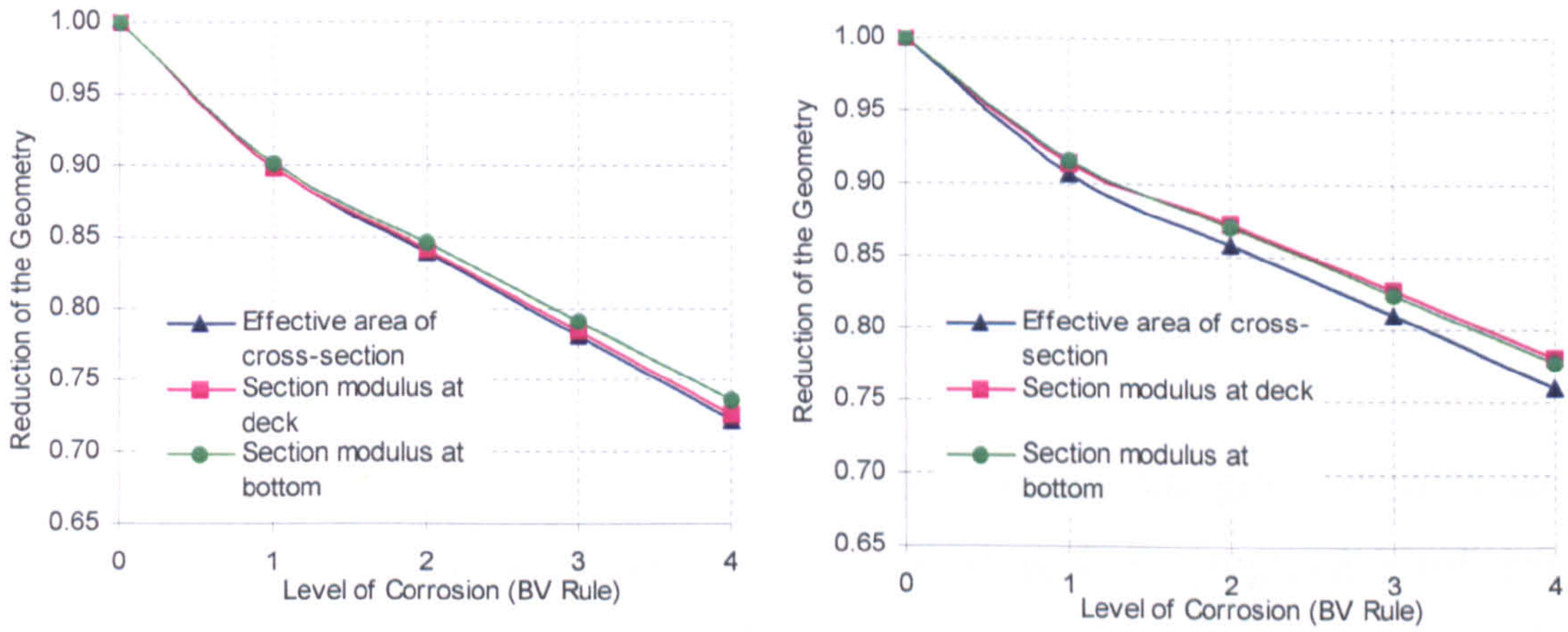

Figure 4.16: Effect of corrosion level on effective area and section modulus for Double Hull VLCC and Single Hull VLCC, respectively

Table 4.14: Corrosion additions t_c , in mm. (Bureau Veritas Rules)

Compartment Type		General
Ballast Tank		1.00
Cargo oil tank and fuel oil tank	-Ordinary stiffeners and primary supporting members	0.75
	-Plating of horizontal surfaces	0.75
	-Plating of non-horizontal surfaces	0.50
Dry bulk cargo hold	General	1.00
	-Inner bottom plating -Side plating for single hull ship -Inner side plating for double hull ship -Sloping stool plate of hopper tanks and lower stool -Transverse bulkhead plating	1.75
	Ordinary stiffeners and primary supports	1.00

4.9 Discussion & Conclusion

Through the research and investigation activities of Chapter 4, it has been found that:

- ✓ The available methods for evaluation of the ultimate hull girder strength can be classified into two groups. One way is to perform progressive collapse analysis and the other is to calculate the ultimate hull girder strength directly applying empirical/theoretical formulae.
- ✓ The potentially most accurate method for progressive collapse analysis may be the elastoplastic large deflection analysis applying the FEM. Such an analysis is fundamentally possible but is presently not practical to perform due to large requirement to computer resource and modelling work.
- ✓ An alternative method of progressive analysis is the Smith's method, which is a simplified method but is capable of simulating the progressive collapse behaviour of a ship hull girder subjected to longitudinal bending with relatively high accuracy. The ISUM can also be used for progressive collapse

analysis. However, more accurate and sophisticated stiffened plate element has to be developed to achieve reliable results.

- ✓ The accuracy of adopted procedure is examined by seven different methods as well as experiment results on the examples used in the benchmark calculations. It was shown that the adopted method predicts the hull girder ultimate strength very accurately.
- ✓ In simplified methods of progressive collapse analysis, the accuracy of the calculated results largely depends on how accurately the collapse behaviour of individual structural members can be determined. From this point of view, benchmark calculations were examined on ninety (90) stiffened plates with and without welding residual stresses applying existing simplified methods as well as the FEM.
- ✓ Some scatters were observed among calculated results applying different methods. On the other hand, it was shown that a simplified method predicts the ultimate strength very accurately if the assumed collapse mode is the same as the actual one. The most crucial point for a simplified method is that it is able to simulate the occurrence of overall buckling as a stiffened plate including tripping of longitudinal stiffeners.
- ✓ Benchmark calculations were conducted also on four existing ship hull girders and one test girder to evaluate the ultimate hull girder strength under pure bending. It was shown that the buckling/plastic collapse of the deck and the bottom dominates the overall collapse of the cross-section under the sagging and the hogging condition, respectively.
- ✓ The thickness reduction due to corrosion reduces the ultimate hull girder strength. It was reported that strength reduction is almost linear to the corrosion level introduced by Bureau Veritas Rules.
- ✓ The present design criteria related to longitudinal strength were investigated in relation to the ultimate hull girder strength. It was found that the safety factor for the sagging condition is in general lower than that for the hogging condition. It was concluded that design characteristics dependent on ship types should be taken into account for the design of individual ship types.

Chapter 5

Investigation of Coupled Bending Moment on Hull Girder Ultimate Strength

5.1 Introduction

A ship is in general subjected to both vertical and horizontal bending moments, particularly in a rough sea with significant roll motions. The ultimate hull girder strength under horizontal bending is generally higher than vertical bending. This is because the ship's breadth is usually larger than its depth. Yao (1994) studied on the ultimate hull girder strength interaction relationship under combined vertical and horizontal bending for double hull tanker. Mansour *et al.* (1995) presented an empirical interaction equations based on the results of calculations of one tanker, one container ship and one cruiser. Paik *et al.* (1996) discussed the ultimate hull girder strength under combined vertical and horizontal bending moment using ALPS/ISUM

program for eleven vessels: five tankers, two bulk carriers, two container vessels and two cruisers. It was found that the ultimate strength interaction relationship for combined loading was unaffected by the level of initial imperfections, even though the ultimate strengths itself would be reduced as the initial imperfections increase. The simple expression was proposed, regardless of initial imperfection level. Another interaction equation was proposed by Gordo & Soares (1997) based on the results for five tankers and six container ships. Rizzuto (1997) also discussed on this subject. Hu *et al.* (2001) analysed the ultimate longitudinal strength of a typical bulk carrier by using a simplified method under combined vertical and horizontal bending moments. An interaction equation suitable for bulk carrier was proposed based on the results of the investigated ship. Recently Ozguc *et al.* (2005a) have calculated the ultimate coupled vertical and horizontal bending moment capacity on single side skin and double side skin bulk carriers which corresponding to intact and investigated various collision damage scenarios, in which a progressive collapse analysis based on Smith's method was carried out. It has been noted that the combined effect of the vertical and horizontal bending moments is important, especially when the ship is damaged.

This chapter presents the most extensive investigation of the hull girder ultimate strength under coupled bending moment. The main objective of the present study is to develop hull girder ultimate strength interaction relationships useful for the ship designs subject to a combination of vertical and horizontal bending moments, where the ordinary Smith's method is employed using a developed computer code NEPTUNE with average stress – average strain relationship of element. The procedure adopted is applied to analyse on the seventeen ships such as nine tankers, five bulk carriers, one general cargo and two container vessels. The findings obtained are used to develop a rapid procedure for the assessment of the ultimate capacity of the hull girder. The interaction expressions proposed by other researchers are also addressed to discuss simple equations presented by this study.

5.2 Collapse Analysis under Combined Bending

Ships have some particular behavioural problems subject to coupled vertical and horizontal bending moment due to interactions of their particular geometry. The maximum stresses are normally taken place at the conjunction between the deck and side under coupled moment. This is mainly because, the ultimate strength of stiffened plate the slenderness ratios are different from each others; thus different maximum axial carrying capacity is expected to occur. The ultimate carrying capacity of side structure is usually lower than that of the deck. As a result, the impact on the vertical and horizontal moment of these stress – strain distributions near collapse is different since the side strength is more important for the horizontal bending while the deck strength is more important for the sagging moment.

The angle of the resultant bending moment vector and the angle of the curvature vector is changing during the load process. If the direction of one of them is kept constant, the minimum carrying capacity of the section to sustain the bending moment is obtained at angles near but not equal to the horizontal bending.

5.2.1 Features of the method

A progressive collapse analysis based on Smith method (1977) is carried out in this study. In this approach, the ultimate hull girder bending moment capacity is defined as the peak value of the curve with vertical bending moment versus the curvature of the ship cross section. The curve is obtained by means of an incremental – iterative approach. Each step of the incremental procedure is represented by the calculation of the bending moment, which acts on the hull transverse section as the effect of an imposed curvature. For each step, the curvature value is obtained by summing an increment of curvature to the value relevant to the previous step. This increment of the curvature corresponds to an increment of the rotation angle of the hull girder transverse section around its horizontal axis. This rotation induces axial strains in each hull structural element, whose value depends on the position of the element. In hogging condition, the structural elements above the neutral axis are lengthened,

while the elements below the neutral axis are shortened. Vice-versa in sagging condition.

The stress induced in each structural element by the strain is obtained from the load-end shortening curve of the element, which takes into account the behavior of the element in the non-linear elastic-plastic domain. The distribution of the stresses induced in all the elements composing the hull transverse section determines, for each step, a variation of the neutral axis position, since the relationship is non-linear. The new position of the neutral axis relevant to the step considered is obtained by means of an iterative process, imposing the equilibrium among the stresses acting in all the hull elements. Once the position of the neutral axis position of the neutral axis is known and the relevant stress distribution in the section structural elements is obtained, the bending moment of the section around the new position of the neutral axis, which corresponds to the curvature imposed in the step considered, is obtained by summing the contribution given by each element stress. In applying the procedure described in above, the following assumption are generally made,

- The ultimate strength is calculated at the hull transverse sections between two adjacent transverse webs
- The hull girder transverse section remains plane during each curvature increment
- The hull material has an elastic-plastic behaviour
- The hull girder transverse section is divided into a set of elements, which are considered to act independently
- Overall grillage collapse is avoided by sufficiently strong transverse frames

5.2.2 The followed steps

The vertical bending moment is indeed the most important load effect when considering the hull girder collapse. However, in many types of ships, the combined effect of the vertical and the horizontal bending moments is important. It is well known the basic equations that relates the applied vertical and horizontal bending moments to the longitudinal stress are very simple and may be summarized:

$$\sigma_i = \frac{M_x.y_i}{I_x} - \frac{M_y.x_i}{I_y} \tag{5.1}$$

or it may be expressed as a function of the total moment by:

$$\frac{\sigma_i}{M} = \frac{y_i.\cos\varphi}{I_x} - \frac{x_i.\sin\varphi}{I_y} \tag{5.2}$$

Where φ is the angle that the bending moment vector makes with the baseline, and x_i and y_i are the coordinates of the element i in the referential located in any point of the neutral axis. For given points of the cross section, this relation is constant until the yield stress of the material is reached in any point of the section. Once the cases mentioned above occur, the neutral axis moves away from its original position and thus the constancy of the relation may be broken. Similarly, the relation between the angle of the resultant bending moment vector φ and the angle of the curvature vector θ is constant in the linear elastic range. This relation may be express by:

$$tg\varphi = \frac{I_y}{I_x} tg\theta \tag{5.3}$$

When the curvature is increased the angle changes slightly towards the neutral axis, but this shift becomes very quick for curvatures near the buckling of the bottom and side plating, which corresponds to the maximum horizontal component of the bending moment. The moment vector moves its direction towards the neutral axis until the maximum of the vertical component, and even further that that, because of the unloading in the horizontal moment. This behaviour is shown in Figure 5.1.

The most general case corresponds to that in which the ship is subjected to curvature in the x and y directions respectively denoted as C_x, C_y. The overall curvature C is related to these two components by:

$$C = \sqrt{C_x^2 + C_y^2} \tag{5.4}$$

or

$$C_x = C.\cos\theta \quad \text{and} \quad C_y = C.\sin\theta \tag{5.5}$$

Adopting the right-hand rule, where θ is the angle between the neutral axis and the x-axis and is related to the components of the curvature by:

$$tg\theta = \frac{C_y}{C_x} \tag{5.6}$$

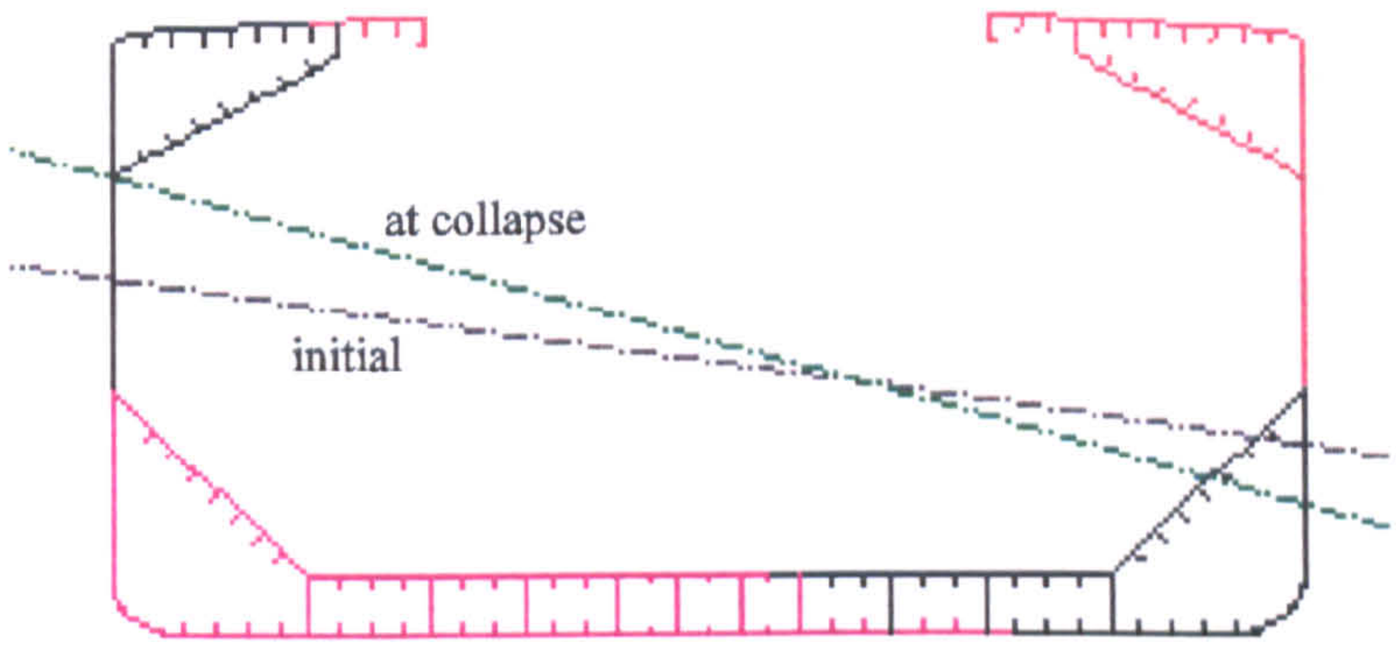

Figure 5.1: Initial and at collapse position of the neutral axis under combined bending moment

The strain at the centroid of an element i is ε_i which depends on its position and on the hull curvature, as given by:

$$\varepsilon_i = y_{gi}.C_x - x_{gi}.C_y \tag{5.7}$$

Where (x_{gi} , y_{gi}) are the coordinates of the centroid of the element i referred to the central point at each curvature. Once the state of strain in each element is determined, the corresponding average stress may be calculated according to the method described above, and consequently the components of the bending moment for a curvature C are given by:

$$M_x = \sum y_{gi} . \sigma_i A_i \tag{5.8}$$

$$M_y = \sum x_{gi} . \sigma_i . A_i \tag{5.9}$$

Where σ_i represents the stress of element i at (x_{gi} , y_{gi}). A_i represents the cross sectional area of element i. This is the bending moment on the cross section after calculating properly the instantaneous position of the intersection of the neutral axis associated with each curvature and the centreline (called the centre of force). The condition to determine the correct position of neutral axis is:

$$\sum \sigma_i A_i = 0 \tag{5.10}$$

A trial and error process has to be used to estimate its position correctly. The total net load in the section, NL, or the error in the shift estimate ΔG should be less than or equal to a sufficiently low value (Gordo & Soares 1996). In this paper, the following equation is used.

$$NL = \sum \sigma_i A_i \leq 10^{-6} \sigma_{0i} \sum A_i \tag{5.11}$$

Where σ_{0i} is the material yield stress of element *i*.

5.3 Structural Modelling of Vessels

Hull girder ultimate strength analysis of seventeen ship hulls is conducted through NEPTUNE computer program. Table 5.1 through Table 5.4 illustrate the principal dimensions and section properties of the investigated ship designs. A total of 17 ships are analysed such as nine tankers (one single side and eight double side), five bulk carriers (four single side and one double side), one general cargo and two container vessels. The single hull tanker included is the *Energy Concentration*, which collapsed during off-loading of cargo in July 1980.

5.3.1 Bulk carriers

The hull girder ultimate strength of five bulk carrier vessels is analysed under combined vertical and horizontal bending moments. The midship cross-section of five bulk carriers is shown in Figure 5.2. Interaction curves are obtained from a series of calculation for the hull bending with different angles of the curvature vector from hogging of vertical bending (the angle of the curvature vector θ = 0 degree) through horizontal bending (θ = 90 degree) to sagging of the vertical bending (θ = 180 degree).

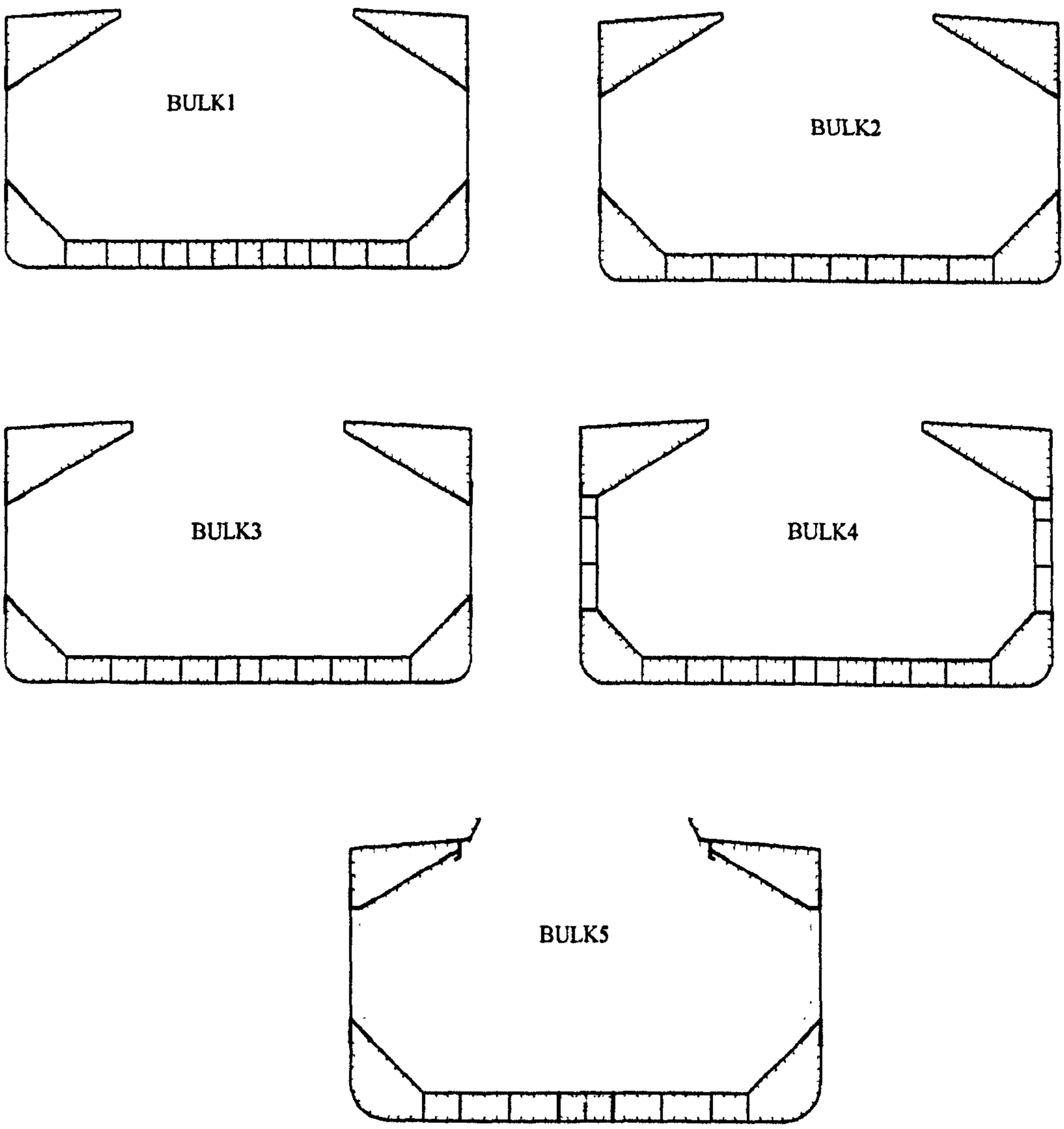

Figure 5.2: Midship cross-section of five bulk carriers

Table 5.1: Hull sectional properties of the Tankers

Items	DHT1	DHT2	DHT3	DHT4	SHT	DHT5	DHT6	DHT7	DHT8
LBP (m)	139.5	112.6	140.0	121.25	313.0	315.0	310.0	142.0	103.5
Breadth (m)	21.6	18.8	21.6	19.6	48.2	58.0	58.0	22.0	16.0
Depth (m)	11.3	10.5	11.5	10.4	25.2	30.3	31.0	11.5	7.25
Draft (m)	8.6	8.1	8.7	8.0	19	22.0	22.0	8.8	5.7
Block coefficient	0.795	0.824	0.795	0.769	0.833	0.823	0.821	0.797	0.771
Speed (knots)	15.0	13.5	14.5	14.0	15.0	15.5	15.5	15.0	12.0
DWT	15000	10000	16000	10500	254000	313000	310000	16000	6500
Cross-sectional area (m^2)	2.217	1.545	2.027	1.831	7.744	9.709	10.624	2.217	1.270
Neutral axis above base line (m)	5.786	4.645	5.170	4.548	12.306	12.937	13.560	5.786	3.561
I (m^4)									
Vertical	51.766	26.052	40.243	27.055	851.466	1354.920	1465.074	51.766	11.946
Horizontal	111.274	63.975	109.047	77.527	2039.219	3854.925	4160.668	111.274	38.719
Z (m^3)									
Deck	9.388	4.449	6.565	4.623	66.037	77.587	78.179	9.388	3.237
Bottom	8.946	5.609	7.783	5.948	69.189	104.733	108.043	8.946	3.355
σ_Y (MPa)									
Deck	HT32	MILD	HT32	MILD	HT32	HT32	HT32	MILD	MILD
Bottom	MILD	MILD	MILD	MILD	HT32	HT32	HT32	MILD	MILD
M_P (GNm)									
Vertical	2.844	1.504	2.230	1.655	23.253	31.577	34.610	2.392	0.703
Horizontal	3.778	2.085	3.711	2.571	34.782	54.135	58.673	3.778	1.242
M_U (GNm)									
Vertical Hog.	2.392	1.289	1.877	1.349	20.562	29.243	30.310	2.392	0.561
Vertical Sag.	1.869	0.949	1.406	0.995	19.113	24.151	25.245	1.869	0.446
Horizontal	2.911	1.669	2.825	1.926	29.184	45.712	47.476	2.889	0.886

NOTES: I = Moment of inertia, Z = Section modulus, σ_Y = Yield stress of material, M_P = Fully plastic bending moment, M_U = Ultimate bending moment
DHT = Double hull tanker, SHT = Single hull tanker

Table 5.2: Hull sectional properties of the Bulk Carriers, Container ships and General Cargo.

Items	Bulk1	Bulk2	Bulk3	Bulk4	Bulk5	Cont1	Cont2	GenCargo
LBP (m)	285.0	250.0	278.0	278.0	226.2	230.0	240.1	133.5
Breadth (m)	50.0	43.0	45.0	45.0	32.24	32.2	32.2	21.7
Depth (m)	26.9	23.9	24.1	24.1	18.3	21.0	20.6	11.15
Draft (m)	17.0	17.4	17.7	16.5	12.74	12.5	12.4	8.3
Block coefficient	0.836	0.850	0.860	0.860	0.836	0.680	0.681	0.729
Speed (knots)	15.5	14.5	14.5	14.55	14.0	23	23	14
DWT or TEU	180000	160000	180000	170000	65000	3500 TEU	3500 TEU	13500
Cross-sectional area (m^2)	5.582	4.809	5.887	5.755	3.580	3.901	3.987	1.827
Neutral axis above base line (m)	11.024	10.04	10.631	10.465	8.461	8.693	8.935	4.545
I (m^4)								
Vertical	682.105	458.760	567.944	581.735	201.394	246.536	231.796	31.465
Horizontal	1796.763	1151.692	1575.861	1482.328	481.002	658.637	661.755	120.260
Z (m^3)								
Deck	42.965	33.100	42.167	42.661	20.468	20.033	23.031	4.801
Bottom	61.872	45.692	53.423	55.595	23.802	28.359	25.941	6.923
σ_Y (MPa)								
Deck	HT40	HT36	HT36	HT36	HT32	HT36	HT36	HT32
Bottom	HT32	HT32	HT32	HT32	HT32	HT32	HT32	MILD
M_P (GNm)								
Vertical	19.174	15.112	17.245	17.122	7.424	8.823	9.722	1.846
Horizontal	23.129	24.444	28.460	27.082	10.628	15.148	16.218	3.630
M_U (GNm)								
Vertical Hog.	17.192	14.116	15.612	16.075	6.136	7.360	8.323	1.642
Vertical Sag.	14.075	10.856	12.991	12.836	5.058	7.290	8.814	1.461
Horizontal	23.631	18.692	21.215	21.573	7.907	12.401	14.111	2.995

NOTES: I = Moment of inertia, Z = Section modulus, σ_Y = Yield stress of material, M_P = Fully plastic bending moment, M_U = Ultimate bending moment
Bulk = Bulk Carrier, Cont = Container Vessel, GenCargo = General Cargo

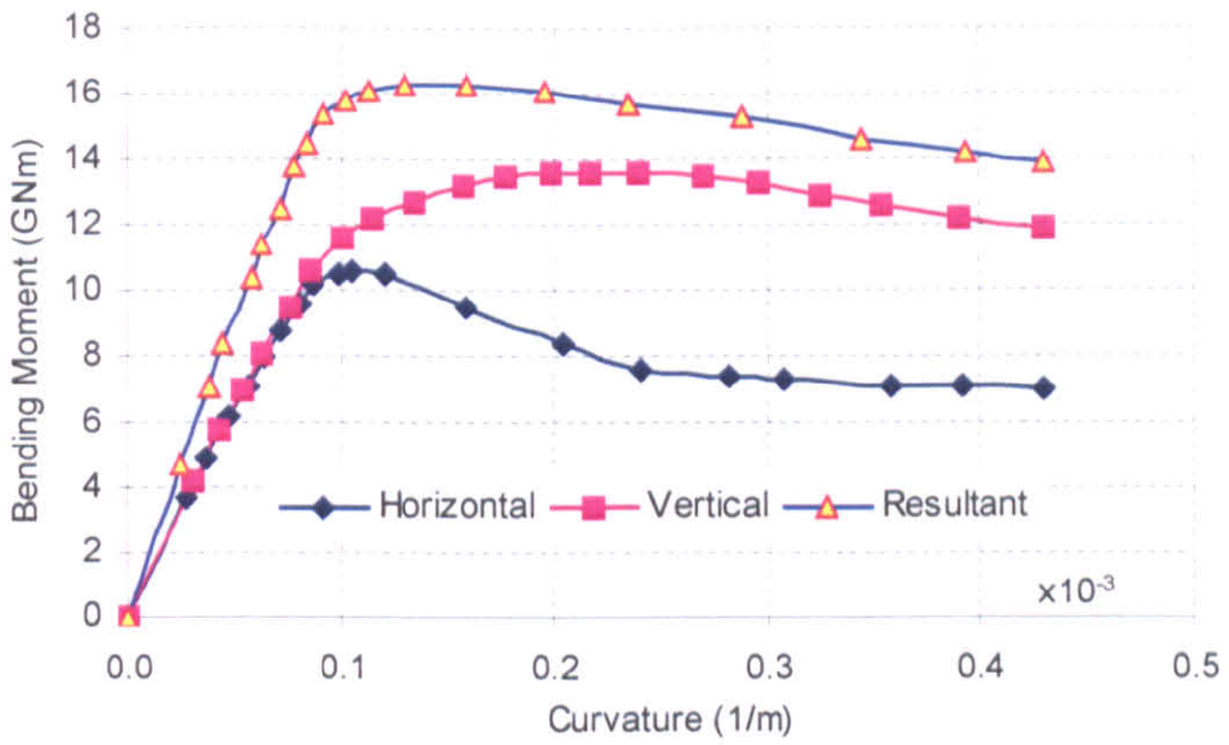

Figure 5.3: Components of bending moment at θ = 20 degree in hogging case for BULK1

In Figure 5.3, the results of Bulk1 are presented in the form of bending moment versus curvature diagram in terms of resultant, vertical and horizontal components. In the present case at an angle of curvature vector θ = 20 degree, a collapse of the section is evident in horizontal bending moment at a curvature of 0.106×10^{-3} 1/m, while vertical bending moment has its maximum value at a curvature of 0.201×10^{-3} 1/m. This is because, the side panels near the bilge collapse first and this collapse is more important for the horizontal than for the vertical modulus due to the greater reduction in effective inertia moment about the vertical than about the horizontal axis. The collapse under the simultaneous action of vertical and horizontal bending moments has been calculated for the different combinations as reflected in the angle between the neutral axis and the horizontal axis.

A series of diagrams is presented in Figure 5.4 to illustrate the behaviour and the ultimate capacity of the analysed bulk carrier vessels' in the case of combined bending moment with respect to analyse of curvature vector. It can be seen that the horizontal component is equal to zero in case of the vertical bending, as the cross section is symmetrical with respect to the vertical axis. Due to lack of symmetry with respect to the horizontal axis, a non-zero value of the vertical component appears.

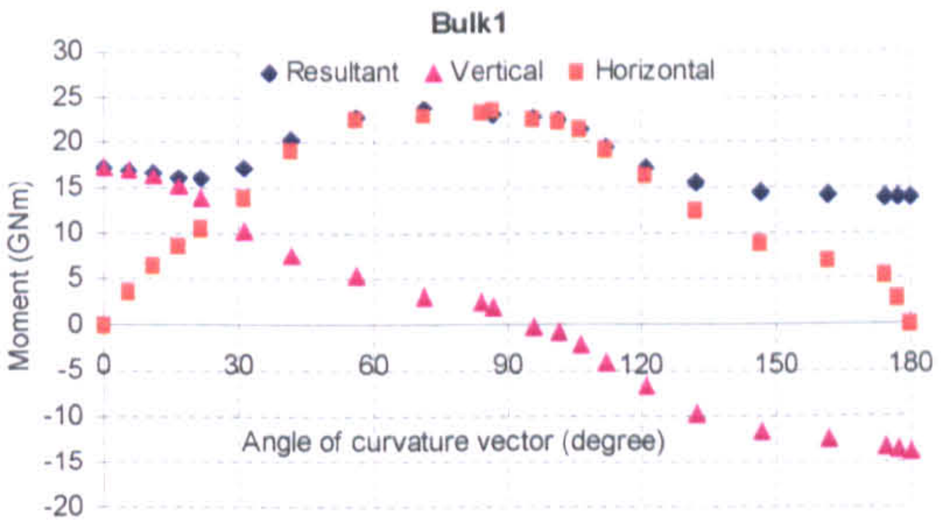

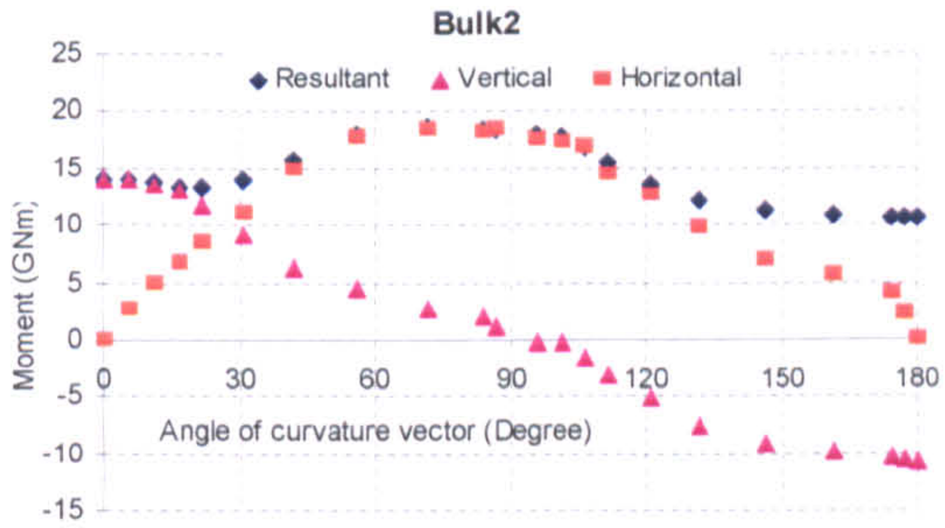

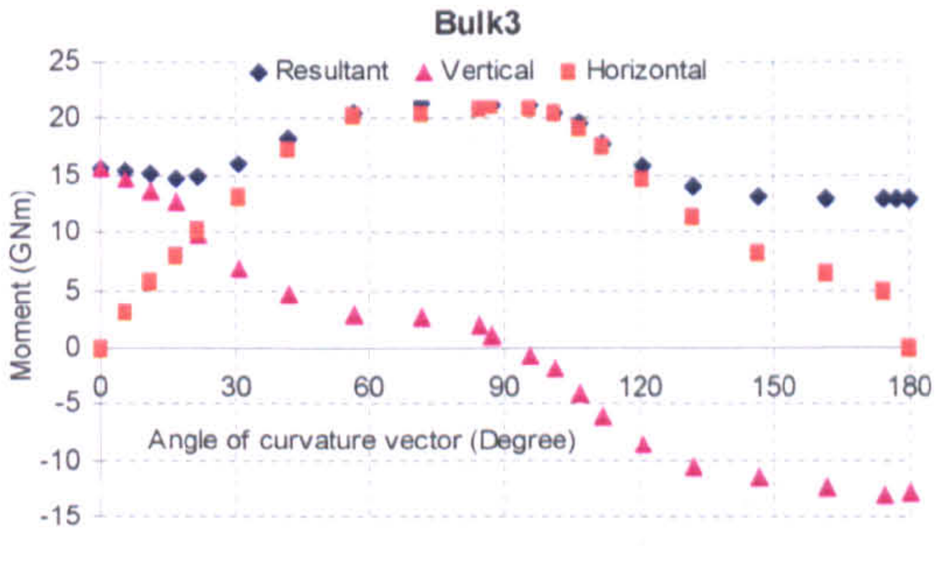

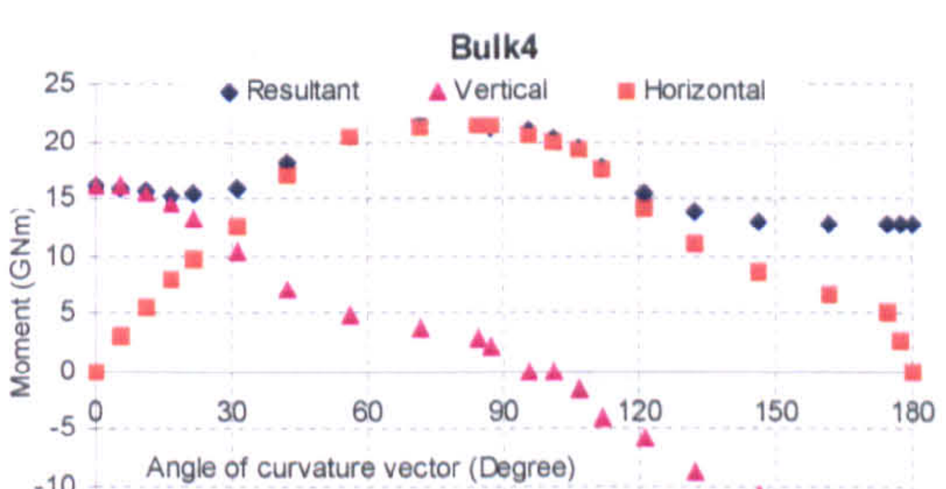

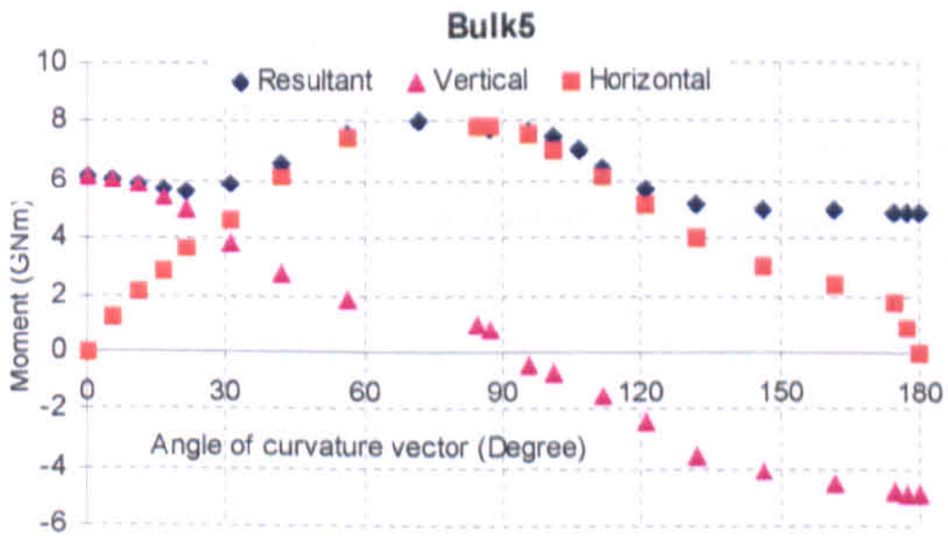

Figure 5.4: The magnitude of the moment components with respect to angle of curvature vector

The relationship between the angles of the curvature vector and the angle of the resultant bending moment vector for the present bulk carrier vessels is plotted in Figure 5.5. It is seen that it is different in general cases. The reason for the asymmetry of the curves is that the hull cross-section of the bulk carrier is not symmetrical about horizontal axis and the behaviour of the structural members under compression is different from that under tension due to the nonlinearity caused by buckling. Therefore, the angle of the curvature vector and the angle of the resultant bending moment vector are not same in general cases.

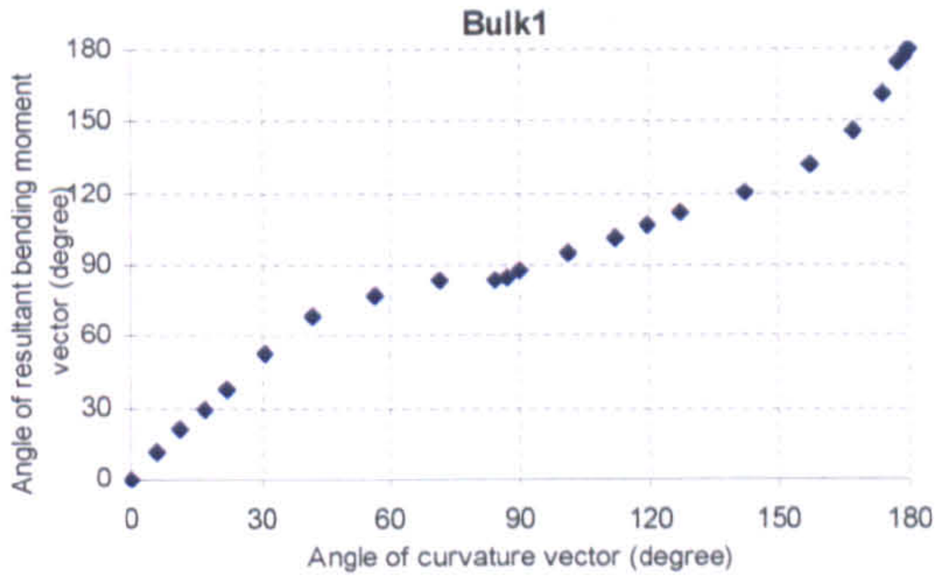

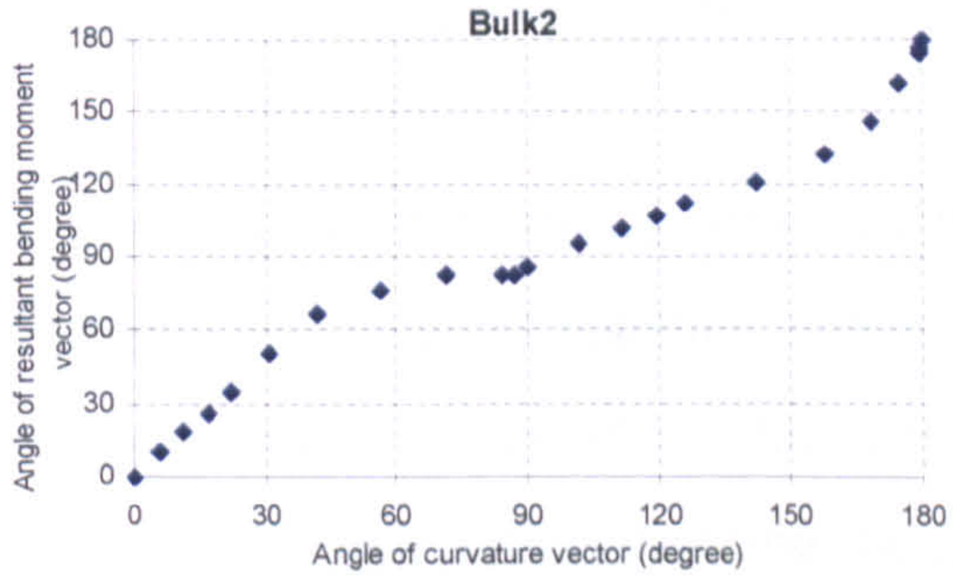

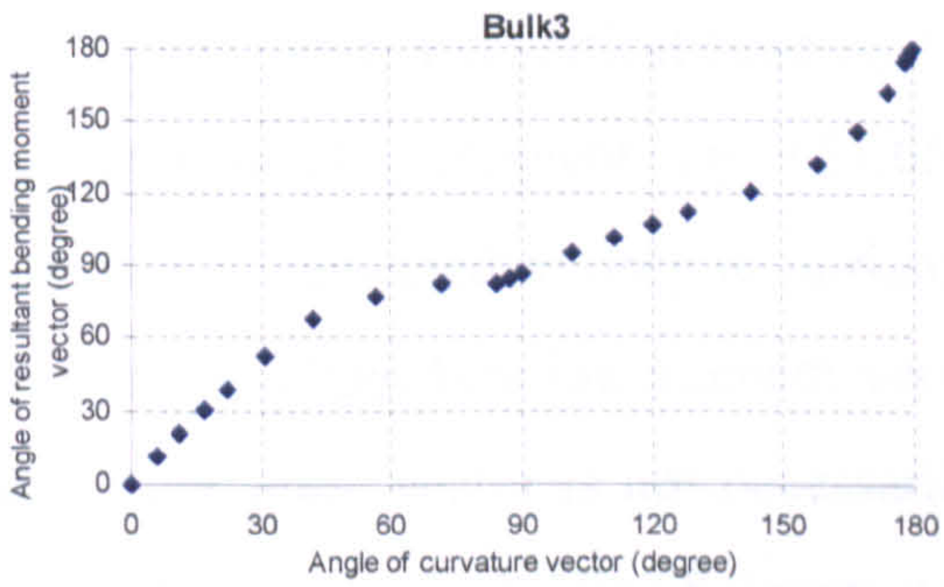

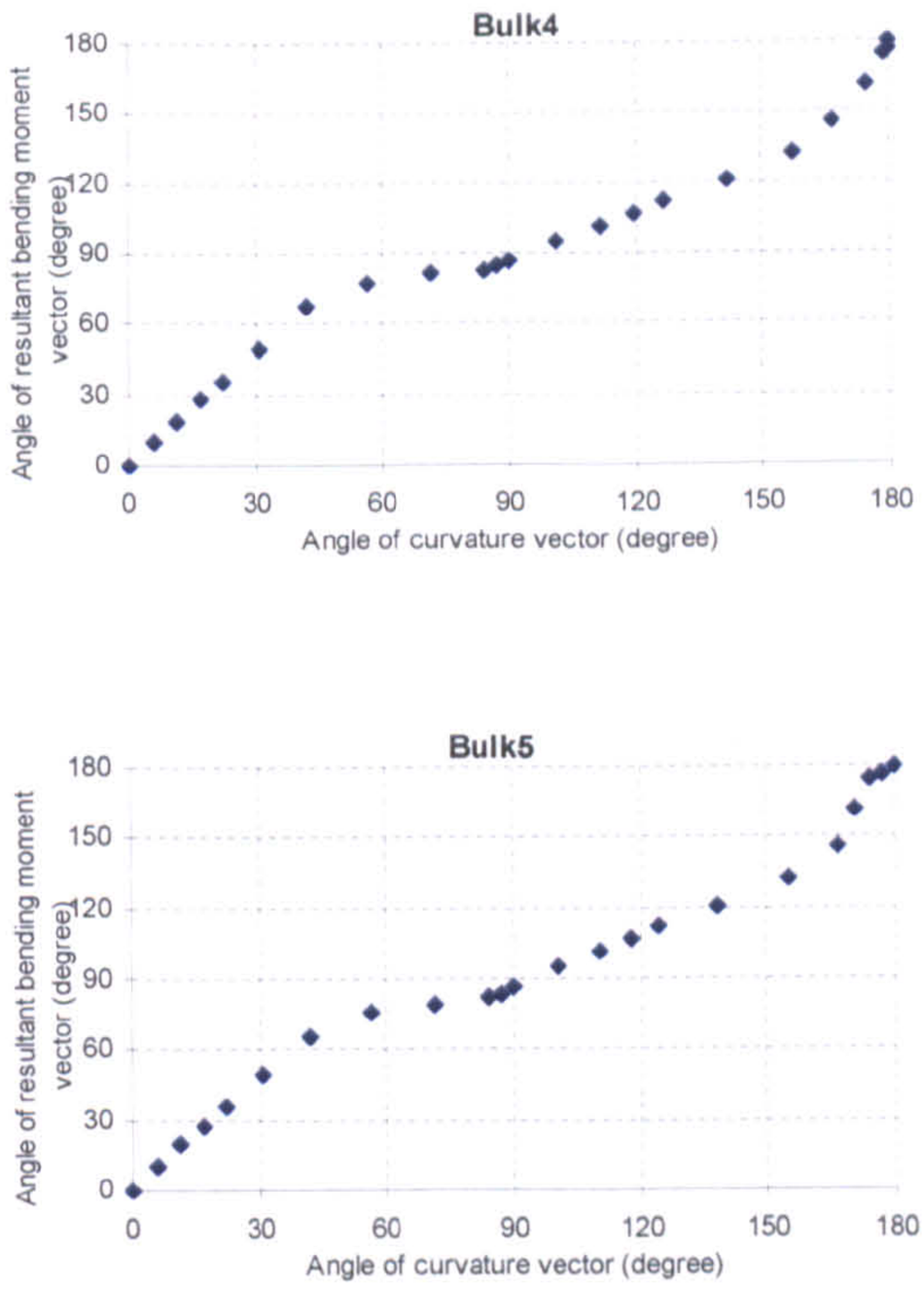

Figure 5.5: Relationship between angle of resultant bending moment and angle of curvature vector

For Bulk1 the following characteristics can be drawn through this investigation.

- When the hull is under horizontal bending, that is, the angle of the curvature vector is $\theta = 90$ degree, the angle of resultant bending moment vector, φ , is not equal to 90 degree due to effect of non-linearity. When $\theta = 90$ degree, there exist both horizontal and vertical bending moments on the hull cross-section. For the present bulk carrier, when $\theta = 90$ degree, the horizontal bending moment is 22.931 GNm and vertical bending moment is 2.072 GNm. The angle of the resultant bending moment is $\varphi = 87.65$ degree.
- If the hull cross-section is subjected to only to horizontal bending moment, that is, the angle of the resultant bending moment vector is $\varphi = 90$ degree, then the angle of the curvature vector is not necessarily equal to 90 degree. The angle of the curvature vector is $\theta = 95.08$ degree when $\varphi = 90$ degree for the investigated bulk carrier vessel.
- The maximum value of the horizontal bending moment occurs neither at $\theta =$ 90 degree nor at $\varphi = 90$ degree. For Bulk1, the maximum value of the

horizontal bending moment takes place at $\theta = 71.58$ degree and $\varphi = 83.18$ degree. The maximum value of the horizontal bending moment is 23.56 GNm. At the moment the horizontal bending moment reaches its maximum, there exists a vertical bending moment on the hull cross-section, which is 2.823 GNm.

For the ultimate strength interaction relationship between vertical and horizontal bending moments, the following simple expression was proposed by Paik et al (1996), regardless of initial imperfection level.

$$\left(\frac{M_x}{M_{xu}}\right)^{1.85} + \left(\frac{M_y}{M_{yu}}\right) = 1 \tag{5.12}$$

Where, M_x is vertical bending moment, M_{xu} is vertical ultimate bending moment, M_y is horizontal bending moment and M_{yu} is horizontal ultimate bending moment.

Another interaction equation was proposed by Gordo & Soares (1997) based on the results for five tankers and six container ships, which is,

$$\left(\frac{M_x}{M_{xu}}\right)^{a} + \left(\frac{M_y}{M_{yu}}\right)^{a} = 1 \tag{5.13}$$

Even though interaction equations proposed by Gordo & Soares were not applied to bulk carriers, even so they have been used in this study. The interactions between vertical and horizontal moments are illustrated in Figure 5. 6. It is seen that the ultimate vertical sagging moment is normally different than the ultimate vertical hogging moment, which requires a separate treatment for hogging and sagging when the ship is subjected to couple horizontal and vertical moment so as to use non-dimensional equations in ship design.

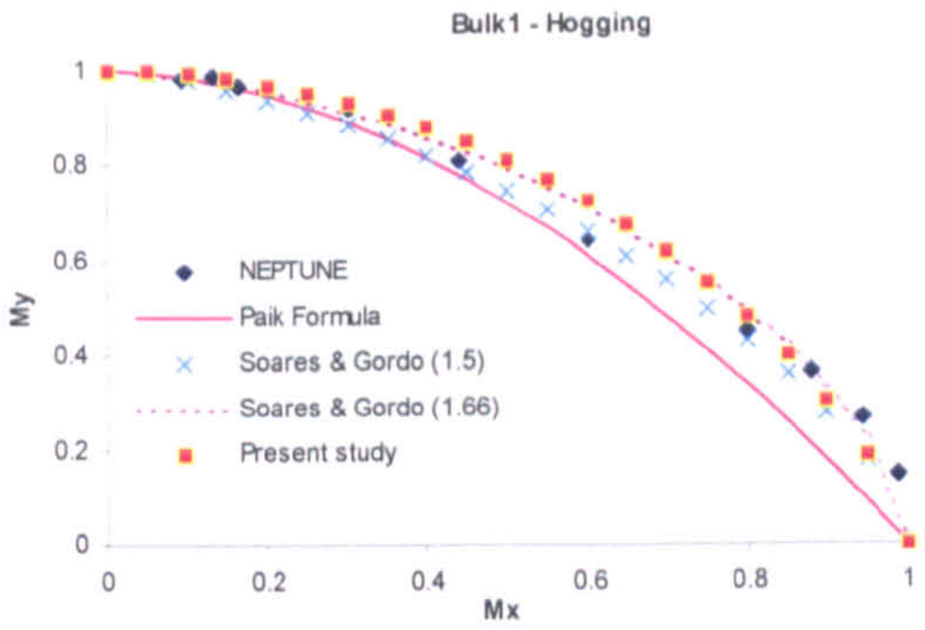
Bulk1 - Hogging
My
Mx
NEPTUNE
Paik Formula
Soares & Gordo (1.5)
Soares & Gordo (1.66)
Present study
0
0.2
0.4
0.6
0.8
1

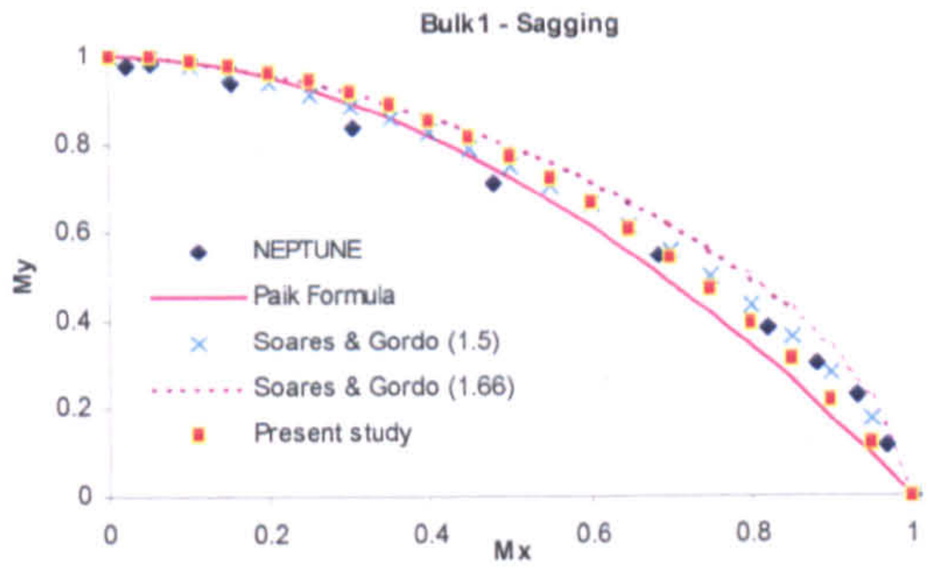
Bulk1 - Sagging
My
Mx
NEPTUNE
Paik Formula
Soares & Gordo (1.5)
Soares & Gordo (1.66)
Present study
0
0.2
0.4
0.6
0.8
1

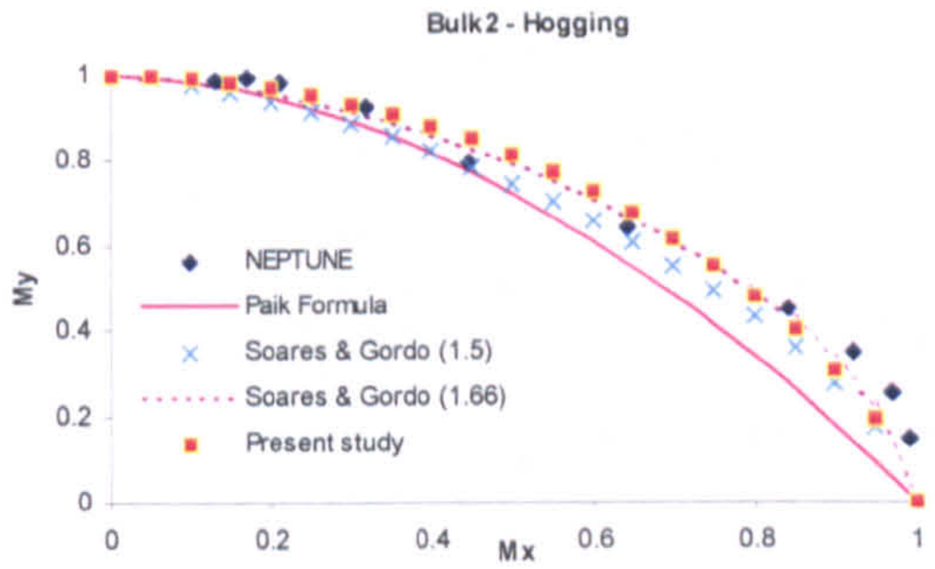
Bulk2 - Hogging
My
Mx
NEPTUNE
Paik Formula
Soares & Gordo (1.5)
Soares & Gordo (1.66)
Present study
0
0.2
0.4
0.6
0.8
1

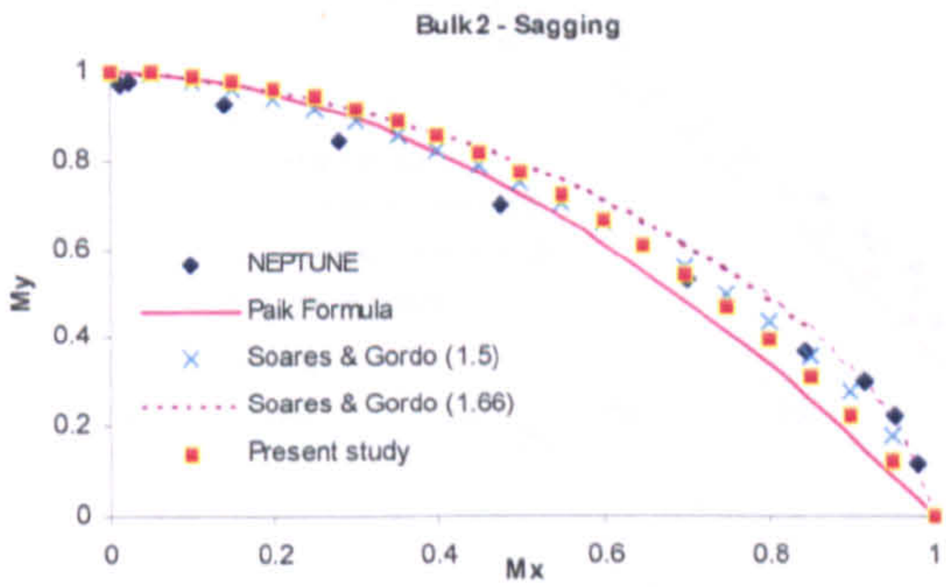
Bulk2 - Sagging
My
Mx
NEPTUNE
Paik Formula
Soares & Gordo (1.5)
Soares & Gordo (1.66)
Present study
0
0.2
0.4
0.6
0.8
1

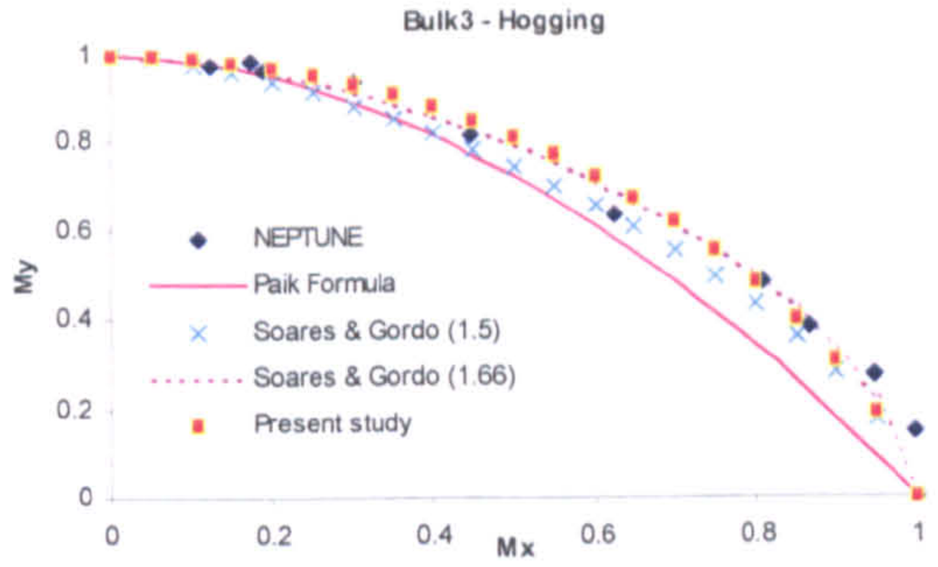
Bulk3 - Hogging
My
Mx
NEPTUNE
Paik Formula
Soares & Gordo (1.5)
Soares & Gordo (1.66)
Present study
0
0.2
0.4
0.6
0.8
1

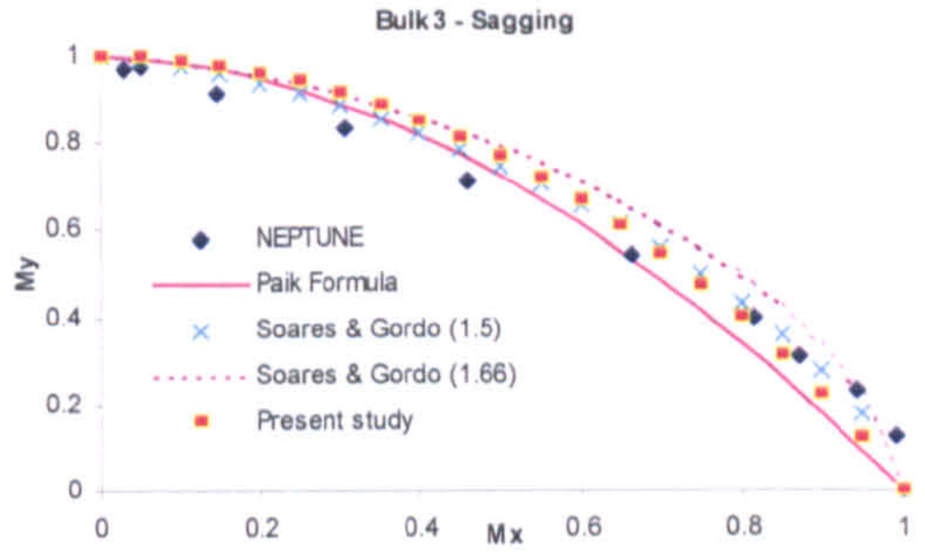
Bulk3 - Sagging
My
Mx
NEPTUNE
Paik Formula
Soares & Gordo (1.5)
Soares & Gordo (1.66)
Present study
0
0.2
0.4
0.6
0.8
1

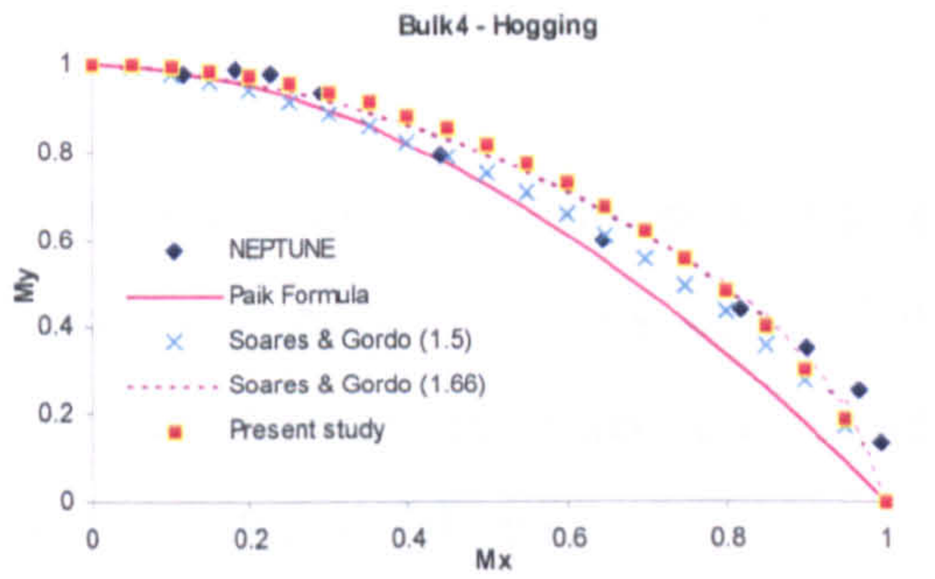
Bulk4 - Hogging
My
Mx
NEPTUNE
Paik Formula
Soares & Gordo (1.5)
Soares & Gordo (1.66)
Present study
0
0.2
0.4
0.6
0.8
1

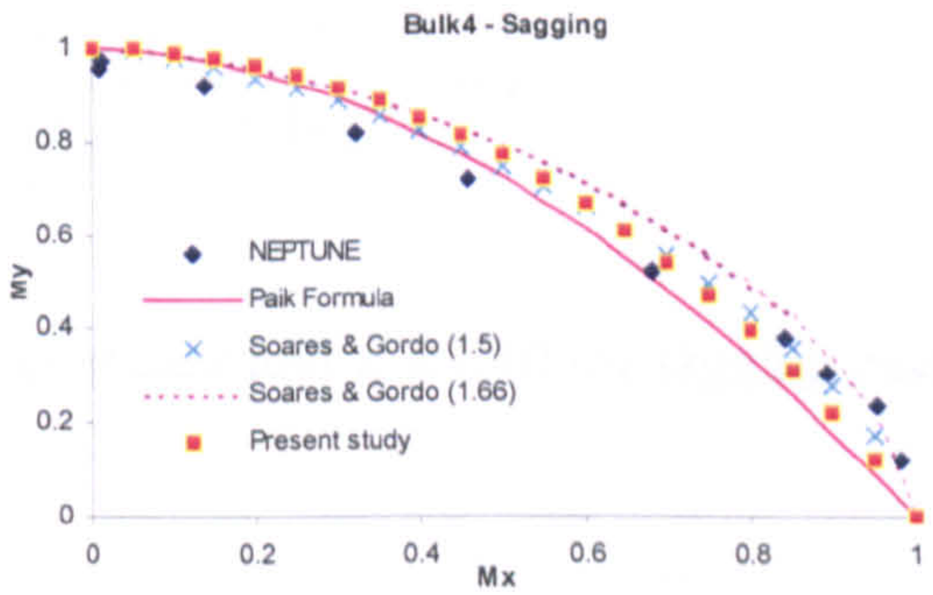
Bulk4 - Sagging
My
Mx
NEPTUNE
Paik Formula
Soares & Gordo (1.5)
Soares & Gordo (1.66)
Present study
0
0.2
0.4
0.6
0.8
1

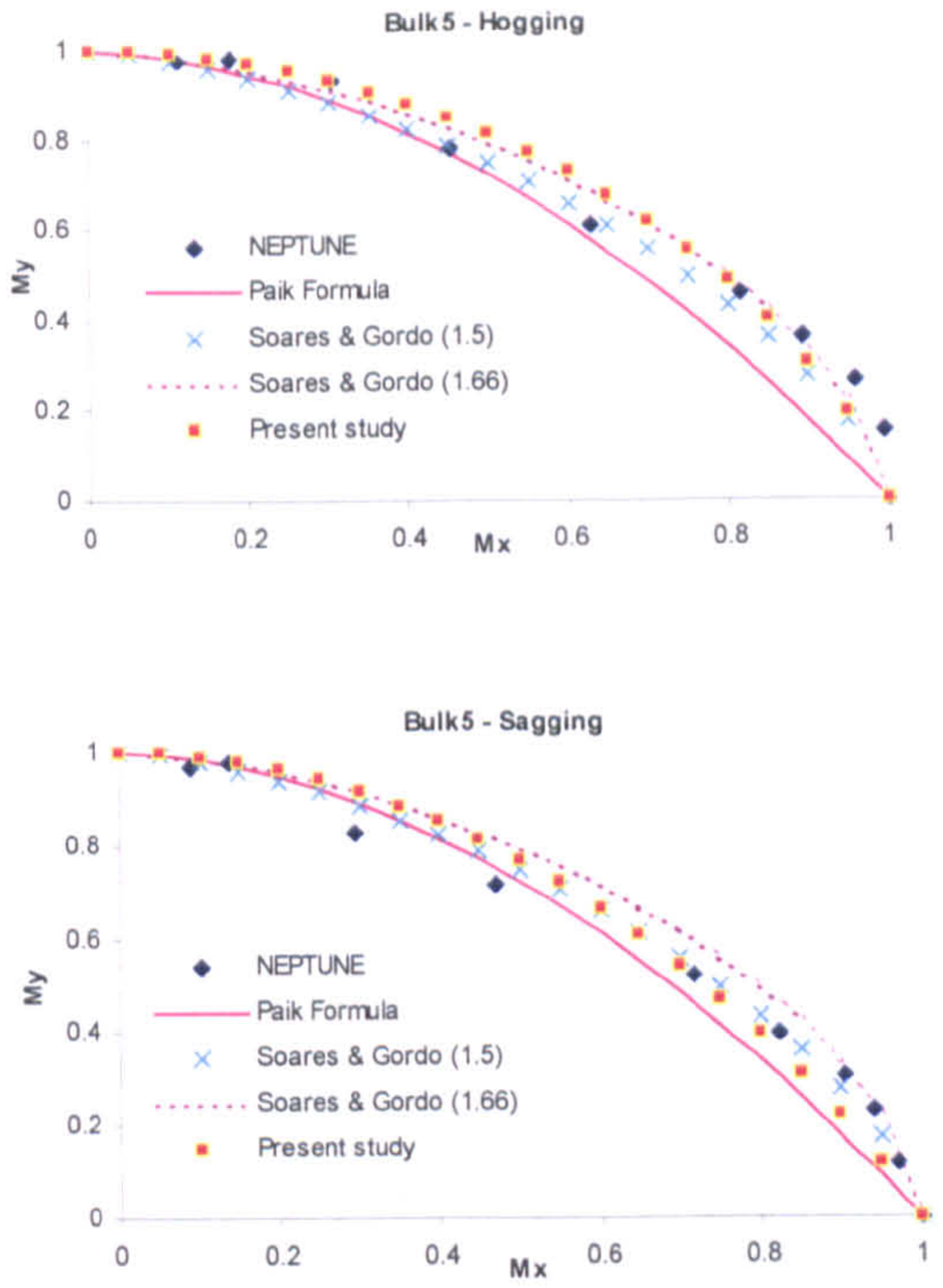

Figure 5.6: Interaction curves for bulk carriers under coupled bending moment

It is shown that the expressions proposed (a=1.66) by Gordo & Soares (1997) fit quite good as compared formulas proposed by Paik et al (1996). However, the present study also proposes interaction formulas to get better results for hogging and sagging cases separately and is presented as follows,

$$\left(\frac{M_x}{M_{xu}}\right)^2 + \left(\frac{M_y}{M_{yu}}\right)^a = 1 \qquad (5.14)$$

Where, $a = 1.40$ for hogging case and $a = 1.10$ for sagging case are proposed.

5.3.2 Tankers

The hull girder ultimate strength of nine tankers is analysed under combined vertical and horizontal bending moments. The midship cross-section of investigated tankers is shown in Figure 5.7.

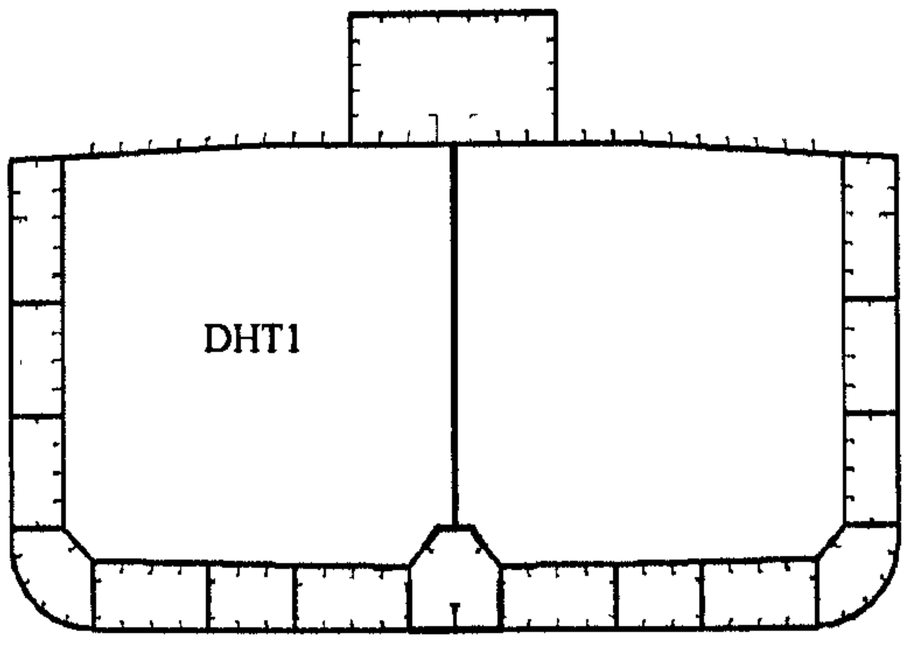
DHT1

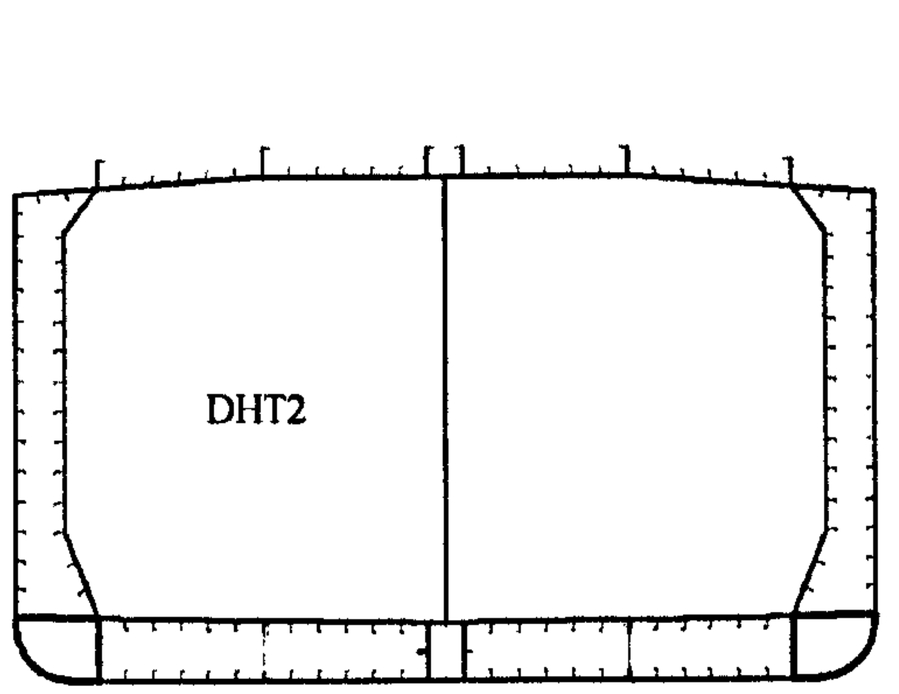
DHT2

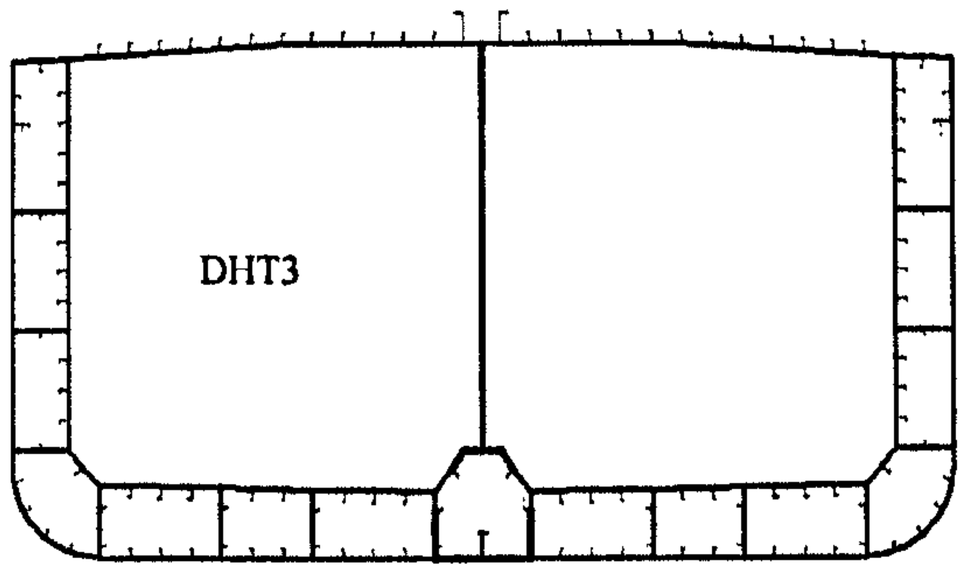
DHT3

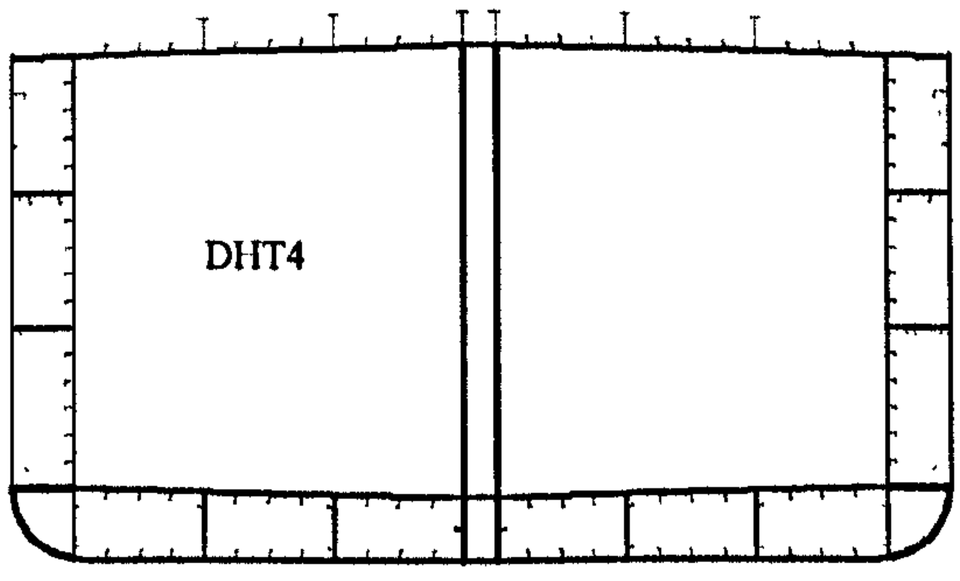
DHT4

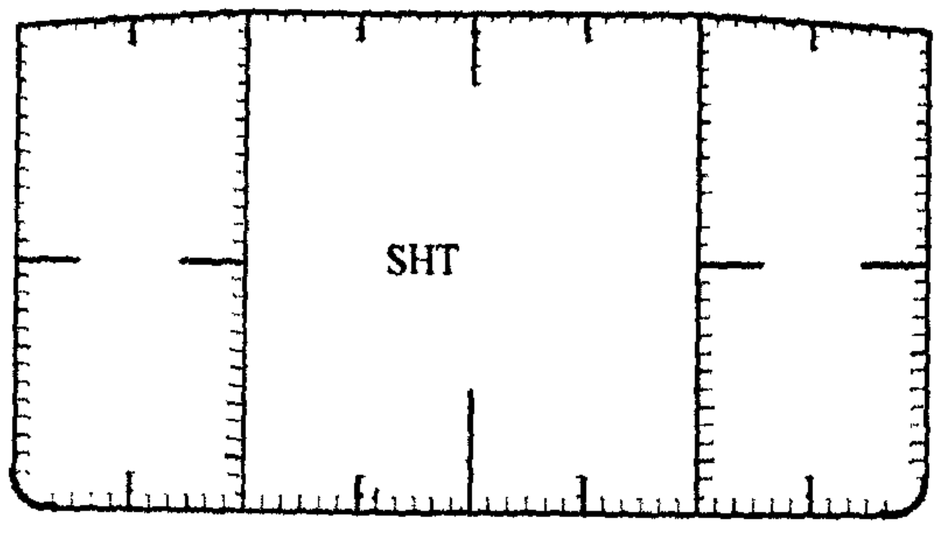
SHT

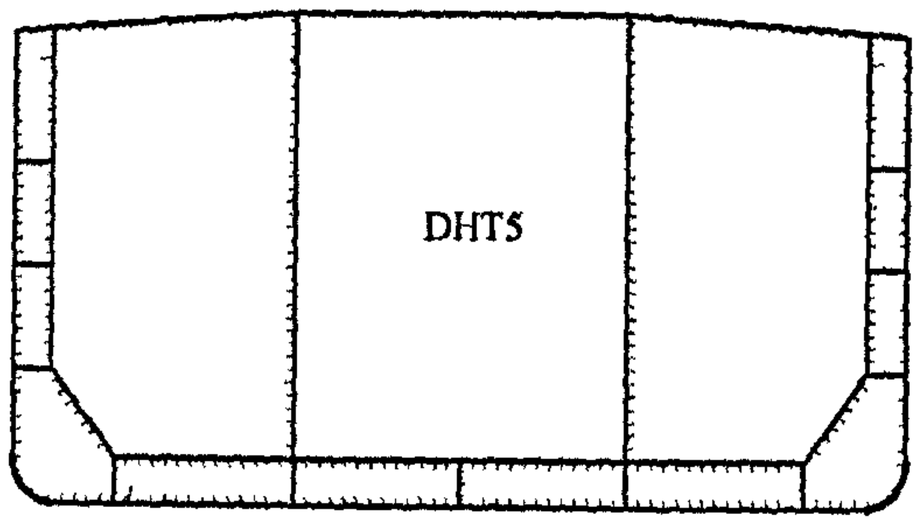
DHT5

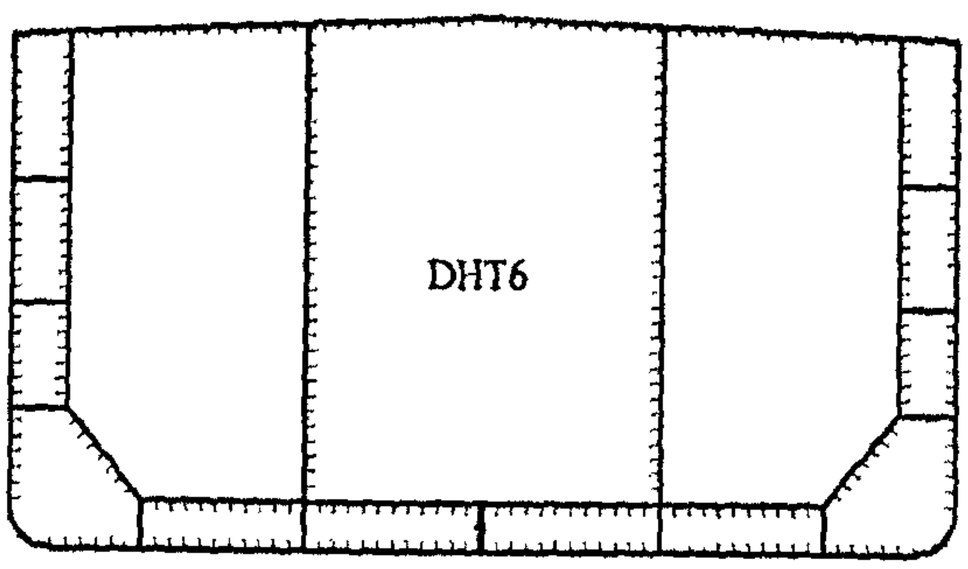
DHT6

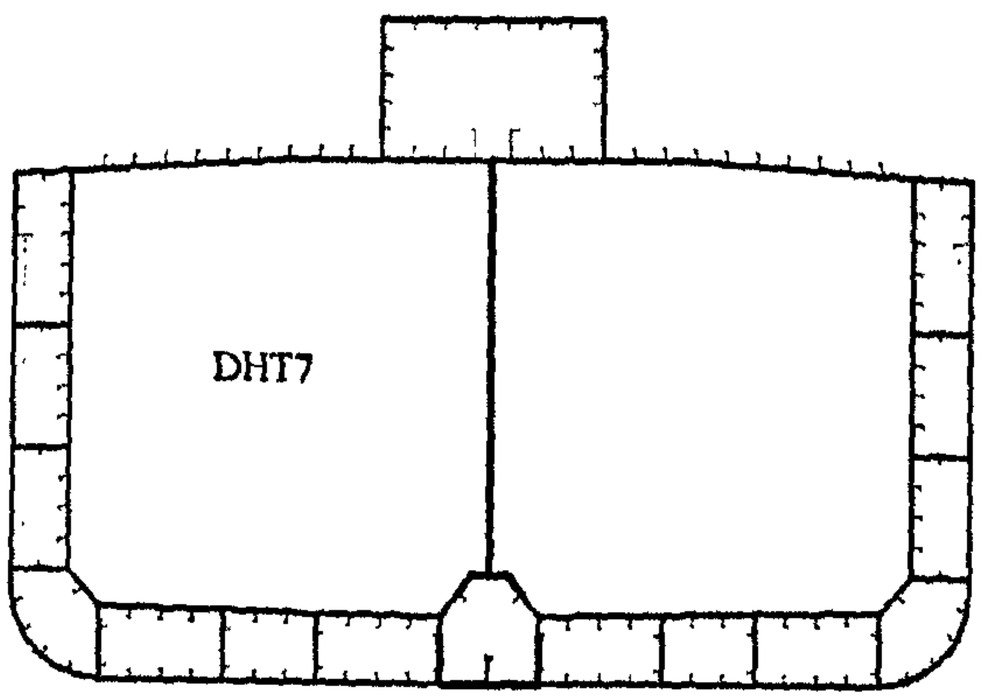
DHT7

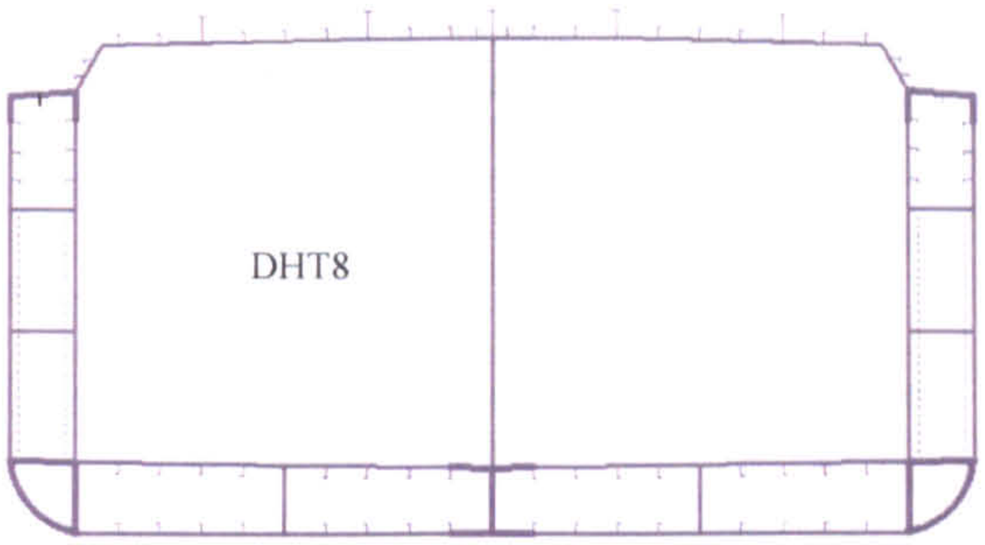

Figure 5.7: Midship cross-section of nine tankers

A series of diagrams is shown in Figure 5.8 to present the response and the ultimate capacity of the analysed tankers under combined bending moments about angle of curvature vector.

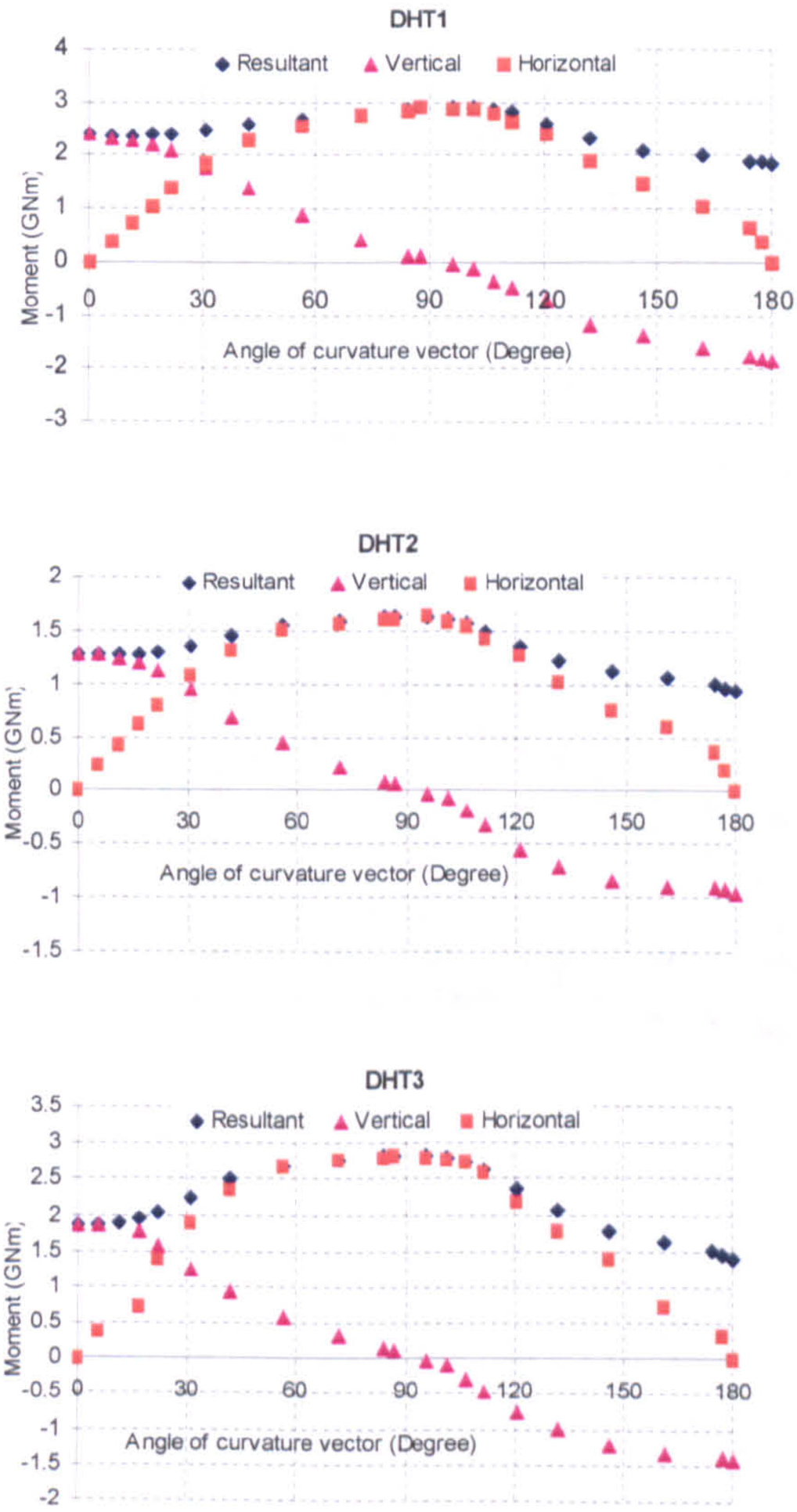

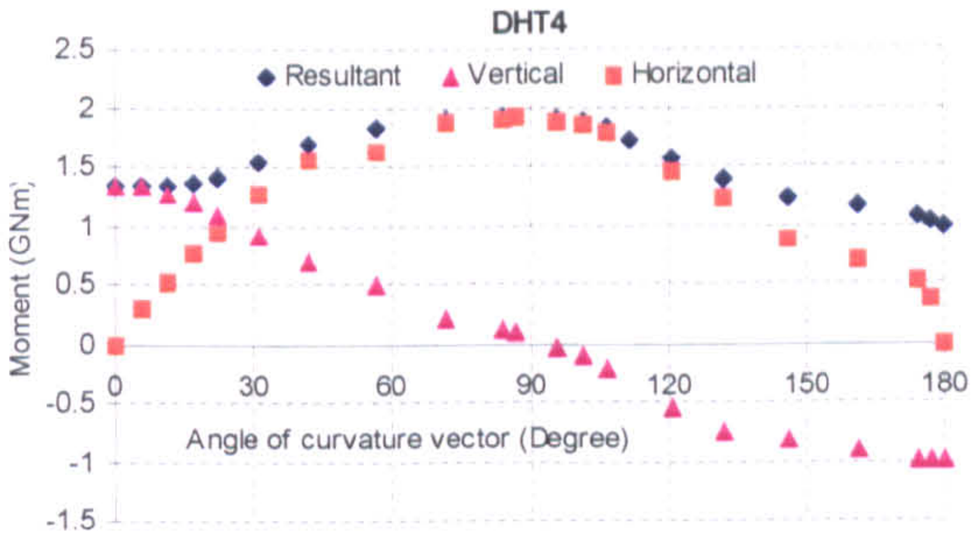
DHT4
Resultant
Vertical
Horizontal
Moment (GNm)
2.5
2
1.5
1
0.5
0
-0.5
-1
-1.5
0
30
60
90
120
150
180
Angle of curvature vector (Degree)

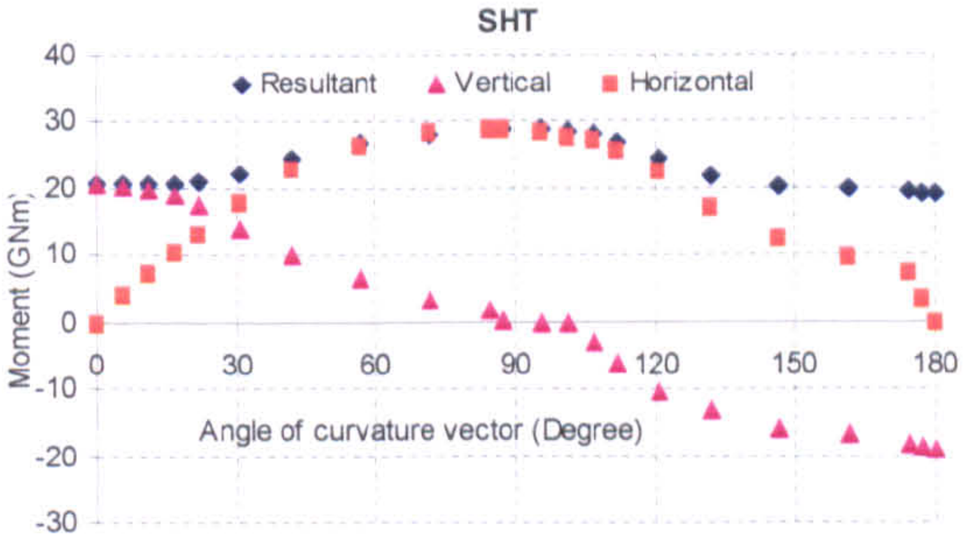
SHT
Resultant
Vertical
Horizontal
Moment (GNm)
40
30
20
10
0
-10
-20
-30
0
30
60
90
120
150
180
Angle of curvature vector (Degree)

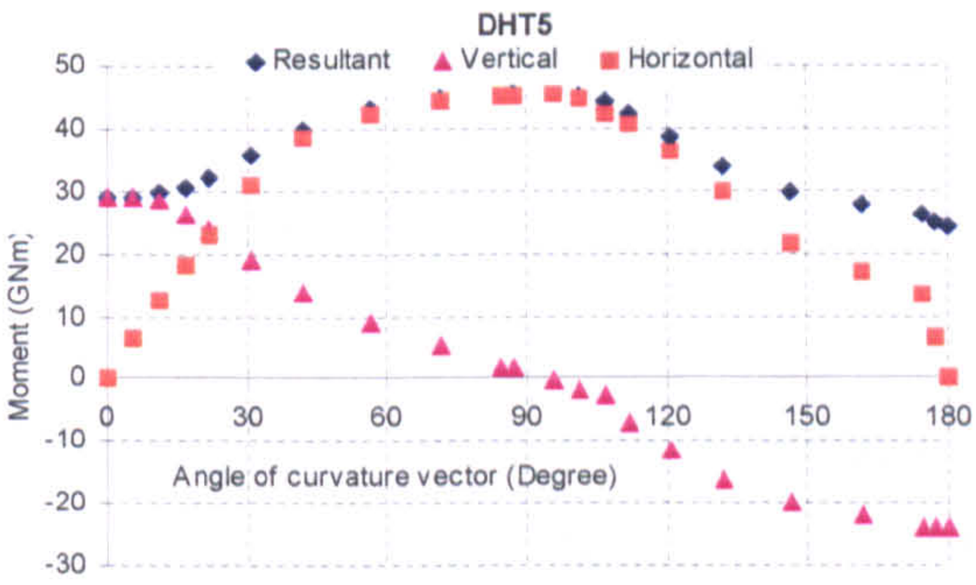
DHT5
Resultant
Vertical
Horizontal
Moment (GNm)
50
40
30
20
10
0
-10
-20
-30
0
30
60
90
120
150
180
Angle of curvature vector (Degree)

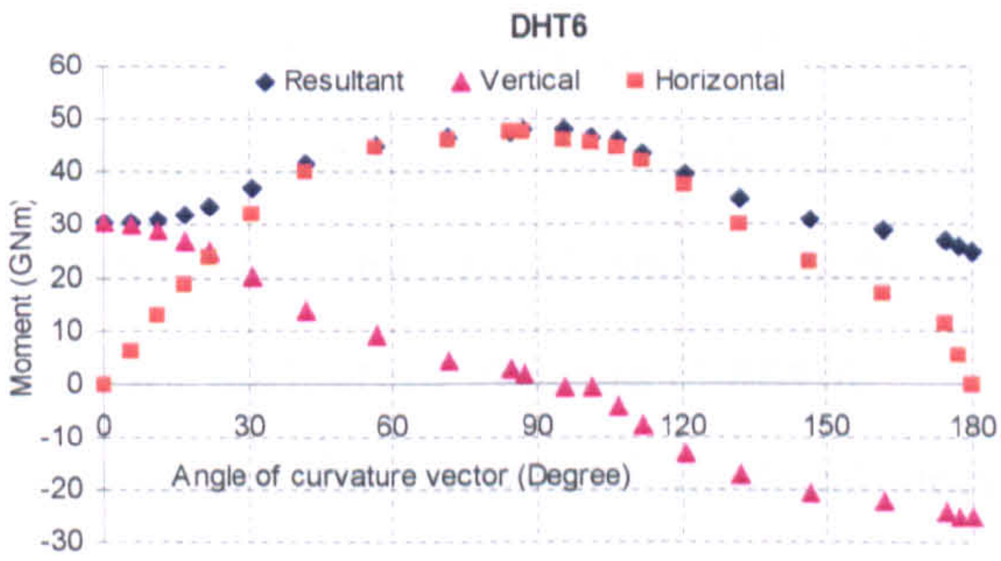
DHT6
Resultant
Vertical
Horizontal
Moment (GNm)
60
50
40
30
20
10
0
-10
-20
-30
0
30
60
90
120
150
180
Angle of curvature vector (Degree)

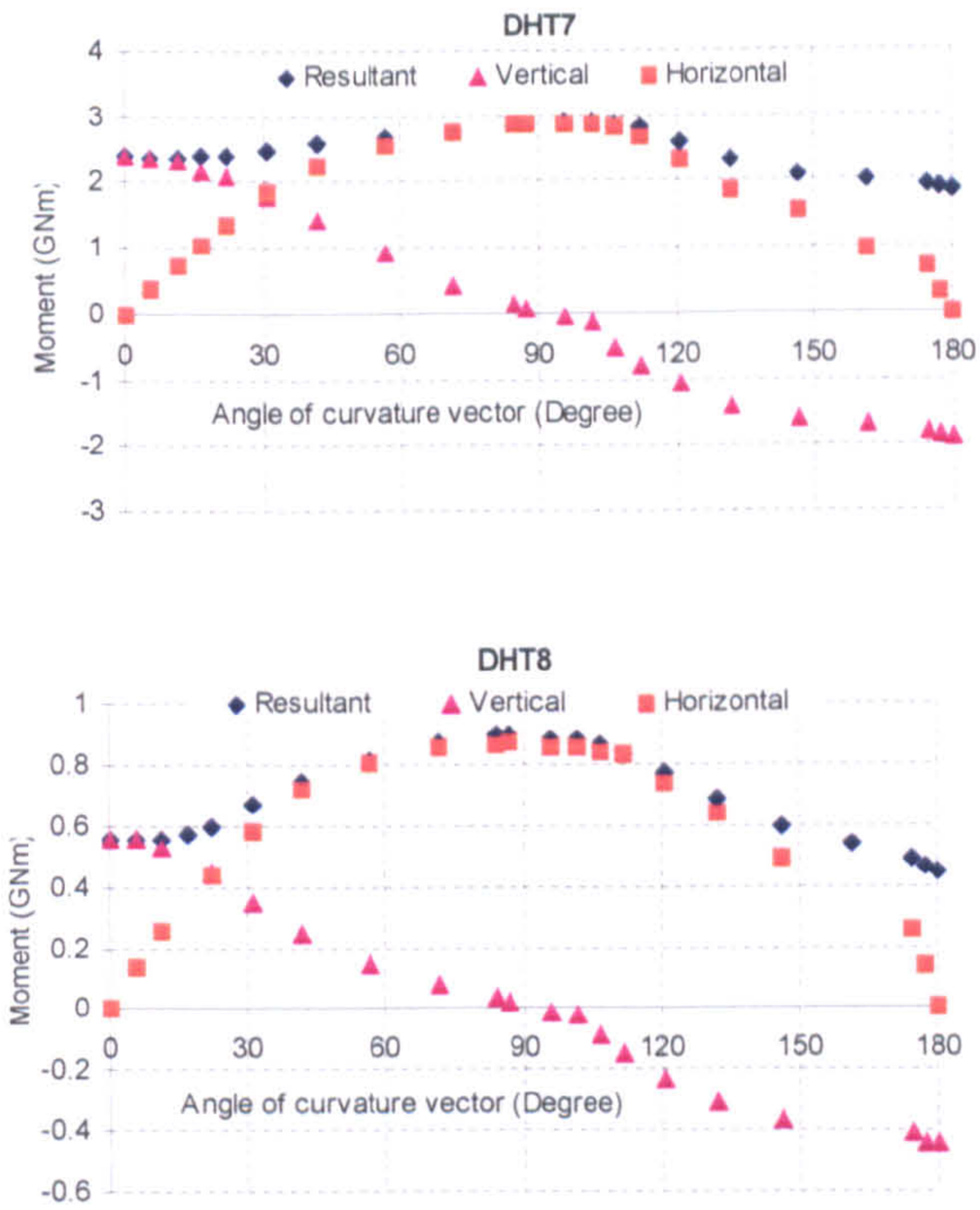

Figure 5.8: The magnitude of the moment components with respect to angle of the curvature vector

For DHT1 following characteristics can be drawn,

- When $\theta = 90$ degree, there exist both horizontal and vertical bending moments on the hull cross-section. When $\theta = 90$ degree, the horizontal moment is 2.898 GNm and vertical bending moment is 0.106 GNm. The angle of the resultant bending moment is $\varphi = 90.94$ degree.
- When $\varphi = 90$ degree is for DHT1 the angle of the curvature vector is $\theta = 95.55$ degree. Thus, both horizontal and vertical bending will take place under action of a pure horizontal bending moment.
- The maximum value of the horizontal moment occurs neither at $\theta = 90$ degree nor at $\varphi = 90$ degree. The maximum horizontal bending moment occurs at $\theta = 86.50$ degree and $\varphi = 87.12$ degree. The maximum value of horizontal bending moment is 2.917 GNm. At the moment the horizontal bending moment reaches its maximum, there exists a vertical bending moment on the hull cross-section, which is 0.119 GNm.

The relationship between the angle of the curvature vector and the angle of the resultant bending moment vector for the tankers is shown in Figure 5.9.

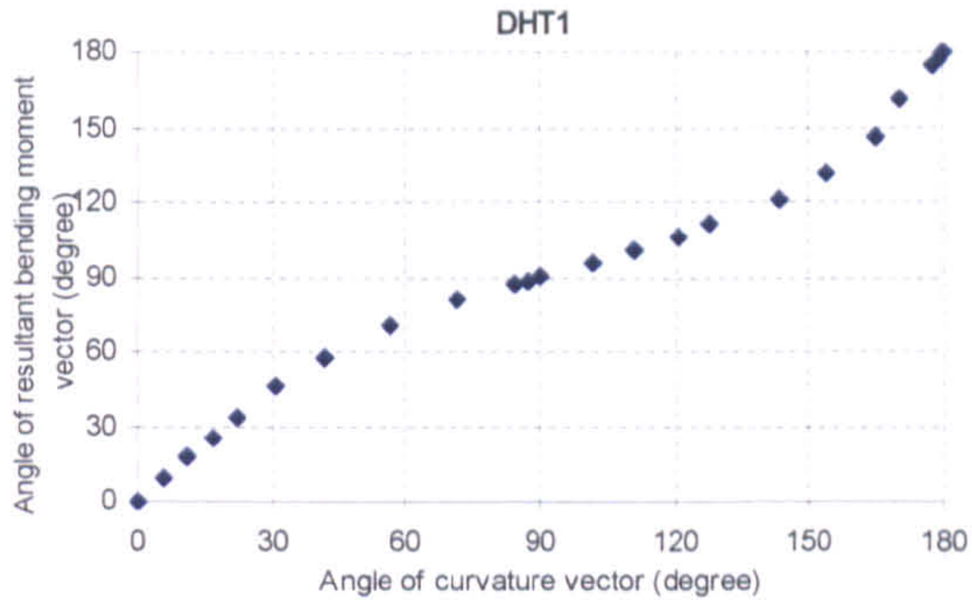

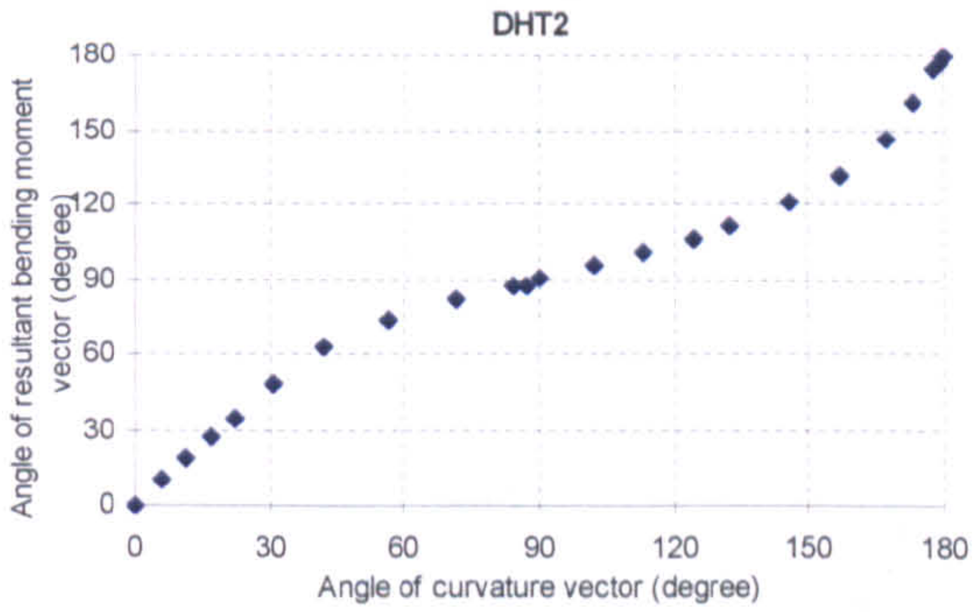

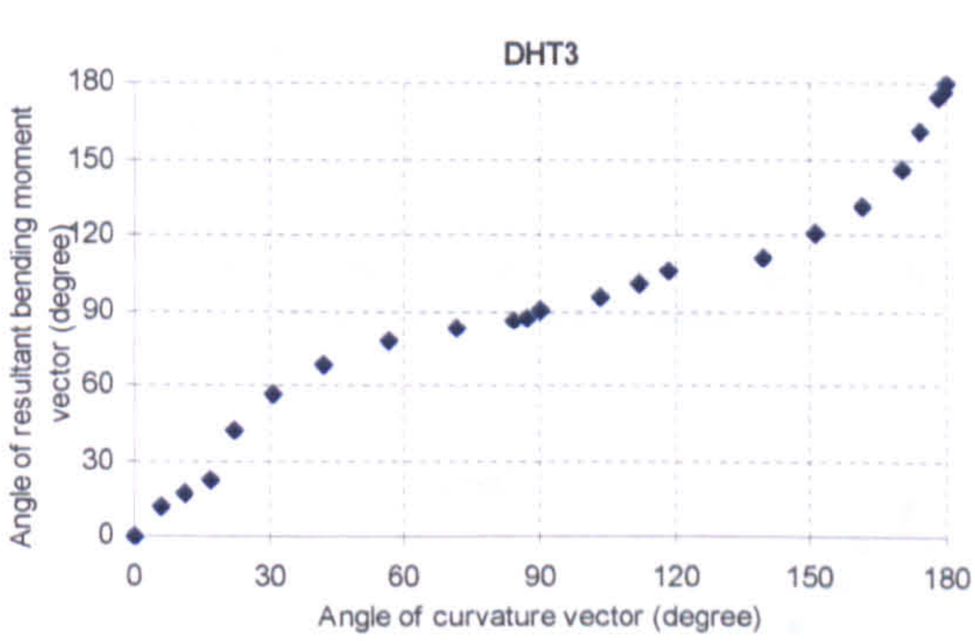

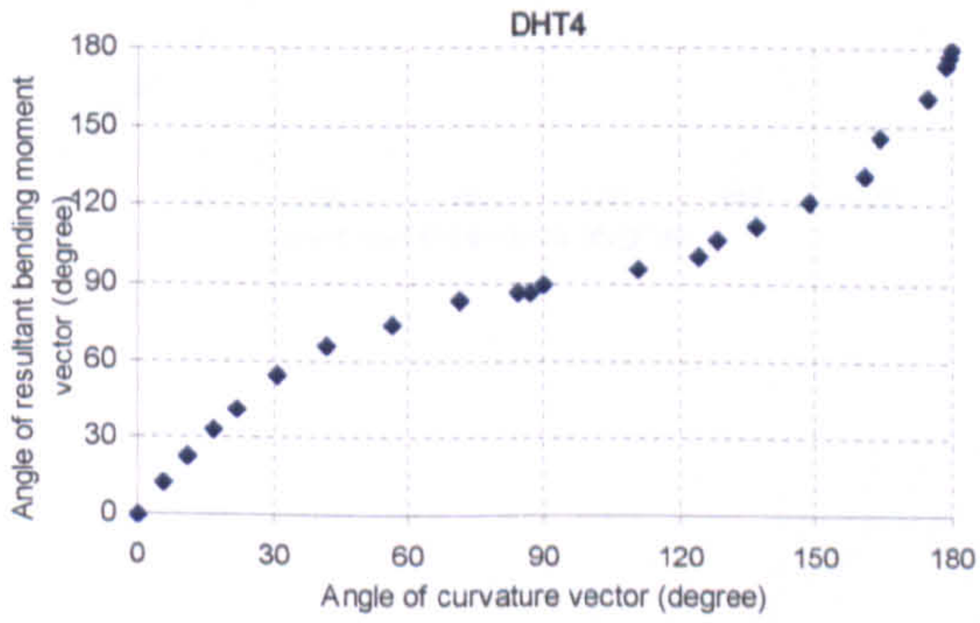

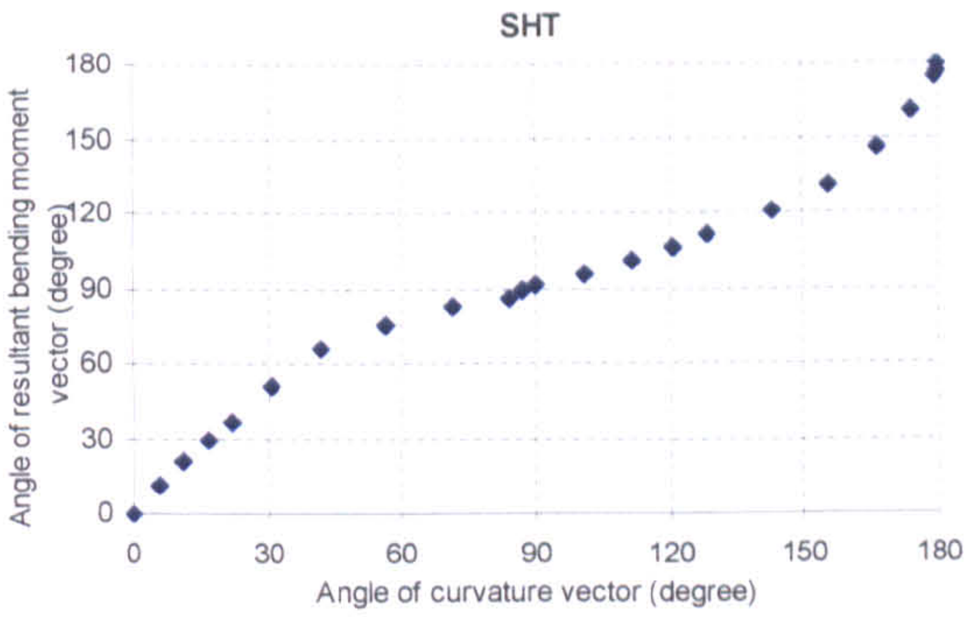
SHT
Angle of resultant bending moment vector (degree)
180
150
120
90
60
30
0
0
30
60
90
120
150
180
Angle of curvature vector (degree)

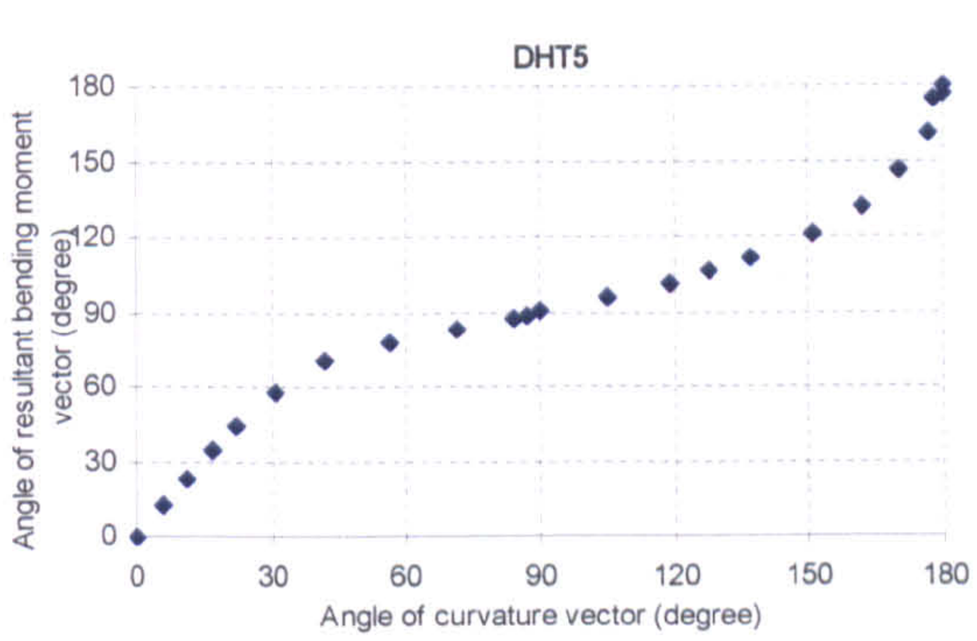
DHT5
Angle of resultant bending moment vector (degree)
180
150
120
90
60
30
0
0
30
60
90
120
150
180
Angle of curvature vector (degree)

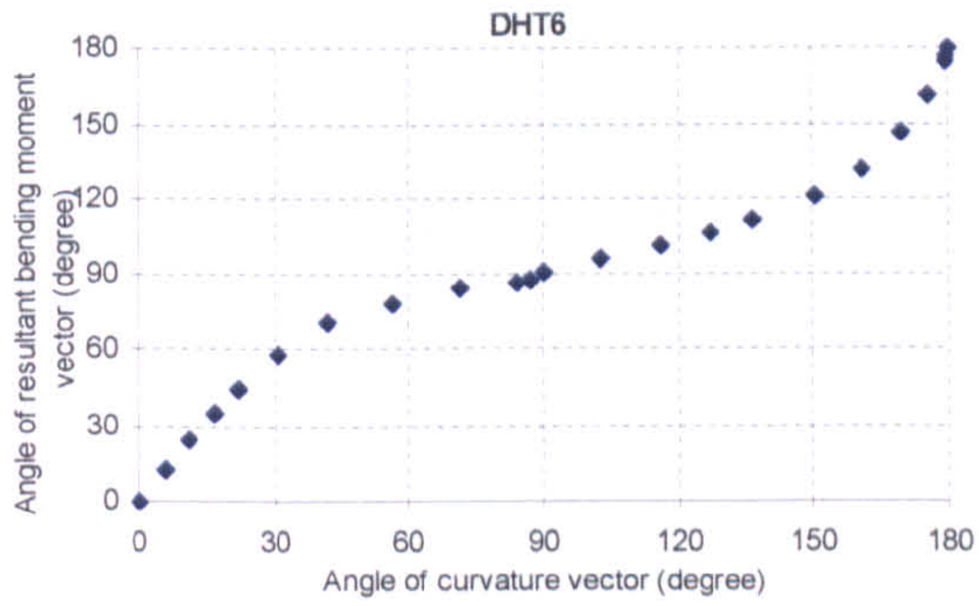
DHT6
Angle of resultant bending moment vector (degree)
180
150
120
90
60
30
0
0
30
60
90
120
150
180
Angle of curvature vector (degree)

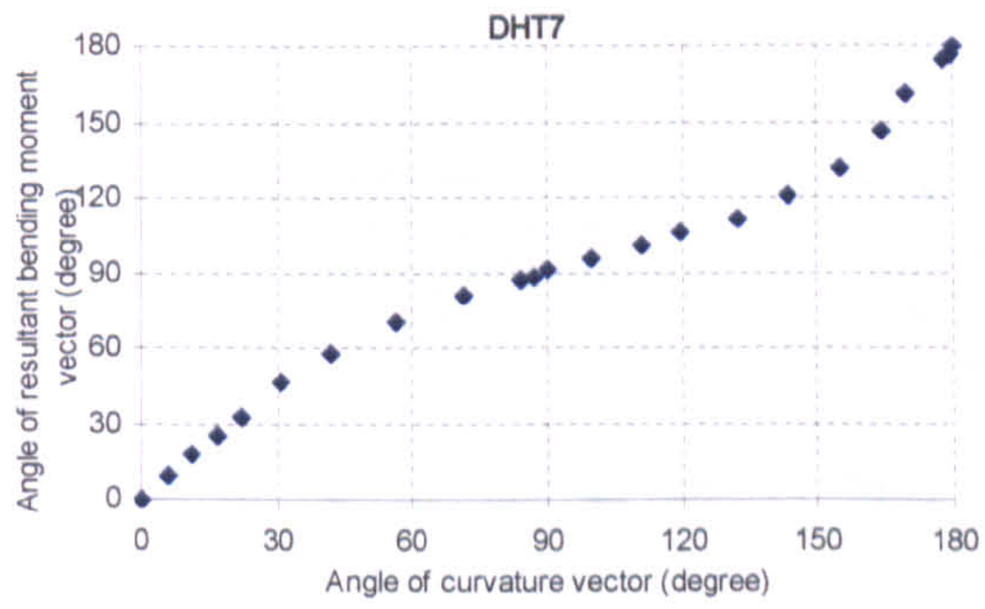
DHT7
Angle of resultant bending moment vector (degree)
180
150
120
90
60
30
0
0
30
60
90
120
150
180
Angle of curvature vector (degree)

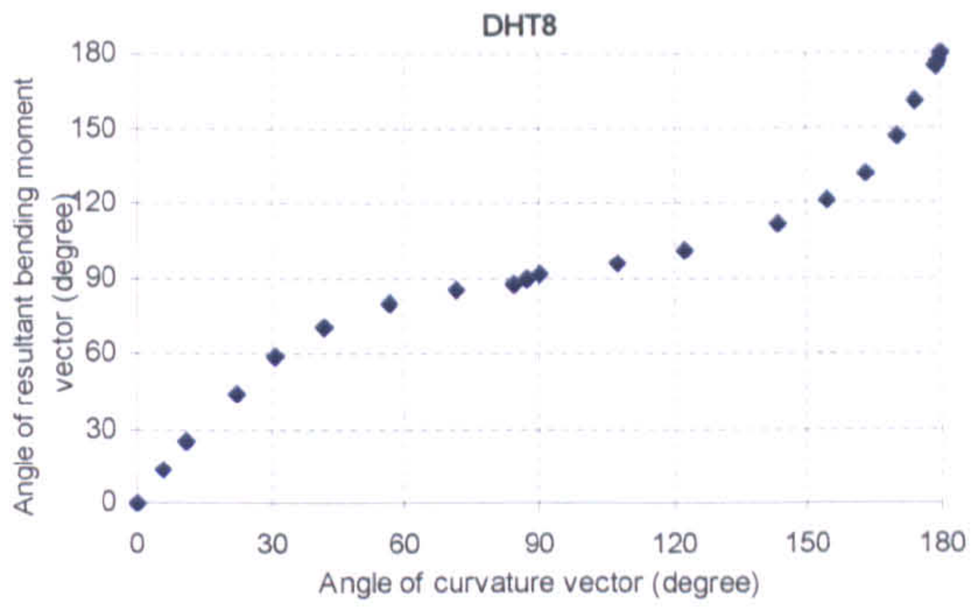

Figure 5.9: Relationship between angle of the resultant bending moment and angle of curvature vector

It is seen that until 20-30 degree of the curvature vector, all tanker figures have a linear variation of the vertical component of the moment vector with an increase in the angle of heel, which means that the horizontal component of the vector moment grows faster than the reduction in the vertical component of the moment. From 95 to 160 degrees in DHT1 and DHT2 these angles are relatively flat, which means that the direction of the moment vector is almost insensitive to the variation of direction of the neutral axis, while the rest tanker figures are far from flat. For angles higher than 173 degree the first behaviour is repeated in sagging condition. The interactions between vertical and horizontal moments are illustrated in Figure 5.10.

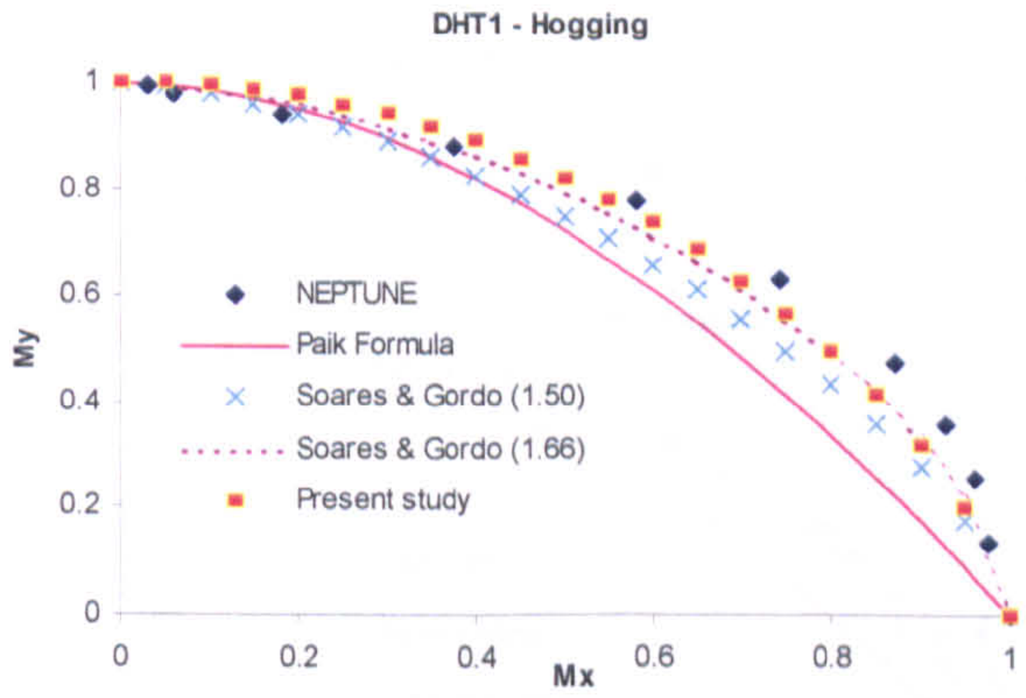

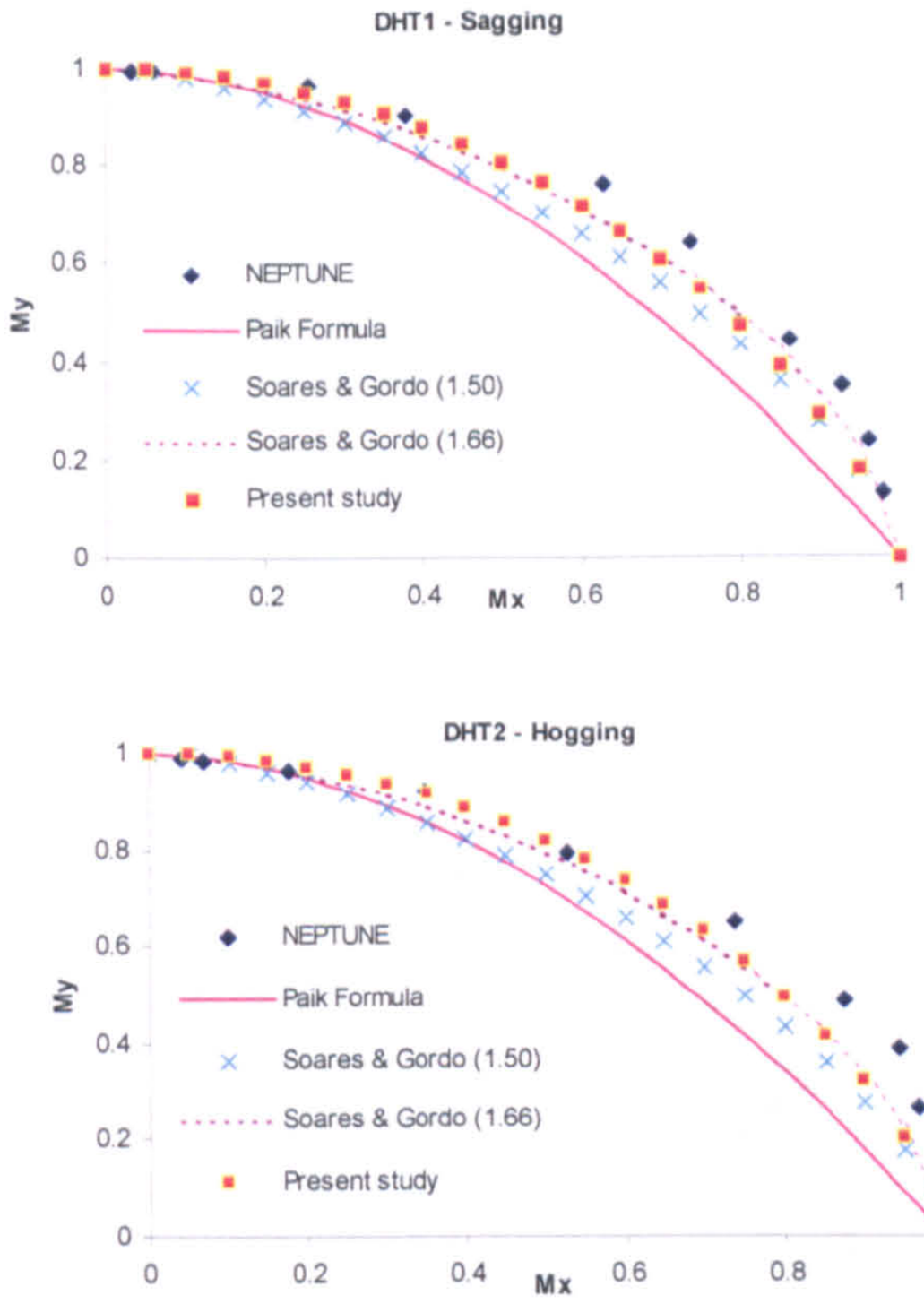
DHT1 - Sagging
My
Mx
NEPTUNE
Paik Formula
Soares & Gordo (1.50)
Soares & Gordo (1.66)
Present study
0
0.2
0.4
0.6
0.8
1

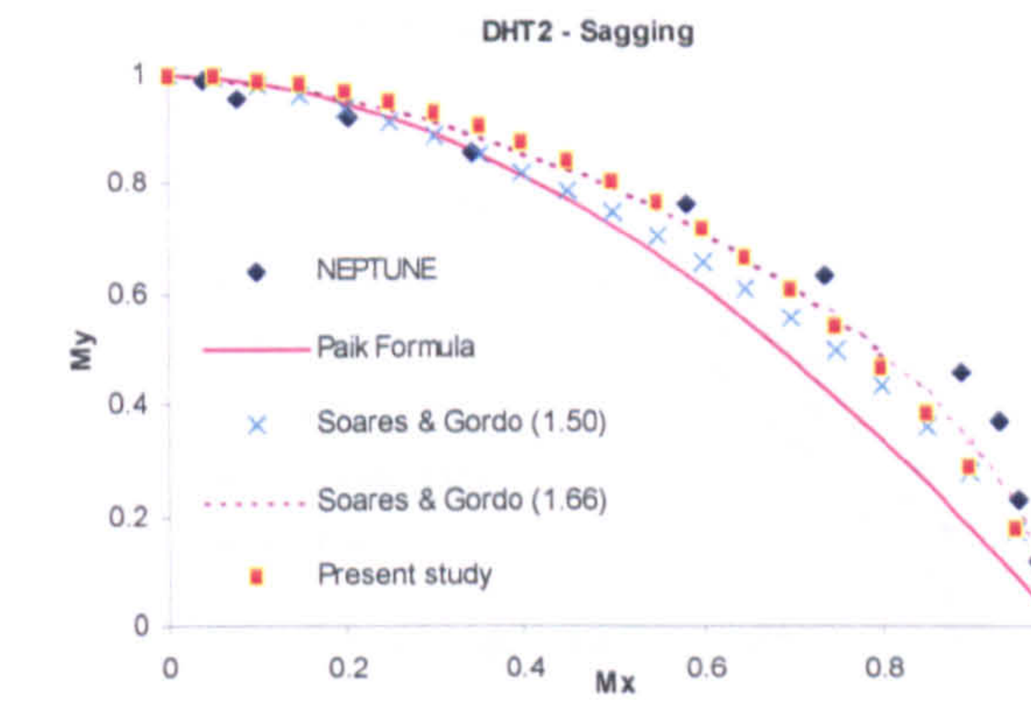
DHT2 - Hogging
My
Mx
NEPTUNE
Paik Formula
Soares & Gordo (1.50)
Soares & Gordo (1.66)
Present study
0
0.2
0.4
0.6
0.8
1

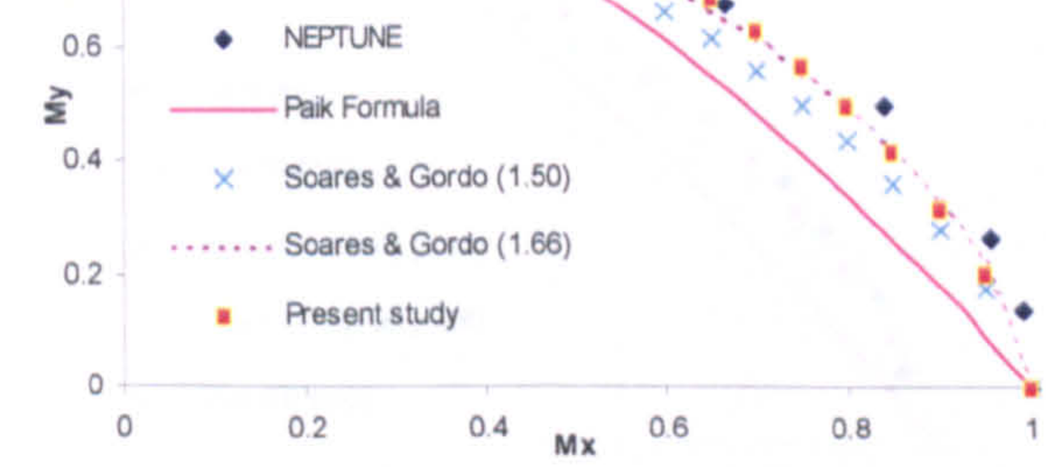
DHT2 - Sagging
My
Mx
NEPTUNE
Paik Formula
Soares & Gordo (1.50)
Soares & Gordo (1.66)
Present study
0
0.2
0.4
0.6
0.8
1

DHT3 - Hogging
My
Mx
NEPTUNE
Paik Formula
Soares & Gordo (1.50)
Soares & Gordo (1.66)
Present study
0
0.2
0.4
0.6
0.8
1

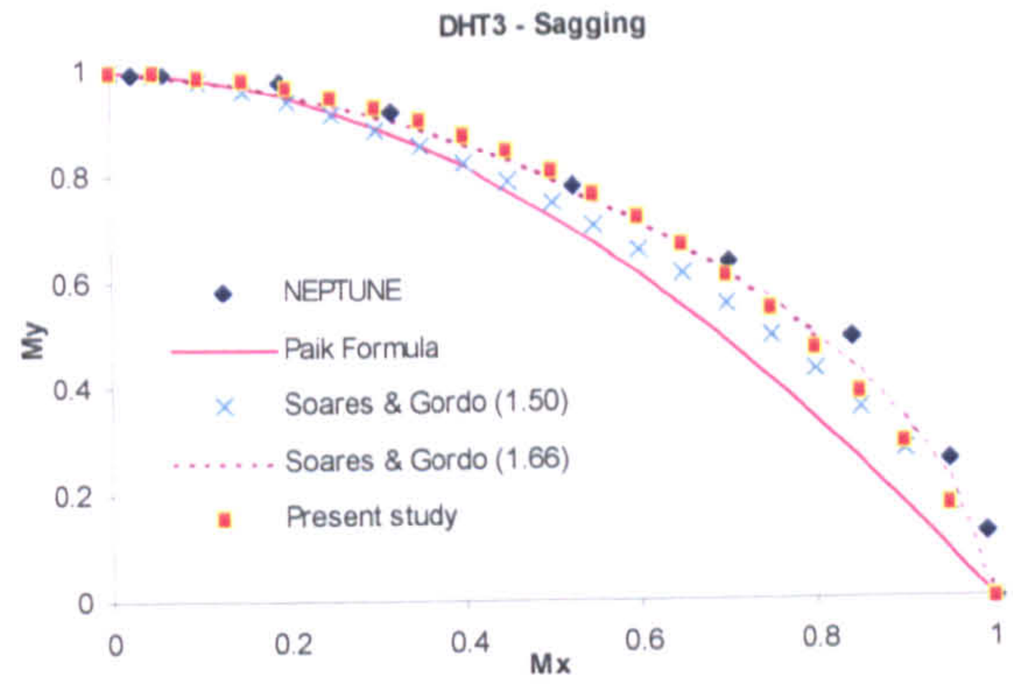
DHT3 - Sagging
My
Mx
NEPTUNE
Paik Formula
Soares & Gordo (1.50)
Soares & Gordo (1.66)
Present study
0
0.2
0.4
0.6
0.8
1

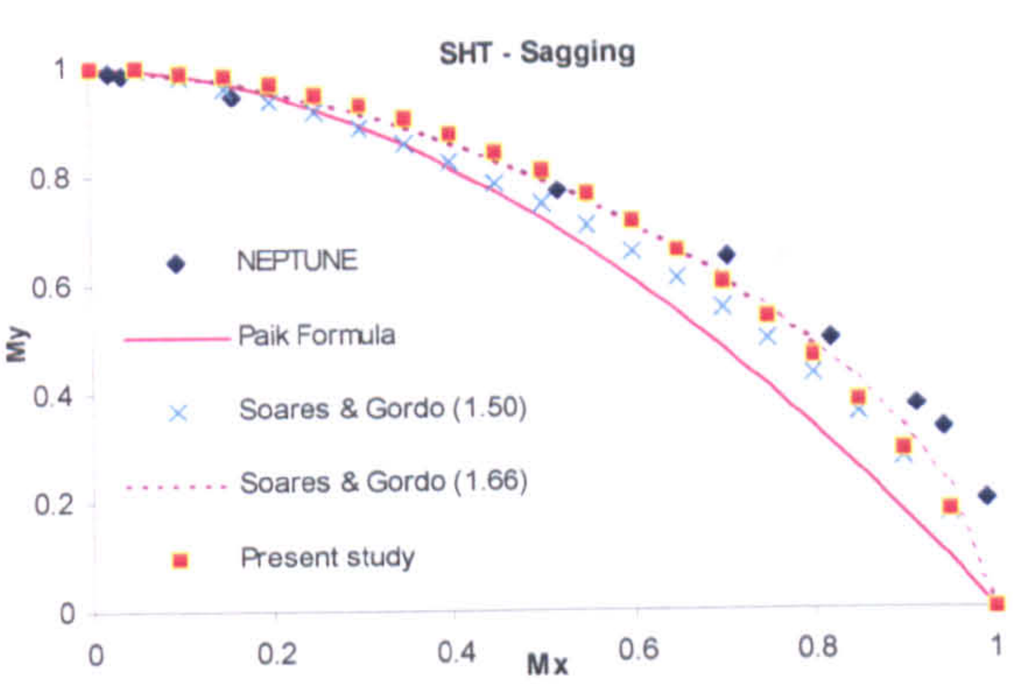
SHT - Sagging
My
Mx
NEPTUNE
Paik Formula
Soares & Gordo (1.50)
Soares & Gordo (1.66)
Present study
0
0.2
0.4
0.6
0.8
1

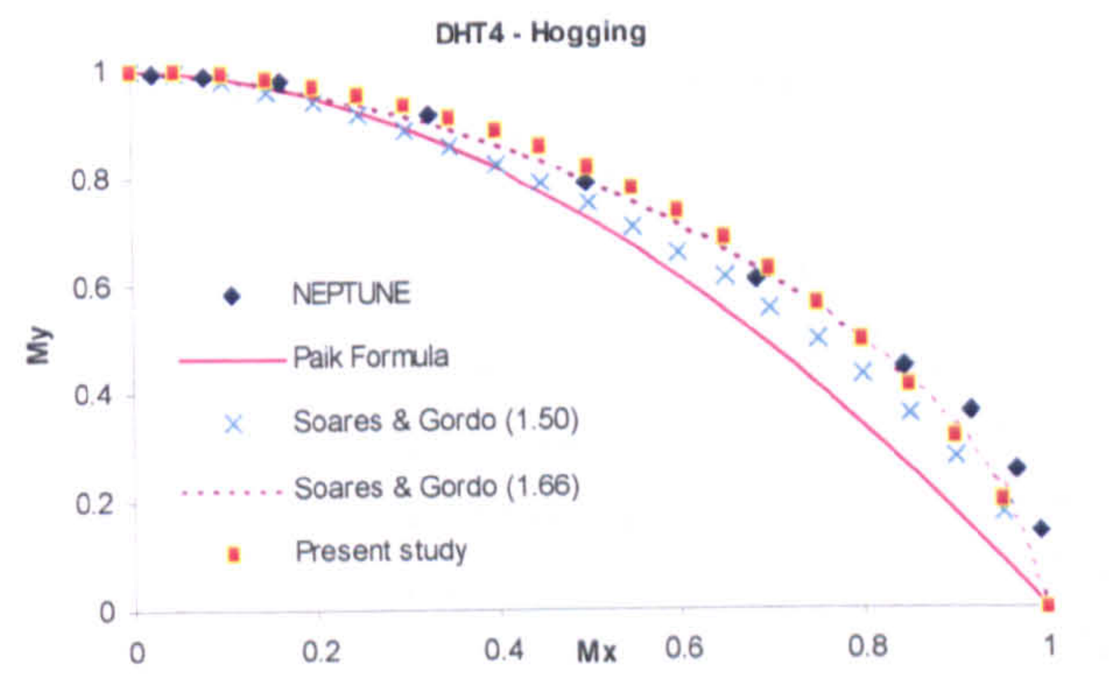
DHT4 - Hogging
My
Mx
NEPTUNE
Paik Formula
Soares & Gordo (1.50)
Soares & Gordo (1.66)
Present study
0
0.2
0.4
0.6
0.8
1

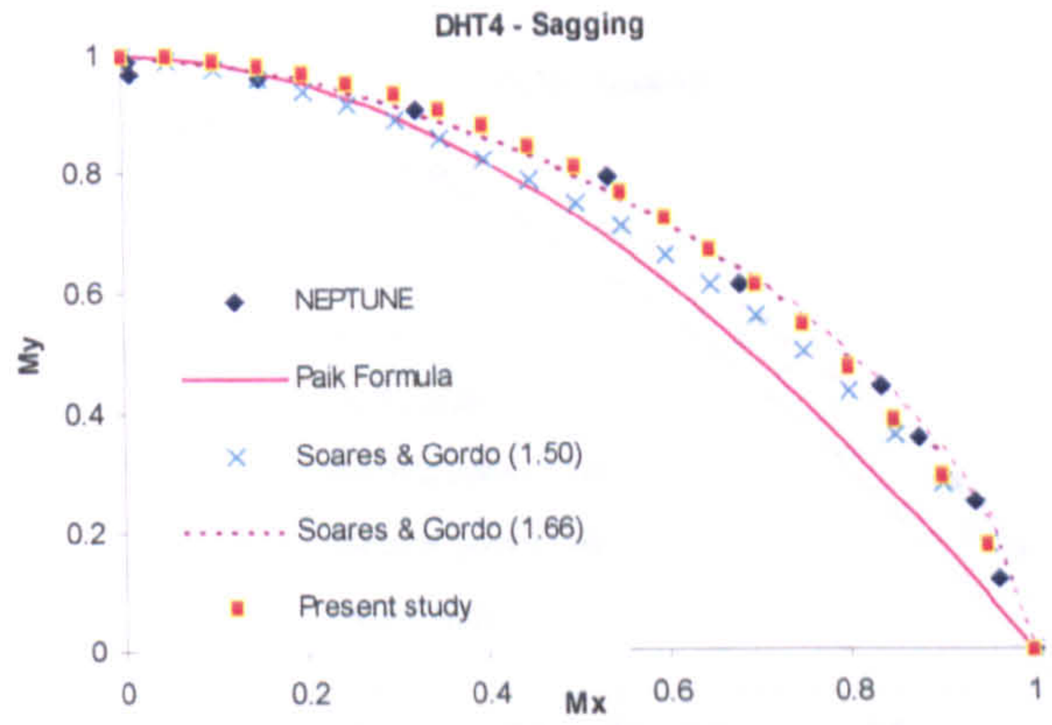
DHT4 - Sagging
My
Mx
NEPTUNE
Paik Formula
Soares & Gordo (1.50)
Soares & Gordo (1.66)
Present study
0
0.2
0.4
0.6
0.8
1

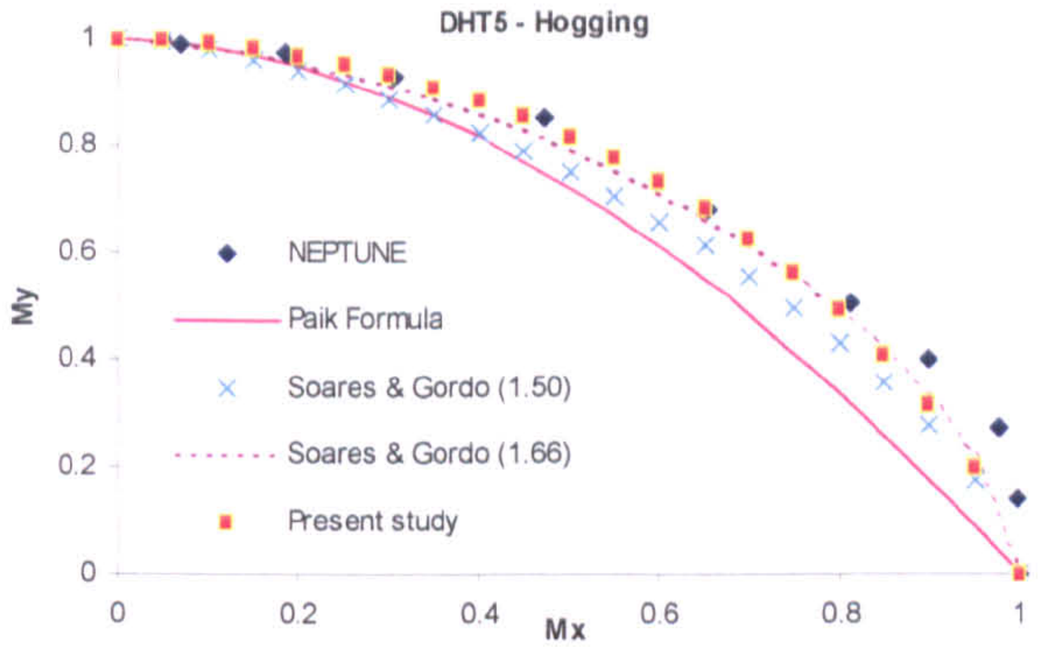
DHT5 - Hogging
My
Mx
NEPTUNE
Paik Formula
Soares & Gordo (1.50)
Soares & Gordo (1.66)
Present study
0
0.2
0.4
0.6
0.8
1

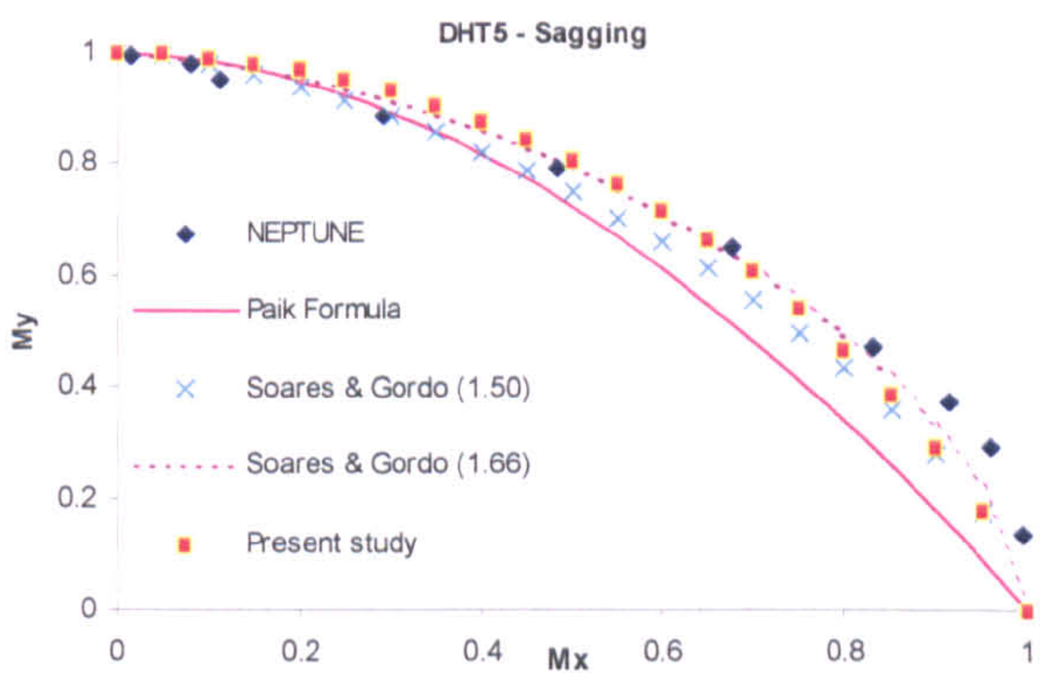
DHT5 - Sagging
My
Mx
NEPTUNE
Paik Formula
Soares & Gordo (1.50)
Soares & Gordo (1.66)
Present study
0
0.2
0.4
0.6
0.8
1

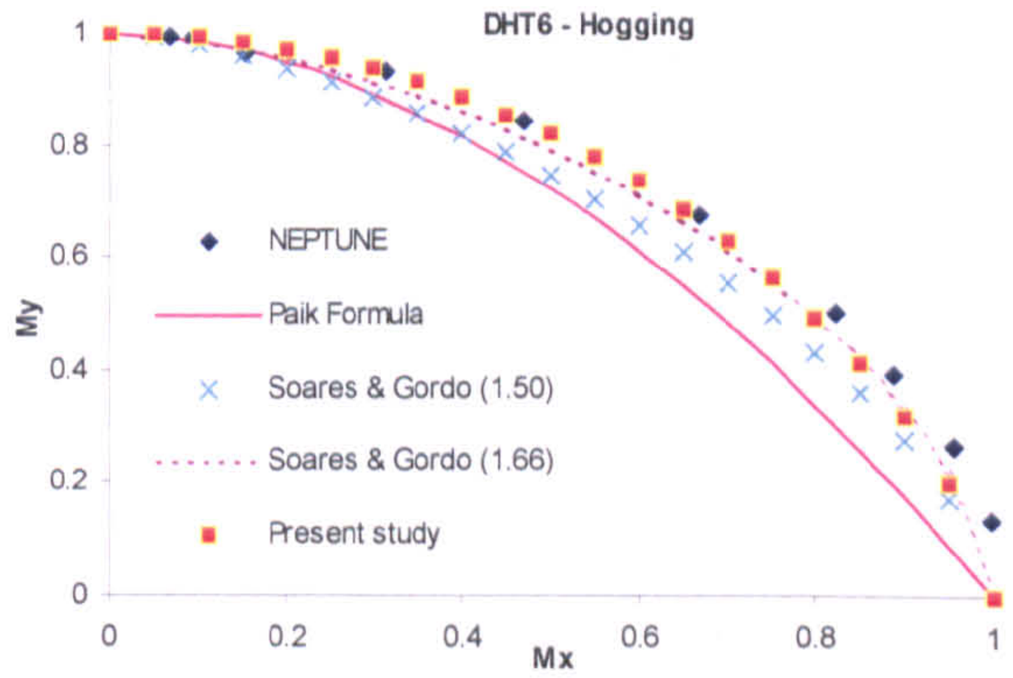
DHT6 - Hogging
My
Mx
NEPTUNE
Paik Formula
Soares & Gordo (1.50)
Soares & Gordo (1.66)
Present study
0
0.2
0.4
0.6
0.8
1

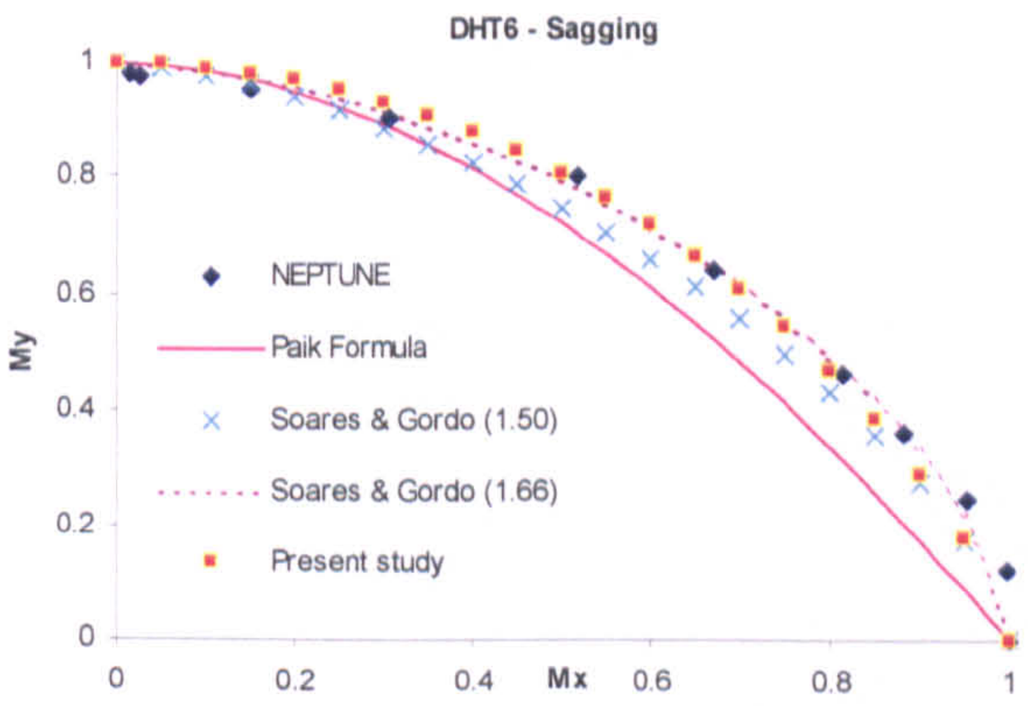
DHT6 - Sagging
My
Mx
NEPTUNE
Paik Formula
Soares & Gordo (1.50)
Soares & Gordo (1.66)
Present study
0
0.2
0.4
0.6
0.8
1

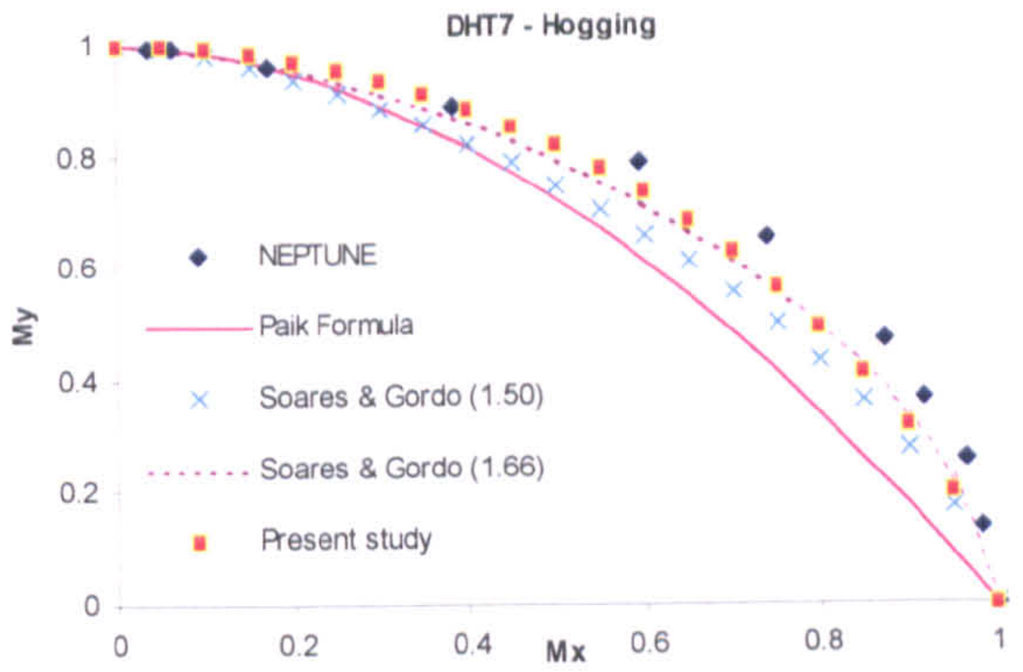

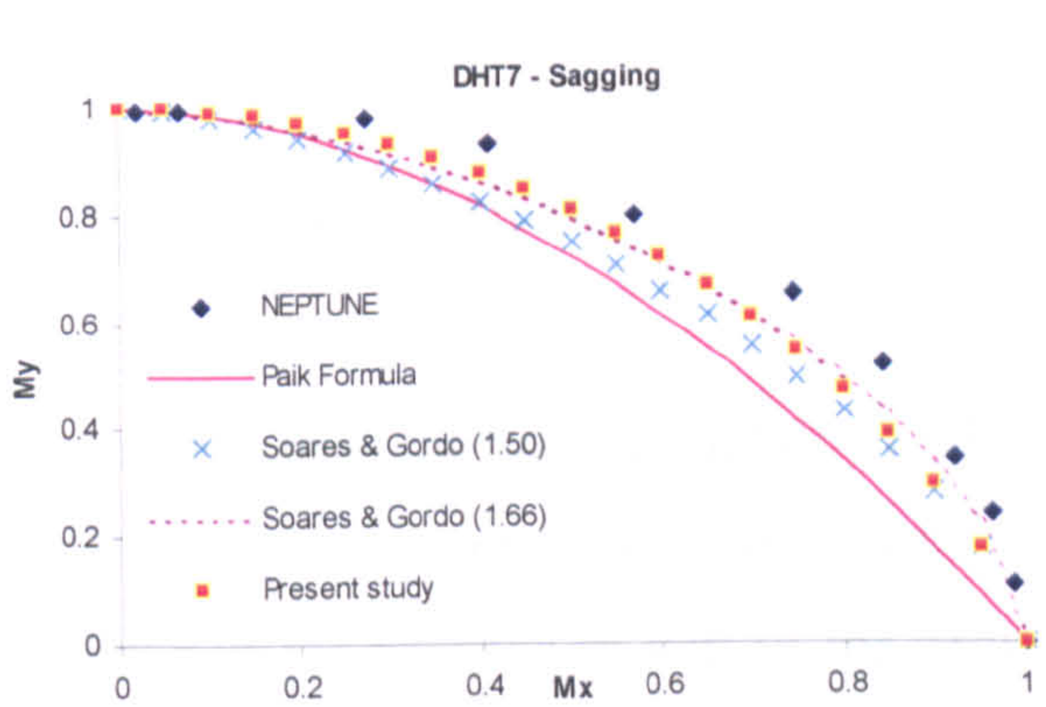

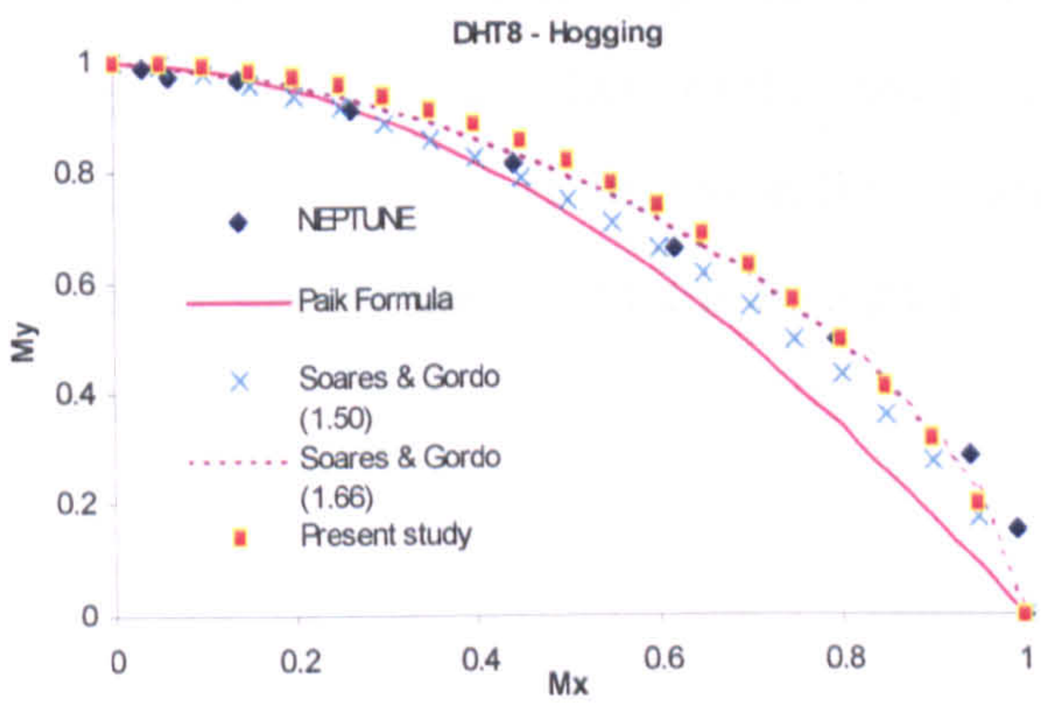

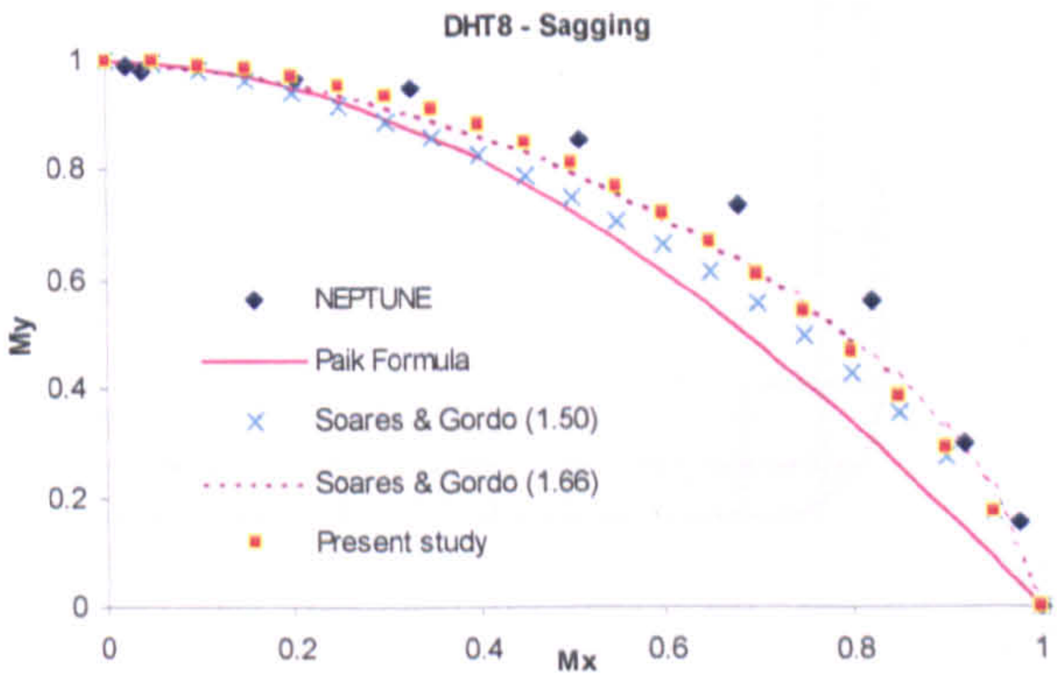

Figure 5.10: Interaction curves for tankers under coupled bending moment

In order to get better correlation for hogging and sagging cases separately in tanker structures following simple expressions are proposed, which is,

$$\left(\frac{M_x}{M_{xu}}\right)^2 + \left(\frac{M_y}{M_{yu}}\right)^a = 1 \qquad (5.15)$$

Where, $a = 1.45$ for hogging case and $a = 1.35$ for sagging case are proposed in this study.

5.3.3 General cargo & Container ships

The process used for tankers and bulk carriers are applied to the container ships and general cargo. The midship sections are shown in Figure 5.11. The principle differences are a consequence of the absence of part of the deck and are due also to the existence of stockier plate elements in this region as compared with those in the tankers. Thus, the container vessels and general cargos are more sensitive to buckling under hogging than sagging in general cases. Due to the low position of the neutral axis in upright bending, which promotes lower strains in the bottom than in the deck, the maximum strength to resist the bending moment is normally achieved at angles of heel lower than 90 degree.

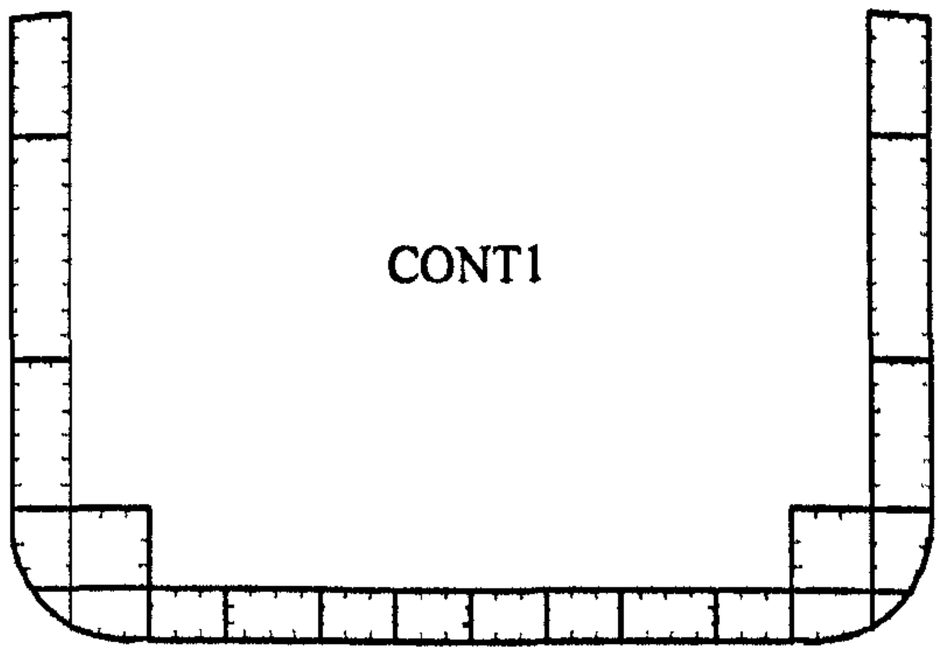

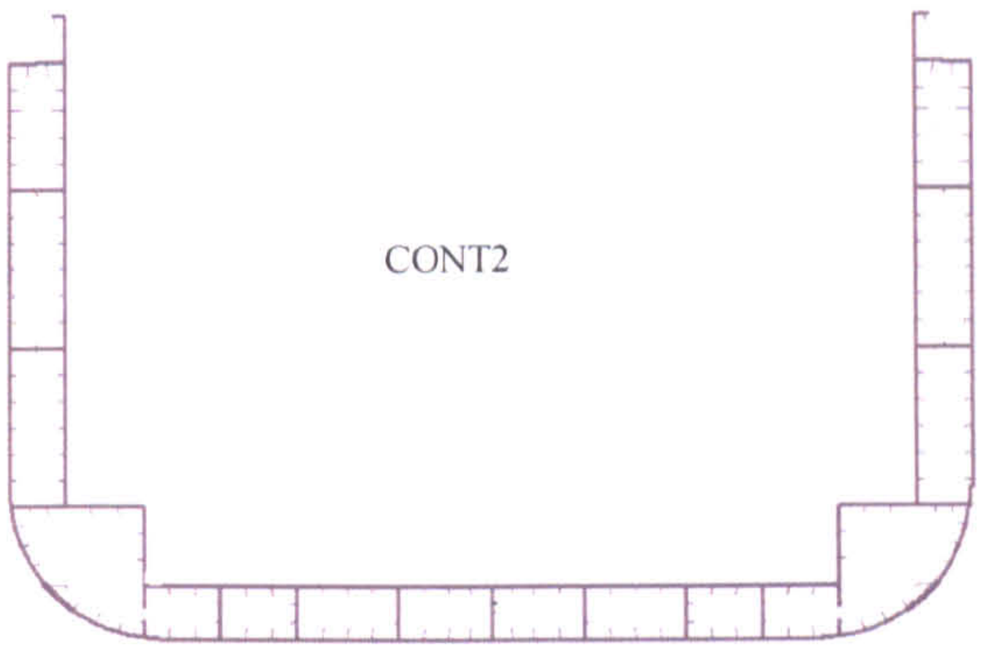

Figure 5.11: Midship cross -section of two container ships and one general cargo

A series of plots is presented in Figure 5.12 to illustrate the behaviour and the hull girder ultimate capacity of container ships and general cargo in case of combined bending moment with respect to angle of curvature vector.

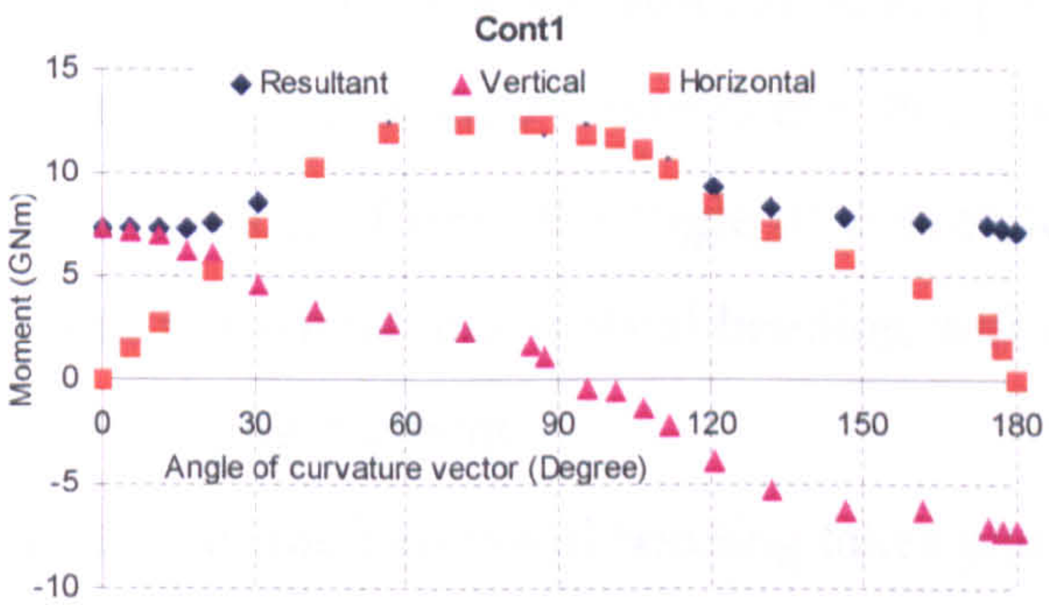

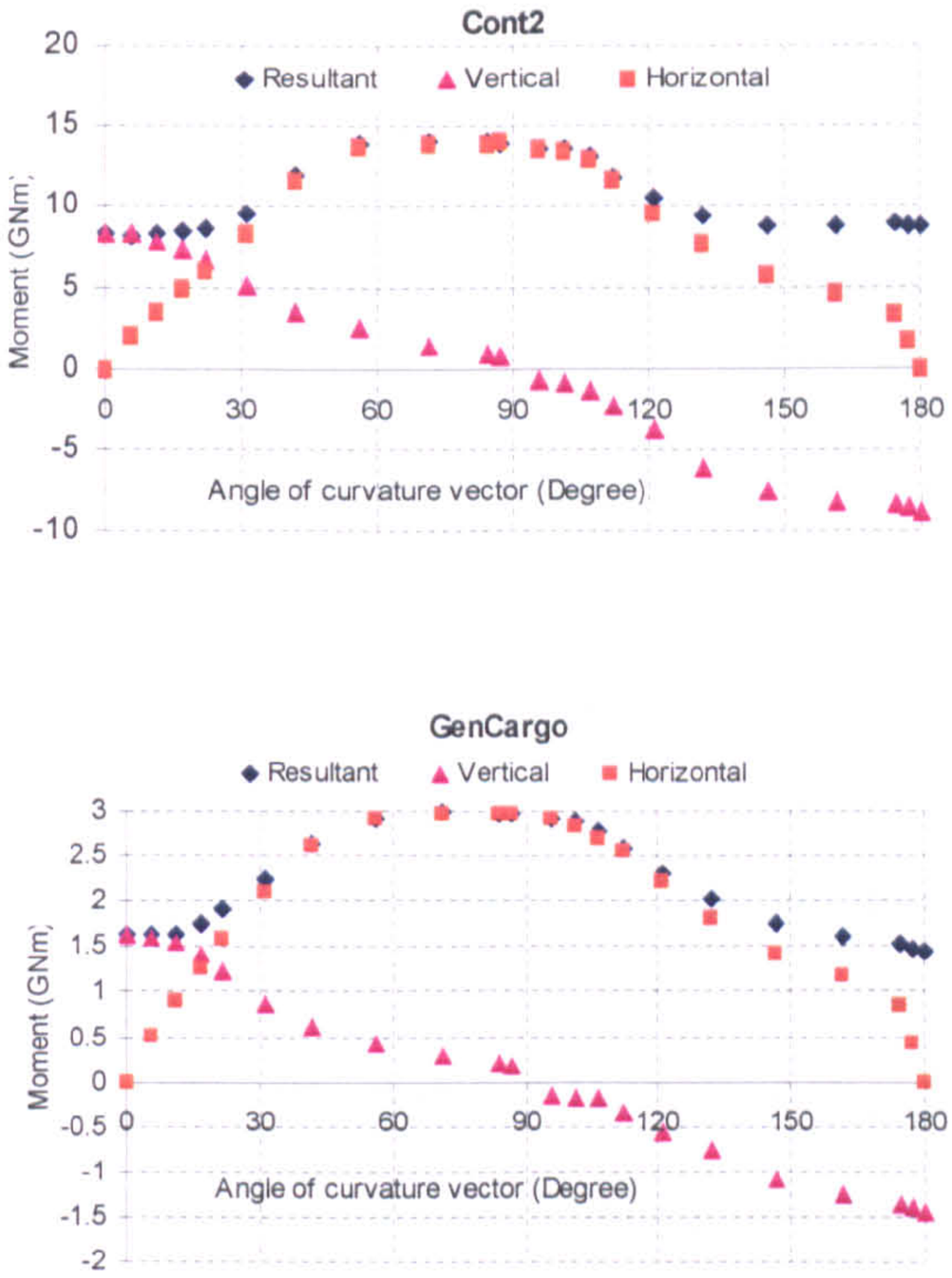

Figure 5.12: The magnitudes of the moment components with respect to angle of the curvature vector

For Cont1 the following characteristics can be drawn through this investigation.

- When $\theta = 90$ degree, there exist both horizontal and vertical bending moments on the hull cross-section. For the Cont1, when $\theta = 90$ degree, the horizontal moment is 12.19 GNm and vertical bending moment is 2.55 GNm. The angle of the resultant curvature vector is $\varphi = 89.60$ degree.
- When $\varphi = 90$ degree is for Cont1 the angle of curvature vector is $\theta = 94.45$ degree. Thus, both horizontal and vertical bending will occur under action of a pure horizontal bending moment.
- The maximum value of the horizontal bending takes place at $\theta = 70.05$ degree and $\varphi = 83.55$ degree. The maximum horizontal bending moment is 12.40 GNm. At the moment the horizontal bending moment reaches its maximum, there exists a vertical bending moment on the hull cross-section, which is 2.80 GNm.

For GenCargo the following characteristics can be drawn through this investigation.

- When $\theta = 90$ degree, the value of horizontal bending moment is 2.966 GNm and vertical bending moment is 0.205 GNm. The angle of the resultant bending moment is $\varphi = 90.15$ degree.
- When $\varphi = 90$ degree, the angle of the curvature vector is $\theta = 100.53$ degree. Thus, both horizontal and vertical bending will occur under action of a pure horizontal bending moment.
- The maximum value of the horizontal bending takes place at $\theta = 71$ degree and $\varphi = 81$ degree. The maximum value of horizontal bending moment is 2.986 GNm. At the moment of horizontal bending moment reaches its maximum, there exists a vertical bending moment on the hull cross-section, which is 0.286 GNm.

The relationship between angle of the resultant bending moment vector and angle of the curvature vector for two container ships and one general cargo is plotted in Figure 5.13. It is seen that it is not same due to non-linearity caused by buckling.

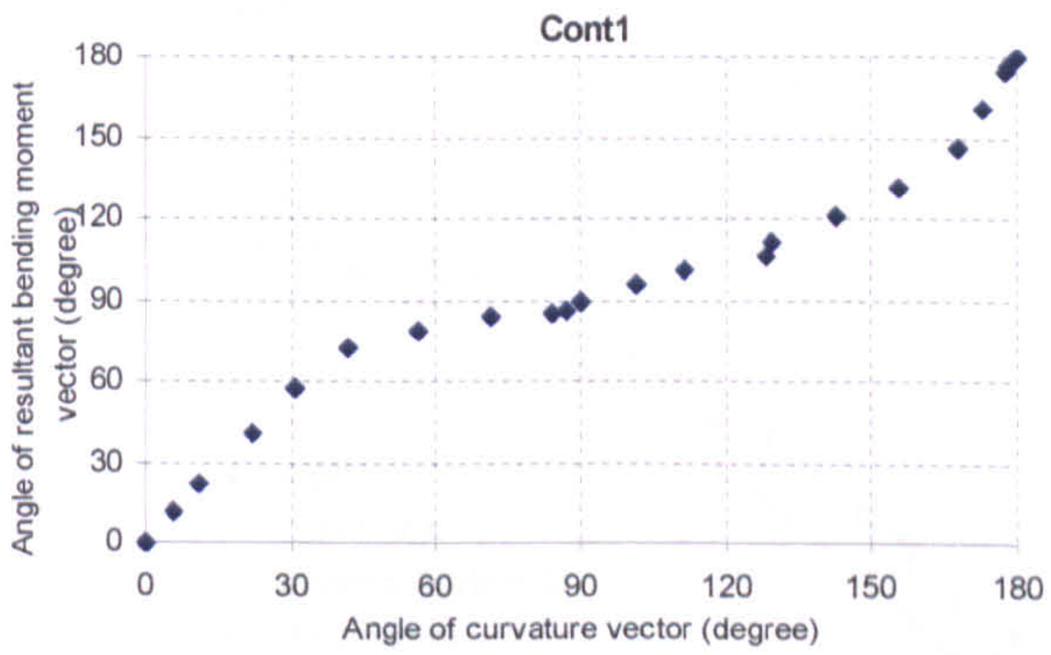

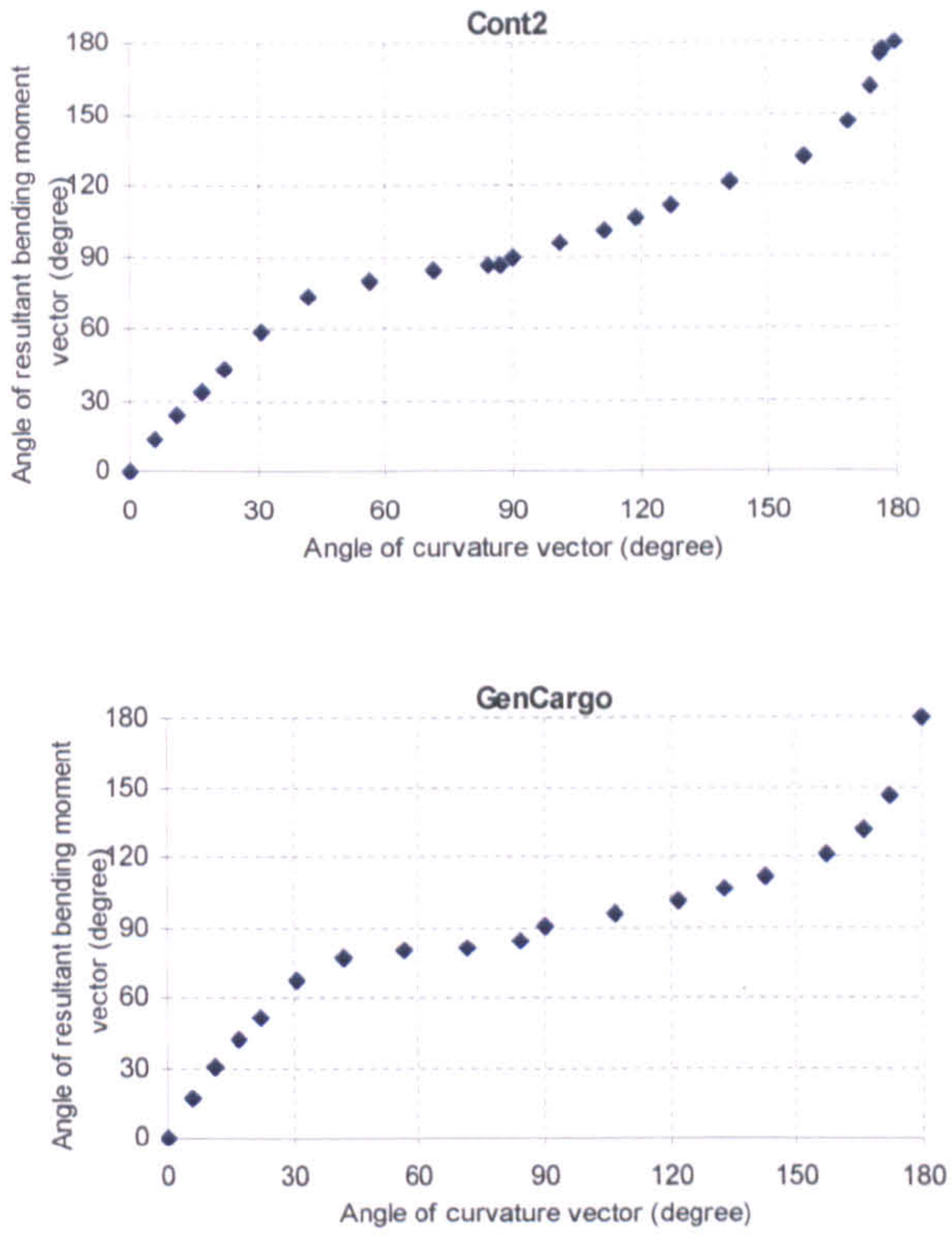

Figure 5.13: Relationship between angle of curvature and resultant bending moment

The interactions between horizontal and vertical components are presented in Figure 5.14. It is also seen that the formula proposed by Gordo & Soares (1997) fits good in hogging case, while it considerably underestimates in sagging case for container and general cargo ships.

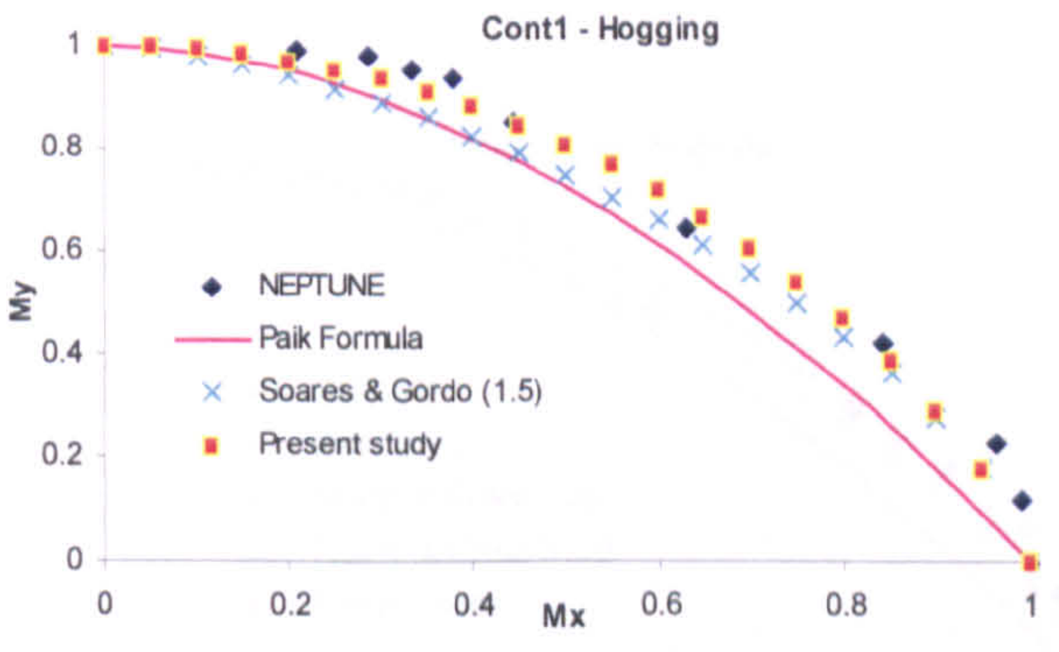

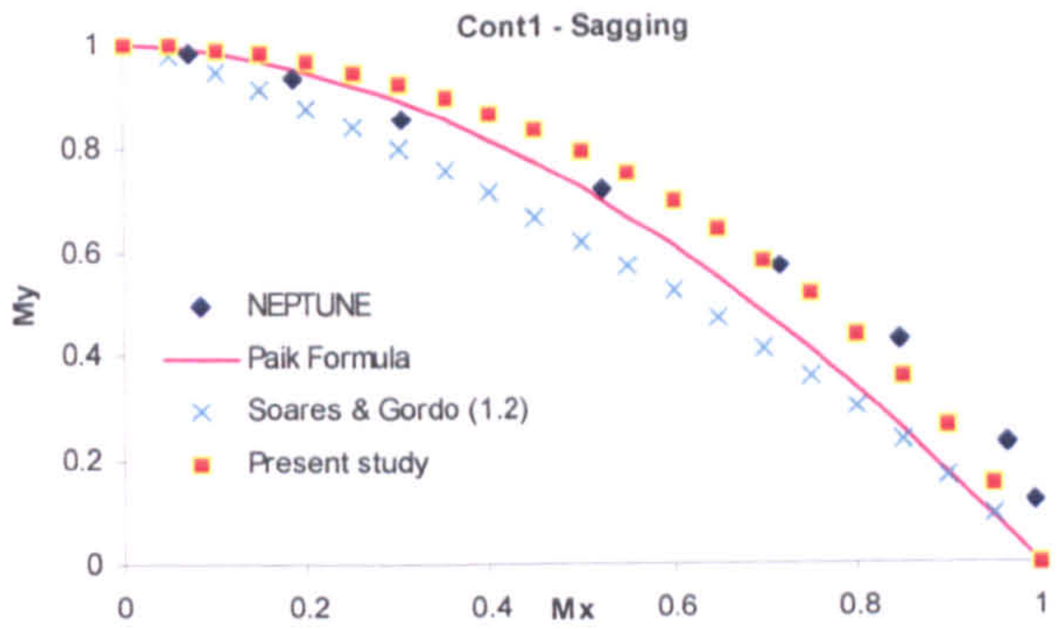
Cont1 - Sagging
My
Mx
NEPTUNE
Paik Formula
Soares & Gordo (1.2)
Present study
0
0.2
0.4
0.6
0.8
1

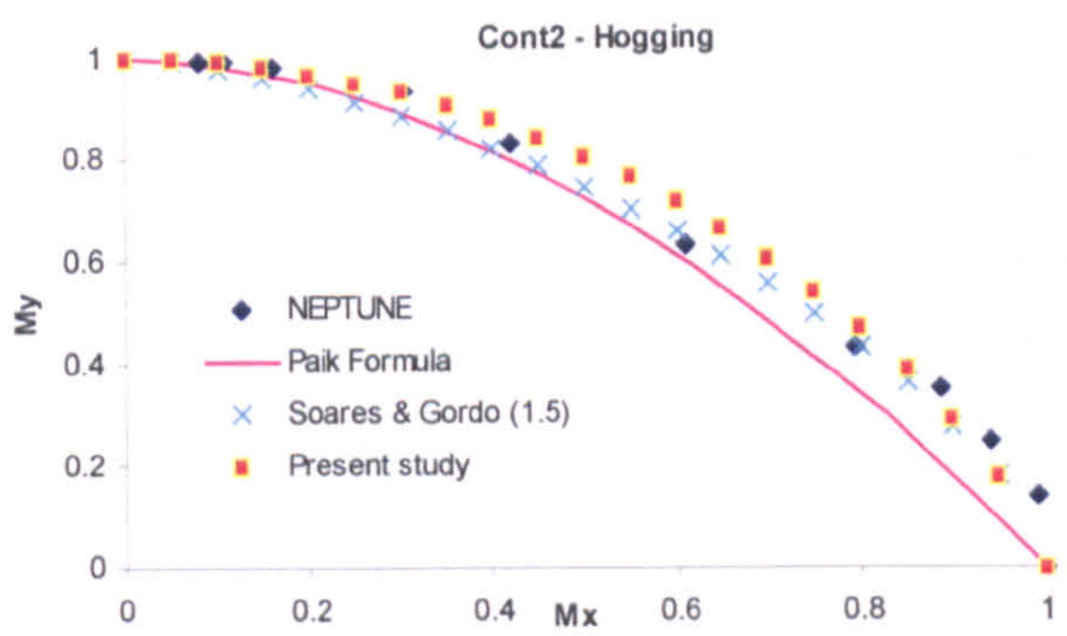
Cont2 - Hogging
My
Mx
NEPTUNE
Paik Formula
Soares & Gordo (1.5)
Present study
0
0.2
0.4
0.6
0.8
1

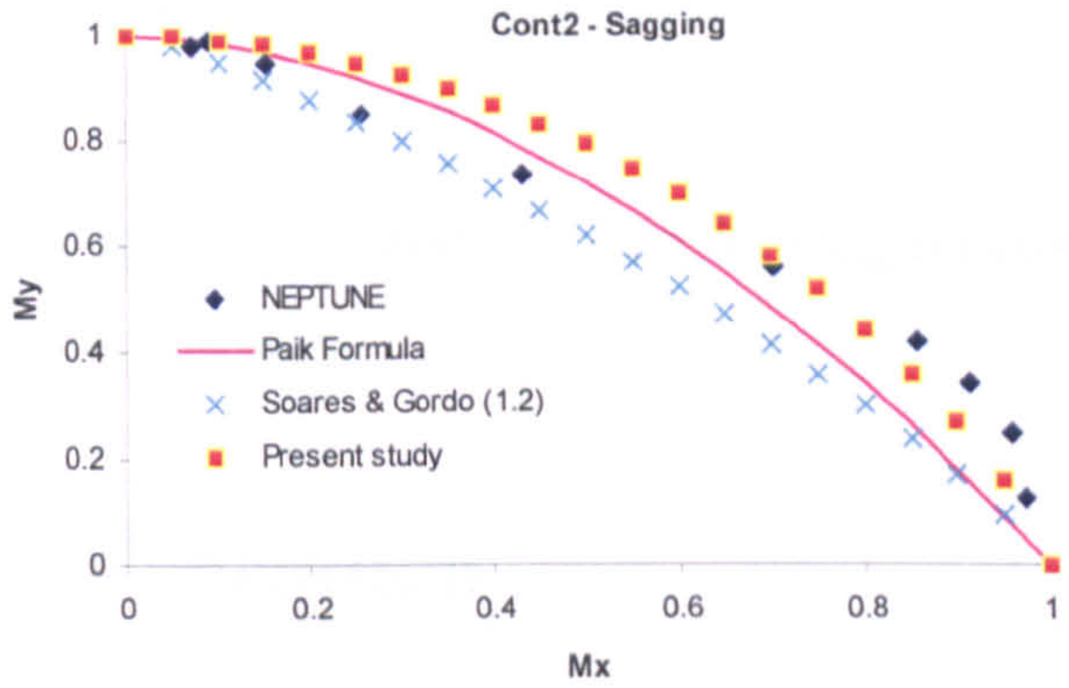
Cont2 - Sagging
My
Mx
NEPTUNE
Paik Formula
Soares & Gordo (1.2)
Present study
0
0.2
0.4
0.6
0.8
1

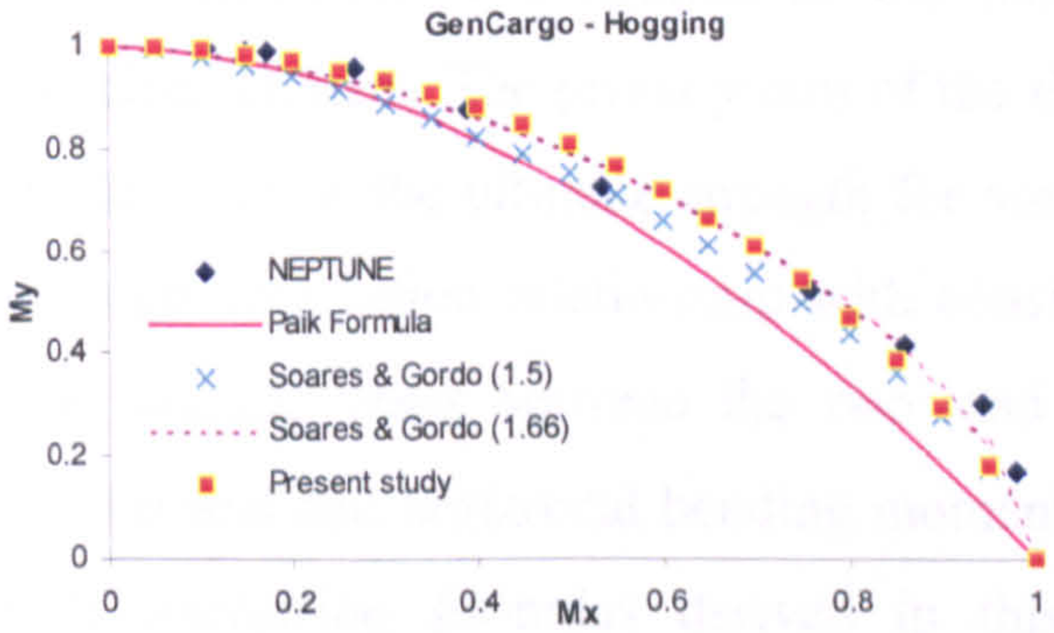
GenCargo - Hogging
My
Mx
NEPTUNE
Paik Formula
Soares & Gordo (1.5)
Soares & Gordo (1.66)
Present study
0
0.2
0.4
0.6
0.8
1

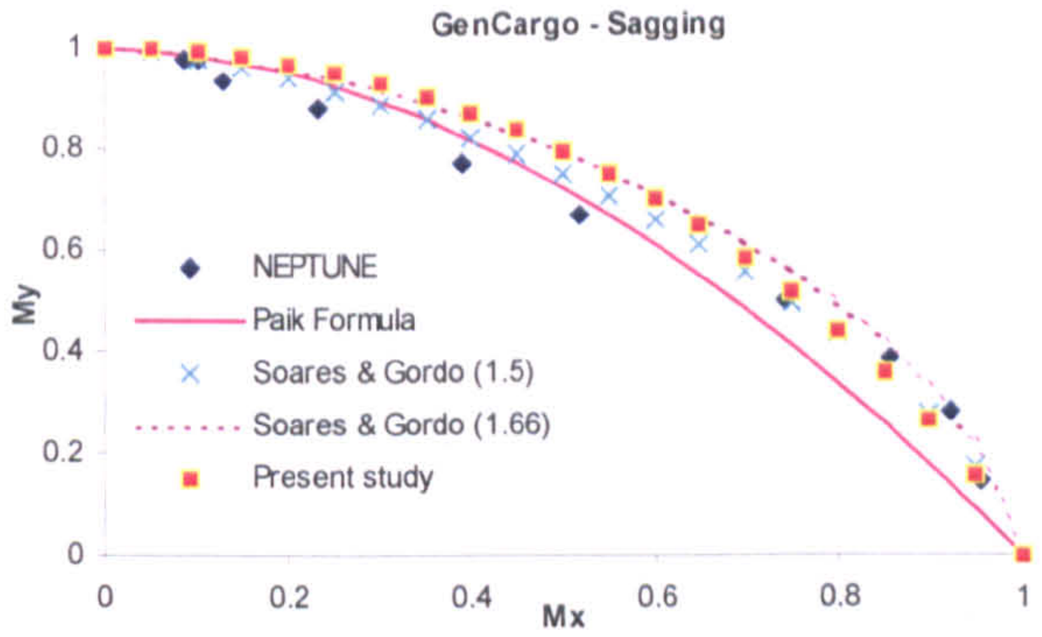

Figure 5.14: Interaction curves for general cargo & container ships under coupled bending moment

For container and general cargo ships the following simple expressions are also proposed. It is seen that from plots the present study's equations have very good correlation with actual NEPTUNE data.

$$\left(\frac{M_x}{M_{xu}}\right)^2 + \left(\frac{M_y}{M_{yu}}\right)^a = 1 \qquad (5.16)$$

Where $a = 1.35$ for hogging case and $a = 1.25$ for sagging case in container and general cargo ships are now proposed.

5.4 Discussion & Conclusion

Chapter-5 presents the most extensive investigation of the hull girder ultimate strength under coupled bending moment. The primary aim of the this research study is to investigate the characteristics of the ultimate strength for various ship designs and to derive a simple strength interaction relationship with considering a separate treatment for hogging and sagging cases between the two load components that normally act on it, namely vertical and horizontal bending moment. It is shown that the ultimate hull strength interaction formulas derived in this paper provided reasonably accurate fits to actual NEPTUNE output. Therefore, the results presented can be extremely useful for the trend analysis in ship design or in the reliability analysis of hull girder collapse.

It is also found that the interaction curve is asymmetrical because the hull cross-section is not symmetrical about the horizontal axis under compression is different from that tension due to non-linearity caused by buckling. The angle of the resultant bending moment vector and that of the curvature vector are different in general cases. The evaluation of the ultimate strength using NEPTUNE is believed to be an adequate estimation of the ultimate load capacity of the ship. Further refinement using non-linear FE analysis requires considerably more engineering and computational effort and is not expected to yield substantially different results.

Chapter 6

Residual Strength Analysis Using Non-linear Finite Element Method for Collision Damage Condition

6.1 Introduction

The ultimate strength of a damaged hull can be predicted either using a 2-D method developed by Smith & Dow (1981a, 1981b) or using a 3-D non-linear finite element analysis as described by Chen *et al.* (1983). The two-dimensional analysis method developed by Smith & Dow is based on the prediction of moment / curvature relationship and hence the collapse strength of a hull girder can be found from the non-linear stiffness characteristics of elements of a hull section by incremental analysis. The method can account for both vertical and horizontal bending and the presence of shear and torsion.

The three-dimensional non-linear analysis method developed by Chen *et al.* takes into account elastic-plastic material properties, geometrically non-linear behaviour of the elements, and their buckling and post buckling strength. The method developed is applicable to a hull girder strength subjected to bending, shear and torsional loads.

The current methods of analysis are possible to assess residual strength that is consistent with the various forms of damage. While the two-dimensional procedure is economical and good for quick assessment of damage consequences, it may predict very conservative results because of the numerous assumptions on the stress fields, boundary conditions and extent of the damage modelled. The three-dimensional method is more fundamental in nature with very few assumptions and overcomes most of the limitations of the two-dimensional method. However, it is not so practical since it is expensive and requires a high level of expertise and considerable amount of computer resources.

The assessment of the true ultimate strength and the progressive collapse behaviour of ship hull girders have been pursued for decades, but assessments using standard non-linear finite element tools started to emerge first in the late 1990's. Before that the lack of computational resources forced the researchers to resort to 2-D simplified analytical methods or specialized finite element methods that enables the use of coarse mesh models. The keys to these methods are element formulations that include the integrated effect of local buckling and inelastic material behaviour in their compressive response characteristics. The accuracy of such codes is highly dependent on the accuracy and physical consistency of the selected characteristics.

Most of the finite element based on progressive collapse analyses published so far seems to be dealing with tankers for oil, where the loading and the structural arrangement allows for modelling and analyses of a single cargo tank or even only a few frame spacing of a tank.

The application of simplified analytical method assumes that individual panels and hard corners will fail individually and there is no interaction between these components and there is no general instability of larger segments or general instability of the complete cross-section. While this is generally true for typical intact ship sections, it may not be the case for a severely damaged structure. Therefore, present chapter is dedicated to investigate on this question, where a new procedures, have not been conducted in the past, are introduced using explicit-to-implicit sequential non-linear finite element solution. The new adopted analyses are capable of taking into account to simulate the bending response of the damaged tanker induced by collision accident and calculate its ultimate load carrying capacity accurately without removing any structural members.

In order to include damage that taken place during ship-ship collision simulation on the residual strength calculations, all elements failed have been removed from the intact original configuration according to LS-DYNA numerical contact simulation for both two methods employed such as the two-dimensional simplified procedure and the three-dimensional non-linear finite element analysis. The results obtained are then compared with the most accurate new approach adopted.

A case study of a tanker vessel is used to carry out progressive collapse analyses of the damaged states considered.

The theory of the basics of the non-linear finite element method is presented in Appendix-1 while the analyses steps are mainly focused on this chapter.

6.2 Description of the Analyses

6.2.1 Vessel particulars

The subject vessel for the analyses is a 5600 DWT chemical tanker built in Turkey in 2003. It has six cargo holds with carrying 1.54 ton / m^3 high-density cargoes. The main particulars of the vessel are:

DWT:	5600 tonnes
L_{OA}:	107.45 m
L_{BP}:	99.95 m
Depth (deck line):	7.25 m
Breadth:	16.0 m
Design draught:	5.80 m
Cargo capacity:	6500 cbm
Material:	Steel Grade A (yield stress = 235 MPa)

The midship cross-section is given in Figure 6.1, while the longitudinal profile section is illustrated in Figure 6.2.

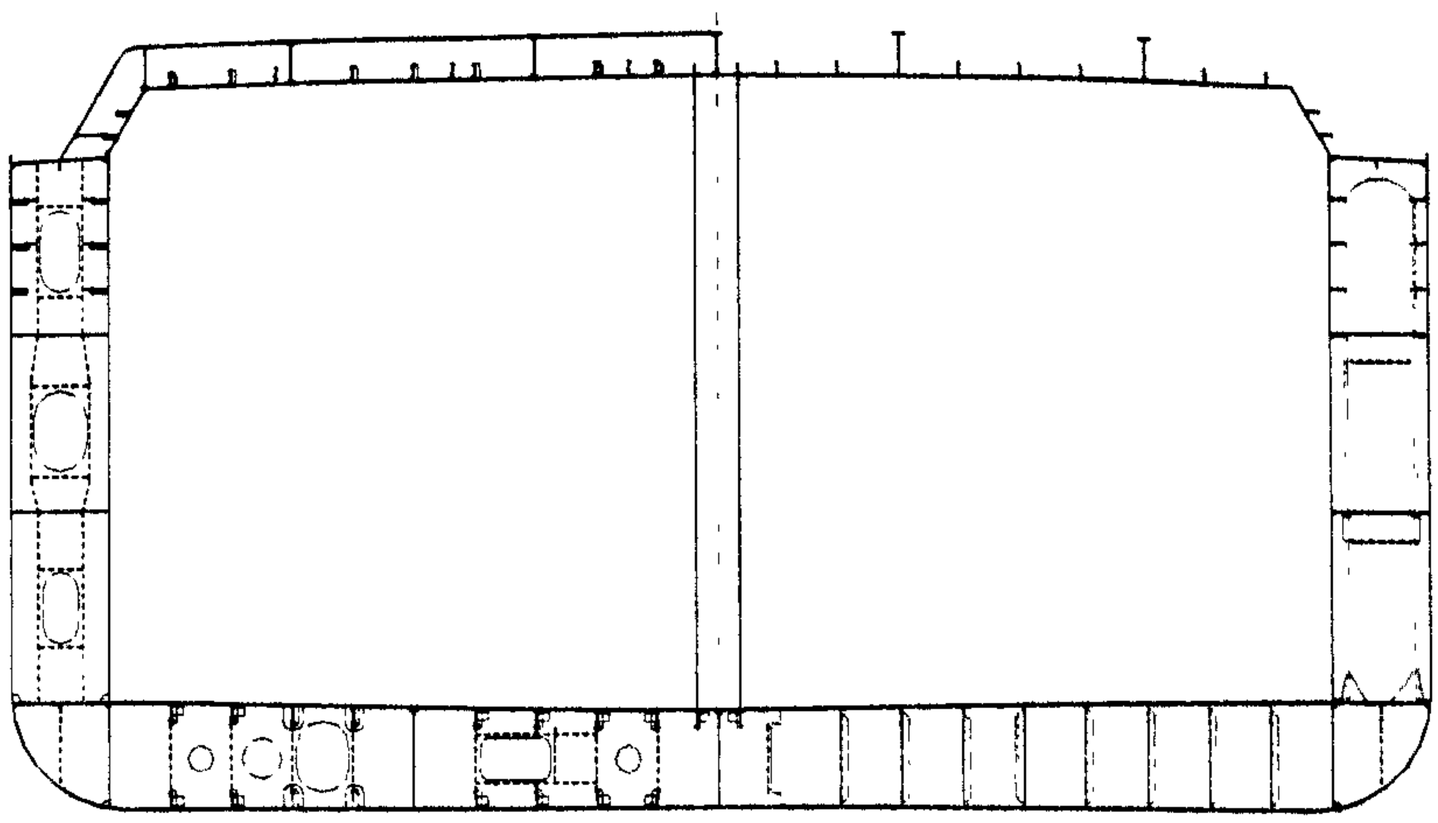

Figure 6.1: Midship cross section of 5600 DWT chemical tanker

As seen from Figure 6.1, the ship studied has been designed by two types of stiffening systems such as transverse and longitudinal.

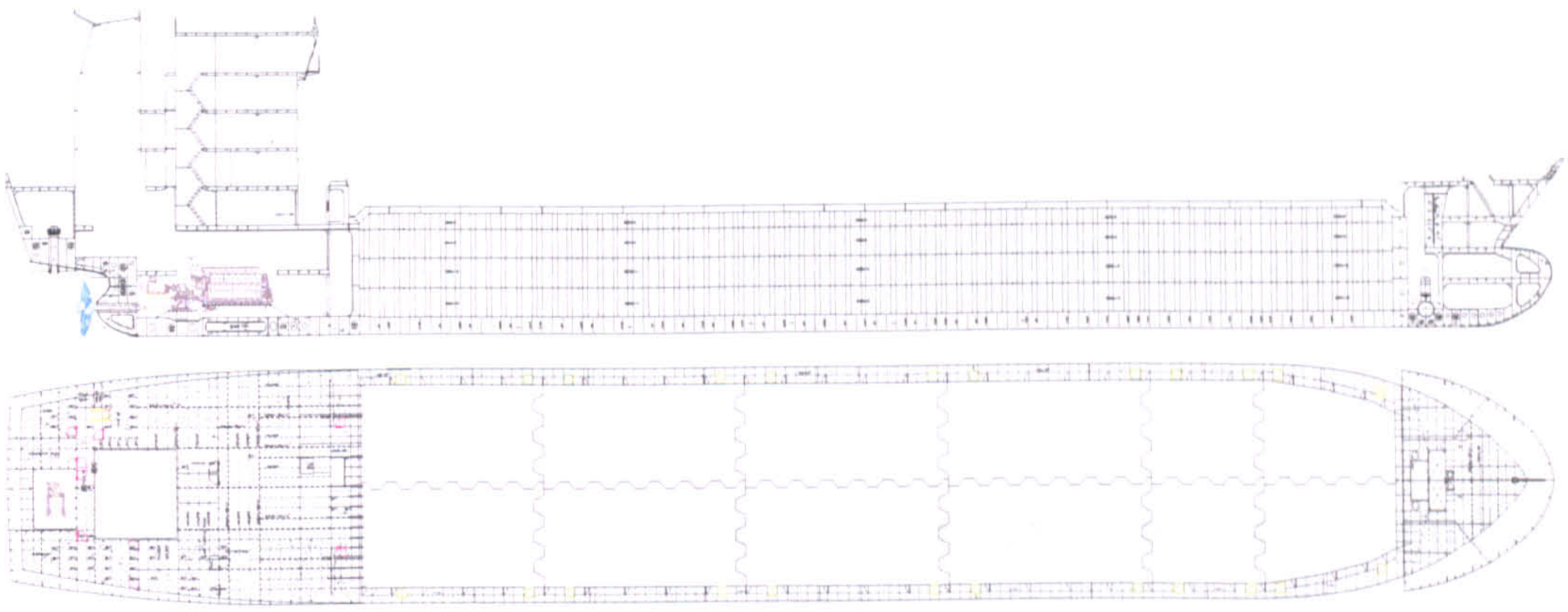

Figure 6.2: Longitudinal section of 5600 DWT chemical tanker

6.2.2 Analysis codes

The two-dimensional analysis on the hull girder ultimate strength of the damaged tanker using simplified method based on an incremental – iterative approach is applied, where a computer code NEPTUNE is developed using the average stress-average strain relationships of elements derived semi-analytically.

The two types of the finite element analyses are carried out using general purpose FEM programs only ANSYS (implicit code) and combination of ANSYS (implicit code) & LS-DYNA (explicit code). When removed structural members to define damage event, ANSYS (implicit) is only considered.

The simulation of new approach finite element processes requires the capabilities of both ANSYS (implicit) and LS-DYNA (explicit) analyses. To solve these problems, both solution methods are need to be used, e.g., an explicit solution followed by an implicit solution. LS-DYNA is an explicit dynamics program intended to solve short duration dynamics problems. Collision analysis is performed by means of LS-DYNA. If an engineering process contains phases that are essentially static or quasi-static, then these phases are best analysed using the ANSYS implicit code. Ultimate hull girder strength analyses of damaged tanker are carried out by means of ANSYS implicit code. Procedures combining the ANSYS

implicit solver with the LS-DYNA explicit solver provide an extremely powerful tool that can be used to simulate many complex residual strength calculations of damaged ship structures.

6.2.3 Finite element model

The model geometry used in the analyses is illustrated in Figure 6.3, and represent the full breadth one cargo hold in the midship area of the vessel. This longitudinal extent is chosen to allow solving converge problems under applied vertical bending moment.

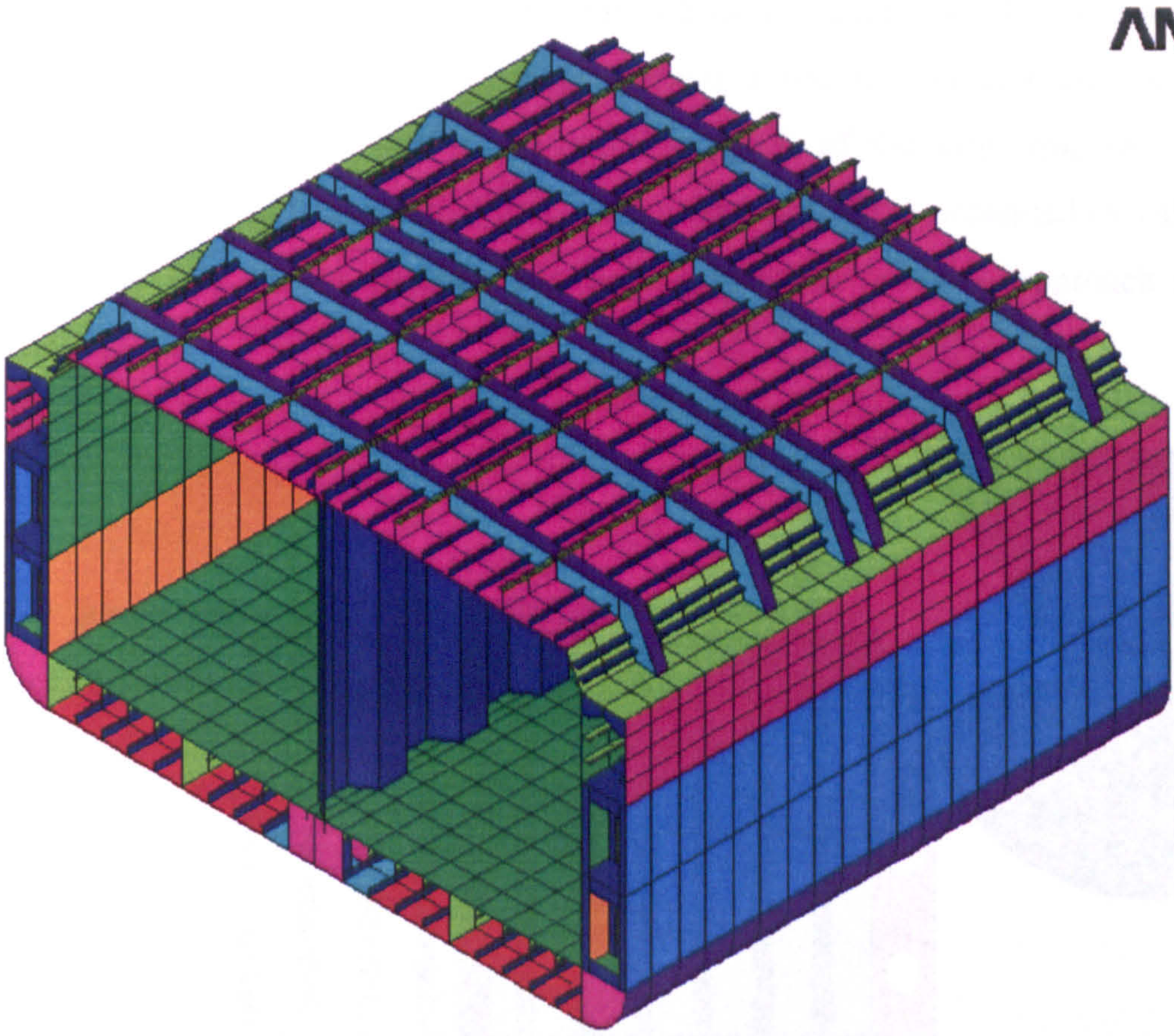

Figure 6.3: The one cargo hold ANSYS model geometry used in the analyses

The structure is analysed with full non-linear capabilities to study on the impact of buckling and inelastic effects on the response of the structure.

The typical shell element is considered for the whole simulated structure, which gave a total number of 42825 shell elements. Collision contact was modelled between striking rigid body and all structural members, including self-contact, where the friction coefficient was assumed as 0.30. Strain rate effects were included in the material model, namely Cowder-Symonds parameters $C_{cs} = 40.4$ (1/sec) and $q = 5.5$.

To overcome hourglassing problem, the stiffeners and the flanges were modelled with fully integrated shell elements with five-integration points through the thickness. The rest of the ship structure was modelled with under integrated Belytschko-Tsay elements with one integration point in plane and five-integration points through the thickness. The collision analysis model is shown in Figure 6.4. The impact speed of the rigid striking ship is 8 m/sec, and the total simulated time is 0.3 sec. The mesh density in the contact region is 100 mm while a slightly coarser mesh is used to be 300 mm in the remaining parts of the ship structure. Plastic-kinematics material is accounted into contact analyses and is presented in Table 6.1. It is noted that failure criterion has been considered on GL's approach (2003), namely 13 %.

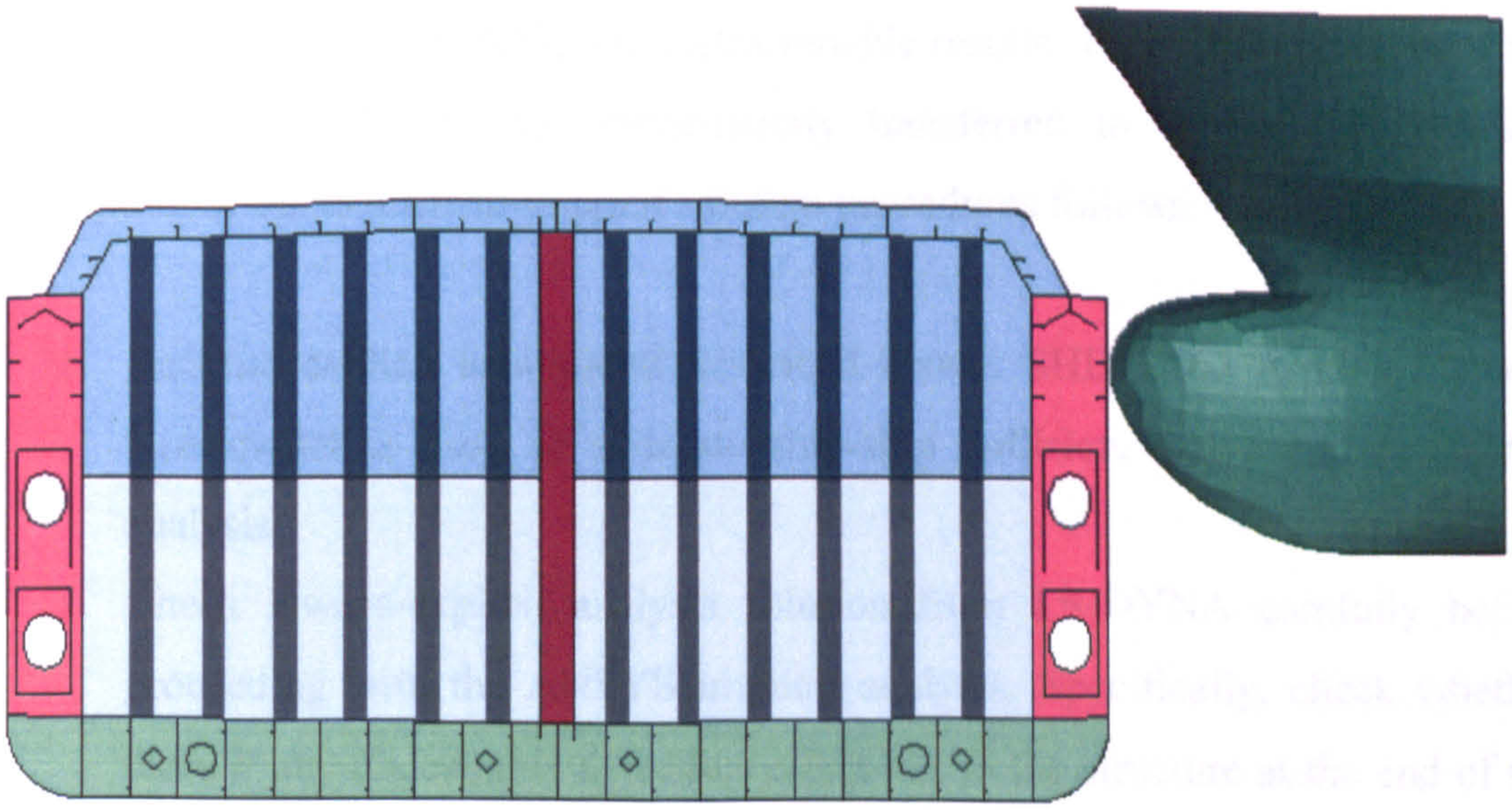

Figure 6.4: Dynamics impact analysis conducted in LS-DYDA explicit FEM code

Table 6.1: Material properties of plastic – kinematics used in LS-DYNA

Density (kg/mm^3)	7.85e-6
Young's modulus (MPa)	210000
Poisson ratio	0.30
Yield strength (MPa)	235
Tangent modulus (MPa)	1280
Hardening parameter	0
Strain rate (C, 1/sec)	40.4
Strain rate (P)	5
Failure Strain (GL Approach, 2003)	0.13

Multiply Processor Computer (MPC) which has 32 CPU (1 CPU has 512 MB RAM) was employed for the tanker's collision simulation. Solution time 0.3 seconds was regarded and CPU time was nearly 4 hours. The finite element model used for the hull girder strength solutions is the same model that has been used for the collision simulations. The model was initially developed for the analysis with the explicit FE code LS-DYNA. For the ultimate load simulations it was decided to use an implicit code. This decision is based on the fact that ANSYS provides the user with a variety of non-linear analysis sequences. Since such a task, namely the calculation of the ultimate bending capability of a damaged ship, has not been performed in the past, it was preferred to use explicit-to-implicit sequential solution methodology that is both stable and yields reliable results. The initial model used for the collision simulations was consequently transferred to ANSYS. A detailed description of the explicit-to-implicit solution procedures follows.

1. Run the explicit analysis as described above. SHELL163 explicit element type model is used to simulate ship-ship collision. Solve and finish the analysis.
2. Check always-explicit analysis solution from LS-DYNA carefully before proceeding with the ANSYS implicit analysis. Specifically, check whether there if any undesirable dynamics effect left in the structure at the end of the explicit run.
3. Convert explicit element types to corresponding companion implicit element types. The companion explicit-implicit element type pairs are SHELL163 – SHELL181.

4. Redefine the key options, shell thickness, material properties, boundary conditions, and loading values on any implicit elements that were converted to SHELL181.
5. Unselect or delete any unnecessary elements (mainly those making up any rigid bodies from the explicit analysis), or convert to null elements. Any explicit elements that remains active in ANSYS, which will produce an error.
6. Turn large deformation effects on. Once analysis is solved, any of the selected ANSYS postprocessing functions are used to review results.

Elastic-plastic material, namely, no strain hardening, is chosen in ANSYS for residual strength calculations. Arc-length static solution algorithm is used to solve converge problem. Vertical bending moment at the model end is gradually increased from low to high versus curvature increased.

6.2.4 Boundary conditions

As mentioned above the hull girder strength analyses are conducted on the one cargo tank. At the foremost and aftermost sections, special boundary conditions are applied. These constraints are shown in Figure 6.5, which are called Multi-Point Constraints (MPCs), are used to link the degree of freedom of several nodes to the degrees of freedom of one node. The degrees of freedom of the latter are independent while of the degrees of freedom of all the other nodes are dependant. In this case examined here, all the nodes of a boundary section are linked to a node at the centre of gravity of the cross-section, forming a rigid point. This way, it is possible to impose correct bending loads to the FE model. The independent nodes at the aftermost cross-section are clamped while a moment is applied at the respective node of the foremost section. This moment is oriented in such a way as to impose a vertical bending moment to the vessel. It should be noted that even tough the boundary sections remain plane after deformation due to the imposed MPCs; this is not case for the sections at the damaged area, since this is bounded by deformable bulkheads.

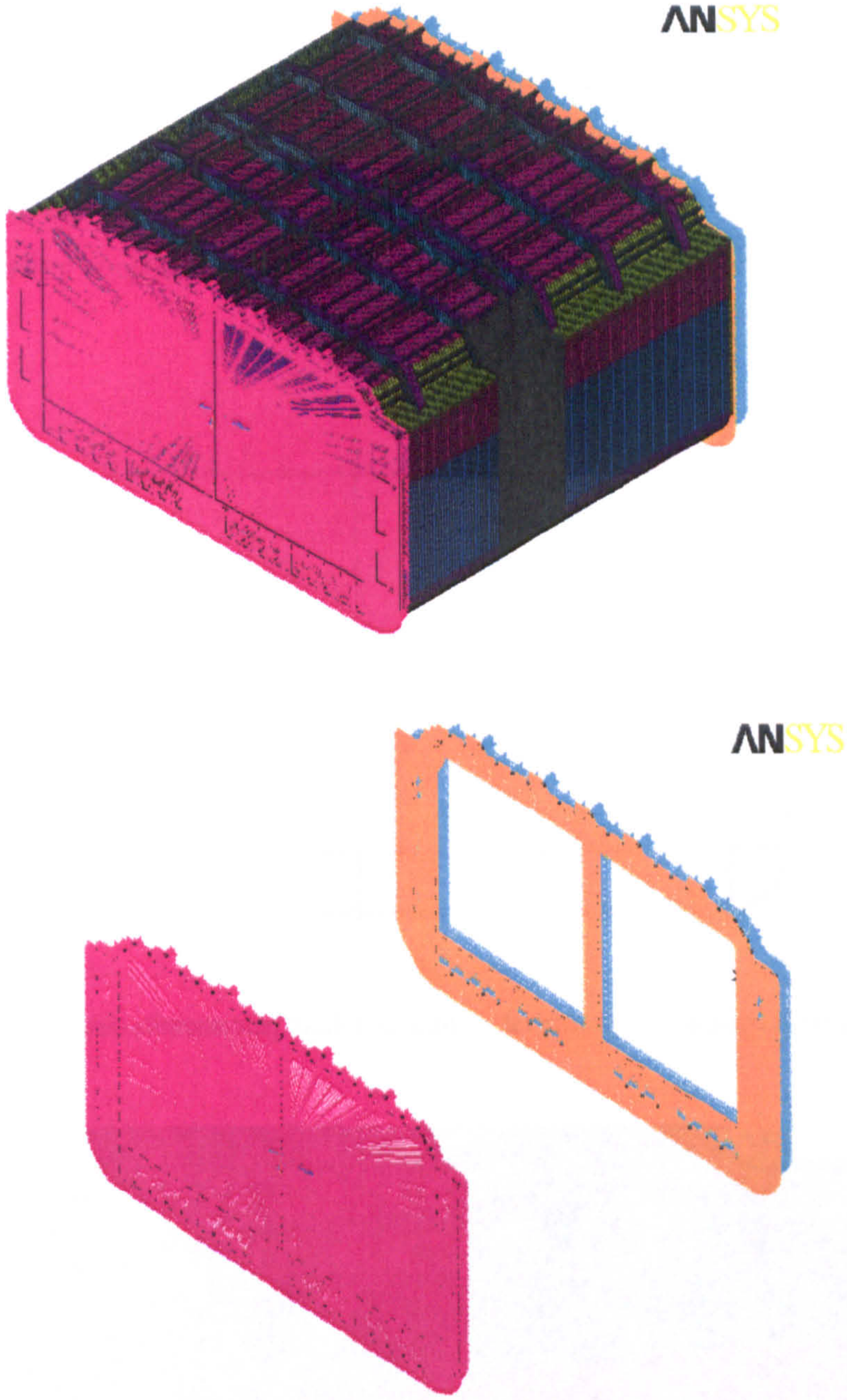

Figure 6.5: The Multi Point Constraints (MPCs) introduced to damaged tanker vessel

6.2.5 Summary of the results

Three different approaches are considered to evaluate hull girder ultimate strength capacity of a damaged tanker vessel. All calculations have been done for perfect cases since initial imperfections are extremely difficult to define in 3-D finite element models.

Figure 6.6 presents the damaged zone investigated on the two-dimensional using a developed computer code, NEPTUNE. Figure 6.7 illustrates that 3-D non-linear FEM approach, where damage zone is introduced with creating elliptical geometry with respect to collision simulation. Figure 6.8 shows that 3-D non-linear FE model, where considering explicit-to-implicit sequential solution procedures (no element removed).

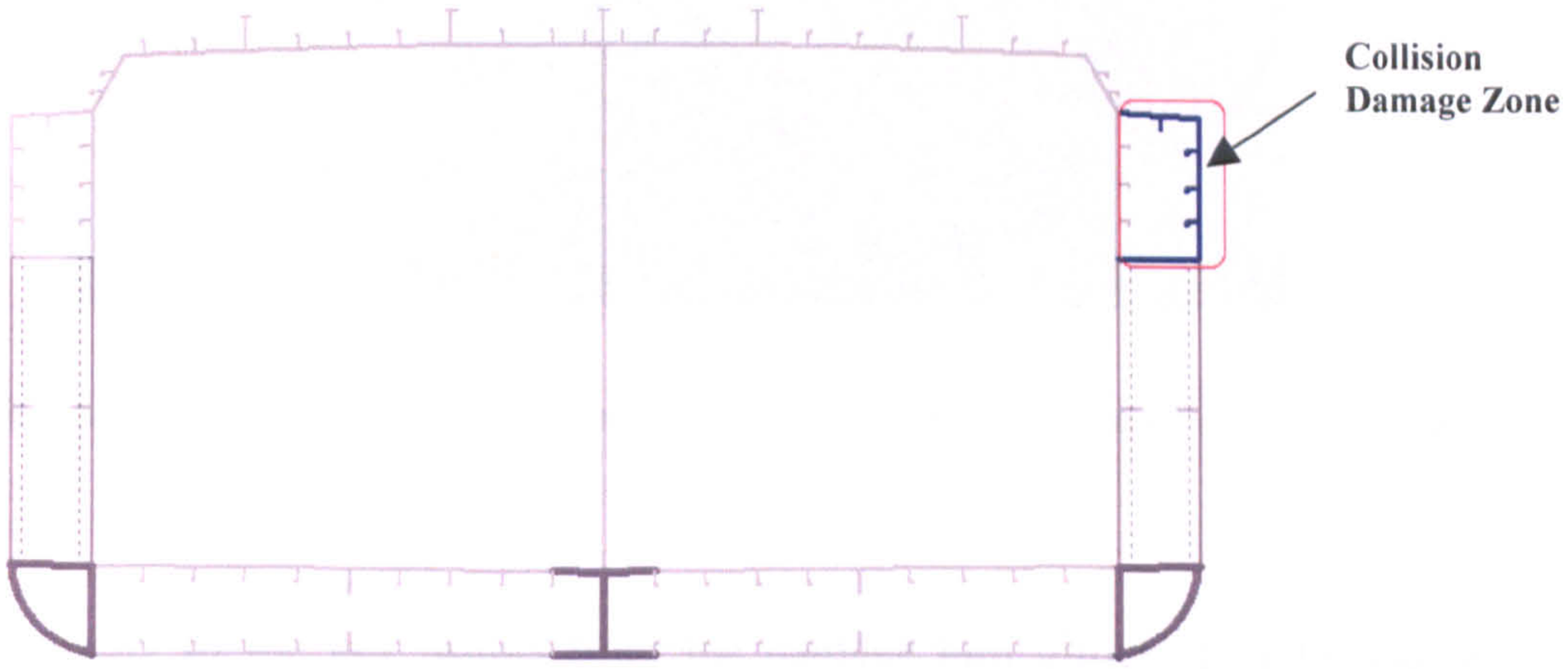

Figure 6.6: The two-dimensional model for hull girder strength of damaged tanker vessel

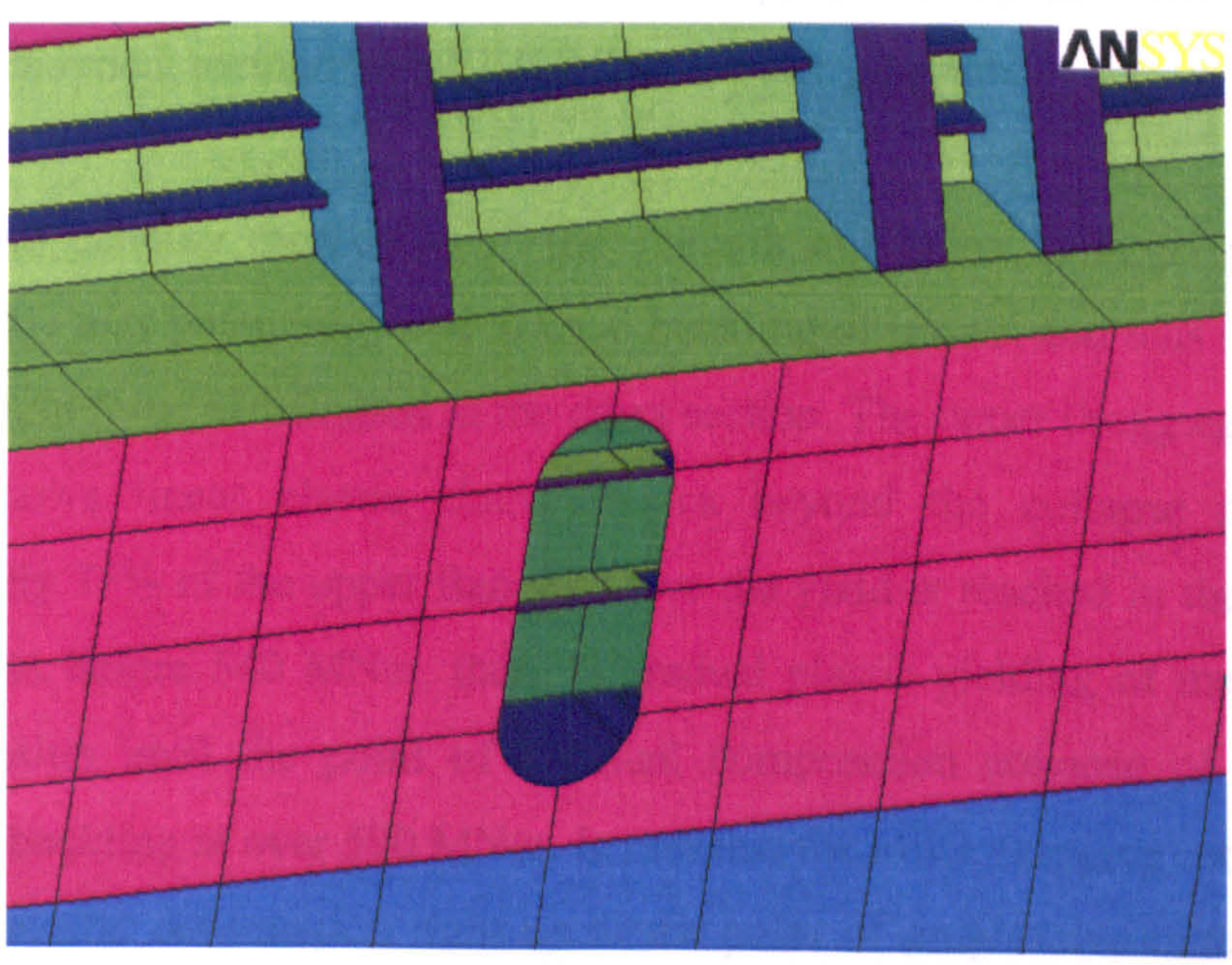

Figure 6.7: The three-dimensional model for hull girder strength of damaged tanker (remove element)

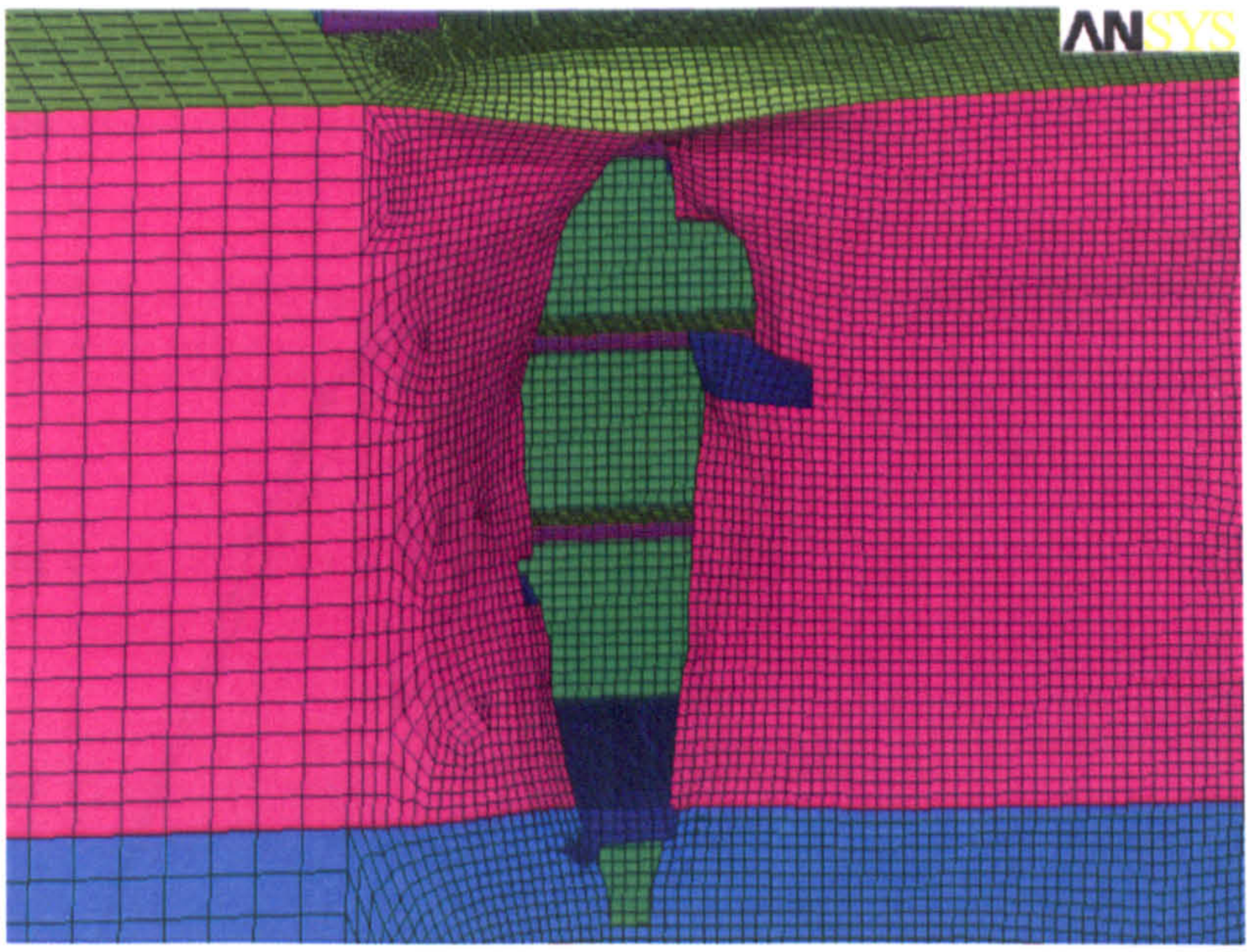

Figure 6.8: The three-dimensional model for hull girder strength of damaged tanker (no remove element)

A summary of the key results from the damage hull girder strength analyses subjected to collision are presented based on the moment versus curvature response shown in Figure 6.9 and in Figure 6.10, where the overall responses obtained by non-linear FEM are compared with the response predicted by the two-dimensional simplified analytical method by NEPTUNE computer program.

Increased bending moments will the strength utilization in larger parts of the structure. This may potentially lead to local buckling of panels, and thus slightly alter the equilibrium force distribution in the cross section. The upper (hogging) portion of the plot shows linear elastic characteristics beyond the collapse moment (at approximately 75% of the upper flange). Once the yield is reached in the uppermost structure, just before 540 MNm, there is gradual plastic yielding of the upper side shell in tension until the point of eventual compression collapse of the bottom structure in buckling at over 590 MNm. In contrast the lower (sagging) portion of the plot shows elastic deformation right up to the point of progressive initiation of the upper side shell and deck structure collapse in total compression at 460 MNm before yielding. The total collapse moment in sagging is fundamentally based on a margin on the critical buckling stress rather than a margin on yield stress.

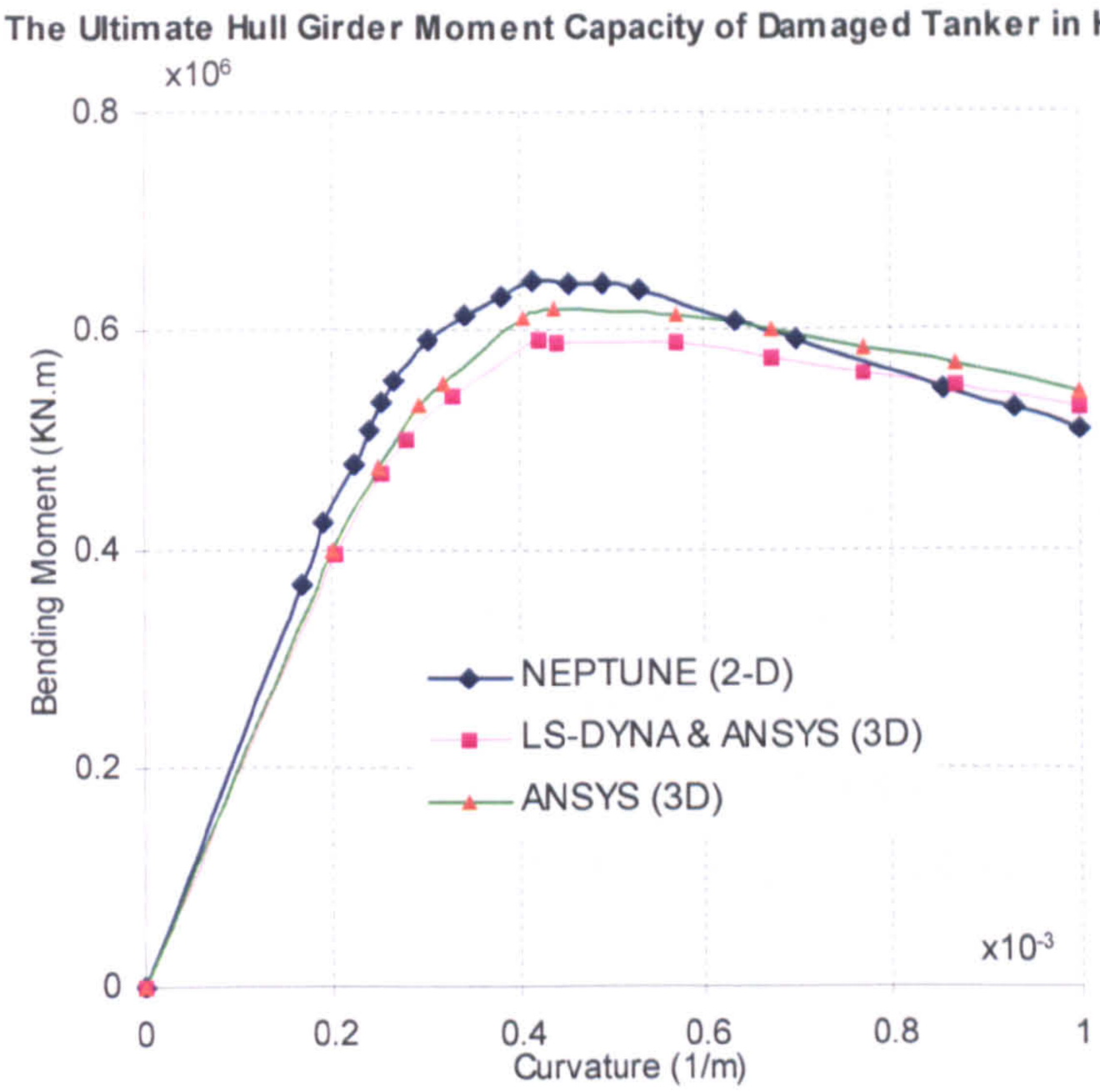

Figure 6.9: Damaged hull girder ultimate strength of the tanker in hogging case

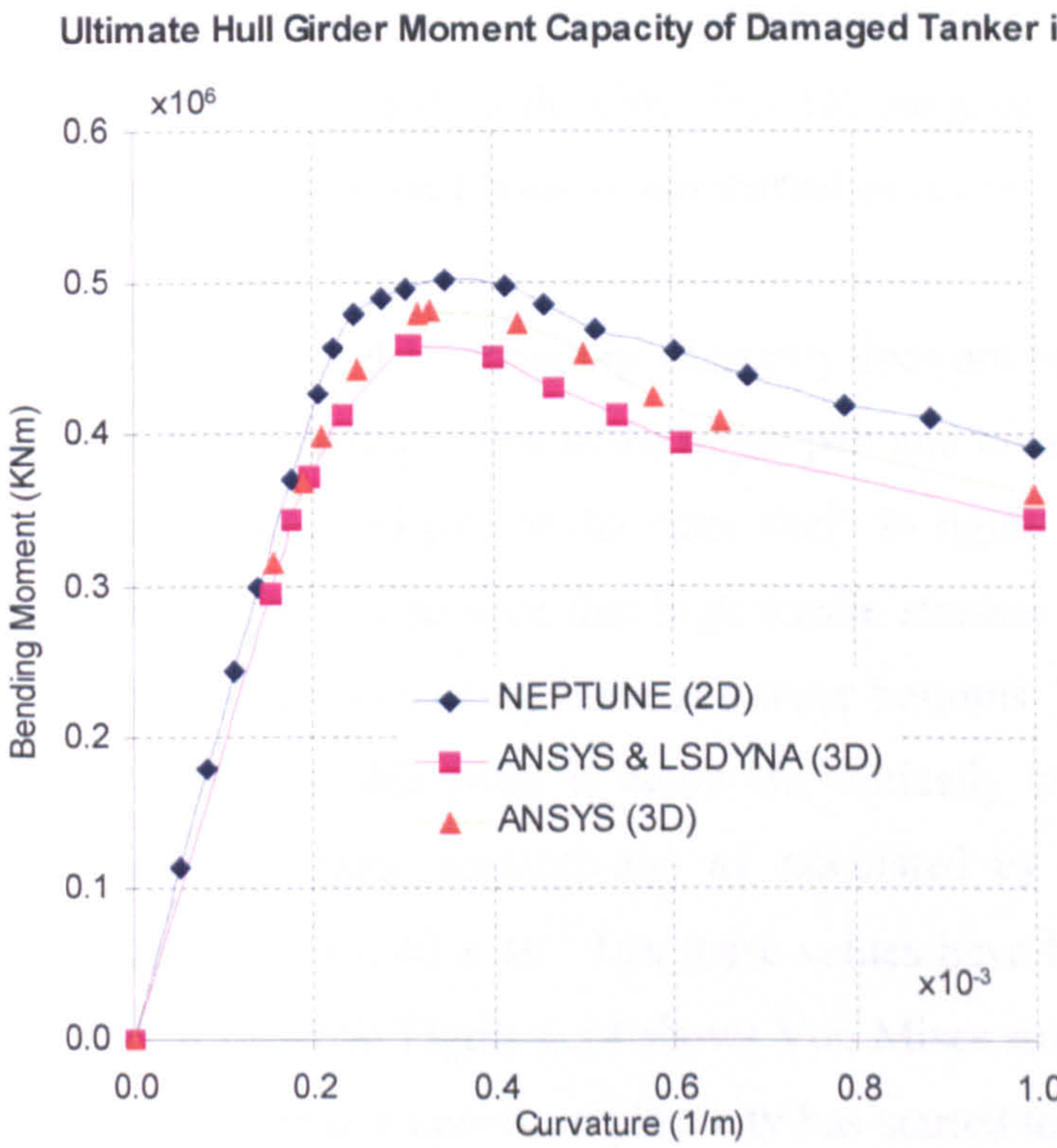

Figure 6.10: Damaged hull girder ultimate strength of the tanker in sagging case

It is seen that 3-D explicit-to-implicit sequential procedure predicts damaged collapse capacity to be 592 MNm in hogging case whereas 3-D non-linear implicit FE method estimates to be 621 MNm and 2-D simplified analytical method is 645 MNm. In sagging condition, 3-D explicit-to-implicit sequential procedure estimates ultimate damaged collapse capacity to be 462 MNm while 3-D non-linear implicit FE method predicts as 482 MNm and 2-D simplified analytical method is 501 MNm. It is noted that in hogging condition, both 2-D NEPTUNE and 3-D ANSYS implicit overestimate results which corresponding to 3-D new LSDYNA & ANSYS FE analyses, which are to be 8.95 % and 4.88 %, respectively. It is noted that in sagging condition, again both 2-D NEPTUNE and 3-D ANSYS implicit overpredict results which corresponding to 3-D new LSDYNA & ANSYS FE analyses, which are to be 8.45 % and 4.33 %, respectively.

In the following figures, Von Mises and longitudinal stress distributions are presented for both hogging and sagging conditions, at different levels of the curvature. For the hogging condition, two levels of the curvature are considered. The first one at 0.25 x 10^{-3} 1/m, when plasticity has not taken place and at 0.40 x 10^{-3} 1/m when the plasticity has started to develop. For the sagging condition, results are presented for the case where the plasticity has started to occur.

Figure 6.11 and Figure 6.12 show that plasticity does not occur at the deck, outer bottom and close to the damage, both at the upper part and lower part. The maximum stresses occur at the damaged part of the outer shell. In figure 6.12, the longitudinal stresses are presented. It can be seen that high tensile stresses develop on the upper deck and compressive stresses at the inner and outer bottoms. The stress level at the inner and outer bottom at this point is below the critically buckling stress for this location (111 and 137 MPa, respectively) as calculated by IACS Rules. On the contrary, at a curvature of 0.40 x 10^{-3} 1/m these values have been exceeded as may be seen in Figure 6.13 while Figure 6.14 shows Von Mises stress distribution of this level curvature value. At this curvature plasticity has started to develop on the upper side shell. These remarks may be used to justify the drastic drop of the bending moment curvature curve in Figure 6.9.

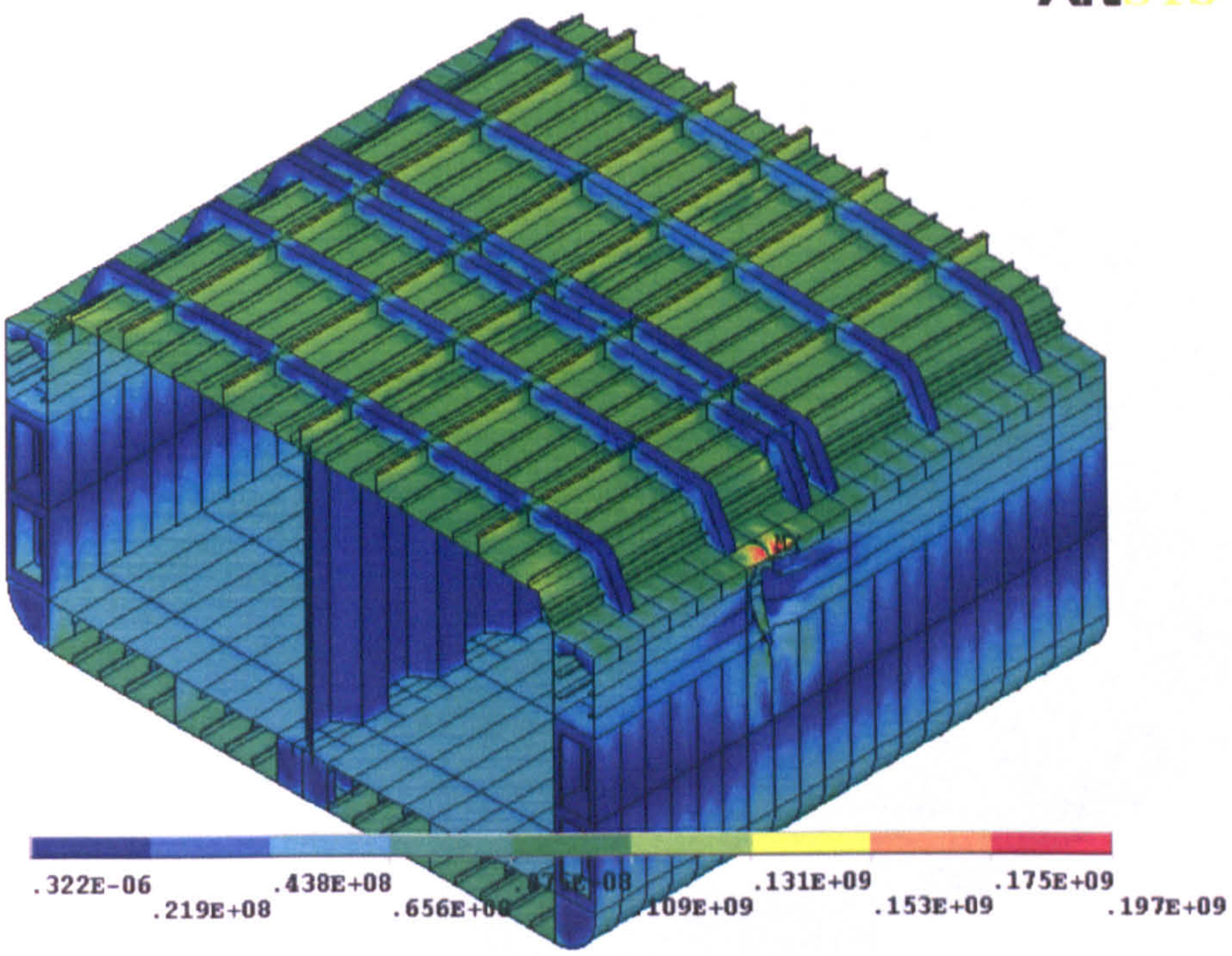

Figure 6.11: Hogging condition: moment 471 MNm, curvature 0.25 x 10^{-3} 1/m (Von Mises stress)

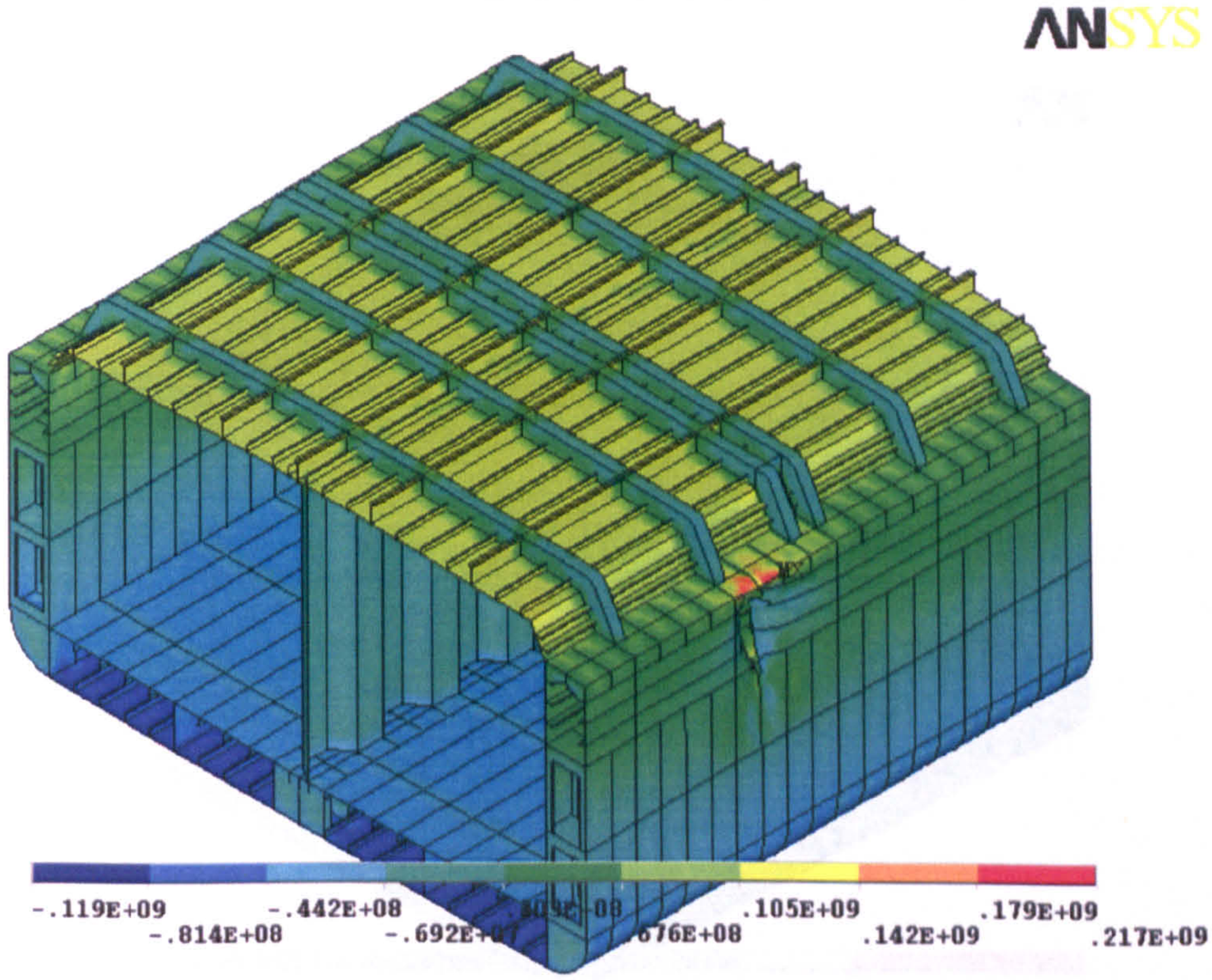

Figure 6.12: Hogging condition: moment 471 MNm, curvature 0.25 x 10^{-3} 1/m (longitudinal stress)

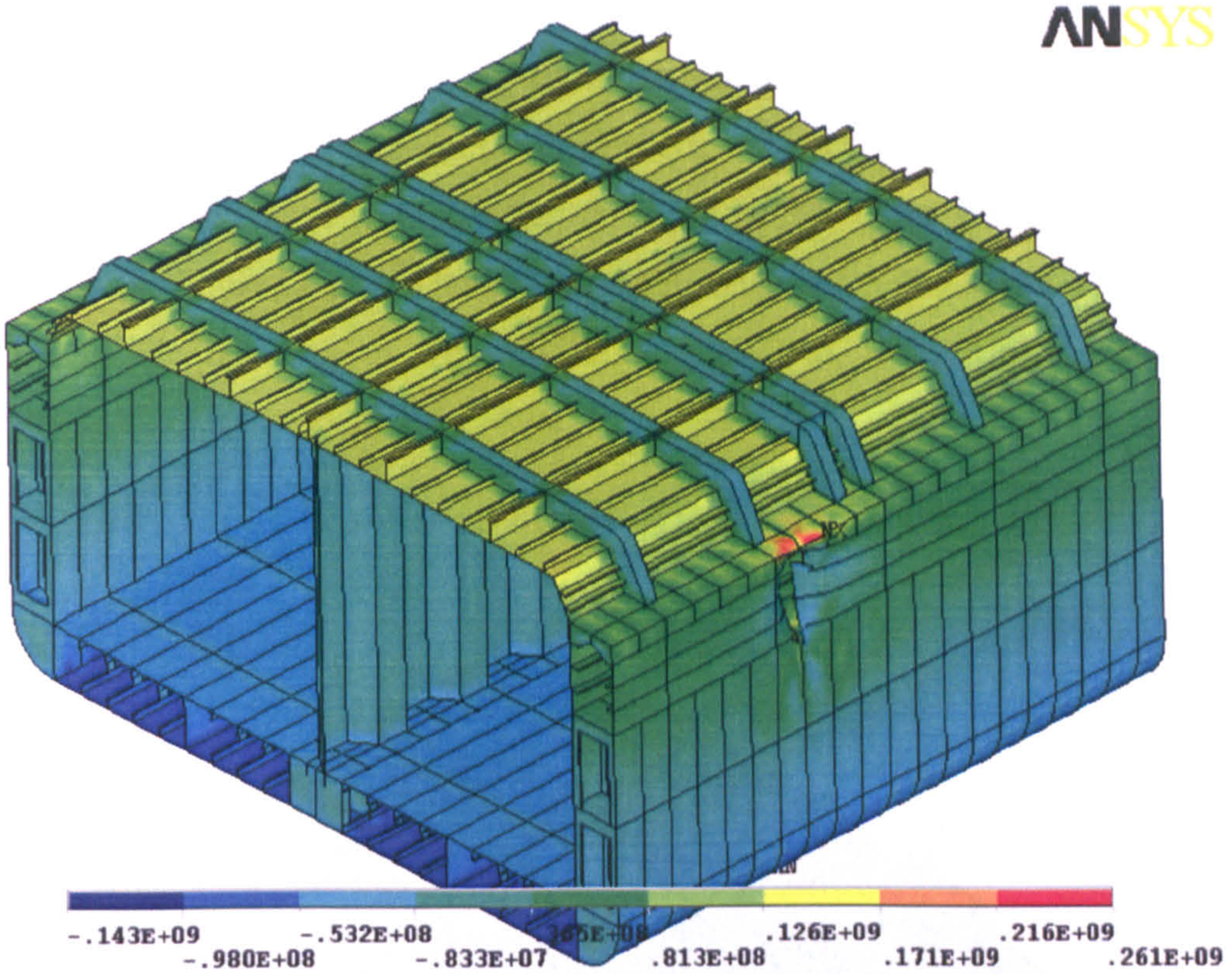

Figure 6.13: Hogging condition: moment 567 MNm, curvature 0.40 x 10^{-3} 1/m (longitudinal normal stress)

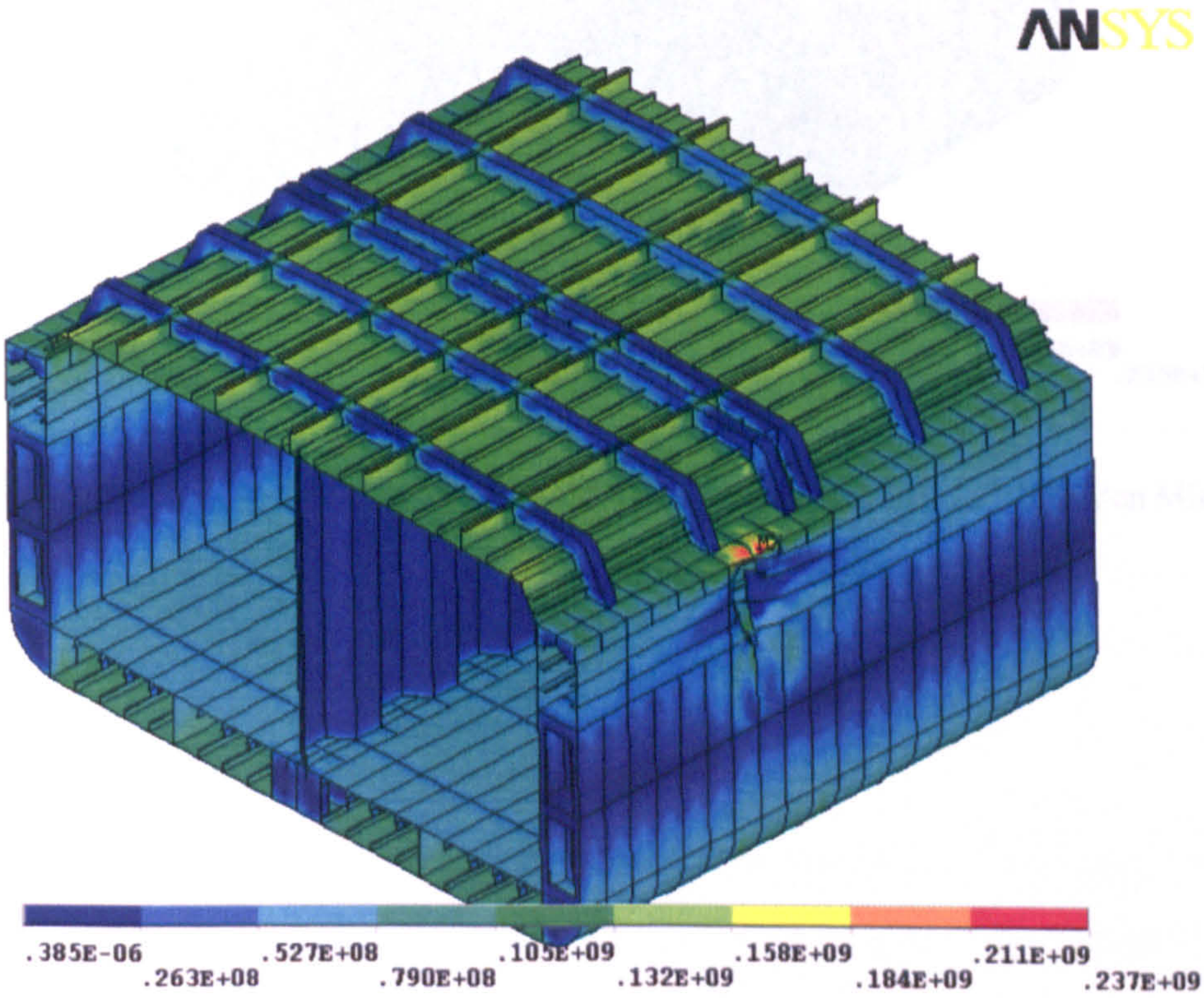

Figure 6.14: Hogging condition: moment 567 MNm, curvature 0.40 x 10^{-3} 1/m (Von Mises stress)

Figure 6.15 and Figure 6.16 show the Von Mises stress and longitudinal normal stress respectively for the sagging condition for the curvature at which 0.30 x 10^{-3} 1/m. The compressive stress at the upper deck is close to the critical buckling stress at this location. Plasticity is slightly observed for the outer side shell of damaged zone and the highest stresses take place the damaged area, the knuckle is mainly due to the elastic buckling of the upper side shell and deck, which occurs for the curvatures larger than 0.30 x 10^{-3} 1/m.

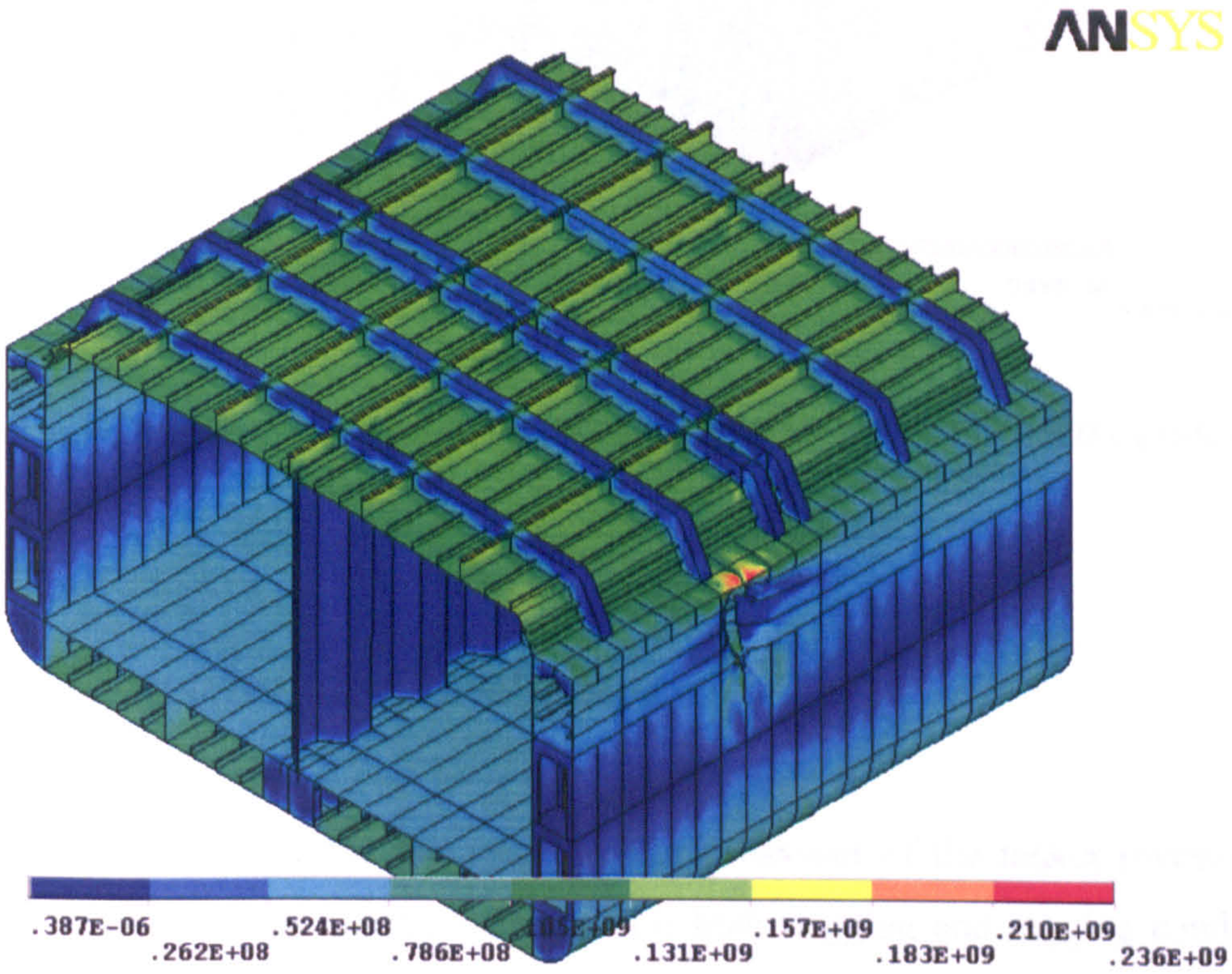

Figure 6.15: Sagging condition: moment 458 MNm, curvature 0.30 x 10^{-3} 1/m (Von Mises stress)

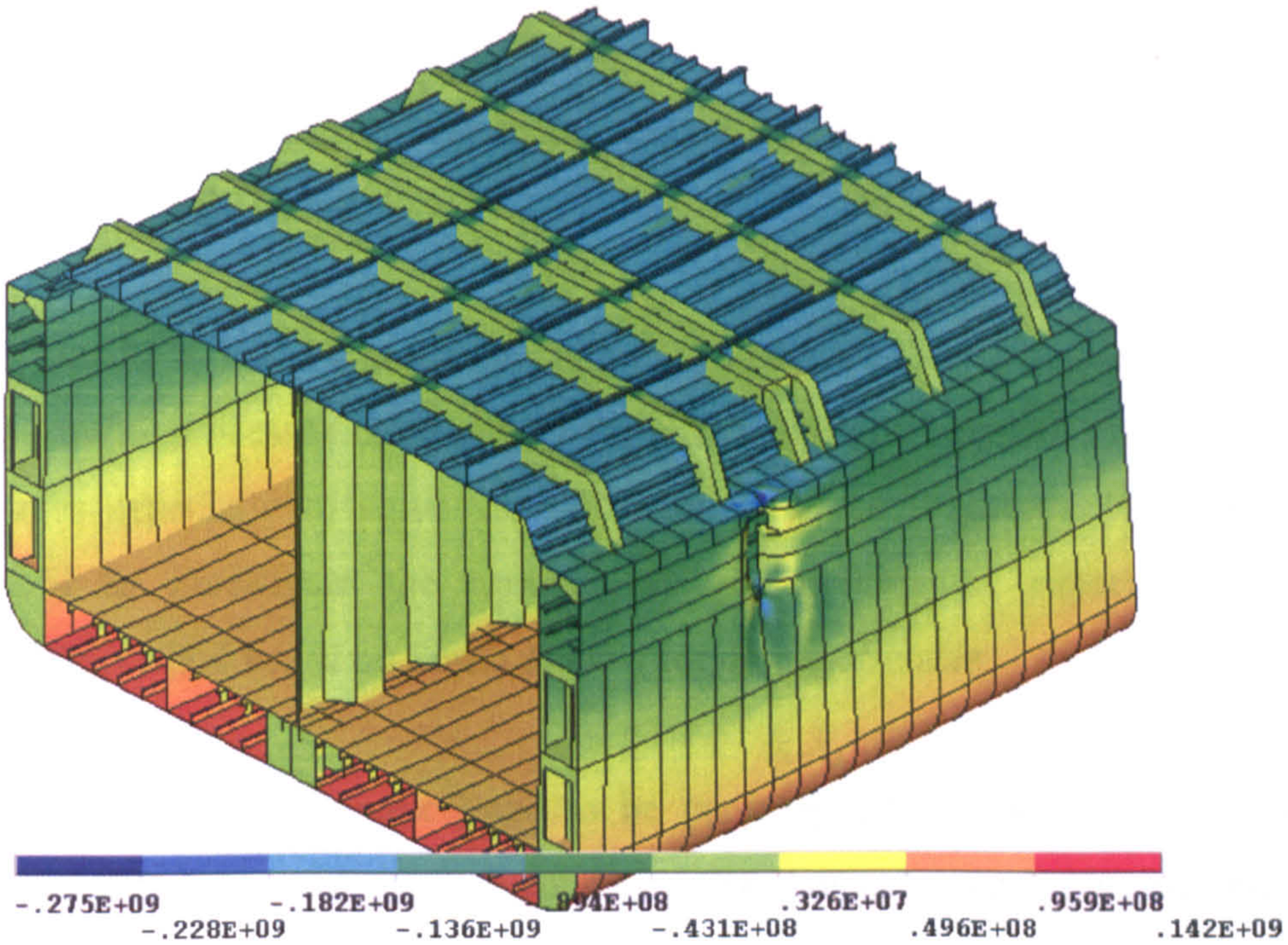

Figure 6.16: Sagging condition: moment 458 MNm, curvature 0.30 x 10^{-3} 1/m (longitudinal normal stress)

6.3 Discussion & Conclusion

A new simulation of the damaged bending behaviour of the tanker investigated in order to calculate her ultimate strength for both hogging and sagging conditions is performed. The simulation is conducted on the assumption that the one compartment modelled is clamped at one end and a vertical bending moment is developed at the other. The results are compared with simplified analytical procedure and 3-D non-linear finite element method, where removed structural members so as to introduce damage occurrence.

Structural investigations of the midship section properties using the program NEPTUNE have established the ultimate collapse strength of the ship in the damaged condition.

It was found that 2-D simplified method slightly overestimated to be 8.95 % for hogging and 8.45 % for sagging cases in this investigated tanker. Therefore, this study shows that the results obtained compare well with simplified analytical results calculated by NEPTUNE.

It should be noted that the new approach is extremely expensive, which 32 CPU having multi processor computers were employed, and requires massive computer resources especially to solve very difficult converge problems. However, it was intended to investigate the accuracy or performance of especially simplified analytical method based on Smith & Dow for damaged states.

This conclusion is anticipated to be generally applicable to a wide range of damaged ship types and sizes on condition that damage zone is properly introduced into calculations.

Chapter 7

A Case Study: A comparative study on the structural integrity of single and double side skin bulk carriers under collision damage

7.1 Introduction

A bulk carrier that experiences flooding of one or more cargo holds or machinery spaces is exposed to the risk of losing its stability and thus suffers the risk of sinking. Several accident scenarios can cause flooding of a bulk carrier, e.g. corrosion and fatigue causing loss of side shell integrity, water ingress through hatch covers in rough seas, grounding and collision with another vessel. From 1980 to mid 1990s, over 150 bulk carriers have been reported lost with a loss of more than 1200 lives. Typically, the bulk carriers have a high number of lives lost in accidents, which shows that the consequences of bulk carrier casualties are more severe than for other ship types (RINA 1998). A search in the database of Lloyd's Maritime Information Service (LMIS) has revealed that between January 1, 1991 and December 31, 2000

there were fewer accidents involving DSS bulk carriers compared to SSS bulk carriers. Only three accident records were retrieved and, notably, all three concerned combination-type vessels. The initiating event each case was contact with another object. Concern over the safety of bulk carriers has risen in recent years and has lead to a number of initiatives from various organizations. The IMO has bulk carrier safety as a priority issue in its work programme and bulk carrier safety is also the central priority of the International Association of Classification Societies (IACS). Recently IACS announced new requirements to enhance the safety of bulk carriers. More than 3484 bulk carriers, with a capacity of up to 173 million DWT, are targeted by the new requirements from January 1, 2003. At the same time, Formal Safety Assessment (FSA) study of bulk carriers is also carried out by an international consortium, which is led by the Royal Institution of Naval Architects (RINA). The aim of the FSA study is to investigate whether the new survivability and structural requirements of SOLAS Chapter XII are sufficient for bulk carriers with double skin side construction.

There are two key advantages identified for the double skin side bulk carrier: the existence of redundancy in case of penetration of the outside shell from a low to moderate energy impact and, more importantly, the fact that primary structural members need no longer suffer from corrosive effects by being in direct contact with the cargo. Furthermore, the hull is protected from damage from cargo loading and offloading equipment Therefore the damage to frames and plating that arise from such contact can be prevented. Double-sided structures have flat sides in the cargo holds and, as a result, the final stages of the cargo discharge process occur without grabs and pipes manoeuvring around awkward frames etc. It is estimated that the steel weight increase in the cargo area of DSS bulk carrier about 4% compared to a SSS bulk carrier for the same cargo hold volume and 3.5% for the same deadweight.

Double hull concept is one effective way to moderate the risk of cargo in collision accidents, even though it is not a whole solution. As long as the inner plating is intact, the cargo will not spill out immediately after an accident although the outer shell plating may have been seriously ruptured. On the other hand, if the

cargo is still on board, there is still a possibility of vessel loss even if the inner shell plating remains intact immediately after collision damage. Such damage or loss can result from hull collapse due to a decrease of the accident-induced sectional forces including during salvage and rescue operations. In this case, it is necessary to compare the structural strength of DSS and SSS bulk carriers in both intact and damaged states.

The primary aim of the present chapter is to investigate the collision resistance and residual strength subject to collision damage of single side skin (SSS) and double side skin (DSS) bulk carriers. The impact dynamics analyses are conducted by means of a non-linear explicit finite element code, ANSYS LS-DYNA for the evaluation resistance forces, energy absorption and penetration depth for various collision scenarios. The struck vessels of Capsize SSS and DSS designs are assumed to be entirely standstill and the striking vessels of an Aframax type oil tanker with different bulbous bow shapes are modelled as rigid bodies. The numerical procedure adopted, findings are compared, where possible, with the analytical calculation tools developed by others by existing analytical tools. Residual strength calculations on SSS and DSS vessels are computed corresponding to all considered collision damage scenarios, where the ordinary Smith's method is applied using a developed computer code NEPTUNE with the average stress – average strain relationships of elements, which are derived semi – analytically. The effect on corrosion is also evaluated by Joint Bulker Project (JBP 2004) rules on the influence of plate and stiffener thickness on the damaged hull girder capacity. The safety assessment of the vessels is determined as a ratio of the ultimate hull girder strength to the applied damaged design-bending moment.

7.2 Collision Problem

Many authors have shown that the analysis of ship collision interaction can be split into two parts such as external dynamics and internal mechanics. Those two parts are studied separately and linked together by the common contact force. External dynamics determines the ship's motion and deal with the energy released for

dissipation in damaged structures and the impact impulse of a collision. Internal mechanics concentrates purely on the structural response, defining the strength or resistance of ship structures in an accident. The methods for simulating the internal mechanics can be classified into four categories such as empirical formulae, simplified analytical methods, non-linear FEM simulations and model experiments.

7.2.1 State of art

One of the earliest attempts to predict ship response to collisions has been made by Minorsky (1959). Energy absorbed in collision and the loss of kinetic energy was determined from simple momentum conservation. Interaction between the vessels and the surrounding water was included by constant added mass. Minorsky also proposed an empirical correlation between the deformed volume of structural members and absorbed collision energy. Proposed relation is valid for high-energy collisions (absorbed energy over 30MJ) and may result in wrong values for minor collisions. Minorsky`s approach is widely used and modified by many researchers. Petersen (1982) developed a transient procedure for time simulation of the outer dynamics in ship collisions with including only the motions in horizontal plane. Arita (1986) carried out theoretical, numerical and experimental studies on the structural crashworthiness of nuclear power vessels, LNG carriers and double hull tankers in collision. A theoretical approach to predict the energy absorption capability of striking and struck vessel structures was proposed and explored. Woisin (1999) developed a simplified analytical procedure for calculating the loss of kinetic energy and impact impulse on entirely plastic ship collisions. Developed model was capable of handling arbitrary collision angles and impact location.

The 1990's were characterized by the remarkable advances in analytical solutions of various damage mechanics in collision accidents. A series of analytical methods were developed and applied by Wierzbicki (1979). Kierkegaard (1993) developed an analytical method for analysis of the internal collision mechanics of the bow structure in a head – on collision with iceberg or other objects. Wang (1995) obtained a simplified theoretical approach for predicting the damage of vessels in a

head-on collision or raking. A variety of failure modes were regarded into Wang's work. Chung (1996) developed a theoretical approach for analysing the damage and crushing strength of a ship's bow in a head-on collision. Zhang (1999) presented a comprehensive set of simplified formulations for the analysis structural damage in ship-ship collisions. These became the main theme of 1990's.

Non-linear finite element method (FEM) is a powerful tool for analysing ship collision problem and has been more and more applications in the recent years. The reliability of the numerical simulation results largely depends on the proper modelling of the phenomenon and realistic consideration of aspects, such as material failure and boundary conditions. The rapid advances in the computer technology make numerical simulation, a formidable task only a couple years ago, a viable choice now. Many powerful special purpose FEM packages, such as DYNA 3D, DYTRAN, ABAQUS and PAM. (ISSC 2003), are now reliable that can account for large deformation, contact, no-linearity in material properties and rupture. Some recent supporting literature on numerical simulations of collision and grounding include Kuroiwa (1996), Kitamura *et al.* (1998, 2001), Servis *et al.* (2002), Tornqvist (2003) and Ozguc *et al.* (2005f).

Since structures behave in many complex patterns, many special modelling techniques are needed. Challenges involved in analysing such a high non-linear problem include among others, structural contact, criteria for material's rupture, crack propagation (Wang, 2002). To analyse a collision and grounding accident involving high non-linearity, contact, friction and rupture, the explicit methodology is suitable. The required calculation efforts are fewer than the commonly used implicit methods. Converge of calculations is much easier to realize.

7.3 Validation of ANSYS LS-DYNA using ISSC Benchmark Collision Test

The Association of Structural Improvement of Shipbuilding Industry of Japan (1993) conducted extensive collision and grounding tests. One of the collision test models is a double side structure model made of mild steel. In the dynamics test the bow model fell freely from a height of 4.8 m above the initial position of the outer hull, which gave an impact velocity of about 9.7 m/sec.

7.3.1 Finite element procedure

The typical shell element size for the whole simulated structure was about 15x15 mm, which gave a total number of 56908 shell elements. Contact was modeled between the indenter and all structural members, including self-contact, where the friction coefficient was assumed to be 0.3. Strain rate effects were included in the material model, namely Cowder-Symonds parameters C_{cs}=3600 (1/s) and q=5.5. In order to avoid hourglassing, the stiffeners and the flanges were modeled with fully integrated shell elements with five-integration points through the thickness. The remaining bottom structure was modeled with the under integrated Belytschko-Tsay elements with one integration point in plane and five-integration points through the thickness.

7.3.2 Results

The force-penetration curve determined from the finite element simulation of the dynamics test is shown in Figure 7.1. Good correlation with the experimental result is achieved, however the contact force is slightly smaller in the finite element simulation, while absorbed energy – penetration curve has excellent correlation between experiment and numerical approach, which is shown in Figure 7.1. Figure 7.

2 present the deformation pattern obtained from ANSYS LS-DYNA, where penetration is 500 mm.

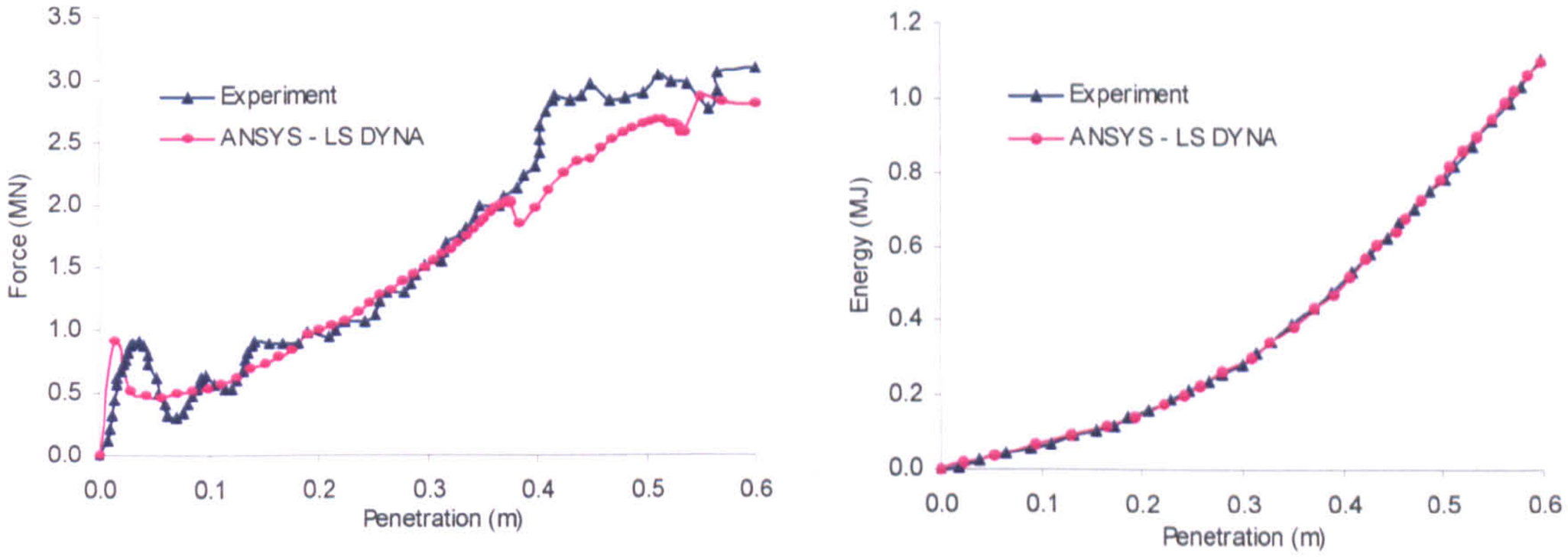

Figure 7.1: Collision force versus penetration (*left*) and absorbed energy versus penetration (*right*)

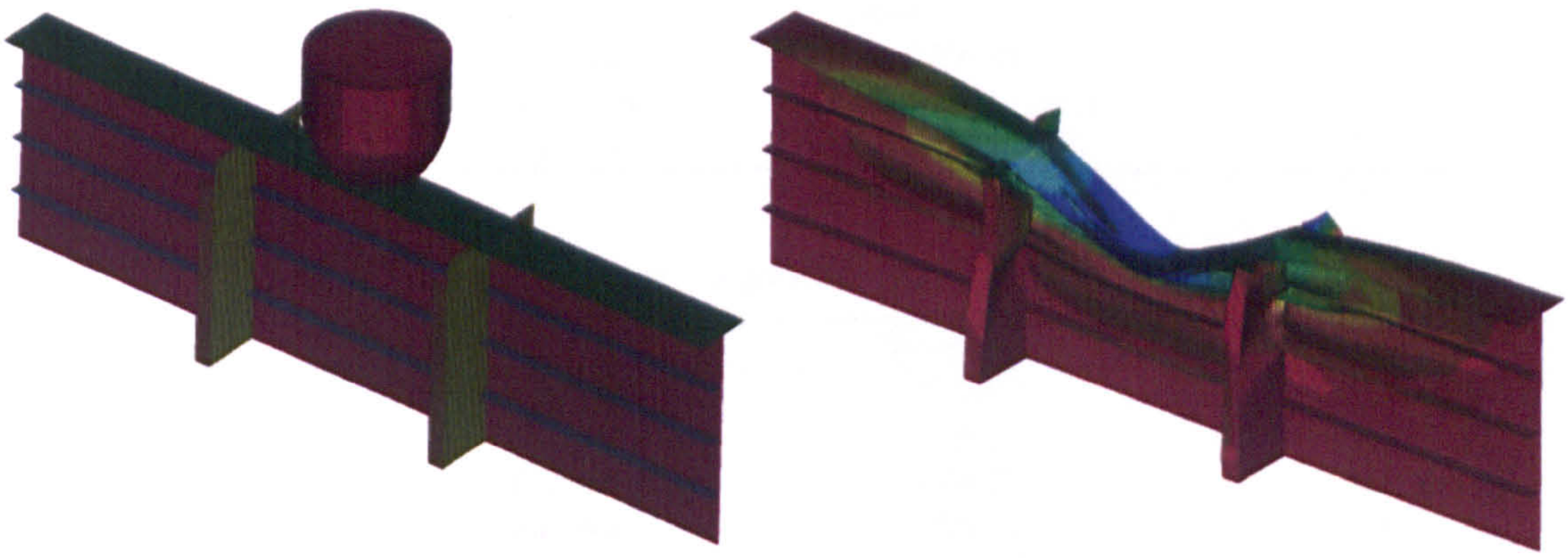

Figure 7.2: Finite element model with very fine mesh (left) and penetration of 500 mm (right)

7.4 SSS & DSS Bulk Carrier Designs

The principal dimensions of the DSS and SSS bulk carrier designs are listed in Table 7.1, while Table 7.2 and Table 7.3 present the material and the scantlings of longitudinal members. The midship cross sections are given in Figure 7.3 and Figure 7.4, while Figure 7.5 presents ANSYS one cargo tank geometry model for SSS & DSS bulk carrier vessels.

Table 7.1: Principal dimensions of SSS & DSS bulk carrier vessels

Items	SSS	DSS
Length overall (m)	279.91	279.29
Length between perpendiculars (m)	279.33	279
Breadth (m)	45	45
Depth (m)	24.1	24.1
Draft (m)	16.5	17.7
Block coefficient	0.86	0.86
Transverse frame spacing (m) Bottom Side shell Deck	 2.68 0.86 5.16	 2.68 0.86 5.16

Table 7.2: The scantlings of longitudinal of SSS bulk carrier vessel

Stiffener no	Type	Dimensions	Yield stress
1	Flat bar	330x26	355
2	Angle bar	400x11.5+100x16	315
3	Angle bar	350x12+100x17	355
4	Flat bar	200x16	315
5	Angle bar	400x13+100x8	315
6	Angle bar	300x13+90x17	315
7	Angle bar	300x11+90x16	315
8	Flat bar	220x20	315
9	Angle bar	150x11.5+125x18	315
10	Angle bar	150x12+90x12	315

Table 7.3: The scantlings of longitudinal of DSS bulk carrier vessel

Stiffener no	Type	Dimensions	Yield stress
1	Flat bar	350x32	355
2	Flat bar	330x22	355
3	Flat bar	350x26	355
4	Flat bar	200x22	315
5	Angle bar	350x12+100x17	315
6	Angle bar	400x11.5+100x16	315
7	Angle bar	450x11.5+125x18	315
8	Angle bar	150x12+90x12	315

The striking ships are chosen with the same main dimensions. Two different types of striking bow shapes are used for the numerical determination of the absorbed energy – penetration curves. Bow shape 1 called has shorter and sharper bulb and a shorter forecastle deck than bow shape 2 called. Figure 7.5 shows the striking ships.

Single Skin

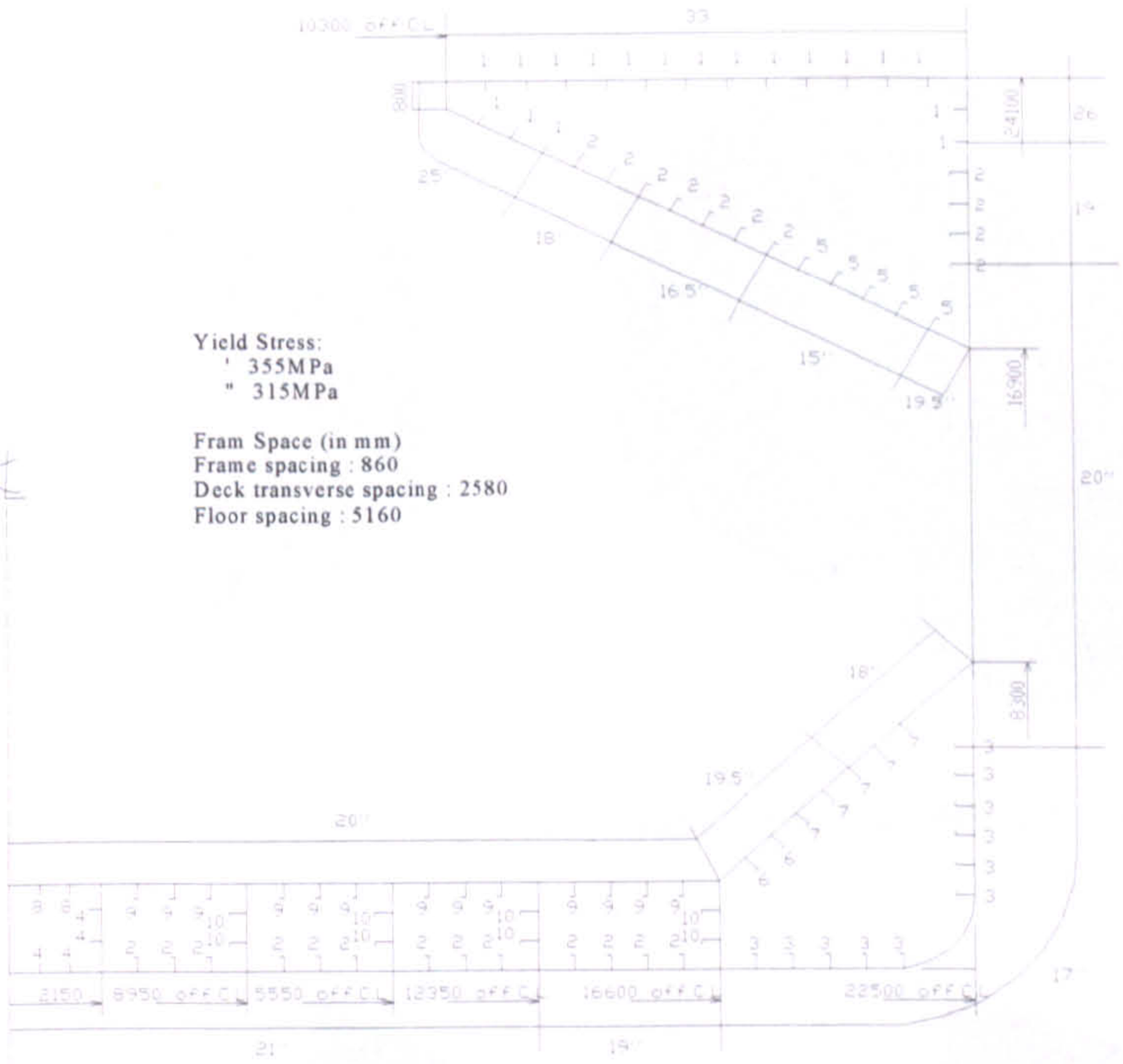

Yield Stress:
' 355MPa
" 315MPa

Fram Space (in mm)
Frame spacing : 860
Deck transverse spacing : 2580
Floor spacing : 5160

Figure 7.3: Midship cross section of SSS Bulk carrier

Double Skin

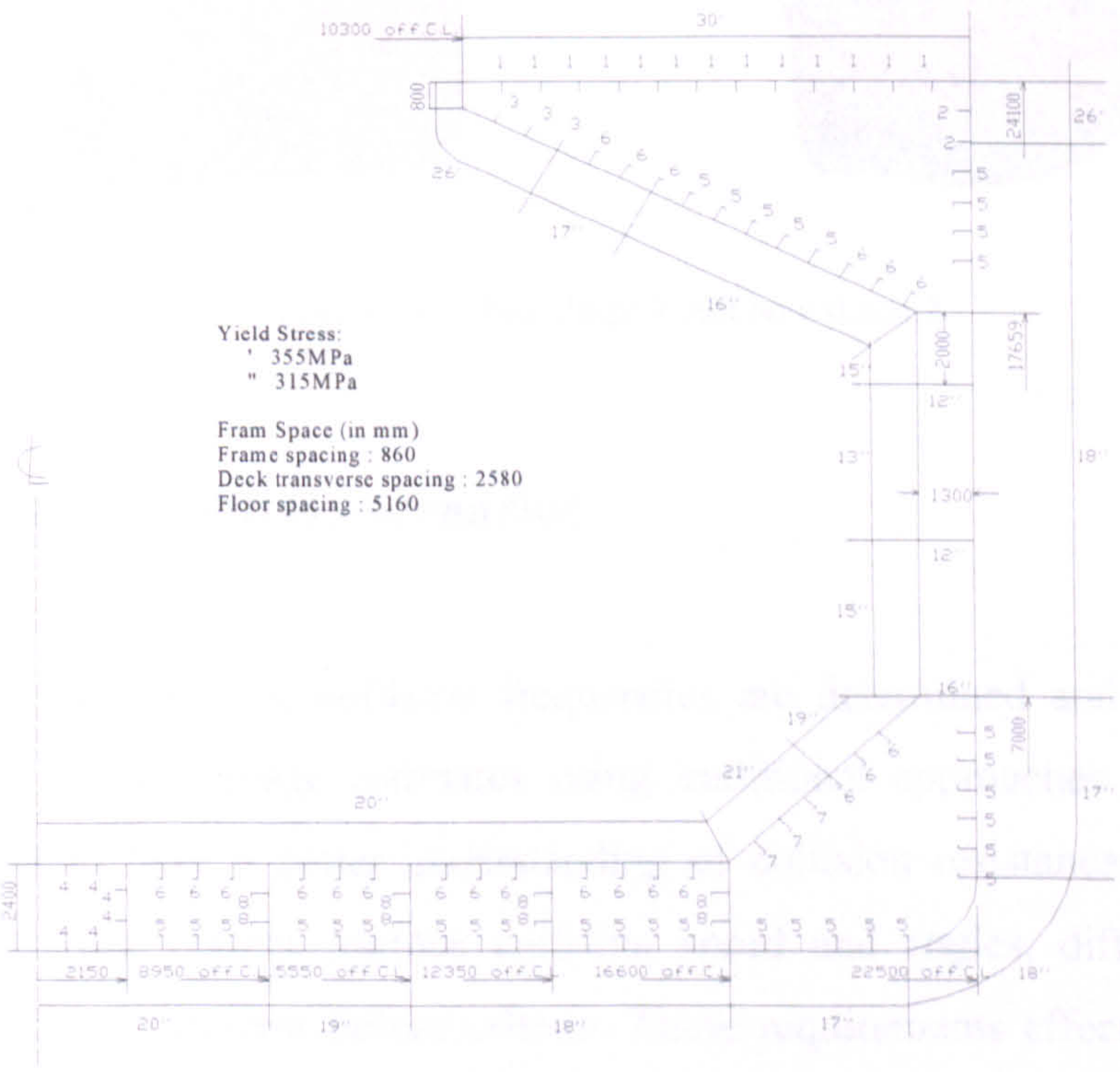

Yield Stress:
' 355MPa
" 315MPa

Fram Space (in mm)
Frame spacing : 860
Deck transverse spacing : 2580
Floor spacing : 5160

Figure 7.4: Midship cross section of DSS Bulk carrier

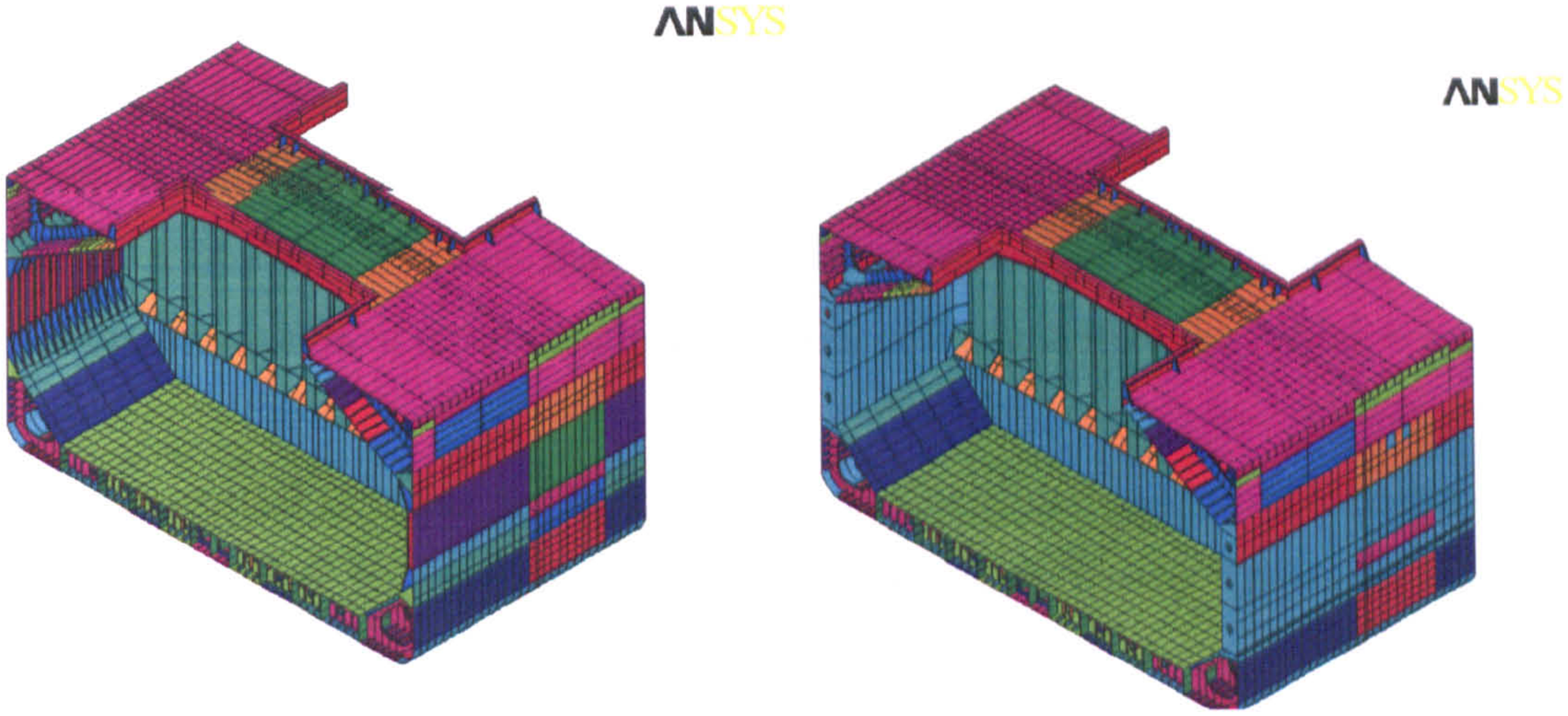

Figure 7.5: ANSYS one cargo tank geometry model for SSS & DSS bulk carrier vessels

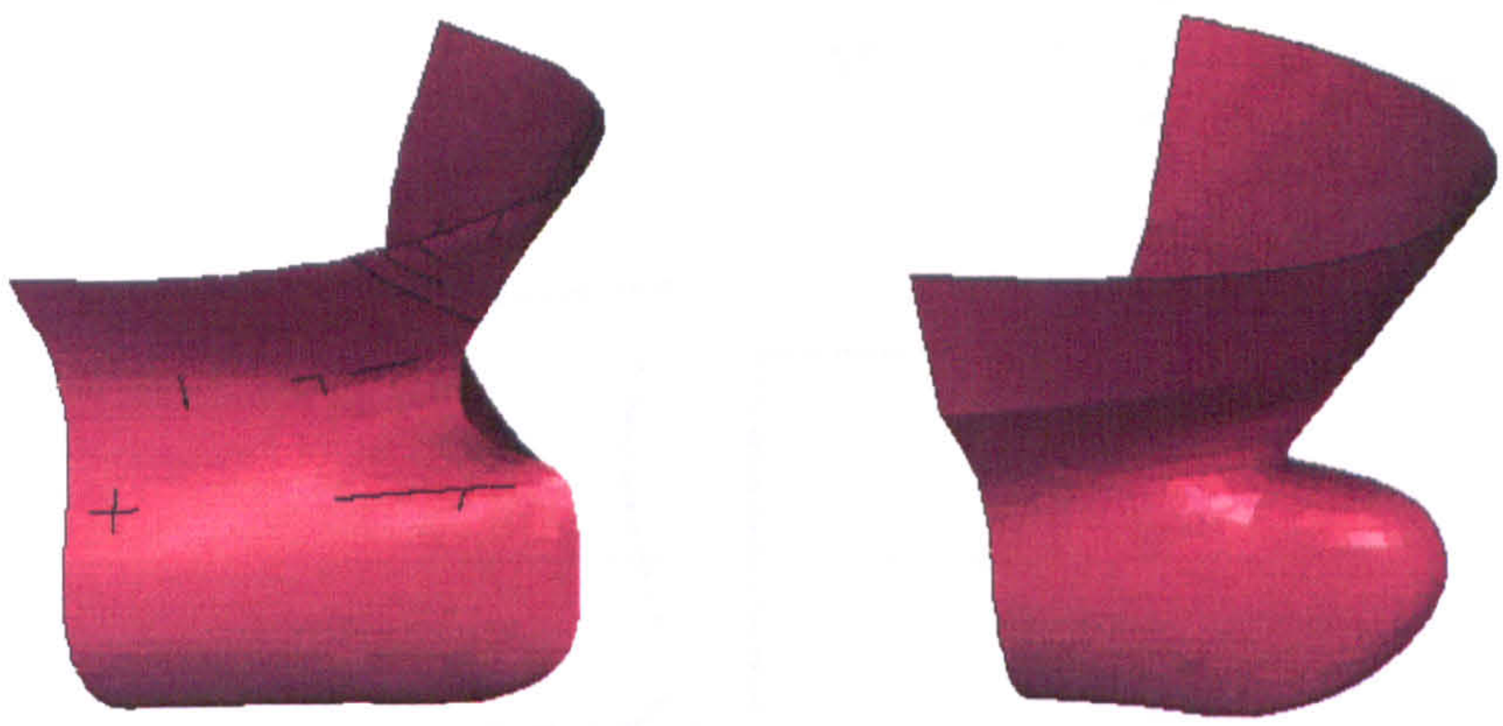

Figure 7.6: Bow shape 1 and bow shape 2

7.4.1 Assumed collision scenarios

During the risk analysis, collision frequencies are determined and limitations are recognized in the damage estimates using traditional approaches. The interested parties want to have a better understanding of collision resistance accounting for different striking vessels, various collision speed and angles, different structural arrangement and different failure criteria. These requirements effectively drove the consequences analysis towards applying the detailed finite element analysis (FEA) for calculating structural damage.

The results of the simulation further depend on two main input parameters such as vertical location, i.e. different vertical position of one ship with respect to the other, longitudinal position of impact - the impact may occur between two web frames or directly on a web frame. These parameters together with the striking bow and the assumption of a right angle and central collision define the collision scenario.

The vertical relevant position of the two ships is defined by their drafts, which are given by the following formulae (GL, 2003) and Figure 7.6 shows the draft differences between striking and struck ships.

$$\Delta T_1 = T_{2\max} - \frac{3.T_{1\min} + T_{1maz}}{4} \qquad \Delta T_2 = T_{2\max} - \frac{3.T_{1\max} + T_{1\min}}{4} \tag{7.1}$$

$$\Delta T_3 = \frac{T_{2\min} + 3.T_{2\max}}{4} - T_{1\max} \qquad \Delta T_4 = \frac{T_{2\max} + 3.T_{2\min}}{4} - T_{1\max}$$

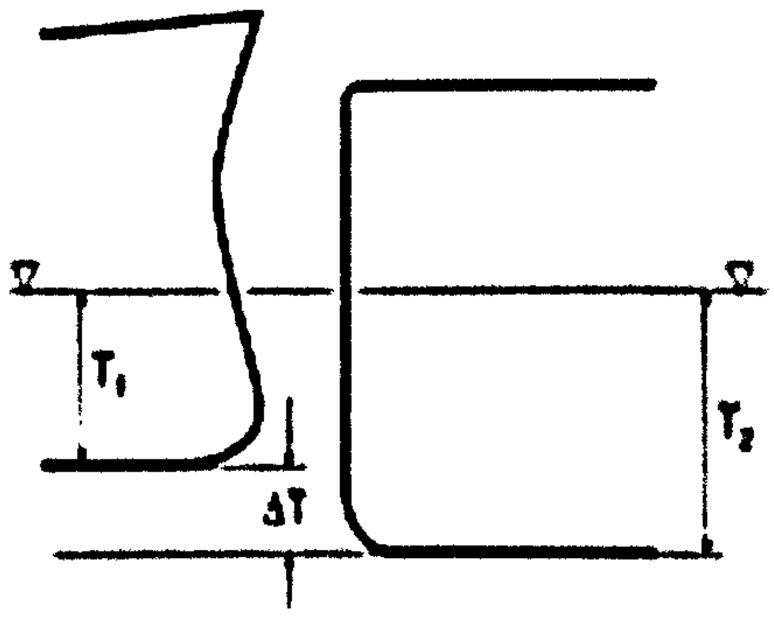

Figure 7.7: Draft differences between striking and struck ships, (GL 2003)

Where $T_{1\max}$ is the design draft of the striking ship and $T_{1\min}$ is the ballast draft of the striking ship respectively while $T_{2\max}$ and $T_{2\min}$ is the design and ballast draft of the struck ship respectively.

16 different collision cases are accounted into non-linear finite element analyses by means of ANSYS LS-DYNA. The impact speed of striking ships is 10.5 m/sec and the total simulated collision scenarios time is 0.3 sec. The density of element mesh size is 125 mm in contact areas while the rest areas is considered to be 375 mm. In order to reduce CPU time consuming only one half-cargo tank is modelled

and two ends are clamped while symmetric boundary condition is introduced to half longitudinal section. Plastic-kinematics material is considered into analyses and is summarized in Table 7.4. The yield function of plastic-kinematics material is given as equation 7.2.

All investigated ship-ship collision scenarios is shown in Table 7.5 through 7.8.

$$\sigma_y = \left[1 + \left(\frac{\dot{\varepsilon}}{C}\right)^{1/P}\right]\left(\sigma_o + \beta E_P \varepsilon_P^{\ eff}\right) \qquad E_P = \frac{E_{\tan} E}{E - E_{\tan}} \tag{7.2}$$

Where σ_o = initial yield stress; $\varepsilon_P^{\ eff}$ = effective plastic strain; E_P = plastic hardening modulus, β = hardening parameter between 0 (kinematics) and 1 (isotropic); and C, P = Cowder – Symonds strain rate parameters.

Table 7.4: Material properties of plastic – kinematics used in this study

Density (kg/mm^3)	7.85e-6
Young's modulus (MPa)	210000
Poisson ratio	0.30
Yield strength (MPa)	315
Tangent modulus (MPa)	625
Hardening parameter	0
Strain rate (C, 1/sec)	3200
Strain rate (P)	5
Failure Strain	0.20

Table 7.5: Bow shape 1at direct web longitudinal position

Case	Bow Shape 1 - DSS	Bow Shape 1 - SSS
Case 1	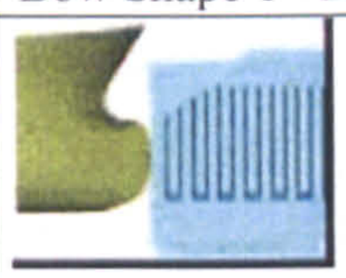 $\Delta T_1 = 5.24$ m	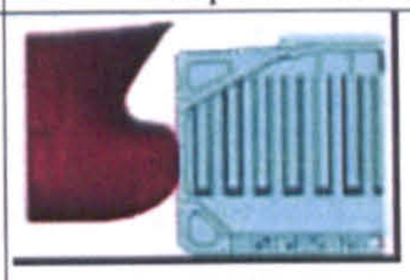 ΔT_1=4.2 m
Case 2	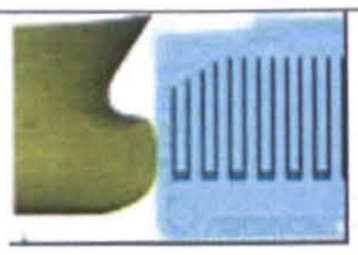 $\Delta T_2 = 2.8$ m	 $\Delta T_2 = 1.6$ m
Case 3	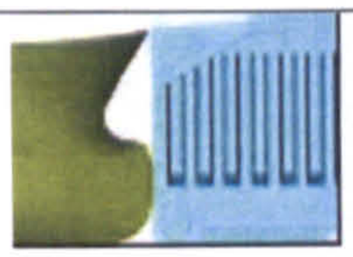 $\Delta T_3 = 0.1$ m	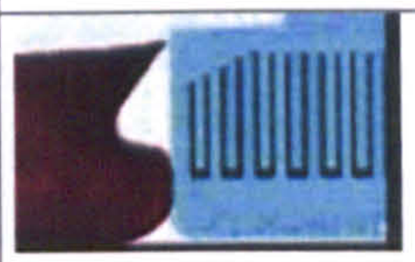 $\Delta T_3 = -1.025$ m
Case 4	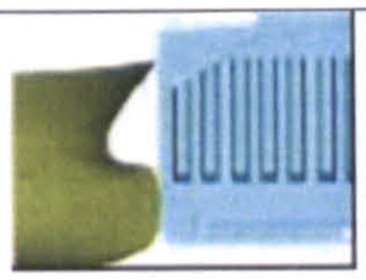 $\Delta T_4 = -2.7$ m	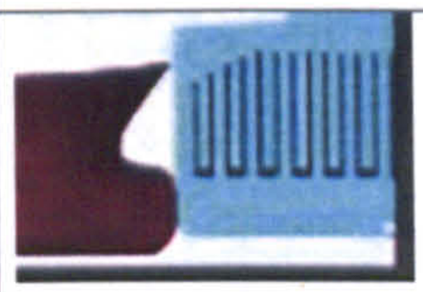 $\Delta T_4 = -3.675$ m

Table 7.6: Bow shape 1 at between webs long. Position

Case	Bow Shape 1 - DSS	Bow Shape 1 - SSS
Case 5	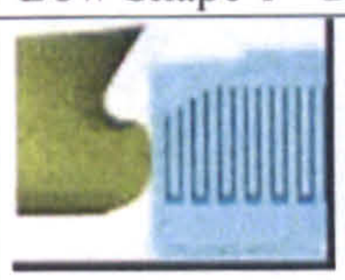 $\Delta T_1 = 5.24$ m	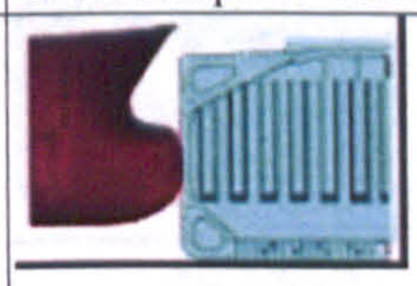 $\Delta T_1 = 4.2$ m
Case 6	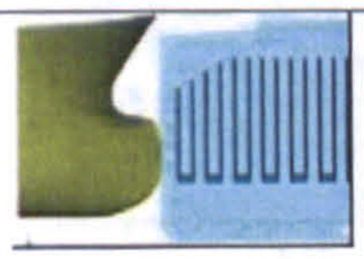 $\Delta T_2 = 2.8$ m	 $\Delta T_2 = 1.6$ m
Case 7	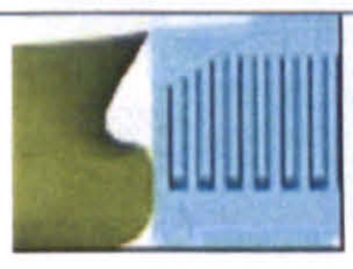 $\Delta T_3 = 0.1$ m	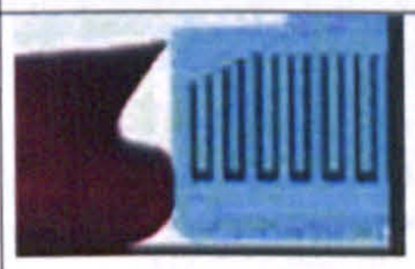 $\Delta T_3 = -1.025$ m
Case 8	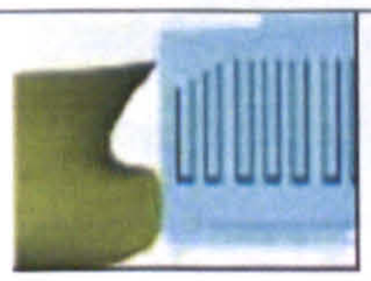 $\Delta T_4 = -2.7$ m	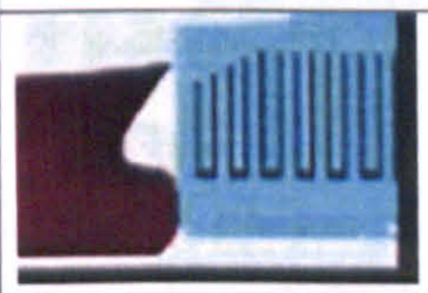 $\Delta T_4 = -3.675$ m

Table 7.7: Bow shape 2 at direct web longitudinal position

Case	Bow Shape 2 - DSS	Bow Shape 2 - SSS
Case 9	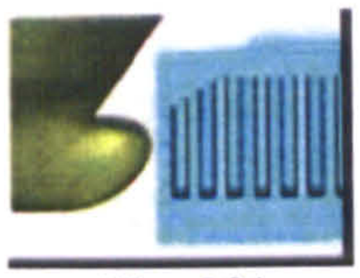 $\Delta T_1 = 5.24$ m	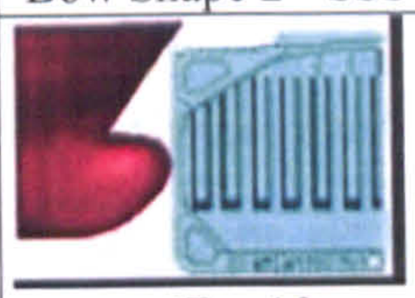 $\Delta T_1 = 4.2$ m
Case 10	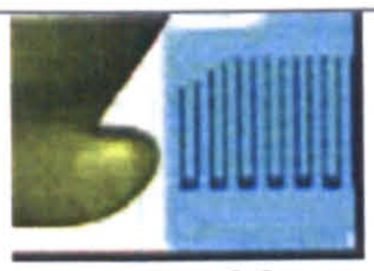 $\Delta T_2 = 2.8$ m	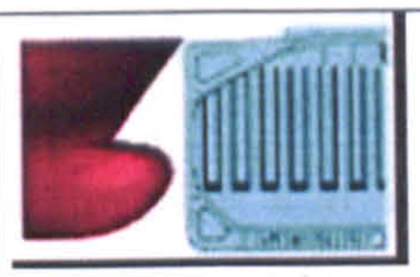 $\Delta T_2 = 1.6$ m
Case 11	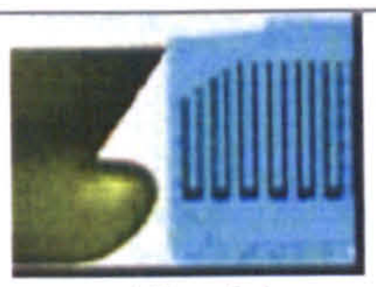 $\Delta T_3 = 0.1$ m	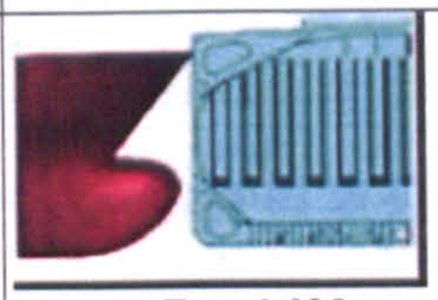 $\Delta T_3 = -1.025$ m
Case 12	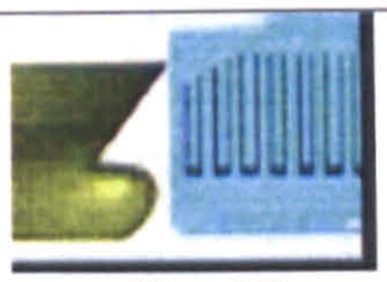 $\Delta T_4 = -2.7$ m	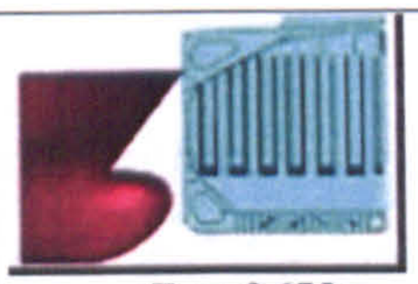 $\Delta T_4 = -3.675$ m

Table 7.8: Bow shape 2 at between webs longitudinal position

Case	Bow Shape 2 - DSS	Bow Shape 2 - SSS
Case 13	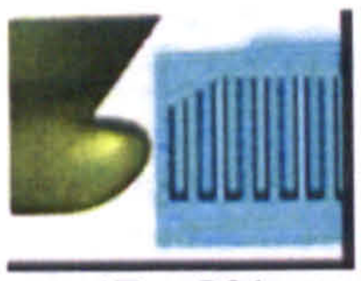 $\Delta T_1 = 5.24$ m	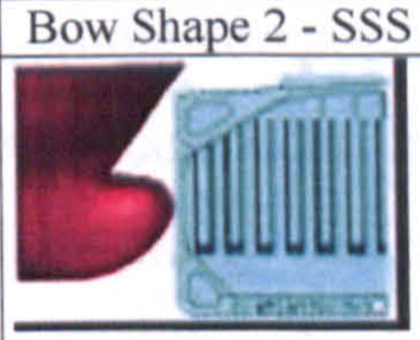 $\Delta T_1 = 4.2$ m
Case 14	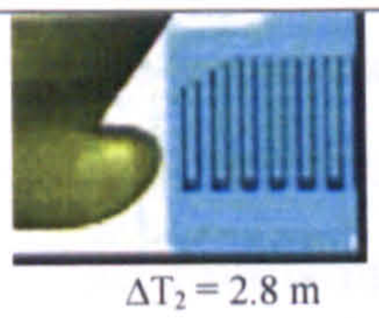 $\Delta T_2 = 2.8$ m	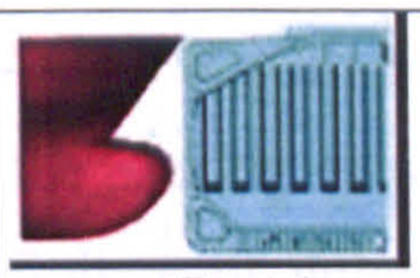 $\Delta T_2 = 1.6$ m
Case 15	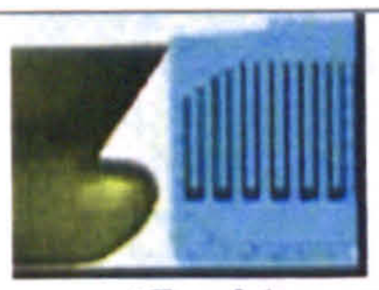 $\Delta T_3 = 0.1$ m	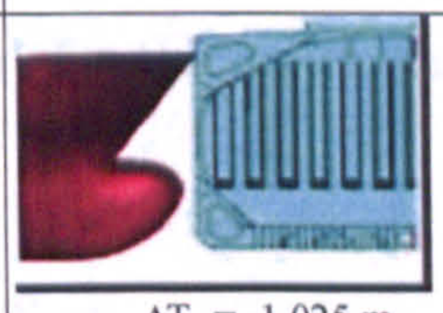 $\Delta T_3 = -1.025$ m
Case 16	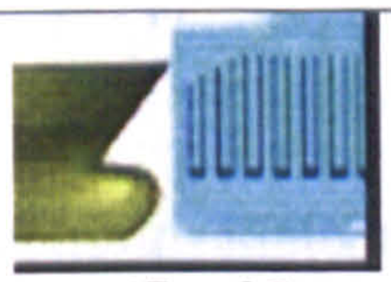 $\Delta T_4 = -2.7$ m	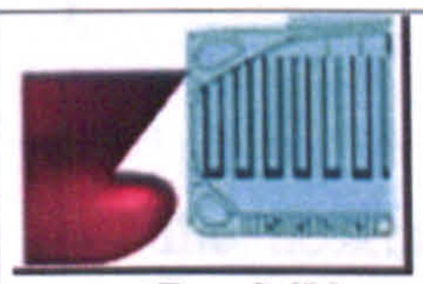 $\Delta T_4 = -3.675$ m

7.4.2 Failure criterion

The failure of ships side structure in case of collision can be described as the tearing of the side shell plating. Hence, a criterion has to be defined for the ultimate strain after which fracture takes place. The rupture strain of the material is a significant function of collision energy absorption capability. It would be thus be of importance to choose the material, welding with good toughens and large critical rupture strain. In fact the rupture of a structural component is a very complicated process and is influenced by many factors. It is directly related to the material characteristic parameters such as the yielding stress, fracture strain and ultimate tensile stress as well.

It is well known from numerous practical experiences and theoretical investigations that the failure depends also on the stress states resulted under complicated loads in the structures. In addition, it is also influenced by manufacture quality and production process. The mesh density, element shape and mesh size has very important role since the development of a fracture process starts from the uniform deformation to continue over the whole component to a local necking in a very small area where extreme large strain values occur. In order to obtain practical failure strain definitions in consideration of many parameters, e.g. element size, stress state and manufacture influence many full-scale thickness measurements on prototype damaged structure components- such as shell plating and stiffeners etc.- have been conducted and uniform strain, the necking as well as the necking length have been determined. The following definition of failure strain is recommended from evaluation of the thickness measurements (Germanischer Lloyd).

$$\varepsilon_f(l_e) = \varepsilon_g + \varepsilon_e \frac{t}{l_e} \tag{7.3}$$

Where, ε_g is the uniform strain and ε_e is the necking, t and l_e is the plate thickness and an individual element length respectively. The values of uniform strain

and the necking achieved from the thickness measurements are related to the calculated stress and they are indicated in Table 7.9.

Table 7.9: Proposed failure strain versus mesh size, GL 2003

Stress States	1-D	2-D
ε_g	0.079	0.056
ε_e	0.76	0.54
Element Type	Beam - Truss	Shell - Plate

7.4.3 Modified Minorsky correlation

In order to compare the numerical results the modified Minorsky approach is employed. Based on the statistics of certain collision accidents, Minorsky [31] suggested an empirical linear correlation between the structural resistance parameter and absorbed energy as follows:

$$W_C = 47.2R_T + 32.7 \tag{7.4}$$

Where, W_C is the total energy absorbed by damage and striking and struck vessels in MJ and R_T is the damaged volume of structural steel in m^3.

$$R_T = \sum_{N=1} P_N L_N t_N + \sum_{n=1} P_n L_n t_n \tag{7.5}$$

Where P_N , P_n = depth of damage for N-th member of striking vessels or for the n-th member of struck vessel, respectively, L_N , L_n = length of damage for the N-th member of the striking vessel or for the n-th member of struck vessel, respectively, and t_N , t_n = thickness of the N-th member of the striking vessel or of the n-th member of the struck vessel, respectively.

Woison (1979) derived a formula, relating the energy absorbed by damage of both striking and struck vessel structures to the damaged volume of structural steel,

which replaces the constant 32.7 in equation (7.5) with the expression $0.49\sum Ht^2$, where H is the height of rupture aperture in the side shell (m) and t is the side shell thickness (cm).

7.4.4 Calculation of internal energy for every collision cases

The calculated plastic deformation energy (internal energy) versus penetration for SSS & DSS vessels subject to 16 different collision cases is summarized with modified Minorsky correlation at t = 0.3 sec in Table 7.10 through Table 7.13 while Figure 7.7 and Figure 7.8 illustrate the deformations at two different time increments for both DSS & SSS bulk carrier vessels respectively.

Table 7.10: Internal energy for SSS at hitting direct web at t = 0. 1 second

SSS	Collision cases	Penetration (m)	Internal Energy (MJ)	
			LS DYNA	Minorsky
Bow shape 1	Case 1	2.36	50.2	54.1
	Case 2	2.48	83.7	81.3
	Case 3	2.73	107.0	93.6
	Case 4	2.79	79.3	89.9
Bow shape 2	Case 9	2.28	60.6	62.5
	Case 10	0.94	65.0	30.9
	Case 11	2.57	84.9	61.7
	Case 12	3.56	86.1	23.4

Table 7.11: Internal energy for DSS at hitting direct web at t = 0.1 seconds

DSS	Collision cases	Penetration (m)	Internal Energy (MJ)	
			LS DYNA	Minorsky
Bow shape 1	Case 1	1.10	61.5	65.4
	Case 2	2.22	73.8	59.1
	Case 3	1.96	90.1	75.8
	Case 4	2.83	69.7	76.3
Bow shape 2	Case 9	2.67	36.7	30.8
	Case 10	2.13	62.1	54.3
	Case 11	1.56	61.2	43.7
	Case 12	2.15	48.1	29.1

Table 7.12: Internal energy for SSS at hitting between web at t = 0.3 seconds

SSS	Collision cases	Penetration (m)	Internal Energy (MJ)	
			LS DYNA	Minorsky
Bow shape 1	Case 5	2.71	73.0	66.5
	Case 6	2.85	121.2	54.8
	Case 7	2.80	120.1	83.8
	Case 8	3.07	104.1	65.7
Bow shape 2	Case 13	2.98	67.8	37.9
	Case 14	2.42	77.2	30.6
	Case 15	2.52	81.1	37.9
	Case 16	2.56	87.5	57.8

Table 7.13: Internal energy for DSS at hitting between at t = 0.3 seconds

DSS	Collision cases	Penetration (m)	Internal Energy (MJ)	
			LS DYNA	Minorsky
Bow shape 1	Case 5	2.38	63.1	74.7
	Case 6	2.41	78.2	80.6
	Case 7	2.62	84.7	76.1
	Case 8	2.72	69.4	81.3
Bow shape 2	Case 13	2.10	37.2	33.5
	Case 14	1.88	37.8	47.4
	Case 15	2.45	58.2	46.8
	Case 16	2.18	48.4	43.8

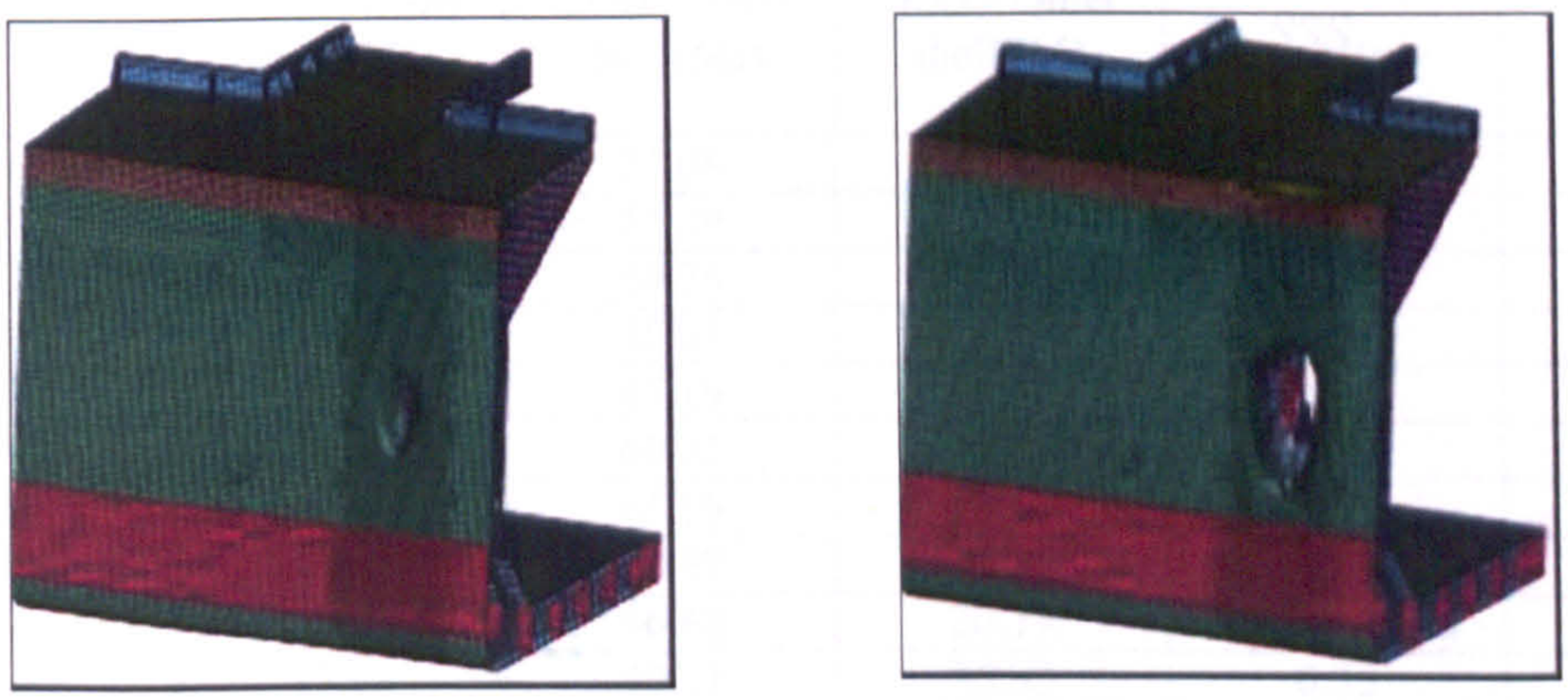

Figure 7.8: Deformations in case 1 for DSS at t = 0.1 and t = 0.3 seconds, respectively

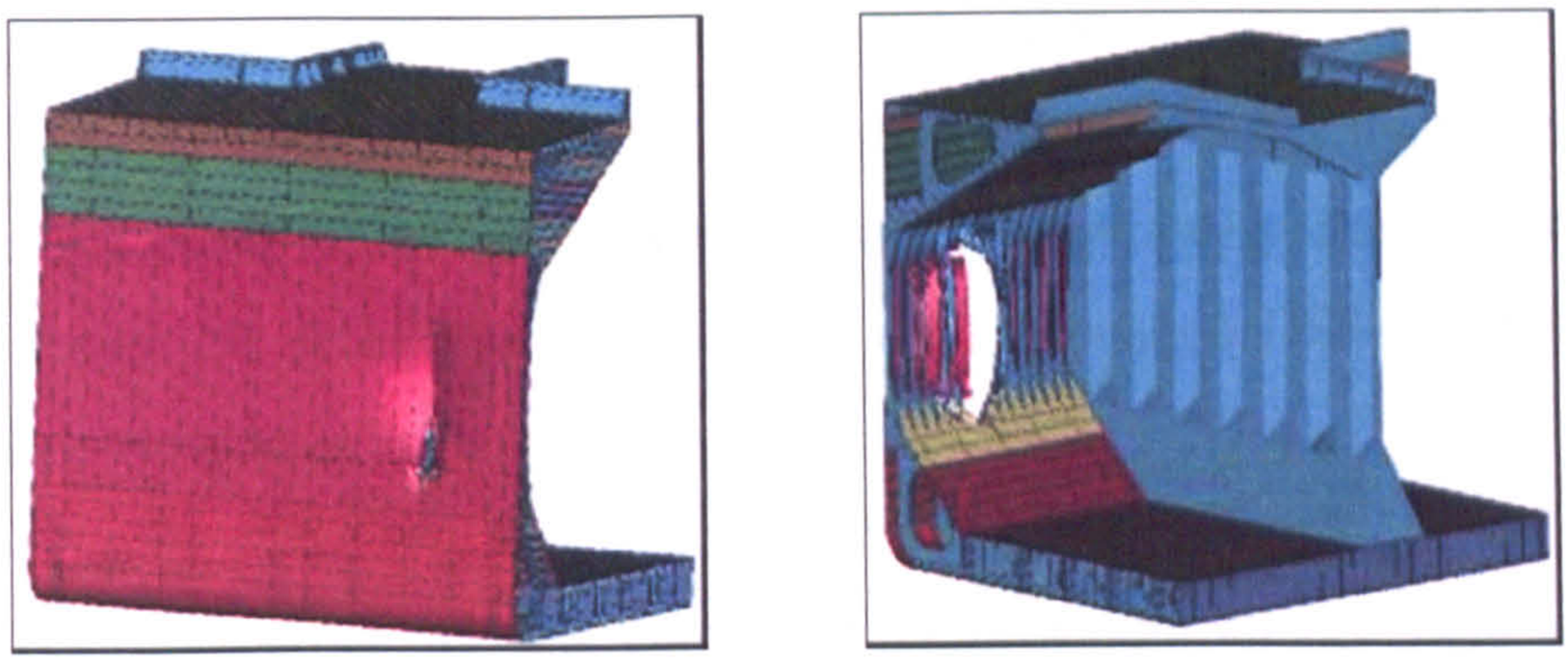

Figure 7.9: Deformations in case 1 for SSS at t = 0.1 and t = 0.3 seconds, respectively

Table 7.12 presents a summary of the results. Column 2 shows the energy absorbed when rupture of the DSS occurs. Column 3 and 4 show the critical energy absorbed when the skin of the cargo hold, i.e. inner shell for DSS (col.3) and outer shell for SSS ruptures (col.4). Column 5 is the ratio of the energies absorbed by the outer skin of the DSS over that of the SSS and column 6 the ratio of the critical energies of the DSS over that of the SSS.

Table 7.14: The summary of the rupture energies of DSS & SSS bulk carrier designs

Case	*DSS* - Outer shell (MJ)	*DSS* - Inner shell (MJ)	*SSS* - Outer shell (MJ	$\frac{DSS_{Outer}}{SSS_{Outer}}$	$\frac{DSS_{Inner}}{SSS_{Outer}}$
1	22.23	51.08	13.84	1.61	**3.69**
2	24.61	50.29	14.76	1.67	**3.41**
3	30.48	69.25	37.35	0.81	**1.85**
4	16.45	40.61	17.17	0.96	**2.36**
5	16.83	47.19	32.12	0.52	**1.47**
6	18.79	60.35	59.20	0.32	**1.02**
7	16.17	61.18	43.45	0.37	**1.41**
8	7.88	43.43	26.75	0.29	**1.62**
9	9.81	36.62	20.19	0.49	**1.81**
10	12.43	40.11	35.92	0.35	**1.12**
11	36.94	No rupture	10.72	3.44	---
12	6.42	No rupture	6.33	1.01	---
13	8.53	30.73	10.35	0.82	**2.97**
14	6.98	50.71	39.44	0.18	**1.28**
15	8.13	No rupture	8.55	0.95	---
16	5.94	No rupture	9.28	0.64	---

Energy absorption when rupture of the outer shell of DSS occurs is approximately 10% less than the energy absorbed by the outer shell of SSS. However, the maximum energy absorbed, i.e. the energy absorbed when the skin of

cargo hold (inner shell for DSS, outer shell for SSS) ruptures, in 2.2 times more for DSS than for the SSS. It is noted that for all cases DSS has higher rupture energy than SSS. However, in case 6 SSS' rupture energy is very close to DSS, which is only lesser 2%. This is because; at the impact location DSS and SSS have very similar structural arrangements.

The comparing of the calculated deformation energy dependent on the penetration for each collision case between DSS & SSS bulk carrier designs with the modified Minorsky correlation is illustrated in Figure 7.9.

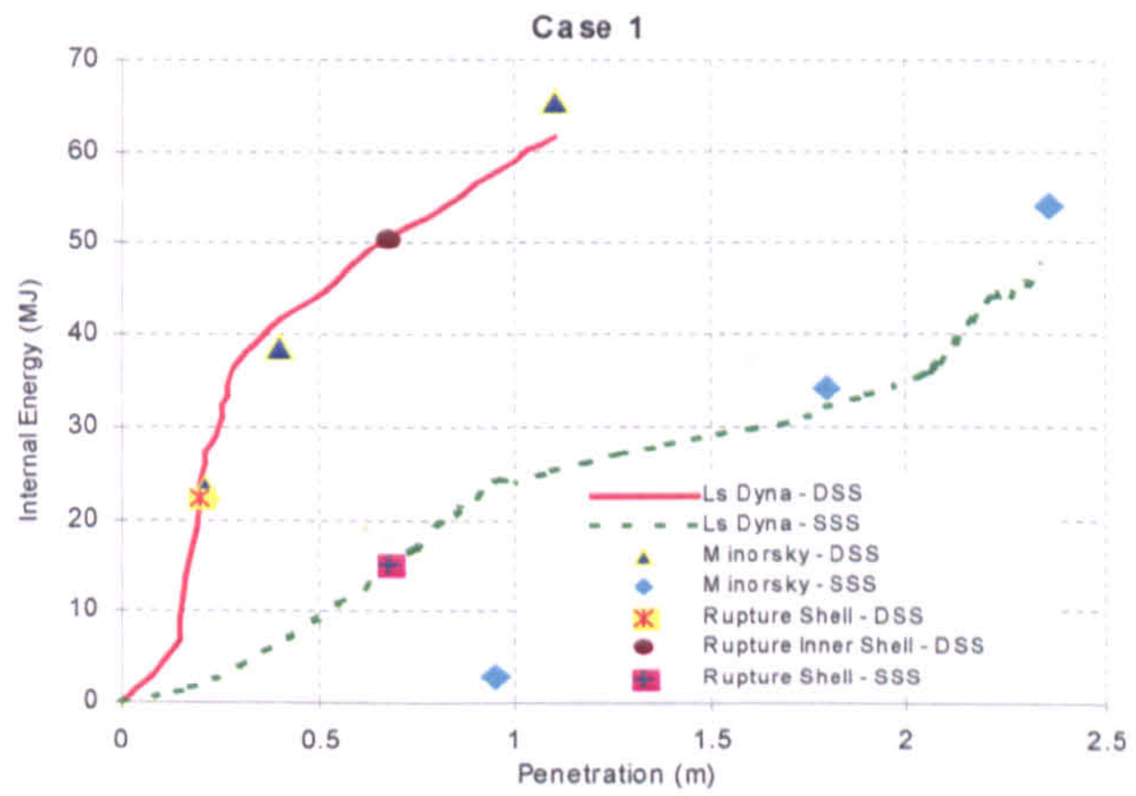

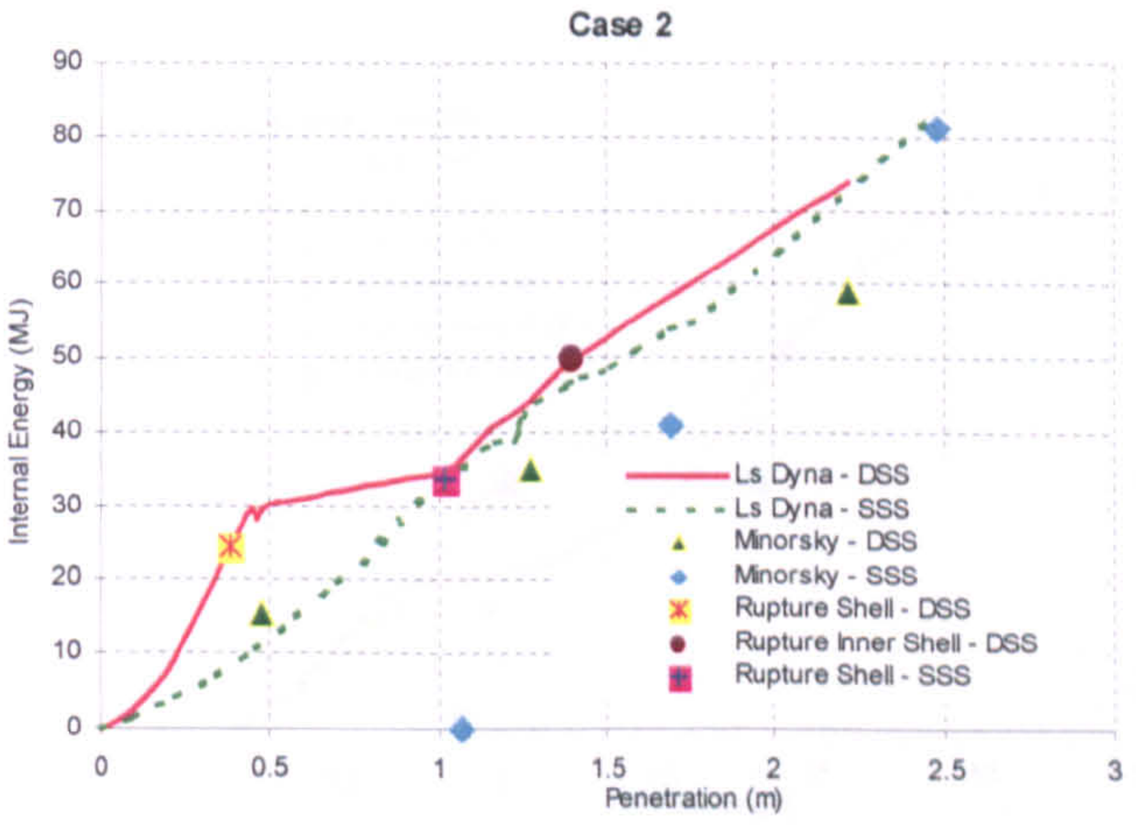

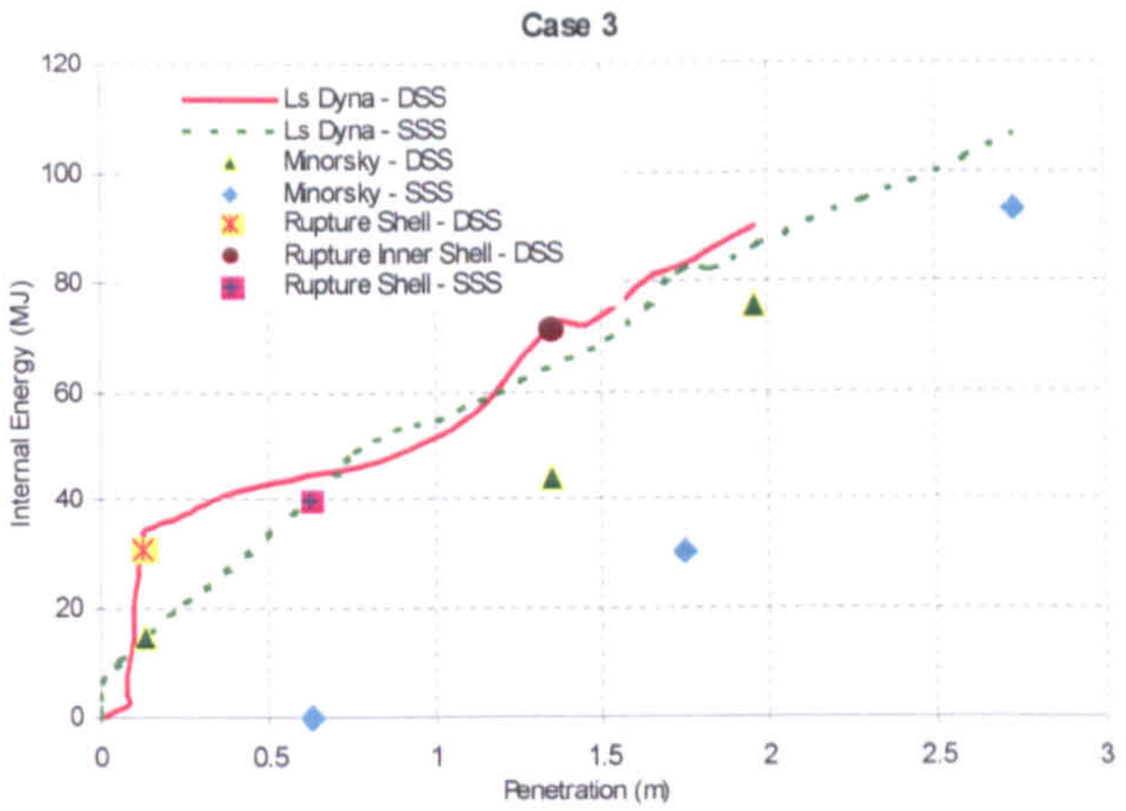
Case 3
Ls Dyna - DSS
Ls Dyna - SSS
Minorsky - DSS
Minorsky - SSS
Rupture Shell - DSS
Rupture Inner Shell - DSS
Rupture Shell - SSS
Internal Energy (MJ)
Penetration (m)
0
20
40
60
80
100
120
0
0.5
1
1.5
2
2.5
3

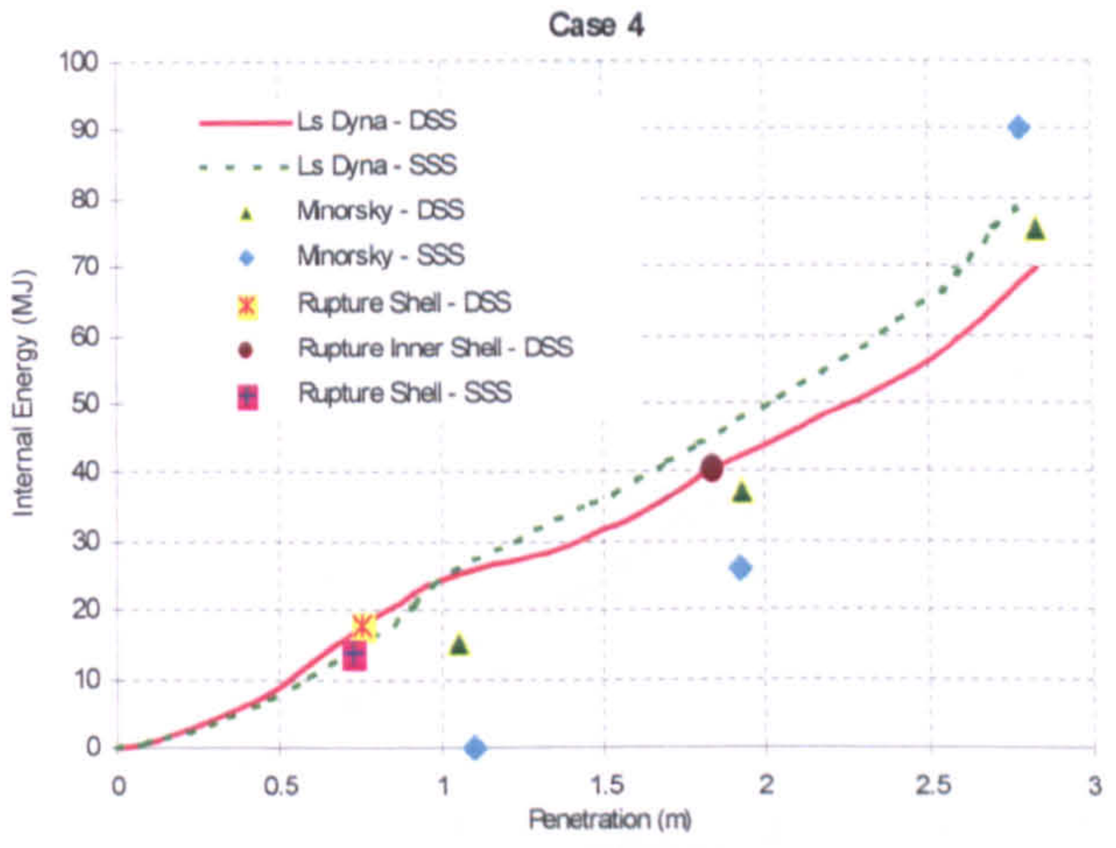
Case 4
Ls Dyna - DSS
Ls Dyna - SSS
Minorsky - DSS
Minorsky - SSS
Rupture Shell - DSS
Rupture Inner Shell - DSS
Rupture Shell - SSS
Internal Energy (MJ)
Penetration (m)
0
10
20
30
40
50
60
70
80
90
100
0
0.5
1
1.5
2
2.5
3

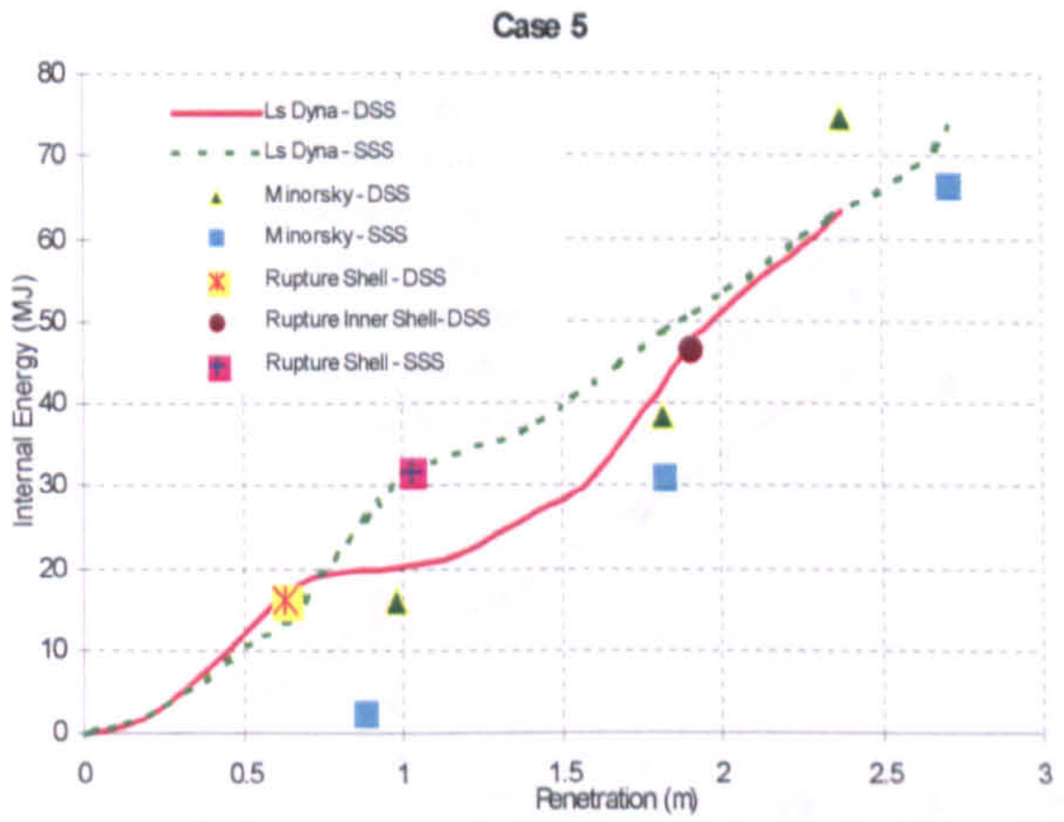
Case 5
Ls Dyna - DSS
Ls Dyna - SSS
Minorsky - DSS
Minorsky - SSS
Rupture Shell - DSS
Rupture Inner Shell- DSS
Rupture Shell - SSS
Internal Energy (MJ)
Penetration (m)
0
10
20
30
40
50
60
70
80
0
0.5
1
1.5
2
2.5
3

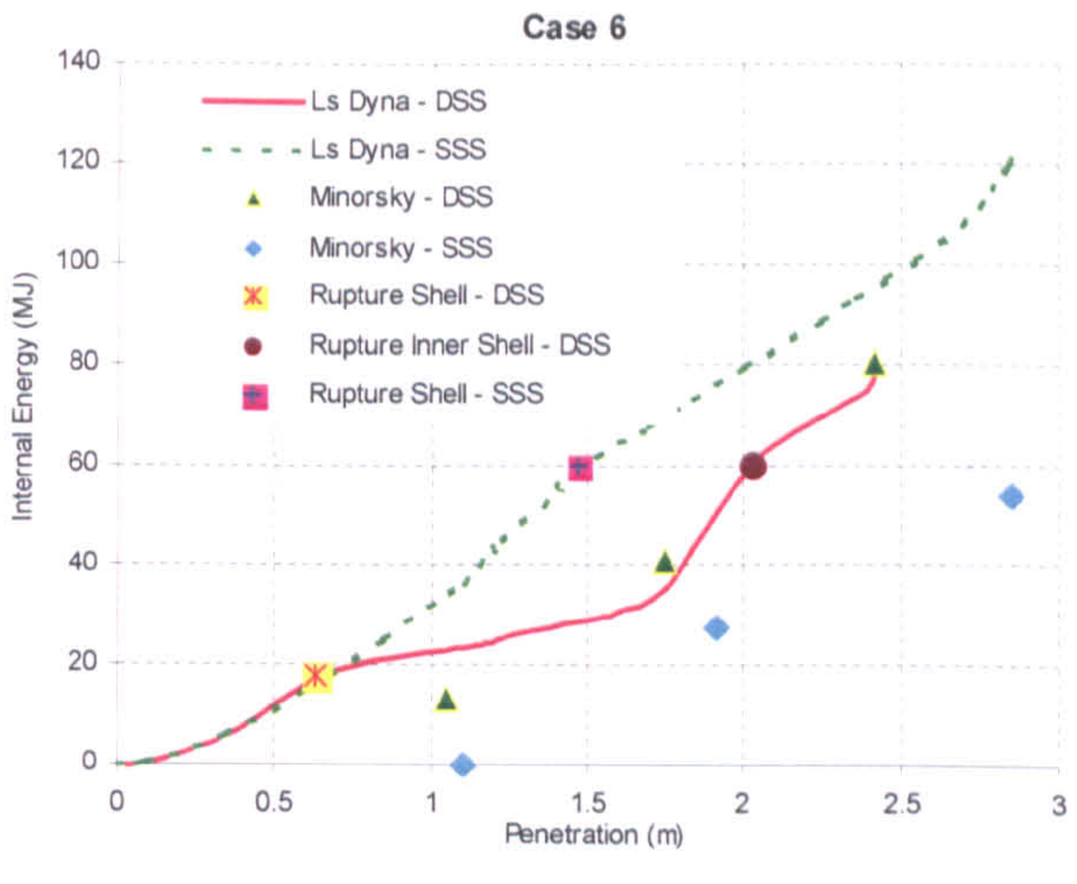
Case 6
Ls Dyna - DSS
Ls Dyna - SSS
Minorsky - DSS
Minorsky - SSS
Rupture Shell - DSS
Rupture Inner Shell - DSS
Rupture Shell - SSS
Internal Energy (MJ)
Penetration (m)
0
20
40
60
80
100
120
140
0
0.5
1
1.5
2
2.5
3

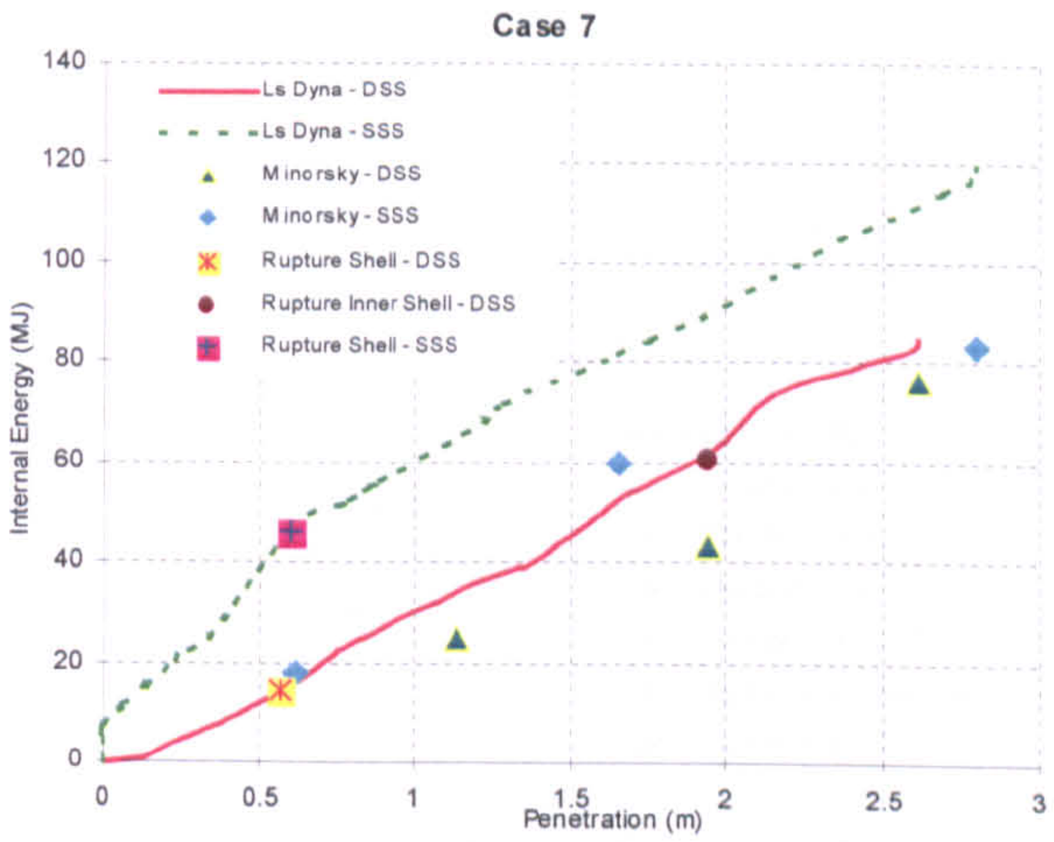
Case 7
Ls Dyna - DSS
Ls Dyna - SSS
Minorsky - DSS
Minorsky - SSS
Rupture Shell - DSS
Rupture Inner Shell - DSS
Rupture Shell - SSS
Internal Energy (MJ)
Penetration (m)
0
20
40
60
80
100
120
140
0
0.5
1
1.5
2
2.5
3

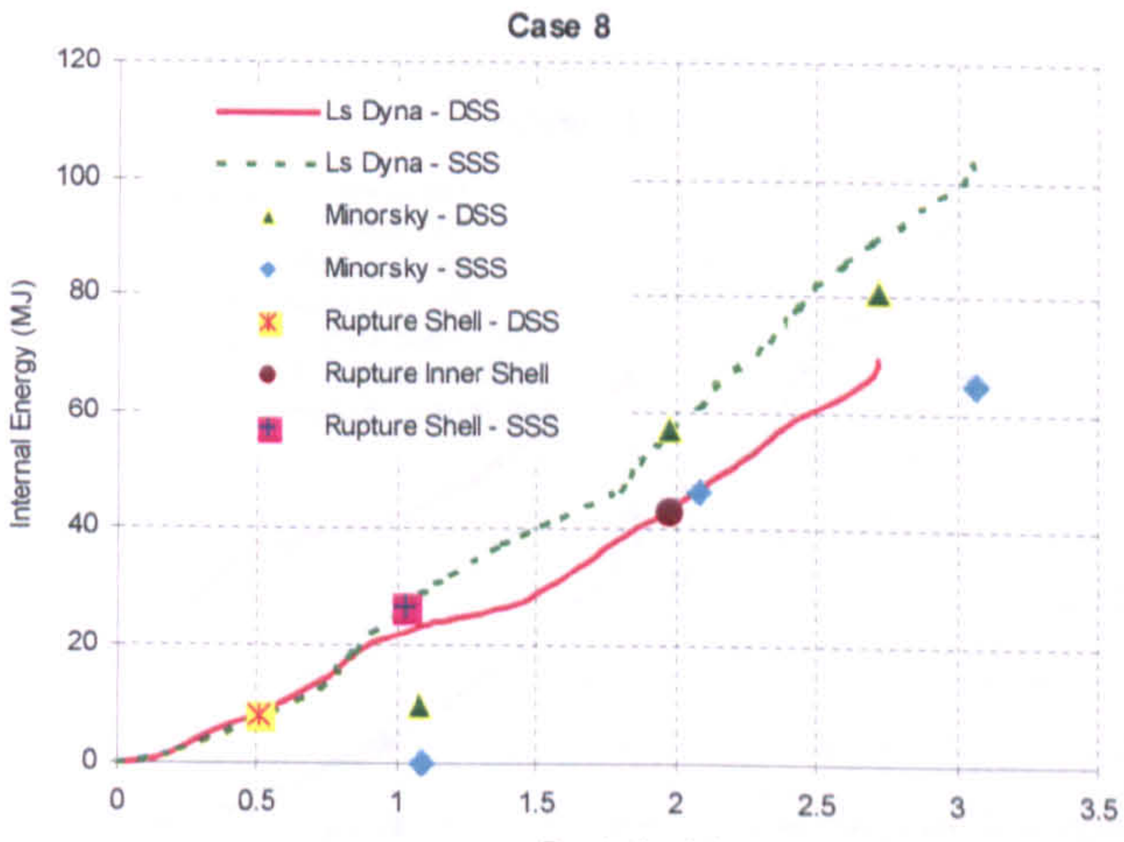
Case 8
Ls Dyna - DSS
Ls Dyna - SSS
Minorsky - DSS
Minorsky - SSS
Rupture Shell - DSS
Rupture Inner Shell
Rupture Shell - SSS
Internal Energy (MJ)
Penetration (m)
0
20
40
60
80
100
120
0
0.5
1
1.5
2
2.5
3
3.5

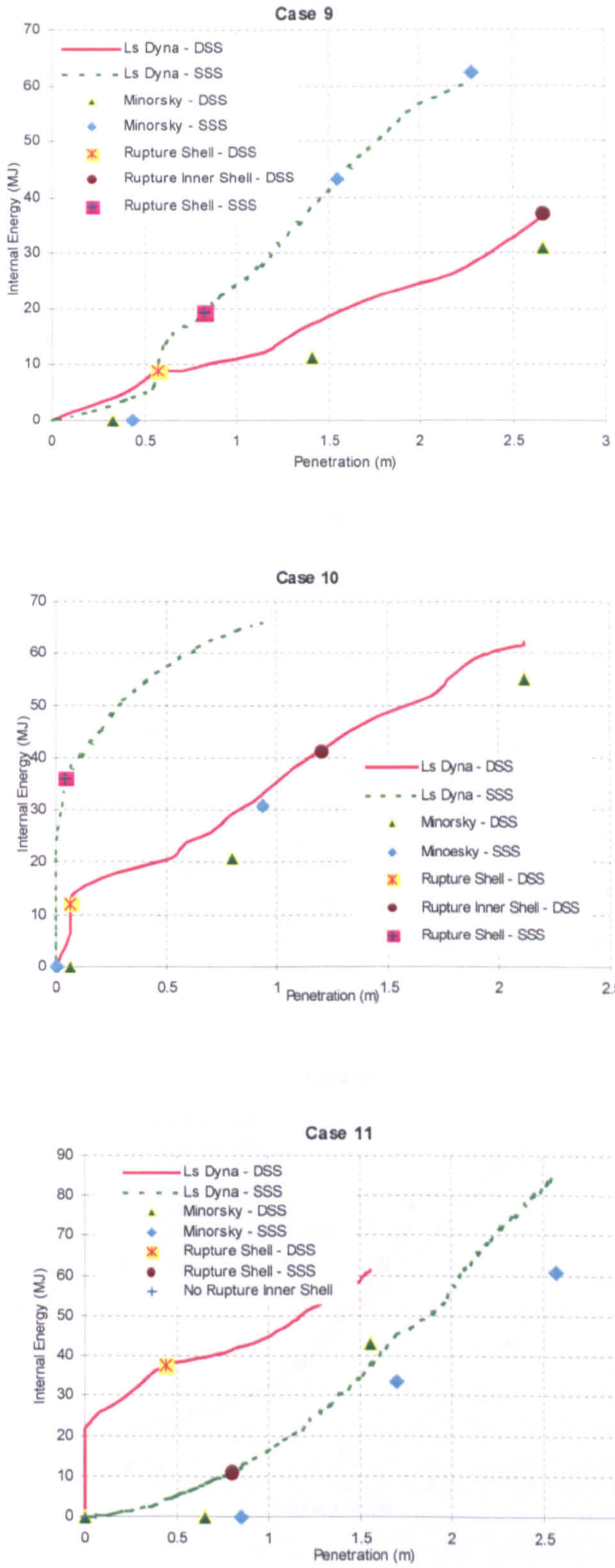
Case 9
Ls Dyna - DSS
Ls Dyna - SSS
Minorsky - DSS
Minorsky - SSS
Rupture Shell - DSS
Rupture Inner Shell - DSS
Rupture Shell - SSS
Internal Energy (MJ)
Penetration (m)
Case 10
Ls Dyna - DSS
Ls Dyna - SSS
Minorsky - DSS
Minoesky - SSS
Rupture Shell - DSS
Rupture Inner Shell - DSS
Rupture Shell - SSS
Internal Energy (MJ)
Penetration (m)
Case 11
Ls Dyna - DSS
Ls Dyna - SSS
Minorsky - DSS
Minorsky - SSS
Rupture Shell - DSS
Rupture Shell - SSS
No Rupture Inner Shell
Internal Energy (MJ)
Penetration (m)

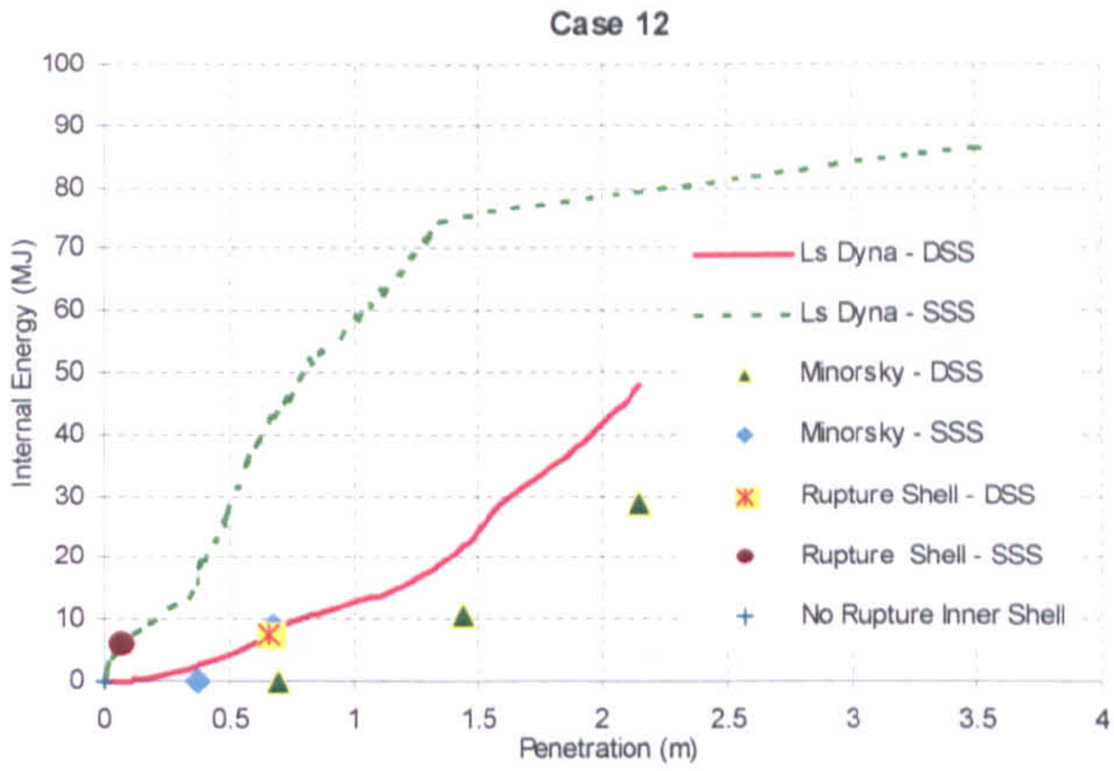
Case 12
Internal Energy (MJ)
Penetration (m)
Ls Dyna - DSS
Ls Dyna - SSS
Minorsky - DSS
Minorsky - SSS
Rupture Shell - DSS
Rupture Shell - SSS
No Rupture Inner Shell

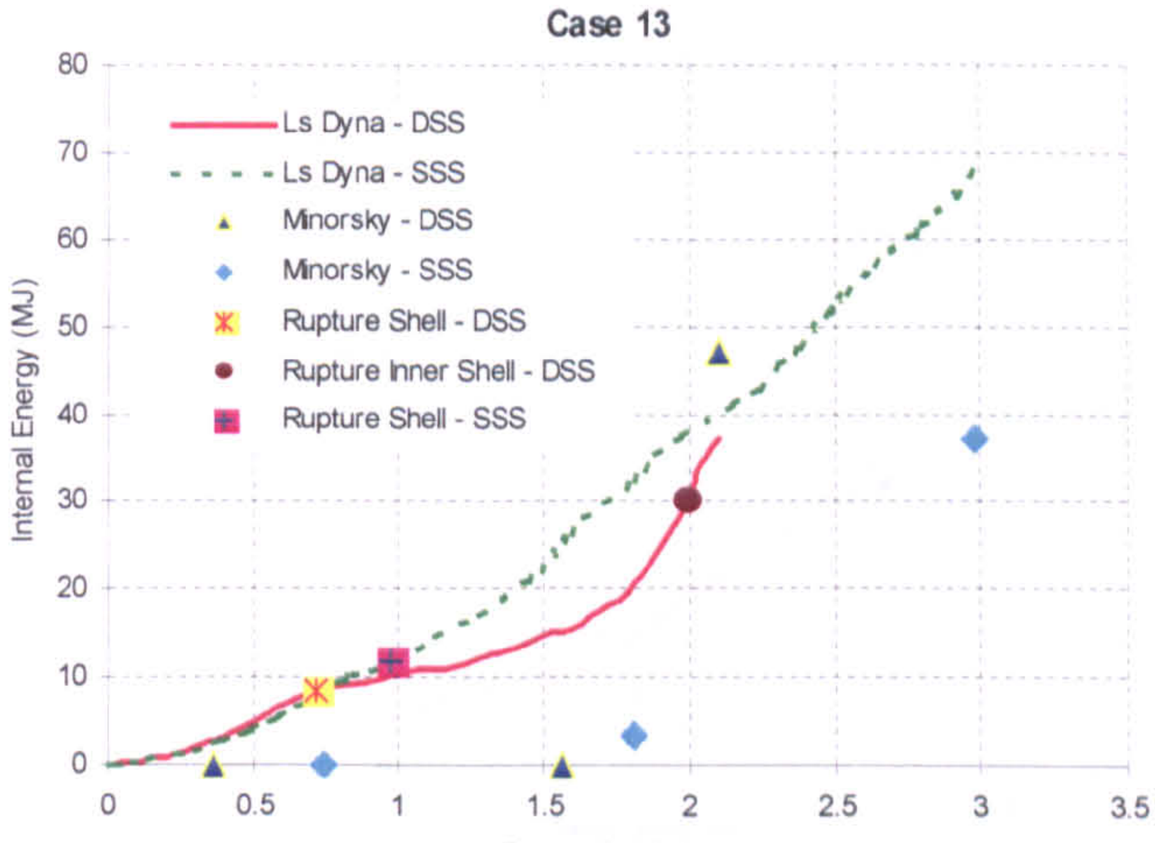
Case 13
Internal Energy (MJ)
Penetration (m)
Ls Dyna - DSS
Ls Dyna - SSS
Minorsky - DSS
Minorsky - SSS
Rupture Shell - DSS
Rupture Inner Shell - DSS
Rupture Shell - SSS

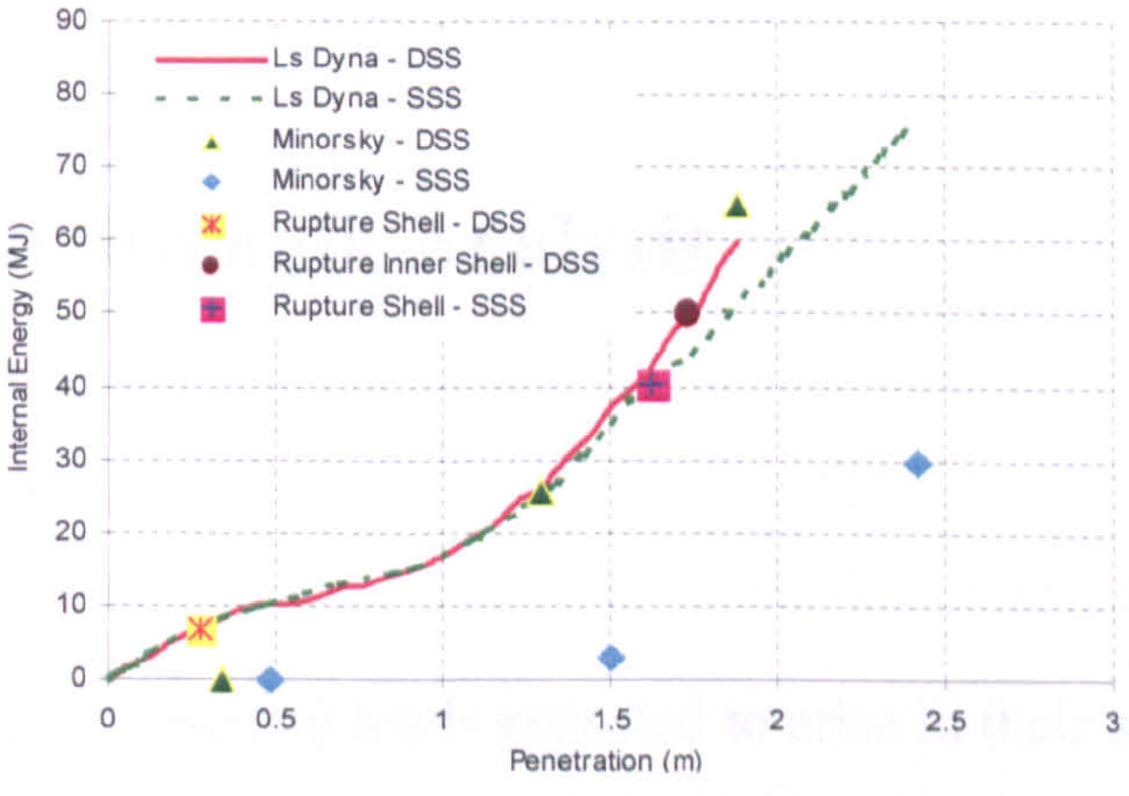
Case 14
Internal Energy (MJ)
Penetration (m)
Ls Dyna - DSS
Ls Dyna - SSS
Minorsky - DSS
Minorsky - SSS
Rupture Shell - DSS
Rupture Inner Shell - DSS
Rupture Shell - SSS

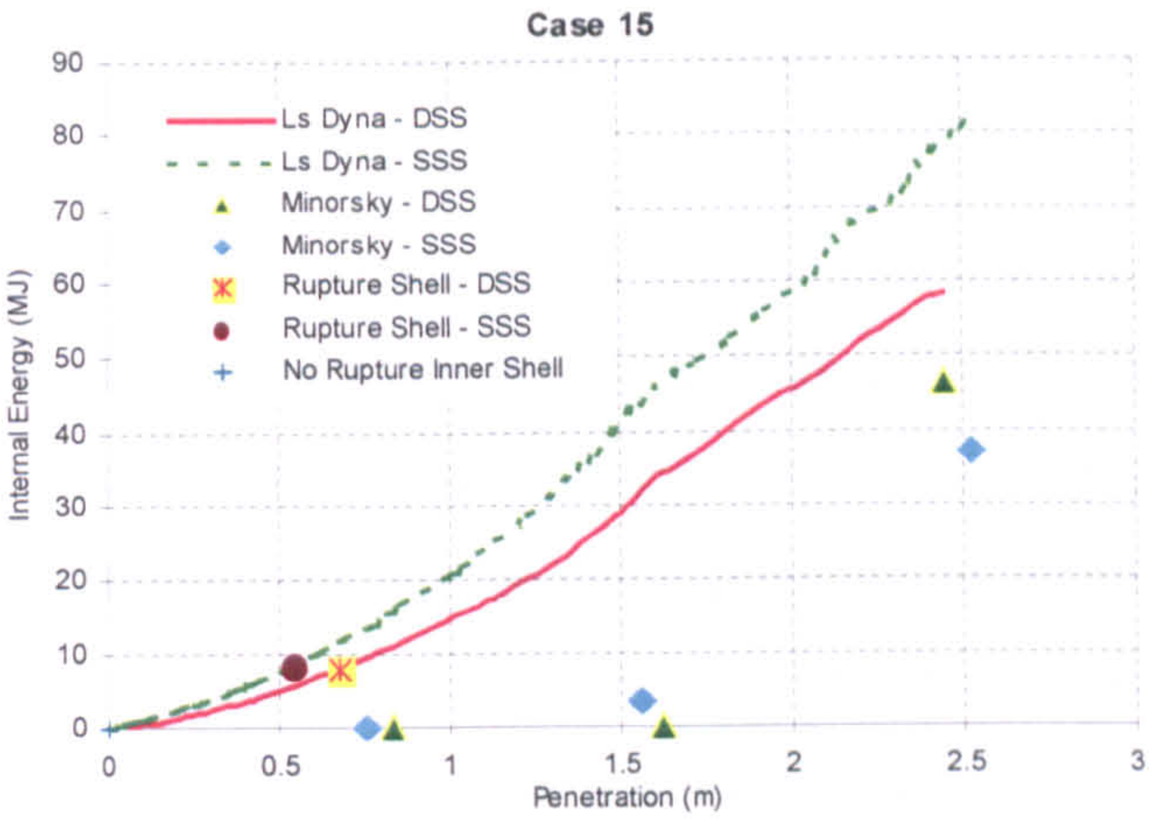

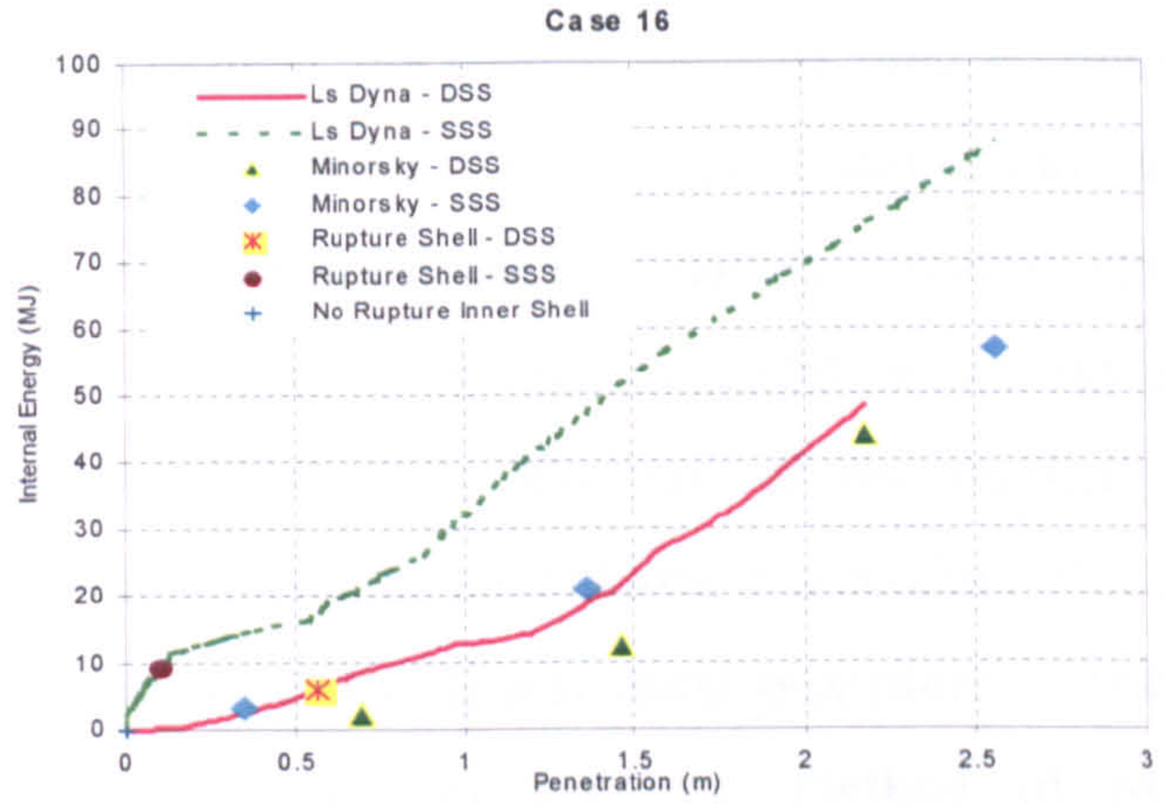

Figure 7.10: Internal energy versus penetration curves for all investigated collision case

7.5 Residual Strength Analysis

7.5.1 State of art

Ships are designed to resist all loads expected to arise in their seagoing environment. The objective in structural design is to maintain a ship structural integrity for normal operating conditions. A combination of the most severe loads is usually selected as the normal design load. However, the damage induced by grounding or collision dramatically decreases the ship hull resistance. The effect that damage has on the overall residual strength of structure is a function of its extent, mode of failure and

relative shipboard location. Conventional design, assessing an adequate structural strength in intact condition, does not necessarily guarantee an acceptable safety margin in damaged conditions. However, when a ship is damaged the operators need to decide the immediate repair actions by evaluating the effects of the damage on the safety of the ship using residual strength assessment procedure. International Maritime Organization (IMO) has therefore proposed an amendment, which states: ' All oil tankers of 5000 tonnes deadweight or more shall have prompt access to computerized, shore-based damage stability and residual structural strength calculation programmes. Earlier, Smith & Dow (1981) conducted a research about the residual strength of damaged ships and offshore structures. A study reported by Ghose *et al.* (1994) reviews the current methods used by marine industry to assess the residual strength. The primary objectives of this report such as introducing the subject of residual strength assessment of damaged marine structures due to normal operating loads and summarize the state of the art technology and methods available for quantifying residual strength. Because of the implicit relationship between residual strength and inspections procedures, a secondary objective of the report was to present an outline for practical analytical procedure to react to detected cracks. Zhang (1996) proposed a semi-analytical method of assessing the residual longitudinal strength of a damaged ship hull. Paik, *et al.* (1998) analysed the residual strength of a ship after collision and grounding. The location and amount of collision and grounding damage were prescribed. The possibility of hull collapse was explored by a comparison of the applied extreme bending moment and the ultimate hull strength which were estimated using design oriented methods and formulas. Two types of residual strength index, namely the section modulus based residual strength index and the ultimate bending strength based residual strength index, were defined. Qi, *et al.* (1999) also proposed a simplified method for assessing residual strength of hull girder of damaged ships, the corresponding reliability of damaged ship is also analysed. Wang *et al.* (2002a) first reviewed the state-of –the-art research on the collision and grounding, focusing on the three issues that a standard for design against accidents needs to address: definition of accident scenarios, evaluation approaches, and the acceptance criteria. Later, Wang *et al.* (2002b) investigated the longitudinal strength of a damaged ship hull for a broad spectrum of collision and

grounding accidents. Both the hull girder section modulus and hull girder ultimate strength, based on the appropriate approach, are calculated. The simple relationships to assess residual hull girder strength are obtained, which may be used as handy and reliable tools to help make timely decisions in the event of an emergency. Kalman *et al.* (2002) investigated the effect of different damage modes of a hull section on the residual longitudinal strength of an impaired ship, based on elastic theory, fully plastic resistance moment theory and ultimate bending moment approach, respectively. The practical application of the computational link between the residual strength contours and a ship's survival is further clarified in the given example. Finally, the use is suggested of constant, residual strength contours of damaged hull girder sections, to enhance assessment of a ship's survival ability when exposed to longitudinal vertical bending after an accident. Santos *et al.* (2002) present a probabilistic methodology of assessing the survivability of damaged passenger Ro-Ro ships through the identification of critical damage scenarios. The static equivalent method was used to calculate the critical sea state the ship can survive in, for a given damage scenario. Monte Carlo simulation is used to take into account the uncertainties in the ship's loading condition at the time of the accident: intact draught, vertical and longitudinal position of the centre of gravity and permeability of the Ro-Ro decks. Recently, Das & Fang (2005) investigated the residual strength capacity subject to grounding and collision based on advanced calculation methods developed for SSS and DSS capsize type bulk carrier vessels. Survivability of SSS and DSS bulk carrier designs after damage scenarios was addressed in detail.

From above review of the residual strength of the damaged ship, the research on this field mainly focuses on the following two aspects:

1. Estimating the influence of damaged ship members (such as damaged panels and damaged stiffeners) on the hull girder ultimate strength.
2. Based on the empirical and semi-analytical methods, assessing the residual longitudinal strength of ship after collision and grounding in order to providing handy tools to help make timely decisions in the event of an emergency, even at some cost of accuracy.

7.6 The Analysis of Residual Strength of SSS & DSS Bulk Carriers under Collision Damage

In order to include damage that occurred during ship-ship collision simulation on the residual strength calculation, all elements failed have been removed from the intact original configuration in accordance with ANSYS LS-DYNA numerical results. All simulated collision scenarios represent the location and extent of structural damage. The resulting damage also varies, so that each accident is different. The residual resistance of damaged ship hull girders are investigated, both in hogging and sagging cases, in which damage scenarios demonstrates in Table 7.15 through 7.22.

Table 7.23 and Table 7.24 gives the ultimate coupled vertical and horizontal bending moment on SSS and DSS bulk carrier vessels which corresponding to 16 different damage conditions and intact as well as the fully plastic bending moments without and with corrosion effect based on JBP Rules respectively. It is seen that ultimate moment of an intact DSS bulk carrier in hogging case is a little less of SSS bulk carrier. This is mainly because there is slight difference of the plating thickness and scantlings of primary members between DSS and SSS bulk carriers. For example, the deck plating thickness is 33 mm for SSS bulk carriers and 30 mm for DSS bulk carriers.

Table 7.15: Bow shape 1at direct web longitudinal position

Case	DSS	SSS
Case 1	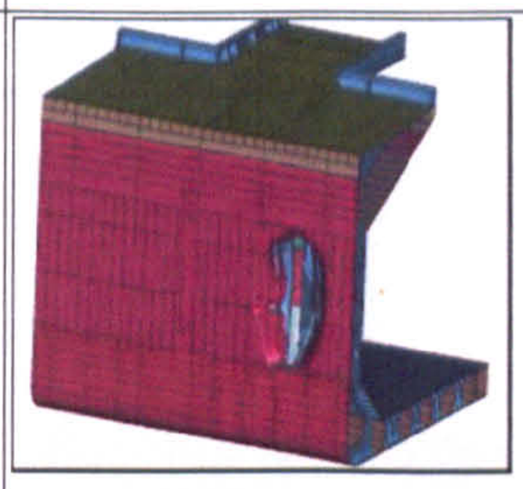	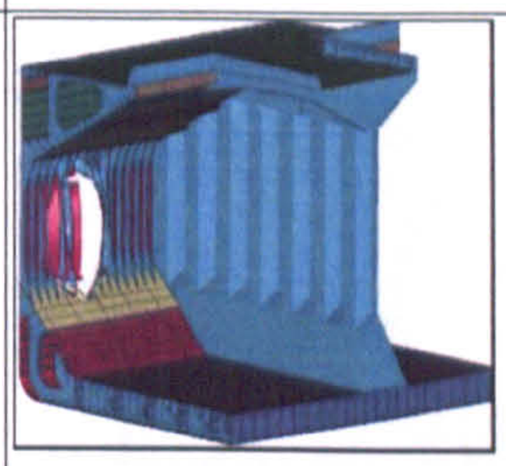
Case 2	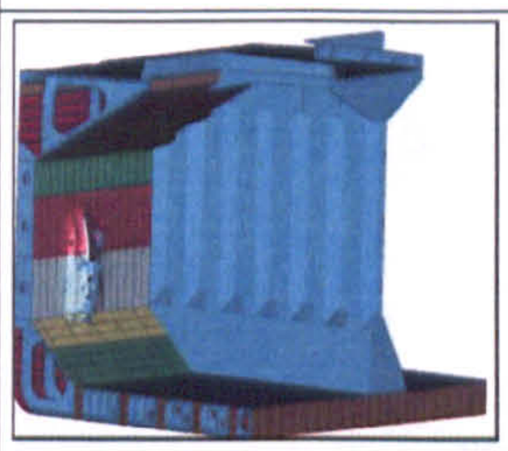	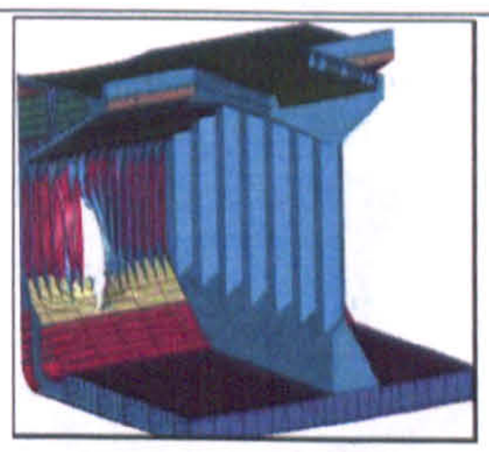
Case 3	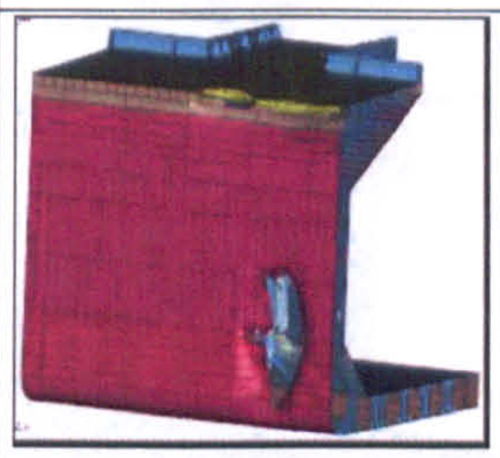	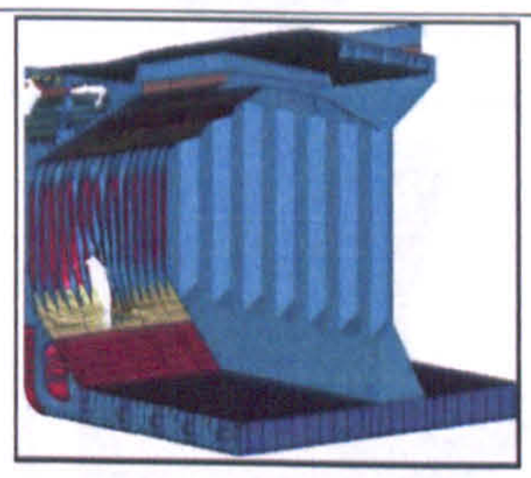
Case 4	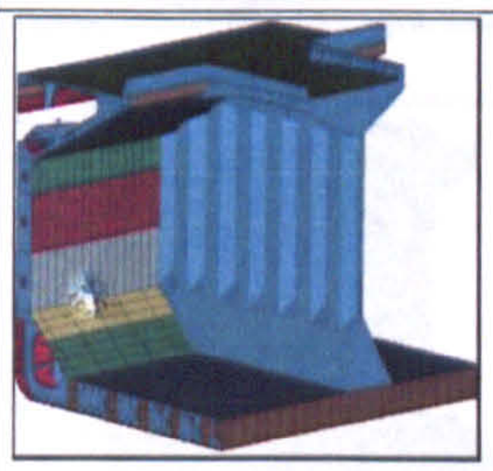	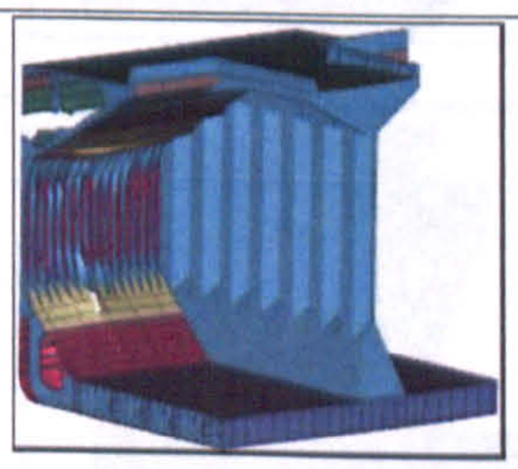

Table 7.16: Bow shape 1 at between web longitudinal position

Case	DSS	SSS
Case 5	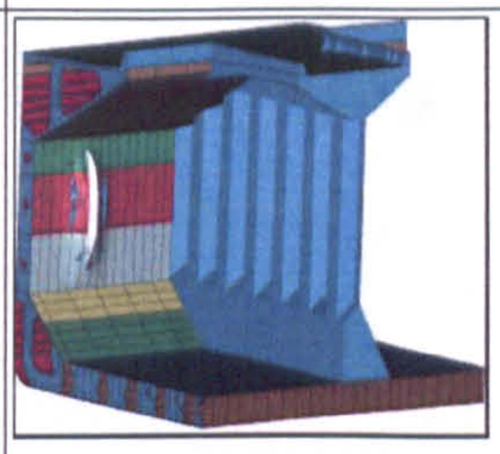	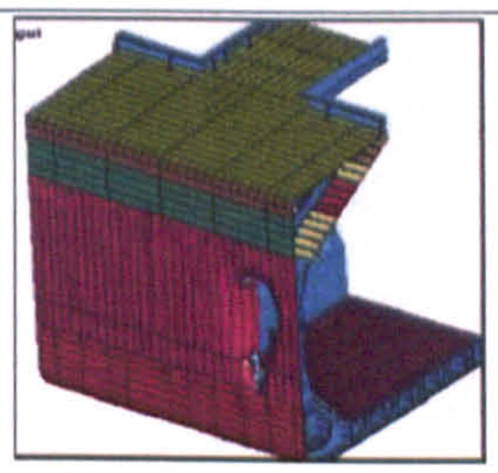
Case 6	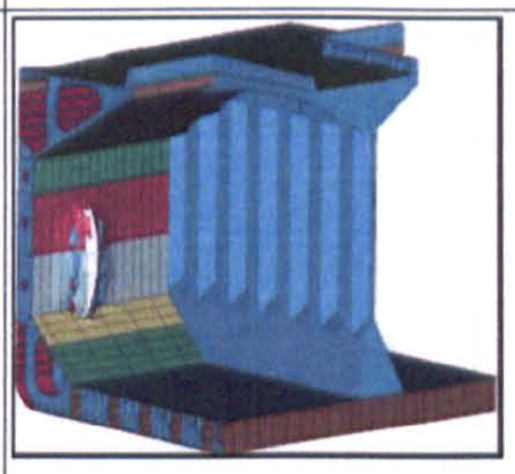	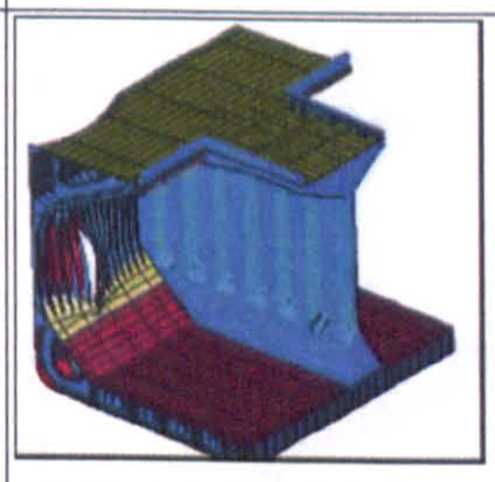
Case 7	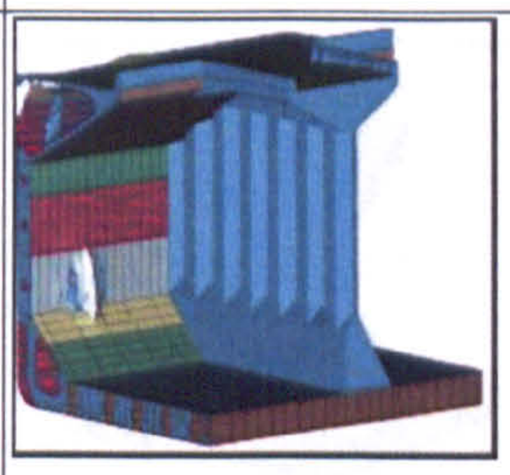	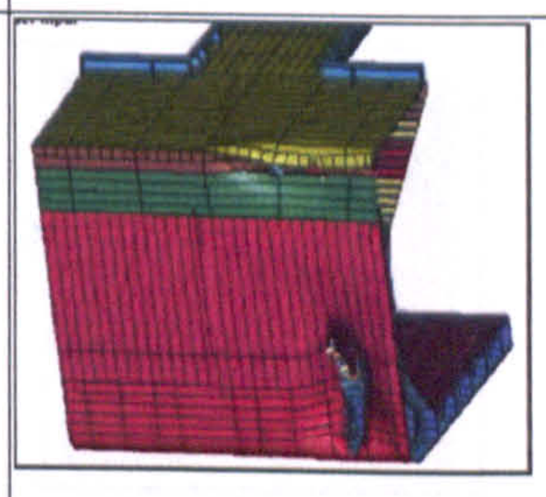
Case 8	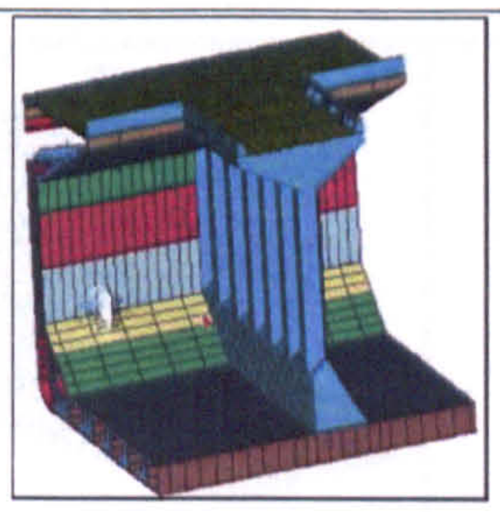	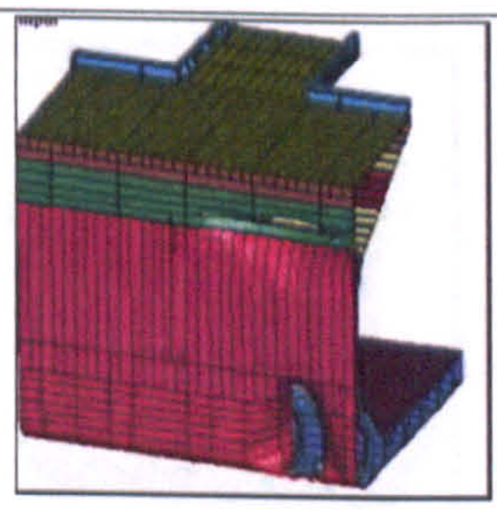

Table 7.17: Bow shape 2 at direct web longitudinal position

Case	DSS	SSS
Case 9	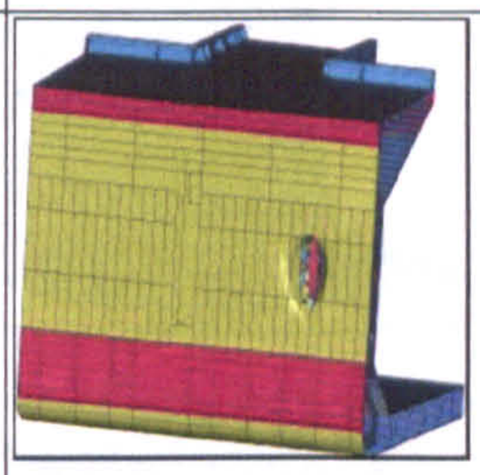	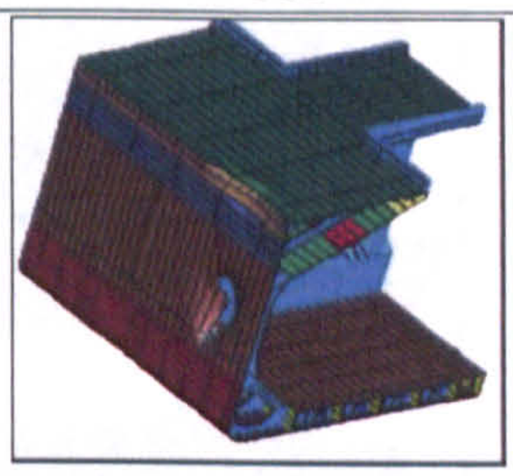
Case 10	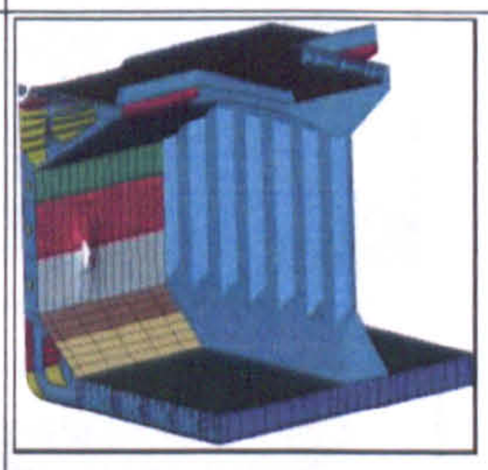	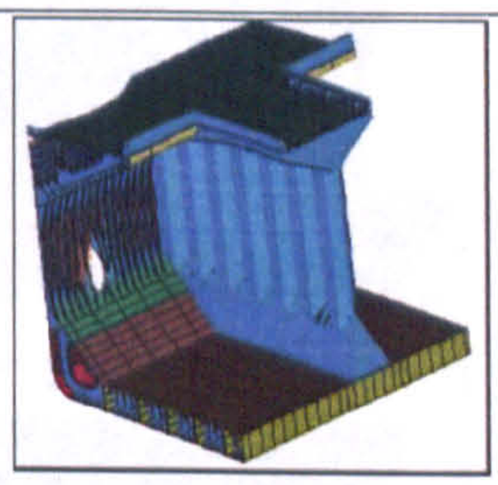
Case 11	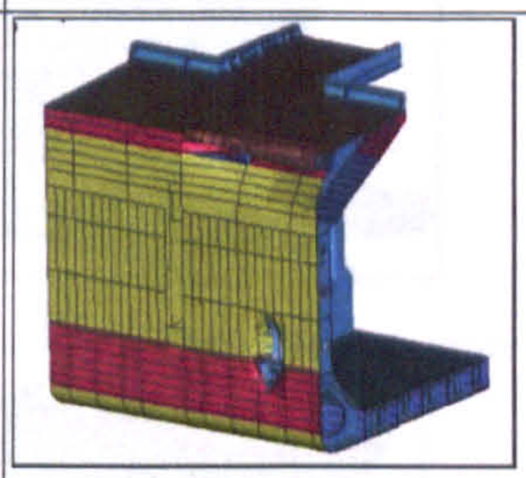	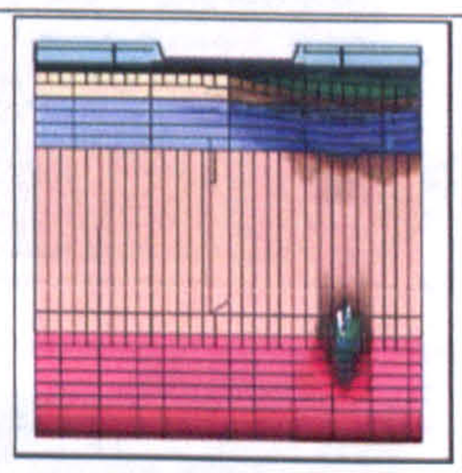
Case 12	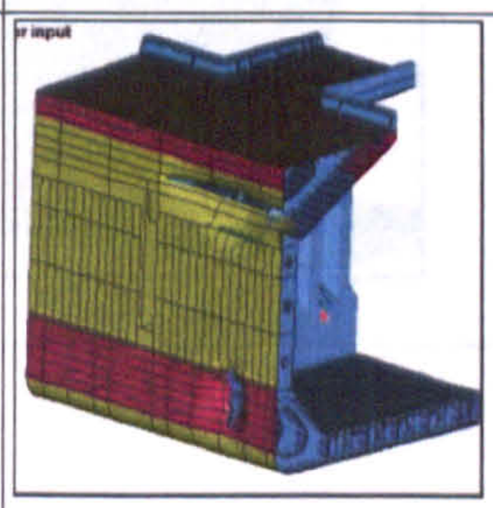	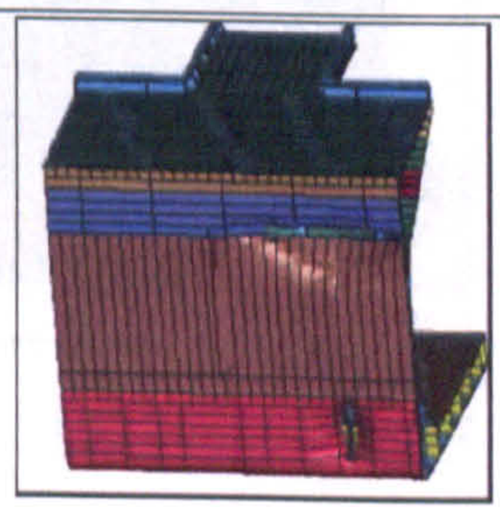

Table 7.18: Bow shape 2 at between web longitudinal position

Case	DSS	SSS
Case 13	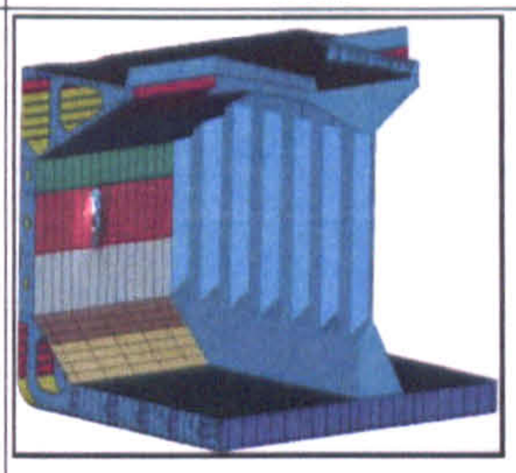	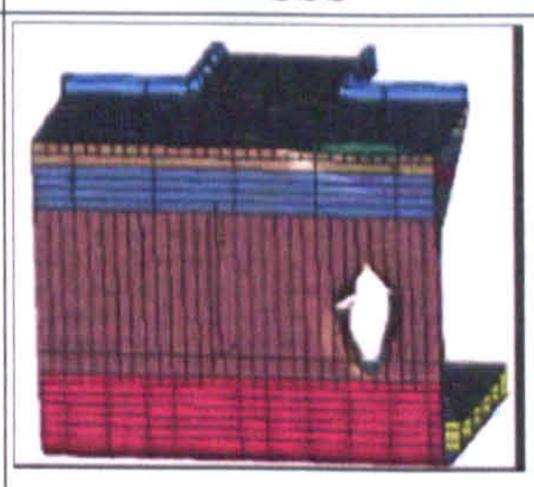
Case 14	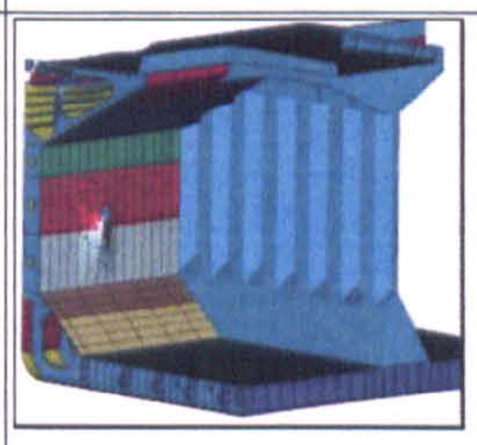	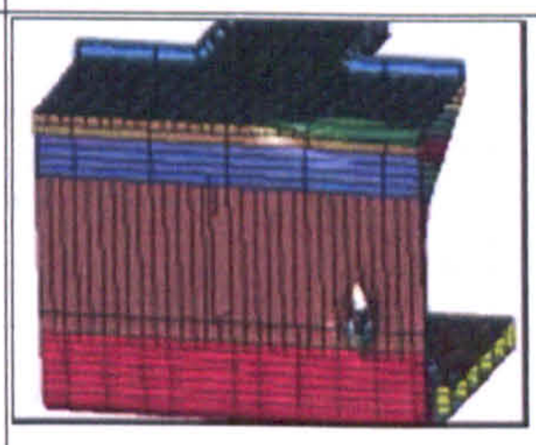
Case 15	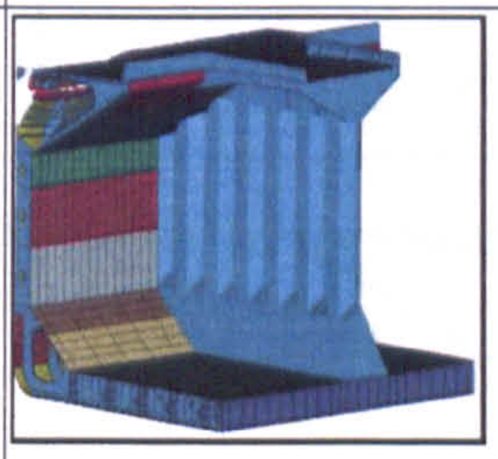	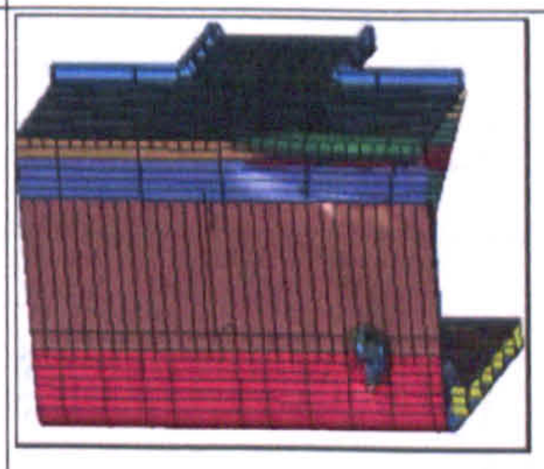
Case 16	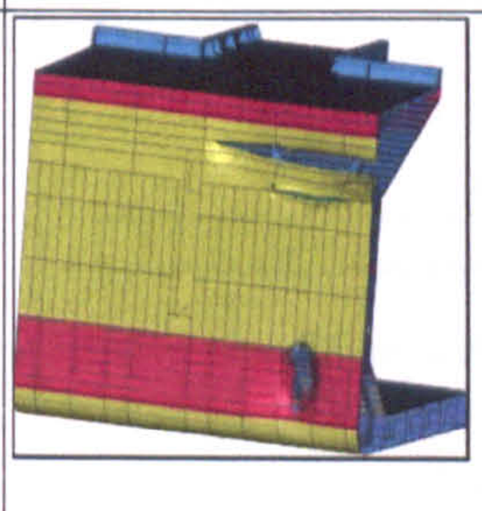	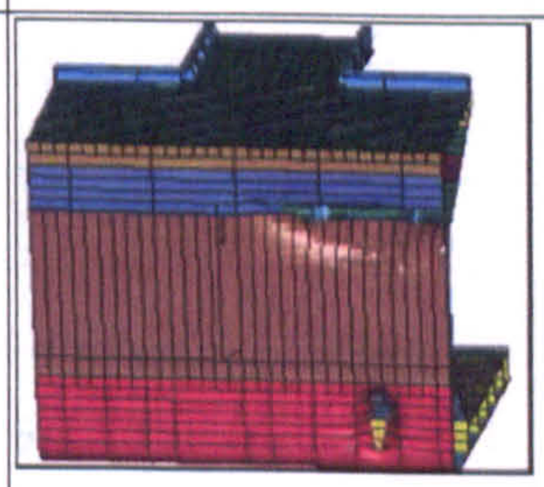

Table 7.19: Bow shape 1at direct web longitudinal position

Case	DSS	SSS
Case 1	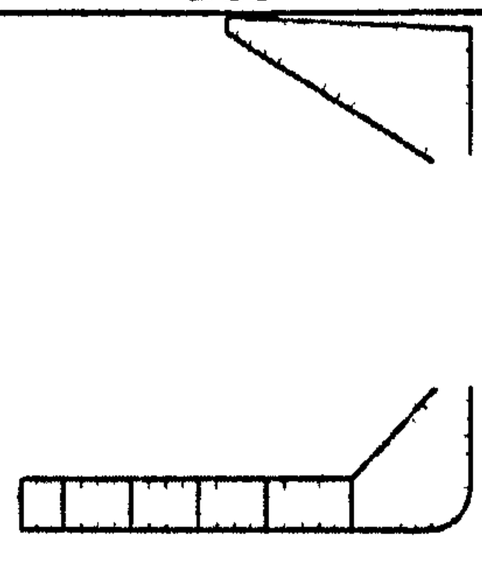	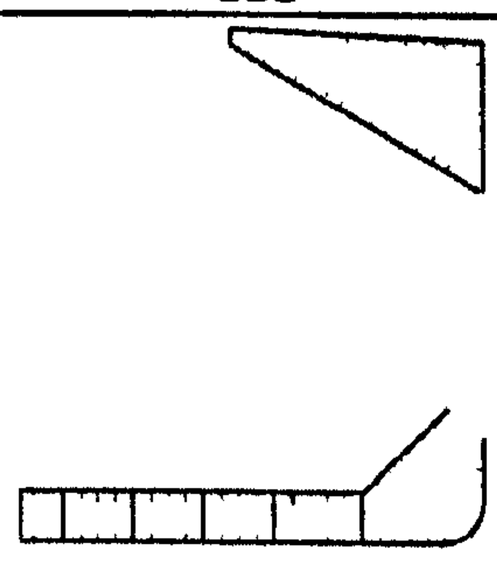
Case 2	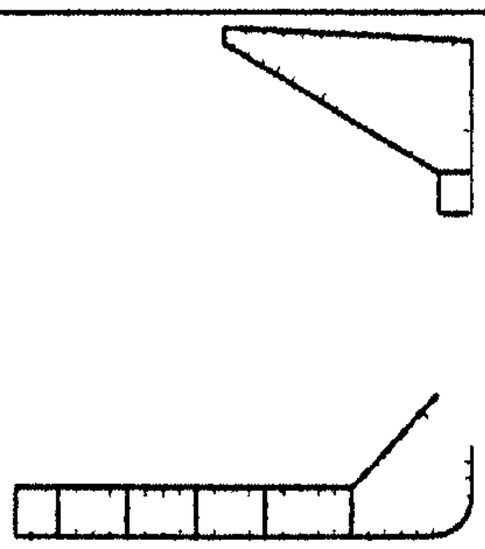	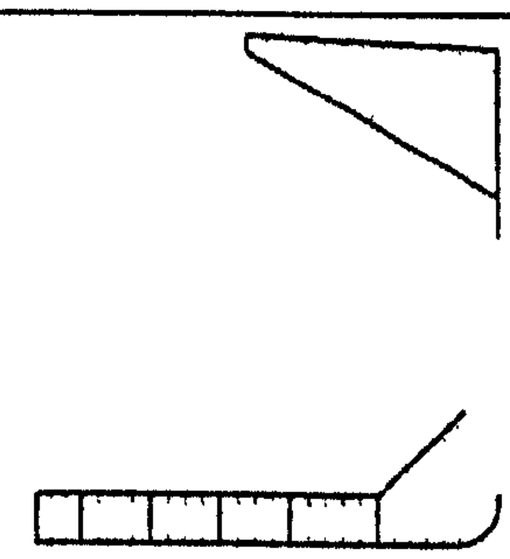
Case 3	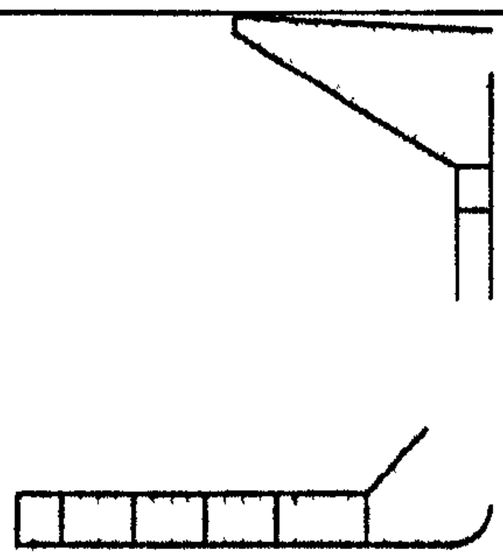	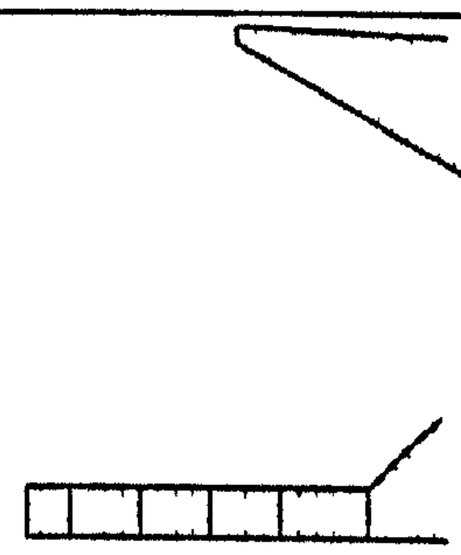
Case 4	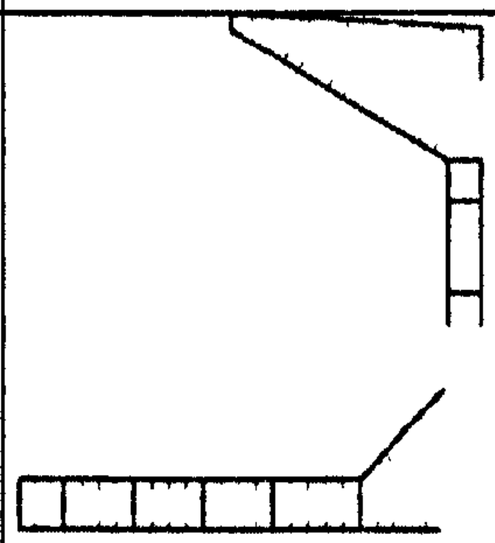	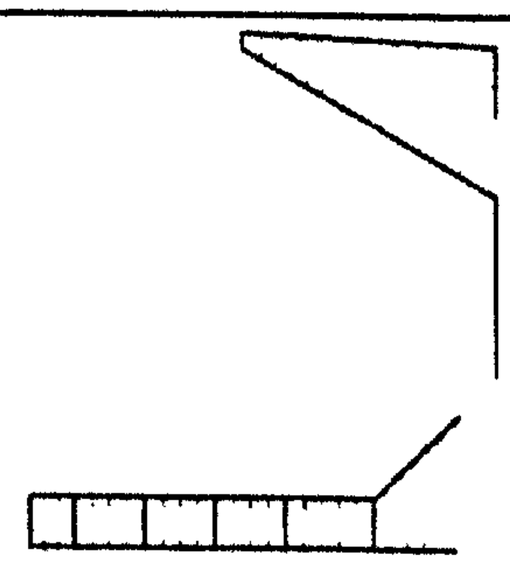

Table 7.20: Bow shape 1 at between web longitudinal position

Case	DSS	SSS
Case 5	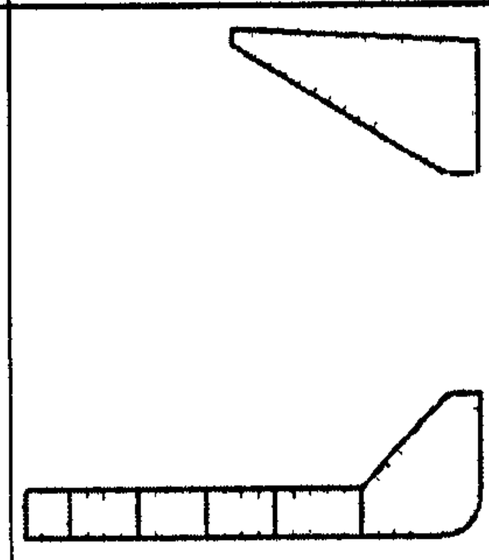	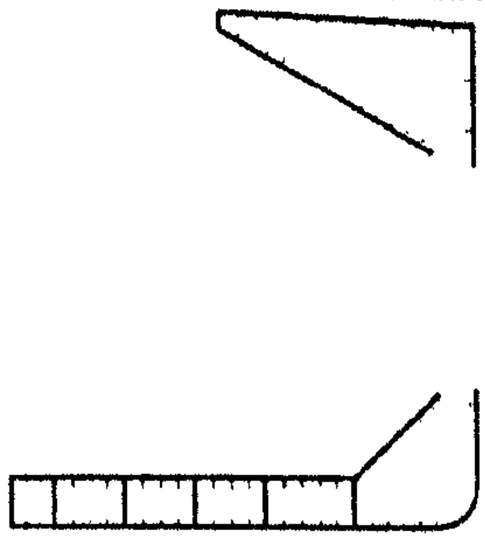
Case 6	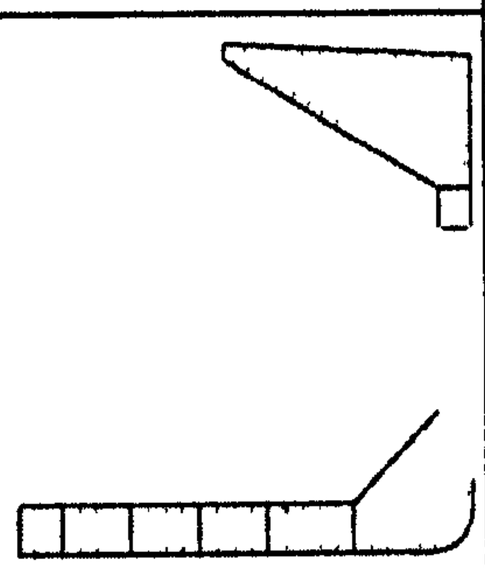	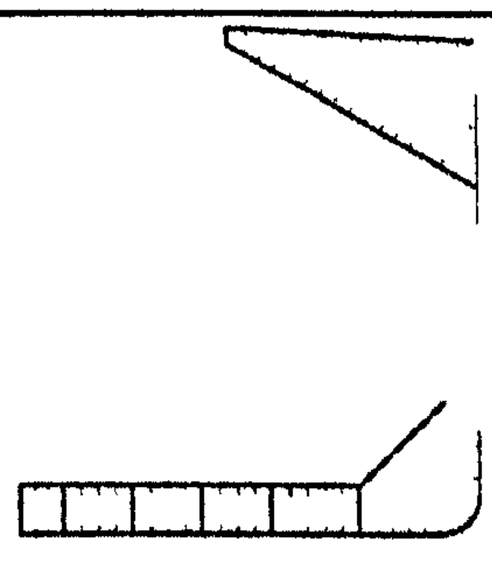
Case 7	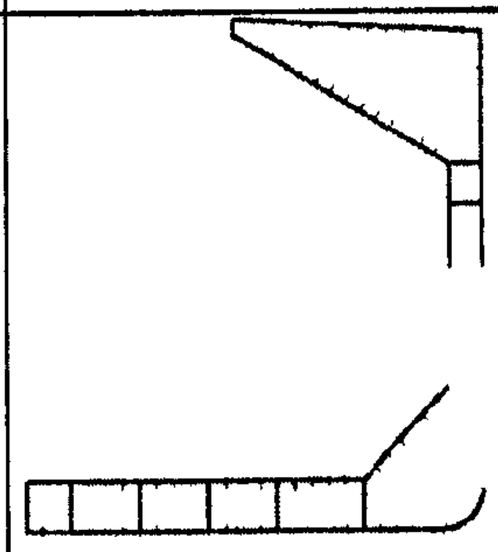	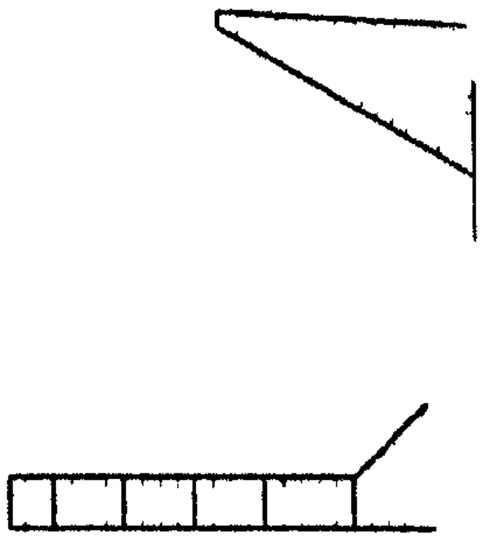
Case 8	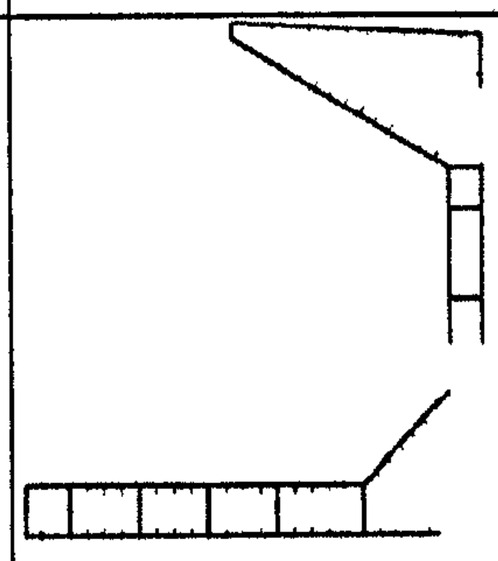	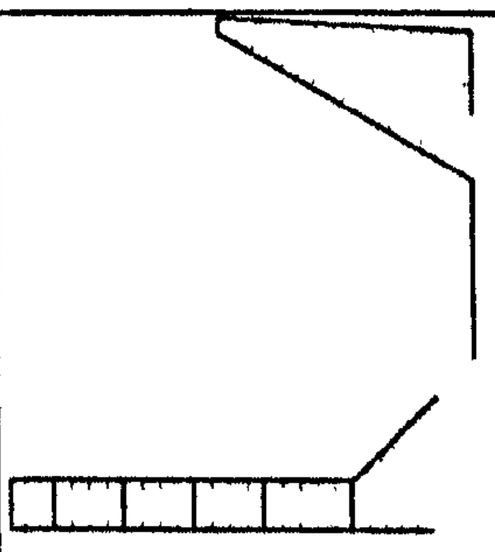

Table 7.21: Bow shape 2 at direct web longitudinal position

Case	DSS	SSS
Case 9	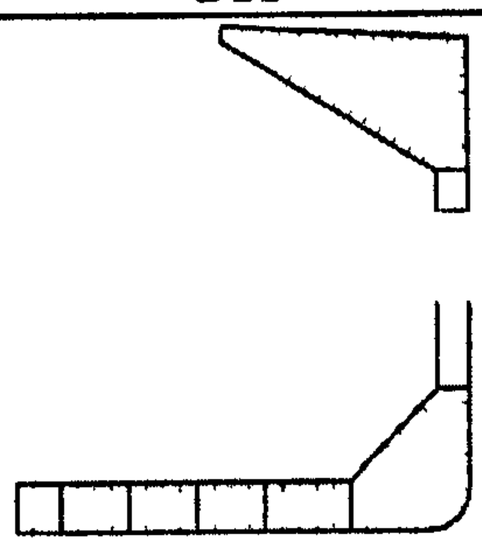	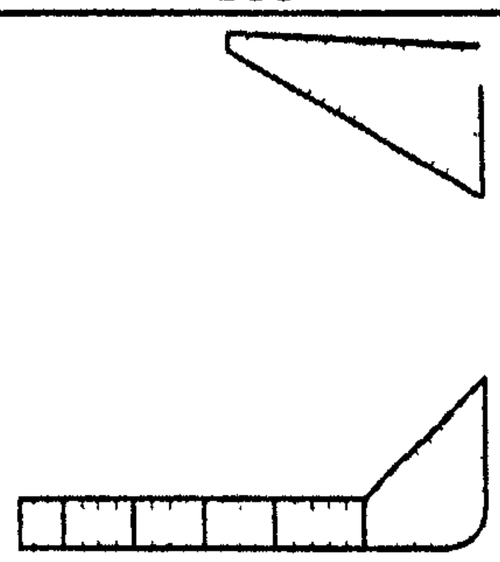
Case 10	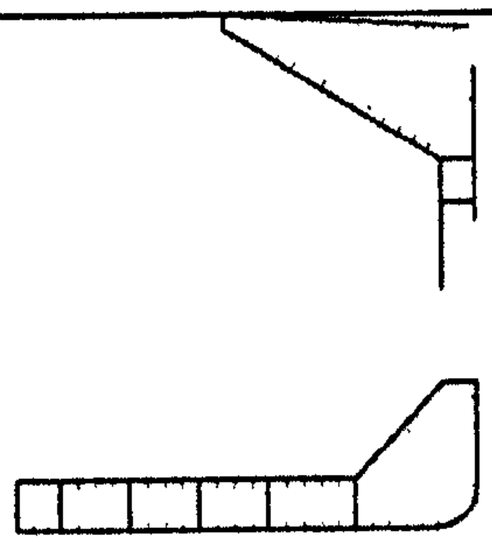	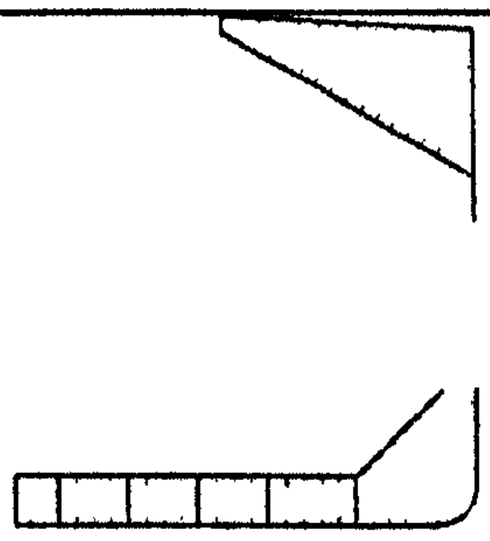
Case 11	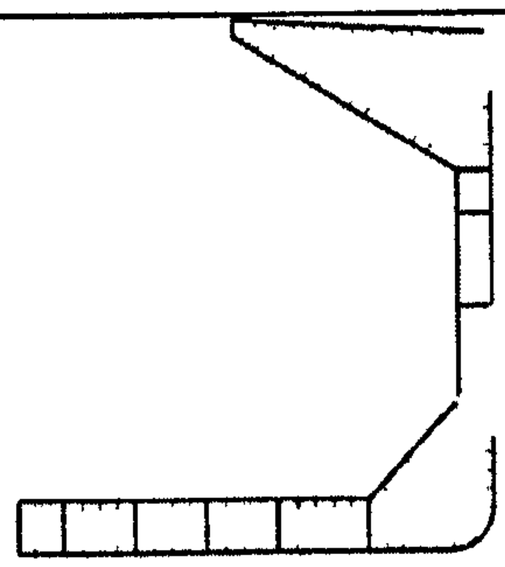	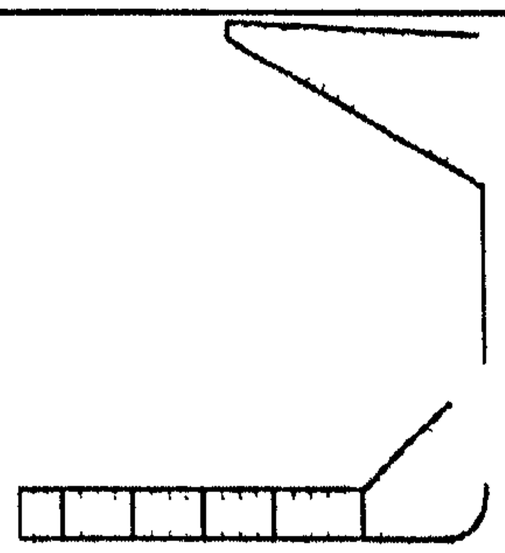
Case 12	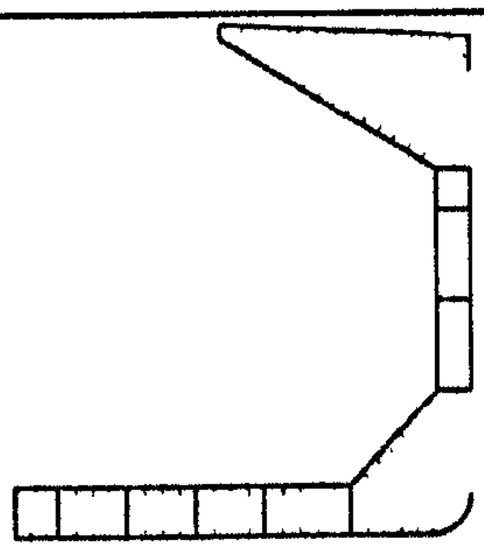	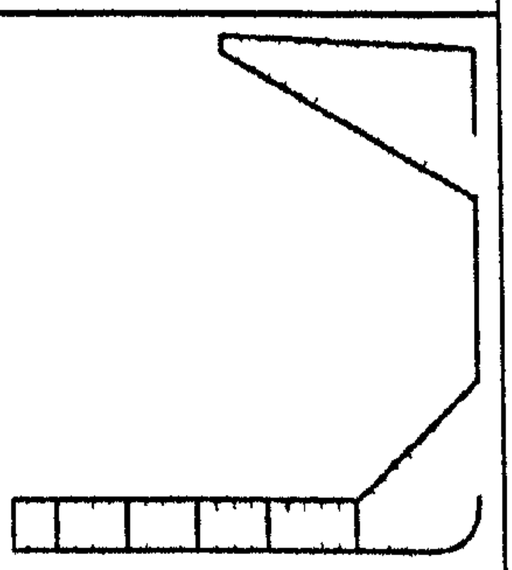

Table 7.22: Bow shape 2 at between web longitudinal position

Case	DSS	SSS
Case 13	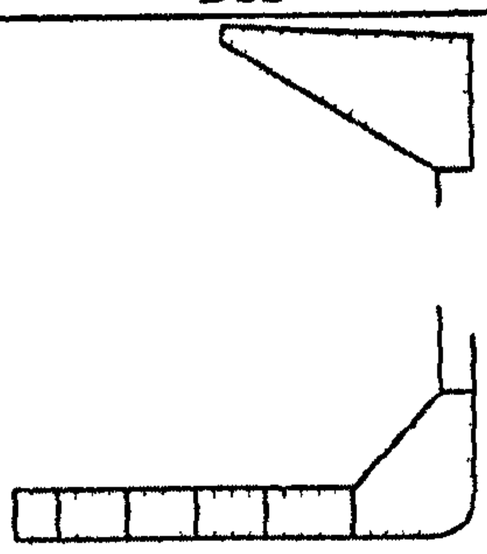	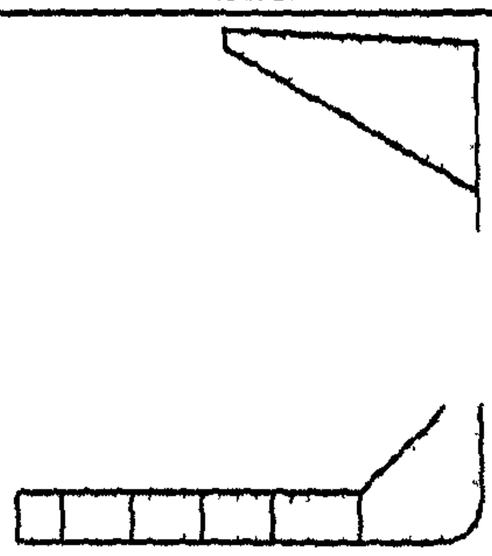
Case 14	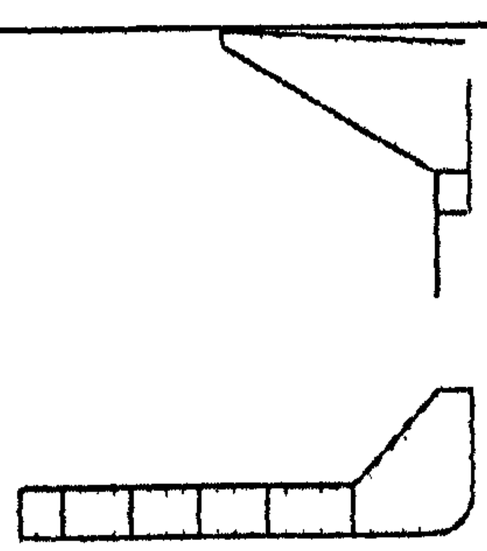	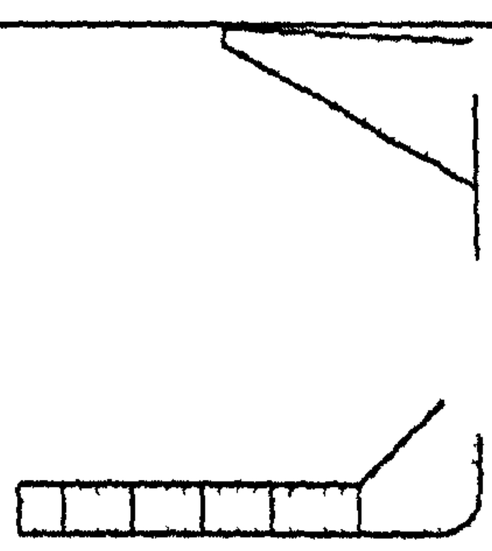
Case 15	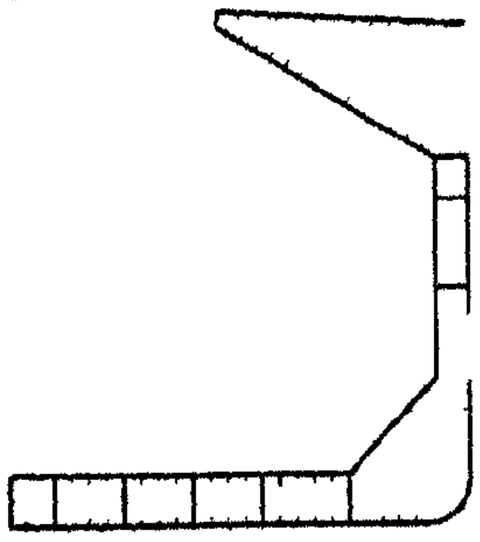	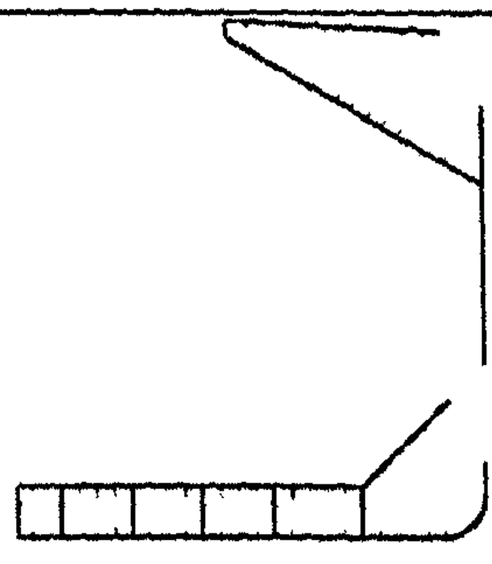
Case 16	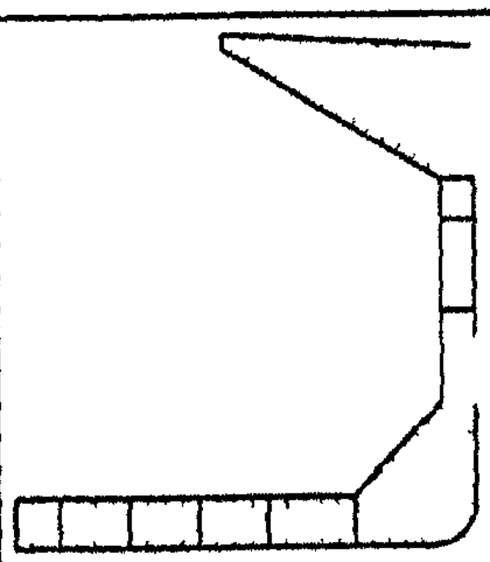	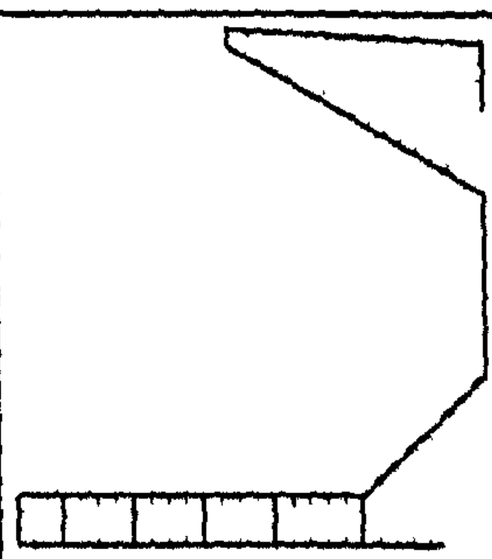

Table 7.23: Residual strength of SSS & DSS bulk carriers both in intact and damage states without corrosion effect

		Single Side Skin Bulk Carrier (SSS)		Double Side Skin Bulk Carrier (DSS)	
		Hogging	Sagging	Hogging	Sagging
M_{Design} (Collision)	M_{swbm}	0.406	0.375	0.406	0.375
	M_{wvbm}	0.605	0.635	0.605	0.605
	M_{total}	0.830	0.820	0.830	0.820
$M_{Plastic}$ (Intact)		1.779	1.779	1.823	1.823
$M_{Only\ Vertical\ Ultimate}$ (Intact)		1.606	1.289	1.570	1.312
$M_{Combined\ Ultimate}$ (Intact)		1.499	1.304	1.493	1.314
$M_{Combine\ Ultimate}$ (Collision)	Case 1	1.392	1.221	1.345	1.241
	Case2	1.384	1.239	1.386	1.244
	Case 3	1.313	1.094	1.341	1.113
	Case 4	1.407	1.191	1.394	1.197
	Case 5	1.374	1.225	1.356	1.249
	Case 6	1.354	1.154	1.386	1.241
	Case 7	1.367	1.151	1.420	1.244
	Case 8	1.324	1.126	1.393	1.201
	Case 9	1.364	1.203	1.420	1.288
	Case 10	1.371	1.191	1.363	1.196
	Case 11	1.347	1.221	1.402	1.216
	Case 12	1.438	1.226	1.403	1.206
	Case 13	1.421	1.245	1.406	1.278
	Case 14	1.427	1.235	1.329	1.180
	Case 15	1.326	1.111	1.368	1.194
	Case 16	1.411	1.196	1.397	1.197

NOTE: 1. $M_{total} = M_{swbm} + 0.7 \times M_{wvbm}$ (Proposed by ABS for hogging and sagging cases in collision)
2. $M_{Combine\ Ultimate}$ is calculated as combine vertical and horizontal bending moment
3.MOMENT (x 10^7 KN.m)

It is seen that the ultimate sagging moments of resistance in intact and damaged SSS & DSS bulk carrier vessels are considerably less than the ultimate hogging moment. Damages in upper side shell and deck structures subject to in-plane compressive loading reduce the residual strength substantially in sagging condition. For DSS and SSS bulk carriers, it also necessary to note that in the hogging condition the stresses of deck elements reach the material yield stress point first and then the bottom structure approaches the critical stress point in the yield zone of that material, with the increasing of ship hull girder curvature. The other hand, DSS and SSS bulk carriers may be attributed to the facts that original position of central position of cross section is closer to the bottom than it is to the deck, and the thicker bottom plating and dense longitudinal in the bottom cause bottom structure collapse in form of plastic buckling rather than elastic buckling.

Table 7.24: Residual strength of SSS & DSS bulk carriers both in intact and damage states with corrosion effect

		Single Side Skin Bulk Carrier (SSS)		Double Side Skin Bulk Carrier (DSS)	
		Hogging	Sagging	Hogging	Sagging
M_{Design} (Collision)	M_{swbm}	0.406	0.375	0.406	0.375
	M_{wvbm}	0.605	0.635	0.605	0.605
	M_{total}	0.830	0.820	0.830	0.820
$M_{Plastic}$ (Intact)		1.539	1.539	1.571	1.571
$M_{Only\ Vertical\ Ultimate}$ (Intact)		1.356	1.114	1.309	1.116
$M_{Combine\ Ultimate}$ (Intact)		1.259	1.104	1.248	1.111
$M_{Combine\ Ultimate}$ (Collision)	Case 1	1.157	1.028	1.118	1.023
	Case2	1.153	1.038	1.155	1.031
	Case 3	1.101	0.919	1.117	0.926
	Case 4	1.166	1.011	1.159	1.002
	Case 5	1.154	1.031	1.126	1.032
	Case 6	1.139	0.971	1.157	1.029
	Case 7	1.149	0.970	1.192	1.039
	Case 8	1.117	0.955	1.161	1.001
	Case 9	1.141	1.008	1.182	1.073
	Case 10	1.151	0.998	1.132	0.991
	Case 11	1.128	0.938	1.167	1.025
	Case 12	1.211	1.033	1.169	1.012
	Case 13	1.168	1.046	1.168	1.063
	Case 14	1.201	1.039	1.114	0.978
	Case 15	1.101	0.930	1.135	0.998
	Case 16	1.178	1.015	1.163	1.001

NOTE: 1. $M_{total} = M_{swbm} + 0.7 \times M_{wvbm}$ (Proposed by ABS for hogging and sagging cases in collision)
2. $M_{Combine\ Ultimate}$ is calculated as combine vertical and horizontal bending moment
3. MOMENT (x 10^7 KN.m)

It is noted that the most reduction of residual strength takes place in Case 3 for both SSS & DSS bulk carriers. This is because; any damage occurred upper side shell and deck structures leads to decrease moment capacity in sagging case significantly.

This study clearly shows that a thickness reduction in the bottom plating largely affects the hogging strength, while a thickness reduction in the deck plating largely reduces the sagging strength. In the intact states, JBP Rules cause to decrease 83.9 % and 84.6 % reductions in hogging and sagging conditions respectively for SSS bulk carrier vessels while 83.5 % and 84.5 % reductions take place in hogging and sagging conditions respectively for DSS bulk carrier vessels. In the damage states, for example the worst condition in case 3, JBP Rules lead to decrease 83.8 % and

84.0 % reductions in hogging and sagging conditions respectively for SSS bulk carrier vessels while 83.3 % and 83.1 % reductions take place in hogging and sagging conditions respectively for DSS bulk carriers. In damaged DSS bulk carries in sagging condition has more reduction value. This is because, the inclusion of tripping formulation in the behaviour of stiffened panels is noticed to be very important in the particular case investigated here. Since the deck stiffeners do not have much torsional rigidity and calculated tripping stress is lower than beam-column stress of the stiffener with associated plate. This fact leads to more reduction of the ultimate bending moment in sagging compared with the moment in hogging, where the bottom is in tension.

Figure 7.10 and Figure 7.11 also shows the calculated results of the ultimate coupled vertical and horizontal bending moment on SSS and DSS bulk carrier vessels versus curvature for case 3 obtained by NEPTUNE with and without JBP Rules corrosion effect.

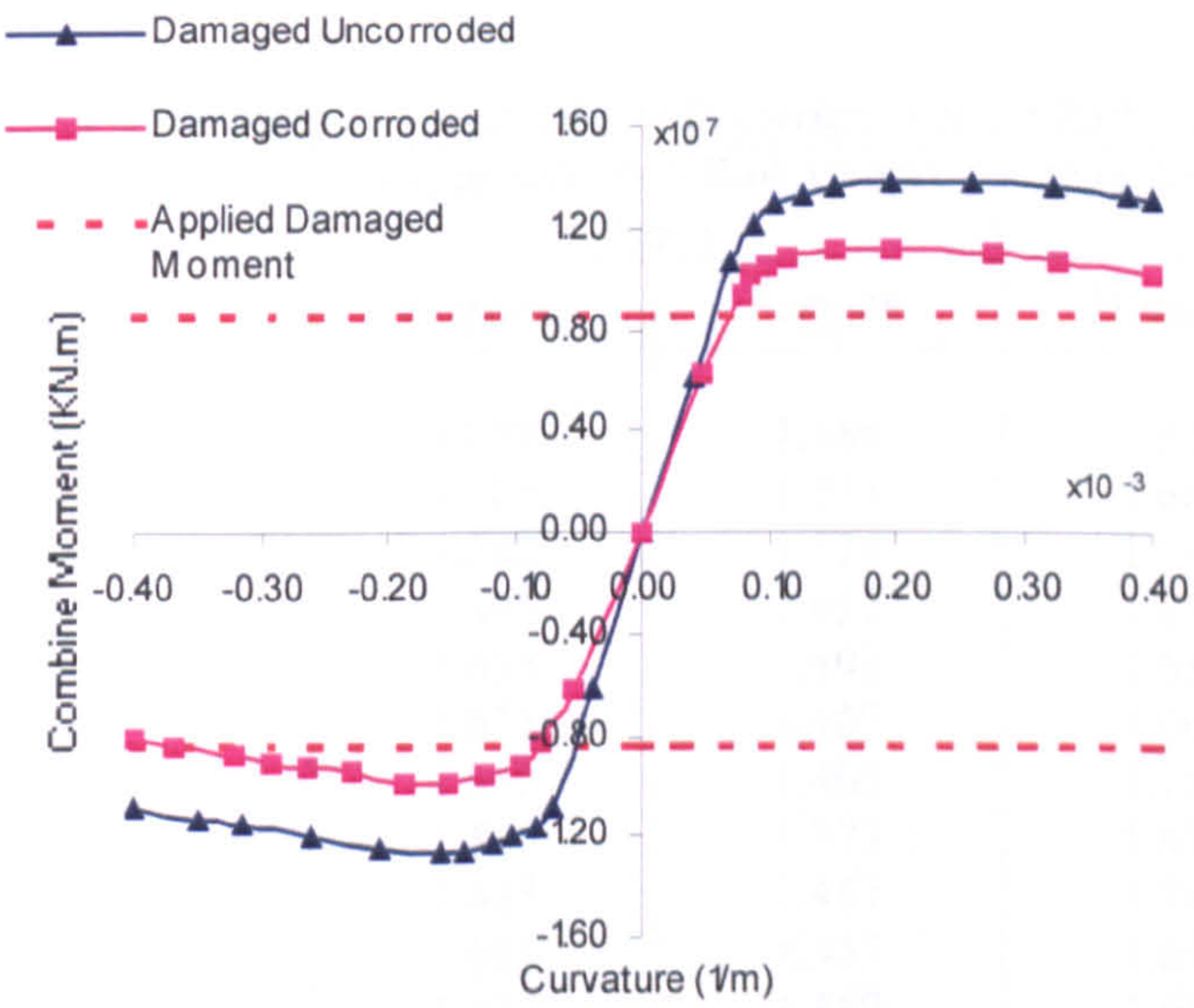

Figure 7.11: Moment – curvature relationship of DSS vessels in Case 3 ($\theta = 21.81$ degree)

It is noted that in case 3 the maximum coupled bending moment takes place at $\theta = 21.81$ degree for DSS vessel while it occurs for SSS vessel at $\theta = 26.56$ degree.

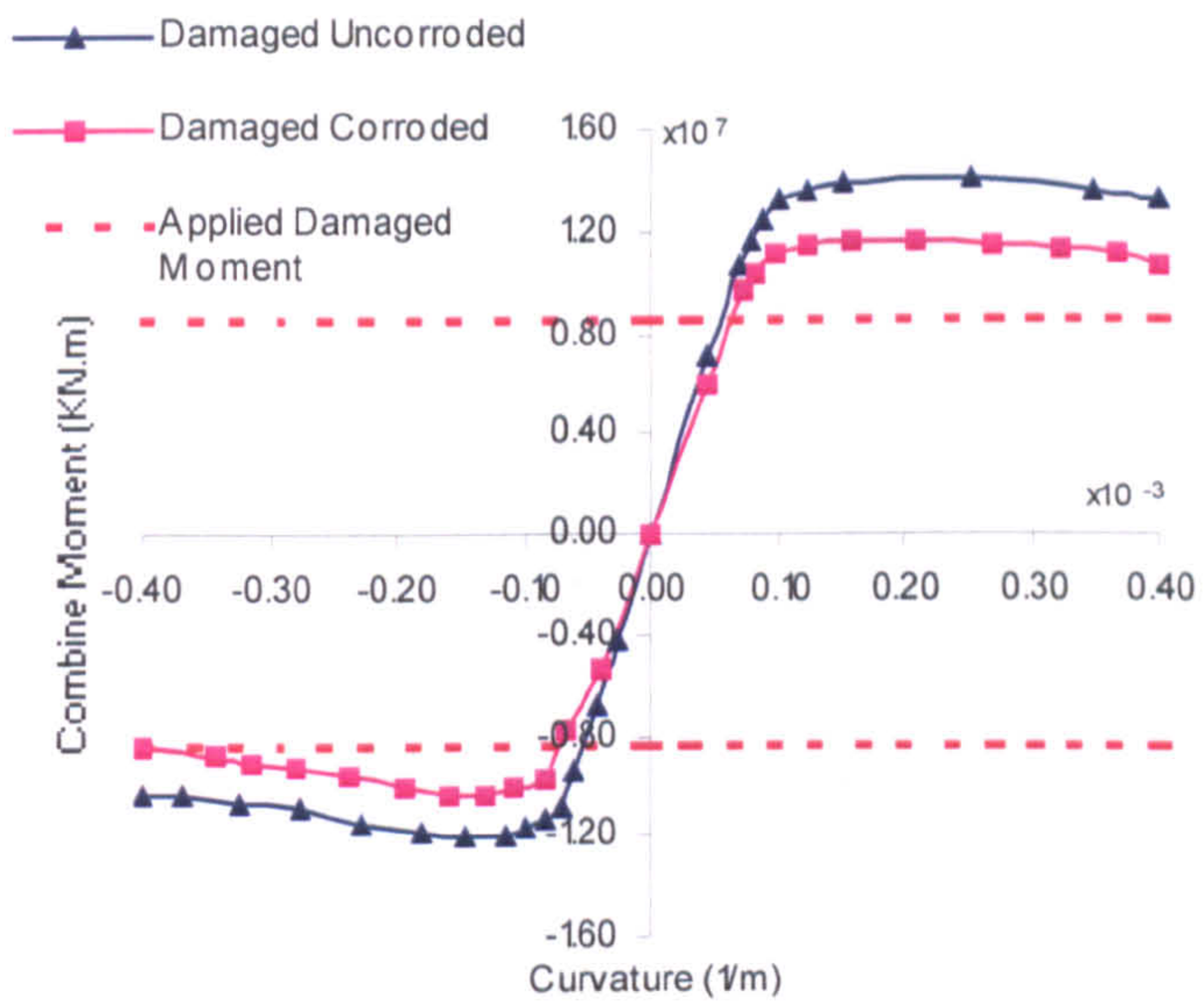

Figure 7.12: Moment – curvature relationship of SSS vessels in Case 3 ($\theta = 26.56$ degree)

The safety margin of SSS and DSS bulk carrier designs is used to judge damage tolerance and survivability can be assessed by a comparison of their ultimate strength with expected extreme hull girder loads and are shown in Table 7.25 and Table 7.26.

Table 7.25: Safety assessment of SSS & DSS bulk carriers without JBP Rules corrosion effect

		Single Side Skin Bulk Carrier (SSS)		Double Side Skin Bulk Carrier (DSS)	
		Hogging	Sagging	Hogging	Sagging
Safety Factor	Case 1	1.677	1.489	1.620	1.513
	Case 2	1.667	1.511	1.669	1.517
	Case 3	1.582	1.334	1.615	1.357
	Case 4	1.695	1.452	1.679	1.459
	Case 5	1.655	1.493	1.633	1.523
	Case 6	1.631	1.407	1.669	1.513
	Case 7	1.646	1.403	1.710	1.517
	Case 8	1.595	1.373	1.678	1.464
	Case 9	1.643	1.467	1.710	1.570
	Case 10	1.651	1.452	1.642	1.458
	Case 11	1.622	1.489	1.689	1.482
	Case 12	1.732	1.495	1.690	1.470
	Case 13	1.712	1.518	1.639	1.558
	Case 14	1.719	1.506	1.601	1.439
	Case 15	1.597	1.354	1.648	1.456
	Case 16	1.700	1.458	1.683	1.459
	Mean	1.657	1.442	1.666	1.486
	(%) COV	2.787	4.119	2.033	3.462

Table 7.26: Safety assessment of SSS & DSS bulk carriers with JBP Rules corrosion effect

		Single Side Skin Bulk Carrier (SSS)		Double Side Skin Bulk Carrier (DSS)	
		Hogging	Sagging	Hogging	Sagging
Safety Factor	Case 1	1.393	1.253	1.346	1.247
	Case 2	1.389	1.265	1.391	1.257
	Case 3	1.326	1.120	1.345	1.129
	Case 4	1.404	1.232	1.396	1.221
	Case 5	1.390	1.257	1.356	1.258
	Case 6	1.372	1.184	1.393	1.254
	Case 7	1.383	1.182	1.436	1.267
	Case 8	1.345	1.164	1.398	1.220
	Case 9	1.374	1.229	1.424	1.308
	Case 10	1.386	1.217	1.363	1.208
	Case 11	1.358	1.143	1.406	1.250
	Case 12	1.458	1.259	1.408	1.234
	Case 13	1.407	1.275	1.407	1.296
	Case 14	1.446	1.267	1.342	1.192
	Case 15	1.326	1.134	1.367	1.217
	Case 16	1.418	1.237	1.401	1.220
	Mean	1.385	1.213	1.387	1.235
	(%) COV	2.664	4.271	2.205	3.293

NOTE: 1. COV = Coefficient of Variation
2. Safety Factor = $M_{Combine\ Ultimate}$ / M_{total}
3. $M_{Combine\ Ultimate}$ and M_{total} refer to Table 7.23 and Table 7.24

For the collision damage scenarios, the safety index is greater in the hogging condition than in the sagging condition. It means that collision damage to the topside has more effect on the decrease of ultimate strength in the sagging state than in hogging state. It is seen that DSS bulk carrier has more safety factor compared that SSS bulk carrier for nine simulated damage cases in both hogging and sagging conditions. However, under JBP Rules corrosion effect, DSS bulk carrier has 1.387 mean values in hogging while SSS bulk carrier has 1.385 mean values. The obtained safety factor mean values may be provided quick estimation for practical ship applications such as rescue and salvage operations of ships after collision. From the calculations, it is noted that the possible collapse is expected to take place in sagging state for both SSS and DSS bulk carrier vessels when subject to collision damage.

7.7 Discussion & Conclusion

This chapter investigates the collision resistance capability and residual strength capacity subject to collision damage of SSS and DSS bulk carriers. Through this investigation, the following conclusions can be drawn:

- ✓ The results of collision behaviour of SSS and DSS bulk carriers present the variation of energy, which is absorbed until rupture versus the relative vertical location of the striking and struck ship, longitudinal location of the impact (impact on a transverse web or between webs) and the shape of the assumed rigid bow.
- ✓ From the comparison of experimental and numerical results using ISSC collision test model, it seems that a non-linear explicit finite element code, ANSYS LS-DYNA is quite adequate to perform ship collision analysis.
- ✓ The failure criterion, which has been used based on GL approach. The value of the maximum plastic strain, which has been selected to be 20 %. However, more effort is needed in order to consider a failure criterion, which would be more confidence in the ship-ship collision simulation.
- ✓ The ship structural design has very significant influence on the collision resistance. The collision energy absorption capability depends on the thickness of outer shell, inner shell, side stringers, transverse webs, width of the side ballast tank and width of lower and upper wing tanks.
- ✓ Energy absorption when rupture of the outer shell of DSS occurs is approximately 10% less than the energy absorbed by the outer shell of SSS. However, the maximum energy absorbed, i.e. the energy absorbed when the skin of cargo hold (inner shell for DSS, outer shell for SSS) ruptures, in 2.2 times more for DSS than for the SSS.
- ✓ Critical locations of damage are a function of ship type and structural configuration

- ✓ It is noted that for all cases DSS has higher rupture energy than SSS. However, in case 6 SSS' rupture energy is very close to DSS, which is only lesser 2%
- ✓ The results obtained from the finite element simulation may be used a) for the assessment of the collision behaviour of a ship under defined collision scenario, b) for the relative comparison of structural arrangements and c) for the validation of analytical techniques for ship collision analysis
- ✓ The existence of damage induced by collision reduces the ultimate resistance of the ship hull girder. However, the degree of reduction, which varies with the damage location and the extents, can be regarded as a function of damage extent, mode of buckling failure and relative shipboard location. Hence the measures taken to avoid collision in service are very important.
- ✓ In order to investigate the influence of the damage location and extent on the residual strength capacity and difference of the survivability between SSS and DSS bulk carriers, a wide range analyses are carried out in both hogging and sagging cases with consideration of the intact and damage scenarios and also considers corrosion effect based on JBP Rules, where the simplified method based on a incremental – iterative approach is employed using a developed computer code NEPTUNE.
- ✓ It is shown that the DSS bulk carriers have higher safety index than the SSS bulk carriers in hogging and in sagging conditions under similar collision damage scenarios, and this index value is greater in the hogging case compared that in the sagging case.
- ✓ Ultimate sagging moments of resistance in intact and damaged hulls are considerably less than ultimate hogging moment. Damages in upper side shell and in deck structures lead to reduce the residual strength significantly when subject to in plane compressive load combinations.
- ✓ The evaluation of the ultimate strength using NEPTUNE is believed to be an adequate estimation of the ultimate load capacity of the ship. Further refinement using non-linear FE analysis requires considerably more engineering and computational effort and is not expected to yield substantially different results

- ✓ Fracture mechanics of ships for the ultimate strength of extensively unsymmetrical damaged section with large damage openings should be investigated in detail especially in case that sea state covering high significant wave height. This issue is investigated on a damaged tanker using elastic-plastic fracture mechanics (EPFM), where extensive non-linear finite element analyses conducted by author in chapter 8.

Chapter 8

Fracture Assessment on Hull Girder Ultimate Strength Subject to Collision Damage

8.1 Introduction

Generally, crack-like discontinuities or flaws exist in the structural elements due to welding. Under cyclic loading, a flaw can develop into a fatigue crack and propagate until fracture occurs. Fracture mechanics is used to analyse and predict the behaviour of a cracked structural element. This chapter assesses the amount of the time following a collision accident before a ship is calculated to suffer a brittle fracture. There have also been cases of ships breaking into two parts as a result of very small cracks e.g. MV Kurdistan Tanker. TWI (World Centre for Materials Joining Technology) investigated possible causes of failure of MV Kurdistan tanker. The report revealed that failure was brittle fracture with presence of defect in bilge keel welds combined with high thermal stresses. This failure also showed how critical the

quality of workmanship can be even for a detail of apparently little significance such as the bilge keel. The summary details given below are provided by TWI's web site (www.twi.co.uk).

On the morning of 15 March 1979 the motor tanker M V Kurdistan left Point Tupper in Nova Scotia bound for Sept-Isles, Quebec. The tanker was carrying a heated cargo of oil for the first time. The weather conditions were not good and the ship was rolling heavily. At about 12.30 the Kurdistan came to the edge of an ice field but, after travelling 2.5km into the ice, the ship was brought to a halt. The ship was turned around and headed back towards the open sea. At 13.50 the Kurdistan cleared the edge of the ice belt and put full ahead. Almost immediately there was a thud and a shudder during a downward pitch of the vessel. (The sea conditions were described as 'very heavy swell'). Oil started to escape from a vertical crack in the sides of No.3 wing tanks. The crack came up to about 3.6m below the main deck level. To reduce the loss, the transfer of oil from No.3 wing tanks to the No.4 tanks was undertaken `while the ship continued on its course. At 18.40 a second shudder was felt and the transfer of oil was stopped. The weather conditions had improved and the wave height was 2m. At 21.30 the ship broke in two: a shudder was felt and the bow rose, hinging about the deck at the No.3 cargo tanks before finally separating from the stern. Almost eight hours had elapsed between the initial fracture of the vessel's shell and it's breaking in two (see Figure 8.1).

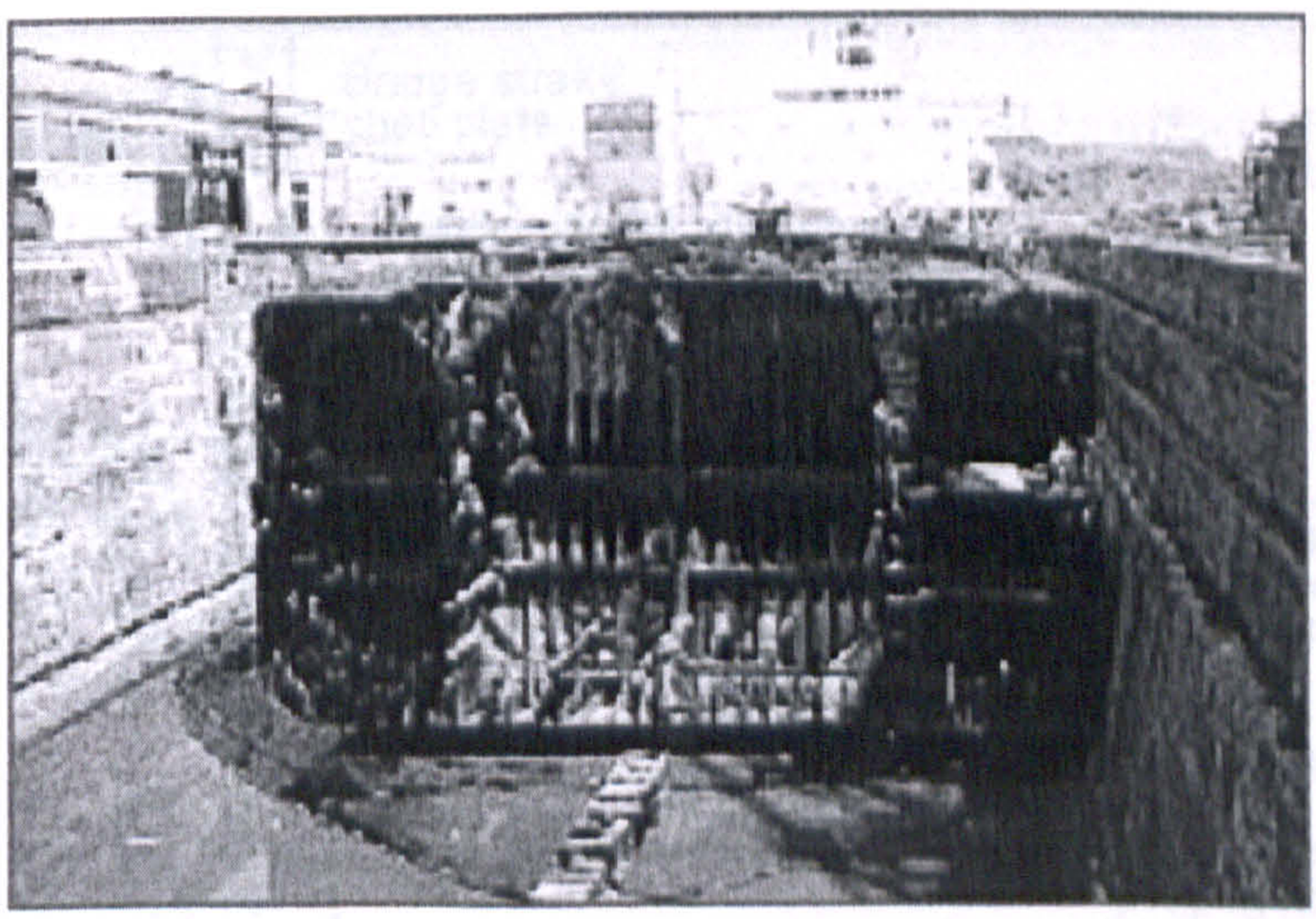

Figure 8.1: M V Kurdistan tanker failure (www.twi.co.uk)

The Kurdistan was built to construction class 'Ice Class I' and completed in 1973. The vessel was longitudinally framed except for the sides where the framing was transverse. With six cargo tanks, each divided into two wing tanks and a centre tank, the overall length of the ship was approximately 182m. The Kurdistan was built almost entirely in Grade A steel (no Charpy requirements). The bottom shell was 19.5mm thick and the bilge strake 14.7mm.

The bilge keel over a length of ship including the region failure consisted of 125 x 11mm ground flat bars butt welded end to end and overlapped on the underside by 300 x 13mm bulb plates, attached by intermittent welding. The bilge keel was connected edge-on to the bilge strake by continuous fillet welds above and below. The design of the keel called for a 25mm crack arrest hole to be drilled in each butt weld joining the ground bars.

Examination of the fracture faces revealed that the initial fracture through the bottom and side shell plates was brittle. The origin of the crack was a defective butt weld in the port bilge keel (see Figure 8.2). There was lack of penetration in the butt weld and, where the bulb plate overlapped the underside of the ground bar, there was no weld at all. The bulb plate was misaligned and the crack arrest hole was missing. This region of the bilge keel had been damaged in 1975 and repaired in 1977. Areas of fatigue crack growth along the lack of penetration at the weld root were found.

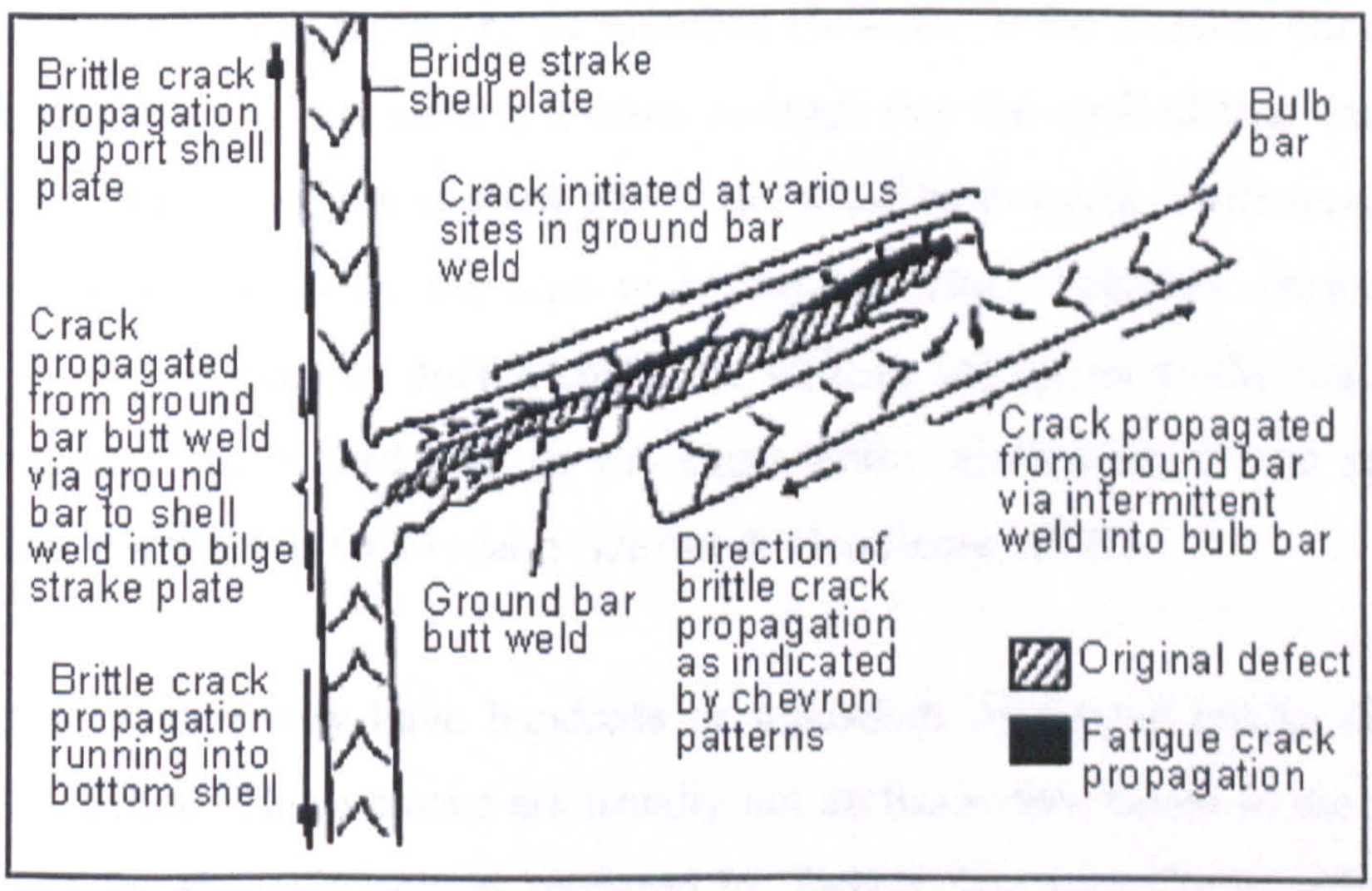

Figure 8.2: M V Kurdistan failure induced by fracture initiation (www.twi.co.uk)

The inquiry into the failure of the Kurdistan did not establish precisely the sequence of failure of the ship's longitudinal structure, which showed both brittle and ductile fracture. Given that the ship's shell plates were found to have 27J Charpy transition temperatures of between 5° and 20°C, the steel in contact with the sea water was close to or below its transition and that in contact with the heated cargo was above. The displacement of oil by water entering the cargo tanks lowered the steel temperature to below its ductile/brittle transition.

Calculations of the thermal stresses in the ship resulting from the carriage of a warm cargo in a cold sea indicated that a high tensile stress level would have been present in the shell and bilge keel. It is thought that the stresses due to the impact of a wave on the bow, superimposed on the high thermal stress and the stresses due to the moderate wave bending moments, triggered the fracture of the Kurdistan's bilge keel. The toughness of the shell plate was insufficient to arrest the propagating crack and complete failure ensued. The initiation of the fracture was due to the classic combination of poor weld metal toughness and high stresses in the presence of a defect.

Fracture toughness and ductility of the structural steel are important for redundancy to be effective. In a steel member, the capacity of the member decreases as the crack propagates further in the member. However, if the member has sufficient fracture toughness, it can tolerate a crack so large that the applied load exceeds the capacity for the net section causing plastic deformation to occur in the member. The plastic deformation allows the load to be shed to other members. However, net-section yielding is not very ductile unless the yielding can spread to the gross section, which requires strain hardening in the stress-strain relationship of the steel, or a reasonably low yield to tensile ratio (Dexter & Gentilcore, 1997).

A large tanker may have hundreds or thousands of fatigue cracks discovered during inspection. These cracks are usually not an immediate threat to the structural integrity of the ship. Guidelines prepared by Tanker Structure Co-operative Forum

are used for the inspection and maintenance of tanker structure (1986, 1995). The tolerance of ships to these cracks is a function of the overall structural redundancy and ductility, as well as fracture toughness of the structural components.

The S-N curve approach is the most common method used for determining the fatigue life of a structural detail. The S-N curve is a lower bound to fatigue test data in terms of the stress range (S) and number of cycles to failure (N). Failure in the test is usually defined as the development of through-thickness cracks (typically about 100 mm in length).

Fracture mechanics of ships for the ultimate strength of unsymmetrical damaged section with large damage openings should be investigated in detail especially in the case that the sea state after damage has a high significant wave height.

In literature, no studies on the crack growth in damaged stiffened plates have been conducted. This chapter mainly focuses on developing a procedure how to take into account fracture assessment on damaged marine structures using elastic-plastic fracture mechanics (EPFM), where extensive non-linear finite element analyses are performed. The models developed in this research are aimed at predicting the growth of cracks after they become through-thickness cracks, and investigating effect of residual stresses, damage extent, structural arrangement, sea states, and redundancy on the crack growth.

8.2 Fundamentals of Fracture Mechanics

Cracks and flaws occur in many structures and components, sometimes leading to disastrous results. The engineering field of fracture mechanics was established to develop a basic understanding of such crack propagation problems. Fracture mechanics deals with the study of how a crack or flaw in a structure propagates under applied loads. It involves correlating analytical predictions of crack propagation and failure with experimental results. The analytical predictions are made by calculating fracture parameters such as stress intensity factors in the crack

region, which you can use to estimate crack growth rate. Typically, the crack length increases with each application of some cyclic load, such as cabin pressurization-depressurisation in an airplane. Further, environmental conditions such as temperature or extensive exposure to irradiation can affect the fracture propensity of a given material.

Structural fracture modes associated with cracks may be classified into three groups, namely brittle fracture, ductile fracture and rupture (Machida, 1984). When the strain at fracture of material is very small, it is called brittle fracture. In steel structures made of ductile material with adequately high fracture toughness, however, the fracture strain can be comparatively large. When the material is broken by necking associated with large plastic flow, it is called rupture. As a failure mode, ductile fracture is an intermediate phenomenon between brittle fracture and rupture.

The progress of ductile fracture from an existing sharp-tipped crack may be separated into four regimes, namely blunting of the initially sharp crack tip, initial crack growth, stable crack growth and unstable crack propagation (Shih *et al.* 1977). The ductile fracture characteristics generally depend on the material toughness, but can also be affected by the loading rate and environmental factors such as corrosion and temperature. For high-toughness materials, the crack tip may be significantly blunted and the stable crack growth regime can be substantial prior to fracture. For low-toughness materials, however, there is likely to be relatively little crack tip blunting and unstable crack extension can occur even without a stable crack growth regime.

In the rare situation when the structure has been weakened by large cracks or large-scale plasticity associated with cracks, resulting in a decrease of structural stiffness, large deformations are likely to develop. Figure 8.3 shows a schematic representation of the non-linear behaviour of cracked steel structures under monotonic loading. It is noted that, for similar structures, the stiffness and ultimate strength of cracked structures is, as expected, smaller than those of uncracked structures.

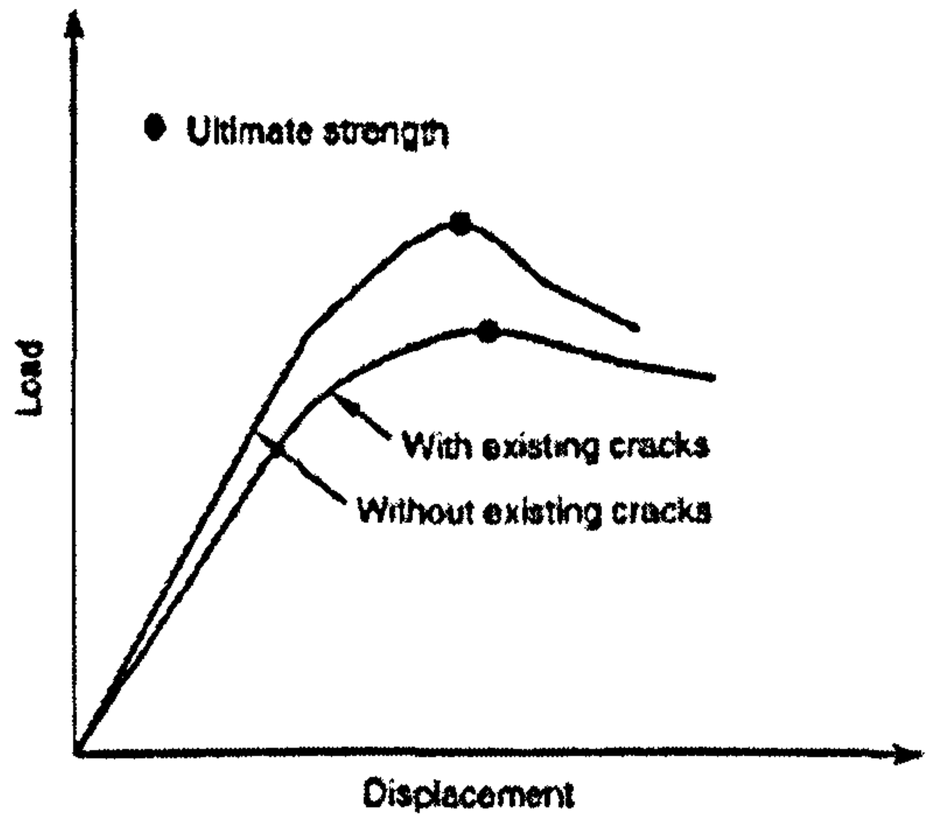

Figure 8.3: A schematic representation of the cracking damage effect on the ultimate strength behaviour of steel structures

Fracture behaviour for ductile materials is quite different from that of brittle materials. Ductile materials generally exhibit slow stable crack growth accompanied by considerable plastic deformation. In other words, there is crack growth resistance during crack extension. The study of the fracture behaviour of materials, components and structures is now known as fracture mechanics. Fracture mechanics is hence the engineering discipline that can be used to quantify the conditions under which a load-bearing structure can fail due to the enlargement of a crack.

It is commonly agreed that the modern era of fracture mechanics originated with the work of A.A. Griffith (1920) who resolved the infinite crack tip stress dilemma inherent in the use of the theory of elasticity for cracked structures. However, the study of fracture remained for some time of scientific interest only. One reason for this was the apparent non-applicability of the Griffith theory to engineering materials whose fracture resistance values are typically orders of magnitude greater than that of brittle materials such as glass.

The next major contributions to the subject were made independently by Irwin (1948) and Orowan (1948) who extended Griffith's approach to metals by including the energy dissipated by local plastic flow. During this same period, Mott (1948) extended Griffith's theory to a rapidly propagating crack.

Irwin (1956) developed the energy release rate concept and related it to Griffith's theory. Using the approach of Westergaard (1939) who developed a method to analyse stresses and displacements ahead of a sharp crack, Irwin (1957) showed that the stresses and displacements near the crack tip could be described by a single parameter, which was related to the energy release rate. This crack tip characterizing parameter is the stress intensity factor. During the same period, Williams (1957) also calculated the stress distribution at the crack tip but using a somewhat different technique from the Irwin approach. Both results were essentially identical.

Linear elastic fracture mechanics (LEFM) is generally found to be accurate for brittle materials. Direct application of LEFM to ductile materials is found to yield overly conservative predictions. In the 1960s it was realized that LEFM is not applicable when large-scale yielding at the crack tip precedes approximate methods, mostly by correcting and expending on LEFM (Dugdale, 1960; Wells, 1961; 1963, Barenblatt, 1962). While Dugdale (1960) proposed an idealized model based on a narrow strip of yielded material at the crack tip, Wells (1961,1963) suggested the displacement of the crack faces as an alternative fracture criterion when large-scale plasticity occurs at the crack tip. The Wells parameter is now known as the crack tip opening displacement (CTOD).

Rice (1968) introduced another parameter to characterize non-linear material behaviour ahead of a crack tip. He generalized the energy release rate to non-linear materials by idealizing plastic deformations as non-linear elastic. The resulting parameter is the J-integral. During this same period, Hutchinson (1968) and Rice & Rosengren (1968) showed that the J-integral could be used to represent the characteristics of crack tip stress fields in the non-linear elastic range of material behaviour.

To apply fracture mechanics to structural design, a mathematical relationship between material toughness, stress and flaw size must be established. While these relationships for linear elastic problems had been available for a time, Shih &

Hutchinson (1976) were perhaps the first to provide the theoretical framework to establish such a relationship for non-linear problems. Shih (1981) also established a relationship between the J-integral and CTOD.

Anderson (1990) reviewed the history and state-of-the art in elastic-plastic fracture mechanics as applied to welded steel structures. Fundamental concepts and underlying assumptions were described. Standardized test methods and developments were reviewed. The results of a parametric study comparing several elastic-plastic design analyses were presented.

Dexter & Pilarski (2000) conducted large-scale testing by integration welded, stiffened panels into a box girder configuration subjected to cyclic fatigue loading. The experiments showed a decrease in the crack rate between stiffeners, which is attributed to compressive residual stress between stiffeners, case residual stress field representation. Numerical modelling was performed using finite element models, with temperature gradients simulating residual stress, to calculate the J-integral around the crack tip at different stages of crack development, and transferring the results into a propagation rate prediction.

BMT Fleet Technology (2003) presented the sample application considered a bulk carrier as a platform for the demonstration of the concepts involved project, which was supported by Ship Structure Committee. The failure assessment process was applied to this vessel to demonstrate the implementation of numerical and analytic modelling techniques by considering the six-step process. These steps include vessel particular identification, structural section, load assessment, definition of local detail characteristics, failure assessment, and application of the results. Results of the failure assessment were discussed to illustrate trends in the results and how they might be applied in practice.

Recently, Dexter & Mahmoud (2004) have conducted fatigue tests on approximately half-scale welded stiffened panels to study propagation of large cracks

as they interact with stiffeners. A linear elastic fracture mechanics analysis was used to simulate the crack propagation and gave reasonable agreement with experiments.

8.3 Basic Concepts for Fracture Mechanics Analysis

Figure 8.4 represents a schematic of approximate approaches for fracture analysis of cracked structures as a function of material fracture toughness. It is seen from Figure 8.4 that for low-toughness materials, brittle fracture is predominant and LEFM is valid. For very high-toughness materials, however, rupture is dominant because of large-scale plasticity until the structure collapses. In this case, limit-load analysis (LLA) is more relevant. There is a transition between brittle fracture and rupture when the fracture toughness is intermediate. This is termed the ductile fracture regime, and in this case non-linear fracture mechanics concept, now generally termed elastic-plastic fracture mechanics (EPFM), will be more relevant to assess failure characteristics of the structure. These various basic concepts of fracture mechanics are described as below:

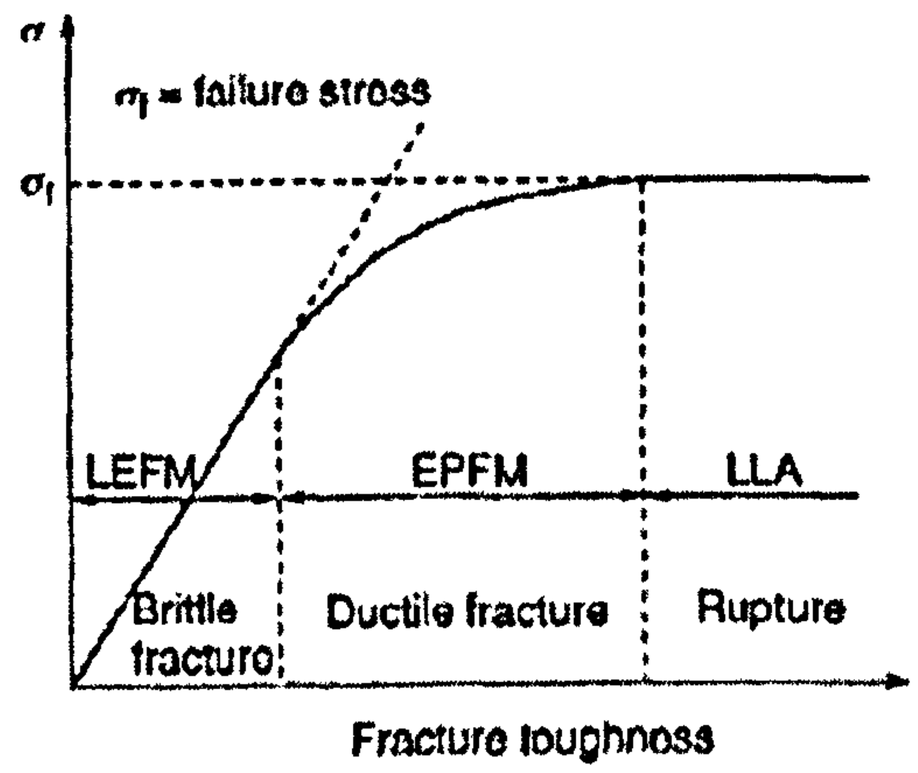

Figure 8.4: A schematic of appropriate approaches for fracture analysis as a function of material fracture toughness (LEFM = linear elastic fracture mechanics, EPFM = elastic-plastic fracture mechanics, LLA = limit-load analysis)

8.3.1 Energy-based concept

In the Griffith energy concept, it is considered that the fracture takes place if crack-growth-related energy exceeds the material's resistance to fracture. Mathematically, the following criterion must be satisfied for fracture to occur:

$$G \geq G_C \tag{8.1}$$

where G is called the strain energy release rate or, alternatively, the crack driving force, and G_C represents the material's resistance to crack growth. For a cracked infinite plate under tensile stress σ, as shown in Figure 8.5, it can be shown that G and G_C are given by:

$$G = \frac{\pi\sigma^2 a}{E} \tag{8.2}$$

$$G = \frac{\pi\sigma_f{}^2 a}{E} \tag{8.3}$$

where E is Young's modulus, a is half crack length and σ_f is failure stress.

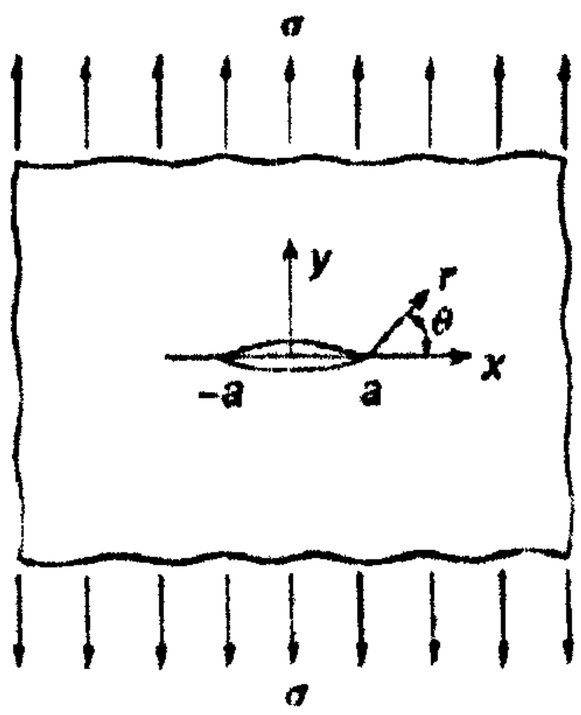

Figure 8.5: A cracked infinite plate under tensile loading

It is surmised from Equations (8.3) and (8.4) that the failure stress, σ_f, is proportional to $1/\sqrt{a}$ for a constant value of G_c, implying that the failure stress decreases in that manner with increase in the flaw size.

8.3.2 Stress intensity factor concept

For a cracked body with a linear elastic material as shown in Figure 8.6, stress components near the crack tip in the xy plane may be shown to be given by:

$$\sigma_x = \frac{K_I}{\sqrt{2\pi r}}\cos\left(\frac{\theta}{2}\right)\left[1-\sin\left(\frac{\theta}{2}\right)\sin\left(\frac{3\theta}{2}\right)\right] \tag{8.4}$$

$$\sigma_y = \frac{K_I}{\sqrt{2\pi r}}\cos\left(\frac{\theta}{2}\right)\left[1+\sin\left(\frac{\theta}{2}\right)\sin\left(\frac{3\theta}{2}\right)\right] \tag{8.5}$$

$$\tau_{xy} = \frac{K_I}{\sqrt{2\pi r}}\cos\left(\frac{\theta}{2}\right)\sin\left(\frac{\theta}{2}\right)\cos\left(\frac{3\theta}{2}\right) \tag{8.6}$$

where K_I is called the Mode I stress intensity factor. Mode I is the direct opening mode for a crack; more will be said about crack modes later.

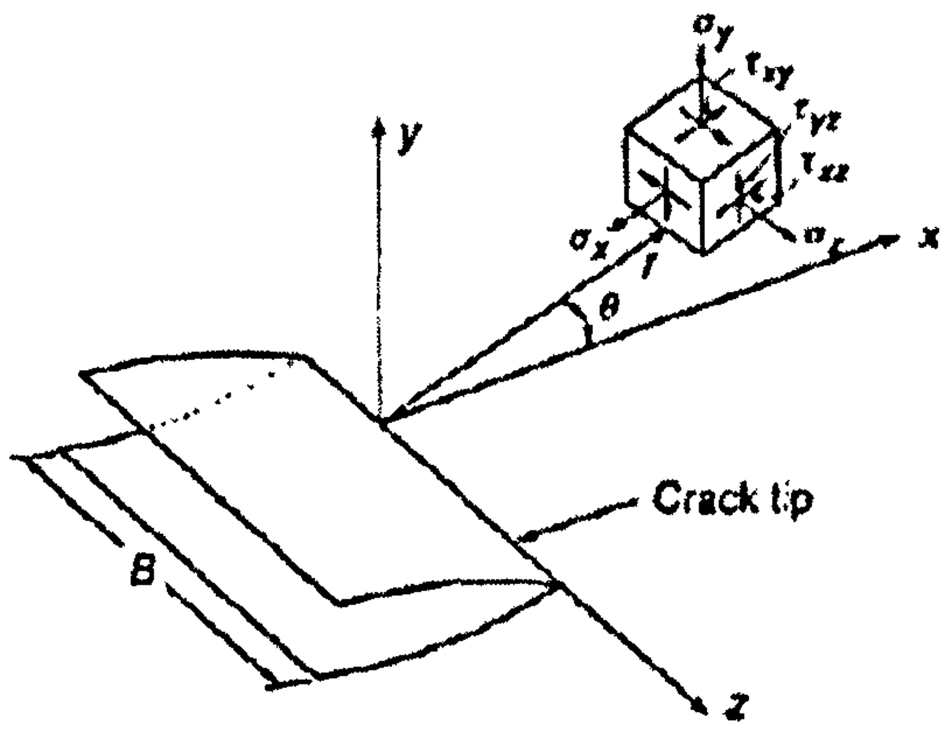

Figure 8.6: Local coordinate system and the resulting stress components for a cracked body (B = plate thickness)

The dimensions of the stress intensity factor are given by [stress] x [length]$^{1/2}$ = [force] x [length]$^{-3/2}$.

It is evident from Equations (8.4), (8.5), and (8.6) that each stress component is proportional to the stress intensity factor.

The stress intensity factor, K, is determined as a function of crack size, geometric properties and loading conditions. An investigation of crack tip stress and displacement fields and their relationship to K is important because these fields are typically the ones that govern the fracture process occurring at the crack tip.

A cracked body as shown in Figure 8.6 is now considered. The crack lies in the xz plane and the crack front is parallel to the y axis. In this case, three basic fracture modes are relevant as depicted by Figure 8.7. Mode I is the opening mode where the crack faces separate symmetrically with respect to xy and xz planes. In Mode II, the sliding mode, the crack faces slide relative to each other symmetrically about the xy plane, but antisymmetrically with respect to the xz plane. In the tearing mode, Mode III, the crack faces also slide relative to each other but antisymmetrically with respect to the xy and xz planes.

For plane problems with homogeneous, isotropic, linear elastic materials, the stress intensity factors corresponding to the three modes are given as follows (Kanninen & Popelar, 1985).

$$K_I = \lim_{r\to 0} \sigma_y \Big| \theta = 0 \sqrt{2\pi r} \tag{8.7}$$

$$K_{II} = \lim_{r\to 0} \tau_{xy} \Big| \theta = 0 \sqrt{2\pi r} \tag{8.8}$$

$$K_{III} = \lim_{r\to 0} \tau_{yz} \Big| \theta = 0 \sqrt{2\pi r} \tag{8.9}$$

where r, θ and the coordinates are defined in Figure 8.5. σ_y , τ_{xy}, and τ_{yz} are stress components as defined in Figure 8.5.

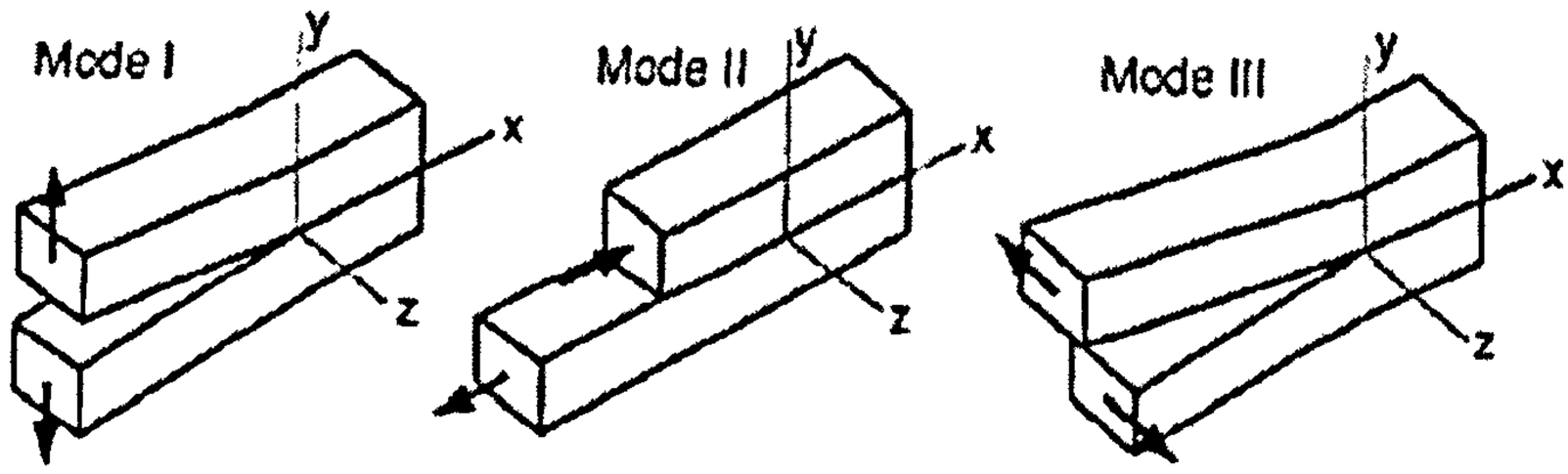

Figure 8.7: Three basic loading modes for a cracked body: (a) Mode I, opening mode; (b) Mode II, sliding mode; (c) Mode III, tearing mode

An elastic body with a crack length of $2a$ and under uniform tensile stress, σ, is considered, although much of the treatment in Equations (8.10) to (8.23) are in fact more general and are applicable to arbitrary types of loading and crack geometry. The local coordinate system of the body is defined as shown in Figure 8.5. The stresses and displacements at the crack tip may be given as follows (Machida, 1984):

$$\begin{Bmatrix}\sigma_x\\ \sigma_y\\ \tau_{xy}\end{Bmatrix}=\frac{K_I}{\sqrt{2\pi r}}\cos\frac{\theta}{2}\begin{Bmatrix}1-\sin(\theta/2)\sin(3\theta/2)\\ 1+\sin(\theta/2)\sin(3\theta/2)\\ \sin(\theta/2)\cos(3\theta/2)\end{Bmatrix} \tag{8.10}$$

$$\tau_{xz}=\tau_{yz}=0 \tag{8.11}$$

$$\sigma_z=\begin{cases}\upsilon(\sigma_x+\sigma_y) & \textit{for plane strain state}\\ 0 & \textit{for plane stress state}\end{cases} \tag{8.12}$$

$$\begin{Bmatrix}u\\ v\\ w\end{Bmatrix}=\frac{K_I}{2\mu}\sqrt{\frac{r}{2\pi}}\begin{Bmatrix}\cos(\theta/2)\left[\kappa-1+2\sin^2(\theta/2)\right]\\ \sin(\theta/2)\left[\kappa+1-2\cos^2(\theta/2)\right]\\ 0\end{Bmatrix} \tag{8.13}$$

where $\kappa = 3-4\nu$ for the plane strain state and $\kappa = (3-\nu)/(1+\nu)$ for the plane stress state, $K_I = \sigma\sqrt{(\pi a)}$, a is crack length, $\mu = E/[2(1+\nu)]$, E is elastic modulus, ν is Poisson's ratio, u, v, w = translational displacements in the x, y and z directions.

It is evident from Equations (8.10), (8.11), (8.12), and (8.13) that the stress or displacement components at the crack tip include a common parameter, K_I. The relative displacements used represent used represent a distance between the crack surfaces. This type of displacement is called Mode I or opening mode, as shown in Figure 8.7(a). A cracked body under shear stress τ is now considered. In this case, the stress and displacement components are given as follows:

$$\begin{Bmatrix}\sigma_x\\ \sigma_y\\ \tau_{xy}\end{Bmatrix} = \frac{K_{II}}{\sqrt{2\pi r}}\begin{Bmatrix}-\sin(\theta/2)[2+\cos(\theta/2)\cos(3\theta/2)]\\ \sin(\theta/2)\cos(\theta/2)\cos(3\theta/2)\\ \cos(\theta/2)[1-\sin(\theta/2)\sin(3\theta/2)]\end{Bmatrix} \tag{8.14}$$

$$\tau_{xz} = \tau_{yz} = 0 \tag{8.15}$$

$$\sigma_z = \begin{cases}\upsilon(\sigma_x+\sigma_y) & \textit{for plane strain state}\\ 0 & \textit{for plane stress state}\end{cases} \tag{8.16}$$

$$\begin{Bmatrix}u\\ v\\ w\end{Bmatrix} = \frac{K_{II}}{2\mu}\sqrt{\frac{r}{2\pi}}\begin{Bmatrix}\sin(\theta/2)[(3-\nu)/(1+\nu)+1+2\cos^2(\theta/2)]\\ -\cos(\theta/2)[(3-\nu)/(1+\nu)-1-2\sin^2(\theta/2)]\\ 0\end{Bmatrix} \tag{8.17}$$

where $K_{II} = \tau\sqrt{(\pi a)}$. In this case, the displacements follow Mode II or the in-plane shear mode as shown in Figure 8.7(b).

When the body is subjected to uniform shear stress, s, in the direction normal to the xy plane, the stress and displacement components are given by:

$$\begin{Bmatrix}\tau_{xz}\\ \tau_{yz}\end{Bmatrix}=\frac{K_{III}}{\sqrt{2\pi r}}\begin{Bmatrix}-\sin(\theta/2)\\ \cos(\theta/2)\end{Bmatrix} \tag{8.18}$$

$$\sigma_x=\sigma_y=\sigma_z=\tau_{xy}=0 \tag{8.19}$$

$$w=\frac{2K_{III}}{\mu}\sqrt{\frac{r}{2\pi}}\sin\frac{\theta}{2} \tag{8.20}$$

$$u=v=0 \tag{8.21}$$

where $K_{III}=s\sqrt{\pi a}$. In this case, the displacements follow Mode III or anti-plane (or out-of-plane) shear mode as shown in Figure 8.7(c).

When the three modes noted above are combined, the stress or displacements components may be given as a sum of those for each mode as follows (Machida, 1984):

$$\sigma_{ij}(r,\theta)=\frac{1}{\sqrt{2\pi r}}\left\{K_I f_{ij}^{\ I}+K_{II} f_{ij}^{\ II}+K_{III} f_{ij}^{\ III}\right\} \tag{8.22}$$

$$u_i(r,\theta)=\frac{1}{2\mu}\sqrt{\frac{r}{2\pi}}\left\{K_I g_i^{\ I}+K_{II} g_i^{\ II}+4K_{III} g_i^{\ III}\right\} \tag{8.23}$$

where $f_{ij}^{\ I}, f_{ij}^{\ II}, f_{ij}^{\ III}$ = stress function of θ for Modes I, II, III as defined in Equations (8.10) to (8.21), $g_i^{\ I}, g_i^{\ II}, g_i^{\ III}$ = displacement functions of θ for Modes I, II, and III as defined in Equations (8.10) to (8.21).

It is apparent that the K parameters are independent of the coordinate system while they are affected by geometric properties and loading conditions such as crack size, dimensions of the structure and can hence be employed as the measure of crack extension resistance at the crack tip as long as the structure remains in the linear elastic regime.

In relation to LEFM, calculations of the stress intensity factor involve the most part of the work. Analytical and numerical approaches can be used to determine the stress intensity factors, many essentially exploiting the relationships between K and the crack tip stress field previously described. Some useful K solutions are now described below.

For steel plates with typical types of cracks under tensile stress as shown in Figure 8.8, the K value for Mode I is approximately given as follows (Broek, 1986):

- Center crack, see Figure 8.7(a)

$$K_I = F\sigma\sqrt{\pi a} \tag{8.24}$$

where

$$F = \left(\sec\frac{\pi a}{b}\right) \tag{8.25}$$

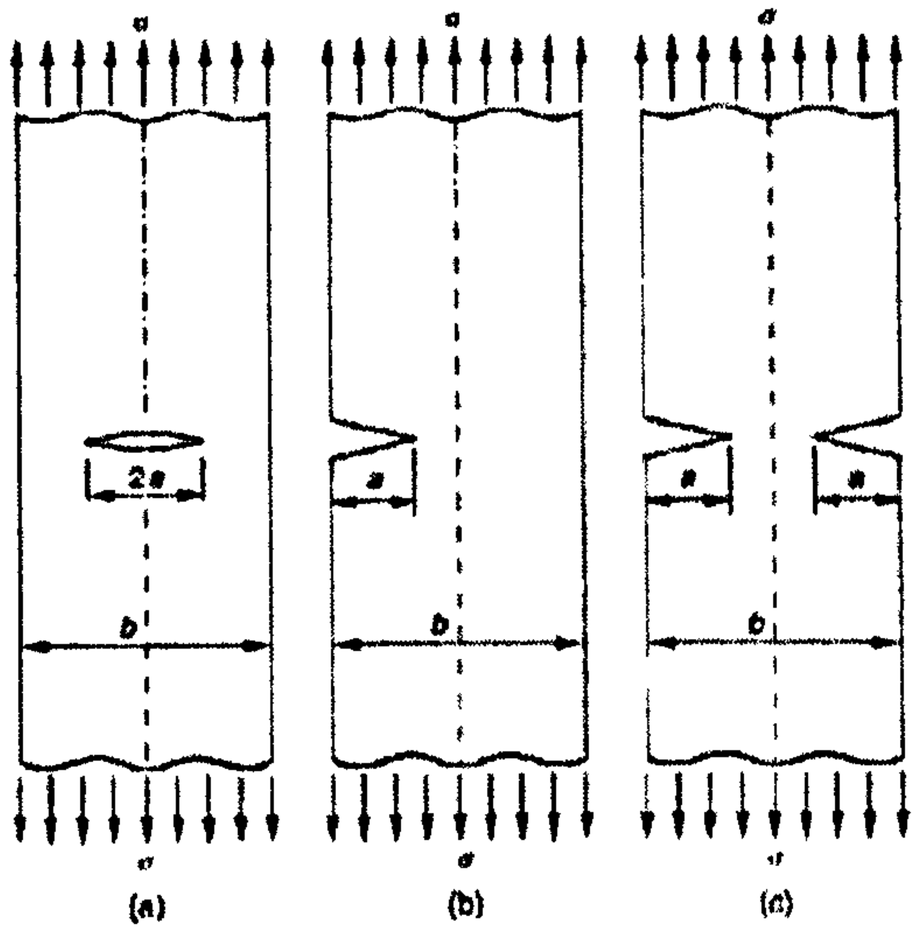

Figure 8.8: Typical crack locations in a plate under tensile stress: (a) center crack; (b) crack on one side; (c) crack on both sides

- Crack on one side, see Figure 8.7(b)

$$K_I = F\sigma\sqrt{\pi a} \tag{8.26}$$

where

$$F = 30.38\left(\frac{a}{b}\right)^4 - 21.71\left(\frac{a}{b}\right)^3 + 10.55\left(\frac{a}{b}\right)^2 - 0.23\left(\frac{a}{b}\right) + 1.12 \tag{8.27}$$

- Crack on both sides, see Figure 8.7(c)

$$K_I = F\sigma\sqrt{\pi a} \tag{8.28}$$

where

$$F = 15.44\left(\frac{a}{b}\right)^3 - 4.78\left(\frac{a}{b}\right)^2 + 0.43\left(\frac{a}{b}\right) + 1.12 \tag{8.29}$$

If the plate width were infinite the solution in the first of the above three cases would revert to the classical exact solution, namely $K_I = \sigma\sqrt{(\pi a)}$ since $F = 1$ in this case.

8.3.3 Fracture toughness testing

Fracture takes place if the K value of the structure reaches the critical K value, K_C, namely

$$K \geq K_C \tag{8.30}$$

where K_C is sometimes called fracture toughness, which is typically determined experimentally for a given material, crack and loading situation. Under plane strain conditions, the notation K_{IC} is used. The fracture toughness parameter, K_C or K_{IC}, must be obtained by testing.

In such testing, K_C is determined once the ultimate fracture loads (or failure loads) and the crack sizes are obtained for a mechanical test specimen with the stress intensity factor known. In general, the fracture toughness, K_C, is affected by strain rate, temperature and plate thickness. As the plate thickness decreases, the K_C value tends to significantly increase. This is because with decrease in the plate thickness the crack tip stress state case, and essentially Mode II or III based on shear fracture and mixtures of these with Mode I are more likely to take place than pure Mode I.

For thicker plates, Mode I fracture associated with the plane strain state is more likely to occur. In this case, the fracture toughness, K_C, is no longer a function of plate thickness. Figure 8.9 shows a schematic representation of the critical K value at the crack tip versus the plate thickness. For a given plate thickness, in contrast to through-thickness cracks, surface cracks may sometimes exhibit plane strain behaviour because of the related conditions at the crack tip. It is noted that the critical stress intensity value given in this section, which is used as a material parameter to define the fracture toughness, should strictly speaking be called the static fracture toughness as it relates to fracture under static loading (Broek, 1986).

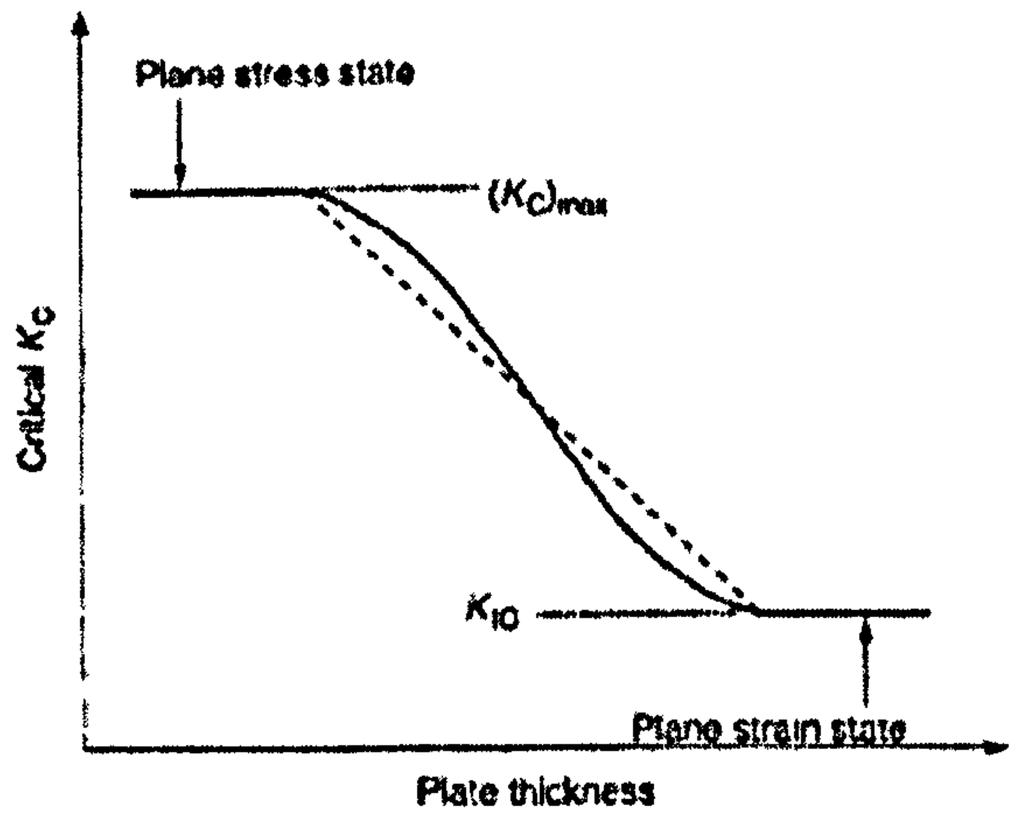

Figure 8.9: A schematic representation of the critical K_I value versus the plate thickness, B

8.4 Elastic-Plastic Fracture Mechanics

In LEFM, the failure stress, $\sigma_f = K_{IC}/F\sqrt{(\pi a)}$, at the crack tip becomes infinite when the crack size, a, approaches zero. This is unrealistic because in real structures behaving in a ductile manner, the crack tip is likely to yield and strictly LEFM may not be valid. For a body with relatively large flaws, LEFM may approximately be dealt with using the K values to an extent, as long as the plastic zone at the crack tip is small in size. The better alternative in this regard is to use the concepts of EPFM. As will now be presented, the concepts of CTOD or the J-integral accommodate the effect of yielding at the crack tip in a more rigorous way. These types of procedure are also variously called non-linear fracture mechanics or post-yield fracture mechanics.

8.4.1 Crack tip opening displacement

Beyond general yield condition, plastic deformation is likely to occur at the crack tip. The crack may propagate if the plastic strain at the crack tip exceeds a critical value. The change of stress at the yielded crack tip may be small when the effect of strain hardening is neglected, and the fracture will take place after a large plastic deformation occurs at the crack tip.

In an effort to account for limited amounts of crack tip yielding as an extension of LEFM, Dugdale (1960), Wells (1961, 1963) and Barenblatt (1962) independently introduced cohesive yield strip zones extending from the crack tip to take account of the inelastic response of real materials in this region. The CTOD concept as now used emanated from these early treatments. The plastic deformation at the crack tip can be measured in terms of the CTOD. Wells (1961, 1963) considered that fracture takes place if the CTOD exceeds a critical value. In LEFM, the crack opening displacement (COD) is given by (see Figure 8.10):

$$COD = 2v = \frac{4\sigma}{E}\sqrt{a^2 - x^2} \tag{8.31}$$

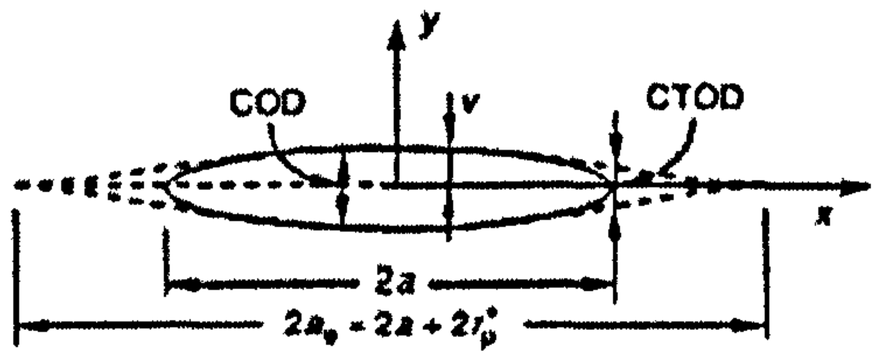

Figure 8.10: Crack opening displacement and CTOD

The maximum COD occurs at the center of the crack, i.e., at $x = 0$, as follows:

$$COD_{max} = \frac{4\sigma a}{E} \tag{8.32}$$

- The Irwin Approach:

Equations (8.31) and (8.32) are the elastic solutions of crack problems while most engineering materials deform plastically. These equations cannot be applied to the crack problems involving the plastic deformations at the crack tip. The size (distance) of the crack tip plastic zone can be approximately calculated by:

$$\sigma_y = \frac{K_I}{\sqrt{2\pi r_p^*}} \quad \text{or} \quad r_p^* = \frac{K_I^2}{2\pi\sigma_y^2} = \frac{\sigma^2 a}{2\sigma_y^2} \tag{8.33}$$

where σ_y = material yield stress, r_p^* = size of the crack plastic zone, see Figure 8.8.

Irwin (1956) assumed that due to occurrence of plasticity, the equivalent crack tip size becomes longer than the physical size. In this regard, the COD is given by applying the plastic zone correction as follows:

$$COD = \frac{4\sigma}{E}\sqrt{\left(a + r_p^*\right)^2 - x^2} \tag{8.34}$$

The CTOD is then found for $x = a$ as follows:

$$CTOD \equiv \delta = \frac{4\sigma}{E}\sqrt{\left(a + r_p^{\bullet}\right)^2 - a^2} \approx \frac{4a}{E}\sqrt{2ar_p^{\bullet}} = \frac{4}{\pi}\frac{K_I^{\,2}}{E\sigma_y} \tag{8.35}$$

It is not straightforward to measure CTOD, but using the K value CTOD can be obtained from Equation (8.35). By substituting Equation (8.35) into Equation (8.34), the following relation between COD and CTOD is approximately obtained by regarding $\left(r_p^{\bullet}\right)^2$ as infinitesimal, namely,

$$COD = \frac{4\sigma}{E}\sqrt{a^2 - x^2 + \left(\frac{E}{4\sigma}\right)^2 \delta^2} \tag{8.36}$$

In testing, the COD can be measured easily so that the CTOD is determined from Equation (8.36) in terms of the maximum COD, i.e., at $x = 0$.

- <u>The Dugdale approach:</u>

Dugdale (1960) treated yielding at the crack tip by replacing the yielded region with the equivalent elastic (unyielded) crack model. As shown in Figure 8.11(a), the crack tip is likely to yield and the yielding may expand around the crack tip. In the Dugdale approach, however, yielding is assumed to be limited inside a region along the straight line of the crack, as shown in Figure 8.11(b). This situation is considered equivalent to a virtual elastic structure which has the crack length of $2b = 2a + 2d$, including the yielded region, and the yielded region is subjected to a 'negative' internal pressure ('tensile' stress) equal to the yield stress, σ_y, on the crack surfaces, which tends to 'close' the virtual crack strip yielding zone opening caused by the external stress as shown in Figure 8.11(c). In this case, the K value at the tip of the virtual elastic crack must be zero, and hence the following applies:

$$K_\sigma + K_y = 0 \tag{8.37}$$

where $K_\sigma = K$ value due to applied stress σ, $K_y = K$ value due to the closure yield stress, which is taken as $K_y = -\sigma_y$. The extent of plastic region, d, can be calculated using Equation (8.37) as follows:

$$d = b - a = a\left[\sec\left(\frac{\pi\sigma}{2\sigma_y}\right) - 1\right] \tag{8.38}$$

where σ_y is material yield stress.

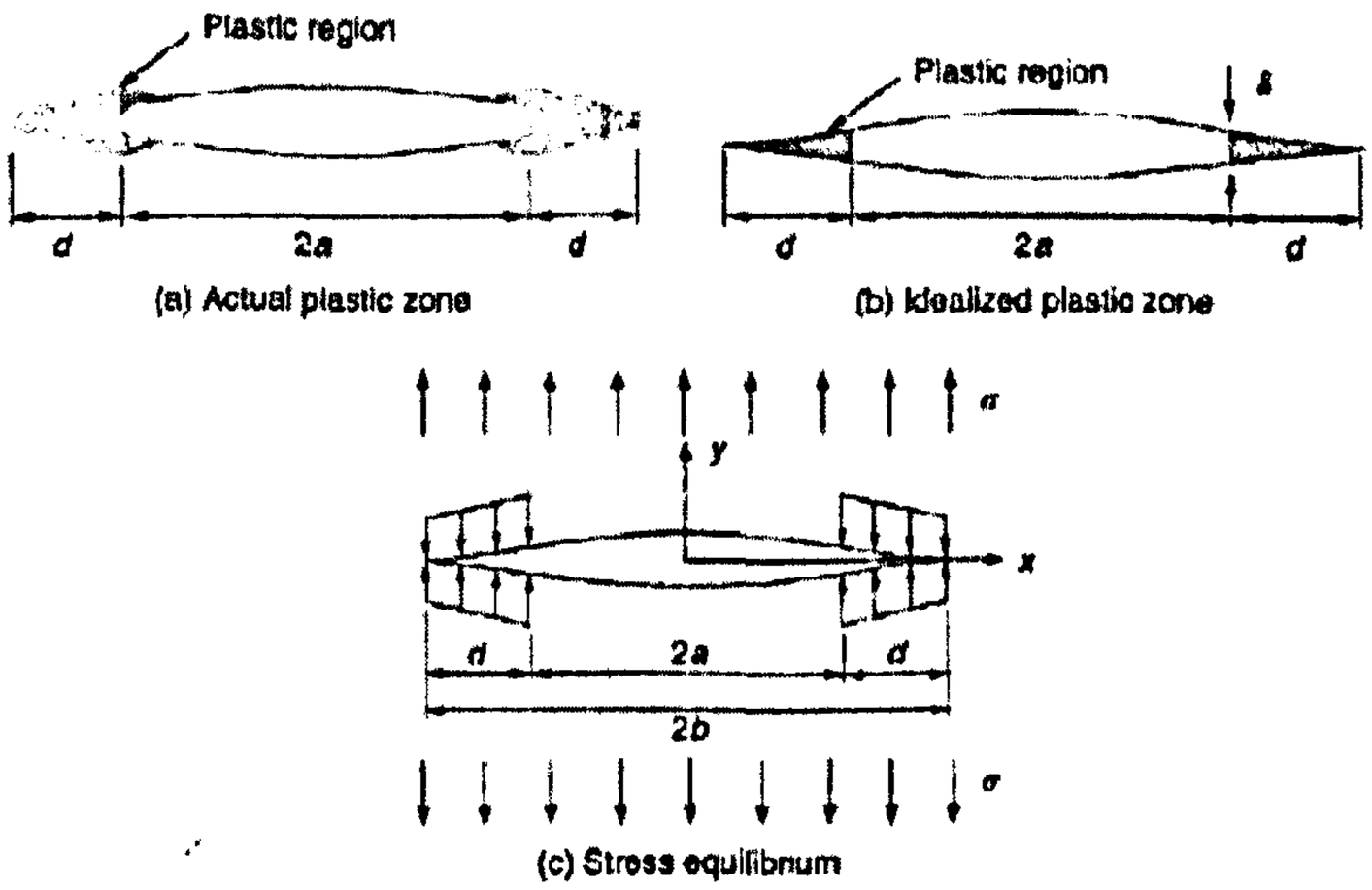

Figure 8.11: A schematic representation of the Dugdale approach (the shaded areas represent the plastic zones)

The CTOD value, δ, at $x = a$ may approximately be considered as the CTOD of the real structure, namely:

$$\delta = \frac{8a\sigma_y}{\pi E}\ln\left[\sec\left(\frac{\pi\sigma}{2\sigma_y}\right)\right] \tag{8.39}$$

when $\sigma \le \sigma_y$, i.e., representing small-scale yielding, Equation (8.39) may be simplified to

$$\delta = \frac{\pi\sigma^2 a}{E\sigma_y} = \frac{G_I}{\sigma_y} = \frac{K_I^{\,2}}{E\sigma_y} = \frac{J}{\sigma_y} \tag{8.40}$$

where G is as defined in Equation (8.3) and J is the J-integral value.

8.4.2 Other EPFM measure: J-integral

The concept of the J-integral is useful to analyse ductile fracture mechanics involving small-scale plasticity at the crack tip in a somewhat rigorous way. The basic work on the J-integral was contributed from a theoretical point of view, primarily by Rice (1968), and by Hutchinson (1968). They envisaged a path-independent integral; called the J-integral; calculated along a contour around the tip of the crack, as a parameter that characterized the fracture behaviour of the crack tip.

It is considerably more important that J is potentially a better parameter to use when it becomes necessary to select the basic of non-linear fracture mechanics for elastic-plastic conditions. Mathematically, J is obtained by evaluating an integral around a path containing the crack tip, namely:

$$J = \int_{\Gamma}\left(W\,dy - T_i\frac{\partial u_i}{\partial x}\right)ds = -\frac{\partial V}{\partial a} \tag{8.41}$$

where: Γ = The contour path, depicted in Figure 8.12

W = Strain energy density

T_i = Components of the traction vector which is normal to the contour

u_i =Components of the displacement vectors

ds = Length increment along the contour Γ

This integral is basically the change in potential energy associated with the virtual crack extension.

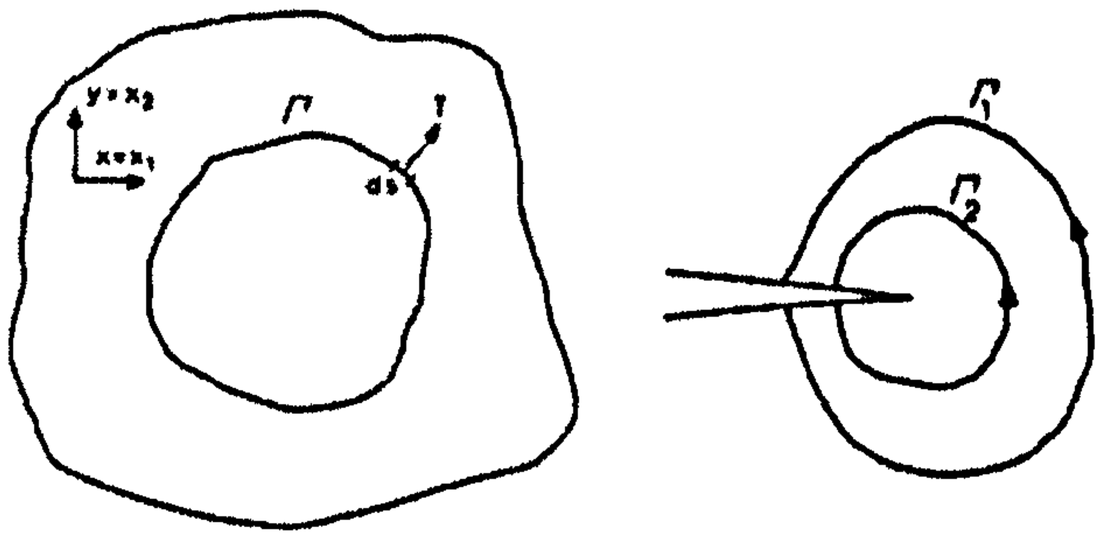

Figure 8.12: Contour path used for J evaluation

The finite element method evaluates Equation (8.41) for a specified node, i.e. the node representing the crack tip, by computing the strain energy density W.

$$w = \int_0^{\varepsilon_{ij}} \sigma_{ij} d\varepsilon ij \tag{8.42}$$

where, σ_{ij} and ε_{ij} are the stress and the strain tensors.

The calculation of J is path independent, which means any chosen path should yield the same value of J as long as it encircles the crack tip. The obtained of J relies on the calculated values of the stress and the strain for the elements on the contour surrounding the crack tip. Therefore, one must be careful when meshing the plate to assure correct values of calculated stresses and strains.

In applying the J-integral criterion to EPFM, it is then considered that fracture takes place if the J-integral value of the structure reaches a critical J-integral value, J_C, namely:

$$J \geq J_C \tag{8.43}$$

8.5 The Crack Growth Resistance Curve

8.5.1 Modelling of fatigue crack growth

The rate of change of crack length (a) with number of cycles (N) in fatigue crack growth can be described using a model having the general form of Equation (8.44).

$$\frac{da}{dN} = f(\Delta K, R) \tag{8.44}$$

where R is the load ratio or the ratio of minimum load to maximum load. Rushton (2001) describes various models that were developed and used to predict fatigue crack growth. Most of the models have the form of a power law, which is associated with curve fitting parameters that do not have a physical significance. One of the most reliable and effective models used for predicting fatigue crack growth is the Paris model, also known as the Paris Law.

8.5.2 The Paris Law

Paris & Erdogan (1963) hypothesized that the range in stress-intensity factor, ΔK, governs fatigue crack growth. The empirical Paris Law represents the crack growth rate data as a straight line when plotted on a log-log scale. However, experimental da/dN versus ΔK data typically exhibit a sigmoid shape when plotted on a log-log scale. There is a ΔK threshold, ΔK_{th}, below which cracks will not propagate. ΔK_{th} can be taken as 3 MPa-m$^{1/2}$ for structural steel. The Paris Law is a fit to the linear portion of the da/dN versus ΔK plot (on a log-log scale) that lies above ΔK_{th}. At relatively high ΔK levels the crack growth rate accelerates, and is accompanied by ductile tearing or increments of brittle fracture in each cycle. The Paris Law is expressed as:

$$\frac{da}{dN} = C(\Delta K)^m \tag{8.45}$$

where:
- a = Half the crack length
- N = Number of cycles
- C = An experimentally determined coefficient
- ΔK = Stress intensity factor range
- m = Material constant

It is difficult to achieve great accuracy in predicting crack growth rate when using fracture mechanics (Kober *et al.* 1990). There is up to a factor of twenty in the scatter of experimental da/dN data. A great deal of the scatter is due to experimental error, especially at low growth rates near the threshold. In this range, the growth rate is affected by the procedure used to pre-crack the specimens at higher ΔK. There is a great deal of inherent variability in the actual growth rates, even if they were to be accurately measured.

The value of m, the exponent in the Paris Law, is typically taken as 3.0 for steel. The relation between the Paris Law describing the stress intensity factor for a specific crack length and the S-N curve is such that the exponent is the same as the inverse slope of the S-N curves when plotted on a log-log scale.

Crack growth rate depends on the load ratio (R) as indicated in Equation (8.45). Different lines may be fitted to the experimental data (on a log-log plot) for different load ratios. There are also empirical equations that account for the effect of the load ratio on the crack growth rate. The proffered approach is to account for the effect of load ratio and associated crack closure in the definition of ΔK. The idea is that the baseline crack growth rate model is defined for high load ratios (greater than 0.7), for which there is negligible crack closure. At lower ratios (less than 0.5) and negative load ratios the crack is closed for part of the load cycle, and only the part of the load cycle where the crack is open effective. An effective ΔK_{eff} is defined as that part of ΔK that contributes to the crack propagation, and then ΔK_{eff} is used in Equation

(8.46), where the parameters of Equation (8.46) are defined by fitting the equation to high R crack growth rate data. This is the approach taken in this research, and the Paris Law will be assumed to be defined for high load ratio (greater than 0.7).

Variance in the crack growth rate is usually expressed by variance in the coefficient C. Most researchers agree that all C-Mn steels have similar crack growth rates, and that the variance observed is just the typical material variation. In other words, there is only scatter. Therefore, most reported values of C are intended to represent a conservative upper bound to the data.

Barsom & Rolfe (1987) established an upper bound for a variety of ferritic steels where C was 6.8×10^{-12} for units of MPa and meters. The Barsom & Rolfe relation seems to be unconservative for high-load-ratio crack growth rates, however, Fisher et. al (1993) performed a study of HSLA-80 steel, which showed that the upper bound value of C for high-load-ratio data was 9.0×10^{-12}. British Standards Institute BS 7910 (1999) recommends an upper bound of 16.5×10^{-12} for C. However, this value seems to be excessively conservative. In a previous version of this document known as PD 6493, a more reasonable upper bound of 9.5×10^{-12} was recommended for C. Table 8.1 shows different values of the constant C from various sources.

Table 8.1: Values of C present in different sources

Reference of C values	C MPa and m
Barsom & Rolfe (1987)	6.8×10^{-12}
Fisher et. al (1993)	9.0×10^{-12}
BS 7910 (1999)	16.5×10^{-12}
BS PD 6493 (1993)	9.5×10^{-12}

8.6 Failure Assessment

The objective of this step in the solution process is to consider the potential for failure including plastic collapse or fracture failure modes for the ship structure containing cracks. This failure assessment will be completed using a failure

assessment diagram approach similar to that outlined in BS 7910. A simplified failure assessment approach that will be used in this analysis was developed based upon a review of available techniques that identified the Level 2 approach in BS 7910:1999 as the most appropriate failure assessment technique. The simplification is made since the stress-strain curve of the material is not likely to be available in most failure assessment cases and the conventional approach is to use the Level 2B FAC. The method that is used in the failure assessment may be summarised as follows:

- Define the cracked detail and material
- Estimate the ultimate state of cracked detail (FAC)
- Estimate the current state of the cracked detail (FAP)
- Estimate fracture toughness of material
- Estimate load on cracked detail
- Estimate crack driving force in cracked detail
- Estimate collapse load of cracked detail
- Determine the safety margin of the cracked detail

A schematic of this method is presented in Figure 8.13 (Reemsnyder, 2002), defining the failure assessment curve (FAC), failure assessment point (FAP), and margin of safety, for scenarios considering no residual stress. The vertical and horizontal axes of the graph in Figure 8.13 represent the fracture or collapse ratios, respectively, indicating the effect of the applied loading towards the onset of fracture or plastic collapse of the flawed structure. As the fracture ratio approaches 1, the flawed structure is said to be at risk of brittle fracture, whereas a structure with a plastic collapse ratio approaching 1 is at risk of a ductile shear or tearing failure.

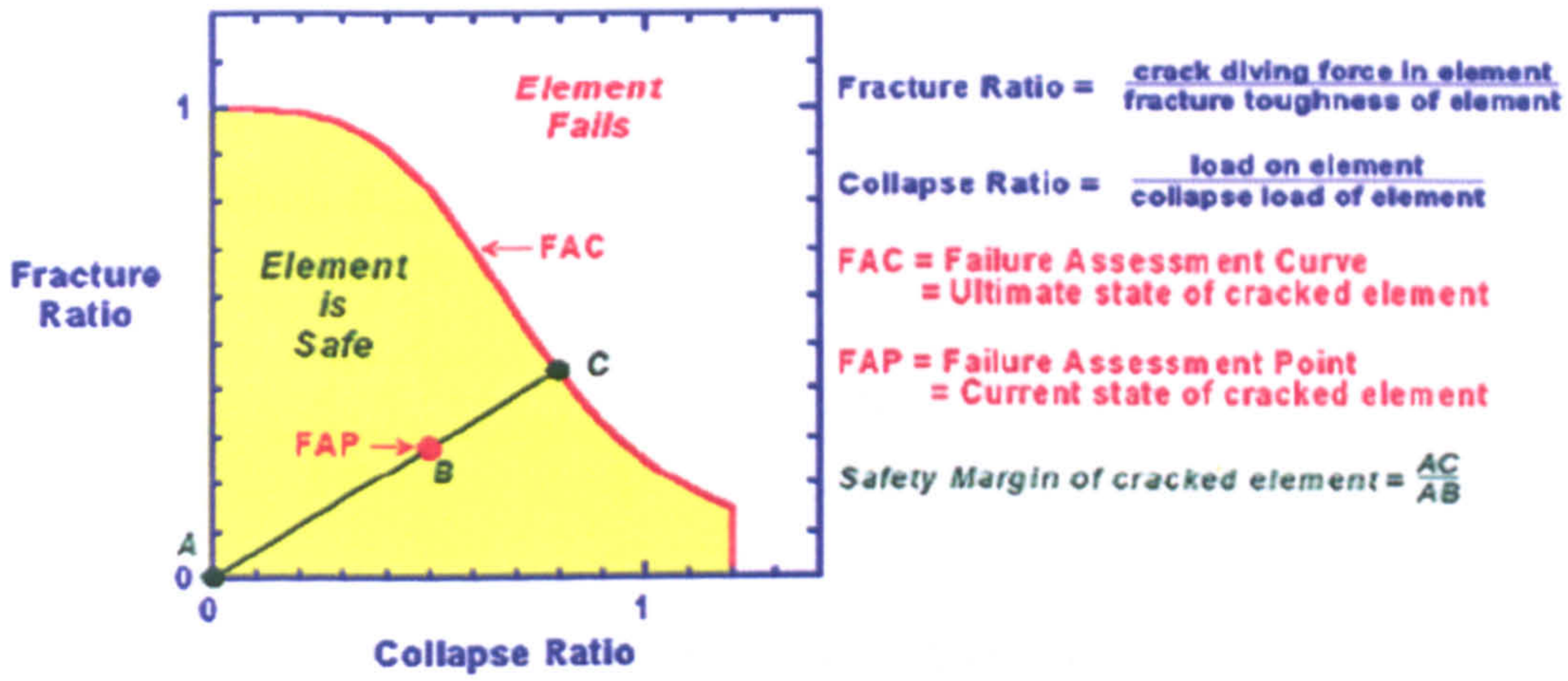

Figure 8.13: A schematic of the generic FAC, the FAP and safety margin (Reemsnyder, 2002)

The simplified Level 2B Failure Assessment Curve (FAC) is expressed as follows and is shown in Figure 8.14.

$$K_r = \frac{1}{\sqrt{1+\frac{L_r^{\,2}}{2}}} \qquad for \qquad L_r \le 1 \tag{8.46}$$

and

$$K_r = 0 \qquad for \qquad L_r > 1 \tag{8.47}$$

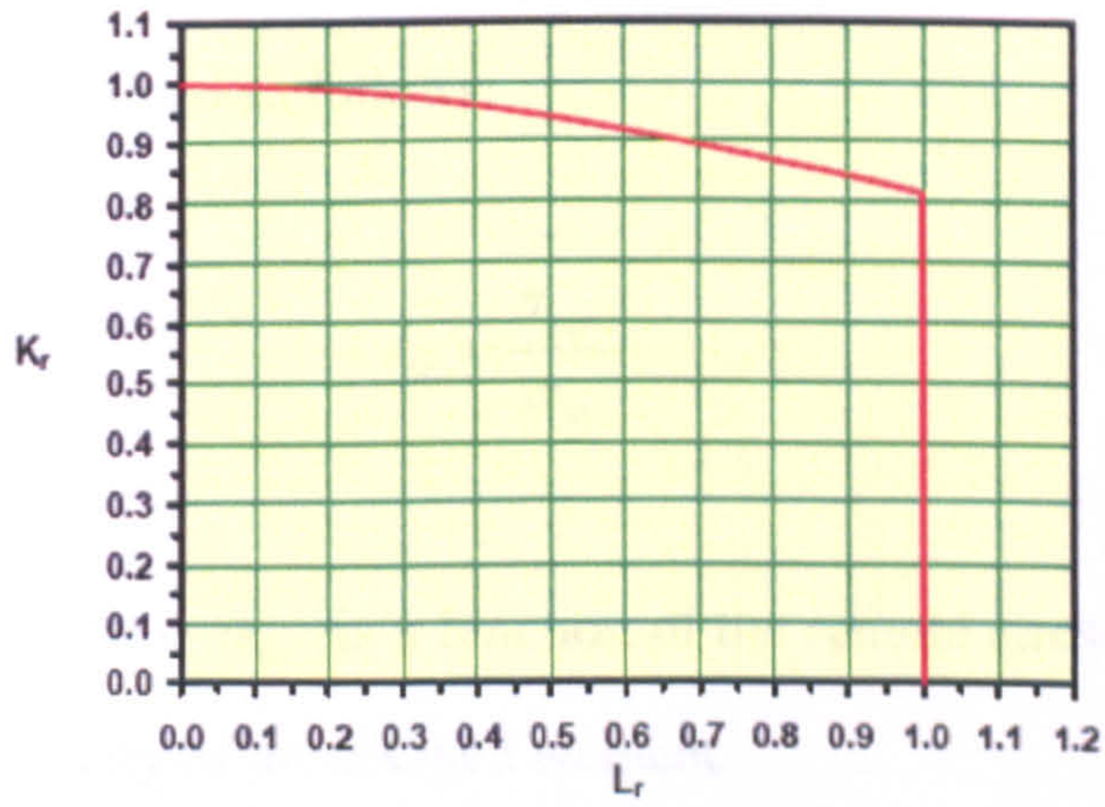

Figure 8.14: Simplified Level 2B, BS 7910

Fracture Ratio and Collapse ratio:

The Fracture Ratio, K_r, (for zero residual stress) is defined as below:

$$K_r = \sqrt{\frac{K_I^{\,2}}{\sigma_y E \delta_c}} + \rho = \sqrt{\frac{\left(K_I^{\,applied} + K_I^{\,residual}\right)^2}{\sigma_y E \delta_c}} + \rho \qquad (8.48)$$

where K_I, σ_y, E and δ_c are, respectively, the elastic crack-driving force, i.e., the stress intensity factor, Young's Modulus, and the CTOD fracture toughness. The plasticity correction factor, ρ, accommodating residual stresses and the concomitant plastic redistribution of stress, is computed from

$$\begin{aligned} &\rho = \rho_1 && for \quad L_r \le 0.8 \\ &\rho = 4\rho_1(1.05 - L_r) && for \quad 0.8 < L_r < 1.05 \\ &\rho = 0 && for \quad L_r \ge 1.05 \; or \; K_I^{\,residual} \le 0 \; or \; K_I^{\,applied} = 0 \end{aligned} \qquad (8.49)$$

where

$$\rho_1 = 0.1\chi^{0.714} - 0.007\chi^2 + 3x10^{-5}\chi^5 \qquad (8.50)$$

The collapse ratio is defined as follows:

$$L_r = \frac{\sigma_{ref}}{\sigma_y} \qquad (8.51)$$

where the reference stress, σ_{ref}, is a function of the remote stress, σ, on the cracked element and the geometry of the cracked element.

8.7 Finite Element Analyses

Finite element analysis is used as a tool to investigate the crack propagation in the stiffened panel. The basis for the definition of stress, strain, and stress intensity transfer functions lies in the development of a global finite element model. Generally, static analysis of stress intensity factors is used to determine the crack propagation rate by comparing factor K_{IC} to the K value associated with a specific crack length.

The static analysis could be done many times to obtain fracture parameters for various crack sizes. These values are then used to determine the number of cycles required to propagate the crack.

Top-down analysis for an entire ship could be employed. It considers the global response of the ship as a whole, and correlates that response to the local response of a certain structural component of the ship. In this case, the global model is a basic shell model created in ANSYS, shown in Figure 8.15.

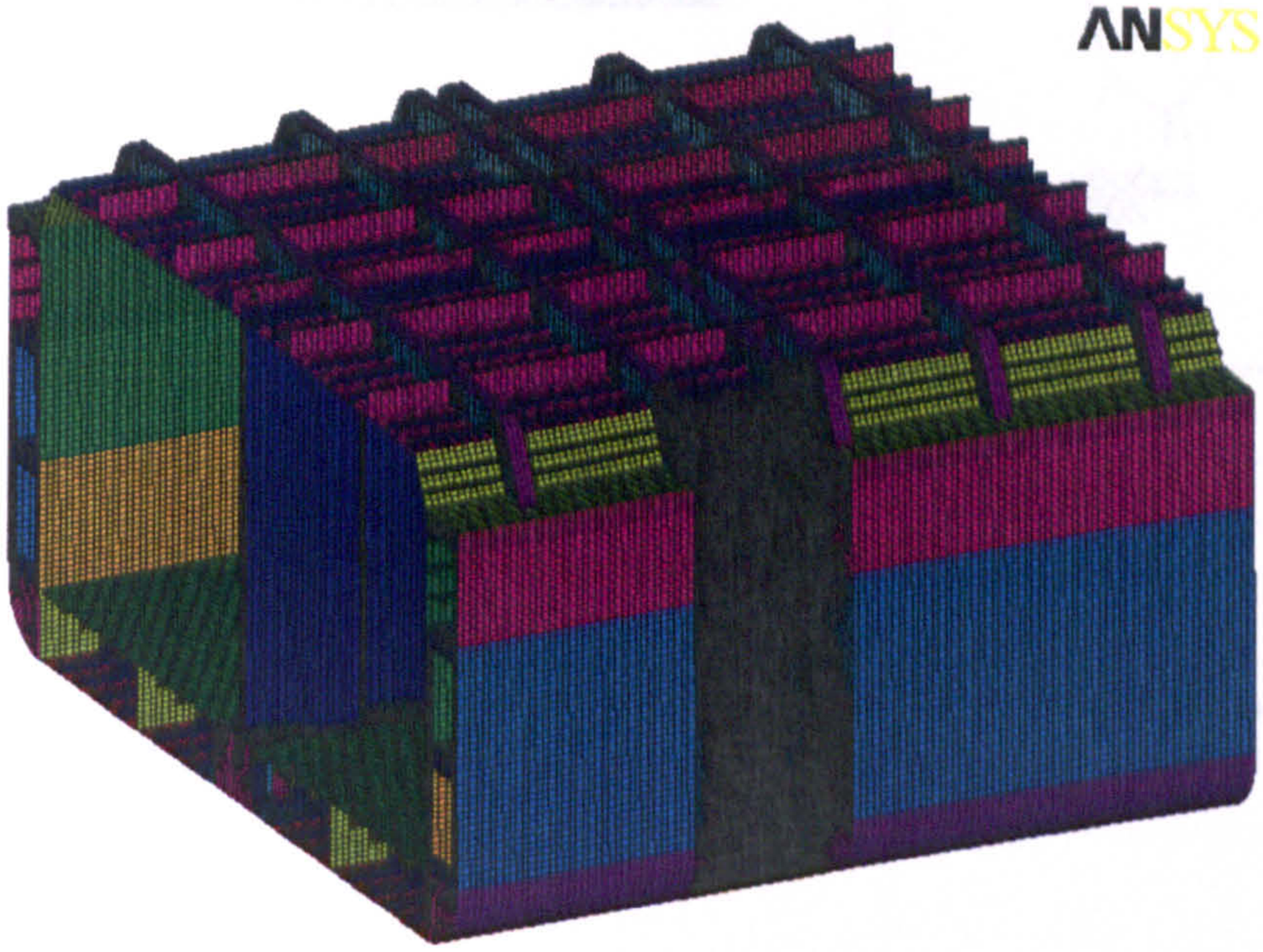

Figure 8.15: The global finite element modelling created by ANSYS

The primary sub-model structure with cracks completed in ANSYS, includes the longitudinal and transverse secondary stiffeners attached to side shell. The damaged-cracked sub-models contain through crack type. Figure 8.16 and Figure 8.17 present the basic primary sub-model geometry used in the study for the fracture assessment of the damaged tanker. These cracked models are used to accurately estimate the fracture parameters. The crack-tip region is modelled using PLANE82 quarter-point (singular) 8-node quadrilateral elements in order to predict more accurate results near the crack. For the through cracked sub-model, approximately 1700 elements are used with a solution time of approximately 10 minutes.

It is noted that the crack tip elements are relatively small (typically about 2% of the crack length) and that elements gradually get larger as the distance from the crack tip increases. This is to ensure that the rapid stress gradient at the crack tip is adequately represented.

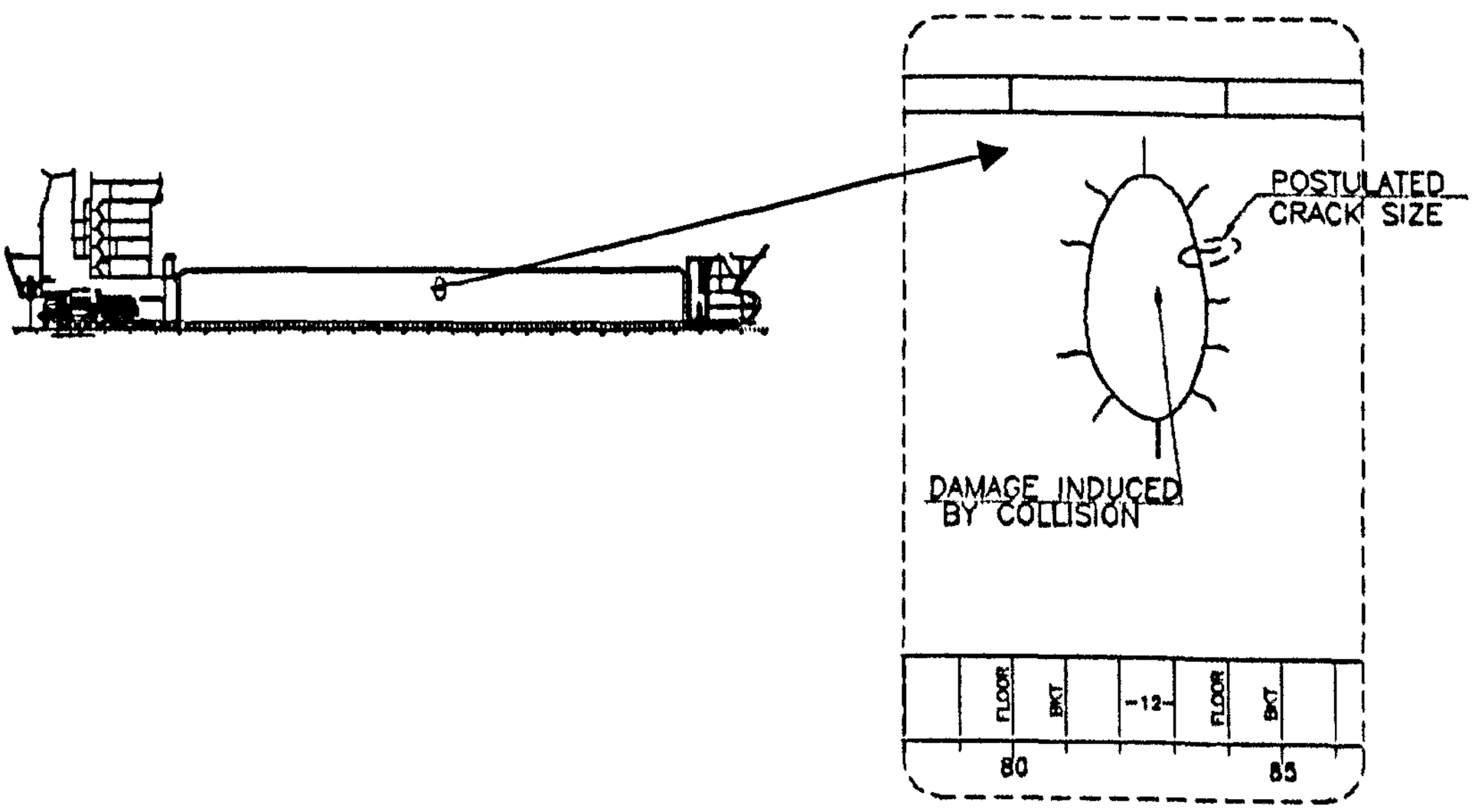

Figure 8.16: Possible crack propagations induced by ship collision incident

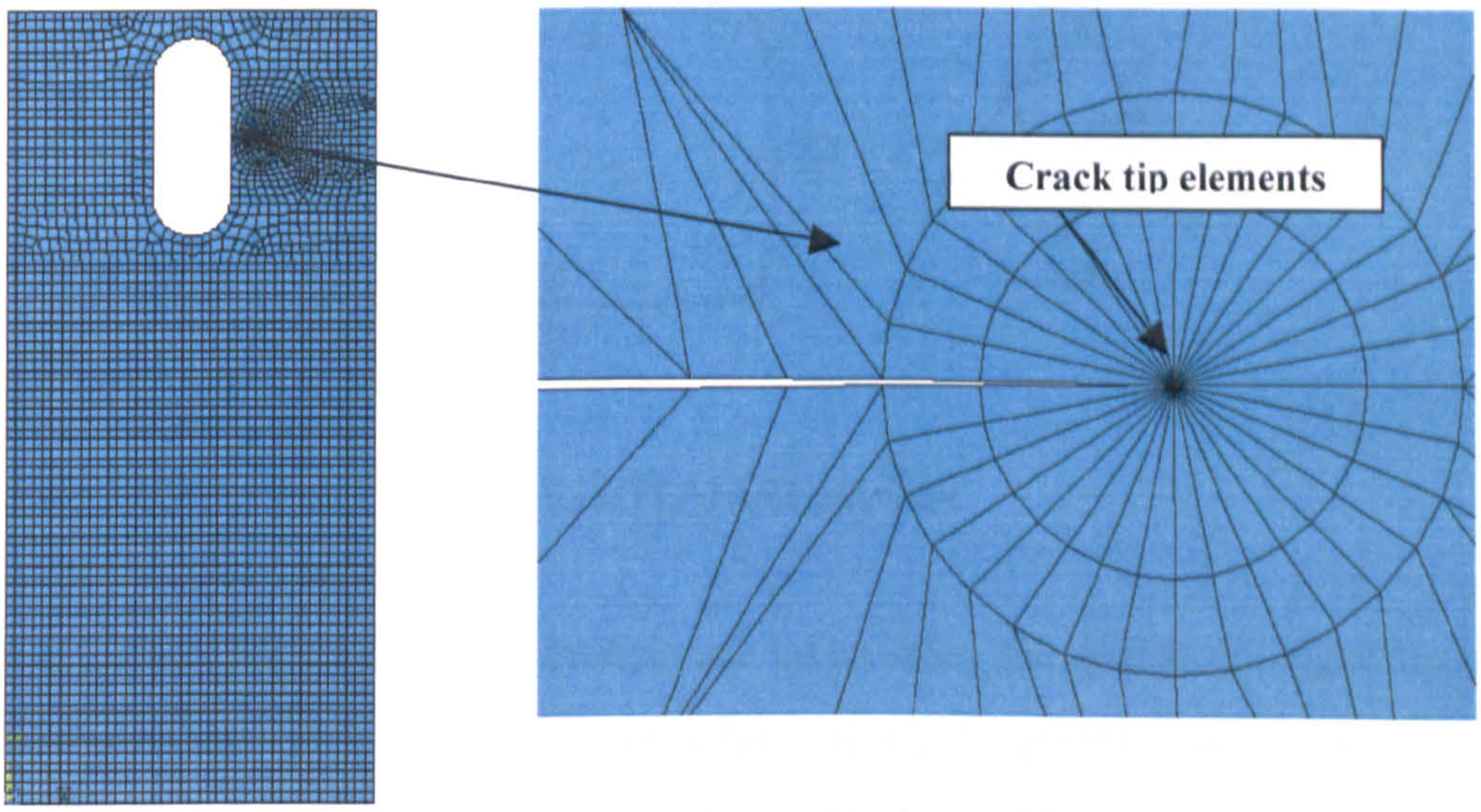

Figure 8.17: Through-crack finite element model for damaged side shell of tanker

PLANE 82 is the highest order version of the 2-D element. It provides more accurate results for mixed (quadrilateral-triangular) automatic meshes and can tolerate irregular shapes without as much loss of accuracy. The 8-node elements have compatible displacement shapes and are well suited to modelling curved boundaries. The 8-node element is defined by eight nodes having two degrees of freedom at each node: translation in the nodal x and y directions. The element may be used as a plane element or as an axisymmetric element. The element has plasticity, creep, swelling, stress stiffening, large deflection, and large strain capabilities. PLANE82 element is shown in Figure 8.18. Ordinary stiffeners attached to outer side shell are modelled as 2D BEAM23 plastic element type. However, the considerations of severed stiffeners are ignored into calculations. Dexter & Mahmoud (2004) have conducted a series of experiment to obtain crack propagation in the stiffened plate. They found that the crack propagation rate in the plate was not largely affected by severing the stiffeners. The reason for that is believed to be that the stiffeners were not effective in carrying the load. This observation was discussed in the experimental results section.

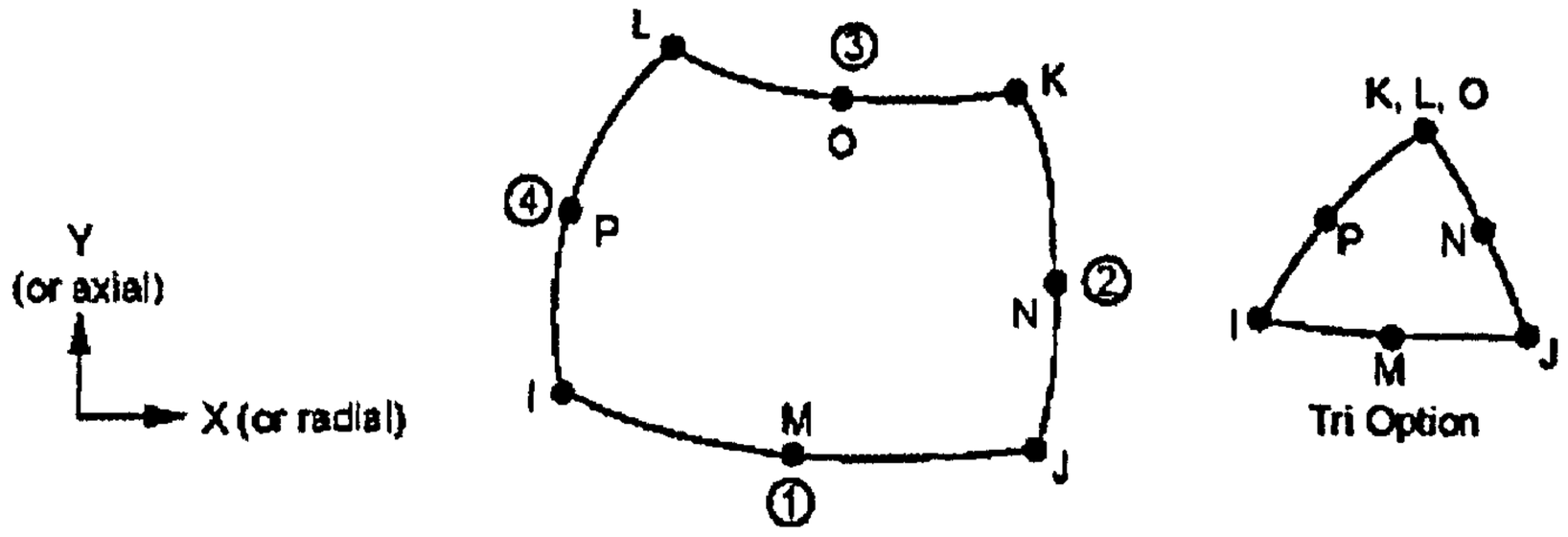

Figure 8.18: PLANE82 geometry

Stress values for cracked sub-models are taken from the global damaged tanker ANSYS modelling, and applied to the edges of elastic-plastic static analysis to calculate desired fracture parameters. In this project, J- Integral values associated with assumed crack lengths are obtained using elastic-plastic non-linear finite element method. For a specified direction cosine of the crack as well as the node number at the crack tip, J-Integral value is computed, and then converted to K value under plane stress condition using Equation (8.52).

$$K = \sqrt{JE} \tag{8.52}$$

Where, J is the J-Integral value and E is the Young's modulus.

When running these analyses, one must be careful to find J-Integral, then convert to K, since J and K do not have a linear relationship. The calculation of J is path independent, which means any chosen path should yield the same value of J as long as it encircles the crack tip. The obtained value of J relies on the calculated values of the stress and the strain for the elements on the contour surrounding the crack tip. Therefore, one must be careful when meshing the plate to assure correct values of calculated stresses and strains.

To determine the value of the J-Integral associated with the new crack length, boundary conditions in the form of constraints are introduced at the crack face, and

released to propagate the crack. Figure 8.19 shows boundary conditions used for the FE analysis.

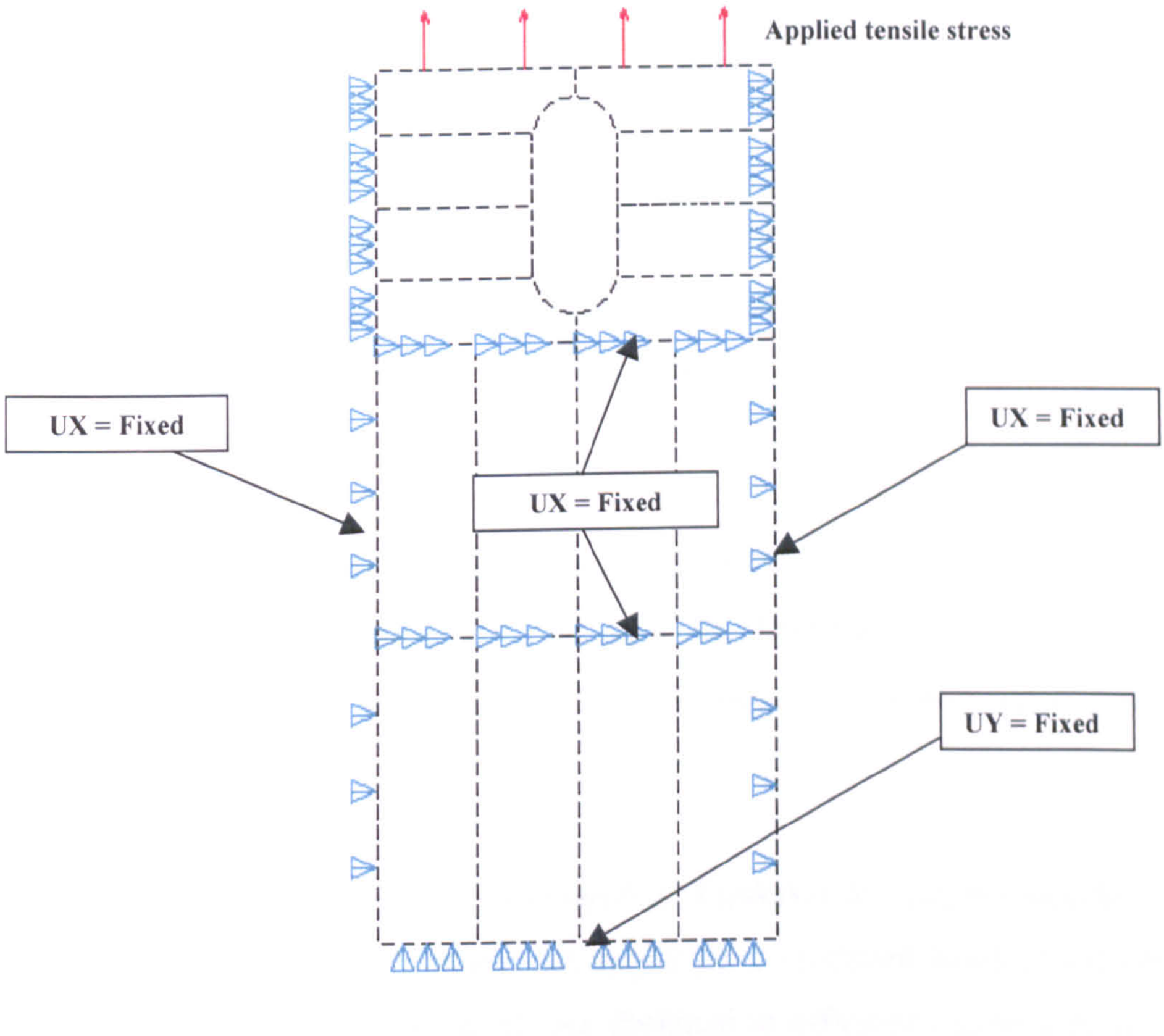

Figure 8.19: Boundary condition adopted into FEA (One transverse frame spacing)

As mentioned before, one must conduct a meshing study, as having too course a mesh size could yield an inaccurate stress gradient at the transition area from tensile to compressive residual stress

8.8 Loading Assessment

The loading used in the analysis was wave induced bending moment. Still water bending moment is not considered since it is a steady, unfluctuating stress, which does not contribute to crack growth. For newly built ships, the design minimum wave-induced bending moment is normally taken as the mean value of the extreme wave-induced bending moment that the ship is likely to encounter during its lifetime,

which is given for unrestricted worldwide service by the International Association of Classification Societies (IACS), as follows:

$$M_w = \begin{cases} +0.19CL^2BC_b & for\ hogging\ in\ KNm \\ -0.11CL^2B(C_B + 0.7) & for\ sagging\ in\ KNm \end{cases} \tag{8.53}$$

Where L is ship length (m), B is ship breadth (m), and C_b is block coefficient at summer load waterline. These equations are concerned with a long-term response of ships. However, the IACS formula does not reflect particular operational conditions and sea states.

For safety and reliability assessment of ship structures in particular cases, short-term-based response analysis may be used to determine M_w when the ship encounters a storm of specific duration and with a specified small encounter probability.

The MIT sea-keeping tables developed by Loukakis & Chryssostomidis (1975) are useful for predicting the short-term based wave –induced bending moments of merchant cargo vessels. These tables are designed to efficiently determine the root-mean-square (rms) value of these bending moments given the values of significant wave height (H_s), B/T ratio, L/B ratio, ship operating speed (V), the block coefficient (C_b), and sea-state persistence time. The USAS-L program (Paik & Thayamballi, 2003) is used for analyses.

A stationary Gaussian process can be used to represent the short-term response of ships in waves when the structural response is assumed to be linear to waves. Mansour (1987, 1990) describes several methods to predict the distribution of the maximum wave load. The extreme value distribution short-term response-based wave-induced bending moments. In this case, the wave-induced bending moment is assumed to follow the distribution function:

$$F_w(w) = \exp\left[-N\exp\left(-\frac{w^2}{2\lambda_o}\right)\right] \tag{8.54}$$

Where $F_w(w)$ is distribution function of variable $w\sqrt{\lambda_o}$ is the non-dimensional root-mean-square value of the short-term wave-induced bending moment process, which is calculated by the MIT sea-keeping tables. Mean value of wave-induced bending moment is then given, as follows (Mansour & Hovem, 1994):

$$M_w = \left[\sqrt{2\lambda_o \ln N} + \frac{0.5772}{\sqrt{2\lambda_o \ln N}}\right]\rho g L^4 \, X \, 10^{-16} \tag{8.55}$$

where N is the expected number of wave bending peaks, which can be estimated from Equation (8.56);

$$N = \frac{S}{T_p} x 3.600 \tag{8.56}$$

where T_p is wave period as calculated below, and S is storm persistence time in hour.

$$T_p = \sqrt{13 H_s} \tag{8.57}$$

where H_s is the significant wave height.

It is noted that the wave-induced bending moment calculations for the purpose of total loss assessment of a vessel in a particular situation must be based on the short-term response analysis that properly reflects operational conditions and sea states involved in the incident.

Table 8.2 shows the magnitudes of wave-induced bending moment of the tanker analysed as a function of the significant wave height (H_s), where USAS-L is employed.

Table 8.2: Wave induced bending moments obtained by USAS-L program

Significant Wave Height H_s (m)	Vertical Wave Bending Moment in Hogging (KNm)	Vertical Wave Bending Moment in Sagging (KNm)	Horizontal Wave Bending Moment (KNm)
16.0	235181	260111	123781
14.5	225655	249575	118766
13.0	216135	239046	113756
11.5	206816	228532	108851
10.0	197143	218041	103761
8.5	187690	207586	98785
7.0	173567	191965	91352
5.5	154395	170761	81260
4.0	123294	136363	64892
2.5	69982	77401	36833

8.9 Assumed Fracture Scenarios

There are mainly four crack scenarios to be addressed and are represented as MC1 (main case 1), MC2 (main case 2), MC3 (main case 3), and MC4 (main case 4). Table 8.3 presents main cases investigated in detail. In order to simulate damaged hole induced by collision accident elliptical geometry is opened in the side shell structure for the numerical calculations. Six different crack sizes are taken into account to determine a critical crack size so as to define as a crack that would be expected to fail at a specified stress level. The following nomenclature is used for identification of all analyses. Namely,

C40: Crack length is 40 mm and, its direction is only right horizontally,

C40s: Crack length is 40 mm and, its direction is right and left horizontally,

CC40: Crack length is 40 mm and, its direction is only up vertically,

CC40s: Crack length is 40 mm and, its direction is up and down vertically,

Table 8.3: All cases investigated in this study

Assumed crack scenarios **(MC1)**	Assumed crack scenarios **(MC2)**	Assumed crack scenarios **(MC3)**	Assumed crack scenarios **(MC4)**
C40	C40s	CC40	CC40s
C60	C60s	CC60	CC60s
C80	C80s	CC80	CC80s
C100	C100s	CC100	CC100s
C120	C120s	CC120	CC120s
C200	C200s	CC200	CC200s

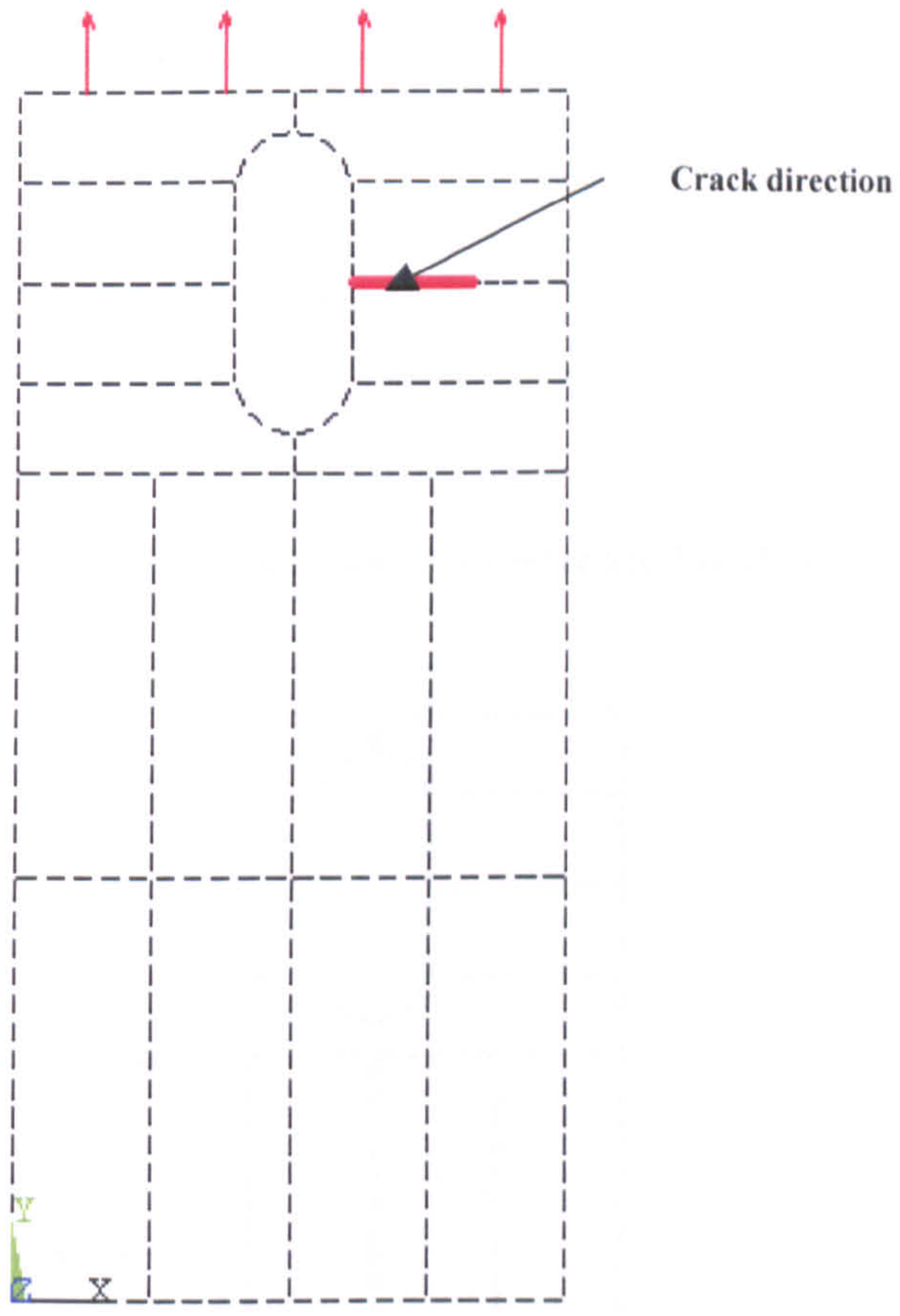

Figure 8.20: Assumed crack location for MC1 (C200)

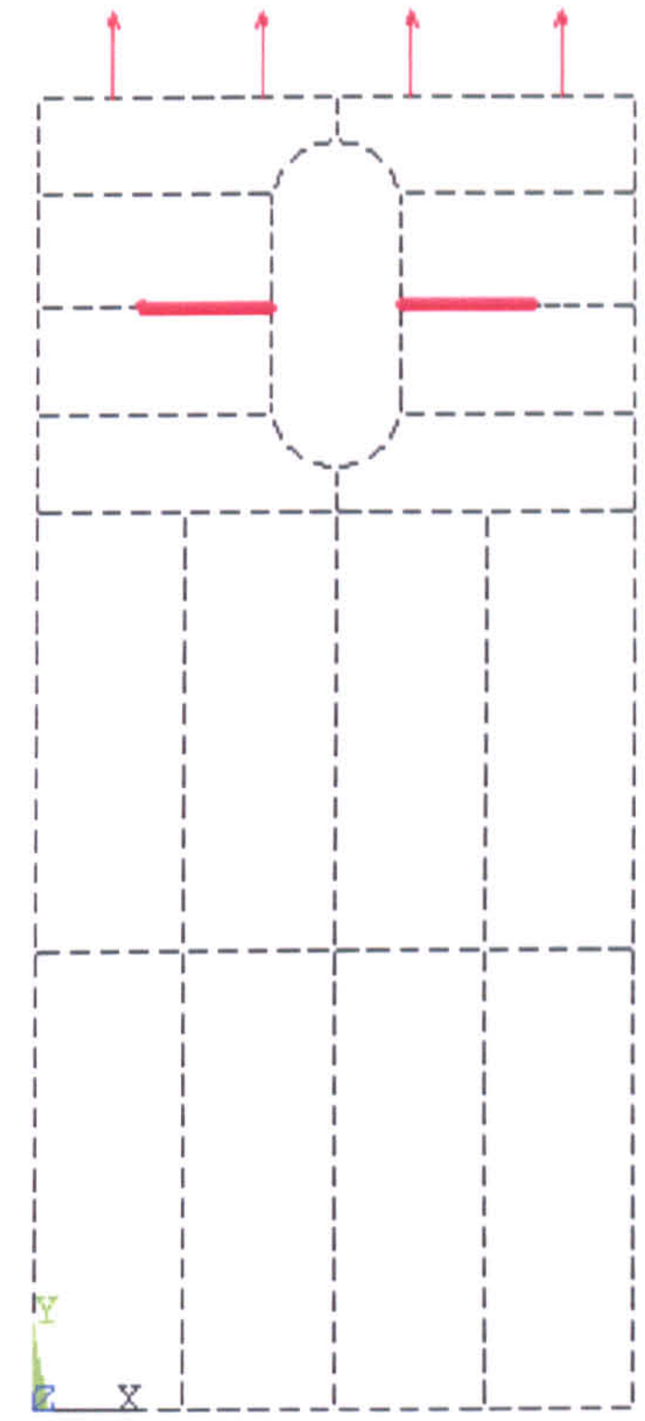

Figure 8.21: Assumed crack location for MC2 (C200s)

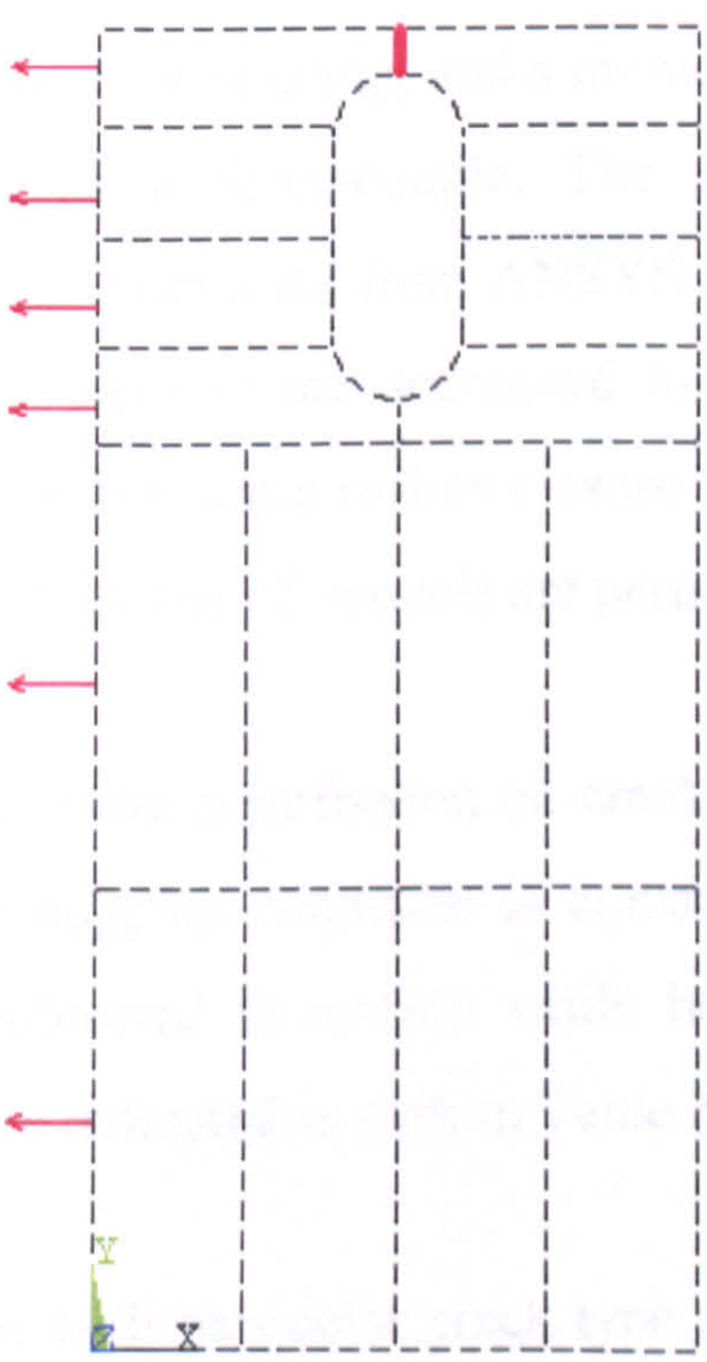

Figure 8.22: Assumed crack location for MC3 (CC80)

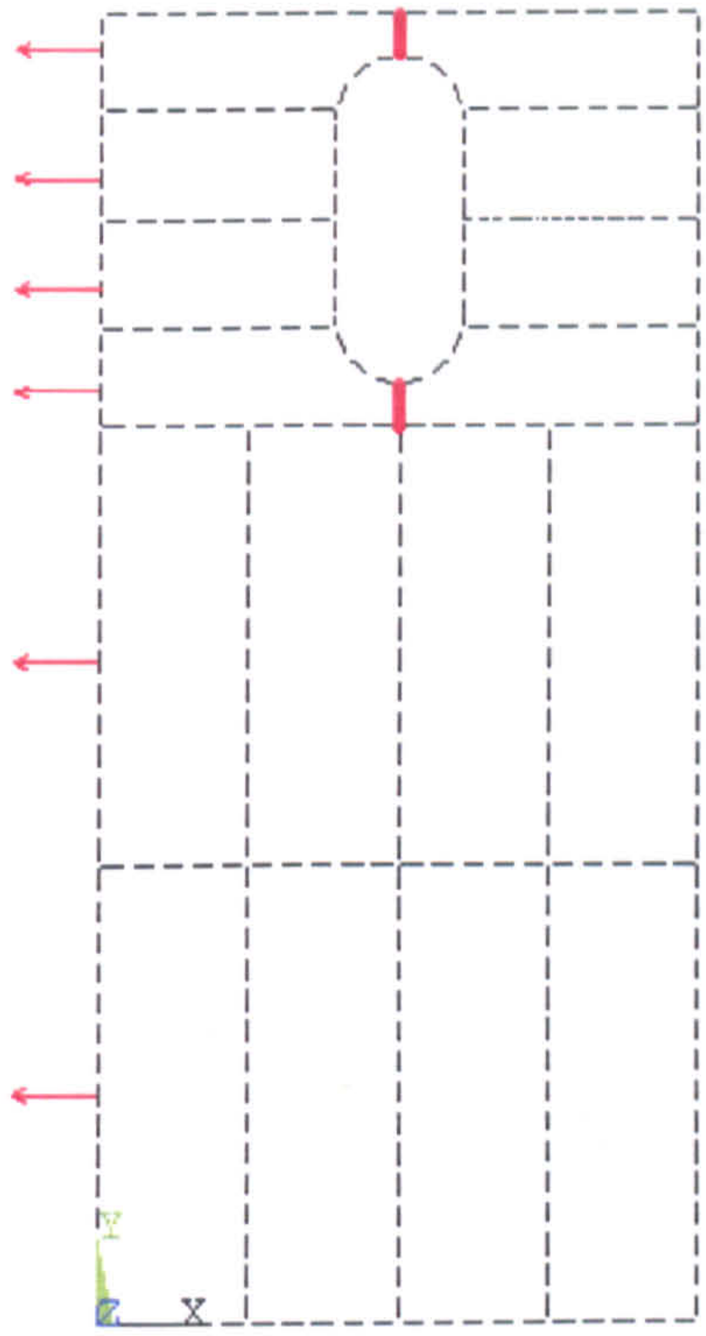

Figure 8.23: Assumed crack location for MC4 (CC80s)

Two load scenarios are applied to the global damaged tanker ANSYS FE model, a moment to produce horizontal bending, and a moment to produce vertical bending. This is achieved by using a force-couple. The stress values such as tensile, compressive and Von misses obtained from ANSYS are summarised in Table 8.4. It is noted that only tensile stresses are accounted into elastic-plastic non-linear FE calculations since compressive stress makes closure crack opening. It is shown that tensile stresses extracted from the FE models are perpendicular to the crack face.

Since tensile stresses have contribution on crack growth, vertical wave-induced bending moment under hogging condition is considered. This is mainly because, above neutral axis is subjected to tension while bottom structure is subjected to compression, and they are indicated as dark in Table 8.4.

The FEA results for each particular crack type and length at each location and load case have a particular J-Integral value. Meanwhile, it is noted that

MC1/MC2/MC3, and MC4 are subjected to operational design loading condition, that is, significant wave height, H_s = 8.5 m.

Table 8.4: Stress summaries subject to wave induced bending moment in hogging and sagging cases

	VWBM in Hogging (KNm)			VWBM in Sagging (KNm)			HWBM (KNm)		
Significant Wave Height (m)	**Tensile stress (MPa)**	Compressive stress (MPa)	Von Misses stress (MPa)	Tensile stress (MPa)	Compressive stress (MPa)	Von Misses stress (MPa)	**Tensile stress (MPa)**	Compressive stress (MPa)	Von Misses stress (MPa)
16.0	**170.0**	-93.1	154.0	102.8	-187.8	171.0	**81.6**	-35.8	103.8
14.5	**163.1**	-89.3	147.9	98.7	-179.9	163.8	**78.3**	-34.7	99.1
13.0	**156.2**	-85.5	141.8	94.6	-172.5	157.7	**75.1**	-33.5	94.8
11.5	**149.1**	-81.8	136.1	90.4	-164.6	150.1	**71.7**	-31.8	90.8
10.0	**141.9**	-78.0	129.0	86.3	-157.0	143.2	**68.2**	-30.4	86.5
8.5	**135.8**	-74.4	122.8	82.1	-150.1	136.5	**65.1**	-29.0	81.5
7.0	**125.0**	-68.8	113.7	76.0	-139.3	125.5	**59.8**	-26.8	75.8
5.5	**111.3**	-61.1	101.1	67.6	-123.1	111.8	**52.8**	-23.9	68.0
4.0	**89.2**	-48.7	80.9	54.1	-98.5	89.4	**42.6**	-18.8	53.2
2.5	**50.5**	-27.7	45.8	30.6	-55.8	50.6	**24.3**	-10.7	30.7

Table 8.5 through Table 8.8 summarize typical fracture parameters of interest such as J-integral and Stress intensity factors (SIF) for various crack sizes, locations, and load cases. It is seen that when the crack progresses vertically under dominantly horizontal bending moment even if horizontal tensile stress value is smaller than vertical stress value fracture parameters have higher value. It is believed that affected cross-section area is bigger, when stiffened plate is subjected to horizontal bending moment and it reduces critical stress value. In some cases, fracture parameters increases almost linear so that no significant plasticity yielding effect appears on the damaged-cracked stiffened plates.

Table 8.5: Numeric and Analytic through crack fracture parameters for MC1 (H_s=8.5m)

Assumed crack scenarios & length	Fracture parameters in plane stress condition	
	J-Integral value (ANSYS FEM)	K value (Converted from analytical formula) in N/mm$^{1.5}$
C40	12.76	1637.5
C60	19.09	2002.4
C80	32.02	2593.3
C100	39.70	2887.4
C120	49.73	3231.7
C200	125.7	5138.5

Table 8.6: Numeric and Analytic through crack fracture parameters for MC2 (H_s=8.5m)

Assumed crack scenarios & length	Fracture parameters in plane stress condition	
	J-Integral value (ANSYS FEM)	K value (Converted from analytical formula) in N/mm$^{1.5}$
C40s	14.27	1731.1
C60s	25.13	2297.3
C80s	38.77	2853.5
C100s	58.38	3501.5
C120s	68.57	3794.9
C200s	276.30	7617.7

(K_{mat} = 2136 N / mm$^{1.5}$)

Table 8.7: Numeric and Analytic through crack fracture parameters for MC3 (H_s=8.5m)

Assumed crack scenarios & length	Fracture parameters in plane stress condition	
	J-Integral value (ANSYS FEM)	K value (Converted from analytical formula) in N/mm$^{1.5}$
CC40	25.82	2328.6
CC60	60.77	3572.4
CC80	171.85	6007.5
CC100	188.80	6296.7
CC120	268.42	7507.9
CC200	907.01	13752.1

(K_{mat} = 2136 N / mm$^{1.5}$)

Table 8.8: Numeric and Analytic through crack fracture parameters for MC4 (H_s=8.5m)

Assumed crack scenarios & length	Fracture parameters in plane stress condition	
	J-Integral value (ANSYS FEM)	K value (Converted from analytical formula) in N/mm$^{1.5}$
CC40s	31.79	2583.7
CC60s	75.13	3972.3
CC80s	199.05	6465.8
CC100s	237.42	7061.1
CC120s	346.01	8524.2
CC200s	1347.20	16820.4

(K_{mat} = 2136 N / mm$^{1.5}$)

8.10 Parametric Studies

Eight parametric studies are performed on MC1 to permit the evaluation of the crack propagation for damaged-cracked stiffened panel. The investigations adopted

vary on the various sea state (various significant wave height), damage extent (hole dimension), existing stiffener effect, and compressive residual stress level.

- Residual stress effect:

Non-linear elastoplastic finite element model are carried out to determine the J-integral fracture parameter, which is then used to predict the crack propagation rate. Residual stresses are incorporated in the model as initial stress.

In this project, Faulkner's model for residual stress distribution is employed to represent the distribution of the stresses, and then incorporated in the finite element model as a simple representation of the actual residual stress present in the stiffened panels. The tensile region resulting from the welding process is balanced by a compression region, which is very beneficial in slowing down the crack.

The values of J-integral parameters are found by running the analysis for every load case separately, then converted to K (SIF) value. Using superposition the total stress intensity value required for the Paris law equation is determined. Table 8.9 presents analytic and numeric through fracture crack fracture parameters for 25 MPa compressive residual stress level.

Table 8.9: Numeric and Analytic through crack fracture parameters including 25 MPa compressive residual stress level (Hs=8.5 m)

Assumed crack scenarios & length	Fracture parameters in plane stress condition	
	J-Integral value (ANSYS FEM)	K value (Converted from analytical formula) in $N/mm^{1.5}$
C40	13.15	1923.7
C60	19.63	2336.1
C80	32.84	3008.3
C100	40.76	3357.1
C120	51.01	3748.2
C200	128.1	5847.1

It is seen that the 25 MPa compressive residual stress level promotes an increase of 2 % for J-integral value and nearly 16 % for K (SIF) value in the above-investigated case.

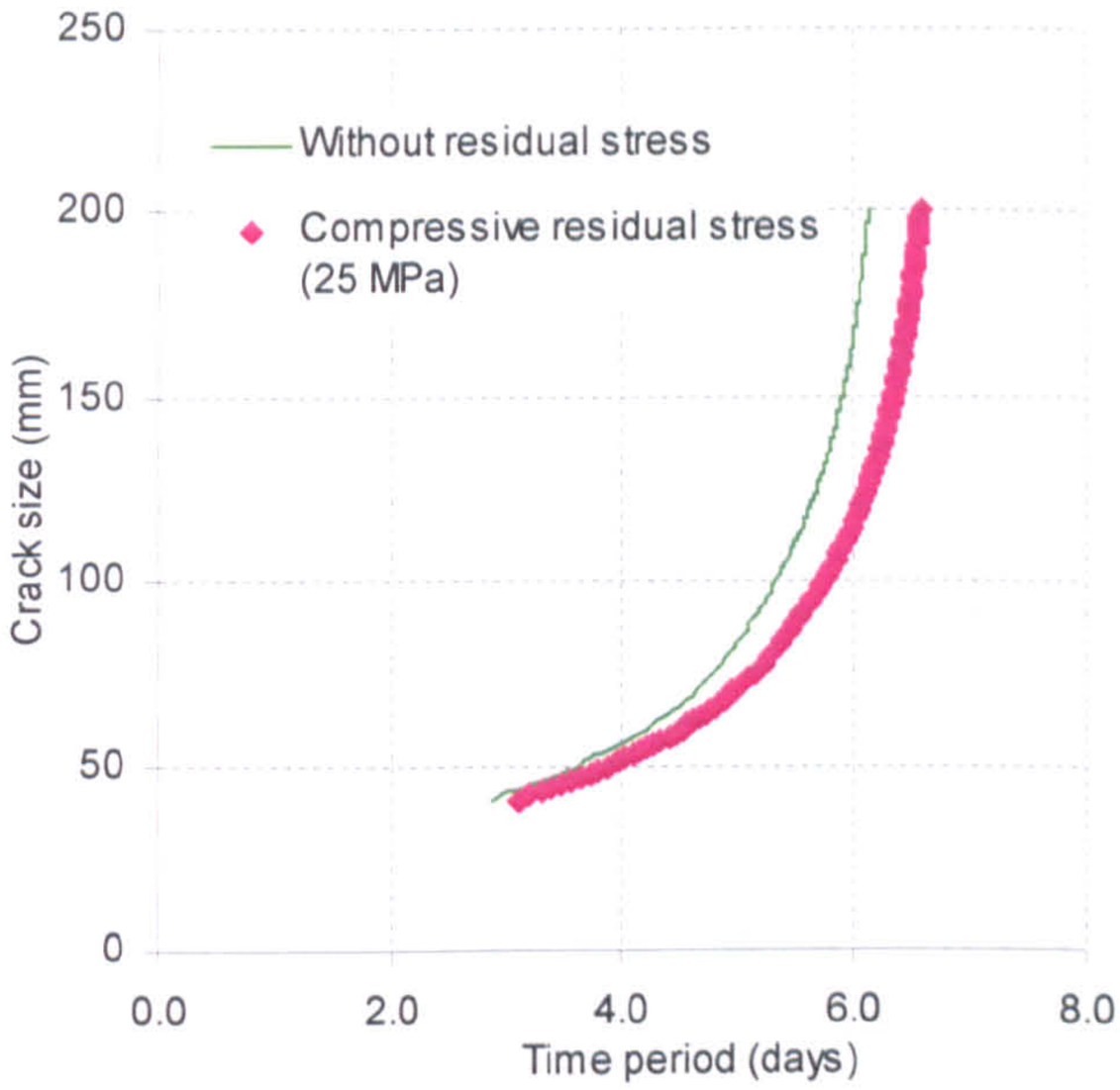

Figure 8.24. Crack extension versus cycles between perfect and imperfect including residual stress cases

Figure 8.24 shows that the compressive residual stress has an obvious effect on the reduction in crack propagation rate as well as the overall number of cycles to fail. However, in case of small crack length it has moderate influence.

- Damage extent effect:

When the damage extent increases, the capacity of load-carrying material decreases significantly. This is due to the fact that the cross-sectional area is reduced by the hole and the initial crack grows as the tensile load increases (i.e., a certain amount of tearing occurs). In order to evaluate the effect of the bigger damage size on the fracture parameters and crack growth, non-linear elastoplastic FE analyses are conducted. Damage hole geometry is expanded from 1500 x 600 elliptical shape to 1800 x 1000 elliptical shape for the sake of calculations. Table 8.10 presents analytic and numeric through crack fracture parameters for 1800 x 1000 elliptical damage geometry investigated.

Table 8.10 Numeric and Analytic through crack fracture parameters for 1800 x 1000 damage shape (H_s=8.5 m)

Assumed crack scenarios & length	Fracture parameters in plane stress condition	
	J-Integral value (ANSYS FEM)	K value (Converted from analytical formula) in N/mm$^{1.5}$
C40	17.21	1901.3
C60	28.31	2437.8
C80	35.22	2719.9
C100	50.65	3261.3
C120	55.42	3410.2
C200	165.10	5888.7

It is seen that 1800 x 1000 bigger damage geometry promotes an increase of minimum value, 10 % and maximum value, 48 % for the J-integral and approximately average 16 % for the K (SIF) value in this investigated case.

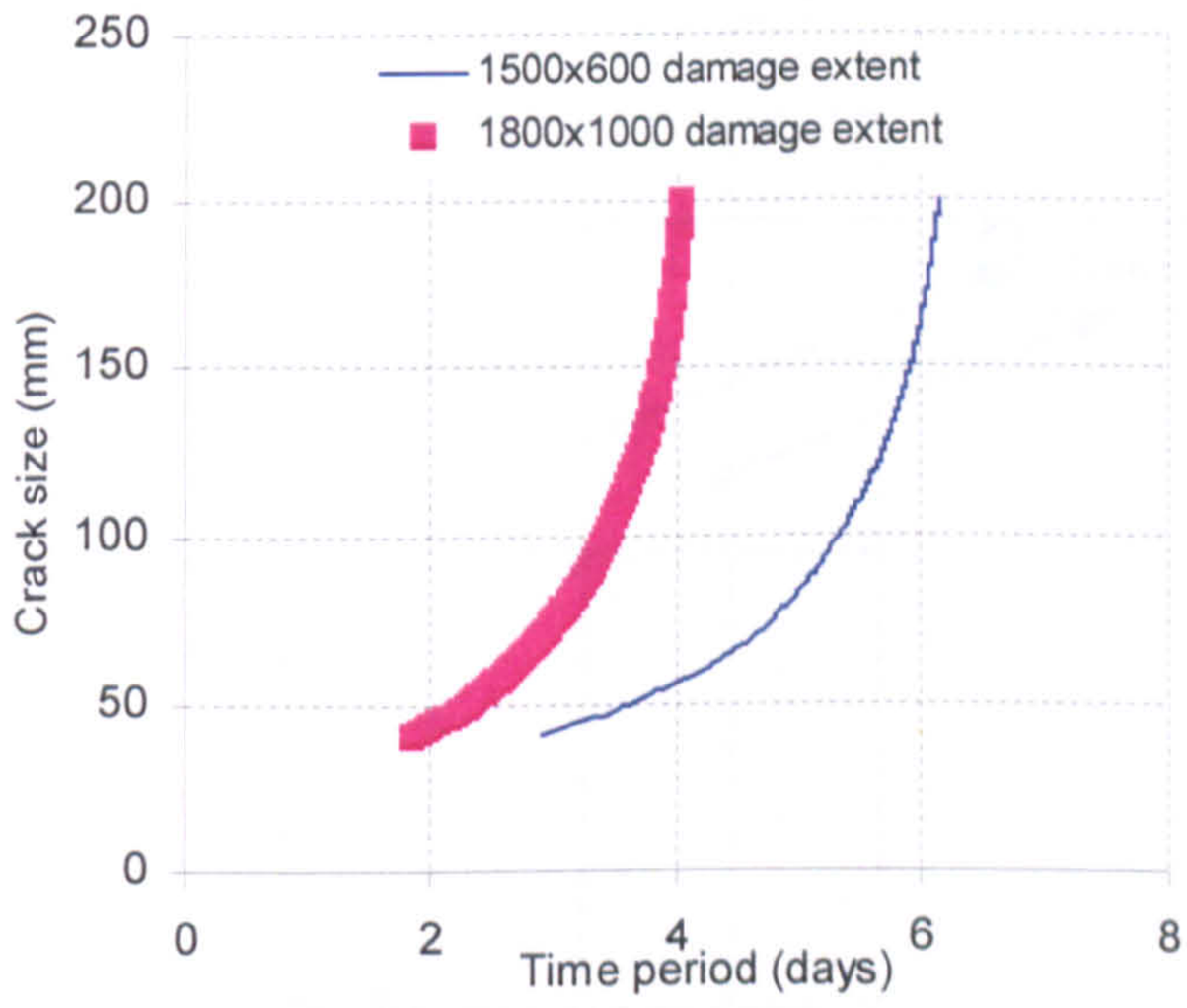

Figure 8.25: Crack extension versus cycles between 1800 x 1000 and 1500 x 600 damage geometries

Figure 8.25 illustrates the crack propagation rate in the stiffened plate is largely affected by extended damage geometry, particularly with increasing crack length.

- Ordinary stiffener effect:

In order to allow the assessment of the effect of the unstiffened plate on the fracture parameters and crack growth, a non-linear elastic-plastic finite element analysis is carried out. Figure 8.26 illustrates the structural arrangement of stiffened panel investigated. As seen there are both longitudinal and transverse stiffeners attached to plate. Table 8.11 presents analytic and numeric through crack fracture parameters for unstiffened plate under only vertical induced bending moment, that is, H_s=8.5 m.

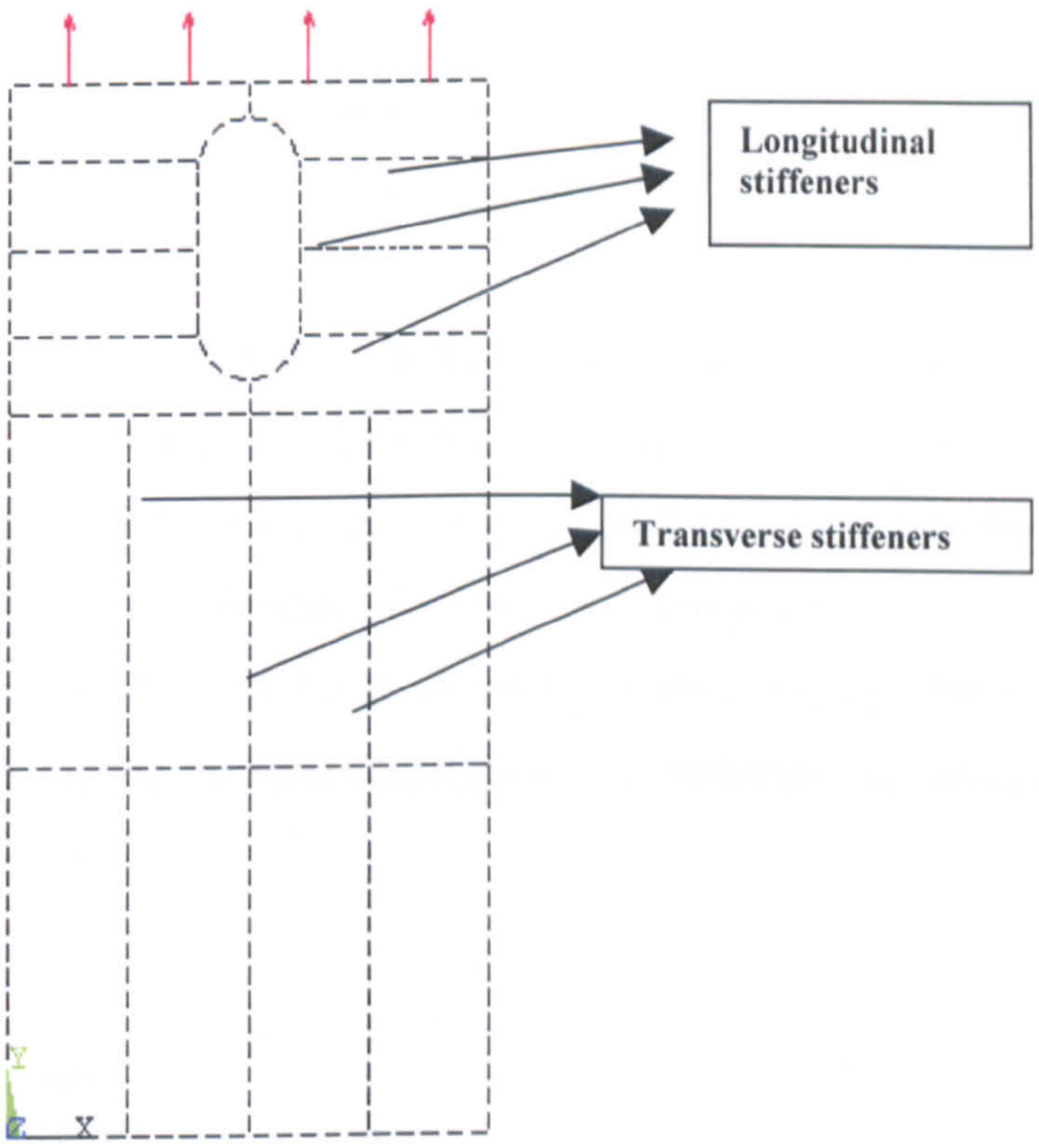

Figure 8.26: The structural arrangement of stiffened panel investigated

Table 8.11: Numeric and Analytic through crack fracture parameters for unstiffened plate (H_s=8.5 m)

Assumed crack scenarios & length	Fracture parameters in plane stress condition	
	J-Integral value (ANSYS FEM)	K value (Converted from analytical formula) in N/mm$^{1.5}$
C40	15.24	1788.9
C60	26.43	2356.1
C80	47.66	3163.8
C100	67.63	3768.7
C120	94.14	4446.3
C200	286.87	7761.7

It is shown that ignoring stiffeners promote an increase of minimum value, 19 % and maximum value, 128 % for the J-integral while minimum value, 9 % and maximum value, 51 % for the K value (SIF) in this investigated case.

The crack propagation rate in the plate is affected by ordinary stiffeners. The reason for that is believed the stiffeners are effective in carrying the load. Figure 8.27 shows that there is a substantial reduction in the crack propagation rate in stiffened plates relative to in a plate without stiffeners. The cycles to propagate one stiffener spacing may increase by a factor of 1.5 to 3.5 for a center-cracked damage stiffened plate. This study clearly presents the restraint effect cause the reduction in the crack propagation rate in a stiffened panel.

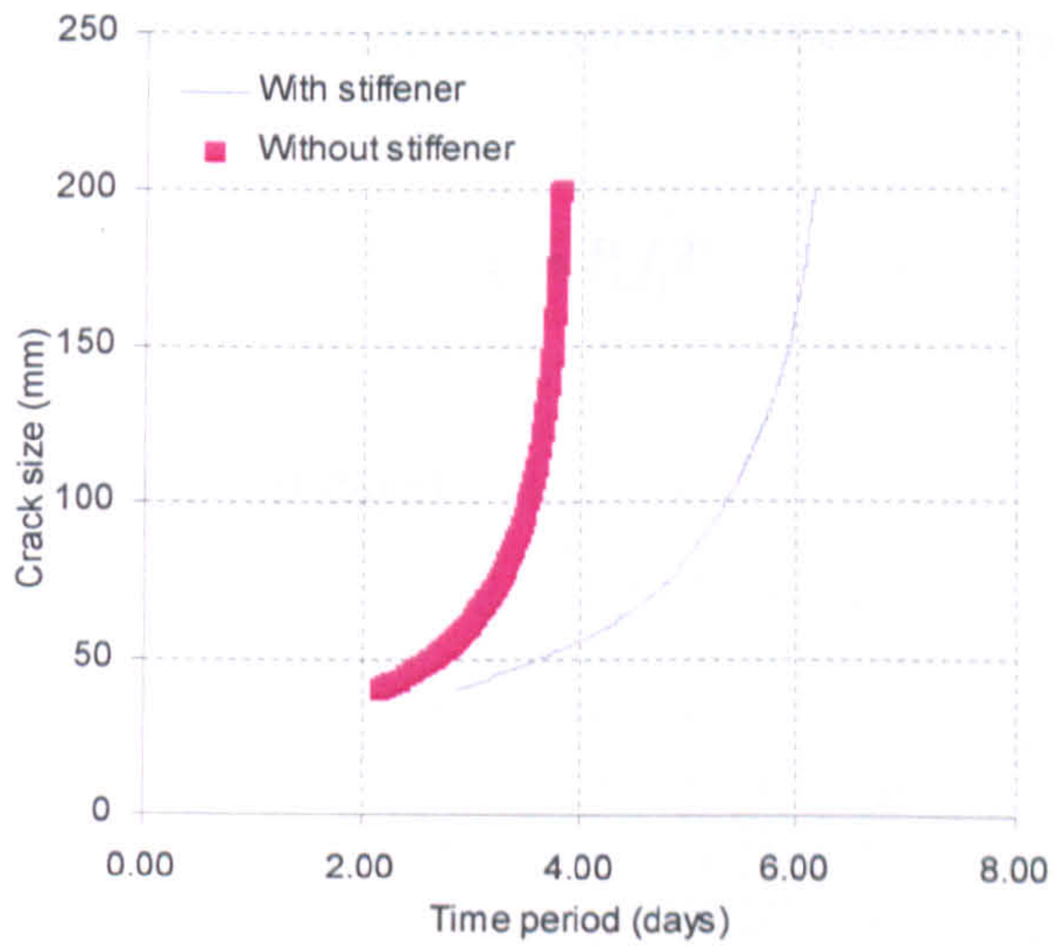

Figure 8.27: Crack extension versus cycles between stiffened and unstiffened panels

- Sea State:

The four loading zone condition is used in investigated parametric examples simply to demonstrate their effects on the fracture parameters of interest, crack propagation, and the critical stress level. These parameters are used to develop critical stress levels and crack propagation rate for each crack length.

In the absence of measured stress spectrum acting on the ship, a stress spectrum is generated from data available from Ghose *et al.* (1994). This data reflects short-term simulated North-Sea condition used for fatigue studies in the offshore industry. This condition consists of eleven wave heights or sea states. The maximum significant wave height is 16 m. For each sea-state, its significant wave height, H_{si}, fraction of time spent in that sea-state, P_i, and its frequency, f_i are presented in Table 8.12. The stress spectrum is obtained by performing finite element analysis.

In this example it is assumed that:

I. The length of each voyage is 30 days or 0.08 year and
II. For short-term damage estimation, the stress spectrum is repeated very month.

The number of cycles, n_i corresponding to a particular stress range is calculated as:

$$n_i = P_i f_i T \tag{8.58}$$

where, $T = 2627895$ sec (30 days)

Table 8.12: Short-term north-sea stress spectrum

Wave Level	H_{si} (m)	P_i	f_i (Hz)	σ_{ri} (MPa)	n_i (cycles)
1	16.0	0.0000368	0.0976	170.0	9
2	14.5	0.0000932	0.1040	163.1	25
3	13.0	0.0003700	0.1090	156.2	106
4	11.5	0.0022000	0.1200	149.1	694
5	10.0	0.0073000	0.1330	141.9	2551
6	8.5	0.0135000	0.1440	135.8	5109
7	7.0	0.0265000	0.1600	125.0	11142
8	5.5	0.0600000	0.1780	111.3	28066
9	4.0	0.2100000	0.1990	89.2	109820
10	2.5	0.4900000	0.2230	50.5	287150
11	1.0	0.1900000	0.2710	20.3	135310

The four sea states (H_s = 7.0, 5.5, 4.0, and 2.5 m) investigated in this study are summarized for numeric and analytic fracture parameters obtained in Table 8.13 through Table 8.16.

Table 8.13: Numeric and Analytic through crack fracture parameters for sea state, H_s=7.0 m

Assumed crack scenarios & length	Fracture parameters in plane stress condition	
	J-Integral value (ANSYS FEM)	K value (Converted from analytical formula) in $N/mm^{1.5}$
C40	9.48	1400.5
C60	14.95	1772.3
C80	18.96	1995.4
C100	30.09	2513.8
C120	42.62	2991.7
C200	76.13	3998.5

Table 8.14: Numeric and Analytic through crack fracture parameters for sea state, H_s=5.5 m

Assumed crack scenarios & length	Fracture parameters in plane stress condition	
	J-Integral value (ANSYS FEM)	K value (Converted from analytical formula) in $N/mm^{1.5}$
C40	6.55	1172.8
C60	10.13	1458.53
C80	14.65	1753.9
C100	18.76	1984.85
C120	24.33	2260.4
C200	28.22	2433.96

It is noted that sea state, H_s = 7 m, causes a reduction of minimum value, 14 %, and maximum value, 39 % for the J-integral while minimum value, 7.4 %, and maximum value, 22 % for the K value (SIF) for this considered case. (All percentage values are with respect to H_s = 8.5 m).

It is noted that sea state, H_s = 5.5 m, causes a reduction of minimum value, 47 %, and maximum value, 77 % for the J-integral while minimum value, 27 %, and maximum value, 52 % for the K value (SIF) for this considered cases. (All percentage values are with respect to H_s = 8.5 m).

Table 8.15: Numeric and Analytic through crack fracture parameters for sea state, H_s=4.0 m

Assumed crack scenarios & length	Fracture parameters in plane stress condition	
	J-Integral value (ANSYS FEM)	K value (Converted from analytical formula) in $N/mm^{1.5}$
C40	4.77	1000.85
C60	7.52	1257.52
C80	11.85	1577.53
C100	15.25	1789.55
C120	20.31	2065.72
C200	24.13	2251.13

Table 8.16: Numeric and Analytic through crack fracture parameters for sea state, H_s=2.5 m

Assumed crack scenarios & length	Fracture parameters in plane stress condition	
	J-Integral value (ANSYS FEM)	K value (Converted from analytical formula) in $N/mm^{1.5}$
C40	3.19	818.51
C60	3.97	914.23
C80	4.91	1015.41
C100	6.32	1152.13
C120	8.51	1336.82
C200	13.95	1711.62

It is noted that sea state, H_s = 4.0 m, causes a reduction of minimum value, 60 %, and maximum value, 80 % for the J-integral while minimum value, 36 %, and maximum value, 49 % for the K value (SIF) for this considered case. (All percentage values are with respect to H_s = 8.5 m).

It is noted that sea state, H_s = 2.5 m, causes a reduction of minimum value, 75 %, and maximum value, 89 % for the J-integral while minimum value, 50 %, and maximum value, 67 % for the K value (SIF) for this considered case. (All percentage values are with respect to H_s = 8.5 m).

Based on assumptions on loading, generation of the sea-spectra and numerical calculations in determining critical crack lengths, an allowable crack lengths of 120 mm for significant wave height, H_s = 8.5 m, 127 mm for H_s=7.0 m, 340 mm for H_s=5.5 m, 443 mm for H_s=4.0 m, and 581 mm for H_s=2.5 m are determined. A crack longer than the permissible value may lead to unstable fracture. Table 8.18 presents maximum allowable crack length versus time period (days) while Table 8.17 shows crack sizes versus time period under various sea states

Table 8.17: Allowable crack length (mm) versus time period (days)

Significant Wave Height H_s (m)	Max. Allowable Crack Length (mm)	Time Period (days)*
8.5	120	5.64
7.0	127	9.13
5.5	340	21.71
4.0	443	34.06
2.5	581	77.97

* From 40 mm initial crack length

The effect of sea state on the propagation of crack could be seen in Figure 8.28. Considering the maximum permissible crack length, sea state, H_s = 2.5 m, has 72.33 more than sea state-H_s = 8.5 m, 68.84 days than sea state-H_s = 7.0 m, 56.26 days than sea state-H_s=5.5 m, and 43.91 days than sea state-H_s=4.0 m.

Table 8.18: Crack sizes versus time period under various sea states

Significant Wave Height, H_s (m)	Time Period for 50mm crack size (days)*	Time Period for 100mm crack size (days)*	Time Period for 200mm crack size (days)*	Time Period for 500mm crack size (days)*
8.5	3.48	5.15	5.92	6.19
7.0	5.82	8.62	9.86	10.63
5.5	9.81	14.73	18.25	24.48
4.0	15.72	22.98	27.55	35.07
2.5	29.89	51.98	66.24	77.02

* From 40 mm initial crack length

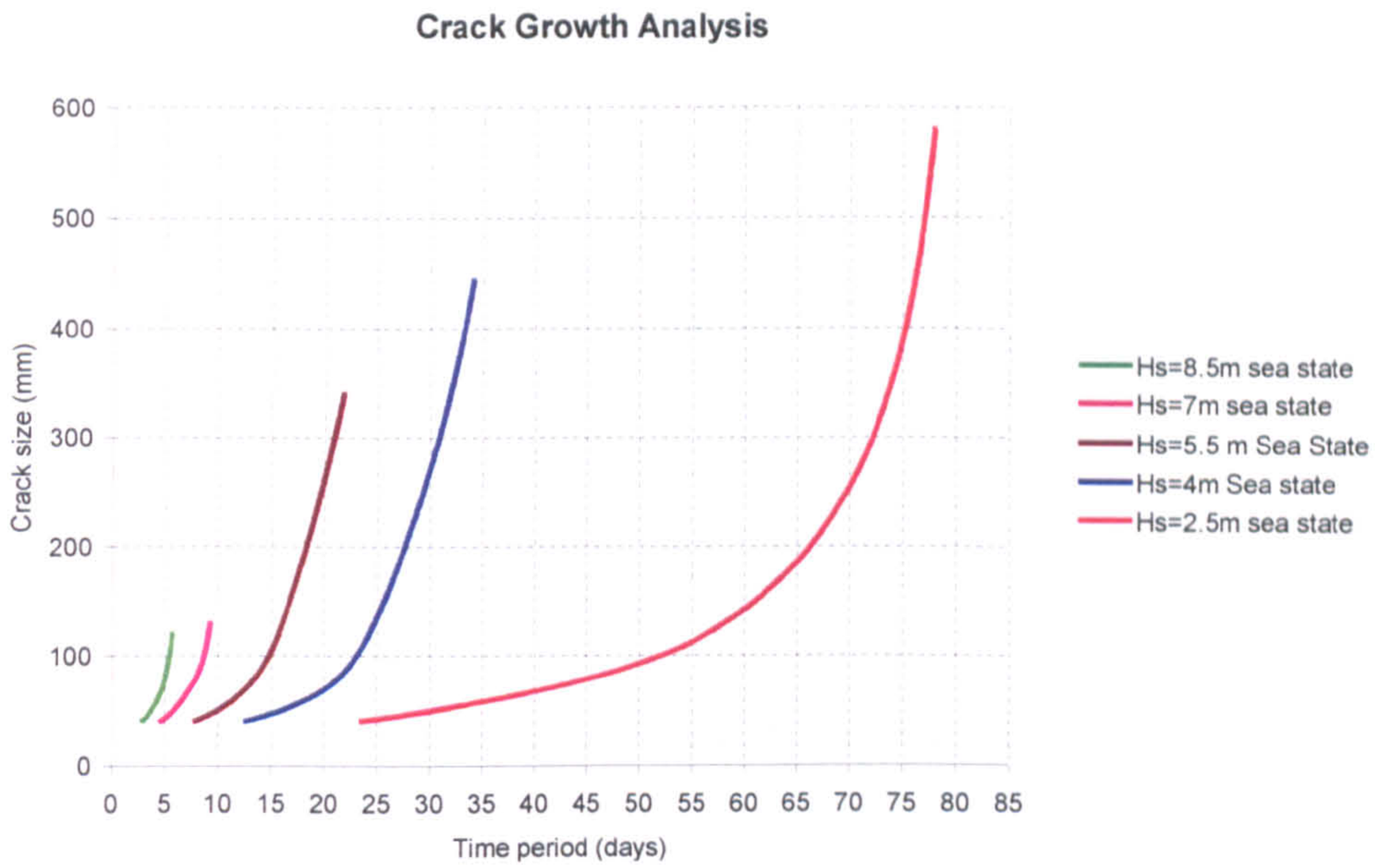

Figure 8.28: Crack extension versus cycles for five loading cases

8.11 Failure Assessment Diagrams

The objective of this step in the solution process is to consider the potential for failure including plastic collapse or fracture failure modes for the ship structure containing cracks. This failure assessment will be completed using a failure assessment diagram approach to that outlined in BS 7910:1999 with the simplified level 2B curve. Failure assessment diagrams are constructed for specific crack size and location to determine critical stress which corresponding to applied loading case.

Figure 8.29 through 8.39 illustrate the Failure Assessment Diagrams for all investigated cases including parametric studies of damaged tanker. Six crack lengths, 40, 60, 80, 100, 120, and 200 mm are considered in Figure 8.29 through 8.39.

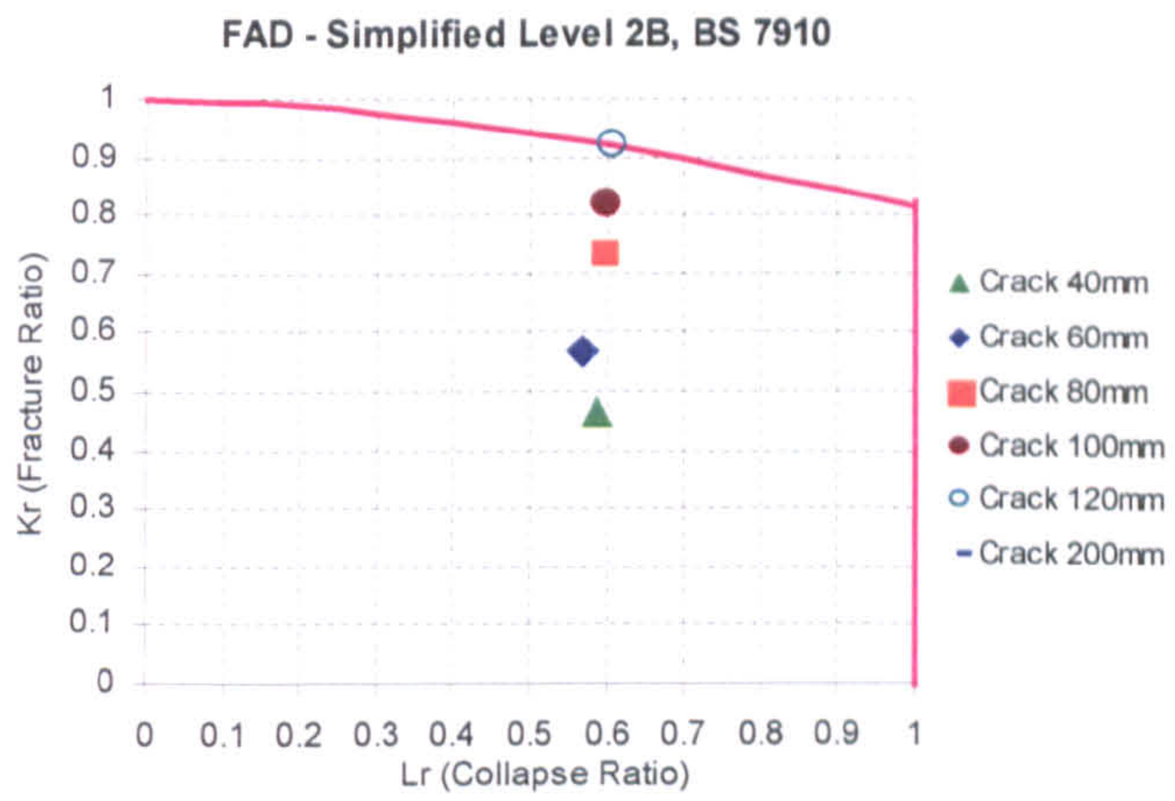

Figure 8.29: Simplified Level 2B FAD for main case-1 (MC1)

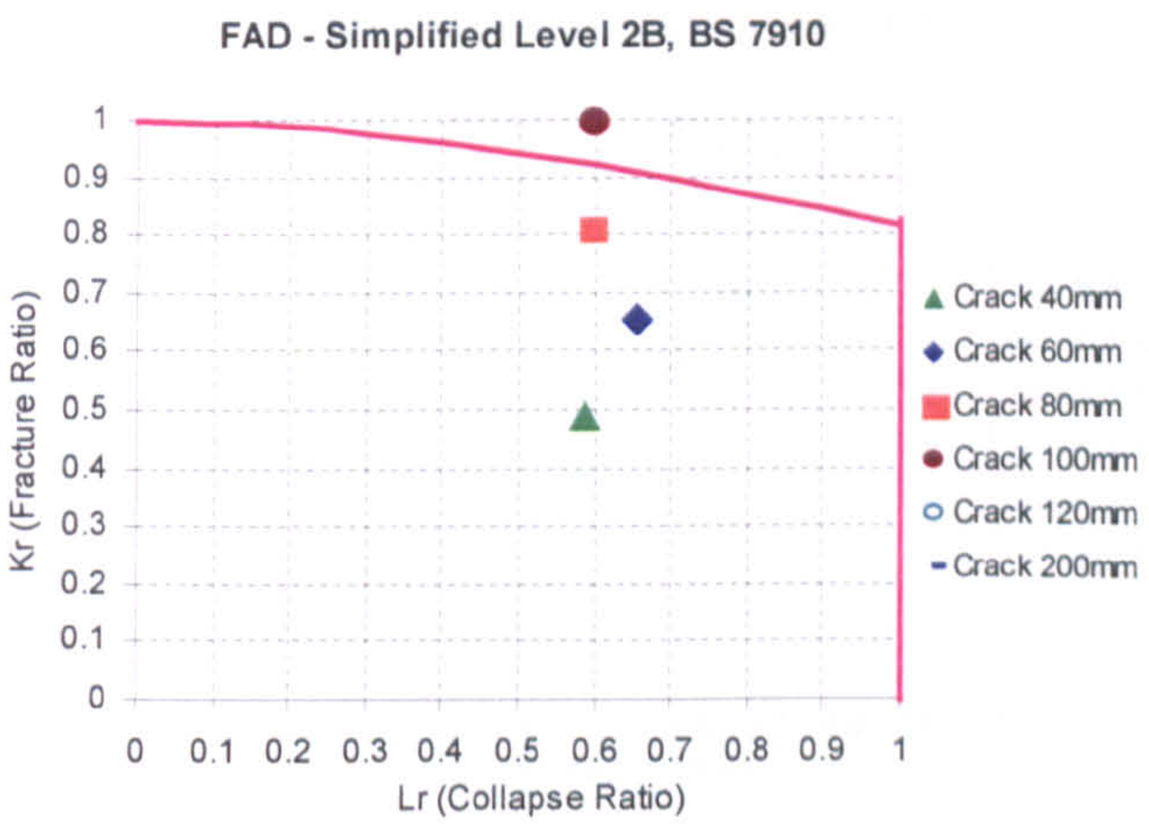

Figure 8.30: Simplified Level 2B FAD for main case-2 (MC2)

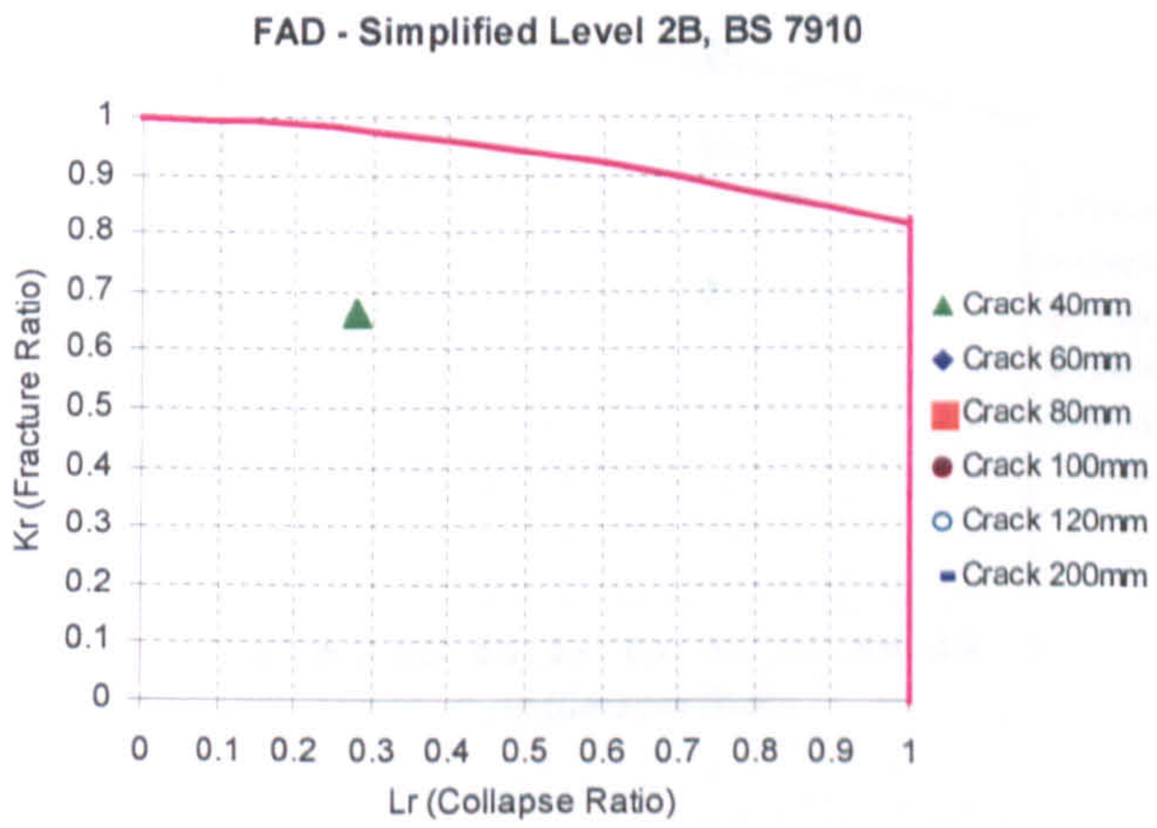

Figure 8.31: Simplified Level 2B FAD for main case-3 (MC3)

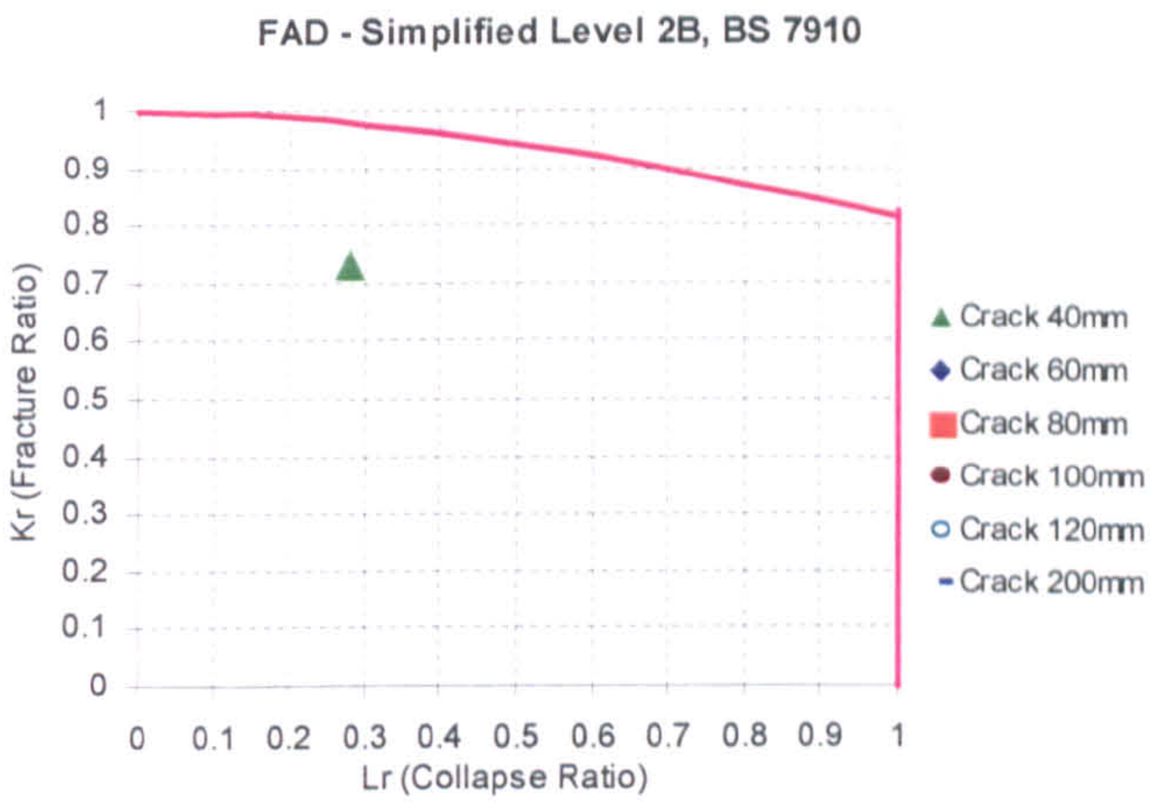

Figure 8.32: Simplified Level 2B FAD for main case-4 (MC4)

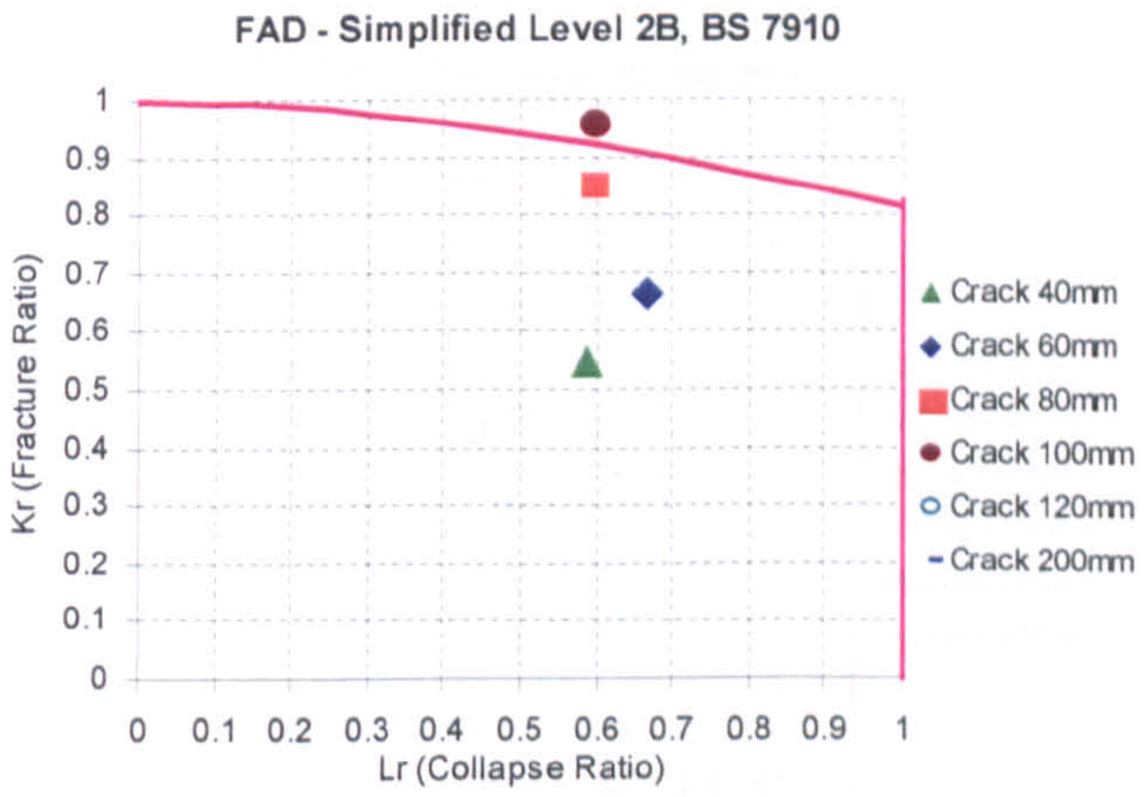

Figure 8.33: Simplified Level 2B FAD for residual stress level (25 MPa) on MC1

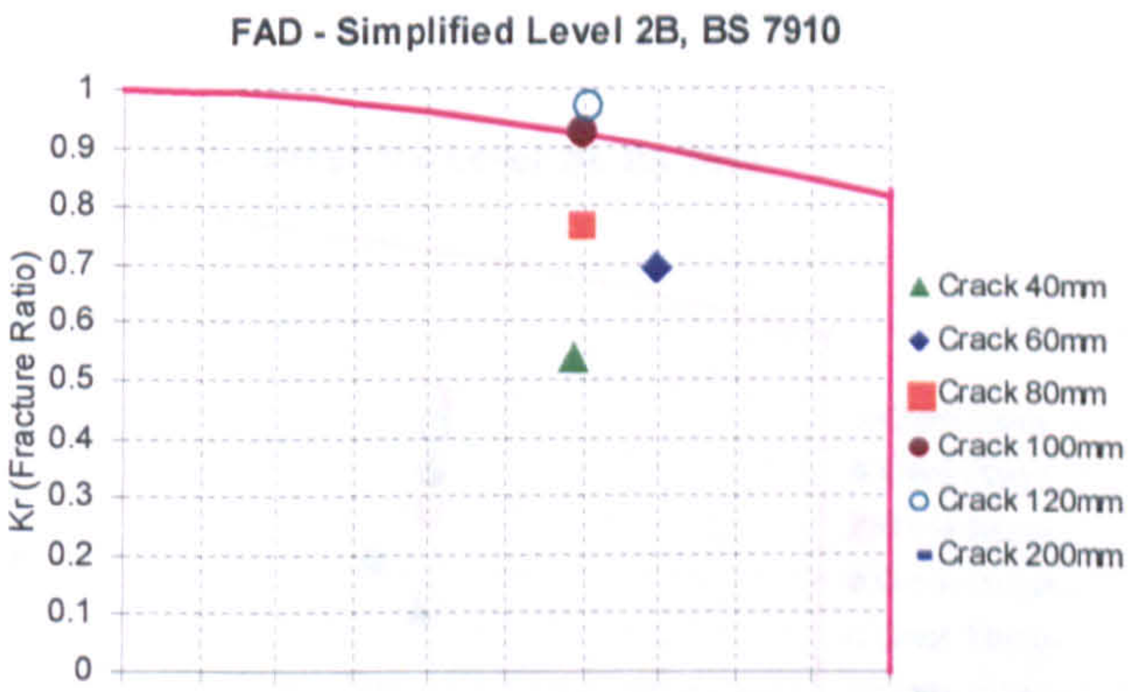

Figure 8.34: Simplified Level 2B FAD for 1800 x 1000 damage extent effect on MC1

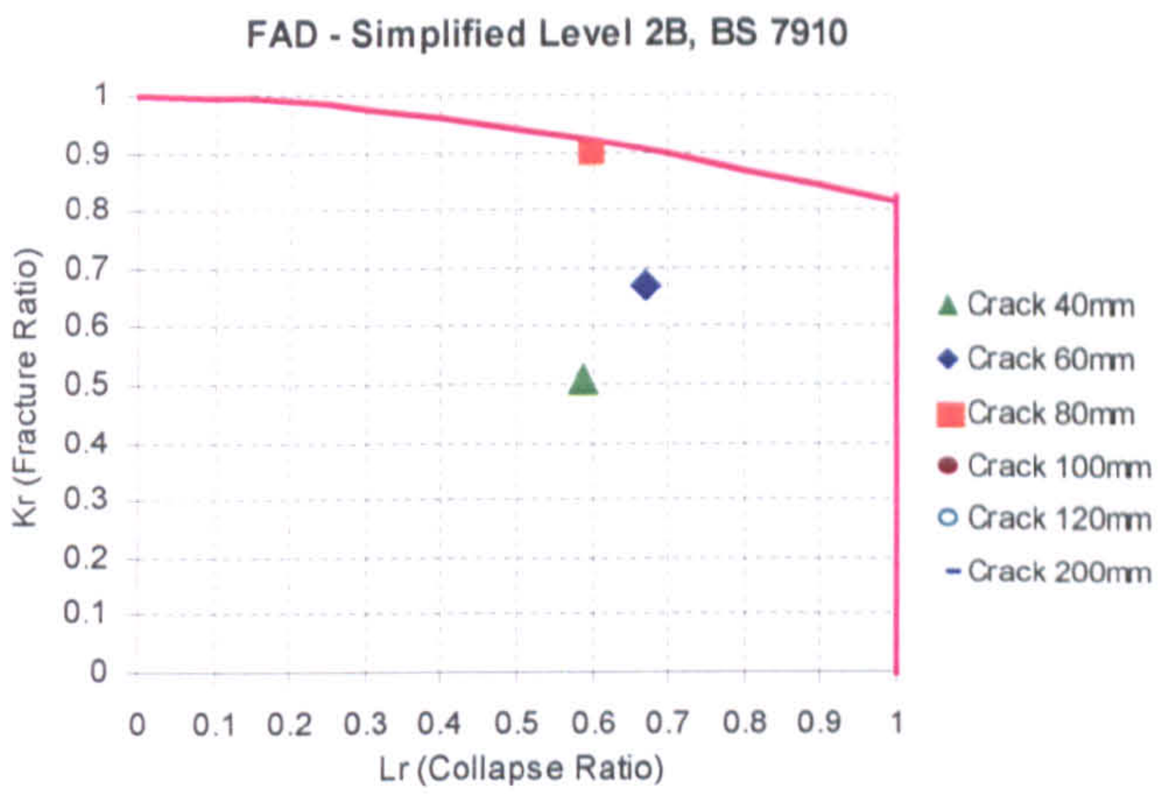

Figure 8.35: Simplified Level 2B FAD for ignoring stiffeners (unstiffened plate) on MC1

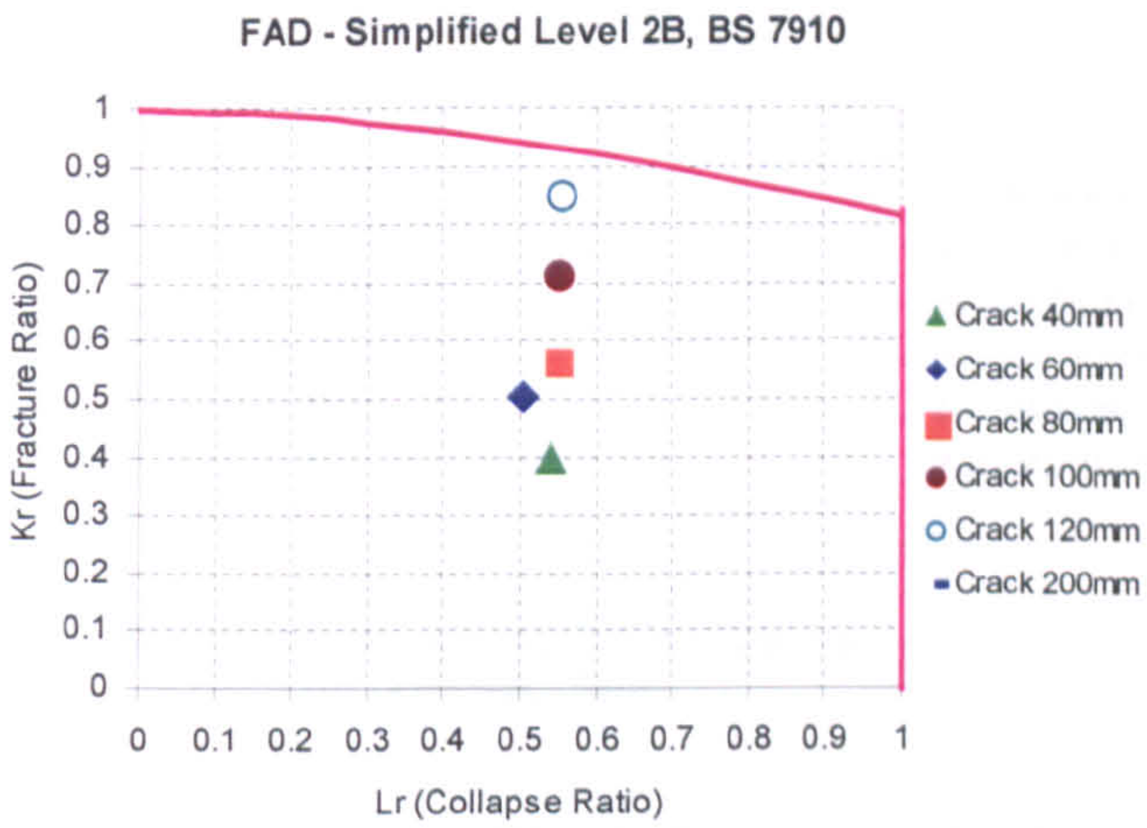

Figure 8.36: Simplified Level 2B FAD for sea state, H_s = 7.0 m on MC1

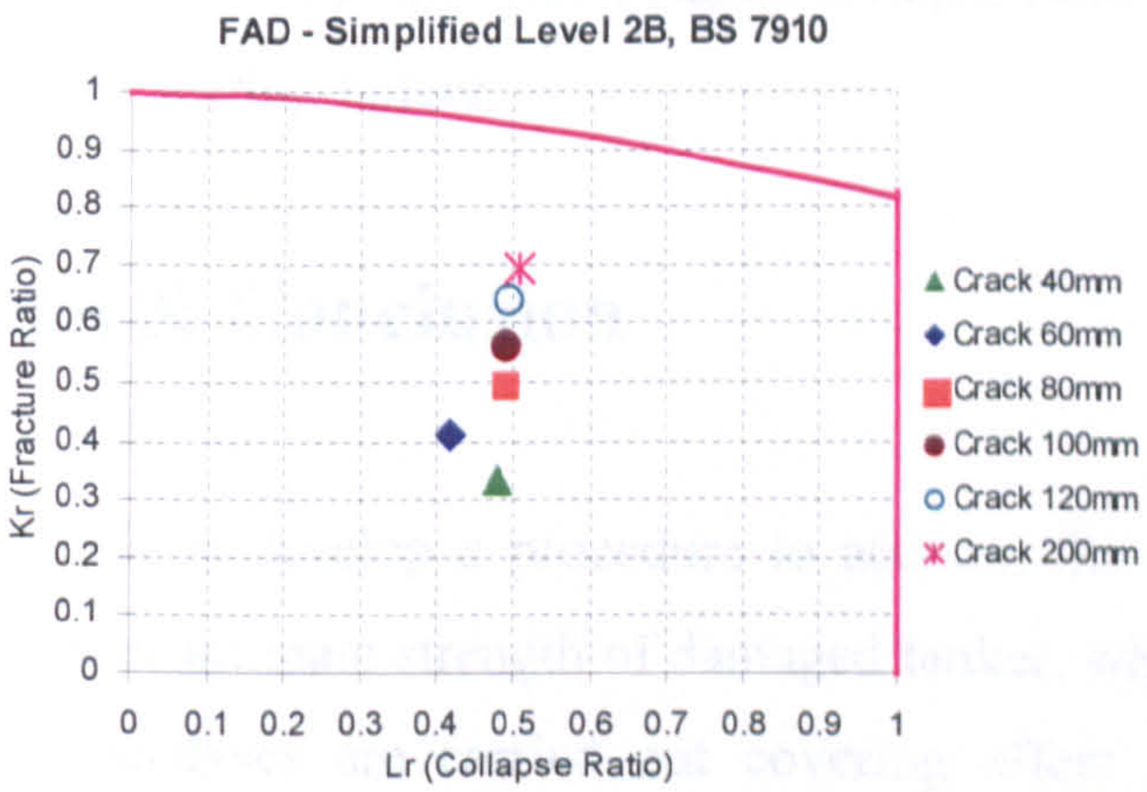

Figure 8.37: Simplified Level 2B FAD for sea state, H_s = 5.5 m on MC1

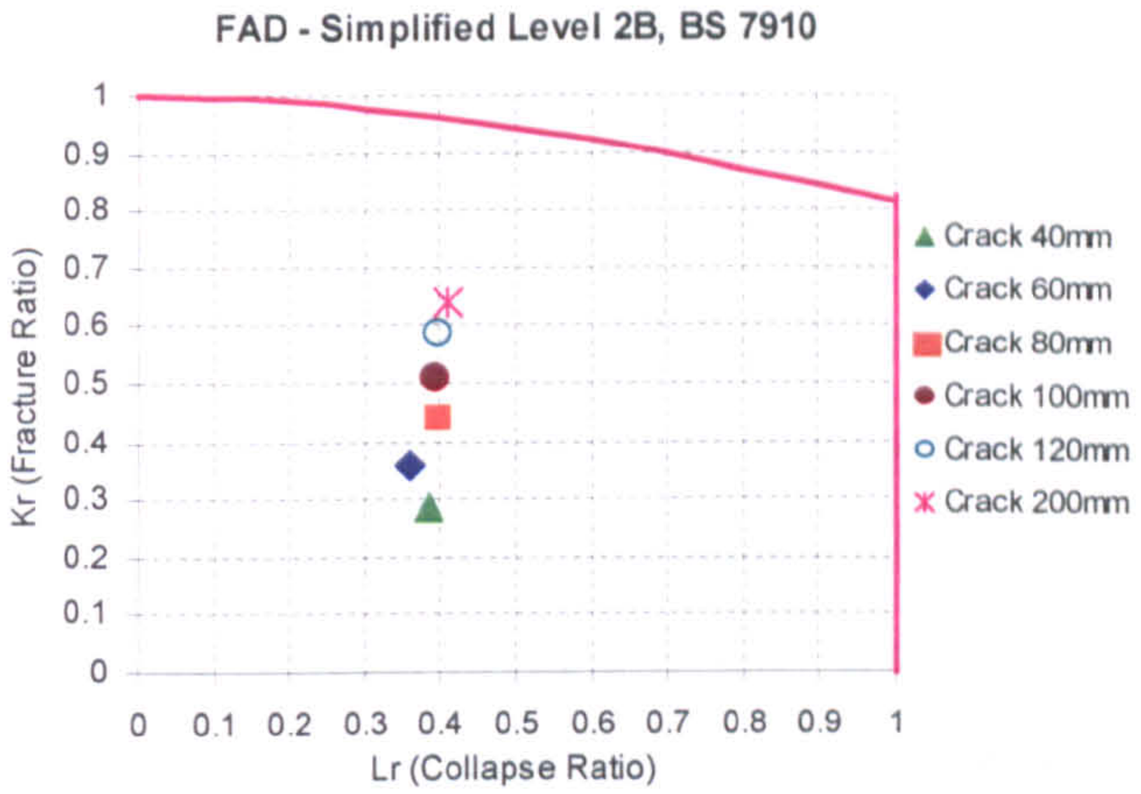

Figure 8.38: Simplified Level 2B FAD for sea state, H_s = 4.0 m on MC1

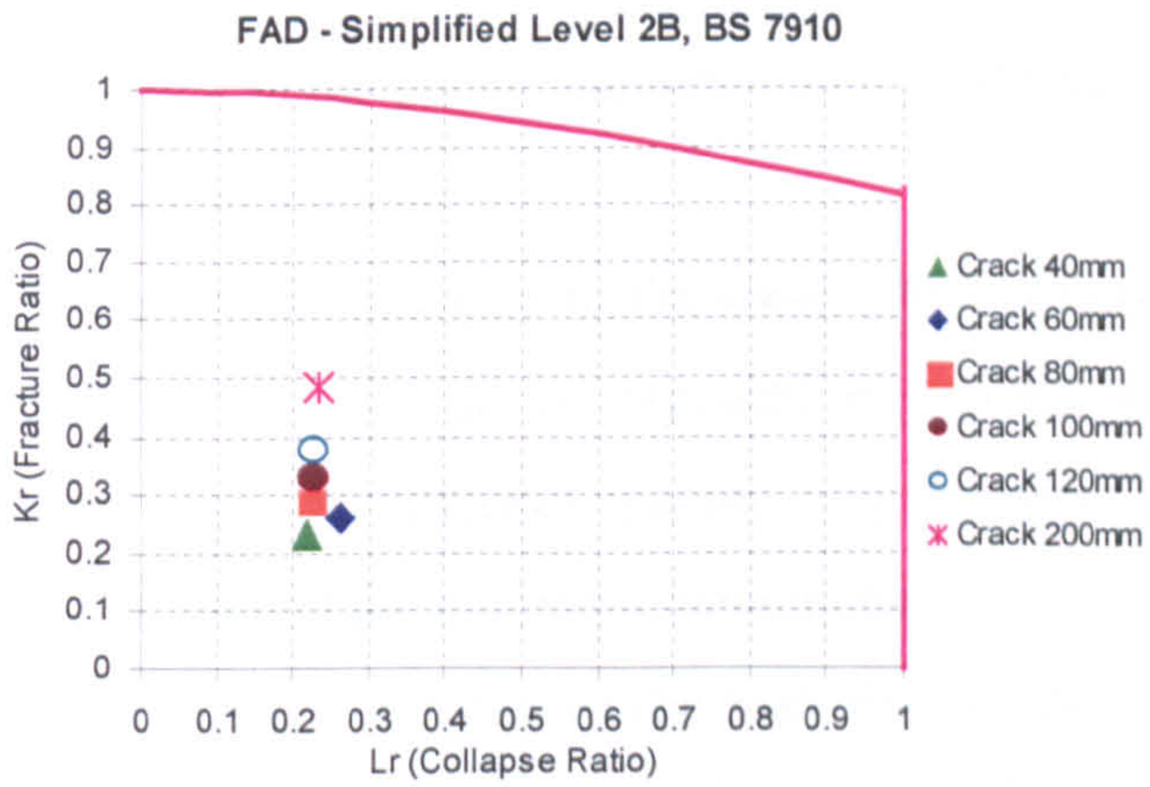

Figure 8.39: Simplified Level 2B FAD for sea state, H_s = 2.5 m on MC1

As the fracture ratio (K_r) approaches 1, the cracked structure is said to be at risk of brittle fracture, whereas a structure with a plastic collapse ratio approaching 1 is at risk of a ductile shear or tearing failure.

8.12 Discussion & Conclusion

This chapter establishes to develop a procedure to account the influence of crack growth on the hull girder ultimate strength of damaged tanker, where extensive non-linear finite element analyses are carried out covering effect of residual stress, damage extent, structural arrangement, and different sea states. The following conclusions have been reached:

- ✓ It is important to note that the response and capability of a marine structure following some form of damage is evaluated by identifying the effect of local member failure on the overall structural integrity. The effects of local damage must be integrated upward to the global structural level to insure that correct load transfer paths are determined realistically simulate the extent damage on the overall system behaviour. This local-global response approach required for assessing the residual strength of damaged marine structures represents a reverse approach from the global-local response approach used in the current structural design process. This was the underlying principle of this investigation.
- ✓ The analyses using the finite element method have been conducted to calculate the range in the stress intensity factor, followed by using Paris' Law to predict crack propagation.
- ✓ There is an important reduction in the crack propagation rate in the stiffened plates relative to what would be expected in a plate without stiffener. The cycles to propagate one stiffener spacing may increase by a factor of 1.5 to 3.0 would be estimated for a center-cracked plate.
- ✓ Compressive residual stress causes the reduction in the crack propagation rate in a stiffened panel as well as the overall number of cycles to failure.
- ✓ Critical stress level decreases with increasing crack length.
- ✓ Failure assessment diagrams (FAD) have been established for specific crack size and location to determine critical stress level under applied dynamic wave loadings.
- ✓ This work shows that fracture assessment would play important role on calculating residual strength of damaged ship structures particularly in the event that sea states having high significant wave height so that it may result in speed up collapse event, therefore it needs to be taken into account.

Chapter 9

Conclusions and Recommendations

9.1 Conclusions

Through this Ph.D. study, the following conclusions can be reached:

- ✓ The one of the objectives of the present thesis has been to develop a simplified analytical method for calculating the ultimate strength of a stiffened plate subject to combine loads, where any type of stiffener profile may be used. A non-linear finite element method has been employed to investigate on 60 ANSYS elastic-plastic buckling analyses of a wide range of typical ship panel geometries. The reduction factors of the collapse strength have been produced from the results of 60 ANSYS inelastic FE calculations.
- ✓ Simplified closed-form interaction formulations for the ultimate capacity assessment of stiffened panels has been developed based on a large number of non-linear finite element analyses using the commercial program ANSYS. It is believed that full non-linear finite element codes are able to predict buckling deflection an accuracy which is sufficient for advanced design

purposes, on condition that the analyses are done properly such as boundary conditions, mesh size, model extent, element types and imperfections. Validation of the proposed interaction model was conducted by use of non-linear finite element calculations and by existing ship rules used by DNV and GL Rules. It was found that present model is generally consistent with results obtained from by ABAQUS and PULS.

- ✓ The accuracy of the proposed method was examined by mechanical test results. The comparisons showed that adopted procedure has excellent correlation when compared to the experimental results. According to two different mechanical experimental results, new expressions have 0.061 values for standard deviation and 0.004 values for variance.
- ✓ ISSC 2000 benchmark calculations were conducted on four existing ship hull girders and also one test girder to verify a computer code NEPTUNE developed. This software has, apart form being highly efficient, also proven to be very robust. This has been achieved through great care taken a consistent attention paid to the achievement of the best-preconditioned analytical formulation of the derived solution scheme. In conclusion, the present procedure has proven capable of accurately predicting the ultimate hull girder strength for the general combined loading condition in a robust and highly proficient manner. This, both for intact and damaged condition of the hull girder. Therefore, it can be stated that the overall objective of the present research has been met by the derivation and implementation of the present procedure.
- ✓ Hull girder ultimate strength interaction relationships useful for the ship designs subject to a combination of vertical and horizontal bending moments have been developed, where the ordinary Smith's method was employed using a developed computer code NEPTUNE with average stress – average strain relationship of element. The procedure adopted was applied to analyse on the seventeen ships such as nine tankers, five bulk carriers, one general cargo and two container vessels. The findings obtained were used to develop a rapid procedure for the assessment of the ultimate capacity of the hull girder.

- ✓ A new simulation of the damaged bending behaviour of the tanker investigated in order to calculate her ultimate strength for both hogging and sagging conditions has been performed. The simulation was conducted on the assumption that the one compartment modelled was clamped at one end and a vertical bending moment is developed at the other. The results were compared with simplified analytical procedure and 3-D non-linear finite element method, where removed structural members so as to introduce damage occurrence. It was intended to investigate the accuracy or performance of especially simplified analytical method based on Smith & Dow for damaged states. This conclusion is anticipated to be generally applicable to a wide range of damaged ship types and sizes on condition that damage zone is properly introduced into calculations.
- ✓ The collision resistance and residual strength subject to collision damage of single side skin (SSS) and double side skin (DSS) bulk carriers have been investigated. The impact dynamics analyses were conducted by means of a non-linear explicit finite element code, ANSYS LS-DYNA for the evaluation resistance forces, energy absorption and penetration depth for various collision scenarios. The struck vessels of Capsize SSS and DSS designs were assumed to be entirely standstill and the striking vessels of an Aframax type oil tanker with different bulbous bow shapes were modelled as rigid bodies. The numerical procedure adopted, findings are compared, where possible, with the analytical calculation tools developed by others by existing analytical tools. Residual strength calculations on SSS and DSS vessels were computed corresponding to all considered collision damage scenarios, where the ordinary Smith's method was applied using a developed computer code NEPTUNE with the average stress – average strain relationships of elements, which are derived semi – analytically. The effect on corrosion was also evaluated by Joint Bulker Project (JBP 2004) rules on the influence of plate and stiffener thickness on the damaged hull girder capacity. The safety assessment of the vessels was determined as a ratio of the ultimate hull girder strength to the applied damaged design-bending moment. The results obtained from the finite element simulation may be used a) for the assessment

of the collision behaviour of a ship under defined collision scenario, b) for the relative comparison of structural arrangements and c) for the validation of analytical techniques for ship collision analysis

- ✓ This thesis established to develop a procedure to account the influence of crack growth on the hull girder ultimate strength of damaged tanker, where extensive non-linear finite element analyses were carried out covering effect of residual stress, damage extent, structural arrangement, and different sea states. It was showed that fracture assessment would play important role on calculating residual strength of damaged ship structures particularly in the event that sea states having high significant wave height so that it may result in speed up collapse event, therefore it needs to be taken into account.

9.2 Recommendations for Future Work

The present research is concluded here. A number of sub-topics remain prone for further investigation that might lead to some improvement of the present study. The research should be continued, the following subjects would be obvious candidates for further investigation:

- ➢ Damage to transverse members should be investigated to show effect on their strength outside of the actual damage zone and could increase the unsupported length (span) of the panels or stiffeners outside the damage zone.
- ➢ The evaluation of dynamics moments was based on vertical bending loads only and an upright ship. Combined vertical and horizontal bending moments on a heeled damage ship may be expected to significantly impact the overall findings and could be considered into non-linear FE analyses as future task.
- ➢ Although not part of this study, the bow or stern flooding scenarios in combination with the hogging wave loading result not only in the largest hogging moments but also the largest shear loadings. In damaged condition, shear flow and the warping part of the torque may be included into FEA to show its influence on ultimate collapse strength.

- A number of the different ship types should be analysed by the explicit-to-implicit sequential solution with considering initial imperfections as well as corrosion to investigate the fracture mechanics of ships having with large damage openings.
- Simplified analytical formulations need to be developed to determine fracture parameters (K value, J-integral value) for damaged stiffened plates with considering severed stiffeners.

Appendix A

The Nonlinear Finite Element Method

A.1 Introduction

The finite element method is one of the most powerful approaches available to analyse the nonlinear behaviour of structures. In a general case, the method requires a large amount of computational effort due to mainly to the large number of unknowns to be addressed in the solution procedure and also because of the fairly complicated numerical integration procedures employed, especially for obtaining the nonlinear stiffness matrices for the finite elements as they deform.

This Appendix presents a useful selected set of nonlinear finite element methods which use special purpose elements for more efficiently analysing the time-independent elastic-plastic large-deflection behaviour of steel-plated structures for the ultimate limit state behaviour.

A.2 Solution procedures for nonlinear problems

In structural mechanics, a problem is linear when the stiffness matrix is determined solely by geometric and material properties of the undeformed structure, i.e., independent of the displacements. However, it is nonlinear if the stiffness matrix varies as the applied loads increase and where the load vector depends on the displacements. For finite element analysis of a time-independent problem expressed by $\{R\}=[K]\{U\}$, where $\{R\}$= load vector, $\{U\}$= displacement vector and $[K]$ = (secant) stiffness matrix, both $[K]$ and $\{R\}$ are regarded as independent of $\{U\}$ is linear analysis, while $[K]$ and/or $\{R\}$ are nonlinear functions of $\{U\}$ in nonlinear analysis.

Nonlinearity in structural mechanics can normally be split into two classes, namely geometric nonlinearity and material nonlinearity, both of which normally interact as the structure deforms. Geometric nonlinearity is associated with changes in geometric configuration (e.g., large deflection or buckling) and material nonlinearity is associated with changes in material properties (e.g., plasticity).

In the following, some of the basic procedures for solving the nonlinear equations are first summarized. As discussed above, the finite element stiffness equation for a time-independent nonlinear problem can be expressed as $\{R\}=[K]\{U\}$, where $[K]$ is a function of $\{U\}$. We are now going to compute $\{U\}$ for a given $\{R\}$. As an illustrative example, a one-dimensional problem is selected, i.e., for a nonlinear spring under load P, as shown in Figure A.1. The secant stiffness of the nonlinear spring is denoted by k which is composed of k_0 and k_N, the former being a constant term and the latter being a function of displacements. Therefore, the nonlinear stiffness equation can in this case be given by,

$$P=(k_0+k_N)u \tag{A.1}$$

where $k_N = f(u)$.

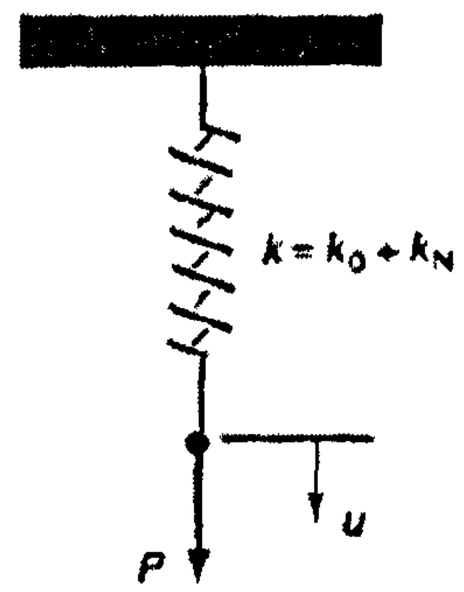

Figure A.1: A nonlinear spring, $k_0 = cons\tan t, k_N = f(u)$

When load P is applied, displacement u is required to compute. However, it is evident from Equation (A.1) that is not straightforward to determine u in terms of P. Iterative procedures described in the following are then needed to compute displacement u for a given load P.

A.2.1 The direct method

When $P = P_A$, we are going to determine $u = u_A$ by applying the direct method. For the first iteration, the stiffness term associated with nonlinearity is set to be zero, i.e., $k_N = 0$. Therefore, we get $u = P_A / k_0 \equiv u_1$ as the first iterative approximation. Using displacement u_1, obtained by the first iteration, the spring stiffness is approximated to $k = k_0 + f(u_1)$. In the second step of iteration, we get $u = [k_0 + (k_N)_1]^{-1} P_A \equiv u_2$, where $(k_N)_1 = f(u_1)$. By generating the sequence of such iteration steps in the process; we get displacement approximation u_{i+1} after the $(i+1)th$ step of iteration is completed, as follows:

$$u = [k_0 + (k_N)_i]^{-1} P_A \equiv u_{i+1} \tag{A.2}$$

where $(k_N)_i = f(u_i)$ and u_i is the displacement obtained as the ith iterative approximation.

A number of iterations are normally required until convergence is attained so that $P_A / u_A \approx k_0 + k_N$ is achieved with a prescribed accuracy, and the solution of the equation may thus be approximated to $u = u_A$. To get the entire relationship between P and u, a series of points on the curve of P versus u are needed, which are obtained by applying the iterative process repeatedly. For a structure with multi-degrees of freedom, k becomes $[K]=[K_0 + K_N]$, P becomes $\{R\}$, and u becomes $\{U\}$.

A.2.2 The incremental method

When the load is incrementally increased the solution procedure is called incremental rather than iterative. From Equation (A.1), the variation of loads with regard to displacements can be given by:

$$\frac{dP}{du} = \frac{d}{du}(k_0 + k_N)u = k_0 + \frac{d}{du}(k_N u) \equiv k_t \tag{A.3}$$

where k_t is typically called the tangent stiffness.

For load increments ΔP, displacement increments Δu can then be approximately computed from Equation (A.3) as follows:

$$\Delta u = (k_t)^{-1} \Delta P \tag{A.4}$$

Starting from $P = 0$ at $k_t = k_0 \equiv (k_t)_0$ since $u = 0$, the displacement u_1, at the first step of load increments ΔP_1, will be $u_1 = (k_t)_0^{-1} \Delta P_1$. Using $u = u_1$ we compute the new tangent stiffness, $k_t = (k_t)_1$, and thus the displacement u_2, at the second step

of load increments ΔP_2, can be determined as $u_2 = u_1 + (k_t)_1^{-1} \Delta P_2$. By generating the sequence of incremental loading steps, we get the displacement u_i at the i th step of load increments as follows:

$$u_i = u_{i-1} + (k_t)^{-1}_{i-1} \Delta P_i \tag{A.5}$$

where $(k_t)_{i-1}$ represents the tangent stiffness which is evaluated at $u = u_{i-1}$.

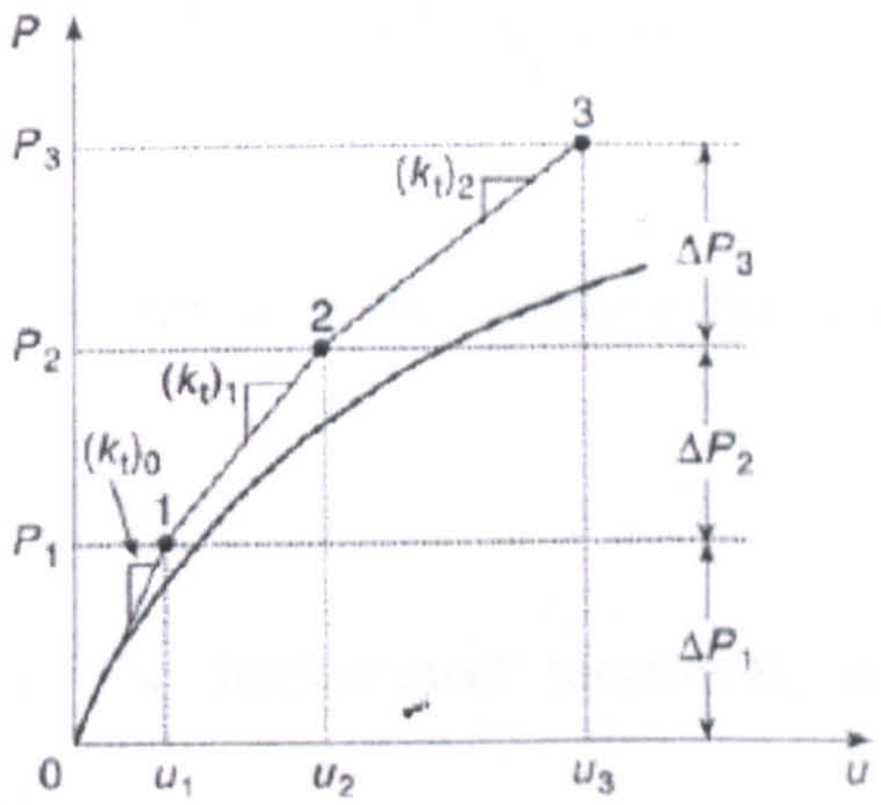

Figure A.2: The incremental method (Cook *et al.* 1989)

In the incremental method, the approximate solution normally drifts further from the exact one as the step of load increments continues, as depicted in Figure A.2. The drift is caused by the difference between the applied loads, $\sum \Delta P_i$, and the internal forces, $\sum (k_t)_{i-1} (u_i - u_{i-1})$. To eliminate the unbalanced forces, the Newton-Raphson method or the modified Newton-Raphson method is widely used.

A.2.3 The Newton-Raphson method

It is considered that the displacement, u_A, has been somehow obtained for the load, P_A. In this case, the stiffness equation can be given from Equation (A.1) as follows:

$$P_A = \{k_0 + (k_N)_A\} u_A \tag{A.6}$$

where $(k_N)_A$ represents that k_N is evaluated at $u = u_A$.

After the load is increased to a value P_{n+1}, we are going to compute the corresponding displacement, u_B. A truncated Taylor series expansion of $P = f(u)$ about u_A, given by

$$f(u_A + \Delta u_1) = f(u_A) + \left(\frac{dP}{du}\right)_A \Delta u_1 \tag{A.7}$$

is used, where $\left(dP/du\right)_A \equiv k_t$ represents the tangent stiffness with k_t being evaluated from Equation (A.3) at $u = u_A$.

At the first iteration, the displacement increment, Δu_1, is computed from Equation (A.7) as follows:

$$\Delta u_1 = (k_t)_0^{-1} (P_B - P_A) \tag{A.8}$$

since $P_B = f(u_A + \Delta u_1)$ and $P_A = f(u_A)(k_t)_0$ represents that k_t is evaluated from Equation (A.3) at $u = u_A \equiv u_0$. As the first displacement approximation, we can determine it as $u = u_A + \Delta u_1 \equiv u_1$.

As indicated in Figure A.3(a), however, there can be some unbalanced forces. For the next iteration, therefore, we obtain a new tangent stiffness, $(k_t)_1$, from Equation (A.3) at $u = u_1$ and the unbalanced force, $P_B - P_1$. The displacement increment, Δu_2, at the second iteration is determined from Equation (A.7) as follows:

$$\Delta u_2 = (k_t)_1^{-1}(P_B - P_1) \tag{A.9}$$

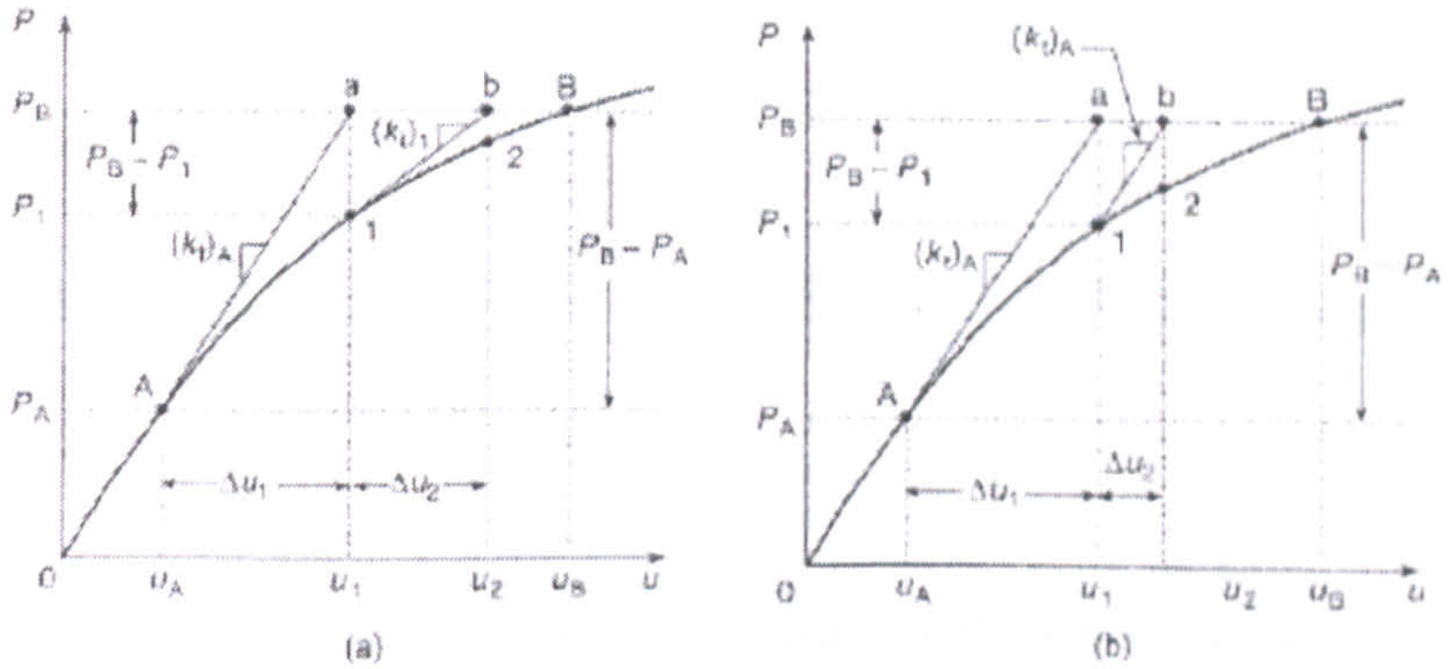

Figure A.3: The (a) original and (b) modified Newton-Raphson methods (Cook *et al.* 1989)

A.2.4 The modified Newton-Raphson method

A major feature of the modified Newton-Raphson method which is different from the original Newton-Raphson method is that the tangent stiffness either is not updated or is updated infrequently, while in the original Newton-Raphson method the tangent stiffness is recalculated with updated displacements after each step of iteration is completed. Figure A.3(b) shows a schematic representation of the modified Newton-Raphson method for a one-dimensional problem.

For a nonlinear analysis with multi-degrees of freedom, the modified Newton-Raphson method can avoid the extensive repetitions of forming, and updating the tangent stiffness matrix. However, more iterative cycles are normally necessary to get an acceptable accuracy in comparison to the original Newton-Raphson method.

A.2.5 The Arc Length method

The methods noted above in Sections A.2.1 to A.2.4 may not be appropriate to apply if the structure displays unstable post-collapse behaviour because they cannot converge to a solution in the post-collapse behaviour; the so-called arc length method (Crisfield 1981) is typically useful.

In the arc length method, the load increment, ΔP, is no longer considered constant, but is varied during the iterative process, which may be given by

$$\Delta P = \lambda_i \; x \; \Delta P_0 \tag{A.10}$$

where ΔP_0 = initial load increment, λ_i = load magnification factor as shown in Figure A.4(a).

To get the coefficient λ_i at the i th iteration process, the arc length, ΔL, as shown in Figure A.4(a), can be defined as follows:

$$\Delta L = \sqrt{\{\Delta u\}^T{}_i \{\Delta u\}_i} \tag{A.11}$$

where $\{\Delta u\}_i$ = incremental nodal displacement vector at the i th iteration process.

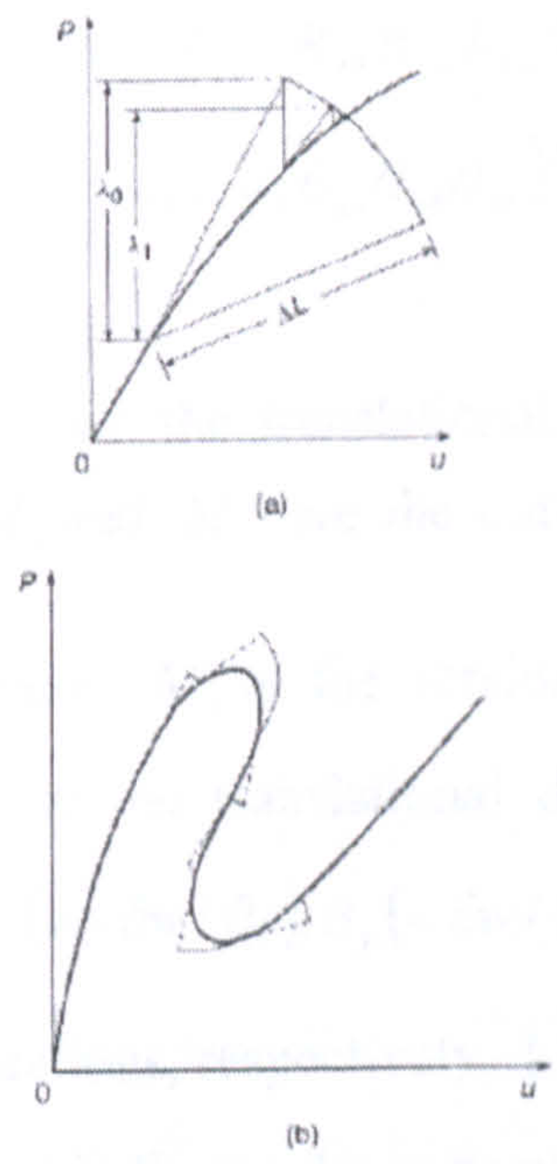

Figure A.4: (a) The arc length method; (b) Application example of the arc length method to the so-called 'snap-through' problem

This procedure is carried out iteratively until the unbalanced force vector converges to zero within some specified tolerance limit. Figure A.4(b) shows an application example of the arc length method to the so-called 'snap-through' problem.

A.3 Formulation of nonlinear rectangular plate-shell element

A.3.1 Nodal forces and nodal displacements

The combined in-plane and out-of-plane deformation behaviour for a rectangular plate element can be expressed by the nodal force vector, $\{R\}$, and the displacement vector, $\{U\}$, with six degrees of freedom at each corner nodal point which is taken to be located in the mid-thickness of the element as shown in Figure A.5, namely

$$\{R\} = \{R_{x1} R_{y1} R_{z1} M_{x1} M_{y1} M_{z1} \ldots R_{x4} R_{y4} R_{z4} M_{x4} M_{y4} M_{z4}\}^T \qquad \text{(A.12a)}$$

$$\{U\} = \{u_1 v_1 w_1 \theta_{x1} \theta_{y1} \theta_{z1} \ldots u_4 v_4 w_4 \theta_{x4} \theta_{y4} \theta_{z4}\}^T \qquad \text{(A.12b)}$$

Where R_x, R_y and R_z are the translational nodal forces in the x, y and z directions, respectively. M_x and M_y are the out-of-plane bending moments with regard to the x
and y directions, respectively; M_z is the torsional moment with regard to the z direction. u, v and w are the translational displacements in the x, y and z directions, respectively. $\theta_x (= -\partial w / \partial y)$, $\theta_y (= \partial w / \partial x)$ and θ_z are the rotations with respect to the x, y and z directions, respectively. $\{\ \}^T$ represents the transpose of the vector. A digit in the subscript indicates the node number of the rectangular element. For a triangular plate element, the number of nodal points will be three and similar expressions for nodal force and displacement vectors can be defined.

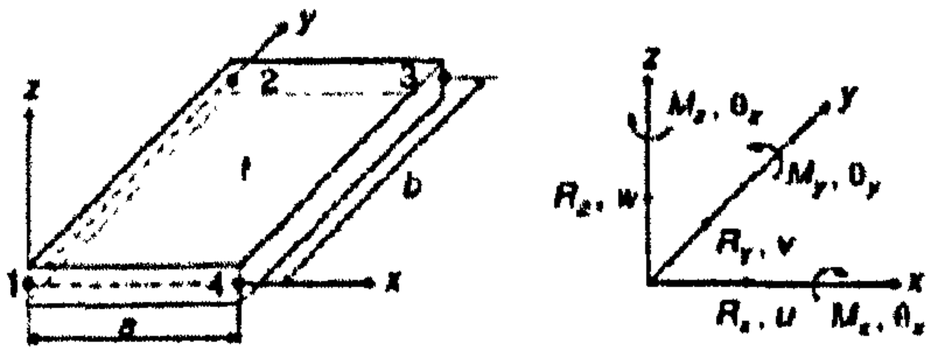

Figure A.5: The local coordinate system for the rectangular plate element with its nodal forces and displacements

A.3.2 Strain-displacement relationship

The strain versus displacement relationship taking into account out-of-plane as well as in-plane large-deformation effects for the element is given in the Cartesian coordinate system by the following:

$$\varepsilon_x = \frac{\partial u}{\partial x} - z\frac{\partial^2 w}{\partial x^2} + \frac{1}{2}\left[\left(\frac{\partial u}{\partial x}\right)^2 + \left(\frac{\partial v}{\partial x}\right)^2\right] + \frac{1}{2}\left(\frac{\partial w}{\partial x}\right)^2 \tag{A.13a}$$

$$\varepsilon_y = \frac{\partial u}{\partial y} - z\frac{\partial^2 w}{\partial y^2} + \frac{1}{2}\left[\left(\frac{\partial u}{\partial y}\right)^2 + \left(\frac{\partial v}{\partial y}\right)^2\right] + \frac{1}{2}\left(\frac{\partial w}{\partial y}\right)^2 \tag{A.13b}$$

$$\gamma_{xy} = \left(\frac{\partial u}{\partial y} + \frac{\partial v}{\partial x}\right) - 2z\frac{\partial^2 w}{\partial x \partial y} + \left[\left(\frac{\partial u}{\partial x}\right)\left(\frac{\partial u}{\partial y}\right) + \left(\frac{\partial v}{\partial x}\right)\left(\frac{\partial v}{\partial y}\right)\right] + \left(\frac{\partial w}{\partial x}\right)\left(\frac{\partial w}{\partial y}\right) \tag{A.13c}$$

where $\varepsilon_x, \varepsilon_y$ and γ_{xy} are the generalized strain components for a plane stress state.

The first term on the right hand side of the above equations represents the small-deformation in-plane strain. The second term denotes the small-deformation out-of-plane strain. The third and fourth terms are nonlinear strain components due to large deflections in plane and out of plane, respectively. It is evident from Equations (A.13) that the component for the rotation with respect to the z axis that is normal to the plane of the element does not affect the strains of the element.

The incremental expressions corresponding to Equations (A.13) are written as:

$$\Delta\varepsilon_x = \frac{\partial \Delta u}{\partial x} - z\frac{\partial^2 \Delta w}{\partial x^2} + \left(\frac{\partial u}{\partial x}\right)\left(\frac{\partial \Delta u}{\partial x}\right) + \left(\frac{\partial v}{\partial x}\right)\left(\frac{\partial \Delta v}{\partial x}\right) + \left(\frac{\partial w}{\partial x}\right)\left(\frac{\partial \Delta w}{\partial x}\right)$$
$$+ \frac{1}{2}\left[\left(\frac{\partial \Delta u}{\partial x}\right)^2 + \left(\frac{\partial \Delta v}{\partial x}\right)^2\right] + \frac{1}{2}\left(\frac{\partial \Delta w}{\partial x}\right)^2 \qquad \text{(A.14a)}$$

$$\Delta\varepsilon_y = \frac{\partial \Delta u}{\partial y} - z\frac{\partial^2 \Delta w}{\partial y^2} + \left(\frac{\partial u}{\partial y}\right)\left(\frac{\partial \Delta u}{\partial y}\right) + \left(\frac{\partial v}{\partial y}\right)\left(\frac{\partial \Delta v}{\partial y}\right) + \left(\frac{\partial w}{\partial y}\right)\left(\frac{\partial \Delta w}{\partial y}\right)$$
$$+ \frac{1}{2}\left[\left(\frac{\partial \Delta u}{\partial y}\right)^2 + \left(\frac{\partial \Delta v}{\partial y}\right)^2\right] + \frac{1}{2}\left(\frac{\partial \Delta w}{\partial y}\right)^2 \qquad \text{(A.14b)}$$

$$\Delta\gamma_{xy} = \left(\frac{\partial \Delta u}{\partial y} + \frac{\partial \Delta v}{\partial x}\right) - 2z\frac{\partial^2 \Delta w}{\partial x \partial y} + \left(\frac{\partial u}{\partial x}\right)\left(\frac{\partial \Delta u}{\partial y}\right) + \left(\frac{\partial u}{\partial y}\right)\left(\frac{\partial \Delta u}{\partial x}\right)$$
$$+ \left(\frac{\partial v}{\partial x}\right)\left(\frac{\partial \Delta v}{\partial y}\right) + \left(\frac{\partial v}{\partial y}\right)\left(\frac{\partial \Delta v}{\partial x}\right) + \left(\frac{\partial w}{\partial x}\right)\left(\frac{\partial \Delta w}{\partial y}\right) + \left(\frac{\partial w}{\partial y}\right)\left(\frac{\partial \Delta w}{\partial x}\right) \qquad \text{(A.14c)}$$
$$+ \left(\frac{\partial \Delta u}{\partial x}\right)\left(\frac{\partial \Delta u}{\partial y}\right) + \left(\frac{\partial \Delta v}{\partial x}\right)\left(\frac{\partial \Delta v}{\partial y}\right) + \left(\frac{\partial \Delta w}{\partial x}\right)\left(\frac{\partial \Delta w}{\partial y}\right)$$

where the prefix Δ denotes an infinitesimal increment of the variable.

For convenience in the formulations of the element, the nodal displacement vector, $\{U\}$, is split into three components, namely the in-plane components, $\{S\}$, the out-of-plane components, $\{W\}$, and the component for the rotations about the z axis. Thus Equations (A.4) can be rewritten in matrix form using the vectors $\{S\}$ and $\{W\}$, as follows:

$$\{\Delta\varepsilon\} = [B_p]\{\Delta S\} - z[B_b]\{\Delta W\} + [C_p][G_p]\{\Delta S\} + [C_p][G_p]\{\Delta W\}$$
$$+ \frac{1}{2}[\Delta C_p][G_p]\{\Delta S\} + \frac{1}{2}[\Delta C_b][G_b]\{\Delta W\} = [B]\{\Delta U\} \qquad \text{(A.15)}$$

Where $\{\Delta\varepsilon\}=\{\Delta\varepsilon_x \Delta\varepsilon_y \Delta\gamma_{xy}\}^T$ = increment of strain vector, $\{U\}=\{SW\}^T$ = nodal displacement vector, $\{S\}=\{u_1 v_1 u_2 v_2 u_3 v_3 u_4 v_4\}^T$ = in-plane displacement vector, $[B]$ = strain versus displacement matrix, and,

$$\left\{\frac{\partial u}{\partial x}\frac{\partial v}{\partial y}\frac{\partial u}{\partial y}+\frac{\partial v}{\partial x}\right\}^T=[B_p]\{S\},\quad \left\{\frac{\partial^2 w}{\partial x^2}\frac{\partial^2 w}{\partial y^2}2\frac{\partial^2 w}{\partial x\partial y}\right\}^T=[B_p]\{W\},$$

$$\left\{\frac{\partial u}{\partial x}\frac{\partial v}{\partial x}\frac{\partial u}{\partial y}\frac{\partial v}{\partial y}\right\}^T=[G_p]\{S\},\quad \left\{\frac{\partial w}{\partial x}\frac{\partial w}{\partial y}\right\}^T=[G_b]\{W\}$$

$$[C_p]=\begin{bmatrix}\partial u/\partial x & \partial v/\partial x & 0 & 0\\ 0 & 0 & \partial u/\partial y & \partial v/\partial y\\ \partial u/\partial y & \partial v/\partial y & \partial u/\partial x & \partial v/\partial x\end{bmatrix},$$

$$[C_b]=\begin{bmatrix}\partial w/\partial x & 0\\ 0 & \partial w/\partial y\\ \partial w/\partial y & \partial w/\partial x\end{bmatrix}$$

A.3.3 Stress-strain relationship

The membrane stress increments, $\{\Delta\sigma\}$, due to the strain increments, $\{\Delta\varepsilon\}$, can be calculated for a plane stress state as follows:

$$\{\Delta\sigma\}=[D]^E\{\Delta\varepsilon\}^E \tag{A.16}$$

Where E represents the elastic component of the variable. $\{\Delta\sigma\}=\{\Delta\sigma_x\ \Delta\sigma_y\ \Delta\tau_{xy}\}^T$ is the increment of average membrane stress components for a plane stress state, and is the elastic stress versus strain matrix, E Young's modulus and υ Poisson's ratio.

$$[D]^E=\frac{E}{1-\upsilon^2}\begin{bmatrix}1 & \upsilon & 0\\ \upsilon & 1 & 0\\ 0 & 0 & (1-\upsilon)/2\end{bmatrix} \tag{A.17}$$

A.3.4 Elastic tangent stiffness matrix

Two approaches, namely the total Lagrangian formulation and updated Lagrangian formulation, are widely used for calculating the nonlinear finite element stiffness matrix. The latter will be used in the present finite element method. In the following, it is convenient to deal separately with the matrix components related to the rotations with regard to the z axis that is normal to the plane of the element.

The Total Lagrangian Approach

Consider that an elastic structure under the nodal forces $\{R\}$, resulting in the internal stresses $\{\sigma\}$, is in an equilibrium condition. Assume that the structure remains in equilibrium even after the increase of the virtual displacement increments, $\delta\{\Delta\varepsilon\}$, which will develop the nodal forces $\{\Delta R\}$ and the resultant stresses $\{\Delta\sigma\}$.

By applying the principle of virtual work, the following equation should be satisfied:

$$\delta\{\Delta U\}^T\{R+\Delta R\}=\int\delta\{\Delta\varepsilon\}^T\{\sigma+\Delta\sigma\}dVol \qquad (A.18)$$

Where the term on the left hand side represents the external work undertaken by the virtual displacement increments and on the right hand side denotes the strain energy dissipated by the deformation during the applied loading. $\int(\,)dVol$ indicates integration over the entire volume of the element and δ indicates a virtual value.

The virtual value of strain components, $\delta\{\Delta\varepsilon\}$, can be obtained by the differentiation of Equation (A.15) with respect to the increment of displacements as follows:

$$\delta\{\Delta\varepsilon\} = [B_p]\delta\{\Delta S\} - z[B_b]\delta\{\Delta W\} + [C_p + \Delta C_p][G_p]\delta\{\Delta S\} + [C_b + \Delta C_b][G_b]\delta\{\Delta W\} \tag{A.19}$$

Substituting Equations (A.16) and (A.19) into Equations (A.18) and neglecting the infinitesimal terms having higher than second-order increments, the elastic stiffness equation for the element can be shown to be given by

$$\{L\} + \{\Delta R\} = [K]^E \{\Delta U\} \tag{A.20}$$

Where $[K]^E$ is the elastic tangent stiffness matrix for the element, $\{L\} = \{R\} - \{r\}$ is the unbalanced forces caused by the differences between the total external forces, $\{R\}$, and the total internal forces, $\{r\}$, which in turn is calculated by

$$\{r\} = \int_V [B_p]^T \{\sigma\} dVol + \int_V [G_p]^T [C_p]^T \{\sigma\} dVol + \int_V [G_b]^T [C_b]^T \{\sigma\} dVol \tag{A.21}$$

Where $\{\sigma\} = \{\sigma_x \quad \sigma_y \quad \tau_{xy}\}^T$ is the total average membrane stress component. The unbalanced forces should be eliminated at every step of load increments. For that purpose, the Newton-Raphson method or the modified Newton-Raphson method is used.

The elastic tangent stiffness matrix, $[K]^E$, in Equation (A.20) can generally be subdivided into four terms, namely

$$[K]^E = [K_p] + [K_b] + [K_g] + [K_\sigma] \tag{A.22}$$

On the right hand side of the above equation, the first and second terms represent the stiffness matrices related to the in plane and the out-of-plane small deformations, respectively. The third term is the so-called initial deformation stiffness matrix, which in turn consists of three terms representing the geometric nonlinear effects associated with the in-plane and out-of-plane deformations and their interactions.

The fourth term is the so-called initial stress stiffness matrix, which is produced by the initial stresses for the element, in which a term related to their interactions does not appear.

Each term mentioned above can be developed in more detail as follows:

$$[K_p]=\begin{bmatrix}[K_1] & 0\\ 0 & 0\end{bmatrix},\quad [K_b]=\begin{bmatrix}0 & 0\\ 0 & [K_2]\end{bmatrix},\quad [K_g]=\begin{bmatrix}[K_3] & [K_4]\\ [K_4]^T & [K_5]\end{bmatrix} \tag{A.23}$$

$$[K_\sigma]=\begin{bmatrix}[K_6] & 0\\ 0 & [K_7]\end{bmatrix}$$

where

$$[K_1]=\int_V [B_p]^T[D]^E[B_p]dVol,\quad [K_2]=\int_V [B_p]^T[D]^e[B_b]z^2 dVol$$

$$[K_3]=\int_V [G_p]^T[C_p]^T[D]^E[B_p]dVol+\int_V [B_p]^T[D]^E[C_p][G_p]dVol$$

$$+\int_V [G_p]^T[C_p]^T[D]^e[C_p][G_p]dVol$$

$$[K_4]=\int_V [B_p]^T[D]^E[C_b][G_b]dVol+\int_V [G_p]^T[C_p]^T[D]^E[C_b][G_b]dVol$$

$$[K_5]=\int_V [G_b]^T[C_b]^T[D]^E[C_b][G_b]dVol,\quad [K_6]=\int_V [G_p]^T[\sigma_p][G_p]dVol$$

$$[K_7]=\int_V [G_b]^T[\sigma_b][G_b]dVol$$

$$[\sigma_p]=\begin{bmatrix}\sigma_x & 0 & \tau_{xy} & 0\\ 0 & \sigma_x & 0 & \tau_{xy}\\ \tau_{xy} & 0 & \sigma_y & 0\\ 0 & \tau_{xy} & 0 & \sigma_y\end{bmatrix},\quad [\sigma_b]=\begin{bmatrix}\sigma_x & \tau_{xy}\\ \tau_{xy} & \sigma_y\end{bmatrix}$$

In calculating Equation (A.23), the terms involving the first order of the variable z would become zero after completing the integration for the entire volume of the element in the elastic regime. Even in the elastic-plastic regime, the plasticity is considered into the plastic nodes and the inside of the element, except for the plastic nodes, is assumed to be elastic in the present method. Thus these terms can be eliminated from the expressions.

The updated lagrangian approach

The tangent stiffness matrix, $[K]^E$, in Equation (A.22) was derived by the total Lagrangian approach considering that the local coordinate system for the element is fixed with regard to the global coordinate system, which makes possible the use of an identical transformation matrix throughout the whole incremental loading process.

On the other hand, in the so-called updated Lagrangian approach one needs to update the local coordinate system at every incremental loading process such that the transformation matrix from the local coordinate to the global system is newly set up each time. The benefit of the updated Lagrangian approach is that the initial deformation at the beginning of every incremental loading process can be set to zero. Therefore, the tangent elastic stiffness matrix, $[K]^E$, can simplify to

$$[K]^E = [K_p] + [K_b] + [K_\sigma] \tag{A.24}$$

Stiffness matrix for the displacement component, θ_z

The stiffness matrix components for the rotations with respect to the z axis may normally be set to zero, but this can in some cases produce numerical instability in the computation of the structural stiffness equation. To get a stabilizing effect in the numerical computation, the stiffness matrix components for the displacement component, θ_z, can be added to the stiffness matrix, Equation (A.24). The stiffness equation for the displacement component, θ_z, may be given by (Zienkiewicz, 1977).

$$\begin{Bmatrix} M_{z1} \\ M_{z2} \\ M_{z3} \\ M_{z4} \end{Bmatrix} = \alpha EAt \begin{bmatrix} 1 & -1/2 & -1/2 & -1/2 \\ -1/2 & 1 & -1/2 & -1/2 \\ -1/2 & -1/2 & 1 & -1/2 \\ -1/2 & -1/2 & -1/2 & 1 \end{bmatrix} \begin{Bmatrix} \theta_{z1} \\ \theta_{z2} \\ \theta_{z3} \\ \theta_{z4} \end{Bmatrix} \tag{A.25}$$

Where t is the plate thickness, and A the surface area of the element. The constant α may normally be taken to be a very small value, e.g., 5.0×10^{-5}.

A.3.5 Displacement (Shape) function

To attain a uniform state of shear stresses inside the element, a nonlinear function is in the present finite element method assumed for the in-plane displacements, u and v, while a polynomial function is assumed for the out-of-plane displacement, w, which is expressed in terms of 12 parameters. We thus have,

$$u = a_1 + a_2 x + a_3 y + a_4 xy + \frac{b_4}{2}\left(b^2 - y^2\right) \tag{A.26a}$$

$$v = b_1 + b_2 x + b_3 y + b_4 xy + \frac{a_4}{2}\left(a^2 - x^2\right) \tag{A.26b}$$

$$\begin{aligned} w = {} & c_1 + c_2 x + c_3 y + c_4 x^2 + c_5 xy + c_6 y^2 + c_7 x^3 + c_8 x^2 y \\ & + c_9 xy^2 + c_{10} y^3 + c_{11} x^3 y + c_{12} xy^3 \end{aligned} \tag{A.26c}$$

Where $a_1, a_2, \ldots\ldots, c_{12}$ are unknown coefficients which are expressed in terms of nodal displacements $\{U\}$.

For the rectangular plate element with a length of a and a breadth of b, the coefficients of the displacement functions can be obtained by substituting local coordinates and displacements at nodes into Equation (A.26).

A.3.6 Yield condition

Plasticity in the element is checked at the element corner nodal points located in the middle plane of the element thickness by applying the Ueda plastic node concept. A fully plastic condition under combined in-plane loads through the thickness of the element is used as the yield condition.

By applying the Mises-Hencky yield condition, the yield function, f_i, for the ith nodal point can be expressed in terms of the resultant membrane stress and generalized bending stress components as follows:

$$f_i = n_i^2 + |m_i| - 1 = 0 \tag{A.27}$$

where

$$n_i^2 = n_{xi}^2 - n_{xi}n_{yi} + n_{yi}^2 + 3n^2{}_{xyi}, \quad m_i = \left(m_{xi}^2 - m_{xi}m_{yi} + m_{yi}^2 + 3m^2{}_{xyi}\right)^{1/2}$$

$$n_{xi} = \frac{\sigma_{xi}}{\sigma_Y}, n_{yi} = \frac{\sigma_{yi}}{\sigma_Y}, n_{xyi} = \frac{\tau_{xyi}}{\sigma_Y}, m_{xi} = \frac{2\sigma_{xbi}}{3\sigma_Y}, m_{yi} = \frac{2\sigma_{ybi}}{3\sigma_Y}, m_{xyi} = \frac{2\tau_{xybi}}{3\sigma_Y}$$

$\{\sigma_i\} = \{\sigma_{xi} \quad \sigma_{yi} \quad \tau_{xyi}\}^T =$ nodal membrane and bending stress components, $\{\sigma_{bii}\} = \{\sigma_{xbi} \quad \sigma_{ybi} \quad \tau_{xybi}\}^T$ = nodal maximum generalized bending stress components in the outer fiber of the cross-section, σ_Y = yield stress of the element material.

The resultant membrane and bending stress components used in Equation (A.27) can be calculated by accumulating the increments of the corresponding stress components in the i th nodal point are calculated by

$$\{\Delta\sigma_i\} = [D]^E \{\Delta\varepsilon\}^E = [D]^E [B_i]\{\Delta U\}^E \tag{A.28a}$$

$$\{\Delta\sigma_{bi}\} = -\frac{t^2}{6}[D]^E \{\Delta\varepsilon\}^E = -\frac{t^2}{6}[D]^E [B_{bi}]\{\Delta W\}^E \tag{A.28b}$$

Where $[B_i]$ and $[B_{bi}]$ can be defined by substituting the local coordinates for the ith nodal point into the matrices $[B]$ and $[B_b]$, respectively, in Equation (A.15).

The yield function, f_i, may be represented as shown in Figure A.6 where the curve represents the yield surface. If the value of the yield function at any nodal

point is less than zero, indicating that the value is located inside the yield surface, e.g., the point A of Figure A.6, the nodal point is still in elastic. As the applied loads increase incrementally, the value of the yield function will reach zero so that its value is just on the yield surface, i.e., the points B or B` of Figure A.6. In this case, it is assumed that the node becomes plastic, and the plastic node is inserted at the nodal point even if the inside of the element except for the plastic nodes is considered to be elastic. The value of the yield function should in any case not be greater than zero.

Since the structural response is nonlinear, it is normally not an easy task to ensure that the value of the yield function is just on the yield surface as the applied loads increase incrementally. One of the methods used to facilitate this is to apply the smallest load increment so that the most highly stressed elastic node is just yielded. In this method, the elastic nodes are yielded one by one through the incremental loading step so that the value of the yield function will always be just on the yield surface.

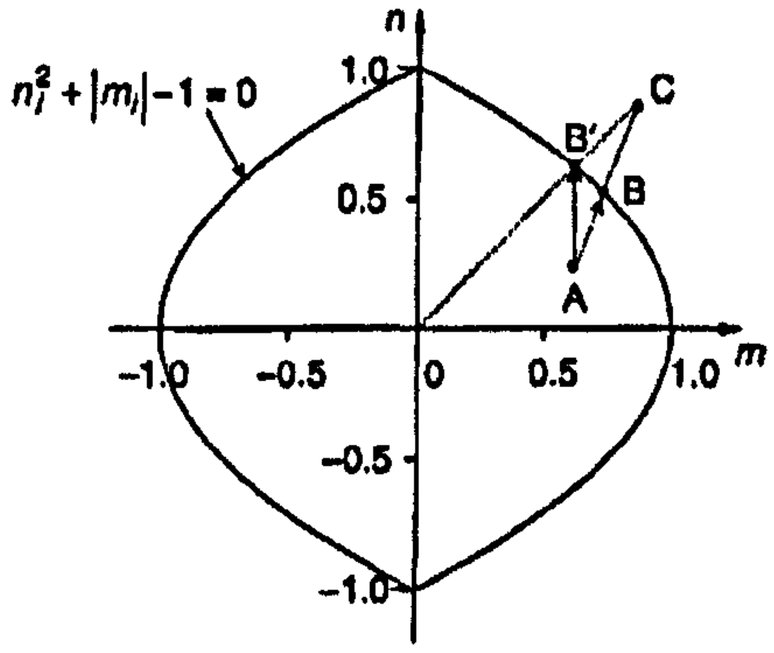

Figure A.6: A diagram of the yield surface

The smallest load increment necessary to yield the most highly stressed elastic node can be defined by a load magnification factor with regard to the initial standard load increments. For an elastic node, it is assumed that the node just yields by applying a load increment of $\beta\{\Delta R\}$, where $\{\Delta R\}$ is the prescribed initial standard load increment β is a positive multiplier. Therefore, at the node one must satisfy the yield condition as follows:

$$
\begin{aligned}
&(n_x+\beta\Delta n_x)^2-(n_x+\beta\Delta n_x)(n_y+\beta\Delta n_y)+(n_y+\beta\Delta n_y)^2+3(n_{xy}+\beta\Delta n_{xy})^2\\
&+\left[(m_x+\beta\Delta m_x)^2-(m_x+\beta\Delta m_x)(m_y+\beta\Delta m_y)(m_y+\beta\Delta m_y)^2\right.\\
&\left.+3(m_{xy}+\beta\Delta m_{xy})^2\right]^{1/2}-1=0
\end{aligned}
\tag{A.29}
$$

where the prefix Δ denotes the increment.

By neglecting the infinitesimal terms, i.e., those with higher than the second-order of the increments, this equation becomes a quadratic equation with regard to the multiplier as follows:

$$
\left(C_1+\frac{C_4}{2\sqrt{C_6}}\right)\beta^2+\left(C_2+\frac{C_5}{2\sqrt{C_6}}\right)\beta+C_3+\sqrt{C_6}-1=0 \tag{A.30}
$$

where

$$
\begin{aligned}
&C_1=\Delta n_x{}^2-\Delta n_x\Delta n_y+\Delta n_y{}^2+3\Delta n_{xy}{}^2\\
&C_2=(2n_x-n_y)\Delta n_x+(2n_y-n_x)\Delta n_y+6n_{xy}\Delta n_{xy}\\
&C_3=n_x{}^2-n_xn_y+n_y{}^2+3n_{xy}{}^2,\quad C_4=\Delta m_x{}^2-\Delta m_x\Delta m_y+\Delta m_y{}^2+3\Delta m_{xy}{}^2\\
&C_5=(2m_x-m_y)\Delta m_x+(2m_y-m_x)\Delta m_y+6m_{xy}\Delta m_{xy}\\
&C_6=m_x{}^2-m_xm_y+m_y{}^2+3m_{xy}{}^2
\end{aligned}
$$

The positive solution of this equation will then give the minimum load multiplier, β, as follows:

$$
\beta=\frac{-\alpha_2+\sqrt{\alpha_2{}^2-4\alpha_1\alpha_3}}{2\alpha_1} \tag{A.31}
$$

where

$$\alpha_1 = C_1 + \frac{C_4}{2\sqrt{C_6}}, \alpha_2 = C_2 + \frac{C_5}{2\sqrt{C_6}}, \alpha_3 = C_3 + \sqrt{C_6} - 1$$

If the actual numerical process for the structural response analysis, the smallest value of β for all elastic nodes can be determined. The next step of the load increment will then continue by applying the load increment of $\beta\{\Delta R\}$ so that the most highly stressed elastic node just yields.

In some cases, the value of the yield function may be found to be apparently located outside the yield surface, e.g., the point C of Figure A.6, implying that the prescribed load increment is too large. In these cases, an iterative procedure is needed until the desired accuracy is obtained so that the value of the yield function is just on or very near the yield surface.

A.3.7 Elastic-plastic tangent stiffness matrix

As previously mentioned, the elastic-plastic tangent stiffness matrix for the element in the local coordinate system is derived by applying the plastic node method. While the strain hardening effect can be taken into account without difficulty, the elastic-perfectly plastic model for the stress-strain relation is adopted in the present formulation, as shown in Figure A.7. Upon attaining convergence of the unbalanced forces, $\{L\}$, required to secure the equilibrium of the structure, the elastic tangent stiffness equation for the element will become

$$\{\Delta R\} = [K]^E \{\Delta U\}^E \tag{A.32}$$

where $[K]^E$ = elastic tangent stiffness matrix for the element, $\{\Delta U\}^E$ = elastic component of displacement increments which are equal to the total load displacement increments, $\{\Delta U\}$, if the element behaviour is still in elastic regime.

Since the nodal force vectors are related to only the elastic components of the displacements, this equation should be available even for elastic-plastic regime. If the resultant stress components at any nodal point of the element satisfy the yield condition, plastic nodes are inserted and plastic deformation will be produced. Therefore, the total displacement increments, $\{\Delta U\}$, in the elastic-plastic regime can be calculated by the sum of the elastic and plastic components of the displacement increments as follows:

$$\{\Delta U\} = \{\Delta U\}^E + \{\Delta U\}^P \tag{A.33}$$

Where $\{\Delta U\}^E$ and $\{\Delta U\}^P$ are the elastic and plastic components of the displacement increments, respectively.

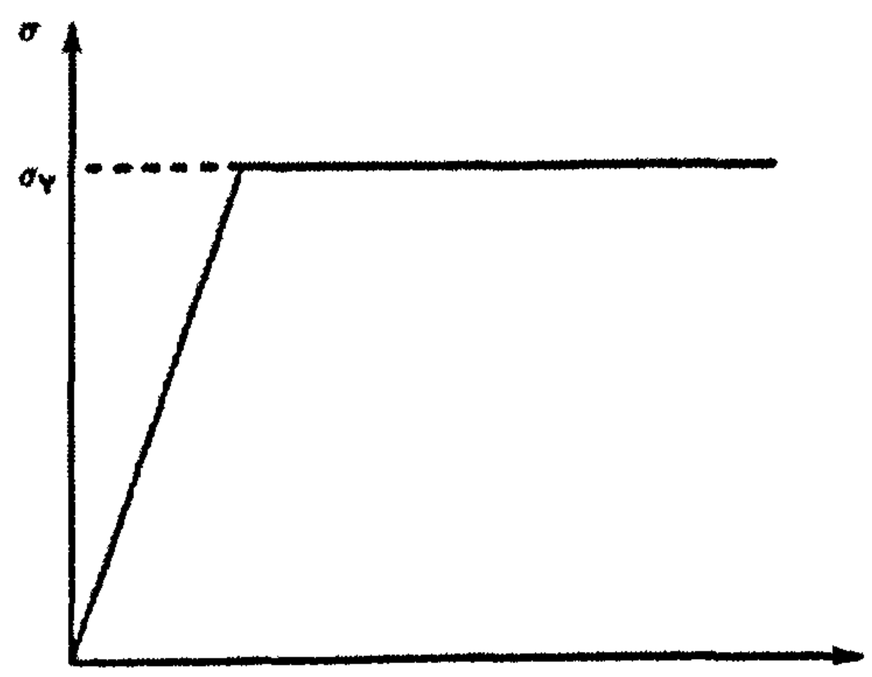

Figure A.7: The elastic-perfectly plastic model for the stress-strain relationship

By applying plastic flow theory, the plastic components of the displacement increments after the i th node has yielded can be calculated by

$$\{\Delta U\}^P = \Delta\lambda_i \{\phi_i\} \tag{A.34}$$

Where $\{\phi_i\} = \{\partial f_i / \partial R\}$ and $\Delta\lambda_i$ is a positive scalar characterizing the magnitude of the plastic displacement. $\{\phi_i\}$ in this equation represents the outward vector

normal to the yield surface which can be expressed in terms of nodal forces as follows:

$$\{\phi_i\} = \sigma_Y{}^2 \left(\left\{ \frac{\partial f_i}{\partial \sigma_i} \right\}^T \left\{ \frac{\partial \sigma_i}{\partial R} \right\} + \left\{ \frac{\partial f_i}{\partial \sigma_{bi}} \right\}^T \left\{ \frac{\partial \sigma_{bi}}{\partial R_e} \right\} \right) \tag{A.35}$$

Where $\sigma_Y{}^2$ appears because the yield function, f_i, of Equation (A.27) was expressed in a non-dimensional form with regard to the yield stress, σ_Y. In this equation, $\{R_w\}$ indicates the out-of-plane component of nodal forces, with the increments of $\{R_w\}$ being calculated by

$$\{\Delta R_e\} = [K_w]\{\Delta W\}^E \tag{A.36}$$

where the subscript w denotes the vector or matrix for the out-of-plane component.

By reducing the degrees of freedom with regard to the rigid-body motion of the element, the relationships between the nodal forces and displacements or between the stresses and displacements can be expressed by

$$\{\Delta R\} = [K^*]^E \{\Delta U^*\}^E \tag{A.37a}$$

$$\{\Delta R_w\} = [K_W{}^*]^E \{\Delta W^*\}^E \tag{A.37b}$$

$$\{\Delta \sigma_i\} = [D]^E [B_i{}^*]\{\Delta U^*\}^E \tag{A.37c}$$

$$\{\Delta \sigma_{bi}\} = -\frac{t^2}{6}[D]^E [B_{bi}{}^*]\{\Delta W^*\}^E \tag{A.37d}$$

where the asterisk indicates the reduced degree of freedom after removing the rigid-body motion of the element.

Calculating the nodal displacements, $\{\Delta U^*\}^E$ and $\{\Delta W^*\}^E$ from Equations (A.37a) and (A.37b), respectively, and substituting them into Equations (A.37c) and (A.37d), the resultant stresses can be expressed as functions of the nodal forces as follows:

$$\{\Delta\sigma_i\} = \frac{[D]^E [B_i^*] ([K^*]^E)^T}{([K^*]^E)^T [K^*]^E} \{\Delta R\} \tag{A.38a}$$

$$\{\Delta\sigma_{bi}\} = -\frac{t^2}{6} \frac{[D]^E [B_{bi}^*] ([K_w]^E)^T}{([K_w^*]^E)^T [K_w^*]^E} \{\Delta R_w\} \tag{A.38b}$$

To calculate the outward normal vector, $\{\phi_i\}$, of Equation (A.35), $\{\partial f_i/\partial\sigma_i\}$ and $\{\partial f_i/\partial\sigma_{bi}\}$ are first computed by differentiating the yield function, f_i, Equation (A.27), with regard to the stresses can be expressed as functions of the nodal forces as follows:

$$\left\{\frac{\partial f_i}{\partial\sigma_i}\right\} = \frac{1}{\sigma_Y^2} \{(2\sigma_{xi} - \sigma_{yi})(2\sigma_{yi} - \sigma_{xi})(6\tau_{xyi})\}^T \tag{A.39a}$$

$$\left\{\frac{\partial f_i}{\partial\sigma_{bi}}\right\} = \frac{1}{3\sigma_Y\sqrt{S}} \{(2\sigma_{xbi} - \sigma_{ybi})(2\sigma_{ybi} - \sigma_{xbi})(6\tau_{xyi})\}^T \tag{A.39b}$$

where $S = \sigma_{xbi}{}^2 - \sigma_{xbi}\sigma_{ybi} + \sigma_{ybi}{}^2 + 3\tau_{xyi}{}^2$

Also, $\left\{\partial\sigma_i/\partial R\right\}$ and $\left\{\partial\sigma_{bi}/\partial R_w\right\}$ are computed by differentiating Equations (A.38a) and (A.38b) with regard to the nodal forces as follows:

$$\left\{\frac{\partial\sigma_i}{\partial R}\right\} = \frac{[D]^E [B_i^*] ([K^*]^E)^T}{([K^*]^E)^T [K^*]^E} \tag{A.40a}$$

$$\left\{\frac{\partial \sigma_{bi}}{\partial R_w}\right\} = -\frac{t^2}{6}\frac{[D]^E\left[B_{bi}^{\ *}\right]\left([K_w]^E\right)^T}{\left(\left[K_w^{\ *}\right]^E\right)^T\left[K_w^{\ *}\right]^E} \tag{A.40b}$$

Then the outward normal vector, $\{\phi_i\}$, can be computed by substituting Equations (A.39) and (A.40) into Equation (A.35). In the numerical computation process, a drift in the value of the yield function from be located just on the yield surface can occur and this should be prevented to get the desired accuracy of solution.

When the resultant stress components of the ith nodal point satisfy the yield condition, the value of the yield function must be located just on the yield surface, e.g., the point O of Figure A.8(a), in which the outward normal vector denoted $\{\phi_i\}_0$ will be developed. As the external loads increase, the nodal force vector at the plastic node should move along the yield surface in the tangent direction and thus the point O may move to a point outside the yield surface, e.g., the point A of Figure A.8(a) where the outward normal vector, $\{\phi_i\}_A$, will be produced. Likewise, in the next step of load increments, the point A may move to a point which is more distant from the yield surface, e.g., the point B of Figure A.8(a) with the outer normal vector $\{\phi_i\}_B$.

In fact, as long as the value of the yield function is located outside the yield surface, the outward normal vector is not real and if its drift from the yield surface is too big the resulting response obtained in the subsequent loading step may no longer be reliable. It is hence of importance to control and remove the drift of the value of the yield function during the incremental loading process.

Several useful approaches, namely the iterative method (Wen & Farhoomand 1970), five-step correction method (Orbison *et al.* 1982) and two-step correction procedure (Paik & Kim 1989) have been proposed to reduce the drift of the value of the yield function. In the illustrative examples of this appendix, the two-step correction method is applied. The method is described in the following.

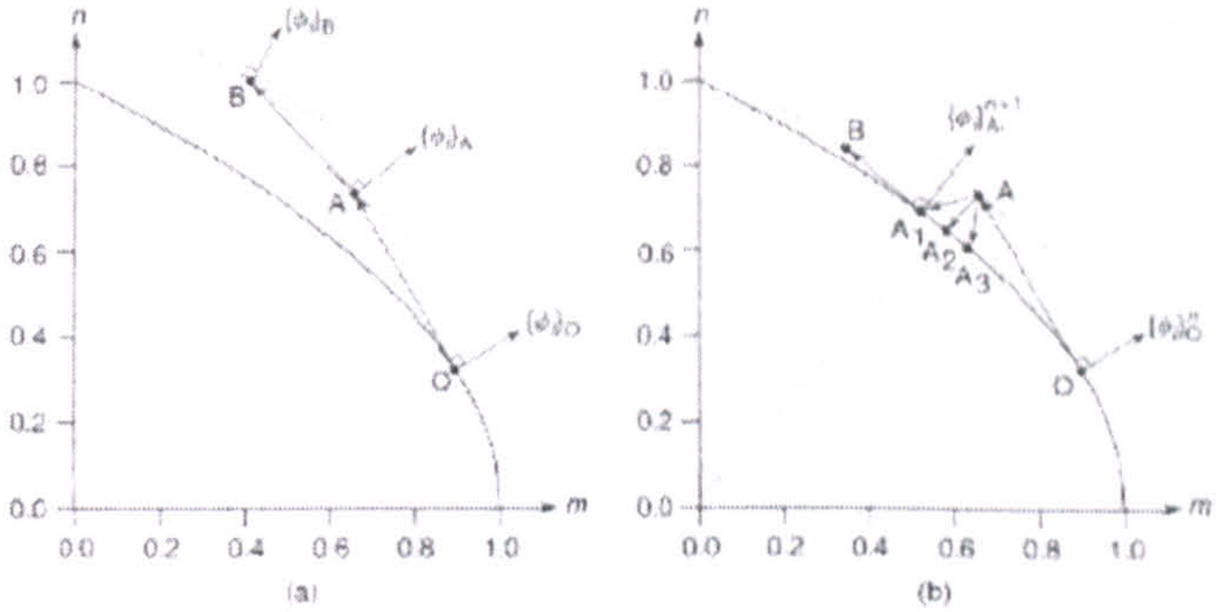

Figure A.8: (a) The drift in the value of the yield function; (b) A two-step procedure for convergence to the yield condition

As previously noted, the elastic nodes of the structure are yielded one by one through the incremental loading step so that the value of the yield function will be located just on or very near the yield surface. It is considered that at the n th step of load increment the value of the yield function for the i th plastic node is just on the yield surface, e.g., the point O of Figure A.8(b) with the outward normal vector, $\{\phi_i\}^n{}_O$. Assume that the value of the yield function moves to the point A along the tangent vector OA in the next (i.e., (n+1)th) step of load increments. If the drift of the point A from the yield surface exceeds an acceptable tolerance, the location of the point A is corrected by multiplying by the linearly determined correction factor can be estimated in a similar manner to the computation of the load magnification factor indicated in Equation (A.31). If the point A returns to the yield surface, e.g., at the point A_1, the nodal forces will produce the outward normal vector, $\{\phi_i\}_{A1}{}^{n+1}$, and the tangent vector, A_1B, for the $(n+1)$th step of load increments. This approach is quite simple to handle and gives sufficient accuracy for practical use.

If m numbers of the nodal points for an element are in the plastic condition, the plastic component of displacement increments can then be computed by the superposition of Equation (A.34) as follows:

$$\{\Delta U\}^P = \sum_{i=1}^{m} \Delta\lambda_i \{\phi_i\} \tag{A.41}$$

where the maximum number of m will be four for the rectangular plate element since the number of nodal points is four.

Substituting Equations (A.33) and (A.41) into Equation (A.32), the tangent stiffness equation for the element becomes

$$\{\Delta R\} = [K]^E \left(\{\Delta U\} - \sum_{i=1}^{m} \Delta\lambda_i \{\phi_i\} \right) \tag{A.42}$$

Neglecting the strain-hardening effect, i.e., considering an elastic-plastic fully plastic material, the following equation should be satisfied at every plastic node as long as the loading process continues:

$$\Delta f_i = \{\phi_i\}^T \{\Delta R\} = 0 \tag{A.43}$$

Substitution of Equation (A.42) into Equation (A.43) leads to

$$\{\Delta\lambda\} = \frac{[\phi]^T [K]^E}{[\phi]^T [K]^E [\phi]} \{\Delta U\} \tag{A.44}$$

where $[\phi] = [\{\phi_1\} \quad \{\phi_2\} \quad \ldots \quad \{\phi_m\}]^T$, $\{\Delta\lambda\} = \{\Delta\lambda_1 \quad \Delta\lambda_2 \quad \ldots \quad \Delta\lambda_m\}^T$

By substituting Equation (A.44) into Equation (A.42), the tangent stiffness matrix for the element in the elastic-plastic regime can be written as follows:

$$\{\Delta R\} = \left([K]^E - \frac{[K]^E [\phi][\phi]^T [K]^E}{[\phi]^T [K]^E [\phi]} \right) \{\Delta U\} = [K]^P \{\Delta U\} \tag{A.45}$$

where

$$[K]^P = [K]^E - \frac{[K]^E [\phi][\phi]^T [K]^E}{[\phi]^T [K]^E [\phi]}$$

is the elastic-plastic tangent stiffness matrix of the element.

It is evident from Equation (A.45) that the elastic-plastic tangent stiffness matrix, $[K]^P$, can be calculated by a matrix operation without having to perform the numerical integration over the volume of the element once the elastic tangent stiffness matrix, $[K]^E$, is obtained. In the calculation of Equation (A.45), the loading state for every plastic node should be checked, and when unloading is detected, i.e., if $\Delta\lambda_i < 0$. For the i th plastic node, the node should be treated as an elastic one.

A.3.8 Treatment of the Bauschinger effect

The bauschinger effect may play an important role in the nonlinear response of steel structures which are likely to be subjected to cyclic extreme loading. In this case, the so-called sublayer model may be relevant for the elastic-perfectly plastic material.

When the strain-hardening effect is of primary concern, the kinematic hardening model or combined isotropic and kinematic hardening model is typically used where the origin of the yield function can be moved as stress components vary, as shown in Figure A.9. The kinematic hardening model keeps the shape and size of the yield function, while the combined model may allow for expansion of the yield function. In contrast, the isotropic hardening model, which neglects the Bauschinger effect, has a fixed origin of the yield function which can expand due to the strain-hardening effect.

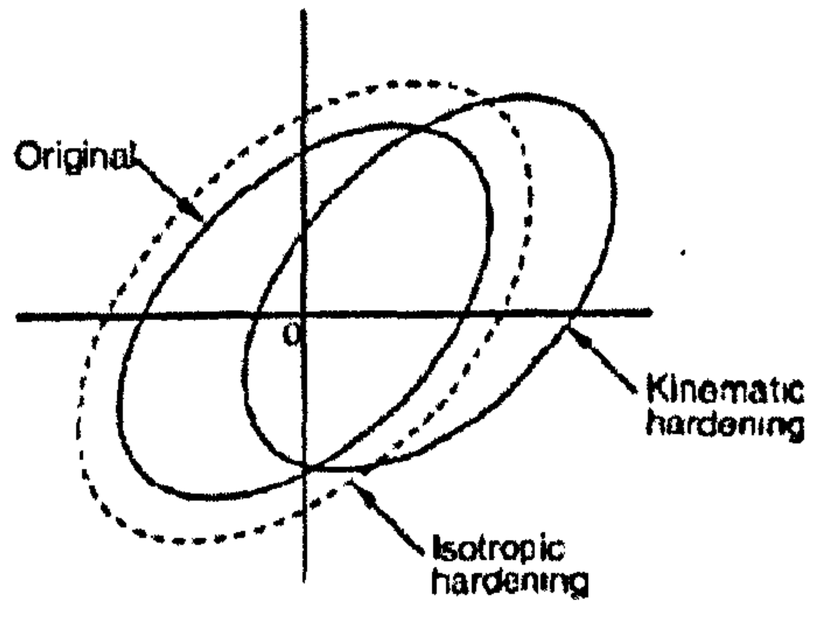

Figure A.9: The isotropic hardening versus the kinematic hardening

A.3.9. Local to global transformation matrix

An exact formulation of the transformation matrix for a rectangular plate element is difficult to define. In the approximate formulation, it is normally considered that the element is in a plane containing at least three nodal points of the element. The transformation matrix, $[T]$, from the local coordinate system to the global coordinate system can then be obtained in Cartesian terms (i.e., as functions of global coordinates at nodal points). Therefore, the element stiffness matrix in the local coordinate system can be transformed to the global system coordinate as follows:

$$[K]_g = [T]^T [K]_l [T] \tag{A.46}$$

Where $[K]_l$ and $[K]g$ are the element stiffness matrices in the local and global coordinates, respectively, and $[T]$ is the transformation matrix from the local coordinate system to the global coordinate system. All element stiffness matrices in the global coordinate system are then assembled in the usual manner for the finite element procedure to obtain the stiffness matrix for the entire structure. By solving the resulting stiffness equations for prescribed load increments and boundary conditions, the structural response is obtained.

REFERENCES:

1. Anderson, T.L. (1995). Fracture mechanics: fundamentals and applications, Second Edition, CRC Press, London, UK.
2. Antoniou, A.C. (1980). On the maximum deflection of plating in newly built ships, Journal of Ship Research, 24(1): 31-39.
3. Arita, K. (1986). A study on the collision strength of ships, Ph.D. thesis, Osaka University, Osaka, Japan.
4. ASIS. (1993). The conference on "Prediction Methodology of Tanker Structural Failure & Consequential Oil Spill", Association of Structural Failure & Consequential Oil Spill", Association of Structural Improvement of Shipbuilding Industry of Japan.
5. Bedair, O.K. (1996). On the post-buckling behaviour of plates under stress gradient, Structural Engineering and Mechanics, 4:397-413.
6. Bleich, F. (1952). Buckling strength of metal structures, McGraw-Hill, New York.
7. BMT Fleet Technology. (2003). Fracture toughness of a ship structure, Report SSC-430, Ship Structure Committee, Washington, D.C.
8. Bonello, M.A., Chryssanthopouls, M.K. and Dowling, P.J. (1993). Ultimate strength design of stiffened plates under axial compression and bending, Marine Structure, 6:532-552.
9. Bureau Veritas (2005). Rules for construction of ships.
10. Caldwell, J.B. (1965). Ultimate longitudinal strength, Trans RINA, 107: 411-430.
11. Carlsen, C.A. and Czujko, J. (1978). The specification of post-welding distortion tolerance for stiffened plates in compression, The Structural Engineer, 56A(5); 133-141.
12. Chen, W.F. and Atsuta, T. (1976). Theory of beam-columns, Vol.1, In-plane behaviour and design, McGraw-Hill, New York.
13. Chen, Y. (2002). Ultimate strength analysis of stiffened panels using a beam-column method. PhD Dissertation, Virginia Polytechnic Institute and State University, Blacksburg, VA.

14. Chen, Y.K., Kutt, L.M., Piaszczyk, C.M. and Bieniek, M.P. (1983). Ultimate strength of ship structures, The Transactions of the Society of Naval Architects and Marine Engineers, 91: 149-168.

15. Chung, J.Y. (1996). On bow collision strength of ships, Ph.D. thesis, Pusan National University, Pusan, Korea.

16. Cook, R.D, Malkus, D.S. and Plesha, M.E. (1989). Concepts and applications of finite element analysis, John Wiley & Sons, New York.

17. CRC (1971). Handbook of structural stability, Column Research Committee of Japan, Corona Publishing Co., Tokyo.

18. Crisfield, M.A. (1981). A fast incremental/iterative solution procedure that handles 'snap-through', Computers & Structures, 13:55-62.

19. Cui, W.C and Mansour, A.E. (1998). Effects of welding distortions and residual stresses on the ultimate strength of long rectangular plates under uniaxial compression, Marine structures, 11: 291-303.

20. Cui, W.C., Wang, Y. and Pedersen, P.T. (2002). Strength of ship plates under combined loading. Marine structures 15: 75-97.

21. Daidola, J.C. (1995). Tanker structure behaviour during collision and grounding, Marine Technology, 32(1): 20-32.

22. Das, P.K. and Dow, R. (2000). Hull girder reliability of a naval ship under extreme load, Journal of Ship Technology Research, 47:186-196, Germany.

23. Das, P.K. and Fang, C.L. (2005). Residual strength and survivability of ships after grounding and collision, Journal of Ship Research (sent for publication).

24. Das, P.K. and Garside J.K. (1991). Structural redundancy for continuous and discrete systems, Ship Structure Committee, Report no. SSC-354.

25. Dexter, R.J. and Gentilcore, M.L. (1997). Evaluation of ductile fracture models for ship structural details, Report SSC-393, Ship Structure Committee, Washington, D.C.

26. Dexter, R.J. and Mahmoud, H.N. (2004). Predicting stable fatigue crack propagation in stiffened plates, Report SSC-435, Ship Structure Committee, Washington, D.C.

27. Dexter, R.J. and Pilarski, P.J. (2000). Effect of welded stiffeners on fatigue crack growth rate, Report SSC-413, Ship Structure Committee, Washington, D.C.

28. DNV (1995). Buckling strength analysis, Classification Notes No. 30.1, Det Norske Veritas, Oslo, July.

29. DNV (2003). PULS 1.5 – User's manual, Technical Report No. 2001-0420, Revision No. 07, Det Norske Veritas, Oslo.

30. Dow, R.S. (1980). N106C: A computer program for elastic-plastic, large deflection buckling and post-buckling behaviour of plane frames and stiffened panels. AMTE(S) R80726.

31. Dow, R.S. (1991). Testing and analysis of 1/3-scale welded steel frigate model. Proceedings of the International Conference on Advances in Marine Structures, Dunfermline, Scotland, 749-773.

32. Dow, R.S., Hugill, R.C., Clarke, J.D. and Smith, C.S. (1981). Evaluation of ultimate ship hull strength, Proceedings of SSC-SNAME Symposium on Extreme Loads Response, Arlington, USA

33. Dugdale, D.S. (1960). Yielding of steel sheets containing slits, Journal of Mechanics and Physics of solids, 8:100-108.

34. Dunbar, T.E., Pegg, N., Taheri, F. and Jiang, L. (2004). A computational investigation of the effects of localized corrosion on plates and stiffened panels, Marine Structures, 17:35-402.

35. Endo, H., Tanaka, Y., Aoki, G., Inoue, H. and Yamamoto, Y. (1988). Longitudinal strength of the fore body of ships suffering from slamming. J. Soc. Naval Arch. of Japan, 163, 322-333 (in Japanese).

36. Faulkner, D. (1973). Synthesis of welded grillages to withstand compression and normal loads, Comp. Struct., 3: 221-246.

37. Faulkner, D. (1975). A review of effective plating for use in the analysis of stiffened plating in bending and compression, Journal of Ship Research, 19(1):1-17.

38. Faulkner, J.A., Clarke, J.D., Smith, C.S. and Faulkner, D. (1984). The loss of HMS COBRA – A reassessment, Trans. RINA, 127, 125-151.

39. Frieze *et al.* (1991). Report of ISSC Committee V.1- Applied Design, 11th ISSC Conference, Wuxi, China, Vol.2.

40. Fujikubo, M., Kaeding, P. and Yao, T. (2000). ISUM rectangular plate element with new lateral shape function (1st Report) – Longitudinal and transverse thrust, J. Soc. Naval Arch. of Japan, 187, 256-271.

41. Fujikubo, M., Yao, T. and Khedmat, M.R. (1999). Estimation of ultimate strength of ship bottom plating under combined transverse thrust and lateral pressure, J Soc Naval Archit Japan, 186: 621-630.

42. Germanischer Lloyd. (2003). Development of explanatory notes for harmonized SOLAS chapter ii-1, International Maritime Organization (IMO).

43. Ghose, D.J., Nappi, N.S. and Wiernicki, C.J. (1994). Residual strength of damaged marine structures, Ship Structural Committee Report, SSC-381.

44. Gordo, J.M. and Soares, C.G. (1996). Approximate methods to evaluate the hull girder collapse strength, Marine Structures, 9(3): 449-470.

45. Gordo, J.M. and Soares, G.C. (1993). Approximate load-shortening curves for stiffened plates under uniaxial compression. In: Faulkner, D., Cowling, M.J., Incecik, A., Das, P.K., editors, Integrity of Offshore Structures-5, EMAS, 189-211.

46. Gordo, J.M., Guedes, S.C. and Faulkner, D. (1996). Assessment of the ultimate longitudinal strength of the hull girder, Journal of Ship Research, 40(1): 60-69.

47. Gordo, J.M. and Soares, C.G. (1999) Interaction equation for the collapse of tankers and containership under combined bending moments, Journal of Ship Research, 41: 230-240.

48. Griffith, A.A. (1920). The phenomena of rupture and flow in solids, Philosophical Transactions Series A, 221:163-198.

49. Grondin, G.Y., Chen, Q., Elwi, A.E. and Cheng, J.J.R. (1998). Buckling of stiffened steel plates-validation of a numerical model, Journal of Constructional Steel Research, 45(2):125-148.

50. Grondin, G.Y., Chen, Q., Elwi, A.E. and Cheng, J.J.R. (1999). Buckling of stiffened steel plates – A parametric study, Journal of Constructional Steel Research, 50(2):151-175.

51. Hu, S.Z., Chen, Q., Pegg, N. and Zimmercman, T.J.E. (1997). Ultimate collapse tests of stiffened plate ship structural units, Marine Structure, 10:587-610.

52. Hu, Y. and Chen, B. (2001). Limit state of torsion of ship hulls with large hatch openings, Journal of Ship Research, 45:(2): 95-102.

53. Hu, Y., Zhang, A. and Sun, J. (2001). Analysis on the ultimate longitudinal strength of a bulk carrier by using a simplified method, Marine Structures, 14: 311-330.

54. Hughes, O.F., Ghosh, B. and Chen, Y. (2004). Improved prediction of simultaneous local and overall buckling of stiffened plates, Thin-Walled Structures, 42:827-856.

55. Hutchinson, J.W. (1968). Singular behaviour at the end of a tensile crack in a hardening material. Journal of the Mechanics and Physics of Solids, 16:13-31.

56. Irwin, G.R. (1948). Fracture dynamics, In fracturing of Metals, The American Society for Metals, Cleveland, OH, 147-166.

57. Irwin, G.R. (1956). Onset of fast crack propagation in high strength steel and aluminium alloys, Singapore Research Conference Proceedings, 2:289-305.

58. ISSC. (2003). Committee V.3 Collision and Grounding. 15th International Ship and Offshore Structures Congress (ISSC), San Diego, USA.

59. Joint Bulker Project Rules, 2004.

60. JTP Background Document. (2004a). Common structural rules for double hull oil tankers, Section 9- Design verification, September.

61. JTP Draft. (2004b). Draft common structural rules for double hull oil tankers, Section 10-buckling and ultimate strength.

62. Kalman, Z. and Manta, P. (2002). Tracing the ultimate longitudinal strength of a damaged ship girder. International Shipbuilding Progress, 49(3): 161-176.

63. Kierkegaard, H. (1993). Ship collisions with icebergs, Ph.D. thesis, DTU.

64. Kitamura, O. (2001). FEM approach to simulate of collision and grounding damage, The Second International Conference on Collision and Grounding of the Ships, Copenhagen, Denmark.

65. Kitamura, O., Kuroiwa, T., Kawamoto, Y. and Kaneko, E. (1998). A study on the improved tanker structure against collision and grounding damage, Proceedings of the 7th PRADS, 173-179.

66. Kmiecik, M., Jastrzebski, T. and Kuzniar, J. (1995). Statistics of ship plating distortions, Marine Structures, 8: 119-132.

67. Kuroiwa, T. (1996). Numerical simulation of the actual collision and grounding experiments, International Conference on Design and Methodologies for Collision and Grounding Protection of Ships, San Francisco, USA.

68. Machida, S. (1984). Ductile Fracture Mechanics, Daily Engineering Newspaper Company, Tokyo.

69. Maestro, M. and Marino, A. (1989). An assessment of the structural capacity of damaged ships: The plastic approach in longitudinal unsymmetrical bending and the influence of buckling, International Shipbuilding Progress, 36:408, 255-265.

70. Mansour, A.E. (1971). Post –buckling behaviour of stiffened plates with small initial curvature under combined loads, International Shipbuilding Progress 18: 1-71.

71. Mansour, A.E., Lin, Y.H. and Paik, J.K. (1995). Ultimate strength of ships under combined vertical and horizontal moments, Proceedings of 6th International Symposium on Practical Design of Ships and Mobile Units PRADS'95, Seoul.

72. Masaoka, K., Okada, H. and Ueda, Y. (1998). A rectangular plate element for ultimate strength analysis, Proc. 2nd Int. Conference on Thin-Walled Structures, Singapore, 1-8.

73. Minorsky, V.U. (1959). An analysis of ship collision with reference to protection of nuclear power ships, Journal of Ship Research, 3: 1-4.

74. Moan, T., Amlashi, H.K.K., and Dong, G. (2005). Critical assessment of ultimate hull girder capacity of ships from a reliability analysis point' of view, IMAM Conference, 26-30 September, Lisbon, Portugal.

75. Mott, N.F. (1948). Fracture of metals: theoretical considerations, Journal of Engineering, 165:16-18.

76. Murray, N.W. (1973). Buckling of stiffened panel loaded axially and in bending, Structure Engineer, 51(8):285-301.

77. Narayan, R. and Chan, L. (1985). Ultimate capacity of plates containing holes under linearly varying edge displacements, Comp. Struct., 21:841-849.

78. Nishihara, S. (1983). Analysis of ultimate strength of stiffened rectangular plate (4th Report) – On the ultimate bending moment of ship hull girder, Soc. Naval Arch. of Japan, 154, 367-375 (in Japanese).

79. Okamoto, T., Hori, T., Tateishi, M., Rashed, S.M.H. and Miwa, S. (1985). Strength evaluation of novel unidirectional-girder-system product oil carrier by reliability analysis. SNAME Trans., 93, 55-77.

80. Orbison, J.G., McGuire, W. and Abel, J.F. (1982). Yield surface applications in nonlinear steel frame analysis, Journal of Computer Methods in Applied Mechanics and Engineering, 33(1-3):557-573.

81. Orowan, E. (1948). Fracture and strength of solids, Reports on Progress in Physics, XII:185-232.

82. Ostapenko, A. (1981). Strength of ship hull girders under moment, shear and torque. Proc. SSC-SNAME Symposium on Extreme Loads Response, Arlington, USA, 149-166.

83. Paik, J.K. and Kim D.H. (1997). A benchmark study of the ultimate strength formulations of stiffened panel on a benchmark study on the stiffened plate strength, Joint PNU-ABS research project, Final report.

84. Paik, J.K. and Kim, C.Y. (1989). A simplified finite element method for the ultimate strength analysis of plates with initial imperfections, Journal of Society of Naval Architects of Korea, 26(1):24-38.

85. Paik, J.K. and Mansour, A.E. (1995). A simple formulation for predicting the ultimate strength of ships, Journal of Marine Science and Technology, The Society of Naval Architects of Japan, 1(1): 52-62.

86. Paik, J.K. and Thayamballi, A.K. (2002). Ultimate strength of ageing ships, Journal of Engineering for the Maritime Environment, 216(M1): 57-77.

87. Paik, J.K. and Thayamballi, A.K. (2003). Ultimate limit state design of steel plated structures, John Wiley & Sons.

88. Paik, J.K., Hughes, O.F. and Mansour, A.E. (2001). Advanced closed form ultimate strength formulation for ships, Journal of Ship Research, 45(2): 111-132.

89. Paik, J.K., Thayamballi, A.K. and Jung, S.C. (1996). Ultimate strength of ship hulls under combined vertical bending, horizontal bending, and shearing forces, Trans.SNAME, 104: 31-59.

90. Paik, J.K., Thayamballi, A.K. and Yang, S.H. (1998). Residual strength assessment of ships after collision and grounding, Marine Technology, 35(1): 38-54.

91. Paik, J.K., Thayamballi, A.K., Sung, K.K. and Soo, H.Y. (1998). Ship hull ultimate strength reliability considering corrosion, Journal of Ship Research, 42:2, 154-165.

92. Pei, Z. and Fujikubo, M. (2005). Application of idealized structural unit method to progressive collapse analysis of ship's hull girder under longitudinal bending, *ISOPE*, June 19-24, Seoul, Korea.

93. Petersen, M.J. (1982). Dynamics of ship collisions, Ocean Engineering, 9(4): 295-329.

94. Pu, Y., Das, P.K. and Faulkner, D. (1997). Ultimate compression strength and probabilistic analysis of stiffened Plates, Journal of OMAE 119: 270-275.

95. Qi, E., Cui, W., Peng, X. and Xu, X. (1999). Reliability assessment of ship residual strength after collision and grounding, Journal of Ship Mechanics, 3(5): 40-46.

96. Rahman, M.K and Chowdhury, M. (1996). Estimation of ultimate longitudinal bending moment of ships and box girders, Journal of Ship Research, 40(3):244-257.

97. Rice, J.R. (1968). A path independent integral and the approximate analysis of strain concentrations by notches and cracks, Journal of Applied Mechanics, 35:379-386.

98. Rice, J.R. and Rosengren, G.F. (1968). Plane strain deformation near a crack tip in a power-law hardening material, Journal of the Mechanics and Physics of Solids, 16:1-12.

99. Rigo, P., Moan, T., Frieze, P.A. and Chryssanthopoulos, M. (1995). Benchmarking of the ultimate strength prediction for longitudinally stiffened panels, Proc.of the 6th international symposium on practical design of ships and mobile units (PRADS`95), Seoul, 869-882.

100. RINA. (1998). Proceedings of the International Conference on Design and Operation of Bulk Carriers, London.

101. Rizzuto, E. (1997) Discussion of Committee II.1 Report of ISSC'1997, Proceedings *of* 13th ISSC, T.Moan and S.Berge (eds), Pergamon Press – Elseiver Science, 13: 69-71.

102. Rutherford, S.E. and Caldwell, J.B. (1990). Ultimate longitudinal strength of ships, Trans. SNAME, 98: 441-471.

103. Sadovsky, Z., Teixeira, A.P. and Soares, C.G. (2004). Degradation of the Compressive Strength of Rectangular Plates due to Initial Deflection, Thin-Walled Structures, Article In Press, 1-18.

104. Santos, T.A. and Soares, S.C. (2002). Probabilistic survivability assessment of damaged passenger Ro-Ro ships using Monte-Carlo simulation, International Shipbuilding Progress, 49(4): 275-300.

105. Schultz, H.G. (1964). Über die effective Breite druckbeanspruchter Schiffsplaten und das effective Widerstandsmoment des Schiffkastenträgers mit ausbeulenden Längsverband, Schiff und Hafen, 8:730-739.

106. Servis, D.P., Samuelides, M., Louka, T. and Voudouris, G. (2002). The implementation of finite element codes for the simulation of ship-ship collisions, Journal of Ship Research, 46(4): 239-247.

107. Sheikh, I.A., Elwi, A.E. and Grondin, G.Y. (2003). Stiffened steel plates under combined compression and bending, Journal of Constructional Steel Research, 59: 911-930.

108. Shih, C.F. (1981). Relationship between the J-integral and the crack opening displacement for stationary and extending cracks, Journal of the Mechanics and Physics of Solids, 29:305-326.

109. Shih, C.F., deLorenzi, H.G. and Andrews, W.R. (1977). Studies on crack initiation and stable crack growth, The American Society for Testing and Materials, Atlanta, GA, November 64-120.

110. Smith, C. and Dow, R. (1981). Residual strength of damaged steel ships and offshore structures, Journal of Constructional Steel Research, 1: No. 4, September.

111. Smith, C.S. (1976). Compressive strength of welded steel ship grillages, Trans. RINA, 118: 325-359.

112. Smith, C.S. (1977). Influence of local compressive failure on ultimate longitudinal strength of a ship's hull, Proc. Int. Symp. On Practical Design in Shipbuilding, Tokyo, Japan, 73-79.

113. Smith, C.S., Anderson, N., Chapman, J.C., Davidson, P.C. and Dowling, P.J. (1992). Strength of stiffened plating under combined compression and lateral pressure, Trans. RINA, 134: 131-147.

114. Smith, C.S., Anderson, P.C., Chapman, J.C. and Dowling, P.J. (1988). Strength and stiffness of ship's plating under in-plane compression and tension, Trans. RINA, 130:277-296.

115. Soares, G.C. (1992). Design equation for ship plate elements under uniaxial compression, J Construct Steel Research, 22: 99-114.

116. Steen, E. and Valsgard, S. (1984). Simplified buckling strength criteria for plates subjected to biaxial compression and lateral pressure, SNAME –84: 251-272.

117. Steen, E., Byklum, E., Vilming, K. and Ostvolds, K. (2004). Computerized buckling models for ultimate strength assessment of stiffened ship hull panels, 9th Symposium on Practical Design of Ships and Other Floating Structures, Luebeck, Germany.

118. Tanaka, Y. and Endo, H. (1988). Ultimate strength of stiffened plates with their stiffeners locally buckled in compression (in Japanese), J of the Society of Naval Architects of Japan, 164: 456 –467.

119. Tanker Structure Co-operative Forum. (1986). International Chamber of Shipping and Oil Companies International Marine Forum, Guidance manual for the inspection and condition assessment of tanker structures, London, England, Witherby & Co.

120. Tanker Structure Co-operative Forum. (1995). International Chamber of Shipping and Oil Companies International Marine Forum, Guidance manual for the inspection and condition assessment of tanker structures, London, England, Witherby & Co.

121. Tornqvist, R. (2003). Design of crashworthiness ship structures, Ph.D. thesis, Denmark Technical University (DTU).

122. Ueda, Y. and Rashed, S.M.H. (1991). Advances in the application of ISUM to marine structures, Proc. Int. Conf. On Advances in Marine Structures-2, ARE, Dunfermline, Scotland, 628-649.

123. Ueda, Y. and Tall, L. (1967). Inelastic buckling of plates with residual stresses, Publication of International Assoc. Bridge Structure Engineering, 211-72.

124. Ueda, Y. and Yao, T. (1985). The influence of complex initial deflection modes on the behaviour and ultimate strength of rectangular plate in compression. Journal of Constructional Steel Research, 5, 265-302.

125. Valsgaard, S. (1979). Ultimate capacity of plates in transverse compression, Det norske Veritas Technical Report No 79-0104.

126. Viner, A.C. (1986). Development of ship strength formulation, Proc. Int. Conf. On Advances in Marine Structures-2, ARE, Dunfermline, Scotland, 152-173.

127. Walker, A.C. (1967). In Thin Walled Structures (Edited by A.H.Chilver), Chattoe and Windus, London.

128. Wang, G. (1995). Structural analysis of ships' collision and grounding, Ph.D. thesis, University of Tokyo, Tokyo, Japan.

129. Wang, G. (2002). Some recent studies on the plastic behaviour of plates subjected to very large load, Journal of ASME, 124 (3): 125 –131.

130. Wang, G., Chen, Y., Zhang, H. and Peng, H. (2002a). Longitudinal strength of ship with accidental damages, Marine Structures, 15: 119-138.

131. Wang, G., Spencer, J. and Chen, Y. (2002b) Assessment of a ship's performance in accidents, Marine Structures, 15: 313-333.

132. Wells, A.A. (1961). Unstable crack propagation in metals: cleavage and fast fracture, Proceedings of the Crack Propagation Symposium, Cranfield, UK, 210-230.

133. Wells, A.A. (1963). Application of fracture mechanics at and beyond general yield, British Welding Research Association, Report No. M13/63.

134. Wen, R.K. and Farhoomand, F. (1970). Dynamics analysis of inelastic space frames, Journal of Engineering Mechanics Division, ASCE, 96(5):667-687.

135. Westergaard, H.M. (1939). Bearing pressure and cracks, Journal of Applied Mechanics, 6:49-53.

136. Wierzbicki, T. (1979). Crushing behaviour of plate intersections, Proc. Of the First Int. Symposium on Structural Crashworthiness, University of Liverpool, 66-95.

137. Williams, M.L. (1957). On the stress distribution at the base of a stationary crack, Journal of Applied Mechanics, 24:109-114.

138. Woisin, G. (1979). Design against collision. Proc of the First Int. Symposium on Advances in Marine Technology, Norway.

139. Wood, R.H. (1961). Plastic and inelastic design of slabs and plates, The Ronald Press, New York, USA.

140. www.imo.org (International Maritime Organisation's Official Web Site).

141. www.twi.co.uk (TWI - World Centre for Materials Joining Technology).

142. Yao, T. (2000). Ultimate hull girder strength, Proceedings of the 14th International Ship and Offshore Structures Congress (ISSC), Nagasaki, Japan, 321-391.

143. Yao, T. (2003). Hull girder strength, Marine Structures, 16: 1-13.

144. Yao, T. and Nikolov, P.I. (1993). Ultimate longitudinal strength of a bulk carrier, Proc. 3rd Int. Offshore and Polar Engineering Conf., Singapore, 497-177.

145. Yao, T. and Nikolov, P.I. (1993). Ultimate longitudinal strength of a bulk carrier, Proc. 3rd Int. Offshore and Polar Engineering Conf., Singapore, 497-177.

146. Yao, T. et al (2000). Ultimate hull girder strength, Proceedings of the 14th International Ship and Offshore Structures Congress (ISSC), Nagasaki, Japan, 321-391.

147. Yao, T., Fujikubo, M., Kondo, K. and Nagahama, S. (1994). Progressive collapse behaviour of double hull tanker under longitudinal bending, 4th ISOPE Conference. Osaka, Japan.

148. Yao, T., Yonedo, M., Kitamura, O., and Kusuba, M. (2002). Simulation of progressive collapse of ship hull girder under longitudinal bending, Proc. World Congress on Computational Mechanics, Vienna, Austria.

149. Zhang, S. (1999). The mechanics of ship collisions, Ph.D. thesis, DTU.

150. Zhang, S., Yu, Q. and Mu, Y.A. (1996). Semi-analytical method of assessing the residual longitudinal strength of damaged ship hull, ISOPE Conference; 510-516.

151. Zienkiewicz, O.C. (1977). The finite element method, Third Edition, McGraw-Hill, London & New York.

List of Author's Articles Published or Submitted during this Ph.D. Study

1. **Ozguc, O.**, Das, P.K. and Barltrop, N.D.P. (2005a). A comparative study on the structural integrity of single and double side skin bulk carriers under collision damage, Marine Structures. (In Press)
2. **Ozguc, O.**, Das, P.K. and Barltrop, N.D.P. (2005b). Rational interaction design equations for the ultimate longitudinal strength of tankers, bulk carriers, general cargo and container ships under coupled bending moment, Journal of Ship Research. (Submitted to publication)
3. **Ozguc, O.**, Das, P.K. and Barltrop, N.D.P. (2005c). A proposed method to evaluate hull girder ultimate strength. Journal of Ships & Offshore Structures. (In Press)
4. **Ozguc, O.**, Das, P.K. and Barltrop, N.D.P. (2005d). The new simple design equations for the ultimate compressive strength of imperfect stiffened plates, Ocean Engineering. (Accepted to publication)
5. **Ozguc, O.**, Das, P.K. and Barltrop, N.D.P. (2005e). Simplified closed-form interaction formulations for evaluation of structural response of stiffened plates, International Shipbuilding Progress. (Accepted to publication)
6. **Ozguc, O.**, Samuelides, M. and Das, P.K. (2005f). A comparative study on the collision resistance of single and double side skin bulk carriers, International Congress of International Maritime Association of the Mediterranean (IMAM), 26-30 September, Lisbon, Portugal.
7. **Ozguc, O.**, Das, P.K. and Barltrop, N.D.P. (2006a). Analysis on the hull girder ultimate strength of a bulk carrier using simplified method based on an incremental – Iterative approach, The 25th International Conference on Offshore Mechanics and Arctic Engineering (OMAE), 4-9 June, Hamburg, Germany.
8. **Ozguc, O.**, Das, P.K. and Barltrop, N.D.P. (2006b). Hull girder ultimate strength of a damaged tanker with considering fracture assessment, 3rd International ASRANET Colloquium, 10-12 July, Glasgow, United Kingdom.

9. **Ozguc, O.**, Das, P.K. and Barltrop, N.D.P. (2006c). Numerical modelling of ship collision based on finite element codes, 3rd International ASRANET Colloquium, 10-12 July, Glasgow, United Kingdom.
10. Dimou, D., Samuelides, M., Incecik, A., **Ozguc, O.** and Tabri, K. (2006d). Collision scenarios for the assessment of the performance of a ship involved in a collision, 3rd International ASRANET Colloquium, 10-12 July, Glasgow, United Kingdom.